Hot Interstellar Matter in Elliptical Galaxies

For further volumes:
http://www.springer.com/series/5664

Astrophysics and Space Science Library

EDITORIAL BOARD

Chairman

W. B. BURTON, *National Radio Astronomy Observatory, Charlottesville, Virginia, U.S.A. (bburton@nrao.edu); University of Leiden, The Netherlands*
(burton@strw.leidenuniv.nl)

F. BERTOLA, *University of Padua, Italy*
J. P. CASSINELLI, *University of Wisconsin, Madison, U.S.A.*
C. J. CESARSKY, *Commission for Atomic Energy, Saclay, France*
P. EHRENFREUND, *Leiden University, The Netherlands*
O. ENGVOLD, *University of Oslo, Norway*
A. HECK, *Strasbourg Astronomical Observatory, France*
E. P. J. VAN DEN HEUVEL, *University of Amsterdam, The Netherlands*
V. M. KASPI, *McGill University, Montreal, Canada*
J. M. E. KUIJPERS, *University of Nijmegen, The Netherlands*
H. VAN DER LAAN, *University of Utrecht, The Netherlands*
P. G. MURDIN, *Institute of Astronomy, Cambridge, UK*
F. PACINI, *Istituto Astronomia Arcetri, Firenze, Italy*
V. RADHAKRISHNAN, *Raman Research Institute, Bangalore, India*
B. V. SOMOV, *Astronomical Institute, Moscow State University, Russia*
R. A. SUNYAEV, *Space Research Institute, Moscow, Russia*

Dong-Woo Kim • Silvia Pellegrini
Editors

Hot Interstellar Matter in Elliptical Galaxies

Springer

Editors
Dong-Woo Kim
Harvard Smithsonian Center for Astrophysics
Garden Street 60
02138 Cambridge Massachusetts
USA
kim@head.cfa.harvard.edu

Silvia Pellegrini
Dipartimento di Astronomia
Università di Bologna
Via Ranzani 1
40127 Bologna
Italy
silvia.pellegrini@unibo.it

Cover figure: Chandra image of NGC 7619. From Kim et al. (2008). Reproduced by permission of the AAS.

ISSN 0067-0057
ISBN 978-1-4614-0579-5 e-ISBN 978-1-4614-0580-1
DOI 10.1007/978-1-4614-0580-1
Springer Heidelberg Dordrecht London New York

Library of Congress Control Number: 2011938147

© Springer Science+Business Media, LLC 2012
This work is subject to copyright. All rights are reserved, whether the whole or part of the material is concerned, specifically the rights of translation, reprinting, reuse of illustrations, recitation, broadcasting, reproduction on microfilm or in any other way, and storage in data banks. Duplication of this publication or parts thereof is permitted only under the provisions of the German Copyright Law of September 9, 1965, in its current version, and permission for use must always be obtained from Springer. Violations are liable to prosecution under the German Copyright Law.
The use of general descriptive names, registered names, trademarks, etc. in this publication does not imply, even in the absence of a specific statement, that such names are exempt from the relevant protective laws and regulations and therefore free for general use.

Cover design: eStudio Calamar S.L.

Printed on acid-free paper

Springer is part of Springer Science+Business Media (www.springer.com)

Preface

The physical properties of the hot interstellar matter (ISM) in elliptical galaxies are directly related to the formation and evolution of these systems, via star formation episodes, the passive evolution of their aging stellar population, environmental effects such as stripping, infall, and mergers, and the growth of supermassive black holes. The recent successful X-ray space missions Chandra and XMM-Newton have provided a large amount of unprecedented high quality observational data on the hot ISM in elliptical galaxies. Thanks to the outstanding angular resolution of Chandra and the large collecting area of XMM-Newton, the fine structure of the hot gas has been imaged in detail, and key physical quantities have been accurately measured, so that theoretical predictions can be compared and tested against the observational results. At the same time, theoretical studies with numerical simulations and analytical modeling of the dynamical and chemical evolution of elliptical galaxies and their hot gas have made significant progress, and start to predict various observable quantities. With contributions from eight leading experts in this field, we intend in this book to review the most significant improvements to our understanding of the hot ISM in elliptical galaxies, and present in detail a number of key discoveries obtained during the last 10 years of the Chandra and XMM-Newton missions, and the corresponding theoretical work.

The need for this book originally emerged during the Joint Discussion between the "Galaxies" and "ISM" IAU Divisions, organized for the XXVII IAU General Assembly of 2009 in Brazil; upon this occasion both observers and theorists in the field were brought together to identify important, but unsolved problems for further investigation, with special emphasis on the spectral and spatial properties of the hot ISM and the comparison with recent theoretical models. Throughout this Joint Discussion, it became clear that time was ripe for an extensive publication, covering a large amount of new important material, and acting as a useful reference for students who approach this field, as well as for experts in related fields.

As this book is primarily intended for graduate students and non-specialists, we provide first in each chapter an introductory and historical background, followed by state-of-the-art results, with a special emphasis on the balance between

observational and theoretical aspects. Throughout the book, the chapters are arranged in such a way that the observational and theoretical results can be compared side by side. Among the eight chapters, roughly half are observationally oriented and the other half are theoretically oriented. All chapters are cross-referenced whenever necessary, so that the readers can easily overview and grasp a coherent picture by finding the related materials discussed in the different parts of the book.

By nature of the state-of-the-art science that is continuously advanced through arguing and counter-arguing, there may be occasionally differing views on an issue, and this is the case for the last two chapters of the book. While we try to minimize any potential confusion, conflicting views are unavoidable sometimes, so the two different positions are presented as they are, and we ask the readers to carefully consider the arguments of both. We hope that this case provides an excellent example for the students to start building their own research framework for their solid future.

Cambridge *Dong-Woo Kim*
Bologna *Silvia Pellegrini*

Contents

Chapter 1
The Hot ISM of Elliptical Galaxies: A Brief History

Giuseppina Fabbiano

This chapter reviews the history of the discovery of a hot gaseous interstellar medium (ISM) in normal E and S0 galaxies with the imaging X-ray telescope of the *Einstein Observatory*. It also highlights the ensuing two-decade long debate on the ubiquity and properties of this medium, and on the suitability of X-ray observations for measuring the gravitational mass of early-type galaxies. Fundamental questions explored during this period included: How much of the X-ray emission is truly from a hot ISM? Is this ISM in hydrostatic equilibrium? Can the data constrain the physical and chemical evolution of this hot medium? While the debate went on, a deeper understanding on the evolution of the hot ISM was generated. Some of these outstanding questions have now been solved with the high spatial resolution observations of the *Chandra X-ray Observatory* and with the high signal-to-noise spectra of *XMM-Newton*.

1.1 X-ray Astronomy and the Discovery of Hot Gaseous Halos

The first extended extragalactic X-ray sources were discovered early in the history of X-ray astronomy with the *Uhuru* satellite (Giacconi et al. 1971) in the Virgo (Kellogg et al. 1971) and Coma (Gursky et al. 1971) clusters. These discoveries were extended soon after to several other galaxy clusters (e.g., Forman et al. 1972; Gursky et al. 1972; Kellogg and Murray 1974). Gursky et al. (1971) pointed out that the temperature of a hot gas derived from a fit to a bremsstrahlung model of the X-ray spectrum of the Coma cluster (73×10^6 K $\sim$ 7 keV), would give thermal velocities of $1{,}050 \pm 90\,\mathrm{km\,s^{-1}}$, comparable with the velocity dispersion of the galaxies in the cluster ($1{,}470\,\mathrm{km\,s^{-1}}$). Although observational confirmation that the diffuse emission was indeed the thermal emission of hot plasma had to await later

G. Fabbiano (✉)
Harvard-Smithsonian Center for Astrophysics, 60 Garden St., Cambridge, MA 02138, USA

D.-W. Kim and S. Pellegrini (eds.), *Hot Interstellar Matter in Elliptical Galaxies*,
Astrophysics and Space Science Library 378, DOI 10.1007/978-1-4614-0580-1_1,
© Smithsonian Institution 2012

measurements (Mushotzky et al. 1978; Fabricant et al. 1978; Lea et al. 1979), it was soon realized that these halos could be hydrostatic, adiabatic atmospheres trapped in the cluster potential. Thus the halos could provide a means for measuring the mass of the associated self-gravitating body (Lea et al. 1973; Gull and Northover 1975; Cavaliere and Fusco-Femiano 1976).

The central Virgo Cluster galaxy, M87, was the first galaxy associated with extended X-ray emission, from a 2–3 keV temperature plasma embedded in a hotter Virgo cluster medium (Lea et al. 1973; Malina et al. 1976; Gorenstein et al. 1977; Mushotzky et al. 1978; Fabricant et al. 1978; Lea et al. 1979; Fabricant et al. 1980). Early modeling of this halo suggested a huge extended halo of dark matter in M87 (Bahcall and Sarazin 1977; Mathews 1978). Fabricant et al. (1980) confirmed this result with stringent observational constraints obtained with the first imaging X-ray telescope, the *Einstein Observatory* (Giacconi et al. 1979).

With the angular resolution and sensitivity allowed by the *Einstein* mirrors, extended emission was discovered in several other early-type galaxies in the Virgo cluster (Forman et al. 1979): the clear displacement of the X-ray isophotes from the optical body of the galaxy in M86 made a strong case for the discovery of a hot gaseous halo, dynamically interacting with the hotter cluster gaseous medium, and suggested that hot halos may be widespread in E and S0 galaxies. This was the beginning of the study of the hot interstellar medium (ISM) of early-type galaxies. Although now we all know that hot X-ray emitting gas is found in E and S0 galaxies, it is worth noting that this was not expected at the time, since the lack of cold ISM in these galaxies had convinced astronomers that winds were likely to occur, dissipating the gaseous stellar ejecta outside the parent galaxy (e.g., Faber and Gallagher 1976; Mathews and Baker 1971). The presence of hot ISM in early-type galaxies could only be discovered with X-ray astronomy.

In summary, *Einstein* observations provided convincing proof of the existence of hot halos in elliptical galaxies:

1. As mentioned above, the images of a few galaxies revealed a displacement of the X-ray isophotes from the stellar body, suggesting a non-stellar source of the X-ray emission (e.g., M86, Forman et al. 1979; NGC4472, see Fig. 1.1 from Trinchieri et al. 1986.)
2. The X-ray spectra of X-ray luminous elliptical galaxies where found to be softer than those of spiral galaxies, suggesting thermal emission from hot coronae (see e.g. Trinchieri et al. 1986 versus Fabbiano and Trinchieri 1987; Kim et al. 1992, Fig. 1.2).
3. The slopes of the correlation between integrated X-ray (L_X) and optical (L_B) luminosity were found to differ between E + S0 and spiral galaxies. In the spiral sample (Fabbiano and Trinchieri 1985), $L_X \sim L_B$, as it would be expected for an X-ray emission dominated by stellar binary sources, which would be a nearly constant fraction of the overall stellar population of the galaxy; instead in the E + S0 sample (Trinchieri and Fabbiano 1985 – TF85), $L_X \sim L_B^{\geq 1}$, suggesting the presence of an additional non-stellar emission component (hot ISM) in some galaxies.

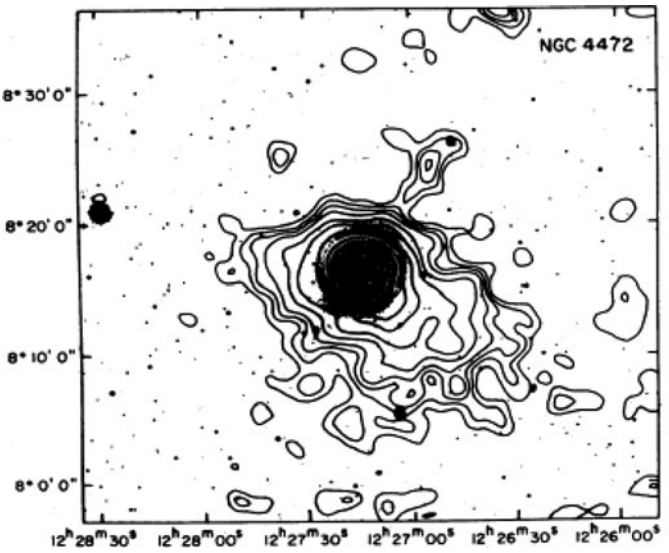

Fig. 1.1 Einstein isophotes of the (0.2–4.0 keV) X-ray emission of the Virgo cluster galaxy NGC 4472, showing a displacement relative to the stellar body of the galaxy (Trinchieri et al. 1986)

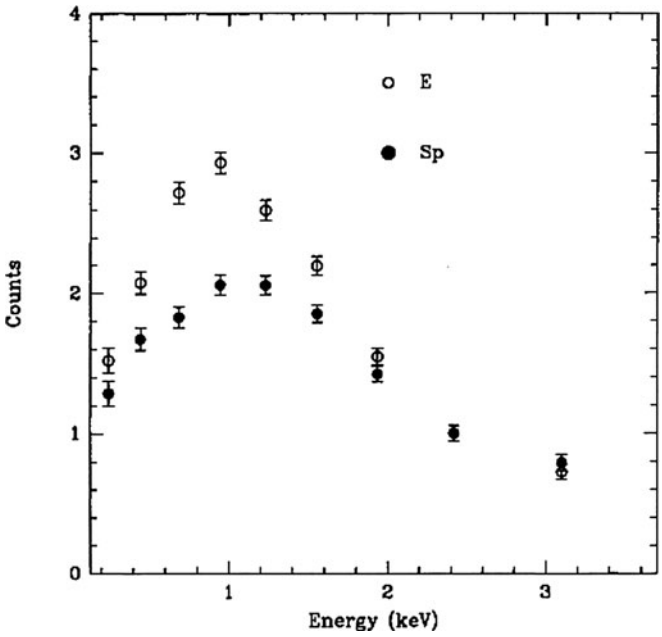

Fig. 1.2 Average X-ray spectral count distributions of the samples of E and Spiral galaxies observed with Einstein (Kim et al. 1992); note the relative excess of counts at the lower energies of the E sample

Although convincing evidence of the existence of hot ISM and gaseous halos in some elliptical galaxies was produced by the *Einstein* observations, it soon became evident that several of these galaxies may not have these hot halos. The detection of extended X-ray emission in Virgo cluster galaxies was not in itself proof of the existence of gaseous halos, because a population of X-ray binaries could not have been possibly resolved with *Einstein* at that distance. These X-ray binary populations were detected in nearby galaxies, such as M31 (see Fabbiano 1989 and references therein). The extent to which the X-ray emission was dominated by a hot hydrostatic halo soon became the subject of intense debate.

In what follows, I will discuss more fully some of the early observations of E and S0 galaxies, and highlight the debate resulting from the *Einstein* and subsequent observations with the *ROSAT* (Truemper 1990) and *ASCA* (Tanaka et al. 1994) X-ray satellites. This discussion provides the background for the more recent *Chandra* (Weisskopf et al. 2000) and the ESA X-ray satellite *XMM-Newton* results, which are only mentioned here when needed, and are more thoroughly discussed in other chapters of this book. A more complete review of the early *Einstein* results can be found in Fabbiano (1989). Here, I will focus the discussion on four topics: Disentangling hot halos from other X-ray emission components (Sect. 1.2); Physical evolution of the hot ISM (Sect. 1.3); Chemical evolution of the hot ISM (Sect. 1.4); and X-ray constraints to galaxy masses (Sect. 1.5).

1.2 The Halo Debate: How Much of the X-ray Emission of E and S0 Galaxies is from a Hot Halo and How Much from X-ray Binaries?

Following the work on M87 mentioned in Sect. 1.1, the discovery of hot gaseous emission in other Virgo elliptical galaxies (Forman et al. 1979) led to an important prospect. *If the X-ray emission of E and S0 galaxies were dominated by hot halos in hydrostatic equilibrium*, these observations could provide a ready means for measuring the masses of the galaxies and detecting the associated dark matter. Forman et al. (1985 – FJT85) presented the results of *Einstein* observations of a sample of early-type galaxies (Sa, S0, E), arguing for hot coronae in hydrostatic equilibrium. Under this assumption, FJT85 derived measurements of the gravitational masses, suggesting widespread substantial dark halos in early-type galaxies.

However, the prevalence of hydrostatic hot coronae in most early-type galaxies could not be proved observationally. The quality of these first X-ray images did not allow disentangling a truly diffuse gaseous emission from the unresolved contribution of populations of low-mass X-ray binaries (LMXBs). Moreover, the associated spectra could not constrain meaningfully multiple emission components.

These were important questions that had to be answered, before the general validity of X-ray mass measurements could be accepted (see also Sect. 1.5).

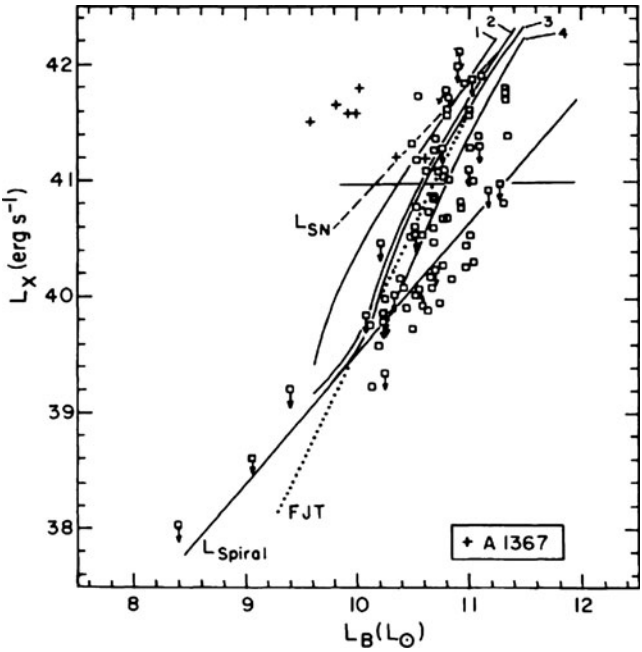

Fig. 1.3 The distribution of early-type galaxies (*squares and crosses*) observed in X-rays with Einstein (see CFT87). The diagonal *solid line* is the TF85 and CFT87 estimate of LMXB luminosity. The *dotted line* represents the FJT85 law of halo emission. The *dashed line* is the CFT87 estimate of energy input from SNe Ia, and curve represent different cooling flow models from Sarazin and White (1988; see also Sect. 3.1)

1.2.1 The L_X–L_B Diagram

A tool used in several of these early studies, and in much later work, was the L_X–L_B diagram. The X-ray (L_X) and B-band luminosity (L_B) are correlated, with a large scatter and a power-law slope steeper than linear (TF85; FJT85; see also Canizares et al. 1987 – CFT87; Fabbiano 1989, Fig. 1.3). The interpretation of this diagram has been central to the 'halo' debate (see also Sect. 1.3). Although the *Einstein* L_X–L_B diagram must be at a certain level the expression of halo evolution and physics (FJT85), it is also 'biased' by the contribution of unresolved LMXB populations.

TF85 first raised the LMXB problem, based on a comparison with the bulge of M31 and the integrated emission properties of bulge-dominated spiral galaxies. In M31 the LMXB population could be easily detected with *Einstein* (Van Speybroeck et al. 1979), leaving no doubt as to the nature of the dominant X-ray emission. Bulge-dominated spirals have L_X/L_B ratios consistent with those of 'X-ray faint' elliptical galaxies. In spirals the X-ray and optical luminosities are roughly linearly correlated, as expected from the integrated contribution of populations of X-ray binaries (Fabbiano and Trinchieri 1985). Based on these results, TF85 (see also

review Fabbiano 1989) concluded that integrated LMXB emission– not gaseous halos – is responsible for most or all of the X-ray luminosity of a very substantial fraction of early-type galaxies.

1.2.2 X-ray Spectra

The importance of LMXB emission was confirmed by the spectral characteristics of the emission. Harder X-ray emission, a signature of LMXB populations (see Fabbiano et al. 1987 using M31 as a spectral benchmark), was found by analyzing the average X-ray colors and the coadded spectra of the sample of X-ray faint elliptical galaxies observed with *Einstein* (Kim et al. 1992). Subsequent deeper observations of some of these galaxies with *ROSAT* (Fabbiano et al. 1994) confirmed this result. Later, with the CCD spectra of ASCA, Matsushita et al. (1994) found a clear signature of hard LMXB emission also in halo-dominated galaxies. Interestingly, the spectra of the least X-ray luminous galaxies showed an additionalvery soft emission component (Kim et al. 1992). Pellegrini and Fabbiano (1994) modeled the *ROSAT* spectra, suggesting complex 3-component emission, consisting of LMXBs, some amount of hot ISM, and the integrated X-ray emission of the normal stellar population in these galaxies (Fig. 1.4).

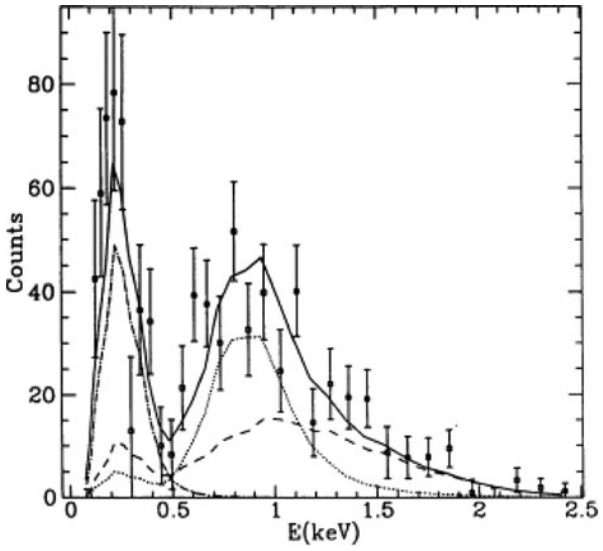

Fig. 1.4 ROSAT X-ray spectrum of NGC 4365, with a 3-component model (*solid line*) including LMXB emission (*dashed*), hot ISM (*dotted*), and a cooler possibly stellar component (*dot-dashed*), from Pellegrini and Fabbiano (1994)

These conclusions, now confirmed with *Chandra* (e.g., Boroson et al. 2011), casted doubts on the presence of dominant hydrostatic coronae in all E and S0 galaxies.

1.2.3 Chandra Images

With the sub-arcsecond telescope of the *Chandra X-ray Observatory*, populations of LMXBs are now ubiquitously detected in the images of elliptical galaxies (see Fabbiano 2006 and refs. therein). These LMXBs in some cases account for the bulk of the X-ray emission, leaving little space for diffuse hot ISM emission (e.g. NGC 3379, NGC 4278; Brassington et al. 2008, 2009; Fig. 1.5).

The debate on the relative fraction of hot ISM and LMXB emission in early-type galaxies has been solved with *Chandra*. This debate, however, has provided a useful framework to reach a deeper understanding of the evolution of early-type galaxies, and their stellar and gaseous components (see also Sects. 1.3 and 1.5).

1.3 Physical Evolution of the Hot Halos: Gravity, Feedback and Interactions

Once the presence of hot ISM and halos – in at least some early-type galaxies – had been established, the observed properties of this hot ISM could be used to constrain its evolution. There is sufficient material from stellar out-gassing to account for the hot halos (FJT85; Faber and Gallagher 1976), if this ISM is trapped by the galaxy gravity. Therefore, the origin of the hot ISM is linked to the evolution of the stellar component of the galaxies. However, the data also suggested that the hot ISM, in X-ray luminous hot-gas-rich galaxiesat least - where this medium was convincingly present -is not in thermal equilibrium with the stellar component. Spectral fits to the *Einstein* data, and the radial behavior of the X-ray surface brightness, indicated temperatures in excess of those implied by the stellar velocity dispersion, suggesting that further heating of the ISM had occurred (see Fabbiano 1989 and references therein).

The sources of energy considered in the early *Einstein* days are Supernova explosions (prevalently SNe Ia, given the old stellar population of elliptical galaxies) and gravity, and to less extent interaction and merging with the surrounding environment and neighboring galaxies. More recently, nuclear/AGN feedback has also been introduced as an important factor in the evolution of the hot halos (see also Sarazin, and Ciotti and Ostriker, this volume).

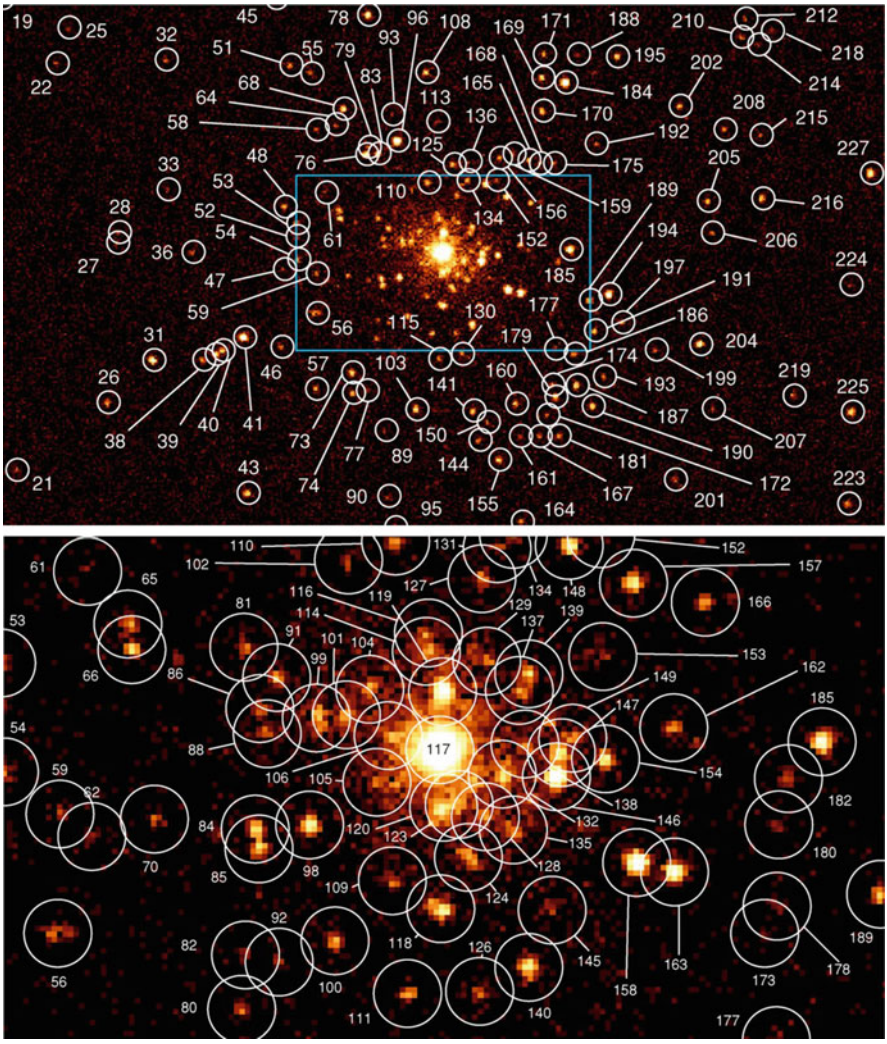

Fig. 1.5 *Chandra* ACIS image of NGC 3379, from Brassington et al. 2008; the bottom panel is an expansion on the blue inner box in the *top panel*; each detected LMXB is identified with a *circle* and a source number. LMXBs account for almost all the X-ray emission of this elliptical galaxy

1.3.1 Supernova and Gravitational Heating

CFT87 (see Fig. 1.3) argued that the distribution of points in the *Einstein* L_X–L_B diagram is roughly bound between two lines: the contribution of X-ray binaries, at the bottom end, and the luminosity that may originate from SN heating at the top. Gravitational heating (see Pellegrini, this volume) is effective, but cannot account for the spread of points in the L_X–L_B diagram.

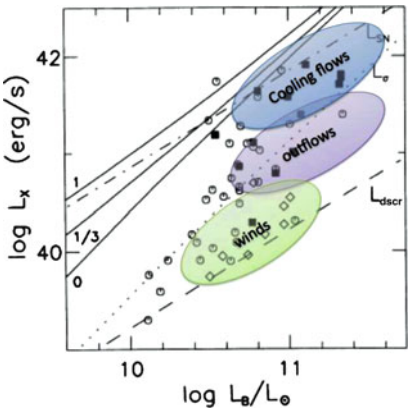

Fig. 1.6 L_X–L_B diagram compared with the evolutionary models of Ciotti et al. 1991. The different physical regimes are indicated by the colored ellipses

Gravitational heating occurs if the hot gas slowly accretes to the center of the galaxies via subsonic cooling flows, caused by faster cooling in the central denser regions of the halos. Gull and Northover (1975) and Binney and Cowie (1981) first pointed out the potential importance of cooling flows for the hot halos of galaxy clusters and M87. This idea enjoyed a vigorous renaissance with the *Einstein* discovery of hot halos in galaxies, where cooling times can be considerable shorter than the Hubble time. Cooling flow models were developed by several authors in the attempt to fit both the data of individual galaxies (e.g. Thomas et al. 1986), and the distribution of points in the *Einstein* L_X–L_B diagram (e.g. Sarazin and White 1988). The Sarazin and White (1988) cooling flow models, plotted in Fig. 1.3, cannot bridge the gap between the two boundary lines even in the absence of dark massive halos and supernova heating; models assuming dark halos and the unescapable supernova heating can only explain the most X-ray luminous galaxies (e.g., Ciotti et al. 1991).

Given all this ready energy input, can we be sure that the halos are in hydrostatic equilibrium? David et al. (1990) modeled the evolution of the ISM of elliptical galaxies with $L_B = 10^{11} L_\odot$, finding an early phase of wind fuelled by SNe II, followed by a long-lasting phase of pure accretion flow resulting in large hot halos within a Hubble time, therefore arguing for 'static' halos. However, more extensive modeling soon after (David et al. 1991; Ciotti et al. 1991) revealed that outflows and wind may be important. David et al. (1991) concluded that except for very high values of the SNe Ia rate most *Einstein* detections are consistent with inflow models. Ciotti et al. (1991) instead reached the opposite conclusion, because in their models the secular variation of the stellar mass loss rate was less steep than that of the supernova rate, in the passive evolution of an old stellar population (see Pellegrini, this volume). The result of this approach is that only the brightest of the galaxies are in inflow/cooling flow, while most of the L_X–L_B diagram would be consistent with outflow models, and the galaxies with the faintest X-ray emission would be in a strong wind phase (Fig. 1.6).

1.3.2 Interactions and Merging

Interactions with the intra-cluster medium and with other galaxies were also suggested as means of alternatively enhancing or reducing the hot halos of galaxies. The hot cluster medium can help confining the hot halos of galaxies (e.g. Vedder et al. 1988; Renzini et al. 1993; Brighenti and Mathews 1998; Brown and Bregman 2000), but can also be effective in ram stripping of these halos (e.g., Forman et al. 1979; Acreman et al. 2003; Sarazin, this volume). Correlations in large samples of galaxies were explored to investigate the importance of this effect, but with inconclusive results. Sarazin and White (1990) reported a correlation between lower X-ray luminosity and a denser environment, suggesting that interactions in clusters may be responsible for the L_X–L_B scatter. However, Mackie and Fabbiano (1997), using the sample of early-type galaxies observed with *ROSAT*, could not confirm this suggestion.

Instead, galaxy merging appears to be an important factor in both galaxy and halo evolution. Recent merging and the related rejuvenation of the stellar populations (causing additional energy input into the ISM) has been connected with smaller or absent hot halos (Fabbiano and Schweizer 1995; Mackie and Fabbiano 1997), a view confirmed by a recent study based on a sample of galaxies observed with *Chandra* (Boroson et al. 2011). Conversely, optical indicators of large gravitational potentials and primordial merging are correlated with the presence of large X-ray halos (e.g., Eskridge et al. 1995; see Kormendy et al. 2009 and refs. therein); these indicators are consistent with the presence of large dark halos in massive systems that have had time to settle into passive evolution, where the hot gaseous halos would be gravitationally confined.

1.3.3 The Effect of Nuclear Super-Massive Black Holes

At the time when people were trying to make sense of the *Einstein* observations of early-type galaxies, it was not yet known that super-massive black holes are present in the nuclei of luminous elliptical galaxies (Magorrian et al. 1998). In fact, Fabian and Canizares (1988) suggested that the absence of cooling-flow-fed AGNs in most elliptical galaxies argued against the ubiquity of nuclear black holes. However, several elliptical galaxies harbor some form of nuclear emission. In the minority of luminous radio galaxies these radio cores are associated with powerful jets and large radio lobes, extending outside the stellar body of the galaxies. In a larger number of galaxies the radio source is faint and confined within the nuclear region. It was speculated that the hot ISM would have a role in causing and shaping these sources (Hummel et al. 1983).

Fabbiano et al. (1987a, 1989) assembled 5 GH observations for a sample of early-type galaxies observed with *Einstein*. Fabbiano (1989), using 84 elliptical and S0 galaxies, found a correlation between core radio power and X-ray to optical ratio,

suggesting that the hot ISM could provide the fuel for the nuclear radio sources. Moreover, they noticed that, for a given radio power, extended radio lobes are associated with X-ray fainter galaxies, pointing to the importance of the hot ISM in disrupting radio jets and confining the radio sources. Furthermore, there is a continuum of radio/X-ray properties from radio-faint to radio-loud 3CR galaxies (Fabbiano et al. 1984), suggesting that either radio-faint galaxies are associated with less massive nuclear black holes, or that something impedes cooling flows from accreting onto these nuclei. This was the first inkling of the interplay between nuclear feedback and the hot ISM in early-type galaxies.

The comprehensive multi-variable correlation study of the entire 148 E and S0 sample observed with*Einstein* (Eskridge et al. 1995) confirmed the results of Fabbiano (1989); moreover, these authors find that the *total* radio power of a galaxy is related to the stellar mass (L_B) rather than the presence of hot ISM, and conclude that *'the mass of the black hole is larger in more massive galaxies'* – a result now widely accepted (Magorrian et al. 1998).

AGN feedback has since surfaced as an important energy source. It has been shown in theoretical models that AGN feedback could be strong enough to eliminate hot halos by starting galactic-size winds (e.g. Tabor and Binney 1993; Ciotti and Ostriker 2001). Observationally, with *Chandra* we have set stringent limits on the amount of diffuse emission in some X-ray faint galaxies, demonstrating the presence of winds (Fabbiano et al. 2004; Pellegrini et al. 2007; Trinchieri et al. 2008). However, while it is certain that winds occur, the relative importance of SNe Ia versus AGN energy input is still debatable.

AGN feedback solves the puzzle of the cooling flow interpretation of the *Einstein* X-ray data: the lack of direct observation, in the predicted amount, of the two key consequences of cooling flows: (1) central colder gas, (2) central star formation (e.g. see review McNamara and Nulsen 2007). The morphology and thermal properties of the circum-nuclear hot ISM from *Chandra* observations of some early-type galaxies convincingly prove that AGN feedback is at play (e.g., the circumgalactic hot ring in Cen A, Karovska et al. 2002; the properties of the inner regions of M84, Finoguenov et al. 2008).

1.4 Chemical Evolution of the Halos: Measurements of Metal Abundances and Theoretical Predictions

The physical evolution of the hot halos is closely linked to their chemical evolution, since these halos are enriched in metals by stellar and supernova ejecta. In particular, large hot halos in gravitational equilibrium should have Fe content commensurate to the integrated output of SNe Ia over their lifetimes; in these halos, the Fe to alpha element ratios should be solar or higher, unless inflow of intra-cluster gas, enriched by SNe II-powered winds early in the galaxies lifetimes, alter these values (David et al. 1991; Ciotti et al. 1991; Renzini et al. 1993; Arimoto et al. 1997; Loewenstein

and Davis 2010). Since optically thin hot plasmas with temperatures in the range of the emission of halo-dominated galaxies (∼1 keV) should contain emission lines produced by atomic transitions in elements (see Raymond and Smith 1977), the X-ray spectra may be used to set observational constraints to the metal abundance. This was – and still is – not an easy task, as explained below (see discussion in Fabbiano 1995).

The *Einstein* and *ROSAT* proportional counter spectra lacked the resolution to reveal individual emission lines and absorption edges, with the result that one could not distinguish between excess line emission or excess absorption in a spectrum (e.g., Trinchieri et al. 1986); similarly, the data could be fitted equally well with either an isothermal halo with sub-solar metallicity, or with multi-temperature models and higher metal abundance (Buote and Canizares 1994; Fabbiano et al. 1994). Estimating abundances of different elements separately was basically impossible.

The higher spectral resolution CCD detectors of the Japanese *ASCA* satellite (Tanaka et al. 1994) first revealed emission lines in the spectra, although with some blending. The abundances measured from these early spectra in luminous early-type galaxies were sub-solar, and the elemental ratios consistent with solar, suggesting a lack of significant SNe Ia input (Awaki et al. 1994). The spectra of X-ray faint galaxies suggested low-metallicity cooler gaseous components, in addition to hard LMXB emission (e.g., Kim et al. 1996; Iyomoto et al. 1998). Multi-temperature halo models (Buote and Fabian 1998; see also Trinchieri et al. 1994), resulted in higher – nearly solar – abundances, which however are still below the theoretical prediction (Arimoto et al. 1997). Adding proper weighing of the uncertainties in the Fe plasma emission codes to multi-temperature models (Matsushita et al. 2000), resulted in abundances for the X-ray luminous galaxies near the range of the prediction; this study also suggests lower abundances in X-ray faint galaxies, which could be related to the presence of winds.

We have now realized that spatial resolution, together with spectral resolution, may be needed to get more realistic abundance measurements, especially in the case of X-ray faint E and S0s with small gaseous components. By 'cleaning' the diffuse emission of the contribution of luminous binaries, and by allowing the separate analysis of different emission regions with *Chandra,* abundances higher than the *ASCA* estimates were found in the elliptical galaxy NGC 1316 (Kim and Fabbiano 2003); interestingly, the *ASCA* estimates were reproduced analyzing the entire emission of the galaxy as a whole, disregarding the information provided by the spatial resolution.

Very high signal to noise data also help, as demonstrated in the case of the *XMM-Newton* observations of the luminous hot halo of NGC 507 (Kim and Fabbiano 2004). In this galaxy, where previous reports gave a range of abundances from sub-solar to near solar (Matsumoto et al. 1997; Kim and Fabbiano 1995; Buote and Fabian 1998; Paolillo et al. 2003; Kraft et al. 2004), the analysis of the *XMM* data revealed that the hot ISM is not isothermal and that the Fe abundance is 2–3 times solar within a radius of 40 kpc from the center of NGC 507, then decreasing at larger distances. A full discussion of the present understanding of

the chemical evolution of the halos can be found in the chapters of Pipino and Kim, this volume.

1.5 Can We Measure Galaxy Masses with X-ray Observations?

Having reviewed the debate surrounding the X-ray emission of E and S0 galaxies, we go back here to the issue of using X-ray observations for measuring the mass of these galaxies. As discussed in Sect. 1.1, Fabricant et al. (1980) applied the equation of hydrostatic equilibrium to the X-ray halo of M87 to constrain the binding mass of this galaxy, confirming the presence of an extended dark matter halo. The equation of hydrostatic equilibrium can be expressed as:

$$M(r) = -kT_{gas}/G\mu m_H(d\ log\ \rho_{gas}/d\ log\ r + d\ log\ T_{gas}/d\ log\ r)r$$

Based on this equation, the mass enclosed within the outer detected halo radius is a function of four quantities, which all need to be measured, and for all of which uncertainties need to be estimated. These quantities are the outer radius of the hot halo, the gas temperature at this radius, and the gradients of gas density and temperature at the outer radius.

The above equation was used by FJT85to measure the binding masses of a sample of normal E and S0 galaxies detected in X-rays with *Einstein*. Under the assumption that the X-ray emission of all these galaxies is dominated by hot halos in hydrostatic equilibrium, these measurements led to the conclusion that large amounts of dark matter are associated with these galaxies. But, as discussed in Sects. 1.2 and 1.3, we now know that hot halos do not dominate the X-ray emission of all E and S0 galaxies.

Following on the previous discussion in this chapter, I will revisit the status of these mass measurements, for X-ray luminous and X-ray faint galaxies, separately.

1.5.1 X-ray Luminous Galaxies

Trinchieri et al. (1986) took a critical look at the *Einstein* mass measurements of five X-ray luminous galaxies, where the emission could be dominated by hot halos in or near hydrostatic equilibrium. These authors concluded that, given the quality of the *Einstein* data, taking into account all the sources of measurement uncertainty would lead to inconclusive results even for the most X-ray luminous galaxies (Fig. 1.7). Trinchieri et al. (1986) also expressed concern on the assumption of hydrostatic equilibrium, because asymmetries in the X-ray surface brightness distributions of some of these galaxies suggested strong interaction of the hot galaxy halo with the hotter cluster gaseous medium. Moreover, steep radial profiles in some cases suggested winds or the result of stripping at the outer detectable radii. Subsequently,

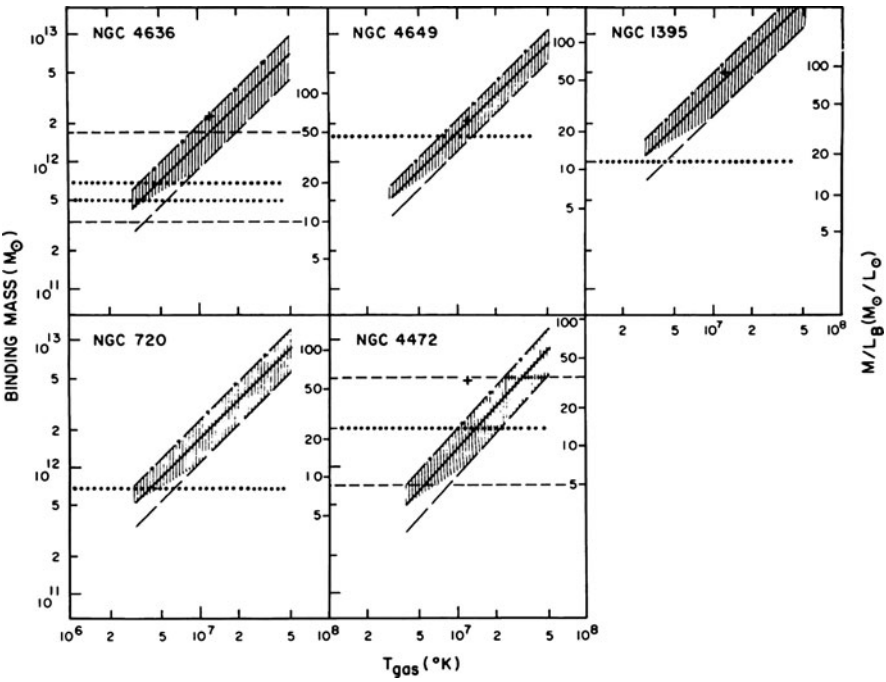

Fig. 1.7 Loci of binding mass allowed by the *Einstein* measurements of five luminous elliptical galaxies (Trinchieri et al. 1986)

Trinchieri et al. (1994), revisited the mass measurement of NGC 4636 with *ROSAT* data, and pointed out additional uncertainties resulting from the possible existence of multi-temperature halos.

Notwithstanding the concerns discussed above, more recent work has confirmed the validity of the X-ray approach to mass measurement – and of the assumption of hydrostatic equilibrium – for X-ray luminous galaxies, even with moderate resolution (10 s to several 10 s of arc-seconds) data. This work is based on deeper X-ray images than those obtained with *Einstein* in clear cases of galaxies with halo-dominated X-ray emission, such as those with L_X/L_B ratios well in excess of the ratios expected from LMXB populations in the L_X–L_B diagram. A good example is given by the *ROSAT*-based measurement of the binding mass of NGC 1399 shown below in Fig. 1.8 (Paolillo et al. 2002).

In NGC 1399 the X-ray isophotes allow the separation of galaxy halo and cluster emission (Ikebe et al. 1996; Paolillo et al. 2002). The X-ray-based *ROSAT* mass profile obtained by Paolillo et al. (2002) is consistent with other X-ray estimates (Rangarajan 1995; Ikebe et al. 1996). More important, this mass profile is also consistent with estimates obtained independently from optical indicators available out to large galactocentric radii (planetary nebulae and GCs, Saglia et al. 2000). This consistency demonstrates that the X-ray mass measurement is correct.

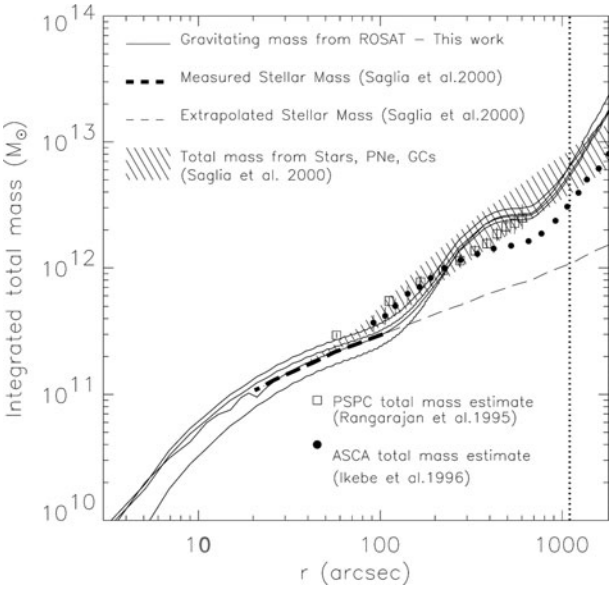

Fig. 1.8 Radial distribution of the enclosed mass in NGC 1399, from different indicators, showing that the X-ray measured mass is consistent with that derived from optical indicators over a large range of radii (Paolillo et al. 2002)

As noted by Paolillo et al. (2003) in the case of NGC 507, the effect of halo/AGN interaction in the central regions of the halos may produce significant departures from equilibrium, so that these regions are best excluded from X-ray mass measurements. However, these are the regions where other non-X-ray measurements are generally available. Therefore, with due caution, deep X-ray observations of luminous hot halos in early-type galaxies are a good means for obtaining mass measurements of these systems, which may be otherwise unobtainable (see Buote and Humphrey, this volume). However, conflicting interpretations of the same data are possible, especially in the case of 'intermediate luminosity' halos (see Buote and Humphrey versus Statler, this volume), all pointing to the significant uncertainties connected with the justification and assumption of hydrostatic equilibrium.

1.5.2 X-ray Faint Galaxies

Instead, moderate angular resolution mass measurements of X-ray faint galaxies are not believable, because it is impossible to disentangle LMXB contamination from halo emission. NGC1316 is a case in question. FJT85 estimated a binding mass of $2.0 \times 10^{12} M_{\odot}$ for this galaxy from the *Einstein* data. This estimate is $\sim$10 times larger than the mass estimated using the radial velocities of planetary

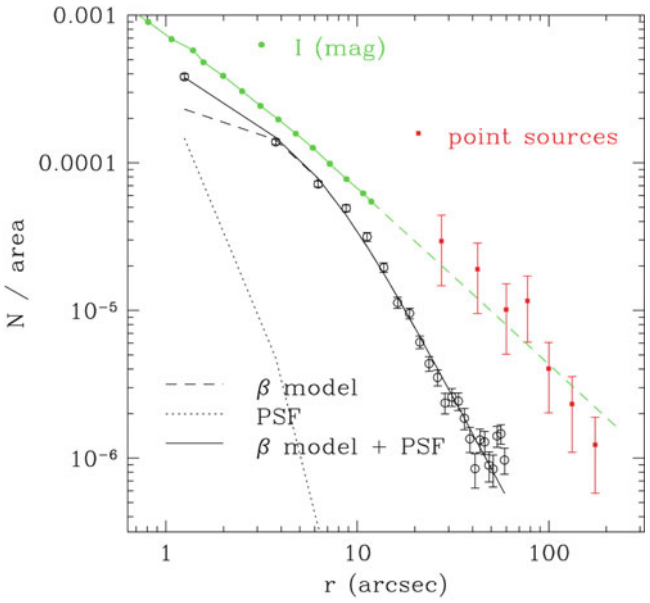

Fig. 1.9 NGC 1316 – radial distribution of stellar surface brightness (*green*), LMXB number counts (*red*), and surface brightness of the hot ISM (*black*), from the *Chandra* measurements of Kim and Fabbiano (2003). This figure shows that the radial distribution of LMXBs is consistent with the optical stellar light, while the gaseous emission has a steeper radial distribution and is concentrated only at the inner radii, see the electronic version for a color version of this figure

nebulae, within a comparable outer radius (Arnaboldi et al. 1998). The *Chandra* observation of NGC1316 (Kim and Fabbiano 2003) revealed that LMXBs dominate the emission at the outer radii out to a radius comparable to that used for the *Einstein* mass estimate, while the hot gas is only detected within less than a 1/3 of this radius (Fig. 1.9); moreover, the temperature of this halo is well constrained with *Chandra* to be ∼0.5 keV, while ∼1 keV was assumed by FJT85.

Therefore, without the sub-arcsecond angular resolution of *Chandra*, and assuming that the X-ray emission is dominated by a halo in hydrostatic equilibrium, the outer radius of the putative hot halo would have appeared mistakenly to be much larger than it is. Moreover, the temperature of this putative halo would have appeared higher because of contamination by the hard emission of LMXBs. All of this would conspire to inflate the mass estimate. Of course in X-ray faint galaxies the halo may not be in hydrostatical equilibrium (see Sect. 1.3), so this method would not be applicable, without appropriate modeling of the halo, even with *Chandra*data (e.g., Ciotti and Pellegrini 2004; Pellegrini and Ciotti 2006).

1.6 Final Remarks

The discovery of hot halos in early-type galaxies was a pivotal result of the first X-ray imaging observatory, *Einstein*. These halos were originally hailed as a new means for measuring the mass of these galaxies and constraining the amount and ubiquity of Dark Matter in the universe. However, the real power of this discovery has been to uncover a new dimension for understanding galaxy evolution. The evolution of the hot halos is the result of a tug of war between the pull of gravity and the push of feedback from stellar evolution (SNe Ia) and AGNs, as well as interactions with the circum-galactic medium and galaxy encounters. This evolution has left observational imprints in both physical properties and chemical composition of the hot gas, which can be exploited to reconstruct the history of both halo and parent galaxy.

The above discussion illustrates that caution must be used when approaching X-ray based mass measurements. In the case of 'dominant' extended hot halos hydrostatic equilibrium may be a good approximation. However, for less X-ray luminous galaxies the halo may be far from equilibrium and also may not dominate the X-ray emission. The analysis of NGC 1316 demonstrates that, for low L_X/L_B galaxies, mass measurements from moderate resolution observations (such as *Einstein*, *ROSAT*, and even *XMM-Newton*) are not to be trusted. For these galaxies, careful analysis of high-resolution X-ray data and hydro-dynamical modeling is required to extract the halo and understand its physical state.

The discovery of these hot halos and the characterization of their properties have been unique contributions of high resolution X-ray telescopes to astronomy. The progress from the first *Einstein* observations to *Chandra* has given us a more complete view of early-type galaxies, including not only their gaseous component, but also their stellar component and their nuclei. To unravel the properties of the hot ISM, we have learnt about the populations of LMXBs in these galaxies, and have now a new tool for studying LMXB evolution. We have also gained a new awareness of the detailed effects of AGN feedback, a key ingredient in the formation and evolution of galaxies in the universe.

This process of understanding has enfolded over the last three decades, and has progressed through discoveries, controversies, setbacks, and more discoveries. While painful at times, this debate has been fruitful, and to me epitomizes the progress of science. I am grateful to have been part of this journey and I am indebted to all other participants, collaborators and competitors, without whom this enterprise would not have been possible.

References

D.M. Acreman, I.R. Stevens, T.J. Ponman, I. Sakelliou, MNRAS **341**, 1333 (2003)
N. Arimoto, K. Matsushita, Y. Ishimaru, T. Ohashi, A. Renzini, ApJ **477**, 128 (1997)
Arnaboldi, K.C. Freeman, O. Gerhard, M. Matthias, R.P. Kudritzki, R.H. Mendez, M. Capaccioli, H. Ford, ApJ **507**, 759 (1998)

H. Awaki et al., PASJ **46**, L65 (1994)
J.N. Bahcall, C.L. Sarazin, ApJL **213**, L99 (1977)
J. Binney, L.L. Cowie, ApJ **247**, 464 (1981)
B. Boroson, D.W. Kim, G. Fabbiano, ApJ **729**, 12 (2011)
N.J. Brassington et al, ApJS **179**, 142 (2008)
N.J. Brassington et al, ApJS **181**, 605 (2009)
F. Brighenti, W.G. Mathews, ApJ **495**, 239 (1998)
B.A. Brown, J.N. Bregman, ApJ **539**, 592 (2000)
D.A. Buote, C.R. Canizares, ApJ **427**, 86 (1994)
D.A. Buote, A.C. Fabian, MNRAS **296**, 977 (1998)
C.R. Canizares, G. Fabbiano, G. Trinchieri, ApJ **312**, 503–CFT87 (1987)
A. Cavaliere, R. Fusco-Femiano, AA **49**, 137 (1976)
L. Ciotti et al, ApJ **376**, 380 (1991)
L. Ciotti, J.P. Ostriker, ApJ **551**, 131 (2001)
L. Ciotti, S. Pellegrini, MNRAS **350**, 609 (2004)
L.P. David, W. Forman, C. Jones, ApJ **359**, 29 (1990)
L.P. David, W. Forman, C. Jones, ApJ **369**, 121 (1991)
P.B. Eskridge, G. Fabbiano, D.W. Kim, ApJ **442**, 523 (1995)
G. Fabbiano, ARAA **27**, 87–F89 (1989)
G. Fabbiano, in *Fresh Views of Elliptical Galaxies, ASP Conference Series*, vol. 86, ed. by A. Buzzoni, A. Renzini, A. Serrano (1995), p. 103
G. Fabbiano, ARAA **44**, 323 (2006)
G. Fabbiano, A. Baldi, S. Pellegrini, A. Siemiginowska, M. Elvis, A. Zezas, J. McDowell, ApJ **616**, 730 (2004)
G. Fabbiano, I.M. Gioia, G. Trinchieri, ApJ **347**, 127 (1989)
G. Fabbiano, D.W. Kim, G. Trinchieri, ApJ **429**, 94 (1994)
G. Fabbiano, U. Klein, G. Trinchieri, R. Wielebinski, ApJ **312**, 111 (1987a)
G. Fabbiano, F. Schweizer, ApJ **447**, 572 (1995)
G. Fabbiano, G. Trinchieri, ApJ **296**, 430 (1985)
G. Fabbiano, G. Trinchieri, ApJ **315**, 46 (1987)
G. Fabbiano, G. Trinchieri, M. Elvis, L. Miller, M. Longair, ApJ **277**, 115 (1984)
G. Fabbiano, G. Trinchieri, L.S. van Speybroeck, ApJ **316**, 127 (1987b)
S.M. Faber, J.S. Gallagher, ApJ **204**, 365 (1976)
A.C. Fabian, C.R. Canizares, Nature **333**, 829 (1988)
D. Fabricant, M. Lecar, P. Gorenstein, ApJ **241**, 552 (1980)
D. Fabricant, K. Topka, F.R. Harnden Jr., P. Gorenstein, ApJ **226L**, 107 (1978)
A. Finoguenov, M. Ruszkowski, C. Jones, M. Bruggen, A. Viklinin, E. Mandel, ApJ **686**, 911 (2008)
W. Forman, C. Jones, W. Tucker, ApJ **293**, 102 – FJT85 (1985)
W. Forman, J. Schwarz, C. Jones, W. Liller, A.C. Fabian, ApJ **234L**, 27 (1979)
R. Giacconi et al., ApJ **234L**, 1 (1979)
R. Giacconi, E. Kellogg, P. Gorenstein, H. Gursky, H. Tananbaum, ApJ **165L**, 27 (1971)
P. Gorenstein, D. Fabricant, K. Topka, W. Tucker, F.R. Harnden Jr, ApJ **216L**, 95 (1977)
S.F. Gull, K.J.E. Northover, MNRAS **173**, 585 (1975)
H. Gursky, E. Kellogg, S. Murray, C. Leong, H. Tananbaum, R. Giacconi, ApJ **167L**, 81 (1971)
H. Gursky, A. Solinger, E.M. Kellogg, S. Murray, H. Tananbaum, R. Giacconi, A. Cavaliere, ApJ **173L**, 99 (1972)
E. Hummel, C.G. Kotanyi, R.D. Ekers, AA **127**, 205 (1983)
Y. Ikebe et al., Nature **379**, 427 (1996)
M. Karovska, G. Fabbiano, F. Nicastro, M. Elvis, R.P. Kraft, S.S. Murray, ApJ **577**, 114 (2002)
E. Kellogg, H. Gursky, C. Leong, E. Schreier, H. Tananbaum, R. Giacconi, ApJ **165L**, 49 (1971)
E. Kellogg, S. Murray, ApJ **193L**, 57 (1974)
D.W. Kim, G. Fabbiano, ApJ **441**, 182 (1995)
D.W. Kim, G. Fabbiano, ApJ **586**, 826 (2003)

D.W. Kim, G. Fabbiano, ApJ **613**, 933 (2004)
D.W. Kim, G. Fabbiano, H. Matsumoto, K. Koyama, G. Trinchieri, ApJ **468**, 175 (1996)
D.W. Kim, G. Fabbiano, G. Trinchieri, ApJ **393**, 134 (1992)
J. Kormendy et al., ApJS **182**, 216 (2009)
R.P. Kraft, W.R. Forman, E. Churazov, N. Laslo, C. Jones, M. Markevitch, S.S. Murray, A. Vikhlinin, ApJ **601**, 221 (2004)
N. Iyomoto, K. Makishima, M. Tashiro, S. Inoue, H. Kaneda, Y. Matsumoto, T. Mizuno, ApJ **503L**, 31 (1998)
S.M. Lea, K.O. Mason, G. Reichert, P.A. Charles, G. Riegler, ApJ **227L**, 67 (1979)
S.M. Lea, J. Silk, E. Kellogg, S. Murray, ApJ **184L**, 105 (1973)
M. Loewenstein, D.S. Davis, ApJ **716**, 384 (2010)
G. Mackie, G. Fabbiano, ASPC, **116**, 401 (1997)
R. Malina, M. Lampton, S. Bowyer, ApJ **209**, 678 (1976)
J. Magorrian, et al., AJ **115**, 2285 (1998)
W.G. Mathews, ApJ **219**, 413 (1978)
W.G. Mathews, J.C. Baker, ApJ **170**, 241 (1971)
H. Matsumoto, K. Koyama, H. Awaki, T. Tsuru, M. Loewenstein, K. Matsushita, ApJ **482**, 133 (1997)
K. Matsushita et al., ApJ **436L**, 41 (1994)
K. Matsushita, T. Ohashi, K. Makishima, PASJ **52**, 685 (2000)
B.R. McNamara, P.E.J. Nulsen, ARAA **45**, 117 (2007)
R.F. Mushotzky, P.J. Serlemitsos, E.A. Boldt, S.S. Holt, B.W. Smith, ApJ **225**, 21 (1978)
M. Paolillo, G. Fabbiano, G. Peres, D.-W. Kim, ApJ **565**, 883 (2002)
M. Paolillo, G. Fabbiano, G. Peres, D.-W. Kim, ApJ **586**, 850 (2003)
S. Pellegrini, A. Baldi, D.W. Kim, G. Fabbiano, R. Soria, A. Siemiginowska, M. Elvis, ApJ **667**, 731 (2007)
S. Pellegrini, L. Ciotti, MNRAS **370**, 1797 (2006)
S. Pellegrini, G. Fabbiano, ApJ **429**, 105 (1994)
F.V.N. Rangarajan, A.C. Fabian, W.R. Forman, C. Jones, MNRAS **272**, 665 (1995)
J.C. Raymond, B.W. Smith, ApJS **35**, 419 (1977)
A. Renzini, L. Ciotti, A. D'Ercole, S. Pellegrini, ApJ **419**, 52 (1993)
R.P. Saglia, A. Kronawitter, O. Gerhard, R. Bender, AJ **119**, 153 (2000)
C.L. Sarazin, R.E. White III, ApJ **331**, 102 (1988)
C.L. Sarazin, R.E. White III, in *Windows on galaxies, Procs. 6th Workshop of the Advanced School of Astronomy of the EttoreMajorana Centre*, Erice, May 21–23, 1989, ed. by G. Fabbiano, J.S. Gallagher, A. Renzini. *Astrophysics and Space Science Library*, vol. 160, p. 279 (Kluwer, Dordrecht, 1990)
G. Tabor, J. Binney, MNRAS **263**, 323 (1993)
Y. Tanaka, H. Inoue, S.S. Holt, PASJ **46L**, 37 (1994)
P.A. Thomas, A.C. Fabian, K.A. Arnaud, W. Forman, C. Jones, MNRAS **222**, 655 (1986)
G. Trinchieri et al., ApJ 688, 1000 (2008)
G. Trinchieri, G. Fabbiano, ApJ **296**, 447–TF85 (1985)
G. Trinchieri, G. Fabbiano, C.R. Canizares, ApJ **310**, 637 (1986)
G. Trinchieri, D.W. Kim, G. Fabbiano, C.R. Canizares, ApJ **428**, 555 (1994)
L. Van Speybroeck, A. Epstein, W. Forman, R. Giacconi, C. Jones, W. Liller, L. Smarr, ApJ **234L**, 45 (1979)
M. Weisskopf, H. Tananbaum, L. Van Speybroeck, S. O'Dell, Proc. SPIE **4012**, 2 (2000)
P.W. Vedder, J.J. Trester, C.R. Canizares, ApJ **332**, 725 (1988)

Chapter 2
Hot Gas Flows on Global and Nuclear Galactic Scales

Silvia Pellegrini

Abstract Since its discovery as an X-ray source with the *Einstein* Observatory, the hot X-ray emitting interstellar medium of early-type galaxies has been studied intensively, taking advantage of observations of improving quality performed by the subsequent X-ray satellites *ROSAT*, *ASCA*, *Chandra* and *XMM − Newton*, and comparing the observational results with extensive modeling by means of numerical simulations. The hot medium originates from the ejecta produced by the normal stellar evolution, and during the galaxy lifetime it can be accumulated or expelled from the galaxy potential well. The main features of the hot gas evolution are outlined here, focussing on the mass and energy input rates, the relationship between the hot gas flow and the main properties characterizing its host galaxy, the flow behavior on the nuclear and global galactic scales, and the sensitivity of the flow to major galaxy properties as the shape of the mass distribution and the mean rotation velocity of the stars.

2.1 Introduction

X-ray observations performed during the late 1970s first revealed that early-type galaxies (ETGs) emit soft thermal X-rays and then host an interstellar medium (ISM), of a mass up to $\sim 10^{10}\, M_{\odot}$, that had not been discovered previously at other frequencies because of its high temperature ($T \sim 10^7$ K; see Fabbiano, this volume). Such a medium was the long sought phase fed by stellar mass losses and predicted by the stellar evolution studies (e.g., Faber and Gallagher 1976, Mathews 1989); in fact, both isolated ETGs and those in groups or clusters emit soft thermal X-rays Fabbiano (1989), which provides simple evidence that the hot ISM

S. Pellegrini (✉)
Department of Astronomy, University of Bologna, via Ranzani 1, 40127 Bologna, Italy
e-mail: silvia.pellegrini@unibo.it

D.-W. Kim and S. Pellegrini (eds.), *Hot Interstellar Matter in Elliptical Galaxies*,
Astrophysics and Space Science Library 378, DOI 10.1007/978-1-4614-0580-1_2,
© Springer Science+Business Media, LLC 2012

is mostly indigenous rather than accreted intergalactic medium. Besides solving a puzzle, this discovery opened the study of an important component of ETGs: it is a major ingredient of galactic evolution, see for example its role in feeding a central supermassive black hole and maintaining an activity cycle and starformation (e.g., Fabian and Canizares 1988, Forman et al. 2005, Kormendy et al. 2009, and Ciotti and Ostriker, this volume), or that in polluting the space surrounding ETGs with metals, via galactic outflows (Renzini et al. 1993, and Pipino, this volume), or finally in responding to environmental effects, as interaction with neighbors, stripping, sloshing, and conduction (e.g., Acreman et al. 2003, Sun et al. 2007, Kim et al. 2008, and Sarazin, this volume).

The most striking X-ray observational feature of ETGs is the wide variation in their luminosity ($L_{\rm X}$) values, of $\gtrsim$2 orders of magnitude at any fixed galactic optical luminosity L_B, when $L_B > 3\times10^{10}L_{B,\odot}$ (Fabbiano 1989, O'Sullivan et al. 2001, Memola et al. 2009, Boroson et al. 2011). This feature cannot be explained by distance uncertainties, since a variation of the same size is present even in the distance-independent diagram of $L_{\rm X}/L_{\rm B}$ versus the central stellar velocity dispersion σ_c (e.g., Eskridge et al., 1995). A number of reasons have been proposed as responsible for this large variation, of environmental nature (see Sarazin, this volume) or linked to the possibility for the gas content to evolve substantially during the ETG lifetime. In this latter context, many studies investigated with numerical simulations the dynamical evolution of the hot ISM in ETGs (Sarazin and White 1988, Loewenstein and Mathews 1987, David et al. 1990, 1991, Ciotti et al. 1991, Pellegrini and Ciotti 1998, Tang et al. 2009). In more recent times, the effect of feedback from a central supermassive black hole (MBH) has revealed as another potential contributor to the variation of the hot ISM luminosity (see Statler, and Ciotti and Ostriker, this volume).

Below I briefly review our current knowledge about the feeding and the energetics of the hot gas flows, concentrating on their dynamical state as a function of galactic mass and other major galaxy properties. Section 2.2 gives an updated summary of the fundamental elements entering the problem, the mass and energy inputs to the flow; Sect. 2.3 presents the general case for the evolution of the flow, pointing out the different behavior on the global and nuclear galactic scales, and making also use of a representative ETG; the effect of a central MBH, acting as a gravitating point mass, and the expectations for accretion feedback, are presented in Sect. 2.4; finally, Sect. 2.5 discusses the observed sensitivity of the flow to major galaxy properties as the flattening of the mass distribution, the mean rotational velocity of the stars, and the shape of the stellar profile.

2.2 Feeding and Energetics of the Hot Gas Flows

In this Section the fundamental processes and quantities at the basis of the origin and evolution of hot gas flows are introduced: their feeding via stellar mass losses (Sect. 2.2.1), their heating via type Ia supernovae explosions (Sect. 2.2.2), and their energy budget (Sect. 2.2.3).

2.2.1 The Stellar Mass Loss Rate

In ETGs the gas is lost by evolved stars mainly during the red giant, asymptotic giant branch, and planetary nebula phases. These losses originate ejecta that initially have the velocity of the parent star, then interact with the mass lost from other stars or with the hot ISM, and mix with it. The details of the interaction are controlled by several parameters, like the velocity of the mass loss relative to the hot phase, or the density of the ambient ISM (Mathews 1990). Parriott and Bregman (Parriott and Bregman 2008, Bregman and Parriott 2009), modeling the interaction with two-dimensional hydrodynamical simulations, found that most of the continuous mass loss from giant stars is heated to approximately the temperature of the hot ISM within few parsecs of the star; in the case of mass ejected by planetary nebulae, about half of the ejecta separates and becomes hot, and the other half creates a narrow wake that remains mostly cool, unless turbulent mixing allows for its heating on larger scales. Far infrared observations allow us to measure directly the stellar mass loss rate for the whole galaxy ($\dot{M}_*$); this was for example derived for nine local ETGs from *ISO* data (Athey et al. 2002). When rescaled by the luminosities of the respective galaxies, the values of $\dot{M}_*$ were found to vary by a factor of $\sim$10, which was attributed to different ages and metallicities. The average of the observed rates was $\dot{M}_* = 7.8 \times 10^{-12}\ L_B(L_{B,\odot})\ \mathrm{M}_\odot\mathrm{year}^{-1}$, and was found to be in reasonable agreement with previous theoretical predictions (Athey et al. 2002).

According to single burst stellar population synthesis models, most of the stellar mass is lost at early times, before an age of $\sim$2 Gyr. For example, the mass lost by stars at an age of 2 Gyr is 25% of the total initial mass, for the Salpeter initial mass function (IMF), and 36% for the Kroupa IMF; at an age of 12 Gyr, the additional loss is of $\sim$4% and 6% of the initial mass, for the same two IMFs respectively (Maraston 2005). Figure 2.1 shows the trend of $\dot{M}_*(t)$ with time, estimated from the models in Maraston (2005) for solar metal abundance. At an age of $\gtrsim$2 Gyr, this trend can be approximated as:

$$\dot{M}_*(t) = 10^{-12}\ A\ \times M_*(M_\odot)\ t_{12}^{-1.3} \qquad (\mathrm{M}_\odot\mathrm{year}^{-1}), \tag{2.1}$$

where M_* is the galactic stellar mass[1] at an age of 12 Gyr, t_{12} is the age in units of 12 Gyrs, and $A = 2.0$ or 3.3 for a Salpeter or Kroupa IMF (see Fig. 2.1).

The relation above agrees well with previous theoretical estimates (Mathews 1989, Ciotti et al. 1991). Taking the stellar mass-to-light ratio in the B-band at an age of 12 Gyr ($M_*/L_B = 9.17$ and 5.81, respectively for the Salpeter and Kroupa IMFs, Maraston 2005), (2.1) gives $\dot{M}_*(12\,\mathrm{Gyr}) = \mathrm{B} \times 10^{-11}\ L_B(L_{B,\odot})\ \mathrm{M}_\odot\mathrm{year}^{-1}$, with B = 1.8 or B = 1.9 for the Salpeter or Kroupa IMF. The latter relation gives a rate that is roughly double as large as the average of the observational estimates

[1]The stellar mass M_* changes very little at late epochs, for example by <1% for a variation of $\pm$2 Gyr at an age of 12 Gyr.

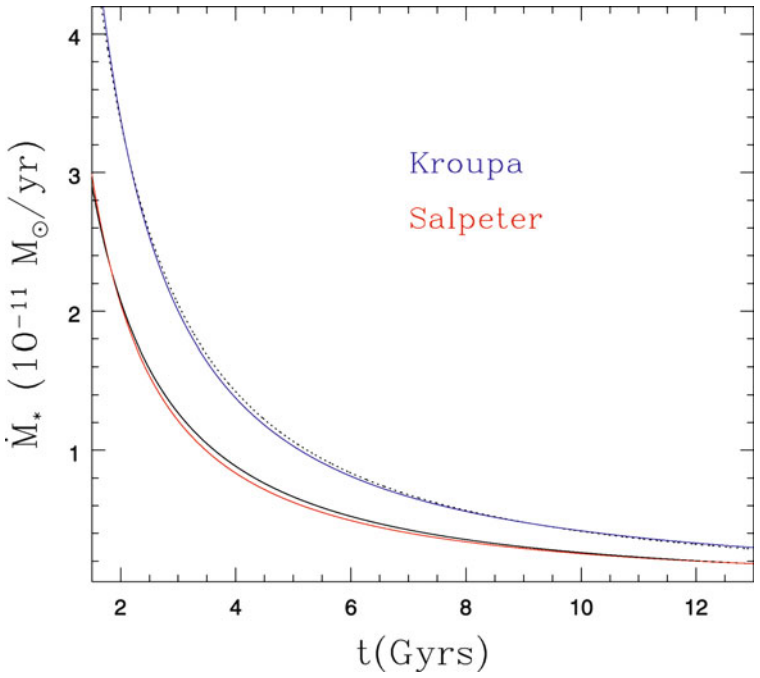

Fig. 2.1 Evolution of the stellar mass loss rate $\dot{M}_*(t)$ according to the models in Maraston (2005), for a Salpeter IMF (*solid line* with best fit of (2.1) in *red*) and for a Kroupa IMF (*dotted line* with best fit of (2.1) in *blue*). Solar abundance is assumed, and a total stellar mass of 1 $M_\odot$ at an age of 12 Gyrs; see the electronic version for a color version of this figure

quoted above (Athey et al. 2002), that however has a large variation around it, partly explained by differences in the ages and metallicities of the observed ETGs.

2.2.2 *The Type Ia Supernovae Mass and Energy Input*

The total mass loss rate of a stellar population $\dot{M}$ is given by the sum $\dot{M}(t) = \dot{M}_*(t) + \dot{M}_{\rm SN}(t)$, where one adds to $\dot{M}_*(t)$ (discussed in the previous Sect. 2.2.1) the rate $\dot{M}_{\rm SN}(t)$ of mass lost by type Ia supernovae (SNe Ia) events, the only ones observed in an old stellar population (e.g., Cappellaro et al. 1999). The mass input due to SNe Ia is $\dot{M}_{\rm SN}(t) = 1.4\ {\rm M}_\odot\ R_{\rm SN}(t)\ {\rm M}_\odot\ {\rm year}^{-1}$, where $R_{\rm SN}(t)$ (in ${\rm year}^{-1}$) describes the evolution of the explosion rate with time, since each SNe Ia ejects $1.4\,{\rm M}_\odot$. In a detailed scenario for the SNe Ia precursors and their subsequent explosion past a burst of star formation (Greggio 2005, 2010), $R_{\rm SN}(t)$ experiences a raising epoch during the first 0.5-1 Gyr, at the end of which it reaches a peak, and then decreases slowly with a timescale of the order of 10 Gyr, and accounts for the present day observed rate. A parameterization of the rate after the peak, in number

of events per year, is

$$R_{\rm SN}(t) = 0.16(H_0/70)^2 \times 10^{-12}\ L_B(L_{B,\odot})\ t_{12}^{-s} \qquad ({\rm year}^{-1}), \tag{2.2}$$

where H_0 is the Hubble constant in units of km s^{-1} Mpc^{-1}, L_B is the present epoch galaxy luminosity, and s describes the past evolution; when $t_{12} = 1$, (2.2) gives the rate for local ETGs in Cappellaro et al. (1999), that has an uncertainty of $\pm 30\%$. Recently, new measurements of the observed rates of supernovae in the local Universe, determined from the Lick Observatory Supernova Search (LOSS; Li et al. 2011), gave a SNe Ia rate in ETGs consistent with that in Cappellaro et al. (1999). For the rate in (2.2), and for $H_0 = 70$ km s^{-1} Mpc^{-1}, one obtains $\dot{M}_{\rm SN}(12\,{\rm Gyr}) = 2.2{\times}10^{-13} L_B(L_{B,\odot})$ M$_\odot$ year^{-1}, that is almost $\sim$100 times smaller than the "normal" stellar mass loss rate $\dot{M}_*$ (12 Gyr) $\approx 2 \times 10^{-11}\ L_B(L_{B,\odot})$ M$_\odot$ year^{-1} derived above (Sect. 2.2.1).

SNe Ia provide also heating (Sect. 2.2.3 below) at a rate $L_{\rm SN}(t)$ that is the product of the kinetic energy injected by one event ($E_{\rm SN} \approx 10^{51}$ erg) times the rate $R_{\rm SN}(t)$. This assumes that the total of $E_{\rm SN}$ is turned into heat of the hot ISM, an assumption that is clearly an overestimate, but not totally unreasonable for the hot diluted gas (Mathews 1989). Then

$$L_{\rm SN}(t) = E_{\rm SN} \times R_{\rm SN}(t) = 5.1(H_0/70)^2 \times 10^{30}\ L_B(L_{B,\odot})\ t_{12}^{-s} \qquad ({\rm erg\ s}^{-1}), \tag{2.3}$$

and is plotted in Fig. 2.2 for $t_{12} = 1$ and $H_0 = 70$ km s^{-1} Mpc^{-1}. The SNe Ia specific heating, given by the total SNe Ia heating per total injected mass (approximated hereafter with $\dot{M}_*$) is

$$\frac{L_{\rm SN}}{\dot{M}_*} = 1.6(H_0/70)^2 \times 10^{50}\ \frac{L_B(L_{B,\odot})}{AM_*(M_\odot)}\ t_{12}^{1.3-s} \quad ({\rm erg\ M}_\odot^{-1}) \tag{2.4}$$

where $\dot{M}_*$ given in (2.1) has been used. At an age $t_{12} = 1$, for $H_0 = 70$ km s^{-1} Mpc^{-1}, and using $\dot{M}_*(12\,{\rm Gyr}) \approx 2 \times 10^{-11}\ L_B(L_{B,\odot})$ M$_\odot$ year^{-1} (valid for both IMFs, see below (2.1)), one gets $L_{\rm SN}/\dot{M}_* \approx 8 \times 10^{48}$ erg M$_\odot^{-1}$, that is a significant heating (with respect to, e.g., the specific binding energy of the gas, see Sect. 2.2.3 and Fig. 2.2).

During the galaxy lifetime, $L_{\rm SN}/\dot{M}_* \propto t^{1.3-s}$, and then can increase or decrease with time increasing, with consequences on the secular gas flow behavior (Loewenstein and Mathews 1987, David et al. 1990, Ciotti et al. 1991; Sect. 2.3). Early hydrodynamical simulations of hot gas flows enlighted the importance of the cosmological evolution of the SNe Ia rate to avoid excessive, and unobserved, mass accumulation at the galactic centers if L_{SN} decreases faster than $\dot{M}_*$ ($s > 1.3$), then at early times it can be large enough to drive the gas lost by stars in a supersonic wind, that later can become subsonic and evolve into an inflow (Ciotti et al. 1991; Sect. 2.2.3 below). Subsequently, mainly following *Chandra* and *XMM − Newton* observations, it was realized that another major source of ISM heating can be

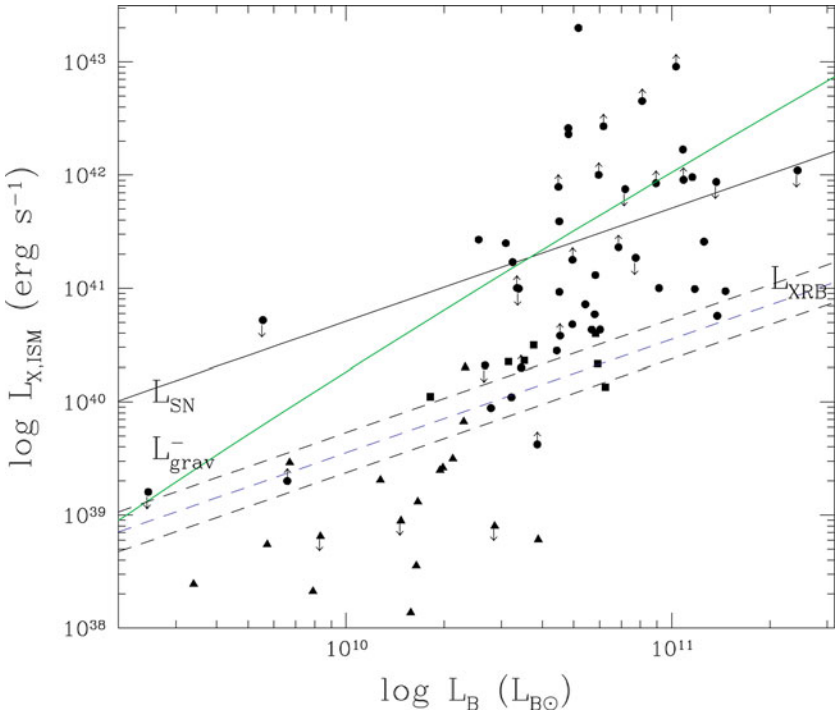

Fig. 2.2 The X-ray luminosity of the hot ISM $L_{X,ISM}$ from *Chandra* observations, versus the galactic L_B (from corrected apparent magnitudes from Hyperleda, and distances from Tonry et al. (2001), Diehl and Statler (2007), for $H_0 = 70$ km s^{-1} Mpc^{-1}). $L_{X,ISM}$ is from Diehl and Statler (2007) (*circles*), David et al. (2006) (*triangles*), Nagino and Matsushita (2009) (*squares*); *downward (upward) arrows* indicate upper (lower) limits. The *dashed lines* show the mean total luminosity from X-ray binaries derived from *Chandra* data (in *blue*), and its $\pm 1\sigma$ uncertainty, from Boroson et al. (2011). All X-ray luminosities have been recalculated for the 0.3–5 keV band, assuming the spectral shape in the original references. The *solid line* is L_{SN} (2.3); the *green line* is $L_{\overline{grav}}$ (2.7), calculated for $\dot{M}_*$ (12 Gyrs) of the Kroupa IMF (Sect. 2.2.1), and representative galactic mass models (see also Sect. 2.3) with: a stellar de Vaucouleurs profile, σ_c from the Faber-Jackson relation, an effective radius R_e from the Fundamental Plane relation (Bernardi et al. 2003), a NFW dark mass profile with a dark-to-luminous mass ratio of 5 in total (Komatsu et al. 2009), and of 0.6 within R_e (Cappellari et al. 2006, Weijmans et al. 2009, Shen and Gebhardt 2010), a ratio of the scale radii of the dark and stellar mass distributions of $r_h/R_e = 1.5$, see the electronic version for a color version of this figure

provided by the central MBH. The MBH heating is not sufficient by itself to avoid long-lasting and massive inflows at early times, but when coupled with the SNe Ia heating, it can help the galaxy degassing and prevent large mass accumulation at the galactic centers, independently of the relative rates of $\dot{M}_*(t)$ and $R_{\rm SN}(t)$ (see Ciotti and Ostriker, this volume). Recent estimates of the slope s agree with a value around $s \sim 1$ (Mannucci et al. 2005, Greggio 2005, 2010, Maoz et al. 2011, Sharon et al. 2010).

2.2.3 Energetics of the Gas Flows

The material lost by stars is ejected at a velocity of few tens of km s^{-1} and at a temperature of $\lesssim 10^4$ K (Parriott and Bregman 2008), and is then heated to high, X-ray emitting temperatures by the thermalization of the stellar velocity dispersion (as it collides with the mass lost from other stars or with the ambient hot gas and is shocked) and of the kinetic energy of SNe Ia events (Sect. 2.2.2). The first process provides heat to the ISM at a rate

$$L_\sigma = \frac{1}{2}\frac{\dot{M}_*(t)}{M_*}\int_0^\infty 4\pi r^2 \rho_*(r)\sigma^2(r)dr, \tag{2.5}$$

where $\rho_*(r)$ is the stellar density profile, and $\sigma(r)$ is the trace of the local stellar velocity dispersion tensor. The latter can be obtained by solving the Jeans equations for an adopted galaxy mass model (e.g., Binney and Tremaine 1987), and for an assumed stellar orbital anisotropy. So doing, one derives that the stellar heating L_σ is a few times lower than that provided by SNe Ia, L_{SN}, for reasonable stellar and dark matter distributions (Ciotti et al. 1991; see also Sect. 2.3.3 and Fig. 2.6 below for an example).

In case of gas flowing to the galactic center (inflow), as the gas falls into the potential well, power is generated that can heat the gas; for a steady inflow of $\dot{M}_*$ through the galactic potential down to the galactic center, this power is given by

$$L^+_{grav} = \frac{\dot{M}_*(t)}{M_*}\int_0^\infty 4\pi r^2 \rho_*(r)[\phi(r) - \phi(0)]dr \tag{2.6}$$

where $\phi(r)$ is the total potential [and the equation above applies only to mass distributions with a finite value of $\phi(0)$]. In outflows, the work done against the gravitational field to extract steadily and bring to infinity the gas shed per unit time $\dot{M}_*(t)$ is

$$L^-_{grav} = -\frac{\dot{M}_*(t)}{M_*}\int_0^\infty 4\pi r^2 \rho_*(r)\phi(r)dr. \tag{2.7}$$

$L^-_{\rm grav}$ is the minimum power required to steadily remove the stellar mass loss, because of energy losses due to cooling, but these are expected to be low in the low density of an outflow. Figure 2.2 shows an example of L^-_{grav} as a function of L_B for representative two-component galaxy mass models.

Even though stationary conditions are unlikely to be verified, the quantities above are useful to evaluate in first approximation the energy budget of the flow, and then predict its dynamical state and the gas content of an ETG. In a more compact notation, the integral in (2.7) can be expressed as

$$L^-_{grav} = \dot{M}_*(t)\sigma_c^2\Gamma^-(\mathscr{R},\beta) \tag{2.8}$$

where σ_c is the central stellar velocity dispersion, and the dimensionless function Γ^- depends on the depth and shape of the potential well, via the variables $\mathscr{R} = M_h/M_*$ (M_h being the total dark halo mass), and $\beta = r_h/r_*$ (r_h and r_* being the scale radii of the dark and stellar mass distributions; see Ciotti et al. (1991), Ciotti and Pellegrini (1992), Pellegrini and Ciotti (1998) for examples of Γ^- for various stellar density profiles). Γ^- increases for increasing $\mathscr{R}$ and decreasing β (see, e.g., Pellegrini 2011).[2] For reasonable galaxy structures, Γ^- does not largely vary with $\mathscr{R}$ and β, as for example empirically demonstrated by the existence of scaling laws as the Fundamental Plane of ETGs (Renzini and Ciotti 1993). Equation 2.8 then shows how the larger σ_c, the harder for the gas to leave the galaxy; for example, per unit gas mass, one has $L^-_{grav}/\dot{M}_* \propto \sigma_c^2$. L^-_{grav} is expected to steeply increase with L_B, since on average the larger is σ_c, the brighter is the optical luminosity of the ETG (from the Faber-Jackson relation $L_B \propto \sigma_c^4$), and since also $\dot{M}_*$ is proportional to L_B (Sect. 2.2.1). For a fixed galaxy structure [i.e., a fixed $\Gamma^-(\mathscr{R}, \beta)$], and using the Faber-Jackson relation, one has $L^-_{grav} \propto L_B^{1.5}$, a trend close to the green line in Fig. 2.2 (that has a slope of $\sim$1.8, though, since it derives from the full $L_B - \sigma_c$ relation for ETGs, that has a shallower slope at the lower L_B, Davies et al. 1983). Since the available heating to extract the gas (L_{SN}) increases with L_B as well, it is useful to evaluate the run of the ratio between the power required to extract the gas (L^-_{grav}) and that given by SNe Ia:[3]

$$\frac{L^-_{grav}(t)}{L_{\rm SN}(t)} \propto t_{12}^{s-1.3}\sigma_c^2\Gamma^-(\mathscr{R}, \beta). \tag{2.9}$$

In a first approximation, (most of) the galaxy will host an outflow if this ratio has always been lower than unity, and an inflow soon after it becomes larger than unity (Ciotti et al. 1991). The time evolution of the ratio is determined by the value of $s - 1.3$; recent progress indicates $s \gtrsim 1$ (end of Sect. 2.2.2), which produces a ratio in (2.9) decreasing with time. This means that with time increasing the gas has a tendency to become hotter and, if outflowing regions are present, the degassing becomes faster (see also Sect. 2.3.3). Equation (2.9) also indicates the underlying cause of the average $L_{X,ISM} - L_B$ correlation (Fig. 2.2), that is the increase of $L^-_{grav}/L_{\rm SN}$ with σ_c^2, and then with L_B (provided that the function Γ^- does not vary widely with L_B, as expected for reasonable galaxy mass models).

The relative size of L^-_{grav} and $L_{\rm SN}$ can be estimated from Fig. 2.2. $L^-_{grav} < L_{SN}$ for $L_B \lesssim 3 \times 10^{10} L_{B,\odot}$, therefore in these ETGs we can expect outflows to be important, and then low L_X values. This "prediction" has been confirmed to be true recently, thanks to *Chandra* observations of low L_B galaxies, probing

[2] An expression equal to that in (2.8) can be written for L^+_{grav}, just replacing Γ^- with a function $\Gamma^+(\mathscr{R}, \beta)$; the latter has the same trend as Γ^- to increase for increasing $\mathscr{R}$ and decreasing β; for reasonable galaxy mass models, $\Gamma^+ \sim 2\Gamma^-$ (see Pellegrini 2011).

[3] In order to account for all the heating sources, one should add to the denominator of (2.9) also L_σ, that has been neglected for simplicity, since typically $L_\sigma << L_{SN}$, as written below (2.5).

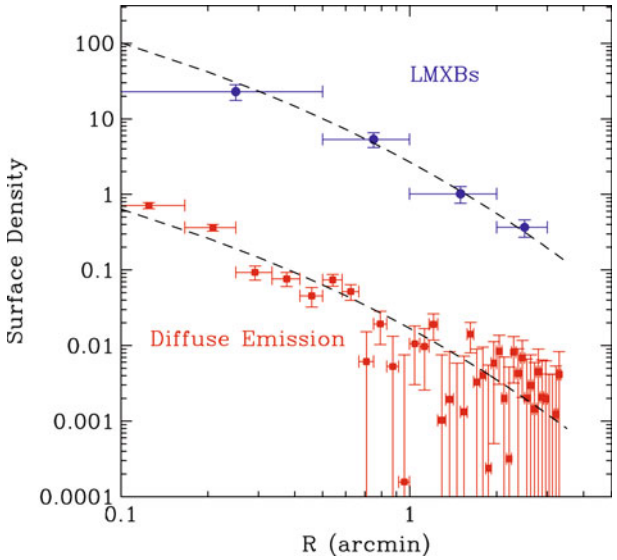

Fig. 2.3 Radial profiles for the ETG NGC821 of: detected point sources (*blue*) in units of number per square arcminute; background-subtracted diffuse emission over 0.3-6 keV (*red*), in units of counts per pixel, from hot gas and unresolved low-mass X-ray binaries; and galactic R-band emission (*dashed lines*, arbitrarily normalized), from Pellegrini et al. (2007). A stringent upper limit on the gas emission could be put exploiting the high resolution of *Chandra* observations (see Fig. 12 of Pellegrini et al. 2007, reproduced with permission of the AAS), see the electronic version for a color version of this figure

for the first time gas emission levels even below those of the X-ray binaries emission (David et al. 2006, Pellegrini et al. 2007, Trinchieri et al. 2008, Boroson et al. 2011; Fig. 2.3). For $L_B > 3 \times 10^{10} L_{B,\odot}$, instead, $L^{-}_{grav} > L_{\rm SN}$ and the SNe Ia heating is insufficient to prevent (at least some) inflow. At high L_B, however, a very large variation of L_X is observed, from values typical of winds to values even larger than predicted by models for global inflows in isolated ETGs (see Sect. 2.3 below). This has a few possible explanations: on one hand, there is the high sensitivity of the gas behavior to variations in the parameters entering (2.9) (the dark and stellar mass, their distribution, the orbital structure, and possibly also L_{SN}, can all vary at fixed L_B), as discussed in Sects. 2.3 and 2.5 below (see also Ciotti et al. 1991, Pellegrini and Ciotti 1998). On the other hand, the simple arguments above do not consider important factors that can influence the hot gas content, as injection of energy from the nucleus (see Ciotti and Ostriker, this volume; Pellegrini et al. 2011), and/or environmental effects (Sarazin, this volume; Pellegrini 1999a, Brown and Bregman 2000, Brighenti and Mathews 1998, Helsdon et al. 2001, Sun et al. 2007, Jeltema et al. 2008, Sun 2009). The considerations in this Section can account for the average trend of $L_{X,ISM}$ with L_B, but significant effects can be superimposed by these factors.

2.3 Decoupled Flows and Variation in $L_{X,ISM}$

In the previous Sect. 2.2.3, a simple evaluation of the energy budget of the hot gas allowed to explain the trend of its content ($L_{X,ISM}$) with L_B (Fig. 2.2): the low $L_{X,ISM}$ at $L_B < 3 \times 10^{10} L_{B,\odot}$ was attributed naturally to the presence of outflows, while the large range of $L_{X,ISM}$ for $L_B > 3 \times 10^{10} L_{B,\odot}$ required that these ETGs can keep widely different amounts of gas. For these brighter ETGs, we here show how variations in the fundamental galaxy parameters, as the total mass or its distribution, can account for much of the observed $L_{X,ISM}$ range (see also Sect. 2.3.3). This point was addressed previously with hydrodynamical simulations of hot gas flows for a set of model ETGs with realistic mass profiles (Pellegrini and Ciotti 1998): their stellar density in the central regions matched the surface brightness observed with the Hubble Space Telescope (*HST*), that is a power law as far in as it can be measured (i.e., $\sim$ a few parsecs in Virgo, Lauer et al. 1995, Côté et al. 2006, Lauer et al. 2007); their dark matter density also followed a peaked $r^{-\nu}$ profile close to the center, with $\nu \simeq 1$, as indicated by high resolution cosmological simulations (Navarro et al. 1997, hereafter NFW profile). The dark mass was constrained to be dynamically important outside 1–2 effective radii R_e, as suggested by dynamical modeling of the stellar and planetary nebulae kinematics out to $\sim$4 R_e and beyond (Saglia et al. 1992, Cappellari et al. 2006, Weijmans et al. 2009, Shen and Gebhardt 2010, Napolitano et al. 2010). Examples of density and surface brightness profiles for representative ETGs with the above characteristics are given Fig. 2.4. For such peaked mass distributions the simulations produced strongly decoupled gas flows (called partial winds, MacDonald and Bailey 1981): an inflow in the central galactic region coexists with an external part that keeps degassing. The inflow is due to the steep mass distribution and the high central stellar (and gas) density, such that the local SNe Ia heating is efficiently radiated away and accretion takes place; the outflow can be sustained where the gas density is lower and the gas is less tightly bound (see also Sect. 2.3.2). Depending on the galaxy model, the external part can be very subsonic or degassing with a velocity of the order of the sonic value (the flow is then usually called a wind).

The partial wind regime settles on a quasi-stationary configuration: if, for example, the specific heating $L_{SN}/\dot{M}_*$ increases with time ($s < 1.3$, Sect. 2.2.3), then during the evolution the stagnation radius r_{st} slowly but steadily moves inward, the central inflow velocity gets lower, and the outer outflow faster (see also Sect. 2.3.3). At the end, r_{st} can range from a small fraction of R_e to few R_e, with corresponding $L_{X,ISM}$ variations by up to a factor of $\sim$100, even at fixed L_B (Pellegrini and Ciotti 1998). Such differences in r_{st} can be produced by a variation of σ_c, of the (dark) mass content $\mathscr{R}$, of the dark and luminous mass concentration (R_e, β), while keeping the model ETGs within the scatter in the observed scaling laws, as the Fundamental Plane relation; or finally by a difference in the heating L_{SN}, within its observed $\pm 30\%$ variation. The highest $L_{X,ISM}$ are of the order of $\sim$ a few $\times 10^{41}$ erg s^{-1}, for the most massive ETGs, with the largest $\mathscr{R}$ and lowest β, that determine the largest L^{-}_{grav} (and then the tendency to a larger inflow), and the

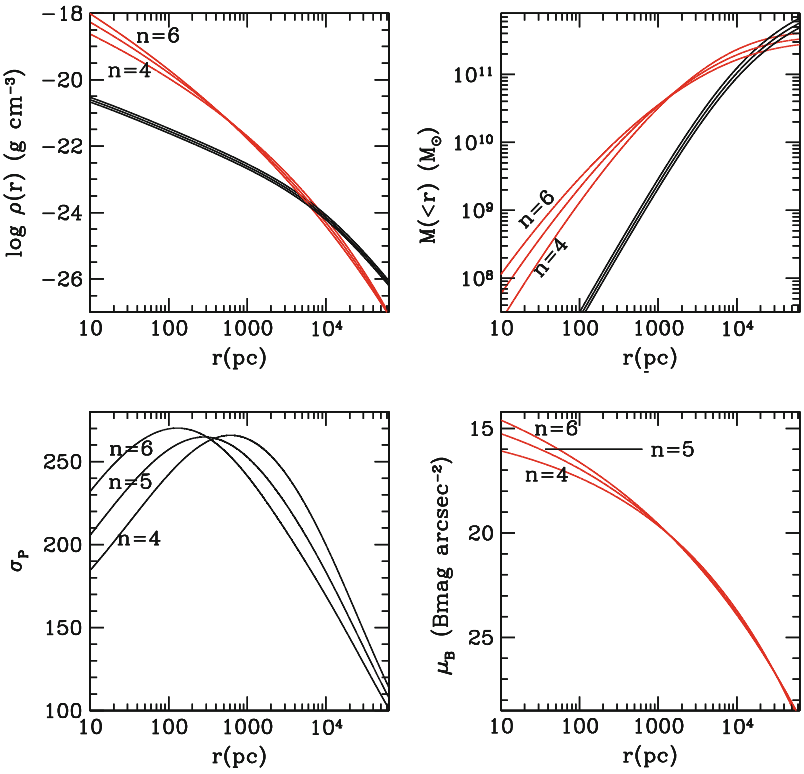

Fig. 2.4 *Upper panels*: density and mass profiles of a two-component galaxy model (stars+dark matter), for a representative galaxy with an aperture velocity dispersion $\sigma_c = 260$ km s^{-1} within $R_e/8$, isotropic orbits, $L_B = 5\times10^{10} L_{B,\odot}$, and then $R_e = 6.46$ kpc, from the Fundamental Plane relation. The stellar (*red*) profiles follow a Sérsic law with index $n = 4, 5, 6$; the dark halo (*black*) has the NFW profile $[\rho_h(r) \propto M_h/4\pi r(r_h + r)^2]$ with $\beta = 1.5, \mathscr{R} = 4$ and then $\mathscr{R}_e = 0.48$ from the Jeans equation (see Sect. 2.3.3). *Lower panels*: the projected velocity dispersion profile, and the B-band surface brightness profile, of the stellar component. The luminosity profile becomes more peaked with n increasing (e.g., *bottom right panel*), therefore the same σ_c is obtained with less total stellar mass (that is the dominating mass component at the center; e.g., M_*/L_B goes from 8.5 to 6.1 for n from 4 to 6); being $\mathscr{R}$ fixed, also M_h becomes lower. The model with $n = 5$ (not labelled in the *upper panels* for clarity) is used in Sect. 2.3.3, see the electronic version for a color version of this figure

largest heating by gravitational compression during infall L^+_{grav} (that is at least in part radiated; Sect. 2.2.3). The highest $L_{X,ISM}$ values of the models are still lower, though, than the highest $L_{X,ISM}$ observed (Fig. 2.2); in fact $L_{X,ISM} \gtrsim 10^{42}$ erg s^{-1} are typical of central dominant ETGs in groups or clusters, where the conditions for gas retention, or even accretion from outside the galaxies, are more favorable (Matsushita 2001, Helsdon et al. 2001, Brighenti and Mathews 1998, Nagino and Matsushita 2009).

2.3.1 Gas Temperature and Galaxy Structure

In the simulations described above (Sect. 2.3), the average emission weighted gas temperature T_{gas} ranges between 0.3 and 0.8 keV, for a large set of galaxy models with different L_B, dark matter fraction and distribution, and SNe Ia rate. This range of T_{gas} compares well with that of the gas temperatures recently determined using *Chandra* data (e.g., Diehl and Statler 2008a, Nagino and Matsushita 2009, Boroson et al. 2011). Both in the observational results and in the models T_{gas} shows a trend to increase with σ_c. For example, the statistical analysis of the gas temperature for a sample of luminous ETGs observed with *ROSAT* indicates a correlation of type $\sigma_c \propto T_{gas}^{0.56\pm0.09}$, although with a large degree of scatter about this fit (O'Sullivan et al. 2003). Both the size of the T_{gas} values and their trend with σ_c behave as expected, since the gas temperature cannot be much different from the virial temperature T_{vir} of the galaxy potential well. In fact T_{vir} is defined as

$$T_{vir} = \frac{1}{3k}\frac{\mu m_p}{M_*}\int 4\pi r^2 \rho_*(r)\sigma^2(r)\, dr \tag{2.10}$$

where k is the Boltzmann constant, μm_p is the mean particle mass, m_p is the proton mass, and $\sigma(r)$ is the three-dimensional velocity dispersion (as in (2.5)); see also Pellegrini 2011. As already done for L^+_{grav} and L^-_{grav} in Sect. 2.2.3, and in analogy with (2.8), T_{vir} can be expressed as $T_{vir} = \mu m_p \sigma_c^2 \Omega(\mathscr{R}, \beta)/k$, with $\Omega < 1$. T_{vir} is then proportional to σ_c^2, which explains the trend of T_{gas} with σ_c present in the models, and is close to the trend shown by the observations (O'Sullivan et al. 2003). A simplified version of the virial temperature in (2.10) is often used, i.e., $T_\sigma = \mu m_p \sigma_c^2/k$; this somewhat overestimates the true T_{vir}, since $\Omega < 1$. One can notice that T_{vir} is also the temperature linked to the gas heating provided by the thermalization of the stellar random motions (2.5). Therefore the values of T_{vir} are expected to represent a lower boundary to the values of T_{gas}, due to the importance of additional heating mechanisms (as that provided by SNe Ia).

In addition to the average increase of T_{gas} with σ_c, at fixed σ_c the models of gas rich galaxies show slightly larger T_{gas} for values of $\mathscr{R}$ larger or β smaller (Sarazin and White 1988, Pellegrini and Ciotti 1998). In fact, Ω shows the same trend as the functions Γ in Sect. 2.2.3 to increase for larger $\mathscr{R}$ and/or lower β. For inflowing gas, this can be understood as a larger gas heating by compression during infall (i.e., a larger L^+_{grav}, (2.6); Ciotti et al. 1991) for a larger dark matter amount or its higher concentration. Since larger $\mathscr{R}$ and/or smaller β also make the gas more bound, they correspond to larger retained hot gas amounts, so that a trend for a larger $L_{X,ISM}$ accompanied by a larger T_{gas} is expected, even at fixed σ_c. Such a trend could be present in the gas temperatures derived recently from the analysis of *Chandra* observations of a large set of ETGs (Boroson et al. 2011). It must be noted, though, that the SNe Ia heating, that is independent of the galaxy structure, is a major source of heating (Sect. 2.2.3), "diluting" the dependence of T_{gas} on the galaxy structure ($\mathscr{R}, \beta$; see Pellegrini 2011).

2.3.2 Reasons for Decoupling

Simulations for steep mass models show typically a central inflowing region, that can be even very small (see Pellegrini et al. 2007 for an example tailored on the hot gas poor ETG NGC 821), and an external outflow (Sect. 2.3). The physical origin of this decoupling can be attributed to two contributing effects: one is the high cooling at the galactic center, due to the high stellar density there, with the consequent high stellar mass loss rate; the other is the large radial variation of the binding energy of the gas. This second effect can be quantified by examining the radial distribution of the energy budget of the gas inside the galaxy models. Instead of (2.9) giving the global L^-_{grav}/L_{SN}, one has now to consider the local energy ratio given by $dL^-_{grav}(r)/dL_{SN}(r)$, where

$$dL^-_{grav}(r) = 4\pi \frac{\dot{M}_*(t)}{M_*} \rho_*(r)|\phi(r)|r^2 dr, \tag{2.11}$$

and

$$dL_{SN}(r) = \frac{L_{SN}(t)}{M_*} 4\pi\rho_*(r) r^2 dr, \tag{2.12}$$

so that

$$\frac{dL^-_{grav}(r)}{dL_{SN}(r)} = \frac{\dot{M}_*(t)}{L_{SN}(t)}|\phi(r)|. \tag{2.13}$$

For a given total mass, the steeper the galaxy density profile, the stronger is the variation of $|\phi(r)|$ across the galaxy, the larger is $|\phi(0)|$; the flow decoupling of highly concentrated systems is then determined by $dL^-_{grav}(r)/dL_{SN}(r)$ being larger than unity in the central galactic regions, which produces accretion, while in the external parts $dL^-_{grav}(r)/dL_{SN}(r) < 1$ and degassing is possible.

The ratio in (2.13) has the same trend with time of (2.9); if $s < 1.3$, then dL^-_{grav}/dL_{SN} decreases with time, so that the radius where $dL^-_{grav}(r)/dL_{SN}(r) = 1$ (and r_{st} in the simulations) moves inward as age increases, and a smaller and smaller part of the galaxy remains inflowing (see for example the case of the test galaxy in the next Sect. 2.3.3, Fig. 2.5). Another important effect, this time on the radial trend of $dL^-_{grav}(r)/dL_{SN}(r)$, is produced by the dark halo, that is generally thought to be more diffuse than the stellar mass distribution and to become dynamically important outside a few R_e (Saglia et al. 1992, Cappellari et al. 2006, Weijmans et al. 2009, Shen and Gebhardt 2010); if for example $\mathscr{R}$ is increased, the gas is more bound in the external regions, and the radius at which $dL^-_{grav}(r)/dL_{SN}(r) = 1$ moves outward (Pellegrini and Ciotti 1998).

In conclusion, a flow with a global $L_{SN} > L^-_{grav}$ can host a central inflow, and one with $L_{SN} < L^-_{grav}$ can still host an external outflow; this is relevant for the possibility of inflowing material on a central MBH, and then for the presence of nuclear activity, even for low mass ETGs in Fig. 2.2 (e.g., those with $L_B < 3 \times 10^{10} L_{B,\odot}$; Pellegrini et al. 2007), and for the possibility of outflowing gas even for ETGs of larger masses.

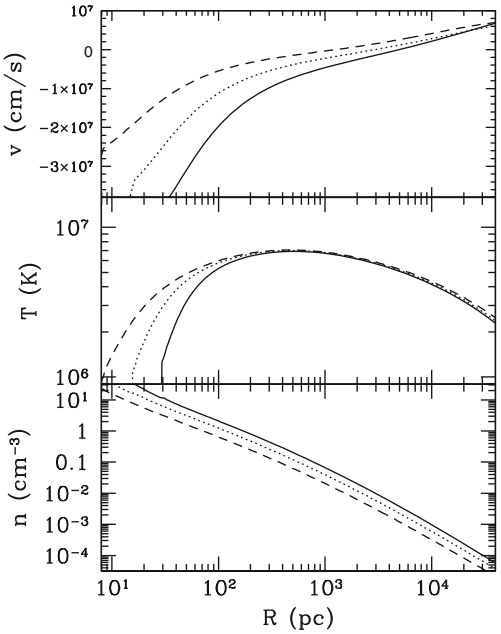

Fig. 2.5 Radial trend of the main hydrodynamical quantities of the gas flow in the testcase ETG described in Sect. 2.3.3: velocity (negative inward), *top*; temperature, *middle*; number density (ρ/m_p), *bottom*. The galaxy age is 5 (*solid*), 8.5 (*dotted*) and 13 (*dashed*) Gyr

2.3.3 The Gas Flow in a Testcase ETG

This Section presents the evolution and the properties of the flow for a testcase ETG, whose optical properties place it where the $L_{X,ISM}$ variation is of ∼2 orders of magnitude (Fig. 2.2): $L_B = 5 \times 10^{10} L_{B,\odot}$ and $\sigma_c = 260$ km s^{-1}, from the Faber-Jackson relation; the stellar mass profile follows a Sérsic law with index $n = 5$, as appropriate for the chosen L_B (e.g., Kormendy et al. 2009); the effective radius $R_e = 6.5$ kpc, from the Fundamental Plane relation (Bernardi et al. 2003). The dark halo has a NFW profile with $\mathscr{R} = 4$ and a scale radius larger than that of the stars ($\beta = r_h/R_e = 1.5$). By solving the Jeans equations for two mass components in the isotropic orbits case, these choices produce $M_* = 3.6 \times 10^{11} M_\odot$, $M_*/L_B = 7.2\, M_\odot/L_{B,\odot}$, and a dark-to-luminous mass ratio within R_e of $\mathscr{R}_e = 0.48$ (this mass model is shown in Fig. 2.4). The stellar mass loss rate is that of (2.1) for the Kroupa IMF; the present epoch SNe Ia rate is that of (2.3) for $H_0 = 70$ km s^{-1} Mpc^{-1}, with the assumption that a factor of 0.85 of L_{SN} is eventually thermalized; the evolution of the rate follows the $s = 1.1$ decay, in agreement with recent results for ETGs (Sect. 2.2.2). The evolution of the galactic flow is obtained by integrating the time-dependent Eulerian equations of hydrodynamics with source terms (e.g., Ciotti et al. 1991), using a numerical code described in Ciotti and Ostriker (2007),

with a sink of the hydrodynamical quantities at the galactic center (see Sect. 2.4 below for the case of the presence of a MBH there). A total of 240 logarithmically spaced gridpoints is used, with the first one placed at a radius of 2.5 pc, the last one at 500 kpc. The distribution of stellar and dark mass is time-independent; star formation is supposed to have occurred all in a single burst at $t = 0$, and the behavior of the mass lost by stars is followed from an age of $\sim$2 Gyrs since the burst, that is after the epoch of SNe II-driven galactic winds ending the formation of the bulk of the stellar population (see Pipino, this volume).

The gas velocity, temperature and density profiles at representative epochs are shown in Fig. 2.5; the time evolution of the various components of the energy budget discussed in Sect. 2.2.3, and of the X-ray luminosity of the gas in the 0.3-8 keV band, is shown in Fig. 2.6; the 0.3-8 keV surface brightness profile at the present epoch is shown in Fig. 2.7. As typical of steep mass models, a central inflowing region is present from the beginning; due to the secular increase of the specific heating of the gas ((2.4), Sect. 2.3.2), with time increasing the infall velocity decreases in modulus, the stagnation radius migrates inward (Fig. 2.5), and a central "cold" region of a few hundreds parsecs gets hotter and hotter. By the present epoch a quasi-stationary configuration establishes, by which the gas leaves the galaxy at a rate almost equal to the rate $\dot{M}_*$ at which gas is injected by stars, and the small difference goes into the central sink. Since $\dot{M}_*$ decreases with time (2.1), the gas becomes uniformly less dense over the whole galaxy, the hot gas mass decreases, and so does its luminosity (Fig. 2.6).

The final gas temperature profile is increasing with radius within the inner $\sim$100 pc; external to this region, the temperature is $\sim$ constant at $\sim 7 \times 10^6$K out to $\sim$1 kpc, and then decreases outside of this broad peak, to reach half its value at a radius of 20 kpc (Fig. 2.5). This kind of profile decreasing outward is common among ETGs observed with *Chandra* (e.g., Matsushita 2001, Fukazawa et al. 2006, Diehl and Statler 2008a; other profiles often occurring are flat or

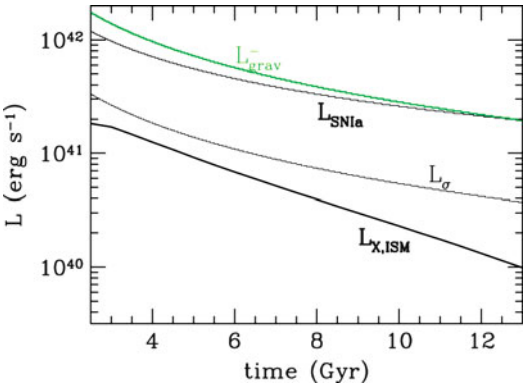

Fig. 2.6 The run with time of the ISM luminosity within $10R_e$, and of L_σ, L_{grav}^{-} and L_{SN}, defined in Sects. 2.2.2 and 2.2.3, for the testcase ETG of Figs. 2.4 and 2.5 (Sect. 2.3.3), see the electronic version for a color version of this figure

outwardly increasing ones (Diehl and Statler 2008a, see also Statler, this volume). To obtain the latter two shapes, other ingredients are required with respect to those included here, as AGN feedback depositing heating outside the central galaxy core, through a jet or rising bubbles (e.g., Finoguenov and Jones 2001, Forman et al. 2005, Diehl and Statler 2008b, Omma et al. 2004), or as an external medium (Sarazin and White 1987, Bertin and Toniazzo 1995, Brighenti and Mathews 1998, Diehl and Statler 2008b).

The brightness profile of the gas is more peaked than that of the stars (the blue and the green profiles in Fig. 2.7, respectively). This feature may have been observed for gas poor galaxies hosting (partial) winds (Trinchieri et al. 2008, Kim and Fabbiano 2003); for gas rich ETGs, instead, this profile is more centrally concentrated than observed (e.g., Loewenstein et al. 2001, Soria et al. 2006), a problem already known since when steady-state cooling flow models were proposed (Sarazin and White 1988). To obtain less peaked gas profiles, distributed mass dropouts were first invoked (Sarazin and Ashe 1989): if the flow is inhomogeneous, a fraction can condense out of it across the cooling region, where the cooling time t_{cool} is lower than the infall time $\lesssim t_{inf}$ (see also Pizzolato and Soker 2010). The mass accretion rate then decreases with decreasing radius, by up to $\sim$1 order of magnitude with respect to the homogeneous flow (Sarazin and Ashe 1989, Quataert and Narayan 2000). For the testcase ETG, within the central $\sim$1 kpc, $t_{cool} \lesssim 10^6$ yr, that is comparable/lower than the infall time (defined at each radius r as $t_{inf} = r/v$, where

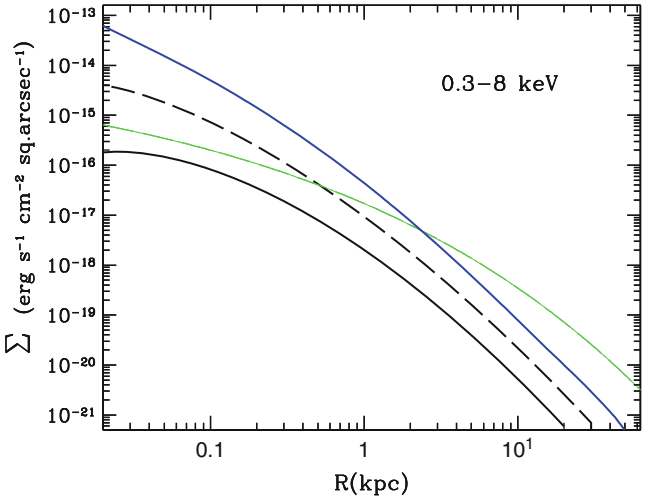

Fig. 2.7 The surface brightness profile for the model in Figs. 2.4–2.6 (*blue line*), and for two other models whose hydrodynamical quantities are shown in the next Fig. 2.8, with the same line type, all at an age of 13 Gyr. The *green line* follows the optical profile of the testcase ETG, and is normalized to the emission of unresolved X-ray binaries, as 20% of their total collective luminosity (the unresolved fraction is <25% for a sample of local ETGs observed with *Chandra*, excluding the very hot gas rich ones; Boroson et al. 2011), see the electronic version for a color version of this figure

v is the local flow velocity; see also Sect. 2.4 below), so that mass loss from the flow due to condensation is possible. However, after *Chandra* and *XMM*-Newton observations, evidence has accumulated for heating from the central MBH, and this phenomenon is likely to be a more straightforward explanation for the observed lack of very peaked profiles (e.g., Tabor and Binney 1993; see Sect. 2.4.2 below).

2.3.3.1 Variations in the Testcase ETG and in $L_{X,ISM}$

To illustrate how the flow properties can vary at fixed L_B and σ_c, three models have been run in all equal to the testcase ETG, except for small differences in the input parameters, within their observed variation for real ETGs. The main

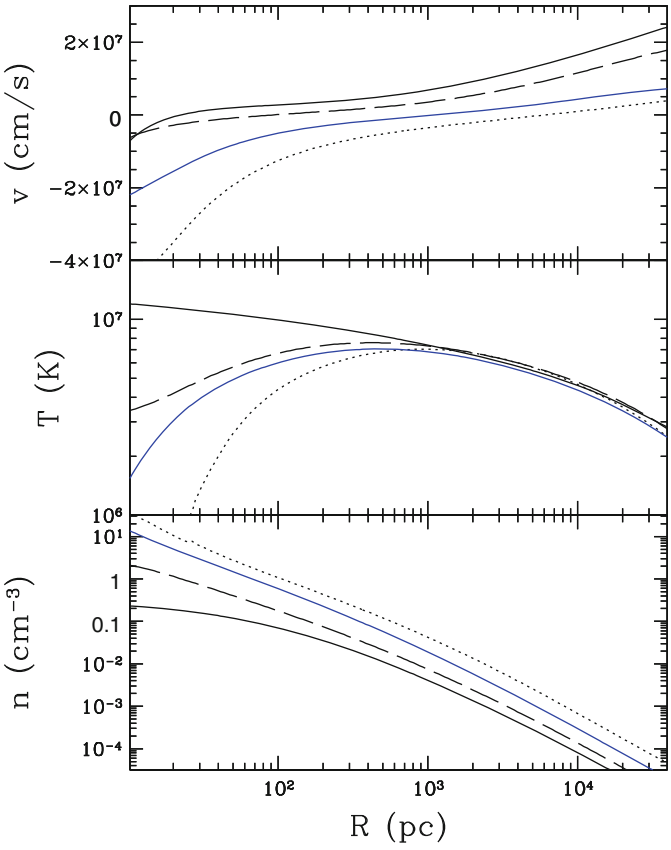

Fig. 2.8 Radial trend of the main hydrodynamical quantities at a galaxy age of 13 Gyr, for the testcase ETG in Fig. 2.5 (*blue lines*), and for three galaxy models with the same L_B and σ_c except for the following differences: a SNe Ia rate increased by 20% (*dashed line*); $n = 6$, $M_*/L_B = 6.1$ (*solid line*); $n = 4$, $M_*/L_B = 8.5$ (*dotted line*). The corresponding gas luminosities are respectively $L_{X,ISM} = 1.1 \times 10^{39}$, 4×10^{38}, 3.0×10^{40} erg s^{-1}. The brightness profiles of the models shown with a *dashed and solid line* are plotted in Fig. 2.7 (see Sect. 2.3.3)

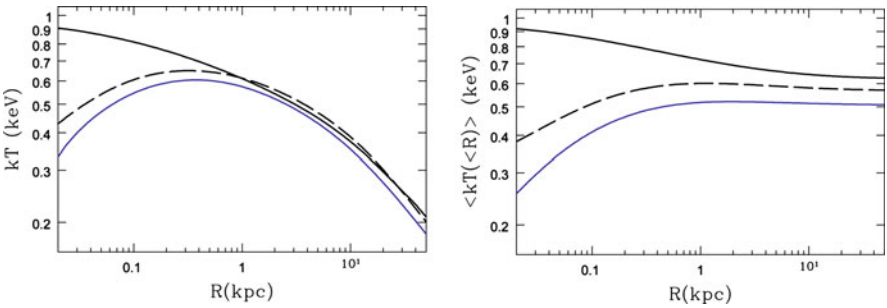

Fig. 2.9 *Left*: The emission-weighted and projected temperature at each radius R (*left*), and the same calculated within the radius R (*right*), for the testcase ETG (*blue line*) and two of the models in Fig. 2.8, with the corresponding line type, all at an age of 13 Gyr, see the electronic version for a color version of this figure

hydrodynamical quantities of the resulting flows at the end of the evolution are shown in Fig. 2.8, and the brightness profiles in Fig. 2.7. A model with a larger SNe Ia rate by 20% ends with a lower r_{st}, and $L_{X,ISM}$ ∼9 times lower (dashed line in Figs. 2.7 and 2.8). A model with $n = 6$ has a more peaked stellar density profile, a lower stellar mass ($M_*/L_B = 6.1$; Fig. 2.4) and then a lower mass loss rate and total mass; the flow is consequently less dense and hotter, less bound, ends with a temperature $T \sim 10^7$ K at the center (solid line), $L_{X,ISM}$ is ∼20 times lower than for the testcase ETG, the brightness profile is less peaked (Fig. 2.7). The third model has $n = 4$, a larger $M_*/L_B = 8.5$, a larger total mass, ends with a larger inflowing region, of lower temperatures and larger densities, so that its $L_{X,ISM}$ is ∼4 times that of the testcase ETG. Figure 2.9 shows the profile of the projected emission weighted temperature, and the profile of the average temperature calculated within radius R. The global emission weighted temperature is 0.5–0.6 keV, as typically observed for the L_B of the testcase ETG (e.g., David et al. 2006, Diehl and Statler 2008a, Humphrey and Buote 2006).

$L_{X,ISM}$ can then change by a factor of ∼80 (from 4×10^{38} to 3.0×10^{40} erg s^{-1}) just by assuming observed differences at fixed L_B in some galaxy properties; this already accounts for a substantial part of the observed $L_{X,ISM}$ range at $L_B = 5 \times 10^{10} L_{B,\odot}$ (Fig. 2.2). However, while the lowest observed $L_{X,ISM}$ are reproduced, the largest ones are not. By increasing the dark-to-stellar mass ratio to $\mathscr{R} = 5$ (corresponding to the baryon-to-total mass ratio of 1/6 of WMAP, Komatsu et al. 2009), still keeping $\mathscr{R}_e < 1$, and decreasing the SNe Ia rate by 20%, while leaving the fundamental galaxy parameters L_B, σ_c and R_e unchanged, the model flow can reach $L_{X,ISM} \sim 8 \times 10^{40}$. Some further deepening of the potential well, as an increase of σ_c, still keeping the galaxy model on the Fundamental Plane, is possible, obtaining a flow with an even larger $L_{X,ISM}$; however, values of $L_{X,ISM} >$ a few$\times 10^{41}$ erg s^{-1} cannot be reproduced (Pellegrini and Ciotti 1998). Accretion of external gas, then, or confinement by an external medium, are needed to explain the X-ray brightest galaxies of the $L_X - L_B$ diagram (Renzini et al. 1993, Brighenti and Mathews 1998, Helsdon et al. 2001, Sect. 2.3).

2.4 The Nuclear Scale

Accretion to the center is commonly present, though from a small region, for the models in Fig. 2.8; therefore, this Section explores what modifications to the flow are expected from the addition of a central MBH. Indeed, following the discovery that a MBH resides at the center of massive spheroids in the local universe (e.g., Ferrarese and Ford 2005), the investigation of the effects on the hot gas flow of accretion feedback due to the MBH has become a very active field of research (see also Ciotti and Ostriker, Statler, and Sarazin, this volume). Feedback from the MBH has been advocated to regulate star formation at early epochs, producing the observed galaxy mass function and colors (e.g., Croton et al. 2006), and to heat galactic flows in later epochs, suppressing QSO activity and preventing large and unobserved mass cooling rates (e.g., Omma et al. 2004, Churazov et al. 2005, Peterson and Fabian 2006, Ciotti and Ostriker 2007, Ciotti et al. 2010). It is now clear that MBH feedback is unavoidable on cosmological timescales; however, for timescales much shorter than the cosmological one, and closer to the present epoch, it is not fully understood yet how it works in detail. It is then interesting to consider a few basics aspects of the flow behavior for models with a central MBH but neglecting feedback, as: how the flow is affected by the MBH gravity, the similarity of the accretion flow with a Bondi flow, how much accretion energy is expected, and how the picture outlined in the previous Sections is modified.

2.4.1 Gravitational Heating from the MBH and Comparison with the Bondi Accretion

The addition to the mass model of the testcase ETG (Sect. 2.3.3) of a central gravitating mass $M_{BH} = 3.6 \times 10^8 M_\odot$, as predicted by the Magorrian relation, that remains constant with time, produces a flow that is not influenced by the MBH in the outer region; within the central $\sim$100 pc, instead, the infall velocity and the temperature become larger (Fig. 2.10), the density lower, and the mass inflow rate to the center $\dot{M}_{in}$ smaller (from 0.12 to 0.06 $M_\odot \text{year}^{-1}$ at a radius of 5 pc). The most relevant difference caused by the addition of the MBH is the higher gas temperature at the center; this is due to the heating of the gas produced by the sharp increase of the stellar velocity dispersion within the sphere of influence of the MBH (of radius of the order of $GM_{BH}/\sigma_c^2 = 20$ pc, where σ_c is the velocity dispersion without the MBH; Fig. 2.11), and by the compression of the gas caused by the gravity of the MBH. The MBH heating succeeds in "filling" the central "hole" in temperature of the model without MBH, and it may even be able to create a small central peak in the gas temperature (Fig. 2.10). The difference in central temperature takes more time to establish for models with larger central gas density (as that with $n = 4$ in Fig. 2.8), and it may even not take place within the present epoch. In models where the flow, without the MBH, keeps hot down to small radii (as that of the black solid

lines in Fig. 2.8), the change in temperature is far less dramatic (an increase by 25% of the central temperature), and $\dot{M}_{in}$ remains substantially unchanged at very small values ($\dot{M}_{in} \sim 10^{-4} - 10^{-3}\, M_{\odot}\mathrm{year}^{-1}$).

Another important property of the flow is the value of its velocity with respect to the sound velocity v_s, calculated for example for the adiabatic case ($\gamma = 5/3$; $v_s = \sqrt{\gamma kT/\mu m_p}$), and also shown in Fig. 2.10. Without a MBH, in cases of "cold" accretion as for the testcase ETG, the flow becomes supersonic close to the galactic center; with a MBH, accretion is hot and keeps subsonic, while the flow tends to reach the sound velocity at the innermost gridpoint (that, for this series of runs, has been put to 1 pc). In fact, in absence of momentum feedback, it is unavoidable for the flow to tend to the free fall velocity close to the MBH, where the potential energy per particle becomes larger than the thermal energy (and this is reproduced by the inner boundary condition of a vanishing thermodynamical pressure gradient).

The MBH heating also causes t_{cool} to become much larger than t_{inf} within the central $\sim$100 pc (Figs. 2.10). Both properties (the inflow velocity that tends to v_s, and $t_{cool} >> t_{inf}$) characterize also the Bondi (1952) solution for spherically symmetric accretion on a central point mass, from a nonrotating polytropic gas with given density and temperature at infinity, in the adiabatic case ($\gamma = 5/3$). This fact provides some support to a commonly used procedure to estimate the MBH mass accretion rate of ETGs (e.g., Loewenstein et al. 2001, Pellegrini 2005a, Soria et al. 2006), that is the use of the analytic Bondi (1952) formula, replacing infinity with a fiducial accretion radius $r_{acc} = 2GM_{BH}/v_s^2$ (Frank et al. 2002), and calculating v_s

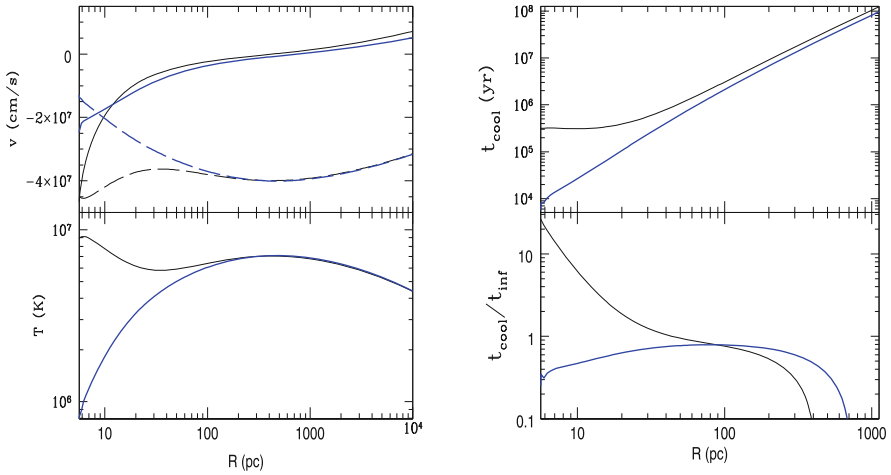

Fig. 2.10 *Left*: the velocity and temperature profiles for the testcase ETG of Sect. 2.3.3 (in *blue*), and for the same galaxy model with a central MBH of mass $3.6 \times 10^8 M_{\odot}$ added (in *black*), at an age of 13 Gyr; the *dashed lines* show $-v_s$ for $\gamma = 5/3$, for the two models respectively. *Right*: the cooling time and its ratio with the infall time, for the models on the left. See Sect. 2.4 for more details, see the electronic version for a color version of this figure

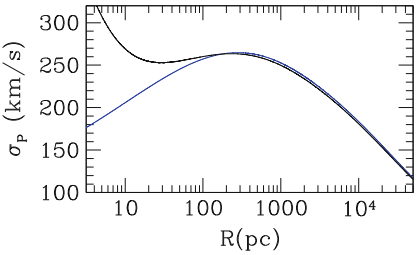

Fig. 2.11 The projected stellar velocity dispersion profile for the galaxy model of the testcase ETG (Sect. 2.3.3, *dotted line*), and for the same model with a central MBH of mass $3 \times 10^8 M_\odot$ discussed in Sect. 2.4 (*solid line*). Both models have an aperture velocity dispersion of 260 km s^{-1} within $R_e/8$, see the electronic version for a color version of this figure

as close as possible to the MBH. This is not a trivial aspect since there are additional ingredients in the galactic flow that are not included in the Bondi (1952) analysis, but are accounted for by the simulations, as: (1) the presence of mass and energy sources, as the stellar mass losses and the SNe Ia heating; (2) the possibility of cooling; (3) the fact that r_{acc} is not a true infinity point, since the gas experiences a pressure gradient there; (4) the contribution of the galactic potential added to that of the MBH. The simulations however have some limits too: for example, the discrete nature of the stellar distribution becomes important where the accretion time on the MBH ($t_{inf} \sim 10^4 - 10^5$ years from 10 pc, in the simulations) is comparable to (or lower than) the time required for the stellar mass losses to mix with the bulk flow (Mathews 1990, Parriott and Bregman 2008), or to the time elapsing between one SNe Ia event and the next (see also Tang and Wang 2010). Another limit is that some form of accretion feedback is also expected, as briefly outlined in the next Section.

2.4.2 The Importance of the Energy Output from Accretion

The mass inflow rates of the models in Fig. 2.8, with a central MBH added, range from $\dot{M}_{in} = 4 \times 10^{-4}$ (model with solid line) to 4×10^{-1} $M_\odot$year^{-1} (model with dotted line), at an inner gridpoint of 5 pc, at the present epoch. If totally accreted, the largest of these $\dot{M}_{in}$ releases an accretion power $L_{acc} \sim 0.1 \dot{M}_{in} c^2 = 2 \times 10^{45}$ erg s^{-1} (Frank et al. 2002), a large value that can have a significant impact on the surrounding hot ISM, depending on the fraction that can interact with the ISM and be transferred to it. L_{acc} is mostly in radiative form at high mass accretion rates; more precisely, the radiative efficiency of the accreting material can be written in a general way as $\epsilon = 0.2 \times 100\dot{m}/(1 + 100\dot{m})$, where $\dot{m} = \dot{M}_{in}/\dot{M}_{Edd}$ is the Eddington-scaled accretion rate, and $\dot{M}_{Edd} = L_{Edd}/0.1c^2 = 2.2 \times 10^{-8} M_{BH}\,(M_\odot)$ $M_\odot$year^{-1} (Ciotti et al. 2010). When $\dot{m} \gtrsim 0.01$, then $\epsilon \sim 0.1 - 0.2$, and L_{acc} is mostly in

radiative form; when $\dot{m} \ll 0.01$, then $\epsilon \sim 20\dot{m}$, as for radiatively inefficient accretion flows (Narayan and Yi 1995), and the radiative output becomes negligible. In the low-ϵ regime, the output of accretion may be dominated by a kinetic form (Blandford 1999, Körding et al. 2006, Allen et al. 2006, Merloni and Heinz 2007). For example, from the energy input by accretion feedback to the hot coronae of a few nearby ETGs, with $\dot{M}_{in}$ calculated using the Bondi rate as described in Sect. 2.4 and $\dot{m} \ll 0.01$, it was found that $\sim 1/5$ of L_{acc} is converted into jet power (Allen et al. 2006). The lowest $\dot{m}$ among the models in Fig. 2.8 is $\sim 10^{-4}$, and then accretion is highly radiatively inefficient, but the largest is $\dot{m} = 0.04$, so that a huge radiative output is expected. The same output must have been released in the past, when $\dot{M}_{in} \gtrsim 1\ M_{\odot}\mathrm{year}^{-1}$, due to the larger gas content and importance of inflows (Fig. 2.5).

At early epochs the two major channels of accretion energy output are then radiation and mechanical energy from AGN winds; the simulations show that these are able to heat the ISM, lead to degassing connected with nuclear outbursts, decrease the gas density in the central galactic regions and prevent large gas mass accumulations (Ciotti and Ostriker, this volume). With the secular decrease of $\dot{M}_*$ (Fig. 2.1), the nuclear outbursts become rarer and less strong, $\dot{M}_{in}$ decreases, and accretion switches to the radiatively inefficient regime. These findings agree with the observations that for a large sample of nearby galaxies with an old stellar population, drawn from the Sloan Digital Sky Survey, the MBH growth is regulated by the rate $\dot{M}_*$ (Kauffmann and Heckman 2009), and that ETGs of the local universe host nuclei of low luminosity or almost quiescent (Ho 2008, Pellegrini 2010). For a representative model with standard input parameter values, the duty cycle (the fraction of the time the AGN is in the "on" state) is of the order of 10^{-2}, for the past 5–7 Gyrs; outside the nuclear bursts, the flow behavior is similar to that described in Sect. 2.3 (Ciotti et al. 2010), with a major difference: the lower central gas density, due to the MBH heating (Pellegrini et al. 2011). This feature is shown for example by the brightness profiles in Fig. 2.12, obtained with the high resolution simulations with radiative and mechanical feedback of Ciotti et al. (2010), for a model similar to the testcase ETG (Sect. 2.3.3). At the present epoch the gas is inflowing within $\sim$100 pc, but with a $\dot{M}_{in}$ much lower ($\dot{m} \sim 10^{-4}$). The profiles in Fig. 2.12 have a variety of shapes, depending on the sources of heating and the presence of an external medium. The confining action of the latter determines an overall increase of the gas content, most noticeable in the outer profile. The effect of the jet heating is to make the brightness profile even flatter, decreasing the gas density significantly within the central few kpc. This kind of study may well require 2D simulations, but it is already clear that the profiles are much less centrally peaked than those in Sect. 2.3.3, as anticipated there, and likely more in agreement with observations.

In addition to this important (positive) effect on the surface brightness profile of the hot gas, how does AGN feedback modify the scenario outlined in the previous Sections? ETGs where $L_{SN} > L^{-}_{grav}$, and then already outflow-dominated, will

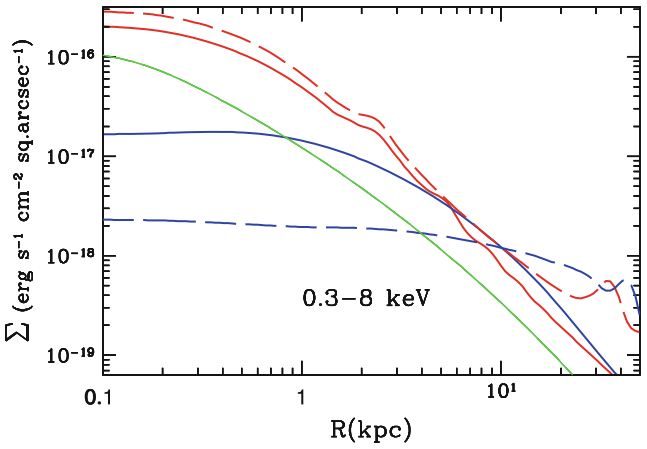

Fig. 2.12 Surface brightness profiles of the stellar emission (in *green*, corresponding to a Sérsic index $n = 6$ and arbitrarily normalized) and of the gas flows at an age of 12 Gyr, for an ETG with the same σ_c and L_B as the testcase ETG (Sect. 2.3.3), but with the radiative and mechanical feedback turned "on"; the mechanical heating is from AGN winds (*red lines*), and also from a jet (*blue lines*), with efficiency $\epsilon_{jet} = 0.1$ (see Ciotti and Ostriker, this volume; Sect. 2.4.2). The *solid lines* refer to an isolated galaxy, the *dashed* ones to models with a low density external medium, as that of the Virgo cluster at a distance of ∼0.5 Mpc from M87. $L_{X,ISM} = 1$ and 0.9×10^{40} erg s^{-1} for the *dashed and solid red* models respectively, and $L_{X,ISM} = 4 \times 10^{39}$ erg s^{-1} and 6×10^{39} erg s^{-1} for the *dashed and solid blue* models respectively

not be affected by further sources of heating. For the other ETGs, the answer depends on how much energy from accretion is transferred to the hot ISM: if this energy is $>>$ L_{SN} then the scenario above will be modified, while if it is $<<$ L_{SN} it will be preserved. In general, it can be noted that the gas modeling based on realistic stellar and dark mass profiles, stellar mass loss and supernova rates and their secular evolution, without accretion feedback can already reproduce reasonably well the fundamental gas properties (e.g., trend of $L_{X,ISM}$ with L_B, wide variation in $L_{X,ISM}$, average gas temperature), therefore such modeling must catch the bulk of the origin and evolution of the hot gas in ETGs. Moreover, even in the context of feedback modulated gas flow evolution, the hot gas content at the present epoch, seem still sensitive to the structural galaxy parameters, in the same sense as described in Sects. 2.2.3 and 2.3 (Ciotti and Ostriker, this volume; Pellegrini et al. 2011). Finally, the modeling without feedback – if any – shows the need for gas accretion from outside or confinement (Sect. 2.3); the nuclear energy input should then mostly readjust the internal gas structure, without causing major degassing at later epochs. The measure in which activity affects the gas content is yet to be established observationally; so far, exploiting *Chandra* resolution, it has just been shown that the nuclear X-ray luminosities of ETGs correlate only weakly with their gas luminosity (Pellegrini 2010).

2.5 Gas Flows and Galactic Shape, Rotation, Stellar Profile

In Sect. 2.3 it was shown how the gas content of an ETG is sensitive to changes regarding the stellar and dark mass components that are in fact allowed for by observations (see, e.g., the scatter around the fundamental scaling laws of ETGs), and by modeling (see, e.g., how model ETGs lying on the Fundamental Plane can be built with different $\mathscr{R}$ and β, Renzini and Ciotti 1993 and Sect. 2.3.3.1). This holds even at fixed L_B, so to account for a significant part of the large observed $L_{X,ISM}$ variation. Below we consider the effects on the hot gas content produced by additional variations in the galactic structure that are observed and have not been considered above, such as the galactic shape, the amount of rotation in the stellar motions, and the central stellar profile.

2.5.1 Galactic Shape and Rotation

Soon after the first large sample of ETGs with known X-ray emission was built from *Einstein* observations, it was found that the hot gas retention capability is related to the intrinsic galactic shape: on average, at any fixed $L_{\rm B}$, rounder systems show larger total X-ray emission $L_{\rm X}$ and $L_{\rm X}/L_{\rm B}$ than flatter elliptical and S0 systems (Eskridge et al. 1995). The relationship defined by $L_{\rm X}/L_{\rm B}$ is stronger than that defined by $L_{\rm X}$. Moreover, galaxies with axial ratio b/a close to unity span the full range of $L_{\rm X}$, while flat systems all have $L_{\rm X} \lesssim 10^{41}$ erg s^{-1} (see, e.g., Fig. 2.13). A similar result holds for the "diskiness" or "boxiness" property of ETGs, that measures the deviation of the isophotal shape from a pure elliptical one (Bender et al. 1989, Kormendy and Bender 1996). This property is described by the a_4/a parameter, in a way that disky ($a_4 > 0$) ETGs show isophotes distorted in the sense of a disk, and boxy ($a_4 < 0$) ETGs have isophotal distortions in the sense of a box. Disky systems are also generally flattened by rotation, while boxy ones have various degrees of velocity anisotropy (see also Pasquali et al. 2007). Boxy ETGs cover the whole observed range of $L_{\rm X}$, while disky ETGs are less X-ray luminous on average (Bender et al. 1989, Eskridge et al. 1995); this result is not produced only by disky galaxies having a lower average galactic luminosity, with respect to boxy ETGs, since it holds even in the range of L_B where the two types overlap (Pellegrini 1999b). The relationship between $L_{\rm X}$ and a_4/a was reconsidered, confirming the above trends, for the *ROSAT* PSPC sample (Ellis and O'Sullivan 2006).

There seems then to be a dependence of the hot gas content on the galactic shape, measured by either $\epsilon = 1 - b/a$ or a_4/a. Since flatter and disky systems also possess, on average, higher rotation levels (Fig. 2.14; Binney and Tremaine 1987), the influence on the hot gas of both the shape of the potential well and of the stellar rotation was called into question. The gas in ETGs that are in part rotationally supported may have a lower "effective" binding energy per unit luminosity compared to the gas in non-rotating ones (a lower effective $L^-_{grav}/L_{\rm B}$

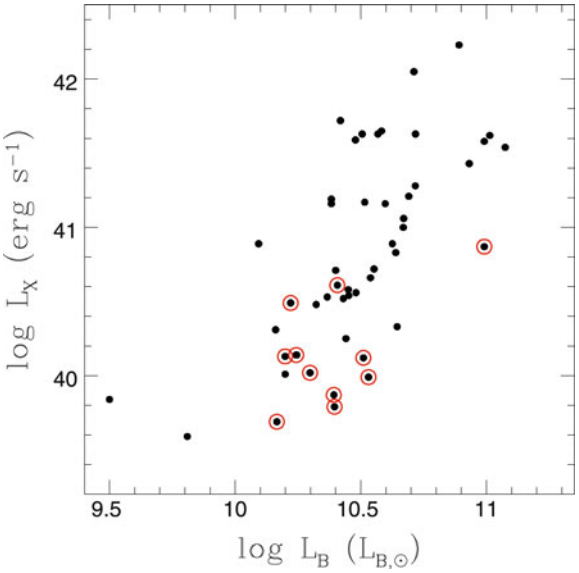

Fig. 2.13 The total X-ray emission (from *ROSAT* PSPC observations, O'Sullivan et al. 2001) versus the *galactic blue* luminosity L_B (from total B-magnitudes in the Hyperleda catalog and distances in O'Sullivan et al. (2001)) for a sample of ETGs with measured optical flattening and stellar rotation (Pellegrini et al. 1997). Galaxies with high flattening ($b/a < 0.6$, see Fig. 2.14) are marked with a *red circle* (see Sect. 2.5.1 for more details), see the electronic version for a color version of this figure

ratio, in the notation of Sect. 2.2.3; see also Sect. 2.5.1.1 below), and then rotating ETGs may be more prone to host outflowing regions. For this reason, the effects on L_X of the ellipticity ϵ of the stellar distribution and of stellar rotation were studied for a sample of 52 ETGs with known L_X, maximum rotational velocity of the stars v_{rot}, and central stellar velocity dispersion σ_c (Pellegrini et al. 1997). Figure 2.15 is an updated version of the results obtained, and shows L_X/L_B, a measure of the galactic hot gas content, versus v_{rot}/σ_c, an indicator of the importance of rotation. The gas content can be high only for values of $v_{rot}/\sigma_c \lesssim 0.4$, while modest or low gas contents, as $\log[L_X(\text{erg s}^{-1})/L_B(L_{B,\odot})] \lesssim 30.2$, are independent of the degree of rotational support. Recently, for the ETGs of the *SAURON* sample, the relationship between soft X-ray emission and rotational properties was investigated again (Sarzi et al. 2010), confirming that slowly rotating galaxies can exhibit much larger luminosities than fast-rotating ones. As for the axial ratio and the isophotal parameter a_4, the trend of L_X/L_B with v_{rot}/σ_c is not produced by the correlation between L_X and L_B: ETGs with high v_{rot}/σ_c cover substantially the same large range in L_B as the whole sample (Fig. 2.16).

In conclusion, rotation seems to have an effect similar to that of shape, and L_X and L_X/L_B show a similar trend with respect to axial ratio, diskiness, and rotation: their variation is large for round, boxy and slowly-rotating systems, while it keeps

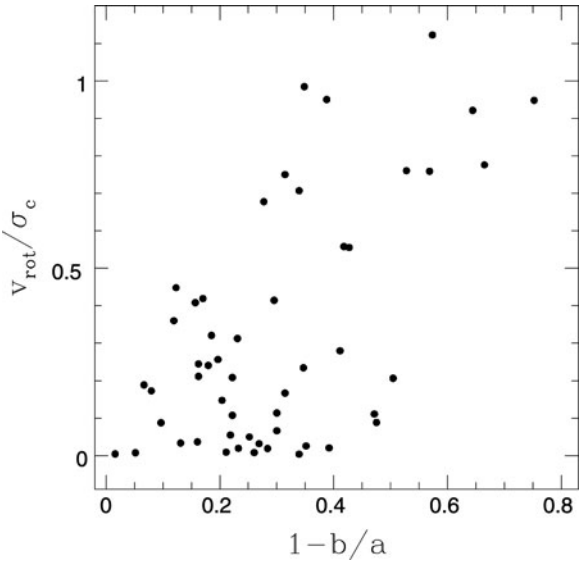

Fig. 2.14 The relation between $v_{\rm rot}/\sigma_{\rm c}$ and the ellipticity of the stellar light $\epsilon = 1 - b/a$, for a sample of ETGs with known X-ray emission, axial ratio b/a (from Hyperleda), $v_{\rm rot}$ and $\sigma_{\rm c}$ (from Pellegrini et al. 1997; see Sect. 2.5.1). Adapted from Pellegrini et al. (1997)

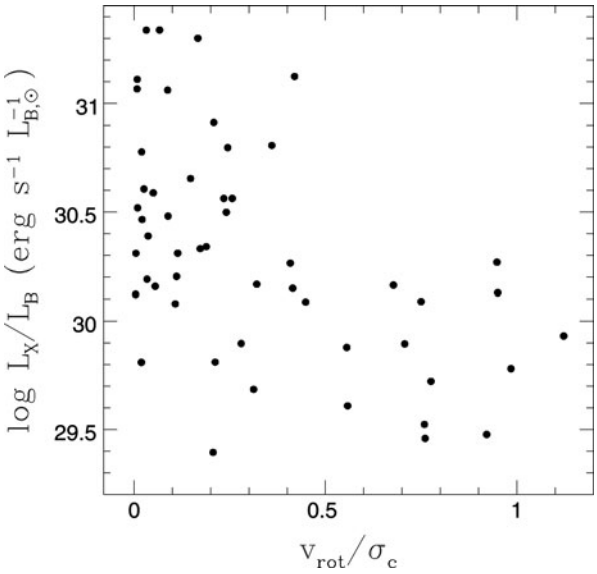

Fig. 2.15 The total X-ray emission normalized to the galactic blue luminosity L_B ($L_{\rm X}$ and $L_{\rm B}$ determined as in Fig. 2.13), versus the indicator of rotational support v_{rot}/σ_c, taken from Pellegrini et al. (1997). Figure adapted and updated from Pellegrini et al. (1997)

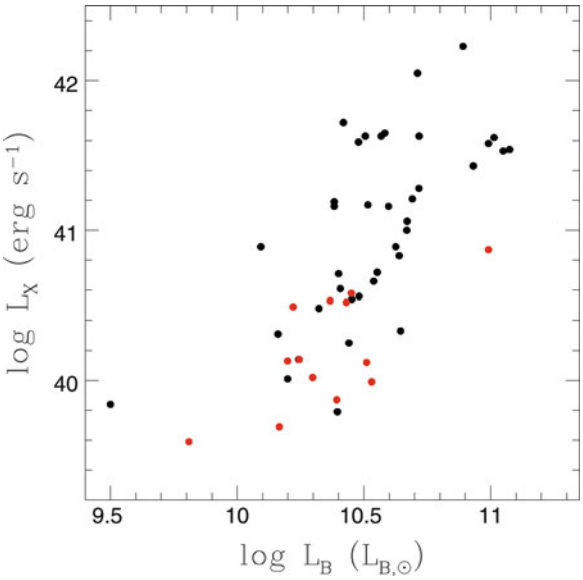

Fig. 2.16 The total X-ray emission versus the galactic luminosity L_B (both determined as in Fig. 2.13), for the sample of ETGs in the previous Fig. 2.15; galaxies with $v_{\rm rot}/\sigma_{\rm c} > 0.5$ are marked with a *red symbol* (see Sect. 2.5.1 for more details)

below a threshold for flatter, disky and high-rotation systems. From observations it remains then undecided which one between axial ratio, diskiness, and rotation is responsible for the trend; more insights is given by the theoretical and numerical analysis discussed below.

2.5.1.1 A Theoretical and Numerical Investigation

The impact of stellar rotation and galactic shape on the hot gas content was also addressed with theoretical and numerical studies (Ciotti and Pellegrini 1996, Brighenti and Mathews 1996, D'Ercole and Ciotti 1998). In principle, the lower gas content of flatter systems could be due to the mass distribution itself, or to a higher rotational level that decreases the effective potential. An analytic investigation showed that flatter systems are less able to retain hot gaseous halos than rounder ones of the same $L_{\rm B}$, due to the effect of the shape more than that of a larger rotational level (Ciotti and Pellegrini 1996). The investigation reconsidered the global estimate of the energy budget of the gas introduced in Sect. 2.2.3, generalizing it for flows in flat and rotating galaxy models. The classical scalar virial theorem for a stellar distribution interacting with a dark matter potential can be written as $2T + \Pi = |W|$, where Π and T are the kinetic energies associated

respectively with the stellar random[4] and ordered motions, and $|W|$ is the potential energy of the stellar component plus the virial interaction energy of the stars with the dark halo. For a fixed total mass and mass distribution (i.e., a fixed $|W|$), the amount of rotational streaming energy T can formally vary from zero to a maximum that depends on the galaxy structure (Ciotti and Pellegrini 1996); in the notation of Sect. 2.2.3, the power L_{rot} related to rotational streaming is $L_{rot} = \dot{M}_* T/M_*$, while that related to random motions is $L_\sigma = 0.5\dot{M}_* \Pi/M_*$. How does L_{rot} enter the energy budget of the gas, for example in (2.9), for a fixed $|W| = 2\,M_*\,(L_{rot} + L_\sigma)\,/\,\dot{M}_*$? In an extreme case, the whole effect of the ordered motion is to produce a change in the effective potential experienced by the gas, if for example the galactic corona is rotating with the same rotation velocity as the stars; in this case L_{rot} is to be subtracted from L^-_{grav}. In the opposite extreme case, all the kinetic energy of the gas, from random and from ordered motions, is eventually thermalized; then L_{rot} is to be added to L_{SN} and L_σ, in the denominator of (2.9). The real behavior, lying between the two extreme cases, can be parameterized re-writing (2.9) as

$$\frac{L^-_{grav} - \alpha L_{rot}}{L_{SN} + L_\sigma + (1-\alpha)L_{rot}} \tag{2.14}$$

with $0 \le \alpha \le 1$. If $\alpha = 0$, the thermalization of L_{rot} is complete, and since the kinetic energy of stellar motions ($L_\sigma + L_{rot}$) will be lower[5] than L_{SN}, then (2.14) coincides with (2.9). If instead $\alpha = 1$, there is no thermalization of L_{rot}, the decrease of L^-_{grav} is maximum, and the effect of rotation is maximum. However, it is found that the role of rotation remains minor, because it can change (2.14) by only a few per cent: the variation of (2.14), between the null and the maximum L_{rot} allowed by realistic galaxy models, is small, even for $\alpha = 1$ (<10%; Ciotti and Pellegrini 1996). Instead, variations of more significant amount that can make the gas significantly less bound (a decrease in L^-_{grav} of ∼20%) can be produced by a change in the galaxy structure, as a reasonable flattening of a round system at fixed $L_{\rm B}$. Therefore, S0s and non-spherical ellipticals are less able to retain hot gaseous haloes than are rounder systems of the same $L_{\rm B}$, and more likely to host outflowing regions.

The results of the purely energetical approach above were tested with numerical studies of gas flows. Two-dimensional simulations for oblate ETGs, with different amounts of ordered and disordered kinetic energies, were carried out for gas in the inflow state (Brighenti and Mathews 1996). In this investigation $L_{\rm X}$ is reduced in rotating models, because the gas cools on a disk before entering the galactic core region, and then L^+_{grav} (2.6) is reduced; since rotation increases on average with flatness, rotation would be the underlying cause of the X-ray underluminosity of flat

[4] In the notation used here and in Sect. 2.2.3, Π is twice the energy due to random motions.

[5] For a totally velocity dispersion supported galaxy, L_σ accounts for the whole energy input to the gas from the stellar motions, that is significantly lower than L_{SN} (Sect. 2.2.3, below (2.5)).

objects. However, the massive, rotationally supported, and extended cold disk that forms in the equatorial plane, due to mass and angular momentum conservation, and comparable in size to the effective radius, is not observed; also, the resulting X-ray images should be considerably flattened towards the equatorial plane out to an optical effective radius or beyond, a phenomenon that is small or absent (Hanlan and Bregman 2000). Other authors (D'Ercole and Ciotti 1998) performed two-dimensional numerical simulations of gas flows for flat systems, but allowing for the gas to be outflowing. The flows then developed a partial wind in flat ETGs that, if spherical, would be in inflow. In this way, the models accumulate negligible amounts of cold gas on a central disk. Rotation could also decrease the X-ray emission (of a factor of two or less), because it favoured the wind. In this scenario, then, flat models, rotating or not, can be significantly less X-ray luminous than spherical ones of the same $L_{\rm B}$, because they are in partial wind when the spherical ones are in inflow; rotation has an additional but less important effect.

2.5.2 The Central Stellar Profile

Hubble Space Telescope observations of the central parts of ETGs revealed that the brightness profiles of galaxies with $M_V \lesssim -19$ show either steep brightness cusps or, interior to a break radius (of typical size <500 pc), they flatten in a cuspy core with respect to an inner extrapolation of the outer profile (Lauer et al. 1995, Faber et al. 1997, Trujillo et al. 2004, Côté et al. 2006, Kormendy et al. 2009). Cores dominate at the highest luminosities and steep cusps at the lowest, with an intermediate luminosity region of coexistence ($-20.5 \geq M_V \geq -23$, Lauer et al. 2007). The inner shape of the brightness profile is related to the formation and evolution of galaxies, with cores likely created during dry merging events by a MBH binary ejecting stars from the center of the new system (Faber et al. 1997, Milosavljevic et al. 2000, Ebisuzaki et al. 2001, Graham 2004, Gualandris and Merritt 2008), and cusps being preserved or (re)generated during gaseous mergings, or nuclear AGN-induced starbursts (Ciotti and Ostriker 2007). The presence of steep cusps or cores correlates with other fundamental galactic properties: core ETGs are generally triaxial systems and slow rotators, with anisotropic velocity distributions, boxy isophotes, and a uniformely old stellar population formed quickly a long time ago; cusp ETGs are generally axisymmetric systems and fast rotators, with isotropic velocity distributions, disky isophotes and a younger (less α-enhanced) stellar population (Kormendy and Bender 1996, Faber et al. 1997). Given the differences in the general galactic properties, one interesting question is whether also the X-ray emission of core and cusp galaxies differ. In fact, core galaxies show a largely different hot gas content, and can be from hot gas poor to very gas rich, while cusp galaxies are confined to a moderate or low hot gas content (Fig. 2.17; Pellegrini 1999b, 2005b). Though core ETGs are more frequent at high $L_{\rm B}$, while cusp ones are more common at low $L_{\rm B}$, they still differ in their soft X-ray luminosities where both types are common, at $\log L_B(L_{B,\odot}) > 10$ (Fig. 2.17). A statistical analysis

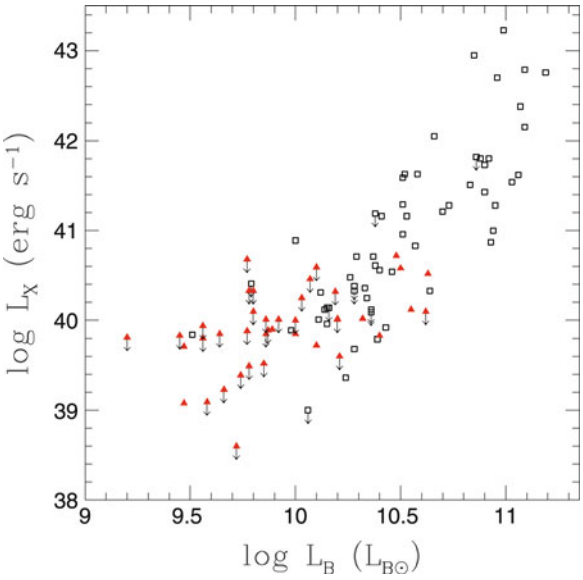

Fig. 2.17 The total X-ray emission versus the galactic luminosity L_B (from O'Sullivan et al. 2001), for ETGs with inner stellar profile classified of the cusp (*red triangles*) or core (*squares*) type by Lauer et al. (2007); *downward arrows* represent upper limits. Updated from Fig. 1 of Pellegrini (2005b), see the electronic version for a color version of this figure

indicates that the brightest cusp ETGs have lower L_X than would be expected from the best fit $L_X - L_B$ relation (Pellegrini 1999b, Ellis and O'Sullivan 2006), i.e., there seems to be an extra factor other than L_B influencing the X-ray luminosity and linked to the inner light profile as well.

Various hypotheses can be put forward for this extra-factor. The first one could be an effect by the light profile itself, but this conjecture is not supported by the results of hydrodynamical simulations for gas flows in ETGs with a luminosity distribution described by a Sérsic law, as observed for cusp ETGs (Côté et al. 2006, Kormendy et al. 2009). In fact, simulations with such a profile down to the smallest radius resolved by the numerical grid (e.g., Sect. 2.3.3) produce decoupled flows, with a central inflow; if any, the presence of a core (that is of an inner flattening of the stellar mass distribution, all the rest equal; e.g., Pellegrini 2010) would make this inflow less significant (Sect. 2.3.2), which would lower L_X and then produce an effect in the opposite direction with respect to what needed. The precise shape of the stellar profile within a radius as small as typical break radii is unlikely to be a driver of major differences in the hot gas content on the galactic scale; this agrees with the absence of an observed trend of L_X with the value of the inner slope of the stellar profile (Pellegrini 1999b, 2005b). A second hypothesis for this extra-factor, again related with the mass distribution but on a global scale, is instead more likely to produce a difference in L_X: cusp ETGs are typically more flattened than core ones of the same L_B (Kormendy and Bender 1996), and flatter systems are observed to be

systematically underluminous in X-rays with respect to rounder ones (Sect. 2.5.1), likely because the gas escape is favoured (Sect. 2.5.1.1).

Other factors presumably important in producing a different average gas content are related with the environmental properties of core and cusp ETGs. Cusp ETGs are preferentially found in the field, and core ones in higher density environments (Faber et al. 1997), where they are often centrally located. The latter position puts core systems in the most favorable conditions to retain the hot gas (Helsdon et al. 2001, Matsushita 2001); in fact, the highest L_X of core ETGs in Fig. 2.17 exceed the maximum L_X predicted by models for isolated galaxies (Sect. 2.3), but these core ETGs are in most cases central members of large groups, subclusters or clusters (Pellegrini 2005b).[6] The environment can contribute to produce the larger spread in L_X of core ETGs also for another reason: during their lifetime, galaxies in denser environments may undergo mutual encounters, close enough to gravitationally perturb their hot gas flows, with a variety of merging and/or tidal interaction conditions (time of the event during the galaxy history, progenitors masses and orbits, and so on); this has a variety of effects on the hot gas content. Two-dimensional, time-dependent hydrodynamical models investigated the impact of such perturbations for a number of representative cases, and found that although the tidal interaction lasts $\lesssim$1 Gyr, its effect extends over several Gyr, with the production of large spikes in the global X-ray luminosity of the gas (D'Ercole et al. 2000). The effect of merging on the hot gas content was instead investigated via an observational survey of the X-ray evolution of on-going mergers: the late stages were found to be underluminous in L_X compared with "normal" ETGs of the same L_B, and in general the remnants appear quite devoid of gas (Fabbiano and Schweizer 1995, Read and Ponman 1998, Brassington et al. 2007). Since to regenerate a massive ($\sim 10^9 - 10^{10} M_\odot$) hot halo through stellar mass losses requires a few Gyrs (Sect. 2.2), hot gas rich core ETGs must have had their last major merger many Gyrs ago.

Finally, the different average hot gas content of core and cusp ETGs was recently suggested to be the key to explain their different global galactic properties (Kormendy et al. 2009). It was proposed that a low hot gas content coupled with a weak AGN feedback could not prevent starbursts in ETGs that, following gaseous mergers, became disky with a central stellar cusp; on the contrary, a large hot gas content coupled with strong AGN feedback quenched starformation and made mergers dry in ETGs that then developed a core, boxy isophotes, anisotropic velocity distributions, and kept an old stellar population. In this context the gas is supposed to be heated by MBH-feedback in the radio (kinetic) mode (Sect. 2.4.2; see Sarazin, and Statler, this volume). Interestingly, the radio luminosity L_R shows the same behavior of the total soft X-ray emission with respect to the inner stellar light profile: cusp ETGs are confined below a threshold in L_R, while core ones span a large range of L_R (Bender et al. 1989, Capetti and Balmaverde 2005, Pellegrini

[6]The inner light profiles of central cluster galaxies are for the vast majority of core type, with cusp profiles only in 10% of the cases (Laine et al. 2003).

2010). Core systems can then reach the highest L_R and possess a conspicuous radio activity cycle, while in cusp galaxies the radio emission keeps smaller, likely because of a rapid jet failure due to the lack of a dense confining medium, or a smaller duty cycle (Pellegrini 2010 and references therein).

Acknowledgements I acknowledge support from the Italian Ministery of Education, University and Research (MIUR) through the Funding Program PRIN 2008.

References

D.M. Acreman, I.R. Stevens, T.J. Ponman, I. Sakelliou, MNRAS **341**, 1333 (2003)
S.W. Allen et al., MNRAS **372**, 21 (2006)
A. Athey, J. Bregman, J. Bregman, P. Temi, M. Sauvage, ApJ **571**, 272 (2002)
R. Bender, P. Surma, S. Doebereiner, C. Moellenhoff, R. Madejsky, A&A **217**, 35 (1989)
M. Bernardi, R.K. Sheth, J.B. Annis et al., AJ **125**, 1866 (2003)
G. Bertin, T. Toniazzo, ApJ **451**, 111 (1995)
J. Binney, S. Tremaine, *Galactic Dynamics* (Princeton University Press, Princeton, NJ, 1987)
R.D. Blandford, M.C. Begelman, MNRAS **303**, L1 (1999)
H. Bondi, MNRAS **112**, 195 (1952)
B. Boroson, D.W. Kim, G. Fabbiano, ApJ **729**, 12 (2011)
N.J. Brassington, T.J. Ponman, A.M. Read, MNRAS **377**, 1439 (2007)
J.N. Bregman, J.R. Parriott, ApJ **699**, 923 (2009)
F. Brighenti, W.G. Mathews, ApJ **470**, 747 (1996)
F. Brighenti, W.G. Mathews, ApJ **495**, 239 (1998)
B.A. Brown, J.N. Bregman, ApJ **539**, 592 (2000)
A. Capetti, B. Balmaverde, A&A **440**, 73 (2005)
M. Cappellari, R. Bacon, M. Bureau et al., MNRAS **366**, 1126 (2006)
E. Cappellaro, R. Evans, M. Turatto, A&A **351**, 459 (1999)
E. Churazov, S. Sazonov, R. Sunyaev, W. Forman, C. Jones, H. Böhringer, MNRAS **363**, L91 (2005)
L. Ciotti, A. D'Ercole, S. Pellegrini, A. Renzini, ApJ **376**, 380 (1991)
L. Ciotti, S. Pellegrini, MNRAS **255**, 561 (1992)
L. Ciotti, S. Pellegrini, MNRAS **279**, 240 (1996)
L. Ciotti, J.P. Ostriker, ApJ **665**, 1038 (2007)
L. Ciotti, J.P. Ostriker, D. Proga, ApJ **717**, 708 (2010)
P. Côté et al., ApJS **165**, 57 (2006)
D.J. Croton, V. Springel, S.D.M. White et al., MNRAS **365**, 11 (2006)
L.P. David, W. Forman, C. Jones, ApJ **359**, 29 (1990)
L.P. David, W. Forman, C. Jones, ApJ **369**, 121 (1991)
L.P. David, C. Jones, W. Forman, I.M. Vargas, P. Nulsen, ApJ **653**, 207 (2006)
R.L. Davies, G. Efstathiou, S.M. Fall, G. Illingworth, P.L. Schechter, ApJ **266**, 41 (1983)
A. D'Ercole, L. Ciotti, ApJ **494**, 535 (1998)
A. D'Ercole, L. Ciotti, S. Recchi, ApJ **533**, 799 (2000)
S. Diehl, T.S. Statler, ApJ **668**, 150 (2007)
S. Diehl, T.S. Statler, ApJ **680**, 897 (2008a)
S. Diehl, T.S. Statler, ApJ **687**, 986 (2008b)
T. Ebisuzaki, J. Makino, T.G. Tsuru et al., ApJ **562**, L19 (2001)
S.C. Ellis, E. O'Sullivan, MNRAS **367**, 627 (2006)
P.B. Eskridge, G. Fabbiano, D. Kim, ApJ **442**, 523 (1995)
G. Fabbiano, ARA&A **27**, 87 (1989)

G. Fabbiano, F. Schweizer, ApJ **447**, 572 (1995)
S.M. Faber, J.S. Gallagher, ApJ **204**, 365 (1976)
S.M. Faber, S. Tremaine, E.A. Ajhar et al., AJ **114**, 1771 (1997)
A.C. Fabian, C.R. Canizares, Nature **333**, 829 (1988)
L. Ferrarese, H. Ford, Space Sci. Rev. **116**, 523 (2005)
A. Finoguenov, C. Jones, ApJ **547**, L107 (2001)
W. Forman, P. Nulsen, S. Heinz et al., ApJ **635**, 894 (2005)
J. Frank, A. King, D. Raine, *Accretion Power in Astrophysics* (Cambridge University Press, Cambridge, 2002)
Y. Fukazawa, J.G. Botoya-Nonesa, J. Pu, A. Ohto, N. Kawano, ApJ **636**, 698 (2006)
A.W. Graham, ApJ **613**, L33 (2004)
L. Greggio, A&A **441**, 1055 (2005)
L. Greggio, MNRAS **406**, 22 (2010)
A. Gualandris, D. Merritt, ApJ **678**, 780 (2008)
P.C. Hanlan, J.N. Bregman, ApJ **530**, 213 (2000)
S.F. Helsdon, T.J. Ponman, E. O'Sullivan, D.A. Forbes, MNRAS **325**, 693 (2001)
L.C. Ho, ARA&A **46**, 475 (2008)
P.J. Humphrey, D.A. Buote, ApJ **639**, 136 (2006)
T.E. Jeltema, B. Binder, J.S. Mulchaey, ApJ **679**, 1162 (2008)
G. Kauffmann, T.M. Heckman, MNRAS **397**, 135 (2009)
D.W. Kim, G. Fabbiano, ApJ **586**, 826 (2003)
D.W. Kim, E. Kim, G. Fabbiano, G. Trinchieri, ApJ **688**, 931 (2008)
E.G. Körding, R.P. Fender, S. Migliari, MNRAS **369**, 1451 (2006)
E. Komatsu, J. Dunkley, M.R. Nolta et al., ApJS **180**, 330 (2009)
J. Kormendy, R. Bender, ApJ **464**, L119 (1996)
J. Kormendy, D.B. Fisher, M.E. Cornell, R. Bender, ApJS **182**, 216 (2009)
S. Laine, R.P. van der Marel, T.R. Lauer et al., AJ **125**, 478 (2003)
T.R. Lauer et al., AJ **129**, 2138 (1995)
T.R. Lauer, et al., ApJ **664**, 226 (2007)
W. Li, et al., MNRAS **412**, 1473 (2011)
M. Loewenstein, W.G. Mathews, ApJ **319**, 614 (1987)
M. Loewenstein, R.F. Mushotzky, L. Angelini, K.A. Arnaud, E. Quataert, ApJ **555**, L21 (2001)
J. MacDonald, M.E. Bailey, MNRAS **197**, 995 (1981)
F. Mannucci, M. Della Valle, N. Panagia, E. Cappellaro, G. Cresci, R. Maiolino, A. Petrosian, M. Turatto, A&A **433**, 807 (2005)
D. Maoz, F. Mannucci, W. Li, A.V. Filippenko, M. Della Valle, N. Panagia, MNRAS **412**, 1508 (2011)
C. Maraston, MNRAS **362**, 799 (2005)
W.G. Mathews, AJ **97**, 42 (1989)
W.G. Mathews, ApJ **354**, 468 (1990)
K. Matsushita, ApJ **547**, 693 (2001)
E. Memola, G. Trinchieri, A. Wolter, P. Focardi, B. Kelm, A&A **497**, 359 (2009)
A. Merloni, S. Heinz, MNRAS **381**, 589 (2007)
M. Milosavljevic, D. Merritt, A. Rest, F.C. van den Bosch, MNRAS **331**, L51 (2000)
R. Nagino, K. Matsushita, A&A **501**, 157 (2009)
N.R. Napolitano, A.J. Romanowsky, M. Capaccioli et al., MNRAS **411**, 2035 (2010)
R. Narayan, I. Yi, ApJ **452**, 710 (1995)
J.F. Navarro, C.S. Frenk, S.D.M. White, ApJ **490**, 493 (1997)
H. Omma, J. Binney, G. Bryan, A. Slyz, MNRAS **348**, 1105 (2004)
E. O'Sullivan, D.A. Forbes, T.J. Ponman, MNRAS **328**, 461 (2001)
E. O'Sullivan, T.J. Ponman, R.S. Collins, MNRAS **340**, 1375 (2003)
J.R. Parriott, J.N. Bregman, ApJ **681**, 1215 (2008)
A. Pasquali, F.C. van den Bosch, H.-W. Rix, ApJ **664**, 738 (2007)
S. Pellegrini, E.V. Held, L. Ciotti, MNRAS **288**, 1 (1997)

S. Pellegrini, L. Ciotti, A&A **333**, 433 (1998)
S. Pellegrini, A&A **343**, 23 (1999a)
S. Pellegrini, A&A **351**, 487 (1999b)
S. Pellegrini, MNRAS **364**, 169 (2005b)
S. Pellegrini, ApJ **624**, 155 (2005a)
S. Pellegrini, A. Baldi, D.W. Kim, G. Fabbiano, R. Soria, A. Siemiginowska, M. Elvis, ApJ **667**, 731 (2007)
S. Pellegrini, L. Ciotti, J.P. Ostriker, ApJ in press (arXiv:1107.3675) (2011)
S. Pellegrini, ApJ **717**, 640 (2010)
S. Pellegrini, ApJ **738**, 57 (2011)
J.R. Peterson, A.C. Fabian, PhR **427**, 1 (2006)
F. Pizzolato, N. Soker, MNRAS **408**, 961 (2010)
E. Quataert, R. Narayan, ApJ **528**, 236 (2000)
A.M. Read, T.J. Ponman, MNRAS **297**, 143 (1998)
A. Renzini, L. Ciotti, ApJ **416**, L49 (1993)
A. Renzini, L. Ciotti, A. D'Ercole, S. Pellegrini, ApJ **419**, 52 (1993)
R.P. Saglia, G. Bertin, M. Stiavelli, ApJ **384**, 433 (1992)
C.L. Sarazin, R.E. White III, ApJ **320**, 32 (1987)
C.L. Sarazin, R.E. White III, ApJ **331**, 102 (1988)
C.L. Sarazin, G.A. Ashe, ApJ **345**, 22 (1989)
M. Sarzi, J.C. Shields, K. Schawinski et al., MNRAS **402**, 2187 (2010)
K. Sharon, A. Gal-Yam, D. Maoz et al., ApJ **718**, 876 (2010)
J. Shen, K. Gebhardt, ApJ **711**, 484 (2010)
R. Soria, G. Fabbiano, A.W. Graham, A. Baldi, M. Elvis, H. Jerjen, S. Pellegrini, A. Siemiginowska, ApJ **640**, 126 (2006)
M. Sun, C. Jones, W. Forman, A. Vikhlinin, M. Donahue, G.M. Voit, ApJ **657**, 197 (2007)
M. Sun, G.M. Voit, M. Donahue, C. Jones, W. Forman, A. Vikhlinin, ApJ **693**, 1142 (2009)
G. Tabor, J. Binney, MNRAS **263**, 323 (1993)
S. Tang, Q.D. Wang, Y. Lu, H.J. Mo, MNRAS **392**, 77 (2009)
S. Tang, Q.D. Wang, MNRAS **408**, 1011 (2010)
J. Tonry, A. Dressler, J.P. Blakeslee et al., ApJ **546**, 681 (2001)
G. Trinchieri, S. Pellegrini, G. Fabbiano et al., ApJ **688**, 1000 (2008)
I. Trujillo, P. Erwin, A.A. Ramos, A.W. Graham, AJ **127**, 1917 (2004)
A.M. Weijmans, M. Cappellari, R. Bacon et al., MNRAS **398**, 561 (2009)

Chapter 3
Feedback and Environmental Effects in Elliptical Galaxies

Craig L. Sarazin

Abstract The role of the environment of an elliptical galaxy on its hot interstellar gas is discussed. In general, the X-ray halos of early-type galaxies tend to be smaller and fainter in denser environments, with the exception of group-central galaxies. X-ray observations show many examples of nearby galaxies which are undergoing gas stripping. On the other hand, most bright galaxies in clusters do manage to retain small coronae of X-ray emission. Recent theoretical and observational results on the role of feedback from AGN at the centers of elliptical galaxies on their interstellar gas are reviewed. X-ray observations show many examples of X-ray holes in the central regions of brightest-cluster galaxies; in many cases, the X-ray holes are filled with radio lobes. Similar radio bubbles are seen in groups and individual early-type galaxies. "Ghost bubbles" are often seen at larger radii in clusters and galaxies; these bubbles are faint in high radio frequencies, and are believed to be old radio bubbles which have risen buoyantly in the hot gas. Low frequency radio observations show that many of the ghost bubbles have radio emission; in general, these long wavelength observations show that radio sources are much larger and involve greater energies than had been previously thought. The radio bubbles can be used to estimate the total energy output of the radio jets. The total energies deposited by radio jets exceed the losses from the gas due to radiative cooling, indicating that radio sources are energetically capable of heating the cooling core gas and preventing rapid cooling.

C.L. Sarazin (✉)
Department of Astronomy, University of Virginia, P.O. Box 400325, Charlottesville, VA 22904-4325, USA
e-mail: sarazin@virginia.edu

D.-W. Kim and S. Pellegrini (eds.), *Hot Interstellar Matter in Elliptical Galaxies*, Astrophysics and Space Science Library 378, DOI 10.1007/978-1-4614-0580-1_3,
© Springer Science+Business Media, LLC 2012

3.1 Introduction

In this chapter, I will review some aspects of the interaction of the hot gas in elliptical galaxies with other physical elements in or around the galaxies. First, the interaction of the hot gas with external aspects of the environment of the elliptical will be discussed. I will concentrate on the question of whether the X-ray luminosity and gas mass of the hot interstellar medium (ISM) in ellipticals is affected by the environment. Is there more or less hot gas and X-ray emission associated with ellipticals in dense as compared to sparse environments? I will also review some of the evidence that gas in ellipticals is stripped by ram pressure due to motions through the external intergalactic gas.

The second major topic is the interaction of the hot gas in ellipticals with the active galactic nuclei (AGNs) often located at their centers. I will describe X-ray and radio evidence for this interactions, and discuss whether the AGNs can heat the X-ray gas and keep it from cooling rapidly. I will discuss evidence for feedback linking the activity by the center supermassive black hole (SMBH) and the heating and cooling of the X-ray gas. I will include both brightest cluster galaxies (BCGs) at the centers of cool core clusters of galaxies, and non-central giant ellipticals. In addition to a general review, I will present some more recent results on sound waves and shocks generated by the radio sources in the BCG in Abell 2052, the extended system of X-ray cavities and tunnels and low frequency radio emission in the BCG in Abell 262, and the southwest radio lobe in Centaurus A, the nearest bright elliptical and nearest radio galaxy.

3.2 Environmental Effects on X-ray Emission

3.2.1 X-ray Luminosity vs. Density

Given the wide range in X-ray luminosities of early-type galaxies of a given optical luminosity, the question naturally arises as to whether part of this dispersion might be due to the effects of environment on their X-ray emission. In particular, are galaxies in dense environments more or less X-ray luminous than galaxies in sparse environments?

One difficulty is deciding what observational probe to use to assess the local density. The best choice physically depends on the mechanism for changing the X-ray luminosity one wishes to consider (e.g., tidal stripping, ram pressure stripping, etc.) Ideally, one should do the comparison for a number of different density measures. Unfortunately, it is difficult to determine the intergalactic gas density in sparse regions. As a result, the galaxy density is often used as a proxy for the density of all forms of matter. In most cases, there is insufficient data to reconstruct the three dimensional galaxy distribution, and the projected galaxy density is used instead. Of course, the fact that a galaxy is projected against a region

of high galaxy projected density is no guarantee that it is actually located in a high density region.

Another complication arises from the fact that current hot gas content of an early-type galaxy probably depends on its history, rather than only on its current location. At the expected stellar mass loss rates, it may require a long time to replenish gas which was removed in the past.

Another issue is separating the X-ray emission from an individual galaxy from that due to the surrounding group or cluster. The higher spatial resolution of Chandra and XMM-Newton observations have helped to separate galaxy and group emission. However, in earlier observations of group-central early-type galaxies, the group emission was often included in the flux of the galaxy. Also, group-central galaxies are often brighter than other optically similar galaxies, and studies have reached very different conclusions depending on whether such galaxies are included or not.

Finally, if one is interested in the hot gas content of elliptical galaxies, one must remove the contribution from a central AGN or X-ray binaries and other stellar sources. The high resolution of Chandra observations has been particularly useful for this.

White and Sarazin (1991) suggested that elliptical galaxies in dense environments were fainter than those in sparse regions. Figure 3.1 illustrates their result, which indicated that X-ray luminous early-type galaxies had fewer neighboring bright galaxies in projection. Their work was based on Einstein observations of early-type galaxies. The local density was characterized by the projected galaxy density in the region around the target galaxy. They suggested that this correlation was due to ram pressure stripping of gas from galaxies (see Sect. 3.2.3 below).

A study of pairs of galaxies based on ROSAT data also found that the galaxies were generally underluminous compared to isolated galaxies (Henriksen and Cousineau 1999). It is unlikely that this is due to ram pressure stripping, but it might be due to tidal effects. A recent Chandra study of galaxies in groups also found an anti-correlation of local density and emission (Jeltema et al. 2008).

An XMM-Newton study of galaxies in the Coma cluster found that, on average, they were 5.6 times less luminous than similar galaxies in lower density locations (Finoguenov et al. 2004); this result was confirmed by a smaller Chandra study of Coma (Hornschemeier et al. 2006). In general, Chandra studies of galaxies in clusters (e.g., Smith 2003, Sun et al. 2007) also seem to confirm a general anti-correlation of local density and X-ray luminosity. In these dense and complex regions, a reduction in the gas mass might be due to ram pressure stripping, viscous or evaporative stripping, gravitational effects, mergers, or some other mechanism.

Alternatively, using ROSAT data Brown and Bregman (2000) argued that early-type galaxies in dense regions were more luminous. They suggested that the hot galactic gas in denser groups was confined by the pressure of intergalactic gas. Their sample included a number of group-central ellipticals; in these systems, it can be uncertain as to what fraction of the emission is due to galactic or group gas.

A number of other studies of the relation between X-ray luminosity and local density based on ROSAT data found no correlation (e.g., O'Sullivan et al. 2001, Helsdon et al. 2001, Ellis and O'Sullivan 2006). Helsdon et al. (2001) studied

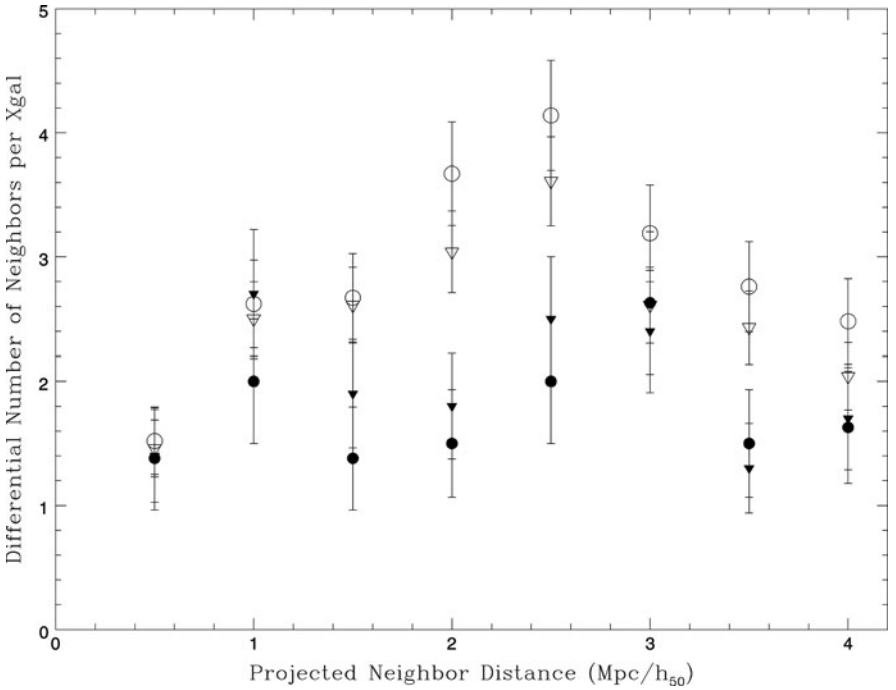

Fig. 3.1 Distribution of the number of bright galaxy neighbors around galaxies with X-ray detections or limits as a function of the projected distance from the X-ray galaxy. This figure is adapted from Fig. 13 of White and Sarazin (1991). The *filled circles (triangles)* are for galaxies with higher than average X-ray luminosities (triangles include upper limits). The *open circles and triangles* are for usually faint X-ray galaxies

galaxies in groups. They separated group and galaxy emission. Group-central early-type galaxies were highly overluminous, and they argued that some of the earlier correlations were driven by the inclusion of these galaxies or of group X-ray emission. They found a significant scatter of X-ray luminosities for a fixed optical luminosity, but no variation with local density.

Recently, Mulchaey and Jeltema (2010) found that the X-ray – optical relationship was steeper for field early-type galaxies than group or cluster galaxies. They suggested that optically faint galaxies in low density environments have their hot gas removed by winds driven by either supernovae or AGNs, and that these outflows are suppressed in regions with denser intergalactic gas. On the other hand, they argued that some galaxies in dense environments have their gas removed by ram pressure stripping, and that this occurs for both massive and low mass galaxies.

At the other end of the range of galactic environments, Memola et al. (2009) studied of four very isolated elliptical galaxies with Chandra, XMM-Newton, and/or ASCA. They found that these galaxies showed a very wide range of X-ray–to–optical luminosity ratios, suggesting that environment alone cannot account for all

of the dispersion in the X-ray properties of ellipticals. They suggest that age may play an important role.

3.2.2 Temperature Gradients vs. Environment

Diehl and Statler (2008) found that the temperature gradient in the outer parts of elliptical galaxies correlated positively with the projected density of galaxies. Galaxies in dense regions had positive gradients, while galaxies in sparse regions had negative temperature gradients. This might be due to intergalactic gas, which might confine the galactic gas, or add to it by inflow, or heat it by thermal conduction.

3.2.3 Ram Pressure Stripping of Hot Gas from Early-Type Galaxies

The environments of elliptical galaxies tend to be denser regions than average, and in many cases have significant amounts of intergalactic gas. This is particularly true in clusters of galaxies. Clusters and groups have significant dark matter halos, which give large masses and deep gravitational potential wells. Thus, most of the galaxies in clusters and rich groups move rather rapidly through the cluster the intergalactic gas, either as a result of their individual orbits or the motions of merging subclusters. The rapid motions through the intracluster gas imply that a large ram pressure from the intergalactic gas will act on the interstellar gas of these galaxies, and may strip the gas (Gunn and Gott 1972). Gunn and Gott considered the stripping of gaseous disks from galaxies, and much of the subsequent work was considered the stripping of disks. However, for ellipticals it is more interesting to consider the stripping of spherical or ellipsoidal halos of hot gas. Then, an approximate condition for stripping in a spherical galaxy is that the ram pressure satisfy

$$P_{\rm ram} \equiv \rho_{\rm IGM} v^2 \gtrsim 2 \frac{G M_{\rm gal}(r) \rho_{\rm ISM}(r)}{r} , \tag{3.1}$$

where $\rho_{\rm IGM}$ and $\rho_{\rm ISM}$ are the mass density of the intergalactic gas and galaxy gas halo, respectively, v is relative velocity of the galaxy and intergalactic gas, $M_{\rm gal}$ is the mass of the galaxy, and r is the radius from the center of the galaxy (Sarazin 1979, McCarthy et al. 2008). Acreman et al. (2003) made a series of simulations of ram pressure stripping of spherical galaxies falling into clusters of galaxies. In addition to ram pressure tails, their simulation showed contact discontinuities ("cold fronts") at the leading edges of the galaxies. Recently, McCarthy et al. (2008) calculated an extensive grid of hydrodynamic simulations of the ram pressure stripping of spherical hot gas halos from galaxies due to ram pressure. They found that a parameterized version of (3.1) when combined with a simple parameterized

expression for the time scale for stripping reproduced the simulations quite well. Other numerical simulations have confirmed this basic conclusion (e.g., Quilis et al. 2000, Roediger and Bruggen 2008), although most of the simulations have been done for spiral galaxies.

Gas stripping can be affected and increased by related transport processes in clusters of galaxies. Viscosity and turbulence may affect the stripping of gas from early-type galaxies (Nulsen 1982). Nulsen found that the time scale for laminar viscous stripping and stripping due to turbulence is given roughly by

$$t_{\rm vs} \approx \frac{4R}{3v} \left(\frac{\rho_{\rm ISM}}{\rho_{\rm IGM}} \right) \left(\frac{12}{\rm Re} + 1 \right)^{-1} , \tag{3.2}$$

where R is the radius of the galaxy, and Re is the Reynolds number of the flow. This can be faster than ram pressure stripping. However, one caution is that the viscous stresses may saturate, since the mean free paths of ions are similar to the sizes of galaxies. Moreover, both viscosity and turbulence may be reduced by the magnetic field.

For early-type galaxies in hot clusters of galaxies, thermal evaporation due to heat conduction may also help to strip any interstellar gas. If one ignores the temperature of the hot interstellar gas, the galaxy gravitational potential, cooling, and full Spitzer (1956) conduction, the rate of stripping is given approximately by Cowie and Songaila (1977)

$$\dot{M}_{\rm ev} \approx \frac{16\pi\mu m_p \kappa R}{25\,k} \approx 700 \left(\frac{T_{\rm ICM}}{10^8\ {\rm K}} \right)^{5/2} \left(\frac{R}{20\ {\rm kpc}} \right) \left(\frac{\ln \Lambda}{40} \right)^{-1} M_\odot\ {\rm yr}^{-1} , \tag{3.3}$$

where μm_p is the mean mass per particle, T is the temperature of the intracluster gas, κ is the thermal conductivity, and $\ln \Lambda$ is the Coulomb logarithm (Spitzer 1956). The evaporation rate will be significantly reduced if the conductivity saturates, as is probably the case at least for disk galaxies. Unfortunately, thermal conductivity also depends critically on the magnetic field geometry. If the conductivity is not suppressed by the magnetic field, this mechanism can play an important role in stripping gas from galaxies.

There is a simple connection between mass loss by evaporation and mass loss by laminar viscosity (the Re term in (3.2)), as pointed out by Nulsen (1982). At low velocities, the viscous term dominates, and the viscous stripping rate is nearly independent of velocity, because the Reynolds number is proportional to velocity. Since both thermal conduction and ionic viscosity are transport processes and the ion and electron mean free paths are essentially equal, the rates of stripping from these two processes are simply related:

$$\dot{M}_{\rm ev} \approx 3.5 \dot{M}_{\rm vs} . \tag{3.4}$$

This expression assumes full Spitzer thermal conduction and viscosity (Spitzer 1956).

Bruggen and De Lucia (2008) used the results from the Millennium Simulation of large scale structure to determine the ram pressure histories of galaxies in clusters. They found that $\gtrsim 64\%$ of the galaxies in clusters today should have experienced strong ram pressures ($>10^{-11}$ dyn cm^{-2}) and thus should have undergone strong gas loss.

The Innsbruck group Domainko et al. e.g., 2006 has made very detailed simulations of the stripping of galaxies in clusters and the effect this has on the abundances of the intracluster medium (ICM). They argue that ram pressure stripping accounts for $\sim 10\%$ of the metals in the ICM, and that stripping should produce complex patterns of stripes and plumes in abundance maps of clusters.

3.2.3.1 Features Due to Ram Pressure Stripping

There are several characteristic features in X-ray images of elliptical galaxies which are expected as a result of ram pressure stripping. First, one expects a tail of hot gas behind the galaxy if the galaxies motion has a significant component in the plane of the sky. Typically, the gas from within the galaxy will be cooler and have higher metallicities than the intergalactic gas through which the galaxy is moving. Thus, the tail will be cooler and and more metal-rich that the nearby intergalactic gas. Since the gas in the tail will tend to be close to pressure equilibrium with the surrounding gas, the density in the cool ram pressure tails will be higher than that of the intergalactic gas. Thus, the tails are expected to be regions of enhanced X-ray surface brightness.

Unless instabilities lead to rapid mixing the the galactic and intergalactic gas, one would expect a sharp contact discontinuity at the front of the galaxy in the direction of its relative motion. This contact discontinuity separates galactic and intergalactic gas. Again, the galactic gas will generally be cooler and more metal-rich, so this contact discontinuity will separate cooler and more metal-rich gas (the inner galactic gas) from hotter, lower abundance gas (the outer intergalactic gas). For this reason, these contact discontinuities are called "cold fronts" (Vikhlinin et al. 2001). A schmatic diagram of a cold front is shown in Fig. 3.2. The discontinuities associated with ram pressure stripping of galaxies are the analogs of the cold fronts associated with subclusters in merging clusters of galaxies (Markevitch et al. 2000, Vikhlinin et al. 2001). For a very comprehensive review of this subject, see Markevitch and Vikhlinin (2007).

Because cold fronts are contact discontinuities rather than shocks, the pressure varies continuously across the center of the cold front. This means that the cooler inner gas will be much denser than the hotter intergalactic gas. Since the X-ray emissivity of a gas depends on the square of its density, this implies that cold fronts will be very strong discontinuities in X-ray surface brightness. Thus, these features tend to be very noticeable in X-ray images.

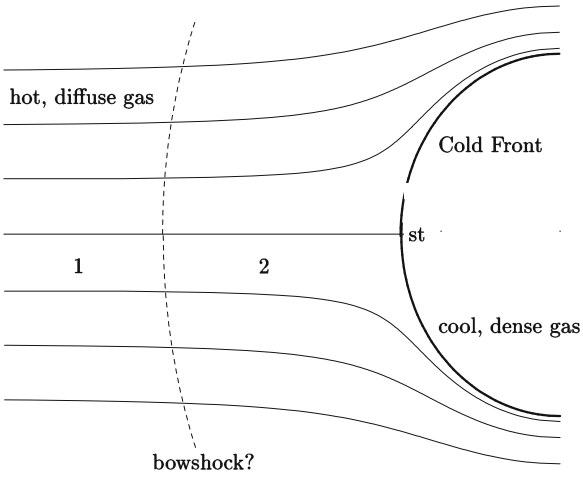

Fig. 3.2 A schematic diagram of flow around a "cold front". The *heavy solid arc* at the right represents the contact discontinuity between the cold, dense galactic gas, and the hotter, more diffuse intergalactic gas. The galaxy is moving toward the left relative to the hotter gas. The *narrow solid lines* are streamlines of the flow of the hotter gas around the cold core. The region labelled "1" represent the upstream, undisturbed hot gas. If the cold front is moving transonically (Mach number $\mathscr{M} > 1$), then the cold front will be preceded by a bow shock, which is shown as a *dashed arc*. The stagnation point, where the relative velocity of the cooler dense gas and hotter diffuse gas is zero, is marked "st"

As discussed extensively in Vikhlinin et al. (2001), Markevitch and Vikhlinin (2007), the variation in the density, pressure, and temperature of the gas in a cold front can be used to determine the relative velocity of cool core. The geometry is illustrated in Fig. 3.2, which is drawn in the rest frame of the cool core. We assume that the cool core has a smoothly curved, blunt front edge. The normal component of the flow of hot gas past the surface of the cool core will be zero. There will be at least one point where the flow is perpendicular to the surface of the cool core, and the flow velocity of the hot gas will be zero at this stagnation point ("st" in Fig. 3.2). Far upstream, the flow of the hot gas will be undisturbed at the velocity of the cool core relative to the hotter gas, v_1. Let c_{s1} be the sound speed in this upstream gas, and $\mathscr{M} \equiv v_1/c_{s1}$ be the Mach number of the motion of the cool core into the upstream gas. If $\mathscr{M} > 1$, a bow shock will be located ahead of the cold front.

The ratio of the pressure at the stagnation point to that far upstream is given by (e.g., Landau and Lifshitz 1959, Sect. 114)

$$\frac{P_{\rm st}}{P_1} = \begin{cases} \left(1 + \frac{\gamma-1}{2}\mathscr{M}^2\right)^{\frac{\gamma}{\gamma-1}} , & \mathscr{M} \le 1 , \\ \mathscr{M}^2 \left(\frac{\gamma+1}{2}\right)^{\frac{\gamma+1}{\gamma-1}} \left(\gamma - \frac{\gamma-1}{2\mathscr{M}^2}\right)^{-\frac{1}{\gamma-1}} , & \mathscr{M} > 1 . \end{cases} \tag{3.5}$$

Here, $\gamma = 5/3$ is the adiabatic index of the gas. The ratio $(P_{\rm st}/P_1)$ increases continuously and monotonically with $\mathscr{M}$. Thus, in principle, measurements of P_1 and $P_{\rm st}$ in the hot gas could be used to determine $\mathscr{M}$. The pressures would be determined from X-ray spectra and images. In practice, the emissivity of the hot gas near the stagnation point is likely to be small. However, the pressure is continuous across the cold front, so the stagnation pressure can be determined just inside of the cool core, where the X-ray emissivity is likely to be much higher. Once $\mathscr{M}$ has been determined, the velocity of the encounter is given by $v_1 = \mathscr{M} c_{s1}$.

If the motion of the cold front is transonic ($\mathscr{M} > 1$), one would also expect to see a bow shock front ahead of the cold front. This would be a second surface brightness discontinuity in the X-ray image. Unlike a cold front, in a bow shock the gas density, temperature, pressure, and entropy would all increase. Unfortunately, bow shock fronts are much less prominent in X-ray images than cold fronts.

The variation in the hydrodynamical properties across a bow shock are determined by the standard Rankine–Hugoniot jump conditions (e.g., Landau and Lifshitz 1959, Sect. 85). Let the subscripts 1 and 2 denote the preshock and postshock gas; thus, $v_1 = v_s$ is the longitudinal velocity of material into the shock (or alternative, the speed with which the shock is advancing into the preshock gas). The jump conditions can be rewritten as:

$$\begin{aligned} \frac{P_2}{P_1} &= \frac{2\gamma}{\gamma+1}\mathscr{M}^2 - \frac{\gamma-1}{\gamma+1} \\ \frac{v_2}{v_1} = \frac{\rho_1}{\rho_2} &\equiv \frac{1}{C} = \frac{2}{\gamma+1}\frac{1}{\mathscr{M}^2} + \frac{\gamma-1}{\gamma+1}\,, \end{aligned} \tag{3.6}$$

where P is the gas pressure, ρ is the gas density, v is the velocity, and $C \equiv \rho_2/\rho_1$ is the shock compression. These expressions can be used to determine the Mach number and speed of a galaxy relative to the intergalactic medium.

If the bow shock can be traced to a large transverse distance and forms a cone, the opening angle of this Mach cone corresponds to the Mach angle, $\theta_M \equiv \csc^{-1}(\mathscr{M})$. This expression could also be used to determine the galaxy Mach number (Sarazin 2002). However, variations in the cluster gas temperature may lead to distortions in this shape.

The bow shock will be located at some distance ahead of the cold front. The distance between the stagnation point and the closest point on the bow shock (the shock "stand-off" distance d_s) can also be used to estimate the Mach number of the motion of the cold front (Vikhlinin et al. 2001, Markevitch and Vikhlinin 2007). The ratio of d_s to the radius of curvature of the cold front $R_{\rm cf}$ depends on the Mach number $\mathscr{M}$ and on the shape of the cold front. Figure 3.3 shows the values of $d_s/R_{\rm cf}$ as a function of $(\mathscr{M}^2-1)^{-1}$ for a spherical cold front (Schreier 1982). The stand-off distance increases as the Mach number approaches unity; thus, this method is, in some ways, a very sensitive diagnostic for the Mach number for the low values which often occur with galaxies in groups or clusters.

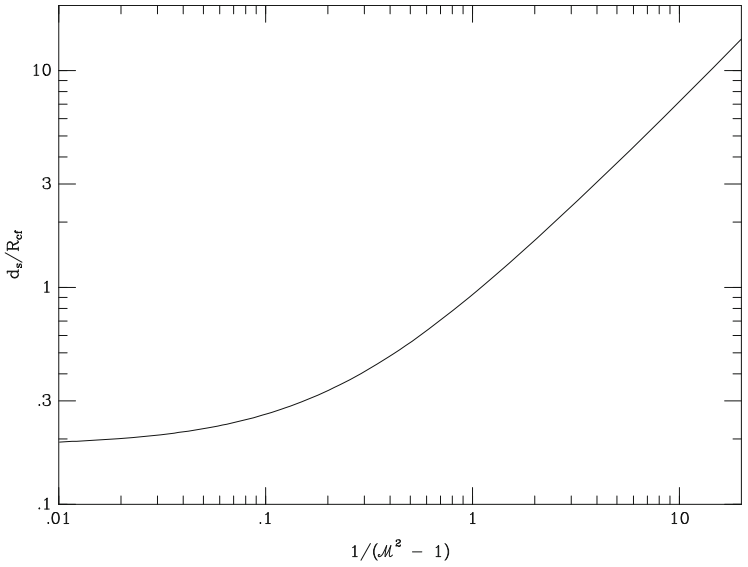

Fig. 3.3 The ratio of the stand-off distance of the bow shock d_s to the radius of curvature $R_{\rm cf}$ of the stagnation region of the cold front, as a function of $1/(\mathcal{M}^2-1)$, where $\mathcal{M}$ is the Mach number. This is for a spherical cold front and $\gamma = 5/3$

3.2.3.2 Examples of Ram Pressure Stripping

Observations of several elliptical galaxies in nearby clusters show evidence for ram pressure stripping.

One of the most prominent X-ray tails associated with ram pressure stripping occurs in the Virgo cluster galaxy NGC 4406 (M86) (Forman et al. 1979, Rangarajan et al. 1995, Randall et al. 2008). It shows a plume to the north, which breaks up into two tails. The total projected length of the plume and tails is 150 kpc. Based on the velocities in the systems, Randall et al. (2008) suggest that the true length is likely to be at least 380 kpc. The total mass of hot gas in the plume and tails exceeds that with the galaxy by a factor of ∼3, indicating that most of the gas from the galaxy is being stripped. Randall et al. (2008) suggest that the position of the plume and the double tails are due to the asymmetric gravitational potential of this galaxy.

The galaxy NGC 4472 (M49) is probably the most luminous galaxy in the Virgo cluster. It is at the center of a group which appears to be falling into the cluster from the south. It shows an extended tail to the southwest, which is probably due to ram pressure (Irwin and Sarazin 1996, Biller et al. 2004, Kraft et al. 2010). Figure 3.4 show the ROSAT X-ray image of NGC 4472 (Irwin and Sarazin 1996). The tail extends at least 36 kpc in projection, and probably at least 100 kpc in three dimensions. There is a sharp bow-shaped surface brightness discontinuity (a cold front) ∼21 kpc to the north of the galaxy (Irwin and Sarazin 1996, Biller et al. 2004, Kraft et al. 2010); XMM-Newton spectra indicate that this feature is a contact

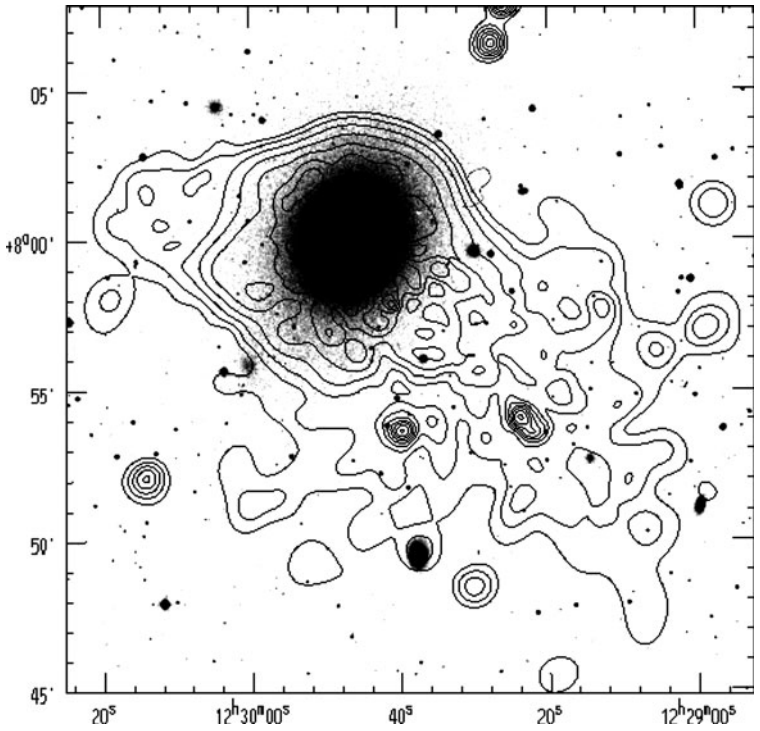

Fig. 3.4 Contours show the ROSAT PSPC+HRI image of the bright elliptical galaxy NGC 4472, adapted from Irwin and Sarazin (1996). The *grey-scale* is the optical image. Note the bow-shock/contact discontinuity feature to the north, and the ram pressure tail to the southwest

discontinuity between the interstellar gas of NGC 4472 and the Virgo intracluster gas (Kraft et al. 2010). The corresponding bow shock is not seen. Another unusual feature is that the cold front (to the north) is not 180° from the tail (to the southwest). Which of these two features represents the true direction of infall of NGC 4472 into the Virgo clusters? Irwin and Sarazin (1996) suggested that NGC 4472 is moving to the north (the direction suggested by the cold front) and that the direction of the tail is affected by the ellipsoidal potential of the galaxy. Alternatively, Kraft et al. (2010) recently argued that NGC 4472 is moving to the northeast as suggested by the direction of the tail, and that location and shape of the cold front are affected by more complex dynamics and by gas motions behind the cold front.

Another Virgo elliptical, NGC 4552 (M89), also shows a ram pressure tail of hot gas (Machacek et al. 2006). It has a cold front as well. It appears to be moving rather rapidly relative to the Virgo cluster gas ($v \approx 1680\,\mathrm{km\,s^{-1}}$, Mach number $\mathscr{M} \approx 2.2$).

NGC 7619 in the Pegasus I group has a long X-ray tail, indicating that it is undergoing ram pressure stripping (Trinchieri et al. 1997, Kim et al. 2008). The high iron abundance in the tail indicates that it came from the galaxy, rather than being a galactic wake, for example. On the opposite side of the galaxy from the tail, there

is a discontinuity in the X-ray surface brightness (Kim et al. 2008, Randall et al. 2009), which may be associated with a jump in temperature as well. This feature is consistent with a slightly supersonic shock (Mach number ∼1), indicating that the galaxy is moving at ∼500 km s^{-1} relative to the intergalactic gas. NGC 7619 is one of two dominant galaxies in the group; the other, NGC 7676, has a cold front which is antiparallel to that of NGC 7619. This suggests that the motions producing the ram pressure on NGC 7619 are due to a merger of two subgroups centered on these two galaxies (Randall et al. 2009).

Some other galaxies with possible ram pressure tails include NGC 1404 in the Fornax cluster (Machacek et al. 2005, Scharf et al. 2005), NGC 1265 in the Perseus cluster (Sun et al. 2005), NGC 1603 in the NGC 1600 group (Sivakoff et al. 2004), NGC 4783 in the NGC 4782 group (Machacek et al. 2007), 4C34.16 (Sakelliou et al. 1996), and C153 in the Abell 2125 cluster (Wang et al. 2004).

3.2.3.3 Cluster Ellipticals Retain Small Coronae

Despite the efficiency of stripping, most bright early-type galaxies in clusters do retain small coronae (Vikhlinin et al. 2001, Sun et al. 2007). Vikhlinin et al. (2001) found that the two D galaxies near the center of the Coma cluster each retain a small corona with a temperature of 1–2 keV, a radius of ∼3 kpc, and a gas mass of $\sim 10^8\ M_\odot$. They suggested that the corona were maintained by a balance between radiative cooling and highly attenuated thermal conduction.

NGC 3309 and NGC 3311, two giant elliptical galaxies near the center of the Abell 1060 cluster have small coronae similar to those in Coma (Yamasaki et al. 2002). The gas at the outer edge of these coronae is in pressure equilibrium with the intracluster gas.

Sun et al. (2005) detected small coronae around four early-type galaxies in the northwest subcluster of Abell 1367. The two larger ellipticals (NGC 3837 and NGC 3842) had larger symmetrical coronae while the two less optically luminous galaxies (NGC 3841 and CGCG 97090) had smaller, disturbed, asymmetric coronae. This indicates that larger galaxies are better able to retain their gas in clusters. Comparisons with other clusters suggested that the coronae get smaller and fainter in X-rays as the ICM pressure increases.

Sun et al. (2007) surveyed 157 early-type galaxies in 25 hot clusters. Most had small coronae; this was true of >60% of galaxies brighter than L^*, the characteristic luminosity of galaxies. The coronae around ellipticals in hot clusters are generally smaller (∼2 kpc in radius), cooler (temperatures ∼1 keV), less luminous in X-rays, and have smaller gas masses ($\sim 10^7\ M_\odot$) than the halos around galaxies in sparser environments, indicating that most of the gas has been stripped. However, these elliptical do retain coronae against the effects of ram pressure, thermal conduction, and input from AGN outbursts (Sect. 3.3 below). Remarkably, these coronae are smaller then the mean-free-path of particles in the ICM, indicating that magnetic fields must retard diffusion. To avoid being evaporated, thermal conduction must be suppressed by at least two orders of magnitude compared to the Spitzer value

(Spitzer 1956). The cooling times of the gas in these small but dense coronae are short, making these systems miniature versions of cluster cool cores around brightest cluster galaxies. The short cooling time implies that the gas would cool quickly; its presence in many cluster ellipticals indicates that there is a heat source to maintain the gas.

X-ray coronae with short cooling times are a common feature of radio AGNs associated with group or cluster galaxies (Sun 2009). When these galaxies are the brightest cluster galaxies (BCGs) at the centers of clusters, the gas forms a cool core in the cluster. When these galaxies are not located in the centers of clusters, the cool cores are the small coronae associated with individual ellipticals.

3.3 AGN Feedback in Early-Type Galaxies

In recent years, evidence has been found for a coupling between supermassive black holes (SMBHs) in the centers of galaxies, and their galaxy hosts. First, the masses of the SMBHs are proportional to the bulge mass of the host, suggesting that star formation and SMBH accretion are connected, and that stellar bulges and SMBHs grow together (e.g., Magorrian et al. 1998, Tremaine et al. 2002). Second, the optical/IR luminosity function of galaxies falls below that expected for dark matter halos at high masses in a way that can be understood if AGN suppress star formation in massive galaxies (e.g., Croton et al. 2006).

Finally, less gas cools to low temperatures at the centers of cool core clusters, groups, and individual ellipticals than expected unless something heats the gas, and AGNs are the leading candidates (see for review Peterson and Fabian 2006, McNamara and Nulsen 2007). In cool core clusters, the central cooling time is less than $\sim 7 \times 10^9$ years, and often is as short as $\sim 10^8$ years (e.g., Hudson et al. 2010). These cool core clusters have positive temperature gradients in their centers, which are consistent with the ICM cooling down to $\sim$1/3 of its initial temperature. Yet, the spectra indicate that $\lesssim$5% of this gas continues to cool down to low temperatures (e.g., Peterson and Fabian 2006). Although there are several other possibilities, the leading candidate for the required heat source is energy input from the central SMBH. In fact, the BCGs at the centers of cool core clusters are, in almost every known case, radio galaxies.

3.3.1 Radio Bubbles in BCGs in Clusters

Chandra and XMM-Newton observations have provided dramatic evidence for the interaction of these radio sources with the intracluster gas. In cool core clusters, X-ray deficits ("radio bubbles") have been found at the locations of the lobes of the radio sources associated with the brightest cluster galaxies (e.g., Fabian et al. 2006, Blanton et al. 2001). Figure 3.5 shows the central region of the BCG in the

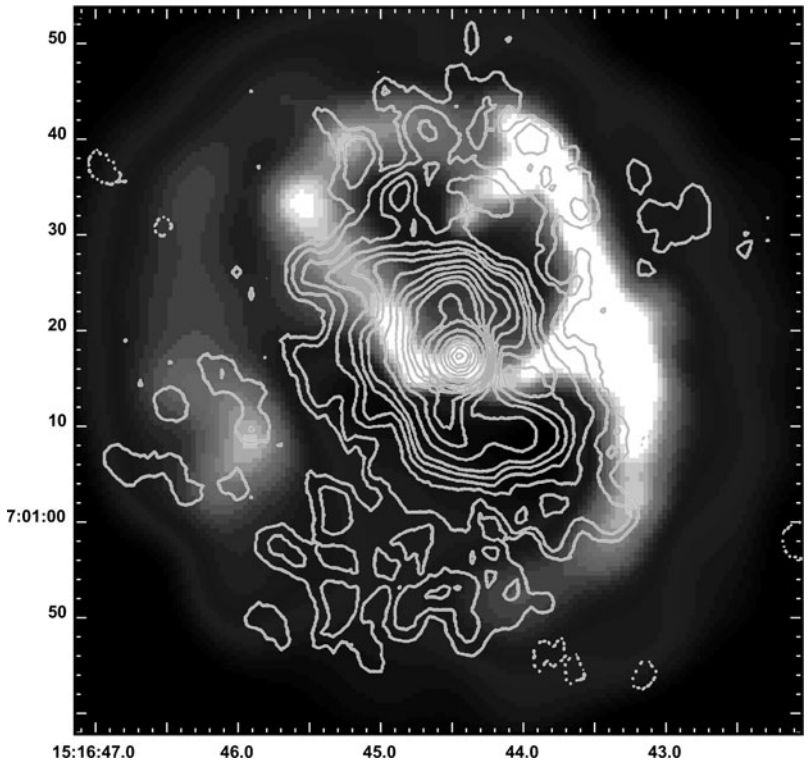

Fig. 3.5 Greyscale is the Chandra X-ray image of the BCG in the cool core cluster Abell 2052, showing holes in the X-ray emission surrounded by bright rims (Blanton et al. 2001, 2003). The contours are the radio emission which fills the X-ray holes. This figure is adapted from Blanton et al. (2001)

Abell 2052 cluster in X-rays and radio (Blanton et al. 2001, 2003). In the X-ray, these radio bubbles generally show two holes in the X-ray surface brightness on opposite sides of the galaxy nucleus. In most cases, the holes are surrounded by bright shells of X-ray emission. The X-ray holes correspond to the lobes of the central radio source. For the systems with a relatively simple geometry, deprojection analysis indicates that the X-ray surface brightness in the holes is consistent with foreground and background cluster emission; that is, the holes appear to be empty of X-ray emitting gas. The masses of X-ray gas in the surrounding shells are consistent with the mass which is missing from the holes (Blanton et al. 2003). All of this is in accord with a picture in which the central radio source has sent out two jets, which have been stopped in the cooling core gas. The jets have inflated two lobes, and the radio plasma has displaced the X-ray gas and compressed it into the two surrounding shells. In a few cases, similar radio bubbles were seen originally with ROSAT (Sarazin et al. 1992, Bohringer et al. 1993, Huang and Sarazin 1998, Rizza et al. 2000). The most spectacular case, in terms of the details in the observations,

is the Perseus cluster, where there is a very long Chandra total exposure (Fabian et al. 2006). The properties of radio bubbles are reviewed in McNamara and Nulsen (2007).

X-ray spectral observations show that the X-ray bright shells around radio bubbles are generally cool, and that the pressures in these shells are similar to those of the surrounding hotter gas. This indicates that these shell are not due to shocks, and that the radio sources are not expanding very supersonically. However, a few clusters have been found in which the radio lobes are surrounded by shells of hot gas, indicating that the radio sources are driving moderately strong shocks. Examples include MS0735.6+7421 (McNamara et al. 2005) which is shown in Fig. 3.6, Hydra A (Nulsen et al. 2005), and Her A (Nulsen et al. 2005).

For the majority of the bubbles which are expanding subsonically or mildly transonically, the pressure within the bubbles must be comparable to the pressure in the X-ray gas external to the bubbles. For the sources with supersonic expansion, the internal pressures must be even higher. However, when the pressures in the radio lobes are estimated by the standard minimum energy or equipartition arguments, they are found to be ∼20 times smaller than required in most cases (e.g., Blanton et al. 2003). This indicates that we have not identified the primary energy content

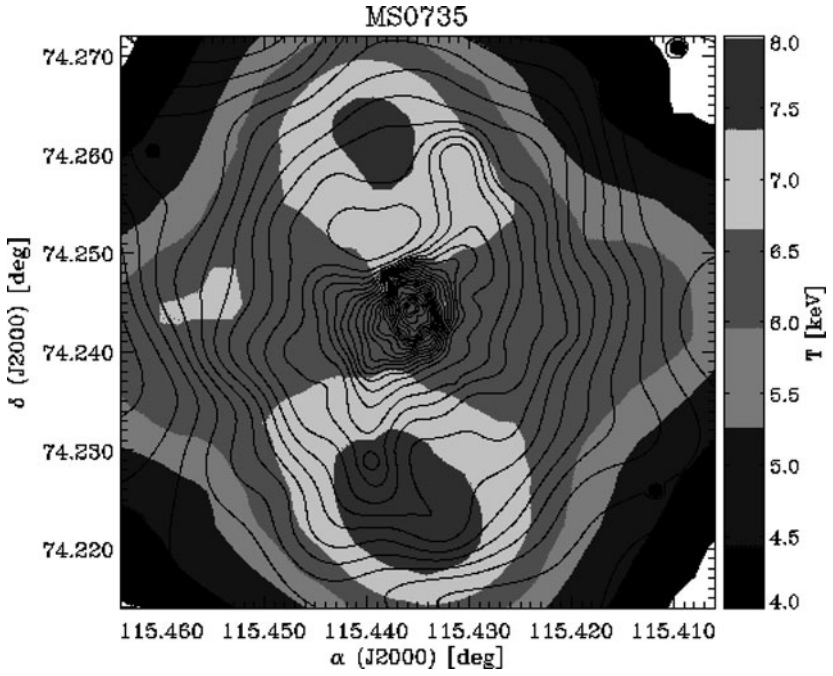

Fig. 3.6 Greyscale is the Chandra temperature map of the center of the cluster MS0735.6+7421, while the contours are the X-ray surface brightness, adapted from McNamara et al. (2005). The radio bubbles in this cluster are bounded by hot regions, which indicates that the radio source is driving shocks into the intracluster gas

and pressure source within radio sources. It may be that the magnetic fields are larger than given by equipartition. The extra pressure might be due to a large population of low energy relativistic electrons, or to a very large population of relativistic ions. Alternatively, the radio sources may contain diffuse but very hot thermal gas, which provides most of the energy and pressure. Within the radio sources, jet kinetic energy is dissipated by shocks or other frictive processes, so it would not be surprising in most of the energy was thermalized. So far, it has been difficult to detect such hot gas in X-ray spectra of the radio lobes (e.g., Blanton et al. 2003). However, it could be detectable with high spatial resolution SZ images (Pfrommer et al. 2005) or hard X-ray images (e.g., Koglin et al. 2009).

Although the radio bubbles generally show an anticorrelation between radio and X-ray emission, in a few systems there is evidence for a form of positive correlation. Specifically, columns of cool, dense gas are seen going from the center of the central galaxy out to the radio lobes. Examples include Virgo/M87 (Young et al. 2002) and Abell 133 (Fujita et al. 2002) (Fig. 3.7). One suggestion is that these X-ray features

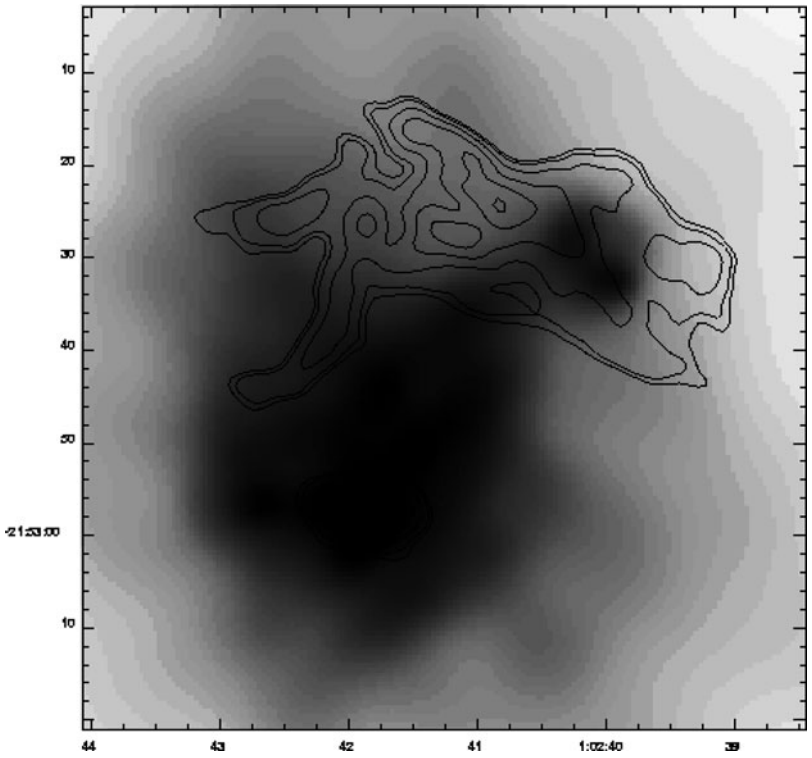

Fig. 3.7 Chandra X-ray image (greyscale) of the center of Abell 133, with radio contours superposed. This figure is adapted from Fujita et al. (2002). There is a column of cool, dense, X-ray bright gas extending from the nucleus (at the *lower left*) to the extended radio source (*upper right*)

are due to cooler gas from the center of the cooling core which has been entrained and uplifted by a buoyant radio lobe.

3.3.2 *Ghost Bubbles in BCGs in Clusters*

In many cooling core clusters, "ghost bubbles" are also seen at larger radii from the center. These are holes in the X-ray emission without associated high frequency radio emission. Figure 3.8 shows Abell 2597, an example of a cooling core with ghost bubbles (McNamara et al. 2001). Low frequency radio images have detected radio emission in many of the ghost bubbles (e.g., Clarke et al. 2005). In general, the properties of the ghost bubbles are consistent with older radio bubbles which

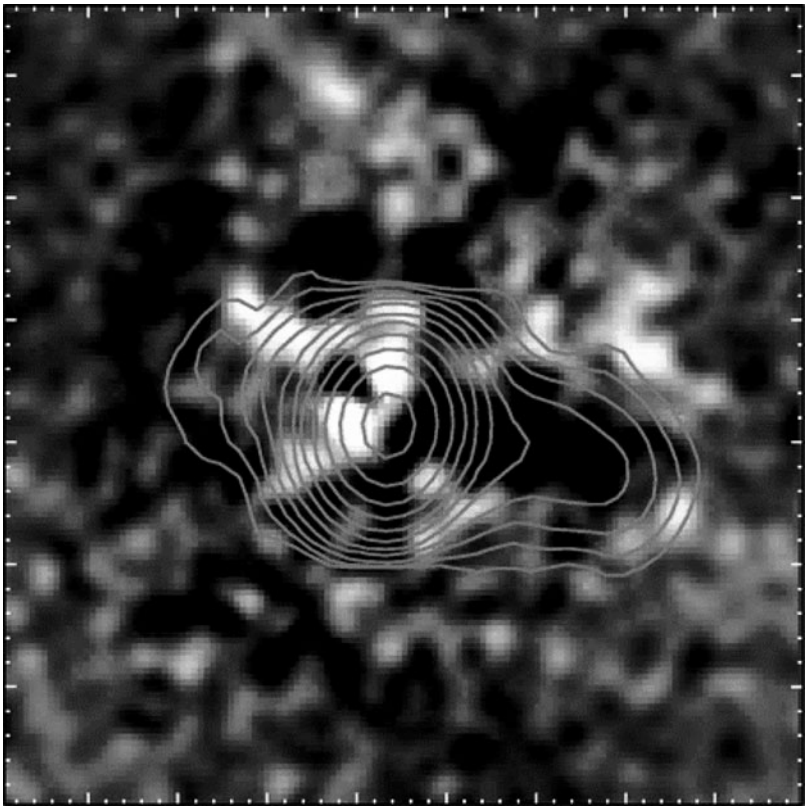

Fig. 3.8 Greyscale is the Chandra residual image of Abell 2597 after subtraction of an elliptical model, with low frequency (330 MHz) radio contours superposed. The figure is adapted from Clarke et al. (2005). The low frequency radio emission extends out into the "ghost bubble" to the west; also, there may be a channel in the X-ray image connecting the ghost bubble with the AGN at the center

have risen buoyantly in the cluster atmosphere. Some examples of ghost bubbles are seen in Perseus (Fabian et al. 2006), Abell 2597 (Clarke et al. 2005), and Abell 262 (Clarke et al. 2009).

3.3.3 Radio Bubbles in Individual Ellipticals and Groups

Similar radio bubbles and ghost bubbles are seen associated with radio AGNs hosted by ellipticals in groups and individual elliptical galaxies. The Chandra X-ray image of M84 shows a series of X-ray shells, some of which correspond to components of the radio source (Finoguenov et al. 2008). X-ray arcs which may be the sides of radio bubbles are also seen in NGC 4636 (Jones et al. 2002, Ohto et al. 2003, O'Sullivan et al. 2005, Baldi et al. 2009). Small bubbles are seen in NGC 4472 (Biller et al. 2004, Kraft et al. 2010). Several groups have small radio bubbles, including NGC 5044 (David et al. 2009), NGC 5098 (Randall et al. 2009), and HCG 62 (Morita et al. 2006, Gitti et al. 2010). Some of the bubbles in ellipticals appear to be open at their outer edges; this may indicate that the radio sources have blown out the elliptical galaxy gas.

There are a number of surveys of the X-ray emission and radio bubbles in individual elliptical galaxies (e.g., Mathews and Brighenti 2003, Jones et al. 2007, McNamara and Nulsen 2007, Nulsen et al. 2007, Diehl and Statler 2008, Dunn et al. 2010). The Jones et al. (2007) sample consisted of 160 nearby gEs, of which 109 had significant X-ray emission from hot gas. The Chandra images of 27 of these ellipticals show evidence for radio bubbles, suggesting that $\gtrsim$25% of early-type galaxies with hot gas have radio bubbles. It is difficult to compare this fraction to that for BCGs in rich clusters due to possible differences in the detectability of bubbles in clusters and gEs. However, the galaxy rate might be similar to the fraction of all clusters which have bubbles, although the fraction of cool core clusters with observed bubbles is higher. A recent radio survey of X-ray-bright ellipticals and S0 found a higher fraction with evidence for radio/X-ray interactions (Dunn et al. 2010).

Surveys of groups find results which are similar to and intermediate between those for clusters and individual galaxies (e.g., Dong et al. 2010).

3.3.4 X-ray Shells as Radio Source Calorimeters

Radio bubbles are very useful systems for determining the total energies supplied by the jets in the radio sources. For the systems which are expanding subsonically, the total energy is the "PdV" work done to displace the X-ray emitting gas, plus the internal energy in the radio bubble (Churazov et al. 2002). (For systems with shocks, the shock energy needs to be included McNamara et al. 2005.) This gives a

total energy of

$$E_{\text{radio}} = P\,V + \frac{PV}{\gamma - 1} = \frac{\gamma}{\gamma - 1}\,PV = (2.5 - 4)\,PV\,, \tag{3.7}$$

where P is the pressure in the radio lobe, V is its volume, and γ is the mean adiabatic index of the contents of the radio lobe. The two terms in the left end of the equation are the work done by the bubble and its internal energy. The range of values at the right of the equation correspond to the range from non-relativistic gas ($\gamma = 5/3$) to relativistic material ($\gamma = 4/3$). For example, in Abell 2052 (Fig. 3.5), the total energy is $E_{\text{radio}} \approx 10^{59}$ ergs (Blanton et al. 2003), which is a typical value. Similar measurements have provided the best direct evidence on the total energy content of radio jets.

3.3.5 Can Radio Sources Offset Cooling in Cluster Cores?

The energy in the radio source can be compared to the cooling X-ray luminosity of the cooling core to see if it is energetically possible for the radio source to inhibit the radiative cooling of the gas. To make this comparison, one needs a time scale for the activity of the radio source; typically, this is given by the buoyancy rise time of the radio bubbles. Then, the total energy injected by the radio source can be divided by the time scale for the activity to give the power injected by the radio source.

A number of surveys have compared the energy injected by the radio sources with the X-ray luminosity of the cool core region of the cluster where the radiative cooling time is short (Birzan et al. 2004, Dunn and Fabian 2006, Rafferty et al. 2006, Dunn and Fabian 2008) In most cases, this comparison indicates that energy from the radio source could balance radiative cooling (e.g., Birzan et al. 2004), although this is not true in all cases. Radio heating (as well as the common occurrence of radio sources in cooling cores) requires that the radio activity be episodic; it may be that the average radio power is more important than the current value.

Also, as deeper low frequency radio observations and deeper X-ray observations have been made of clusters, the sizes of the radio bubbles and their total energies are often found to increase. Figure 3.9 shows an example, the cluster Abell 262. Previous shallower radio and Chandra X-ray images (Blanton et al. 2004) indicated that the radio sources was roughly ten times too weak to offset cooling at the center of this cluster. However, a longer Chandra image revealed a long "X-ray tunnel" to the west, and a shorter tunnel plus three additional bubbles to the east. Sensitive low frequency radio observations with the VLA and GMRT have shown that the radio source extends more than three times further than was seen before. The estimate of the total energy of the radio source was increased by roughly ten times, and now agrees with the cooling luminosity within the errors.

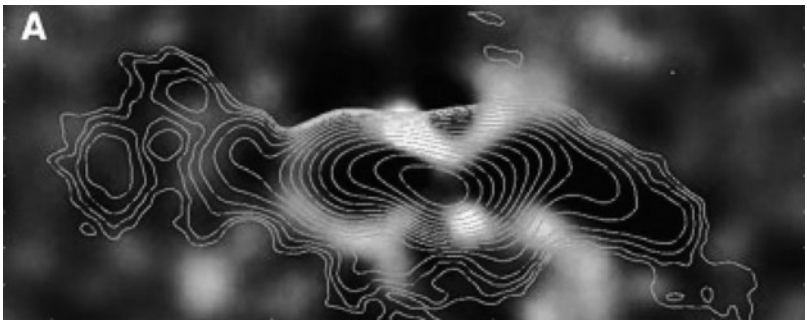

Fig. 3.9 Residual Chandra X-ray image (greyscale) of the center of Abell 262, showing X-ray cavities to the east and a continuous cavity ("X-ray tunnel") to the west. The contours are the GMRT 610 MHz radio image, tapered to show the low surface brightness features. This figure was adapted from Clarke et al. (2009). The X-ray cavities and radio source are three times longer than seen in previous shallower images, and the total radio source energy is roughly ten times higher

3.3.6 Can Radio Source Heating Offset Cooling in Individual Ellipticals?

Similar comparisons of the radio source power and the X-ray cooling luminosity have been made for individual elliptical galaxies (Nulsen et al. 2007, Dunn et al. 2010). For the most X-ray luminous systems, the X-ray cooling luminosity and radio power are in reasonable agreement. However, for ellipticals with lower X-ray cooling luminosities ($\lesssim 5 \times 10^{41}$ erg s^{-1}), the radio power estimated from the radio bubbles significantly exceeds the cooling X-ray luminosity. For these systems, the radio source could heat up and expel the cooling X-ray gas.

3.3.7 Radiative Efficiency of Radio Jets

Radio bubbles allow the estimation of the total amount of kinetic energy deposited by radio jets, and the power or rate at which this energy is deposited. These values can be compared to the radio luminosity of the jets to determine the efficiency of synchrotron emission. These results show that radio jets are generally quite inefficient; the typical value is $\sim$1% (Birzan et al. 2008). The efficiency is also highly variable from radio galaxy to galaxy, with a spread of $\sim 10^2$.

3.3.8 Bondi Accretion vs. Jet Power

Ultimately, the source of the energy in radio jets is thought to be accretion by the SMBH. One can compare the rate of kinetic energy or jet power estimated from the

radio bubbles with possible rates of accretion by the SMBH. Perhaps the simplest mode of accretion would be the direct accretion of hot gas from the surrounding elliptical galaxy and/or cluster cool core. Assuming a spherically symmetric system and no angular momentum, the rate of this accretion should be given approximately by the Bondi (1952) accretion formula,

$$\dot{M}_{\rm Bondi} = \frac{\pi}{4} c_s \rho_A r_A^2 \,, \tag{3.8}$$

where r_A is the accretion radius, c_s is the sound speed in the gas at the accretion radius, and ρ_A is the gas density at the accretion radius. The numerical coefficient in (3.8) assumes that the adiabatic index γ of the gas is $5/3$. Assuming the SMBH dominates the gravity in the region of interest, the accretion radius is given by

$$r_A = \frac{2\,GM_{\rm BH}}{c_s^2} \,, \tag{3.9}$$

where $M_{\rm BH}$ is the mass of the BH. In some nearby elliptical galaxies, this radius is comparable to the resolution of Chandra, so that one could determine the gas properties at the accretion radius directly.

Allen et al. (2006) compared the Bondi accretion rates for nearby ellipticals with the total power in the jets as determined from their radio bubbles. They found that they correlated, and that the jet powers could be produced if $\sim$2% of the rest mass of the material entering the accretion radius was converted in jet kinetic energy by the black hole.

On the other hand, Rafferty et al. found that Bondi accretion might not work for the most luminous systems, which were generally associated with BCGs. One caveat is that these systems are usually further away, so that the Bondi accretion radius was not resolved in the X-ray observations.

3.3.9 The Need for Feedback Coupling AGN and X-ray Cooling

In general, AGNs have a very large range in their luminosities, which presumably reflects, at least in part, a large range in their energy output. Thus, it would seem unlikely that heating by radio sources would balance radiative cooling by X-ray gas in cluster cool core in every case without some sort of "feedback" between the AGN activity and the cooling of the gas. If the AGN is powered by the accretion of cooled X-ray gas, such a feedback loop seems possible. For example, consider a cluster containing a BCG with a supermassive black hole at its center. Assume the cluster formed recently or underwent a major merger, and that there is initially no gas which has cooled at the center of the cluster. Thus, the cluster would lack a cool core, and the AGN would be inactive due to a lack of material to accrete. Eventually, radiative cooling would lead some gas to cool at the center of the cluster where the density

is highest, and thus the cooling time is shortest. This would lead to gas cooling at the center of the cluster, and some small fraction of this gas would reach the central supermassive black hole and be accreted. The AGN would become active, and would launch jets into the surrounding cluster cool core. Assume that these jets are stopped in the cool core and heat the gas there, suppressing cooling. This would stop the cooling, and eventually starve the AGN of fuel. This might either lead to a stable balance in which just enough gas cooled to low temperatures to power the AGN sufficiently to heat the cool core gas enough to prevent further cooling. Perhaps more likely. this would lead to a episodic limit cycle, with periods of cooling and AGN activity, and the average heating rate by the AGN nearly balancing the average cooling rate by the X-ray gas.

3.3.10 Radio Source Heating Mechanism in Cool Cores

Although the radio sources in the centers of cluster cool cores have enough energy, in most cases, to suppress cooling (Sects. 3.3.5 and 3.3.6), the detailed mechanism by which they heat the gas is still poorly understood. How can one get heat preferentially into the cooler gas? How is the heat transported to the outer parts of the cool core without disrupting (e.g., by convection) the cool core and the observed abundance gradients there? It may be that the radio plasma mixes with the X-ray plasma, or that relativistic particles diffuse into the thermal gas, and directly heat the gas. Heat conduction may carry energy from hot gas into cooler gas. The buoyant rise of the bubbles will release gravitational energy and heat the gas. The X-ray gas might be heated by plasma waves, sound waves, or weak shocks generated by the radio source. The deep Chandra image of the center of the Perseus cluster shows ripples which are probably sounds waves and weak shocks from the radio source (Fabian et al. 2006). Figure 3.10 shows an unsharp-masked Chandra image of the center of Abell 2052, which shows similar ripples (Blanton et al. 2009).

The problem of heating is complicated by the fact that the energy is initially in the directed flow of the radio jets. How do initially narrow radio jets heat the X-ray gas in all directions (e.g., Vernaleo and Reynolds 2006)? Sound waves and shocks might be useful for isotropizing the heating. Why don't the jets just punch narrow channels in the gas? Is the collimated outflow disrupted by jet precession, or cluster gas motions, or instabilities? Does most of the energy actually come out in wider jets or winds? The detailed nature of the AGN heating and feedback in cool cores is a very active area of research.

3.3.11 The Southwest Radio Lobe of Cen-A

Centaurus A (Cen A or NGC 5128) is the nearest bright elliptical galaxy, the nearest radio galaxy, and possibly the nearest powerful AGN. This makes it an ideal

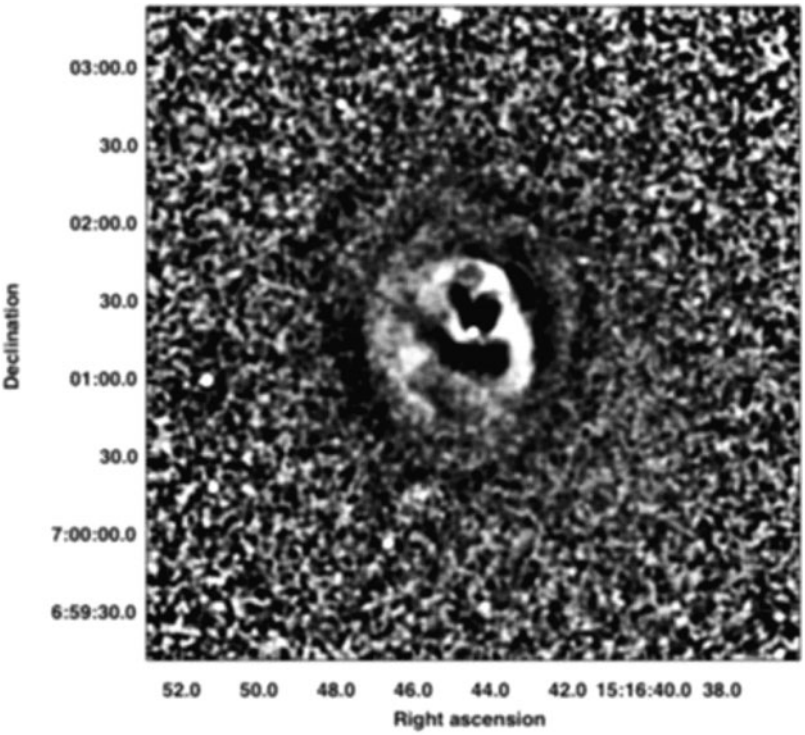

Fig. 3.10 Unsharp-masked Chandra X-ray image of the center of Abell 2052, showing the radio bubbles and a series of ripples. (The result of a shallower Chandra image is shown in Fig. 3.5.) The ripples are consistent with sound waves or weak shocks. This figure was adapted from Blanton et al. (2009)

candidate for the detail study of the interaction between radio sources and the hot gas in ellipticals. Recently, Cen A was observed for roughly 740 ksec with Chandra as part of a Very Large Program (Ralph Kraft PI). Part of this project involved a detailed study of the southwest radio lobe by Croston et al. (2009). Figure 3.11 shows the X-ray and radio images of this region. The SW radio lobe is surrounded by a thin shell of X-ray emission which has a very sharp outer boundary. There is very little diffuse emission from beyond this shell. Based on earlier observations, it had been suggested that this X-ray shell was thermal emission from hot interstellar gas shocked by the expansion of the radio lobe (Kraft et al. 2003). This would make the SW lobe in Cen A similar to the radio bubbles discussed above, but with a much higher Mach number for the expansion. One problem with this suggestion is that the compression required to explain the large increase in X-ray surface brightness at the outer edge of the X-ray shell is much greater than four, the highest value possible for a non-cooling shock.

The new observations from the Very Large Program show that the emission from this shell is actually nonthermal rather than thermal (Croston et al. 2009).

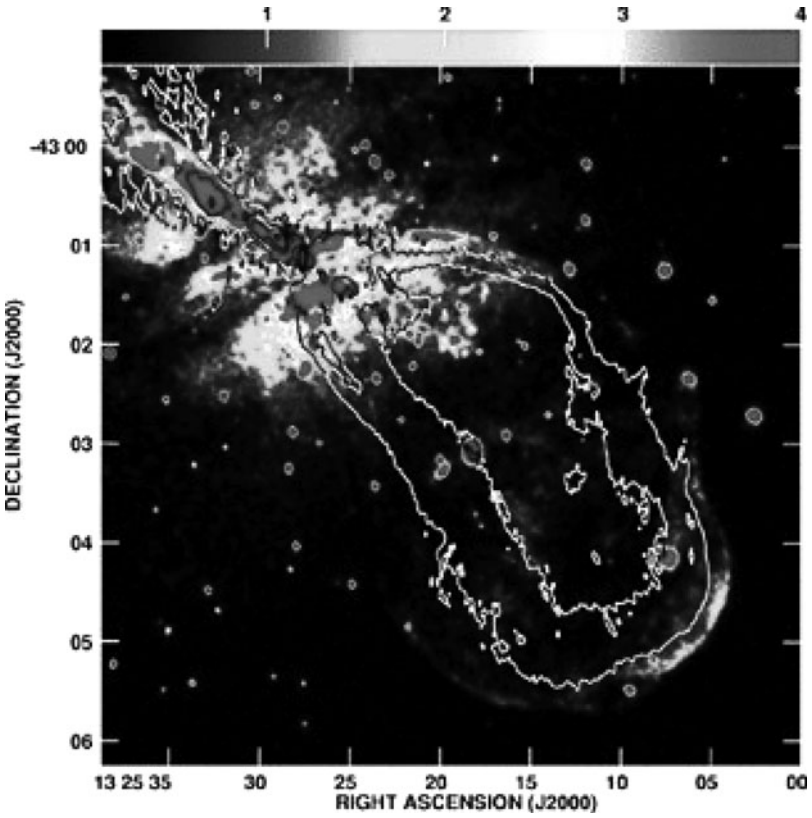

Fig. 3.11 The SW radio lobe of Cen A. The grey scale shows the Chandra X-ray image, while the contours are from the 1.4 GHz radio image. This figure was adapted from Fig. 1 of Croston et al. (2009). Note that the radio lobe is surrounded by a thin shell of X-ray emission, and that the thin shell has a very sharp outer boundary with little emission beyond the shell

Apparently, the gas density in this region is so low that the thermal emission from the shock driven by the expanding radio lobe is too small to detect. The observed X-ray emission is probably X-ray synchrotron emission. Thus, this lobe is similar to the nonthermal supernova remnant shocks, such as in SNR1006. The observations indicate that the lobe is expanding at $\sim$2,600 km s^{-1}, which corresponds to a Mach number of $\sim$8. It is likely that electrons are being accelerated up to energies of $\sim 10^{14}$ eV. These observations suggest that thw SW lobe should be a detectable source of TeV gamma-rays, but that it is probably not the source of the Ultra-High Energy Cosmic Rays which come from the direction of Cen A.

Acknowledgements I thank Liz Blanton, Tracy Clarke, Judith Croston, and Ming Sun for comments and help with the figures for the original talk which led to this chapter. I want to thank Dong-Woo Kim and Silvia Pellegrini for organizing the very useful Joint Discussion at the IAU General Assembly in Rio, and for editing this volume. This work was supported by NASA Chandra

grants GO7-8078X, GO7-8081A, GO8-9083X, GO8-9085X, GO9-0135X, and GO9-0148X, and NASA Herschel grant RSA1373266, and NASA HST grants HST-GO-10597.03-A and HST-GO-11679.01.

References

D.M. Acreman, I.R. Stevens, T.J. Ponman, I. Sakelliou, MNRAS **341**, 1333 (2003). doi: 10.1046/j.1365-8711.2003.06504.x

S.W. Allen, R.J.H. Dunn, A.C. Fabian, G.B. Taylor, C.S. Reynolds, MNRAS **372**, 21 (2006). doi: 10.1111/j.1365-2966.2006.10778.x

A. Baldi, W. Forman, C. Jones, R. Kraft, P. Nulsen, E. Churazov, L. David, S. Giacintucci, ApJ **707**, 1034 (2009). doi: 10.1088/0004-637X/707/2/1034

B.A. Biller, C. Jones, W.R. Forman, R. Kraft, T. Ensslin, ApJ **613**, 238 (2004). doi: 10.1086/423020

L. Bîrzan, D.A. Rafferty, B.R. McNamara, M.W. Wise, P.E.J. Nulsen, ApJ **607**, 800 (2004). doi: 10.1086/383519

L. Bîrzan, B.R. McNamara, P.E.J. Nulsen, C.L. Carilli, M.W. Wise, ApJ **686**, 859 (2008). doi: 10.1086/591416

E.L. Blanton, C.L. Sarazin, B.R. McNamara, M.W. Wise, ApJ **558**, L15 (2001). doi: 10.1086/323269

E.L. Blanton, C.L. Sarazin, B.R. McNamara, ApJ **585**, 227 (2003). doi: 10.1086/345984

E.L. Blanton, C.L. Sarazin, B.R. McNamara, T.E. Clarke, ApJ **612**, 817 (2004). doi: 10.1086/422677

E.L. Blanton, S.W. Randall, E.M. Douglass, C.L. Sarazin, T.E. Clarke, B.R. McNamara, ApJ **697**, L95 (2009). doi: 10.1088/0004-637X/697/2/L95

H. Bondi, MNRAS **112**, 195 (1952)

H. Böhringer, W. Voges, A.C. Fabian, A.C. Edge, D.M. Neumann, MNRAS **264**, L25 (1993)

B.A. Brown, J.N. Bregman, ApJ **539**, 592 (2000). doi: 10.1086/309240

M. Brüggen, G. De Lucia, MNRAS **383**, 1336 (2008). doi: 10.1111/j.1365-2966.2007.12670.x

E. Churazov, R. Sunyaev, W. Forman, H. Böhringer, MNRAS **332**, 729 (2002). doi: 10.1046/j.1365-8711.2002.05332.x

T.E. Clarke, C.L. Sarazin, E.L. Blanton, D.M. Neumann, N.E. Kassim, ApJ **625**, 748 (2005). doi: 10.1086/429717

T.E. Clarke, E.L. Blanton, C.L. Sarazin, L.D. Anderson, Gopal-Krishna, E.M. Douglass, N.E. Kassim, ApJ **697**, 1481 (2009). doi: 10.1088/0004-637X/697/2/1481

L.L. Cowie, A. Songaila, Nature **266**, 501 (1977). doi: 10.1038/266501a0

D.J. Croton, V. Springel, S.D.M. White, G. De Lucia, C.S. Frenk, L. Gao, A. Jenkins, G. Kauffmann, J.F. Navarro, N. Yoshida, MNRAS **365**, 11 (2006). doi: 10.1111/j.1365-2966.2005.09675.x

J.H. Croston, R.P. Kraft, M.J. Hardcastle, M. Birkinshaw, D.M. Worrall, P.E.J. Nulsen, R.F. Penna, G.R. Sivakoff, A. Jordán, N.J. Brassington, D.A. Evans, W.R. Forman, M. Gilfanov, J.L. Goodger, W.E. Harris, C. Jones, A.M. Juett, S.S. Murray, S. Raychaudhury, C.L. Sarazin, R. Voss, K.A. Woodley, MNRAS **395**, 1999 (2009). doi: 10.1111/j.1365-2966.2009.14715.x

L.P. David, C. Jones, W. Forman, P. Nulsen, J. Vrtilek, E. O'Sullivan, S. Giacintucci, S. Raychaudhury, ApJ **705**, 624 (2009). doi: 10.1088/0004-637X/705/1/624

S. Diehl, T.S. Statler, ApJ **680**, 897 (2008). doi: 10.1086/587481

S. Diehl, T.S. Statler, ApJ **687**, 986 (2008). doi: 10.1086/592179

W. Domainko, M. Mair, W. Kapferer, E. van Kampen, T. Kronberger, S. Schindler, S. Kimeswenger, M. Ruffert, O.E. Mangete, A&Ap **452**, 795 (2006). doi: 10.1051/0004-6361:20053921

R. Dong, J. Rasmussen, J.S. Mulchaey, ApJ **712**, 883 (2010). doi: 10.1088/0004-637X/712/2/883

R.J.H. Dunn, A.C. Fabian, MNRAS **373**, 959 (2006). doi: 10.1111/j.1365-2966.2006.11080.x

R.J.H. Dunn, A.C. Fabian, MNRAS **385**, 757 (2008). doi: 10.1111/j.1365-2966.2008.12898.x
R.J.H. Dunn, S.W. Allen, G.B. Taylor, K.F. Shurkin, G. Gentile, A.C. Fabian, C.S. Reynolds, MNRAS **404**, 180 (2010). doi: 10.1111/j.1365-2966.2010.16314.x
S.C. Ellis, E. O'Sullivan, MNRAS **367**, 627 (2006). doi: 10.1111/j.1365-2966.2005.09982.x
A.C. Fabian, J.S. Sanders, G.B. Taylor, S.W. Allen, C.S. Crawford, R.M. Johnstone, K. Iwasawa, MNRAS **366**, 417 (2006). doi: 10.1111/j.1365-2966.2005.09896.x
A. Finoguenov, U.G. Briel, J.P. Henry, G. Gavazzi, J. Iglesias-Paramo, A. Boselli, A&Ap **419**, 47 (2004). doi: 10.1051/0004-6361:20035765
A. Finoguenov, M. Ruszkowski, C. Jones, M. Brüggen, A. Vikhlinin, E. Mandel, ApJ **686**, 911 (2008). doi: 10.1086/591662
W. Forman, J. Schwarz, C. Jones, W. Liller, A.C. Fabian, ApJ **234**, L27 (1979). doi: 10.1086/183103
Y. Fujita, C.L. Sarazin, J.C. Kempner, L. Rudnick, O.B. Slee, A.L. Roy, H. Andernach, M. Ehle, ApJ **575**, 764 (2002). doi: 10.1086/341352
M. Gitti, E. O'Sullivan, S. Giacintucci, L.P. David, J. Vrtilek, S. Raychaudhury, P.E.J. Nulsen, ApJ **714**, 758 (2010). doi: 10.1088/0004-637X/714/1/758
J.E. Gunn, J.R. Gott, III, ApJ **176**, 1 (1972). doi: 10.1086/151605
S.F. Helsdon, T.J. Ponman, E. O'Sullivan, D.A. Forbes, MNRAS **325**, 693 (2001). doi: 10.1046/j.1365-8711.2001.04490.x
M. Henriksen, S. Cousineau, ApJ **511**, 595 (1999). doi: 10.1086/306690
A.E. Hornschemeier, B. Mobasher, D.M. Alexander, F.E. Bauer, M.W. Bautz, D. Hammer, B.M. Poggianti, ApJ **643**, 144 (2006). doi: 10.1086/500798
Z. Huang, C.L. Sarazin, ApJ **496**, 728 (1998). doi: 10.1086/305406
D.S. Hudson, R. Mittal, T.H. Reiprich, P.E.J. Nulsen, H. Andernach, C.L. Sarazin, A&Ap **513**, A37+ (2010). doi: 10.1051/0004-6361/200912377
J.A. Irwin, C.L. Sarazin, ApJ **471**, 683 (1996). doi: 10.1086/177998
T.E. Jeltema, B. Binder, J.S. Mulchaey, ApJ **679**, 1162 (2008). doi: 10.1086/587508
C. Jones, W. Forman, A. Vikhlinin, M. Markevitch, L. David, A. Warmflash, S. Murray, P.E.J. Nulsen, ApJ **567**, L115 (2002). doi: 10.1086/340114
C. Jones, W. Forman, E. Churazov, P. Nulsen, R. Kraft, S. Murray, in *Heating versus Cooling in Galaxies and Clusters of Galaxies*, ed. by H. Böhringer, G. W. Pratt, A. Finoguenov, P. Schuecker (2007), pp. 145–+
D. Kim, E. Kim, G. Fabbiano, G. Trinchieri, ApJ **688**, 931 (2008). doi: 10.1086/592211
J.E. Koglin, H. An, K.L. Blaedel, N.F. Brejnholt, F.E. Christensen, W.W. Craig, T.A. Decker, C.J. Hailey, L.C. Hale, F.A. Harrison, C.P. Jensen, K.K. Madsen, K. Mori, M.J. Pivovaroff, G. Tajiri, W.W. Zhang, in *Society of Photo-Optical Instrumentation Engineers (SPIE) Conference Series*, *Society of Photo-Optical Instrumentation Engineers (SPIE) Conference Series*, vol. 7437 (2009), *Society of Photo-Optical Instrumentation Engineers (SPIE) Conference Series*, vol. 7437. doi: 10.1117/12.826724
R.P. Kraft, S.E. Vázquez, W.R. Forman, C. Jones, S.S. Murray, M.J. Hardcastle, D.M. Worrall, E. Churazov, ApJ **727**, 41 (2011) doi: 10.1086/375533
R. Kraft, W.R. Forman, C. Jones, P.E.J. Nulsen, M.J. Hardcastle, S. Raychaudhury, D.A. Evans, G. Sivakoff, C. Sarazin, ApJ **727**, 41 (2011)
L.D. Landau, E.M. Lifshitz, *Fluid Mechanics* (Pergamon, Oxford, 1959)
M. Machacek, A. Dosaj, W. Forman, C. Jones, M. Markevitch, A. Vikhlinin, A. Warmflash, R. Kraft, ApJ **621**, 663 (2005). doi: 10.1086/427548
M. Machacek, C. Jones, W.R. Forman, P. Nulsen, ApJ **644**, 155 (2006). doi: 10.1086/503350
M.E. Machacek, R.P. Kraft, C. Jones, W.R. Forman, M.J. Hardcastle, ApJ **664**, 804 (2007). doi: 10.1086/519233
M. Markevitch, A. Vikhlinin, Phys. Rep. **443**, 1 (2007). doi: 10.1016/j.physrep.2007.01.001
M. Markevitch, T.J. Ponman, P.E.J. Nulsen, M.W. Bautz, D.J. Burke, L.P. David, D. Davis, R.H. Donnelly, W.R. Forman, C. Jones, J. Kaastra, E. Kellogg, D.W. Kim, J. Kolodziejczak, P. Mazzotta, A. Pagliaro, S. Patel, L. Van Speybroeck, A. Vikhlinin, J. Vrtilek, M. Wise, P. Zhao, ApJ **541**, 542 (2000)

W.G. Mathews, F. Brighenti, ARAA **41**, 191 (2003). doi: 10.1146/annurev.astro.41.090401.094542
B.R. McNamara, P.E.J. Nulsen, ARAA **45**, 117 (2007). doi: 10.1146/annurev.astro.45.051806.110625
J. Magorrian, S. Tremaine, D. Richstone, R. Bender, G. Bower, A. Dressler, S.M. Faber, K. Gebhardt, R. Green, C. Grillmair, J. Kormendy, T. Lauer, AJ **115**, 2285 (1998). doi: 10.1086/300353
B.R. McNamara, M.W. Wise, P.E.J. Nulsen, L.P. David, C.L. Carilli, C.L. Sarazin, C.P. O'Dea, J. Houck, M. Donahue, S. Baum, M. Voit, R.W. O'Connell, A. Koekemoer, ApJ **562**, L149 (2001). doi: 10.1086/338326
B.R. McNamara, P.E.J. Nulsen, M.W. Wise, D.A. Rafferty, C. Carilli, C.L. Sarazin, E.L. Blanton, Nature **433**, 45 (2005). doi: 10.1038/nature03202
I.G. McCarthy, C.S. Frenk, A.S. Font, C.G. Lacey, R.G. Bower, N.L. Mitchell, M.L. Balogh, T. Theuns, MNRAS **383**, 593 (2008). doi: 10.1111/j.1365-2966.2007.12577.x
E. Memola, G. Trinchieri, A. Wolter, P. Focardi, B. Kelm, A&Ap **497**, 359 (2009). doi: 10.1051/0004-6361/200810801
U. Morita, Y. Ishisaki, N.Y. Yamasaki, N. Ota, N. Kawano, Y. Fukazawa, T. Ohashi, PASJ **58**, 719 (2006)
J.S. Mulchaey, T.E. Jeltema, ApJ **715**, L1 (2010). doi: 10.1088/2041-8205/715/1/L1
P.E.J. Nulsen, MNRAS **198**, 1007 (1982)
P.E.J. Nulsen, B.R. McNamara, M.W. Wise, L.P. David, ApJ **628**, 629 (2005). doi: 10.1086/430845
P.E.J. Nulsen, D.C. Hambrick, B.R. McNamara, D. Rafferty, L. Birzan, M.W. Wise, L.P. David, ApJ **625**, L9 (2005). doi: 10.1086/430945
P.E.J. Nulsen, C. Jones, W.R. Forman, L.P. David, B.R. McNamara, D.A. Rafferty, L. Bîrzan, M.W. Wise, in *Heating versus Cooling in Galaxies and Clusters of Galaxies*, ed. by H. Böhringer, G. W. Pratt, A. Finoguenov, P. Schuecker (2007), pp. 210–+
A. Ohto, N. Kawano, Y. Fukazawa, PASJ **55**, 819 (2003)
E. O'Sullivan, D.A. Forbes, T.J. Ponman, MNRAS **328**, 461 (2001). doi: 10.1046/j.1365-8711.2001.04890.x
E. O'Sullivan, J.M. Vrtilek, J.C. Kempner, ApJ **624**, L77 (2005). doi: 10.1086/430600
J.R. Peterson, A.C. Fabian, Phys. Rep. **427**, 1 (2006). doi: 10.1016/j.physrep.2005.12.007
C. Pfrommer, T.A. Enßlin, C.L. Sarazin, A&Ap **430**, 799 (2005). doi: 10.1051/0004-6361:20041576
V. Quilis, B. Moore, R. Bower, Science **288**, 1617 (2000). doi: 10.1126/science.288.5471.1617
S. Randall, P. Nulsen, W.R. Forman, C. Jones, M. Machacek, S.S. Murray, B. Maughan, ApJ **688**, 208 (2008). doi: 10.1086/592324
S.W. Randall, C. Jones, R. Kraft, W.R. Forman, E. O'Sullivan, ApJ **696**, 1431 (2009). doi: 10.1088/0004-637X/696/2/1431
S.W. Randall, C. Jones, M. Markevitch, E.L. Blanton, P.E.J. Nulsen, W.R. Forman, ApJ **700**, 1404 (2009). doi: 10.1088/0004-637X/700/2/1404
F.V.N. Rangarajan, D.A. White, H. Ebeling, A.C. Fabian, MNRAS **277**, 1047 (1995)
D.A. Rafferty, B.R. McNamara, P.E.J. Nulsen, M.W. Wise, ApJ **652**, 216 (2006). doi: 10.1086/507672
E. Rizza, C. Loken, M. Bliton, K. Roettiger, J.O. Burns, F.N. Owen, AJ **119**, 21 (2000). doi: 10.1086/301167
E. Roediger, M. Brüggen, MNRAS **388**, L89 (2008). doi: 10.1111/j.1745-3933.2008.00506.x
I. Sakelliou, M.R. Merrifield, I.M. McHardy, MNRAS **283**, 673 (1996)
C.L. Sarazin, ApL **20**, 93 (1979)
C.L. Sarazin, in *Merging Processes in Galaxy Clusters*, ed. by L. Feretti, I.M. Gioia, G. Giovannini (Kluwer, Dordrecht, 2002), pp. 1–38
C.L. Sarazin, R.W. O'Connell, B.R. McNamara, ApJ **389**, L59 (1992). doi: 10.1086/186348
C.A. Scharf, D.R. Zurek, M. Bureau, ApJ **633**, 154 (2005). doi: 10.1086/444531
S. Schreier, *Compressible Flow* (Wiley, New York, 1982), pp. 182-189
G.R. Sivakoff, C.L. Sarazin, J.L. Carlin, ApJ **617**, 262 (2004). doi: 10.1086/425244
R.J. Smith, MNRAS **344**, L17 (2003). doi: 10.1046/j.1365-8711.2003.06963.x

L.J. Spitzer, *Physics of Fully Ionized Gases* (Interscience, New York, 1956)
M. Sun, ApJ **704**, 1586 (2009). doi: 10.1088/0004-637X/704/2/1586
M. Sun, D. Jerius, C. Jones, ApJ **633**, 165 (2005). doi: 10.1086/452620
M. Sun, A. Vikhlinin, W. Forman, C. Jones, S.S. Murray, ApJ **619**, 169 (2005). doi: 10.1086/425298
M. Sun, C. Jones, W. Forman, A. Vikhlinin, M. Donahue, M. Voit, ApJ **657**, 197 (2007). doi: 10.1086/510895
S. Tremaine, K. Gebhardt, R. Bender, G. Bower, A. Dressler, S.M. Faber, A.V. Filippenko, R. Green, C. Grillmair, L.C. Ho, J. Kormendy, T.R. Lauer, J. Magorrian, J. Pinkney, D. Richstone, ApJ **574**, 740 (2002). doi: 10.1086/341002
G. Trinchieri, G. Fabbiano, D. Kim, A&Ap **318**, 361 (1997)
J.C. Vernaleo, C.S. Reynolds, ApJ **645**, 83 (2006). doi: 10.1086/504029
A. Vikhlinin, M. Markevitch, S.S. Murray, ApJ **551**, 160 (2001)
A. Vikhlinin, M. Markevitch, W. Forman, C. Jones, ApJ **555**, L87 (2001). doi: 10.1086/323181
Q.D. Wang, F. Owen, M. Ledlow, W. Keel, in *IAU Colloq. 195: Outskirts of Galaxy Clusters: Intense Life in the Suburbs*, ed. by A. Diaferio (2004), pp. 78–82. doi: 10.1017/S174392130400016X
R.E. White, III, C.L. Sarazin, ApJ **367**, 476 (1991). doi: 10.1086/169644
N.Y. Yamasaki, T. Ohashi, T. Furusho, ApJ **578**, 833 (2002). doi: 10.1086/342652
A.J. Young, A.S. Wilson, C.G. Mundell, ApJ **579**, 560 (2002). doi: 10.1086/342918

Chapter 4
AGN Feedback in Elliptical Galaxies: Numerical Simulations

Luca Ciotti and Jeremiah P. Ostriker

Abstract The importance of feedback (radiative and mechanical) from massive black holes at the centers of elliptical galaxies is not in doubt, given the well established relation among black hole mass and galaxy optical luminosity. Here, with the aid of high-resolution hydrodynamical simulations, we discuss how this feedback affects the hot ISM of isolated elliptical galaxies of different mass. The cooling and heating functions include photoionization plus Compton heating, the radiative transport equations are solved, and the mechanical feedback due to the nuclear wind is also described on a physical basis; star formation is considered. In the medium-high mass galaxies the resulting evolution is highly unsteady. At early times major accretion episodes caused by cooling flows in the recycled gas produced by stellar evolution trigger AGN flaring: relaxation instabilities occur so that duty cycles are small enough to account for the very small fraction of massive ellipticals observed to be in the QSO-phase, when the accretion luminosity approaches the Eddington luminosity. At low redshift all models are characterized by smooth, very sub-Eddington mass accretion rates. The mass accumulated by the central black hole is limited to range observed today, even though the mass lost by the evolving stellar population is roughly two order of magnitude larger than the black hole masses observed in elliptical galaxies.

L. Ciotti (✉)
Department of Astronomy, University of Bologna, via Ranzani 1, Bologna, 40127, Italy
e-mail: luca.ciotti@unibo.it

J.P. Ostriker
Princeton University Observatory, Peyton Hall, Princeton, NJ 08544-1001, USA

IoA, University of Cambridge, Madingley Road, Cambridge, CB3 0HA, UK
e-mail: ostriker@princeton.edu

D.-W. Kim and S. Pellegrini (eds.), *Hot Interstellar Matter in Elliptical Galaxies*,
Astrophysics and Space Science Library 378, DOI 10.1007/978-1-4614-0580-1_4,
© Springer Science+Business Media, LLC 2012

4.1 Introduction

Supermassive black holes (SMBHs) at the centers of bulges and elliptical galaxies (e.g., see Kormendy and Richstone 1995, de Zeeuw 2001, Ferrarese and Ford 2005) have certainly played an important role in the processes of galaxy formation and evolution (e.g., see among others Silk and Rees 1998, Fabian 1999, Burkert and Silk 2001, Cavaliere and Vittorini 2002, King 2003, Wyithe and Loeb 2003, Haiman et al. 2004, Granato et al. 2004, Sazonov et al. 2005, Murray et al. 2005, Di Matteo et al. 2005, Begelman and Nath 2005, Hopkins et al. 2006, Croton et al. 2006, Pipino et al. 2009, Lusso and Ciotti 2010), as indicated by the observed correlations between host galaxy properties and the masses of their SMBHs (e.g., see Magorrian et al. 1998, Ferrarese and Merritt 2000, Gebhardt et al. 2000, Yu and Tremaine 2002, McLure and Dunlop 2002, Graham et al. 2003, Marconi and Hunt 2003, see also Somerville 2008, Cattaneo et al. 2009, Ciotti 2009).

Of central interest for modern astrophysics is the fact that when gas is added to the central galactic regions for any reason, the SMBH will accrete and emit energy, both as a radiation flow and in some mechanical form. The complex interaction of such energy with the galactic gas, and the consequent effects on the galaxy and on the SMBH itself, are defined as "AGN feedback". A quite widespread view is that, after the end of the galaxy formation epoch, the only way to add fresh gas to the central SMBH is through the merging phenomenon; it follows that the quasar phenomenon should be a secure indicator of (gas rich) galaxy merging over the cosmic epochs. However, this picture is only partially true, as well known to stellar evolutionists and to the "cooling flow" community.

In fact, the mass return rate from the passively evolving stars (primarily from red giant winds and planetary nebulae) in elliptical galaxies can be estimated as

$$\dot{M}_*(t) \simeq 1.5\,10^{-11} L_{\rm B}\, t_{15}^{-1.3} \quad M_\odot {\rm year}^{-1}, \tag{4.1}$$

where $L_{\rm B}$ is the present galaxy blue luminosity in blue solar luminosities, and t_{15} is time in 15 Gyr units (Ciotti et al. 1991, see also Sect. 4.2.2 and Pellegrini, this volume). This metal-rich, recycled gas is the main ingredient of the so-called cooling-flow model (originally developed for clusters, Cowie and Binney 1977, Fabian and Nulsen 1977), that provided the preliminary framework to the interpretation of X-ray halos observed in elliptical galaxies (e.g., see Canizares et al. 1987, Sarazin and White 1987 and Fabbiano, this volume).

However soon it was realized that at least two major problems were faced by the classical cooling-flow scenario. The first is a *luminosity problem*, i.e, the X-ray luminosity $L_{\rm X}$ of local ellipticals is inconsistent with the standard cooling flow model. In fact, low-redshift elliptical galaxies with optical luminosity $L_{\rm B} \gtrsim 3 \times 10^{10} L_\odot$ show a significant range in the ratio of gas-to-total mass at fixed $L_{\rm B}$, with values ranging from virtually zero up to few %, and most of that is seen in X-rays with temperatures close to the virial temperatures of the systems (e.g., see Mathews and Brighenti 2003). The second, and even more severe problem, is the *mass*

disposal problem. In fact, from (1) it follows that the evolving stellar population will inject in the galaxy, over a cosmological time, a gas mass summing up $\approx 10-20\%$ of the total stellar mass M_*. In the classical cooling flow scenario, this gas flows and disappears at the galaxy center, but observations ruled out the existence of such large masses at the center of elliptical galaxies. Young stellar populations observed in the body of ellipticals also cannot account for the total mass released, and alternative forms of cold mass disposal (such as distributed mass drop-out) are not viable solutions (Binney, 2001). The mass disposal problem has been exhacerbated after the discovery of central SMBHs: infact, the total mass of the recycled gas is two orders of magnitude larger than the mass $M_{\rm BH}$ of the central SMBH. In other words, *even in absence of merging, the pure passive stellar evolution injects in the galaxy an amount of gas that, if flowing to the center, would produce a SMBH* $\simeq 100$ *times more massive than what is observed*, $M_{\rm BH} \simeq 10^{-3} M_*$ (e.g., Magorrian et al. 1998).

A (partial) solution to the luminosity and mass problems was proposed in a first series of papers (Loewenstein and Mathews 1987, D'Ercole et al. 1989, David et al. 1990, Ciotti et al. 1991, Pellegrini and Ciotti 1998), by considering the effect of SNe Ia heating of the galactic gas, and exploring the time evolution of gas flows by using hydrodynamical numerical simulations. It was found that SNe Ia input sufficed for low and medium-luminosity elliptical galaxies to produce fast galactic winds, so that the scatter in the $L_{\rm X}$-$L_{\rm B}$ diagram could be nicely reproduced. However, it was also found that more massive galaxies should be in the high-luminosity, permanent cooling-flow regime, so that for massive systems, putative hosts of luminous cooling flows, the mass problem was still unsolved; in addition, if this gas is accreted on the central SMBH, then a bright QSO should be observed in all X-ray luminous elliptical galaxies. These considerations lead naturally to the study of gas accretion on SMBHs at the center of elliptical galaxies, to explore the possibility that radiative and mechanical feedback due to accretion is the solution of the mass disposal problem in cooling flow, and it is the explanation of the maintenance of "small" SMBH masses in presence of very large amounts of recycled gas, and of the shut down of QSO activity in massive ellitpicals (e.g., see Tabor and Binney 1993, Ciotti and Ostriker 1997, Fabian et al. 2006).

In the past years, we dedicated several papers to the AGN feedback in elliptical galaxies (Ciotti and Ostriker 1997, 2001, Ostriker and Ciotti 2005, Sazonov et al. 2005, Ciotti and Ostriker 2007, Ciotti et al. 2009, Pellegrini et al. 2009, 2011, Ciotti et al. 2010, Jang et al. 2010, Shin et al. 2010a,b, Ostriker et al. 2010, Novak et al. 2011). The current most satisfactory models are *combined models*, i.e. models in which both radiative and mechanical feedback effects are at work. In general, all the computed solutions are characterized by relaxation oscillations (e.g., see Ostriker et al. 1976, Cowie et al. 1978, Milosavljevic et al. 2009), and we note that nowadays, several observations support the finding that accretion on central SMBHs is in fact a highly unsteady phenomenon (e.g., see Martini 2004, Goncalves et al. 2008, Hopkins and Hernquist 2009); in addition, evidences of AGN feedback have been clearly detected in the hot gas of nearby elliptical galaxies (e.g., see Jones et al. 2002, Randall et al. 2004, O'Sullivan et al. 2005, Forman et al. 2007, Diehl and Statler 2008, see also Statler, this volume).

From the astrophysical point of view, the emerging picture of the evolution of an isolated, medium-high mass elliptical galaxy consists of four main (repeating) stages.

Stage 1: After the end of the galaxy formation epoch, the galaxy should be in a more or less quiescent phase. Planetary nebulae and other sources of secondary gas, processed through stellar evolution, inject fresh gas in the galaxy at a rate proportional to the stellar density and with an energy due to the stellar motions which gurantees that, when the gas is thermalized, it will be approximately at the local "virial" temperature. Supernovae (Type Ia) are also distributed like the stars and will tend to drive a mild wind from the outer parts of the galaxy, with the inner parts being quite luminous in thermal X-rays. This is a "normal" giant elliptical galaxy. Low mass ellipticals instead can be found permanently in a state of global, low-luminosity galactic wind.

Stage 2: In massive ellipticals, the gas in the dense inner part of the galaxy is radiating far more energy than can be replaced by SNe Ia and stellar motions, and thus a "cooling catastrophe" occurs with a collapsing cold shell forming at ≈ 1 kpc from the center. As this falls towards the center, a starburst occurs, and the galaxy seen as an ULIRG. A radio jet may be emitted, but the AGN flare up is at first heavily obscured and the central source will only be seen in hard X-rays.

Stage 3: Gradually, the gas is consumed, as it is transformed to new stars, and some of it is driven out in a strong wind by the combined effects of feedback from the starburst and the central SMBH, which is now exposed as an optical and then UV "quasar", complete with Broad Line Region (hereafter BLR) wind, optically thick disc of gas, and young stars.

Stage 4: As gas is used up or blown away, a hot cavity is formed at the center of the system and, since a shock has propagated through that volume, it is essentially like a giant supernova remnant and one expects there to be particle acceleration and non-thermal radiation from the central region (Jang et al., 2010). Then, gradually this hot bubble cools and collapses and one returns to the normal elliptical phase at Stage 1.

The paper is organized as follows. In Sect. 4.2 we briefly discuss some class of models that have been studied in the past years, focusing on the radiative or mechanical feedback effects, but not both. In Sect. 4.3 we describe in detail the input physics of the combined feedback models. In Sect. 4.4 we present for the first time a comparison of the effects of combined feedback on three galaxy models of different mass, related to the Reference Model in Ciotti et al. (2010). Finally, in Sect. 4.5 we discuss the main results obtained.

4.2 Previous Works

Due to the importance of the subject, to its implications in different areas of observational and theoretical astrophysics, and to the fact the specific nature of AGN feedback is still not completely understood, it is not surprising that a very

large body of work has been done on the subject. In general, past investigations focused separately on *purely radiative* or *purely mechanical* feedback. Here we briefly describe the main properties and limitations of these two classes of models.

4.2.1 Radiative Feedback

In a first set of papers (Ciotti and Ostriker 1997, 2001, Ostriker and Ciotti 2005, Ciotti and Ostriker 2007), we studied the effects of purely radiative feedback, and we showed its effectiveness to solve in a natural way the long lasting *luminosity* and *mass disposal* problems of cooling flows mentioned in the Introduction.

In Ciotti and Ostriker (1997, 2001), however, a major uncertainty remained about the typical QSO spectrum to adopt, in particular the high energy component of that spectrum, which is most important for heating the ambient gas; in addition, only Compton heating/cooling and electron scattering radiation pressure (with the associated Eddington luminosity limit) were considered. Subsequent works (Sazonov et al. 2004, 2007, 2008), which assessed the full range of observational data of AGNs and computed their Spectral Energy Distribution, concluded that the typical equilibrium radiation temperature was narrowly bounded to values near $10^{7.3}$ K, i.e., of the order of 2 keV. This value, although it is at the lower end of the range adopted in Ciotti and Ostriker (1997, 2001), is still above the virial temperature of all galaxies and, most importantly, well above the central temperature of the cooling flow gas. In addition, as noted by Sazonov et al. (2005), there is a rather large compensating effect also not included in the first two papers: gas heated by radiation with a characteristic temperature near 10^7 K is heated far more effectively by absorption in the atomic lines of the abundant metal species than by the Compton process.

For these reasons, in Ciotti and Ostriker (2007) we adopted the more detailed description of radiative heating, and we also implemented the code with the solution of the radiative transport equation, also considering the effect of dust and its destruction at high temperatures. In this way, we considered other contributions to radiation pressure in addition to electron scattering (e.g., see Shi and Krolik 2008). Finally, consistently with a second generation of metal rich stars observed in SDSS surveys (e.g., see Fukugita et al. 2004, Nolan et al. 2007), we allowed for star formation. All these physical processes are described in Sect. 4.3, and are considered in the current combined feedback models (Sect. 4.4).

The main result of purely radiative models is that, while obviously far better than cooling flow models, they are still clearly inadequate in several respects, in particular because it is found that radiative feedback alone does not sufficie to limit SMBH growth to the observationally allowed degree. The luminosity from young stars is quite high even at relatively low states between bursts, which would produce central regions which are far too blue compared to typical ellipticals. In addition, the AGN during these low states, while at only $10^{-4} L_{\rm Edd}$, is more luminous than

observed low-luminosity AGNs in galaxies of comparable mass (see, e.g., Pellegrini 2005, 2010, Wrobel et al. 2008, Ho 2008, Gallo et al. 2010).

4.2.2 Mechanical Feedback

As we found that despite the richness of the modeling we could not adequately describe the co-evolution of elliptical galaxies and their central SMBHs by using purely radiative feedback, we moved to the study of purely mechanical feedback models.[1]

At variance with the case of radiative heating, the literature about mechanical feedback is quite large (e.g., see Tabor and Binney 1993, Binney and Tabor 1995, Brüggen and Kaiser 2002, King 2003, Omma et al. 2004, Churazov et al. 2005, Begelman and Nath 2005, Begelman and Ruszkowski 2005, Di Matteo et al. 2005, Springel et al. 2005, Antonuccio-Delogu and Silk 2008, King 2010, Gaspari et al. (2011)). In general, two are the natural candidates for mechanical feedback, the most obvious being the interaction of a nuclear jet with the ISM. In fact, collimated jets, especially at low Eddington ratios are observed to put out energy in amounts comparable to the radiative outputs (Allen et al. 2006, even though it is not clear how efficiently such narrow jets can couple to the ambient fluid, see Vernaleo and Reynolds 2006). Another possibility is represented by radiatively driven winds from the BLRs, whose parameters are well observed (e.g., see Crenshaw et al. 2003, Chartas et al. 2007, Blustin et al. 2007, Hamann et al. 2008).

In Ciotti et al. (2009), Shin et al. (2010b) we explored two different prescriptions of mechanical feedback produced by a BLR wind (Sect. 4.3), and we artificially suppressed radiative heating. In the first class of models (Type A), the wind mechanical efficiency is assumed constant, with peak values ranging from $\epsilon_{\rm w}^{\rm M} = 5\,10^{-3}$ (as utilized for example in Di Matteo et al. 2005, Johansson et al. 2008), down to $\epsilon_{\rm w}^{\rm M} = 3\,10^{-5}$. We found that in Type A models with high mechanical efficiency almost all the recycled gas produced by stellar evolution is ejected from the galaxy, and a very negligible amount of mass is added to the central SMBH; star formation is maintained at very low levels. The final X-ray thermal luminosity of the models is far too low, orders of magnitude below that seen from normal giant elliptical galaxies (e.g., see Canizares et al. 1987, O'Sullivan et al. 2003, Mathews and Brighenti 2003). A reduction of the mechanical efficiency does not help, because it leads to a quite strong transition to the situation in which a significant amount of mass is added to the central SMBH. In other words, purely mechanical models with constant wind efficiency appear to be quite "stiff" in their behavior, switching from a strong global wind to a recurrent and significant bursting activity when reducing the efficiency.

[1] However, it should be noted that also a purely radiative feedback produces ultimately some form of mechanical feedback (see Sect. 4.2.1).

In the second class of models (Type B), the wind mechanical efficiency depends on the (Eddington normalized) accretion luminosity, with a maximum value reached at high accretion luminosities. Overall, Type B models perform better than Type A models. For example, the amount of new stars formed is of the same order as in Type A models, but the final mass of the ISM (and its X-ray luminosity) is larger, due to the less efficient feedback during the low luminosity phases. Also, Type B models with a maximum value of wind efficiency identical to Type A models, accrete more mass on their central SMBH, and the differences are mainly established during the low-luminosity phases. The duty-cycles are in general quite small, but larger than in models with constant efficiency and more similar to observationally derived values. Finally, the present-day luminosity ratios of the (optical) accretion luminosity to the Eddington luminosity are much smaller than in the purely radiative models, but still higher than what observed in low-luminosity AGNs. We concluded that also purely mechanical feedback models are inadequate to properly describe AGN feedback in elliptical galaxies.

4.3 Physical Modeling

In this Section we summarize the implementation of the input physics in our 1D code, used to compute the evolution of *combined feedback* models. We now have a more advanced code version, that will be used in future investigations, and we are also working on a 2D code with a multidimensional implementation of the input physics.

4.3.1 Structure and Internal Dynamics of the Galaxy

In Ciotti and Ostriker (1997, 2001) the galaxy models utilized a King (1972) stellar distribution plus a quasi-isothermal dark matter halo. However, the existence of large cores of constant surface brightness has been observationally ruled out (e.g., see Jaffe et al. 1994, Faber et al. 1997, Lauer et al. 2005), so that in Pellegrini and Ciotti (1998) and Ciotti and Ostriker (2007) more appropriate two-components Hernquist models (Hernquist 1990, Ciotti 1996) have been adopted.

These models are also in better agreement with cosmological expectations of dark matter halo central profiles (e.g., see Dubinski and Carlberg 1991, Navarro et al. 1997, Fukushige and Makino 1997), but the Hernquist profile is characterized (as the de Vaucouleurs $R^{1/4}$ profile) by a sizable central depression in the isotropic velocity dispersion, which is not observed, and in addition observations support the idea that ellipticals are characterized by a *total* density distribution well described by a r^{-2} profile over a large radial range (e.g., see Treu and Koopmans 2002, 2004, Rusin and Kochanek 2005, Czoske et al. 2008, Dye et al. 2008). For these reasons, in the studies conducted after Ciotti and Ostriker (2007) we adopt Jaffe (1983) stellar

models embedded in a dark halo so that the total mass profile decreases as r^{-2}. The stellar density profile of the galaxy models is

$$\rho_* = \frac{M_* r_*}{4\pi r^2 (r_* + r)^2}, \tag{4.2}$$

where M_* and r_* are the total stellar mass and the scale-length of the galaxy, respectively, and the effective radius is $R_\mathrm{e} = 0.7447 r_*$. The total density profile is then given by

$$\rho_\mathrm{T} = \frac{\mathscr{R} M_*}{4\pi r_* r^2} = \frac{v_\mathrm{c}^2}{4\pi G r^2}, \tag{4.3}$$

where the dimensionless factor $\mathscr{R}$ controls the amount of dark matter contained within r_*, and v_c is the constant circular velocity.

All the dynamical and phase-space properties of these two-component galaxy models are given in Ciotti et al. (2009), where in particular it is shown that the central projected velocity dispersion $\sigma_\circ$ (obtained by solving and projecting the Jeans equations under the assumption of orbital isotropy[2]) is given by

$$\sigma_\circ = \frac{v_\mathrm{c}}{\sqrt{2}} = \sqrt{\frac{G\mathscr{R} M_*}{2 r_*}}. \tag{4.4}$$

An important ingredient in the energetics of the gas flows, namely the thermalization of the stellar mass losses due to the stellar velocity dispersion (e.g., see Parriott and Bregman 2008), depends on the radial trend of this latter quantity which, for the isotropic models here considered is given by

$$\rho_* \sigma_*^2 = \rho_* \sigma_{*\circ}^2 + \frac{G M_* M_\mathrm{BH}}{4\pi r_*^4} \left[\frac{1 - 2s + 6s^2 + 12 s^3}{3 s^3 (1+s)} - 4 \ln\left(1 + \frac{1}{s}\right) \right], \quad s \equiv \frac{r}{r_*}, \tag{4.5}$$

where $\sigma_{*\circ}$ is the isotropic 1-dimensional stellar velocity dispersion without the contribution of the SMBH. Note that in the thermalization of the stellar mass losses we also consider the (time increasing) contribution of the gravitational field of the central SMBH.

In order to use realistic galaxy models, the mass distribution is determined as follows. We fix a value for $\sigma_\circ$, and we determine the galaxy *present day* model blue luminosity L_B from the Faber–Jakson relation

$$\frac{L_\mathrm{B}}{10^{11} L_{\mathrm{B}\odot}} = 0.23 \left(\frac{\sigma_\circ}{300\,\mathrm{km/s}} \right)^{2.4} + 0.62 \left(\frac{\sigma_\circ}{300\,\mathrm{km/s}} \right)^{4.2} \tag{4.6}$$

[2]The effect of M_BH on $\sigma_\circ$ is not considered, in accordance with estimated values for the radius of the SMBH sphere of influence (e.g., Riciputi et al. 2005). In the new version of the code, fully general stellar and dark matter profiles are allowed.

and then the effective radius R_e (and so r_*) from the Fundamental Plane

$$\log R_e = A \log \sigma_\circ + B \log L_B + C. \tag{4.7}$$

We finally fix the relative amount of dark matter to stars within R_e by assigning $\mathscr{R}$, thus determining the total stellar mass M_* of the galaxy and the stellar mass-to-light ratio $\Upsilon_* \equiv M_*/L_B$. Observational studies (e.g., see Saglia et al. 1993, Bertin et al. 1994, Cappellari et al. 2006, Fabian et al. 1986, see also Binney and Evans 2001) indicate that dark matter begins to be dynamically important at 2-3R_e, and so we adopt $\mathscr{R} = 1$, the minimum admissible value for this class of models.

4.3.2 *Passive Stellar Evolution: SNe Ia Rate and Stellar Mass Losses*

The stellar mass loss rate and the SNe Ia rate associated with the initial stellar distribution are the main ingredients driving evolution of the models. The stellar mass loss rate follows the prescriptions of the stellar evolution theory, with

$$\dot{M}_* = \mathrm{IMF}(M_{TO})|\dot{M}_{TO}|\Delta M, \tag{4.8}$$

where the initial mass function IMF is a Salpeter law, the turn-off mass (in $M_\odot$) of stars at time t (in Gyr) is

$$\log M_{TO} = 0.0558(\log t)^2 - 1.338 \log t + 7.764, \tag{4.9}$$

and

$$\Delta M \equiv M_{TO} - M_{fin} = \begin{cases} 0.945 M_{TO} - 0.503 M_\odot, & (M_{TO} < 9 M_\odot), \\ M_{TO} - 1.4 M_\odot, & (M_{TO} \geq 9 M_\odot), \end{cases} \tag{4.10}$$

(see Ciotti et al. 1991). In the new version of the code, we adopt updated formulae based on the stellar mass losses given by Maraston (2005) and the IMF from Kroupa (2001) (see also Pellegrini, this volume). Also, following the latest observational and theoretical results (Cappellaro et al. 1999, Mannucci et al. 2005, Greggio 2005) we parametrize the time evolution of the SNe Ia rate as

$$R_{SN}(t) = 0.32 \times 10^{-12} h^2 \vartheta_{SN} \frac{L_B}{L_{B\odot}} \left(\frac{t}{13.7\,\mathrm{Gyr}} \right)^{-s} \quad \mathrm{year}^{-1}, \tag{4.11}$$

where the coefficient ϑ_{SN} fixes the present-day SNe Ia rate, and $h \equiv H_\circ/100$ km s^{-1} Mpc^{-1}. Assuming for each supernova event an energy release of $E_{SN} = 10^{51}$ erg, a fraction η_{SN} of which is thermalized in the surrounding ISM, the energy input

per unit time over all the galaxy body is

$$L_{\rm SN}(t) = 1.015\times 10^{31} h^2 \vartheta_{\rm SN}\eta_{\rm SN}\frac{L_{\rm B}}{L_{\rm B\odot}}\left(\frac{t}{13.7\,{\rm Gyr}}\right)^{-s} \qquad {\rm erg\,s^{-1}}. \tag{4.12}$$

The specific value of s is a critical ingredient in the model evolution: when $s \gtrsim 1.3$ the flow evolves from wind to inflow, while the opposite is true for $s \lesssim 1.3$ (e.g., see Ciotti et al. 1991, Pellegrini and Ciotti 1998, and Pellegrini, this volume). Here we restrict to the currently favoured $s = 1.1$ value, even though a more complicate time dependence than a simple power-law seems possible (e.g., Matteucci et al. 2006). We also assume that each SNe Ia ejects $1.4M_\odot$ of material in the ISM, so that the total rate of mass return from the aging initial stellar population is

$$\frac{d\rho_*}{dt} = (\alpha_* + \alpha_{\rm SN})\rho_*, \tag{4.13}$$

where $\alpha_{\rm SN}(t) = 1.4M_\odot\, R_{\rm SN}(t)/M_*$ and $\alpha_*(t) = \dot{M}_*(t)/M_*$ are the specific mass return rates. With these definitions, the SNe Ia kinetic energy injection per unit volume and unit time in the ISM are

$$\dot{E}_{\rm I} = \eta_{\rm SN}E_{\rm SN}\frac{R_{\rm SN}}{M_*}\rho_* = \eta_{\rm SN}E_{\rm SN}\frac{\alpha_{\rm SN}(t)\rho_*}{1.4M_\odot}. \tag{4.14}$$

4.3.3 Star Formation and SNe II Heating

The star formation rate at radius r is estimated from the equation

$$\dot{\rho}_*^+ = \frac{\eta_{\rm form}\rho}{\tau_{\rm form}}, \quad \tau_{\rm form} = \max(\tau_{\rm cool}, \tau_{\rm dyn}), \tag{4.15}$$

where ρ is the local gas density, $\eta_{\rm form} = 0.03 \div 0.4$ (Cen and Ostriker 2006), and the involved time scales are

$$\tau_{\rm cool} \equiv \frac{E}{C}, \quad \tau_{\rm dyn} = \min(\tau_{\rm Jeans}, \tau_{\rm rot}), \quad \tau_{\rm Jeans} \equiv \sqrt{\frac{3\pi}{32G\rho}}, \quad \tau_{\rm rot} \equiv \frac{2\pi r}{v_{\rm c}(r)}. \tag{4.16}$$

E and C are the gas internal energy and the effective cooling per unit volume (Sect. 4.3.6), while $v_{\rm c}(r)$ is the galaxy rotational velocity at radius r. In the code the stars are maintained in the place where they form, and the correspondent sinks of momentum and internal energy are given by the negative of

$$\dot{m}_*^+ = \frac{\eta_{\rm form}m}{\tau_{\rm form}}, \quad \dot{E}_*^+ = \frac{\eta_{\rm form}E}{\tau_{\rm form}}, \tag{4.17}$$

where m is the specific momentum of the ISM (Sect. 4.3.8).

For a total mass ΔM_* of newly formed stars in a given time-step and at a given place we assume a Salpeter IMF ($x > 1$, $M \geq M_{\rm inf} = 0.1 M_\odot$),

$$\frac{dN}{dM} = (x-1)\frac{\Delta M_*}{M_{\rm inf}^2} \times \left(\frac{M}{M_{\rm inf}}\right)^{-1-x}, \tag{4.18}$$

and so the total number of Type II Supernovae is

$$N_{\rm II} = \left(1 - \frac{1}{x}\right)\left(\frac{M_{\rm inf}}{M_{\rm II}}\right)^x \frac{\Delta M_*}{M_{\rm inf}} \simeq 7 \times 10^{-3} \frac{\Delta M_*}{M_\odot}, \tag{4.19}$$

where $M_{\rm II} = 8 M_\odot$, and the numerical value holds for $x = 1.35$. The SNe II efficiency is

$$\epsilon_{\rm II} \equiv \frac{N_{\rm II} E_{\rm SN} \eta_{\rm SN}}{\Delta M_* c^2} = \left(1 - \frac{1}{x}\right)\left(\frac{M_{\rm inf}}{M_{\rm II}}\right)^x \frac{E_{\rm SN}\eta_{\rm SN}}{M_{\rm inf} c^2} \simeq 3.9 \times 10^{-6} \eta_{\rm SN}; \tag{4.20}$$

(usually $\eta_{\rm SN} = 0.85$). The characteristic time for SNe II explosion is fixed to $\tau_{\rm II} = 2 \times 10^7$ year, and from (4.15) and (4.20) their luminosity (per unit volume) at each r is

$$\dot{E}_{\rm II}(t) \equiv \frac{\epsilon_{\rm II} c^2}{\tau_{\rm II}} \int_0^t \dot{\rho}_*^+(t') e^{-\frac{t-t'}{\tau_{\rm II}}} dt'. \tag{4.21}$$

Assuming that each massive star leaves a remnant of $1.4 M_\odot$ (but see also Renzini and Ciotti 1993), the mass return from SNe II progenitors is

$$\frac{M_{\rm II}^{\rm ej}}{\Delta M_*} = \left(\frac{M_{\rm inf}}{M_{\rm II}}\right)^{x-1} - \frac{1.4 N_{\rm II} M_\odot}{\Delta M_*} \simeq 0.2, \tag{4.22}$$

and so the mass return rate per unit volume of the young evolving stellar populations is

$$\dot{\rho}_{\rm II}(t) \simeq \frac{0.2}{\tau_{\rm II}} \int_0^t \dot{\rho}_*^+(t') e^{-\frac{t-t'}{\tau_{\rm II}}} dt'. \tag{4.23}$$

Finally, the code computes the optical and UV luminosity per unit volume of the new stars

$$\dot{E}_{\rm opt}(t) \equiv \frac{\epsilon_{\rm opt} c^2}{\tau_{\rm opt}} \int_0^t \dot{\rho}_*^+(t') e^{-\frac{t-t'}{\tau_{\rm opt}}} dt', \tag{4.24}$$

and

$$\dot{E}_{\rm UV}(t) \equiv \frac{\epsilon_{\rm UV} c^2}{\tau_{\rm UV}} \int_0^t \dot{\rho}_*^+(t') e^{-\frac{t-t'}{\tau_{\rm UV}}} dt', \tag{4.25}$$

respectively, where $\epsilon_{\rm opt} = 1.24 \times 10^{-3}$, $\epsilon_{\rm UV} = 8.65 \times 10^{-5}$, $\tau_{\rm opt} = 1.54 \times 10^8$ year, and $\tau_{\rm UV} = 2.57 \times 10^6$ year are the efficiency and characteristic time of optical and UV emission, respectively (Ciotti and Ostriker 2007).

4.3.4 The Circumnuclear Disk and the SMBH Accretion Luminosity

At the onset of the cooling catastrophe a large amount of gas suddenly flows onto the central regions of the galaxy, and this induces star formation and accretion on the central SMBH, producing a burst of energy. However observations indicate that accretion onto the central SMBH is mediated by a circumnuclear disk. In our treatment the disk is not simulated with hydrodynamical equations, but its description is needed to obtain important quantities required by the code.

The circumnuclear disk, which is the repository of the gas inflowing at a rate $\dot{M}_1^{\rm eff}$ from the first active mesh point R_1 of the hydrodynamical grid, and which feeds the central SMBH at a rate $\dot{M}_{\rm BH}$, contains at any time the mass gas $M_{\rm dg}$ and a total stellar mass $M_{\rm d*} = M_{\rm dl*} + M_{\rm dh*}$ (with a division mass among low and high mass stars at $8M_\odot$). The disk also contains a mass $M_{\rm rem}$ of remnants from the earlier generations of evolved stars. The accretion rate on the central SMBH is Eddington modulated as

$$\dot{M}_{\rm BH} = \frac{\dot{M}_{\rm fid}}{1+\eta_{\rm d}}, \tag{4.26}$$

where

$$\dot{M}_{\rm fid} \equiv \frac{M_{\rm dg}}{\tau_{\rm d}}, \quad \eta_{\rm d} \equiv \frac{\dot{M}_{\rm fid}}{2\dot{M}_{\rm Edd}}, \quad \dot{M}_{\rm Edd} \equiv \frac{L_{\rm Edd}}{\epsilon_0 c^2}, \tag{4.27}$$

and ϵ_0 is defined in (4.29). Equations (4.26)–(4.27) guarantee that when $\eta_{\rm d} \ll 1$ the SMBH accretion rate approaches $\dot{M}_{\rm fid}$, while $\dot{M}_{\rm BH} = 2\dot{M}_{\rm Edd}$ for $\eta_{\rm d} \gg 1$. Following Ciotti and Ostriker (2001) the instantaneous "ADAF-like" bolometric accretion luminosity is

$$L_{\rm BH} = \epsilon_{\rm ADAF}\, \dot{M}_{\rm BH}\, c^2, \tag{4.28}$$

where

$$\epsilon_{\rm ADAF} = \epsilon_0 \frac{A\dot{m}}{1+A\dot{m}}, \quad \dot{m} \equiv \frac{\dot{M}_{\rm BH}}{\dot{M}_{\rm Edd}}, \tag{4.29}$$

so that $\epsilon_{\rm ADAF} \sim \epsilon_0 A\dot{m}$ for $\dot{m} \ll A^{-1}$. In the simulations we fix $A = 100$ (see, e.g. Narayan and Yi 1994, Ciotti and Ostriker 2001 for a preliminary exploration), and we adopt $\epsilon_0 = 0.1$ or 0.2 (e.g., see Noble et al. 2009). We finally introduce the normalized accretion luminosity

$$l \equiv \frac{L_{\rm BH}}{L_{\rm Edd}} = \frac{A\dot{m}^2}{1+A\dot{m}}. \tag{4.30}$$

There are two *lag times* in our problem. The first is the *instantaneous disk lag time*, appearing in (4.27),

$$\tau_{\rm d} \equiv \frac{2\pi}{\alpha}\sqrt{\frac{R_{\rm d}^3}{GM_{\rm BH}}}, \tag{4.31}$$

where $\alpha \simeq 10^{-2} - 10^{-1}$ is the disk viscosity coefficient (Shakura and Sunyaev 1973), and $R_{\rm d}$ is the instantaneous value of the fiducial radius of the circumnuclear disk. From the thin-disk theory

$$R_{\rm d}(t) = f_d\, R_1 \times \left(\frac{M_{\rm BH}}{M_{\rm BH0}}\right)^{2/3}, \tag{4.32}$$

(e.g., see Morgan et al. 2010) where $M_{\rm BH0}$ is the SMBH mass at the beginning of the simulation. We assume $f_d = 0.4$, so that $R_{\rm d}(0) \simeq 2$ pc for an initial SMBH mass of $\simeq 10^8 M_\odot$. The second characteristic time is the instantaneous *infall* lag time from R_1 to the disk, estimated as

$$\tau_{\rm i} = \frac{R_1}{v_{\rm ff}}, \quad v_{\rm ff} \equiv \sqrt{\frac{2GM_{\rm BH}}{R_1}}, \tag{4.33}$$

and the effective rate at which gas accretes on the disk is obtained from

$$\frac{d\dot{M}_1^{\rm eff}}{dt} = \frac{\dot{M}_1 - \dot{M}_1^{\rm eff}}{\tau_{\rm i}}, \tag{4.34}$$

where $\dot{M}_1$ is the instantaneous rate at which gas flows through the first active grid point[3]. It follows that when $\dot{M}_1$ provided by hydrodynamics drops to zero the circumnuclear disk experiences a fueling declining exponentially with time.

The disk total gas mass $M_{\rm dg}$ is not only the source of SMBH accretion, but also of star formation in the disk: we assume that a fraction of $M_{\rm dg}$ is converted into stars at a rate $\eta_* \dot{M}_{\rm fid}$ (where $\eta_* \simeq 10 M_{\rm dg}/M_{\rm BH}$), and that another fraction of $M_{\rm dg}$ is lost as a *disk wind* and as a *jet* at instantaneous rates given by $\eta_{\rm w}\dot{M}_{\rm BH}$ and $\eta_{\rm j}\dot{M}_{\rm BH}$, so that the equation for the gas mass in the disk is

$$\frac{dM_{\rm dg}}{dt} = \dot{M}_1^{\rm eff} - (1 + \eta_{\rm w} + \eta_{\rm j})\dot{M}_{\rm BH} - \eta_* \dot{M}_{\rm fid}. \tag{4.35}$$

The stars formed in the disk are described separately as a function of their mass, i.e., high-mass stars ($M > M_{\rm II}$) produce a total disk mass $M_{\rm dh*}$, and low-mass stars ($M_{\rm inf} < M < M_{\rm II}$) contribute to a disk mass $M_{\rm dl*}$ according to the equations

$$\frac{dM_{\rm dl*}}{dt} = (1 - f_{\rm h})\eta_* \dot{M}_{\rm fid} - \frac{M_{\rm dl*}}{\tau_{*\rm l}}; \quad \frac{dM_{\rm dh*}}{dt} = f_{\rm h}\eta_* \dot{M}_{\rm fid} - \frac{M_{\rm dh*}}{\tau_{*\rm h}}. \tag{4.36}$$

For the characteristic evolutionary times we adopt $\tau_{*\rm l} = \tau_{\rm opt}$ and $\tau_{*\rm h} = \tau_{\rm II}$, while we assume $f_{\rm h} = 0.5$, corresponding to a top-heavy Salpeter-like initial mass function

[3] $\dot{M}_1$ is taken positive in case of accretion and zero in case of outflow at R_1.

(e.g., see Nayakshin and Sunyaev 2005) of slope $x \simeq 1.16$ and minimum mass $M_{\rm inf} = 0.1 M_\odot$. The associated optical ($L_{\rm d,opt}$) and UV ($L_{\rm d,UV}$) luminosities of the stellar disk are calculated as described in Sect. 4.3.7. Finally stellar remnants mass in the disk evolves as

$$\frac{dM_{\rm rem}}{dt} = f_{\rm rem,l}\frac{M_{\rm dl*}}{\tau_{*\rm l}} + f_{\rm rem,h}\frac{M_{\rm dh*}}{\tau_{*\rm h}}, \tag{4.37}$$

where $f_{\rm rem,l} = 0.2$, $f_{\rm rem,h} = 0.09$.

The equation for the mass loss associated with the disk wind is

$$\frac{dM_{\rm dw}}{dt} = \eta_{\rm w}\dot{m} + (1 - f_{\rm rem,l})\frac{M_{\rm dl*}}{\tau_{*\rm l}} + (1 - f_{\rm rem,h})\frac{M_{\rm dh*}}{\tau_{*\rm h}} : \tag{4.38}$$

the first term is a mass loss driven as a wind by the central SMBH, and the second and third are from high mass and low mass stars in the central disk.

Two different classes of models, that we call *Type A* and *Type B*, are explored. In particular, we use for the ratio of the wind outflow rate to the SMBH accretion rate

$$\eta_{\rm w} \equiv \begin{cases} 2, & \text{[A]} \\ \dfrac{3\eta_{\rm w}^{\rm M}}{4}\dfrac{l}{1+0.25l}, & \text{[B].} \end{cases} \tag{4.39}$$

Therefore, in Type B models, the efficiency of ejecting a wind increases with increasing Eddington ratio, and $\eta_{\rm w}^{\rm M}$ fixes the maximum value of $\eta_{\rm w}$ (see Fig. 4.1 in Ciotti et al. 2009). We stress that the scaling of the nuclear wind mass loss rate and mechanical power are based on the results of dedicated numerical simulations (e.g., see Proga et al. 1998, Proga 1999, Proga et al. 2000, Proga and Kallman 2002, 2004, Dorodnitsyn et al. 2008) and observational works (e.g., Ganguly and Brotherton 2008, Holt et al. 2008).

In addition to the nuclear wind, the differential equations for a *nuclear jet* with instantaneous mass flow

$$\frac{dM_{\rm j}}{dt} = \eta_{\rm j}\dot{m}, \quad \eta_{\rm j} = \frac{0.2}{(1+100l)^4}; \tag{4.40}$$

are also considered. The trend of $\eta_{\rm j}$ as a function of l is shown in Fig. 4.1 of Ciotti et al. (2009), where it is apparent how the mass ejected by the jet is always negligible with respect to the wind mass loss in Type A models, while it is slightly dominant over the wind in Type B models at low luminosity ratios.

4.3.5 The Mechanical Feedback Treatment

Another important ingredient of the simulations is how the kinetic energy, momentum and mass of the BLR wind (and of the jet) are transferred to the ISM. The *instantaneous mechanical luminosity* of the disk wind is given by

$$L_{\rm dw} = \epsilon_{\rm w}\dot{M}_{\rm BH}c^2 + \epsilon_{\rm II}c^2(1 - f_{\rm rem,h})\frac{M_{\rm dh*}}{\tau_{*\rm h}}, \tag{4.41}$$

where $\epsilon_{\rm w}$ is the mechanical efficiency of the wind, and the second term describes the energy release due to the SNe II explosions of the high-mass stars in the circumnuclear disk. In analogy with (4.39), we assume

$$\epsilon_{\rm w} \equiv \epsilon_{\rm w}^{\rm M} \times \begin{cases} 1, & \text{[A]} \\ \dfrac{3}{4}\dfrac{l}{1+0.25l}, & \text{[B]}, \end{cases} \tag{4.42}$$

and we consider the range $3\,10^{-5} \le \epsilon_{\rm w}^{\rm M} \le 5\,10^{-3}$ (Di Matteo et al. 2005 adopted $5\,10^{-3}$). In both cases the *instantaneous disk wind velocity* is given by

$$v_{\rm w} \equiv \sqrt{\frac{2L_{\rm dw}}{\dot{M}_{\rm dw}}} \simeq \sqrt{\frac{2\epsilon_{\rm w}}{\eta_{\rm w}}}c. \tag{4.43}$$

In Type A models $v_{\rm w}$ is in the range $2\,10^3 - 2\,10^4$ km s^{-1}, in agreement with observations of BLRs (e.g., Crenshaw et al. 2003). In Type B models we require $v_{\rm w} = 10^4$ km s^{-1}, so that

$$\eta_{\rm w}^{\rm M} = 1800\epsilon_{\rm w}^{\rm M}. \tag{4.44}$$

Similarly, the *instantaneous jet mechanical luminosity* is

$$L_{\rm j} = \epsilon_{\rm jet}\dot{m}c^2, \quad \epsilon_{\rm jet} = \frac{0.0125}{(1+400l)^4}, \tag{4.45}$$

and the jet velocity is given by

$$v_{\rm j} \equiv \sqrt{\frac{2L_{\rm j}}{\dot{M}_{\rm j}}} = \sqrt{\frac{2\epsilon_{\rm jet}}{\eta_{\rm j}}}\,c, \tag{4.46}$$

which, for our chosen parameterization gives high but subrelativistic jet velocity (Fig. 4.1 in Ciotti et al. 2009). The momentum of the wind and jet are

$$m_{\rm w} \equiv \dot{M}_{\rm dw}v_{\rm w}, \quad m_{\rm j} \equiv \dot{M}_{\rm j}v_{\rm j}, \tag{4.47}$$

and the nuclear wind mechanical feedback is distributed over the galaxy ISM as follows. First we introduce the *instantaneous wind lag time*

$$\tau_{\rm w} \equiv \frac{R_1}{v_{\rm w}} \tag{4.48}$$

from the center to the first active grid point R_1, and at each time step we compute the time-lagged values for mass, momentum, and kinetic energy at R_1 by integrating

$$\frac{dX_l}{dt} = \frac{X - X_l}{\tau_{\rm w}}, \tag{4.49}$$

where X_l is the generic lagged variable associated with the instantaneous unlagged value X. Outside R_1 we integrate the differential equation (see Ciotti et al. 2009)

$$\frac{\partial \ln Y_{\rm w}}{\partial \ln r} = -\frac{P_{\rm ISM}(r)}{P_{\rm w}(r)} - \frac{r}{v_{\rm w}}\frac{\partial \ln Y_{\rm w}}{\partial t}, \tag{4.50}$$

where $Y_{\rm w}$ is the mass, momentum and energy of the disk wind/jet component at distance r from the center, $P_{\rm w}(r)$ is the local wind/jet pressure, and for each quantity $Y(R_1) = X_l$. In practice, we first integrate (4.50) for pressure, i.e.,

$$P_{\rm w} = \frac{Y_{\rm w}}{2\Delta\Omega_{\rm w} r^2}, \tag{4.51}$$

where $Y_{\rm w}$ is the effective wind/jet momentum crossing the shell of radius r. Once $P_{\rm w}(r)$ is known over the whole grid, (4.50) for can be integrated for mass and energy. We thus determine how much of the mechanical energy, momentum and returned mass are deposited in the ISM at each radius.

The solid angle in the denominator of (4.51) is the opening angle of each emission cone of the wind. We adopt

$$\Delta\Omega_{\rm w} = \pi \times \begin{cases} 1 & \text{[A]} \\ \min(\sqrt{l^2 + (\Delta\Omega_{\rm j}/\pi)^2}, 1), & \text{[B]}, \end{cases} \tag{4.52}$$

where $\Delta\Omega_{\rm j} = 2.5\ 10^{-2}$ is the jet fiducial opening angle, and case B is designed to mimic the behavior found in radiation driven winds: higher luminosity corresponds to a larger opening angles (see Fig. 4.1 of Ciotti et al. (2009)).

To implement numerically the mechanical feedback terms, we finally compute the nuclear wind mass, momentum and kinetic energy per unit volume deposited in each shell as

$$\text{Source}_{\rm w} = \frac{3}{4\pi}\frac{Y_{\rm w}(R_i) - Y_{\rm w}(R_{i+1})}{R_{i+1}^3 - R_i^3} \tag{4.53}$$

and we add them to the r.h.s. of (4.85)–(4.87). We note that in the current simulations the equations are integrated both for the nuclear wind and the jet, but only the wind feedback component is added to the hydrodynamics. We are currently working on a 2D version of the code, and the first results have been already published (Ostriker et al. 2010, Novak et al. 2011).

4.3.6 Radiative Heating and Cooling

Radiative heating and cooling are computed by using the formulae in Sazonov et al. (2005), which describe the net heating/cooling rate per unit volume $\dot{E}$ of a cosmic plasma in photoionization equilibrium with a radiation field characterized by the average quasar Spectral Energy Distribution (Sazonov et al. 2004, 2007, 2008), whose associated spectral temperature is $T_{\rm X} \simeq 2$ keV. In particular, Compton heating and cooling, bremsstrahlung losses, line and continuum heating and cooling, are taken into account.

The net gas energy change rate per unit volume $\dot{E}$ for $T \gtrsim 10^4$ K (all quantities are expressed in cgs system) is given by

$$\dot{E} = n^2(S_1 + S_2 + S_3) \equiv H - C, \tag{4.54}$$

where n is the Hydrogen number density, and positive and negative terms are grouped together in the heating (H) and cooling (C) functions. The bremsstrahlung losses and the Compton heating and cooling are given respectively by

$$S_1 = -3.8 \times 10^{-27}\sqrt{T}, \tag{4.55}$$

and

$$S_2 = 4.1 \times 10^{-35}(T_{\rm X} - T)\,\xi, \tag{4.56}$$

where $T_{\rm X}$ is the Compton temperature, and finally the sum of photoionization heating, line and recombination continuum cooling is

$$S_3 = 10^{-23}\frac{a + b\,(\xi/\xi_0)^c}{1 + (\xi/\xi_0)^c}\frac{Z}{Z_\odot}, \tag{4.57}$$

where the almost perfect linear dependence on metallicity is explicit, and

$$a = -\frac{18}{e^{25(\log T - 4.35)^2}} - \frac{80}{e^{5.5(\log T - 5.2)^2}} - \frac{17}{e^{3.6(\log T - 6.5)^2}}, \tag{4.58}$$

$$b = 1.7 \times 10^4\, T^{-0.7}, \quad c = 1.1 - \frac{1.1}{e^{T/1.8\,10^5}} + \frac{4 \times 10^{15}}{T^4}, \tag{4.59}$$

$$\xi_0 = \left(\frac{1.5}{T^{0.5}} + \frac{1.5 \times 10^{12}}{T^{2.5}}\right)^{-1} + \frac{4 \times 10^{10}}{T^2}\left[1 + \frac{80}{e^{(T-10^4)/1.5\,10^3}}\right]. \tag{4.60}$$

Equations (4.56)–(4.57) depend on the ionization parameter

$$\xi \equiv \frac{L^{\rm eff}_{\rm BH,photo}(r)}{n(r)r^2}, \tag{4.61}$$

where the effective accretion luminosity is evaluated by numerically solving equation

$$\frac{dL^{\rm eff}_{\rm BH,photo}}{dr} = -4\pi r^2\, H, \tag{4.62}$$

with central boundary condition $L^{\rm eff}_{\rm BH,photo}(0) = L_{\rm BH}(t)$ given by (4.28). The photoionization+Compton opacity associated with radiation absorption is then obtained

$$\kappa_{\rm photo} = -\frac{1}{\rho(r) L^{\rm eff}_{\rm BH,photo}(r)} \frac{dL^{\rm eff}_{\rm BH,photo}(r)}{dr} = \frac{4\pi r^2 H(r)}{\rho(r) L^{\rm eff}_{\rm BH,photo}(r)}. \tag{4.63}$$

Finally, the bolometric ISM luminosity is calculated from the cooling term as

$$L_{\rm r}(r) = 4\pi \int_0^r C r^2 dr. \tag{4.64}$$

4.3.7 Radiation Pressure

An important ingredient in the modelization of the gas flow evolution is the radiation pressure due to the accretion luminosity and to the light produced by the new stars (e.g., see Murray et al. 2005, Thompson et al. 2005). Radiation pressure due to *electron scattering* is

$$(\nabla p_{\rm rad})_{\rm es} = -\frac{\kappa_{\rm es}\rho}{c} \frac{L_{\rm BH} + L_{\rm UV}(r) + L_{\rm opt}(r) + L_{\rm r}(r)}{4\pi r^2}, \tag{4.65}$$

where $\kappa_{\rm es} = 0.35$ in c.g.s. units, from (4.24) to (4.25)

$$L_{\rm UV}(r) = 4\pi \int_0^r \dot{E}_{\rm UV} r^2 dr, \quad L_{\rm opt}(r) = 4\pi \int_0^r \dot{E}_{\rm opt} r^2 dr, \tag{4.66}$$

and all the luminosities used in (4.65) are unabsorbed.

The radiation pressure due to *dust opacity* is

$$(\nabla p_{\rm rad})_{\rm dust} = -\frac{\kappa_{\rm UV}\rho}{c} \frac{L^{\rm eff}_{\rm BH,UV}(r) + L^{\rm eff}_{\rm UV}(r)}{4\pi r^2} - \frac{\kappa_{\rm opt}\rho}{c} \frac{L^{\rm eff}_{\rm BH,opt}(r) + L^{\rm eff}_{\rm opt}(r)}{4\pi r^2} - \frac{\kappa_{\rm IR}\rho}{c} \frac{L_{\rm IR}(r)}{4\pi r^2}, \tag{4.67}$$

where

$$L_{\rm IR}(r) \equiv L^{\rm abs}_{\rm BH,UV}(r) + L^{\rm abs}_{\rm BH,opt}(r) + L^{\rm abs}_{\rm UV}(r) + L^{\rm abs}_{\rm opt}(r), \tag{4.68}$$

is the infrared luminosity due to recycling of photons absorbed from the ISM, and we adopt as estimates for (cgs) opacity in three bands

$$\kappa_{\rm opt} = \frac{300}{1 + T/10^4}, \quad \kappa_{\rm UV} = 4\kappa_{\rm opt}, \quad \kappa_{\rm IR} = \frac{\kappa_{\rm opt}}{150}, \tag{4.69}$$

where the temperature dependent denominator is designed to mimic the destruction of dust at high temperatures. At variance with electron scattering the *effective* luminosities appearing in (4.67)–(4.68) take into account absorption, and are obtained by numerically solving the two lowest spherically symmetric moment equations of radiative transfer in the Eddington approximation (e.g., Chandrasekhar 1960):

$$\frac{dL^{\rm eff}_{\rm UV}}{dr} = 4\pi r^2(\dot{E}_{\rm UV} - \kappa_{\rm UV}\rho J^{\rm eff}_{\rm UV}), \quad \frac{dL^{\rm eff}_{\rm opt}}{dr} = 4\pi r^2(\dot{E}_{\rm opt} - \kappa_{\rm opt}\rho J^{\rm eff}_{\rm opt}). \tag{4.70}$$

$$\frac{dJ^{\rm eff}_{\rm UV}}{dr} = -\frac{3\kappa_{\rm UV}\rho L^{\rm eff}_{\rm UV}}{4\pi r^2}, \quad \frac{dJ^{\rm eff}_{\rm opt}}{dr} = -\frac{3\kappa_{\rm opt}\rho L^{\rm eff}_{\rm opt}}{4\pi r^2}, \tag{4.71}$$

The central boundary conditions for stellar luminosities are $L^{\rm eff}_{\rm UV}(0) = L_{\rm d,UV}$, $L^{\rm eff}_{\rm opt}(0) = L_{\rm d,opt}$, $J^{\rm eff}_{\rm UV}(0) = L_{\rm d,UV}/4\pi R_{\rm I}^2$ and $J^{\rm eff}_{\rm opt}(0) = L_{\rm d,opt}/4\pi R_{\rm I}^2$.

The effective accretion luminosities $L^{\rm eff}_{\rm BH,UV}$ and $L^{\rm eff}_{\rm BH,opt}$ are computed with two equations similar to (4.70), where the distributed source term is missing, $J = L^{\rm eff}_{\rm BH}/4\pi r^2$, and in the UV and optical bands $L^{\rm eff}_{\rm BH,UV}(0) = 0.2L_{\rm BH}(t)$ and $L^{\rm eff}_{\rm BH,opt}(0) = 0.1L_{\rm BH}(t)$, respectively.

The last contribution to radiation pressure comes from *photoionization opacity*,

$$(\nabla p_{\rm rad})_{\rm photo} = -\frac{\rho\kappa_{\rm photo}}{c}\frac{L^{\rm eff}_{\rm BH,photo}(r)}{4\pi r^2}, \tag{4.72}$$

where the photoionization opacity and the absorbed accretion luminosity are calculated as described in Sect. 4.3.6.

4.3.8 Hydrodynamical Equations

The evolution of the galactic gas flows is obtained integrating the time–dependent Eulerian equations of hydrodynamics

$$\frac{\partial\rho}{\partial t} + \nabla\cdot(\rho v) = \alpha\rho_* + \dot{\rho}_{\rm II} - \dot{\rho}^+_* + \dot{\rho}_{\rm w}, \tag{4.73}$$

$$\frac{\partial m}{\partial t} + \nabla\cdot(mv) = -(\gamma-1)\nabla E - \nabla p_{\rm rad} + g\rho - \dot{m}^+_* + \dot{m}_{\rm w}, \tag{4.74}$$

$$\frac{\partial E}{\partial t} + \nabla \cdot (Ev) = -(\gamma - 1)\, E \nabla \cdot v + H - C \qquad (4.75)$$
$$+ \frac{(\alpha \rho_* + \dot{\rho}_{\rm II})(v^2 + 3\sigma_*^2)}{2} + \dot{E}_{\rm I} + \dot{E}_{\rm II} - \dot{E}_*^+ + \dot{E}_{\rm w}.$$

ρ, m, and E are the gas mass, momentum and internal energy per unit volume, respectively, and v is the gas velocity. The ratio of the specific heats is $\gamma = 5/3$, and $g(r)$ is the gravitational field of the galaxy (stars and dark matter), plus the contribution of the central SMBH. The gravitational field is updated at each time step by considering the SMBH mass growth; for simplicity, we do not take into account neither the ISM contribution, nor the mass redistribution due to the stellar mass losses and star formation. The total radiative pressure gradient is $\nabla p_{\rm rad} = (\nabla p_{\rm rad})_{\rm es} + (\nabla p_{\rm rad})_{\rm dust} + (\nabla p_{\rm rad})_{\rm photo}$, while $H - C$ is the radiative heating and cooling term. The energy source terms associated with stellar evolution are obtained under the assumption of a null streaming velocity of the sources, neglecting the small contributions of the internal energy of the injected gas, and of the kinetic energy of stellar wind when compared to the local stellar velocity dispersion contribution (Recchi et al. 2000). Note that the term proportional to the stellar velocity dispersion becomes dominant near the SMBH, as described in (4.5), so that hotter and hotter gas is injected near the SMBH. For physical consistency, the first active grid point R_1 is placed within the Compton radius

$$R_{\rm X} = \frac{2GM_{\rm BH}\mu m_{\rm p}}{3k_{\rm B}T_{\rm X}} \simeq 3.6\mu \frac{M_{\rm BH}}{10^8 M_\odot} \frac{10^7 {\rm K}}{T_{\rm X}} \quad {\rm pc}, \qquad (4.76)$$

so that at R_1 we can impose the physical condition of a vanishing *thermodynamical* pressure gradient, leading to gas free-fall on the circumnuclear disk when the radiation pressure is negligible.

4.4 Results

We now illustrate the main properties of model $B3_{02}$ (discussed in Ciotti et al. 2010) and two variants obtained by increasing ($B3^{\rm h}_{02}$) and decreasing ($B3^{\rm l}_{02}$) its central velocity dispersion, while keeping the remaining input physics identical. The galaxy models are constructed as described in Sect. 4.3.1, and their structural parameters are given in Table 4.1. For sake of comparison, we recall that for model $B3_{02}$ the initial stellar mass is $M_* \simeq 2.9 \times 10^{11} M_\odot$, the Fundamental Plane effective radius $R_{\rm e} \simeq 6.9$ kpc, and the central aperture velocity dispersion $\sigma_{\rm a} = 260$ km s^{-1}. The initial mass of the central SMBH is assumed to follow the present day Magorrian relation ($M_{\rm BH} \simeq 10^{-3} M_*$), as it is believed that the bulk of the SMBH mass is assembled during the process of galaxy formation (e.g., Haiman et al. 2004, Sazonov et al. 2005, Lusso and Ciotti 2010), a process which is not addressed with the present

Table 4.1 The structural parameters of model $B2_{02}$ and its low and high mass variants, and the relevant mass budgets (discussed in Sect. 4.4.2) at the end of the simulations

Model	σ_0	R_e	L_B	M_*	$\log \Delta M_{BH}$	$\log \Delta M_*$	$\log \Delta M_w$	$\log M_{ISM}$
$B3^l_{02}$	240	5.77	3.78	2.04	8.36	9.22	10.21	9.13
$B3_{02}$	260	6.91	5.03	2.87	9.06	10.22	10.31	9.34
$B3^h_{02}$	280	8.20	6.59	3.95	9.41	10.58	10.40	9.75

Velocity dispersions are in km/s, effective radii in kpc, luminosities are in $10^{10} L_\odot$, stellar masses in $10^{11} M_\odot$. In the logarithms, masses are in Solar Masses

simulations. Note that these models are not appropriate as initial conditions for cosmological simulations, because their parameters are fixed to reproduce nearby early-type galaxies (at $z = 0$), and also because of the outflow boundary conditions imposed at the galaxy outskirts (~ 250 kpc).

The initial conditions for the ISM are represented by a very low density gas at the local thermalization temperature. The establishment of such high-temperature gas phase at early cosmological times is believed to be due to a "phase-transition" when, as a consequence of star formation, the gas-to-stars mass ratio was of the order of 10% and the combined effect of shocks, SN explosions and AGN feedback became effective in heating the gas and driving galactic winds (e.g., see Renzini et al. 1993, Ostriker and Ciotti 2005, Di Matteo et al. 2005, Springel et al. 2005, Johansson et al. 2008).

Important quantities associated with the model evolution are the mass (luminosity) accretion weighted EM and mechanical efficiencies

$$< \epsilon_{ADAF} > \equiv \frac{\int \epsilon_{ADAF} \dot{M}_{BH}\, dt}{\Delta M_{BH}}; \quad < \epsilon_w > \equiv \frac{\int \epsilon_w \dot{M}_{BH}\, dt}{\Delta M_{BH}} \tag{4.77}$$

where ΔM_{BH} is the mass accreted by the SMBH over the time interval considered. In addition to the time-averaged quantities introduced above, we also compute the *number of bursts* of each model (each burst being counted when L_{BH} becomes larger than $L_{Edd}/30$), the total time spent at $L_{BH} \geq L_{Edd}/30$ (bolometric), the total time spent at $L^{eff}_{BH,UV} \geq 0.2 L_{Edd}/30$ (UV, after absorption), and at $L^{eff}_{BH,opt} \geq 0.1 L_{Edd}/30$ (optical, after absorption). The two numerical coefficients take into account the fraction of the bolometric luminosity used as boundary condition to solve the radiative transfer equation in each of the two bands (Sect. 4.3).

4.4.1 Luminosities

The central panel of Fig. 4.1 shows the evolution of the accretion luminosity of model $B3_{02}$, fully discussed in Ciotti et al. (2010). After a first evolutionary phase in which a galactic wind is sustained by the combined heating of SNe Ia

and thermalization of stellar velocity dispersion, the central "cooling catastrophe" commences. In absence of the central SMBH a "mini-inflow" would be then established, with the flow stagnation radius (i.e., the radius at which the flow velocity is zero) of the order of a few hundred pc to a few kpc. These "decoupled" flows are a specific feature of cuspy galaxy models with moderate SNe Ia heating (Pellegrini and Ciotti 1998). However, after the central cooling catastrophe, the feedback caused by photoionization, Compton heating, and mechanical feedback, strongly affects the subsequent evolution, as can be seen in Fig. 4.1 where we show the luminosity evolution of the central AGN with time-sampling of 10^5 years. The corresponding Eddington limit is represented by the almost horizontal solid line. As already discussed in previous papers, the major AGN outbursts are separated by increasing intervals of time (set by the cooling time and by mass return rate from the evolving stellar population), and present a characteristic temporal substructure, whose origin is due to the cooperating effect of direct and reflected shock waves.

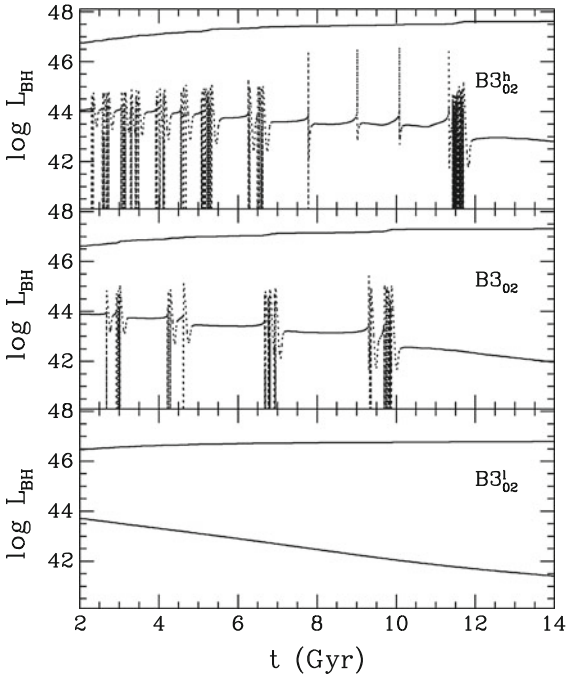

Fig. 4.1 *Dotted lines* are the optical SMBH luminosity corrected for absorption $L^{\rm eff}_{\rm BH,opt}$ (i.e, as would be observed from infinity) for the three models. We recall that at the center we fixed $L^{\rm eff}_{\rm BH,opt}(R_1) = 0.1 L_{\rm BH}$. The almost horizontal *solid line* is $L_{\rm Edd}$. The structural properties of the galaxy models are given in Table 4.1. The feedback is of Type B, i.e. with a nuclear wind mechanical efficiency dependent on the (normalized) accretion luminosity $l \equiv L_{\rm BH}/L_{\rm Edd}$, and with a peak mechanical efficiency of $\epsilon^{\rm M}_{\rm w} = 3\,10^{-4}$ and a peak radiative efficiency of $\epsilon_0 = 0.2$. The model in the central panel is discussed in detail in Paper III. (Adapted from Ciotti et al. 2010 by permission of the AAS)

These outflowing shocks are a likely place to produce emission of synchrotron radiation and cosmic rays (Jang et al. 2010, Sijacki et al. 2008). At $t \simeq 10$ Gyr the SNe Ia heating, also sustained by a last strong AGN burst, becomes dominant, a global galactic wind takes place and the nuclear accretion switches to the optically thin regime.

The top and the low panels show instead the accretion luminosity for the galaxy models with higher (top panel) and lower (bottom panel) velocity dispersion. The differences are apparent, and are in line with energetic expectations. In fact, it is well known that big elliptical galaxies are more bound (per unit mass) than low mass systems (as dictated by the Fundamental Plane and Faber–Jackson relations), while the specific heating provided by SNe Ia is independent of the galaxy mass. For this reason, in model $B3^{h}_{02}$ not only the bursting activity begins earlier than in model $B3_{02}$, but also lasts longer. The opposite case is represented by model $B3^{l}_{02}$, where the SMBH accretion is found, over all the evolution, in the highly sub-Eddington (ADAF), hot and optically thin regime, with absence of central bursts. We note that the SMBH accretion luminosities of the three models are far below the Eddigton limit at the current epoch, in rough agreement with current observations, but clearly still more luminous than the average low-luminosity objects (e.g., see Pellegrini 2005, Ho 2008, 2009, Pellegrini 2010). The need of an additional form of feedback in the low-luminosity phases will be briefly addressed in the Conclusions.

In the top panels of Fig. 4.2 we show the coronal X-ray luminosity $L_{\rm X}$ (emitted by gas at $T \geq 5 \times 10^6$ K), due to the hot galactic atmosphere integrated within $10 R_{\rm e}$ for the three models. Of course, in model $B3^{l}_{02}$ no bursts are observed, consistently with the smooth nuclear accretion regime. Instead, in the other two models the spikes in the X-ray luminosity are clearly reminescent of the SMBH accretion history. These peaks are due to sudden increases in the X-ray surface brightness profiles in the central regions ($\approx$ 100 pc scale), consequence of AGN feedback. This is apparent from inspection of Figs. 4.6 and 4.7 (top left panels). If the central regions are excluded from the computation of $L_{\rm X}$, this quantity would be seen to evolve in a much smoother way, with fluctuations similar to those of the blue lines ($M_{\rm ISM}$) in the top panels of Fig. 4.3. During more quiescent phases, $L_{\rm X}$ attains values comparable to the observed ones, with present times mean values of $L_{\rm X}$ lower than in the standard "cooling flow" model: it is expected that a central galaxy in a cluster will reach higher values, due to confining effects of the ICM, while stripping effects of the ICM in satellite galaxies will lead to a further reduction (Shin et al. 2010b). Curiously, the $L_{\rm X}$ values at the end of the simulations are comparable. Of course, only a systematic exploration of the parameter space determining the galaxy structure can confirm if this is a robust result or just a fortuitous coincidence. The most natural explanation of the similarity of the $L_{\rm X}$ values is that $L_{\rm X}$ of models $B3_{02}$ and $B3^{h}_{02}$ has been finally reduced by the series of bursts (absent in model $B3^{l}_{02}$): in fact, note how the interburst $L_{\rm X}$ of the two models is much higher than in the low-mass model. In the middle panels we show instead the estimated IR luminosity $L_{\rm IR}$ due to the reprocessing of the radiation emitted by the new stars and by the SMBH and absorbed by the ISM inside $10 R_{\rm e}$. Again, in the low mass model only a smooth evolution is visible. Instead, in the other two models the bulk of

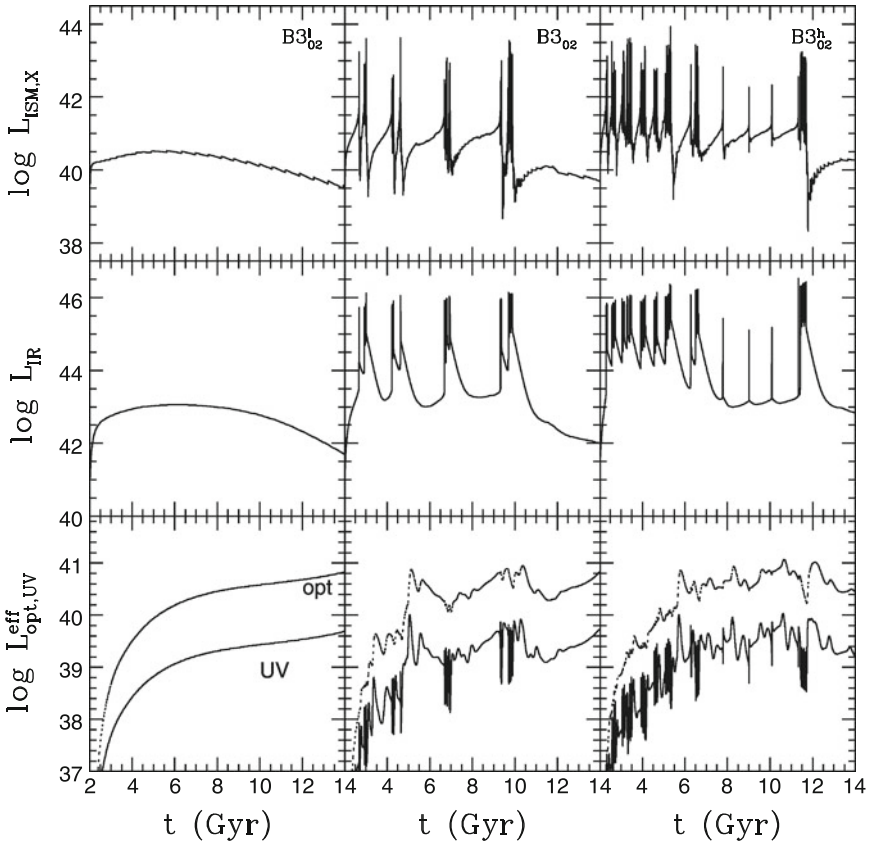

Fig. 4.2 Time evolution of the galaxy X-ray coronal luminosity $L_{\rm X}$ (*top*), recycled infrared $L_{\rm IR}$ (*middle*), and UV and optical luminosities (*bottom*), corrected for absorption. The infrared luminosity is due to the reprocessing of the radiation emitted by the new stars and by the SMBH and absorbed by the ISM inside $10R_{\rm e}$. (Adapted from Ciotti and Ostriker 2007 by permission of the AAS)

the reprocessed radiation comes from AGN obscuration, while the lower envelope is determined by radiation reprocessing of the new stars. Note that the values of high luminosity peaks ($L_{\rm IR} \sim 10^{46}$ erg s^{-1}, or more) are similar to those reported for ULIRGs (e.g., see Pope et al. 2006, Nardini et al. 2010). In addition, peaks of nuclear IR emission coupled with nuclear radio/X-ray emission have been recently reported in a sample of elliptical galaxies (Tang et al. 2009). The bottom panels present the temporal evolution of the optical and UV luminosities of the new stars (corrected for absorption). A large fraction of the starburst luminosity output (in the bursting models) occurs during phases when shrouding by dust is significant (e.g., see Rodighiero et al. 2007, Brusa et al. 2009). At the end of the burst phase, the new stars in the central regions will emit in UV and optical for $\approx 10^7$ year, in the range

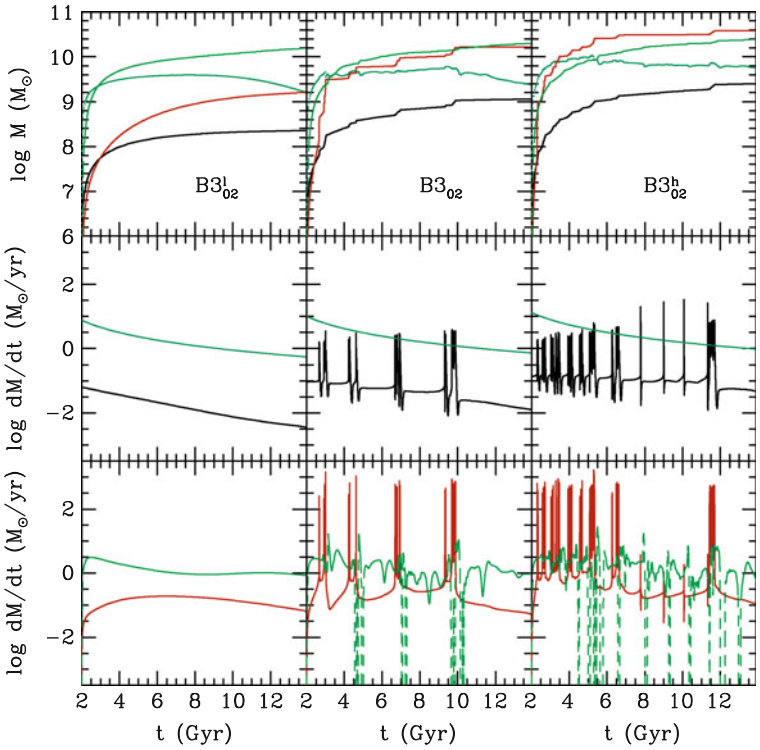

Fig. 4.3 Mass budget evolution of the models $B3^{l}_{02}$ (*left column*), $B3_{02}$ (*central column*), and $B3^{h}_{02}$ (*right column*). *Top panels*: total hot gas mass in the galaxy (within $10R_e$, M_{ISM}, *blue lines*), accreted mass on the central SMBH (ΔM_{BH}, *black lines*), mass lost as a galactic wind at $10R_e$ (ΔM_w, *green lines*), and total mass of new stars (ΔM_*, *red lines*). *Middle and bottom panels*: time rates of the quantities in the *top panels*, with corresponding colours

seen in bright E+A sources. Nowadays, the different time-scales of nuclear accretion and associated star formation can be measured, with very interesting results (Wild et al. 2010).

As anticipated, we compute the duty-cycle as the total time spent by the AGN at high luminosity phases, normalized to the age of the system at the specified time. In practice, we estimate the observable duty-cycle as the fraction of the total time that the AGN is in the "on" state. The resulting values are very similar to the luminosity-weighted values. First, the low-mass model, consistently with the absence of bursts, has a null duty-cycle in the different bands. Cumulative duty-cycles (i.e, spanning the whole simulation time) of model $B3_{02}$ are $\simeq (4.8\,10^{-2}, 2.7\,10^{-2}, 1.9\,10^{-2})$, in the bolometric, optical and UV after absorption. As expected (at each time) the larger duty-cycles are in the bolometric, followed by absorbed optical and finally by absorbed UV. Values for the more massive $B3^{h}_{02}$ are $\simeq (7.9\,10^{-2}, 3.6\,10^{-2}, 2.3\,10^{-2})$. By construction these values cannot take

into account the temporal decline of the accretion activity over the Hubble time. For example, by restricting the computation to the temporal baseline of the last 6 Gyr, the resulting duty-cycle values drop by an order of magnitude. These values compare nicely with observational estimates (e.g., see Heckman et al. 2004, Greene and Ho 2007).

4.4.2 Mass Budgets: SMBH, ISM, and Starformation

In Fig. 4.3 we show the time evolution of some of the relevant mass budgets of the models (summarized in Table 4.1), both as time-integrated properties and instantaneous rates: black lines refer to the SMBH accretion ($\Delta M_{\rm BH}$), green lines to the gas mass ejected as a galactic wind ($\Delta M_{\rm w}$), red lines to the new stars (ΔM_*), and finally the blu lines to the gas content in the galaxy. Of course, the SMBH accretion rate parallels the luminosity evolution discussed in the previous Section. A few expected trends are apparent. For example, from the top panels it results that the final accumulated SMBH mass is higher in the more massive models. This is due to two reasons: first because the mass return from the evolving stars in a galaxy scales linearly with the stellar mass, and second, because the gas is more bound (per unit mass) in more massive systems. The total mass ejected as a galactic wind increases with the galaxy mass, but the remarkable fact here is the strong dependence of the star formation history from the galaxy mass. This is due, as already found and described in previous papers, by the fact that in our models star formation is actually stimulated by peak AGN activity. Therefore, AGN activity not only quenches star formation (during the low-luminosity accretion phases), but it can also be a trigger, especially during the "passive" evolution of early-type galaxies. In any case, star formation episodes end abruptly after major SMBH outburts. The coincidence of vigorous star formation episodes with accretion events and AGN activity can be clearly seen from the middle and bottom panels, by comparison of the black and red lines. Note also how the peaks in the green lines (galactic wind mass loss rate, $\Delta M_{\rm w}$)) are temporally displaced with respect to the starburst-AGN episodes, due to the sound crossing time in the galaxy. About the galaxy mass loss, it is also important to note that the bulk of the degassing is *not* due to AGN feedback events, but to the secular heating provided by SNe Ia: absent this ingredient, all galaxy models host gas inflows, with the consequent series of accretion events and final SMBH masses well above the observed range.

As already mentioned above, these violent star formation episodes are induced by accretion feedback,[4] and are spatially limited to the central 10–100 pc; thus, the bulk of gas flowing to the center is consumed in the starburst. It is then expected that the final surface brightness profile of the galaxy will be modified. In fact, this

[4]However, bursting star formation is not necessarily associated with AGN feedback (Krügel and Tutukov 1993).

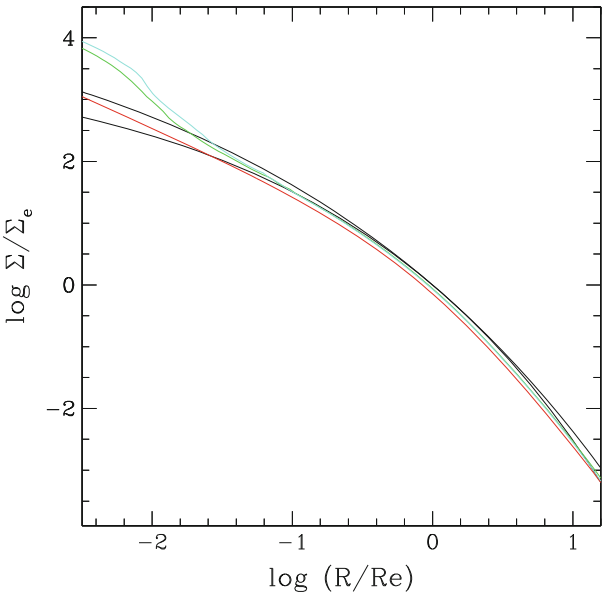

Fig. 4.4 Final stellar projected surface density profiles of model $B3^{l}_{02}$ (*red*), $B3_{02}$ (*green*, see Paper III), and $B3^{h}_{02}$ (*blue*). Each profile is normalized to the surface density at the effective radius, while the radius is normalized to the effective radius. The *two black lines* are the normalized global best-fit Sersic profiles of the initial and final projected profiles, with best-fit Sersic index $m \simeq 4.5$ and $m \simeq 6$, respectively. (Adapted from Ciotti and Ostriker 2007, Ciotti et al. 2010 by permission of the AAS)

can be seen in Fig. 4.4, where we show the final projected stellar density profile of the models, together with Sersic (Sersic 1968, Ciotti and Bertin 1999) best-fit of the initial and final profiles

$$\Sigma(R) = \Sigma_0 \mathrm{e}^{-b(R/R_\mathrm{e})^{1/m}}, \quad b = 2m - 1/3 + 4/405m + \mathscr{O}(m^{-2}). \tag{4.78}$$

The profiles show an increase with time of the best-fit Sersic parameter m, from $\simeq 4.5$ up to $m \simeq 6$, within the range of values commonly observed in ellipticals: also, in the final $B3_{02}$ and $B3^{h}_{02}$ models we note the presence of a central nucleus originated by star formation which stays above the best fit profile. Without entering the debated field of the morphological classification of the centers of elliptical galaxies (e.g., see Faber et al. 1997, Graham 2004, Graham and Driver 2005, Lauer et al. 2005, Davies et al. 2007, Kormendy et al. 2009, Shapiro et al. 2010, see also Ciotti 2009), we notice that the "light spikes" in our models are strikingly similar to the light spikes characterizing "nucleated" or "extra-light", and that usually are attributed to galaxy merging (e.g., see Hopkins et al. 2009), and references therein). Observational evidence is also accumulating that the central parts are quite metal rich (e.g., see Chilingarian et al. 2009, Lee et al. 2010 and, as noticed in Lauer et al.

2005, where colors and luminosities of the nuclear regions of elliptical galaxies are studied, on average the "nuclear" clusters are bluer than the surrounding galaxy, as would be expected if the origin were from infalling gas recycled from evolving stars. Finally, several observational indications exist that, while the majority of the stellar mass in elliptical galaxies may have formed at high redshifts, small but detectable star formation events (summing up to $\lesssim 5-10\%$ of the total stellar mass) have occurred at low redshift (e.g., see Watabe et al. 2008, Pipino et al. 2009, Helmboldt et al. 2008, Trager et al. 2008).

4.4.3 Hydrodynamics

We can now move to describe the most important aspects of the hydrodynamical evolution of the models. For simplicity, we restrict to model $B3_{02}$ (fully discussed in Ciotti et al. 2010). In Fig. 4.5 we show the temperature and density in the central regions of the model: note how the SMBH bursts heat the central gas, causing the density to drop, and launching gas at positive velocities of the order of thousands of km s^{-1}. The Compton temperature is shown by the horizontal dashed line, and during the bursts the local gas is heated above this limit. Note also how the gas

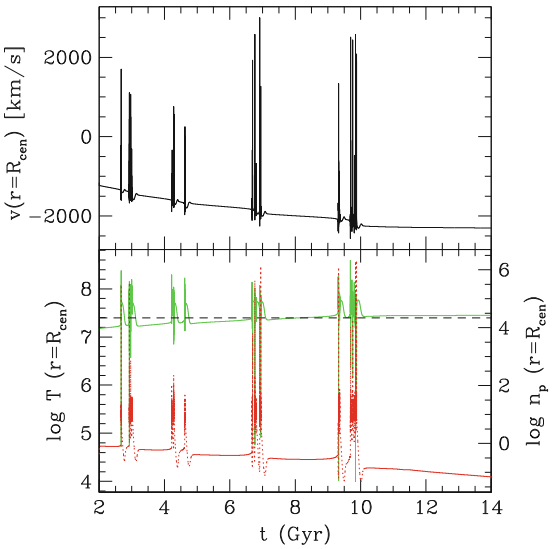

Fig. 4.5 Model $B3_{02}$. *Top panel*: gas velocity at 5 pc from the SMBH. Note how the SMBH growth affects the lower envelope of velocity values. *Bottom panel*: Gas number density (*dotted line*, scale on the right axis) and temperature at 5 pc from the SMBH (*solid line*). Low-temperature, high-density phases end when accretion luminosity $L_{\rm BH}$ increases sharply heating the ambient gas to a high-temperature, low-density state. The horizontal *dashed line* is the model Compton temperature $T_{\rm X} = 2.5 \times 10^7$ K. (Adapted from Ciotti and Ostriker 2007 by permission of the AAS), see the electronic version for a color version of this figure

accretion velocity (between bursts) increases, due to the increasing gravitational field of the growing SMBH, while the gas number density correspondingly decreases, due to the secular evolution of the mass return rate from the evolving stellar population of the galaxy.

In Figs. 4.6–4.8, we show the radial distribution of hydrodynamical quantities at three representative epochs of the evolution, i.e., at the beginning, around 6 Gyr, and at the end of the simulation. In each figure, the three different lines refer to times separated by 500 Myr. In Fig. 4.6, the two unperturbed profiles are snapshots of the galaxy just before and after the first big burst (e.g., see Fig. 4.5): the galaxy would appear as a "normal", X-ray emitting elliptical. Instead, during the burst (dotted lines), two cold and dense shells are apparent. One is traveling outward, while the outer is falling to the center. In fact, the so-called "cooling catastrophe" starts with the formation of a *cold shell* placed around the galaxy core radius (Pellegrini and Ciotti 1998, Ciotti and Ostriker 2001). In the figure, the first shell has already fallen to the center, a radiative shock propagated and accumulated material forming the outer shell, while another accretion event launched the inner shock. The two shells will then interact, producing the complex temporal structure of the bursts (especially visible in the last burst around 10 Gyr in Fig. 4.5). It is important to note that the

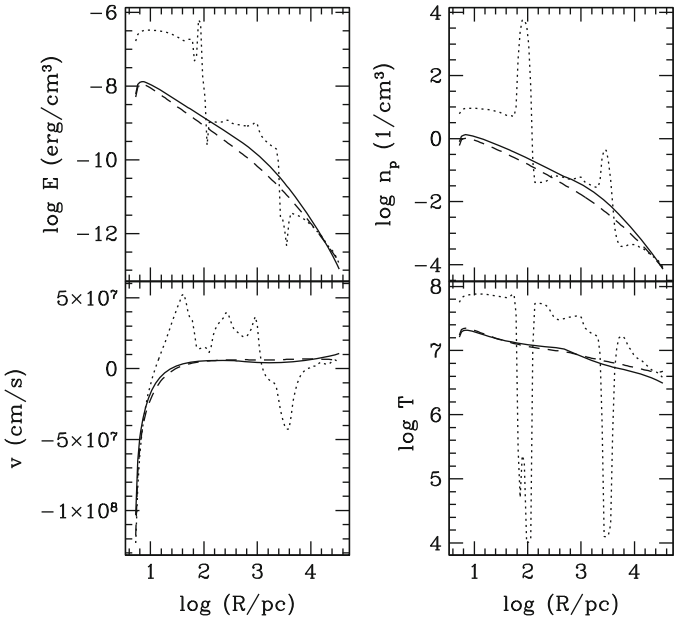

Fig. 4.6 Three snapshots of the radial distribution of internal energy per unit volume, number density, velocity, and temperature, of model $B3_{02}$ starting at (2.554 Gyr, just before the first burst), separated by 500 Myr (in order, *solid, dotted and dashed lines*). After (*solid*) and before (*dashed*) the central burst the profiles are almost unperturbed, while during the burst (*dotted*) we can observe two cold and high density shells, with the inner shell moving outward, while the external cold shell is falling to the center. (Adapted from Ciotti and Ostriker 2007 by permission of the AAS)

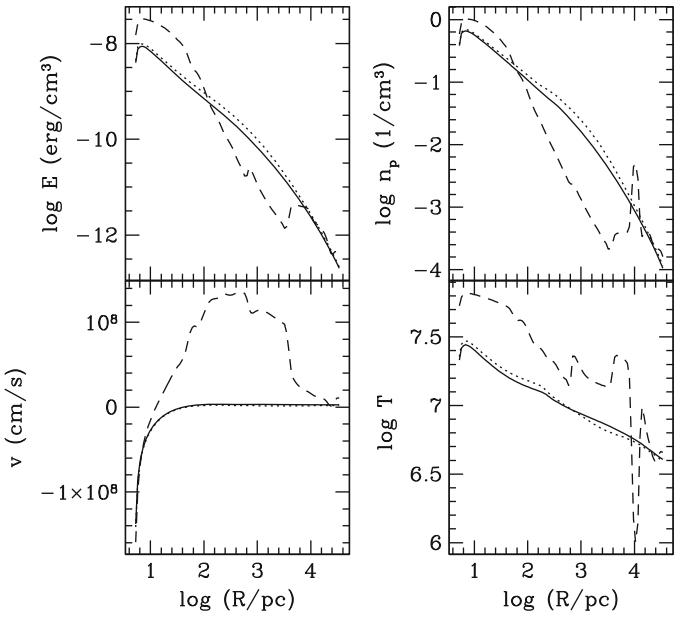

Fig. 4.7 Time evolution during the third burst of model $B3_{02}$ (see Fig. 4.5). *Solid, dotted, and dashed* lines refer to 6, 6.5, and 7 Gyr. The final, global degassing event is apparent, with positive velocities $> 10^3$ km s^{-1} over the galaxy body. (Adapted from Ciotti and Ostriker 2007 by permission of the AAS)

shells are cold and dense, and the star formation rate reaches there very high values. We also notice that these shells are possibly Rayleigh-Taylor unstable, so that 2D hydrodynamical simulations are required to properly study this aspect of the model evolution. This cycle of shell formation, central burst, and expanding phase, repeats during all the bursting evolution of models $B3_{02}$ and $B3^{h}_{02}$, but it is absent in the low mass model $B3^{l}_{02}$. In Fig. 4.7 we show the model evolution at the epoch of 6 Gyr, and the solid and dotted lines are the profiles before the burst that can be easily identified in Fig. 4.5. In particular, the dashed line catches the evolution almost exactly at the end of the burst, when positive velocities are present over a large radial interval, and a global degassing event will soon take place. Finally, (Fig. 4.8), when the specific SNe Ia heating becomes dominant over the decline of fresh mass input from evolving stars, the galaxy hosts a wind, the accretion becomes stationary without oscillations, and the central SMBH is in a very sub-Eddington regime (Hopkins et al. 2006).

In general, the temperature profiles are characterized by a negative gradient (with the exception of very short time intervals during bursts), while it is known that also positive temperature gradients are observed (Statler, this volume), in particular in galaxies with ongoing nuclear activity. A detailed study of the ISM temperature profiles of the present class models is in preparation (Pellegrini et al. 2011, see also Pellegrini et al. 2009), and here we just point out that two important ingredients, that could alter the temperature and surface brightness profiles, are still missing in

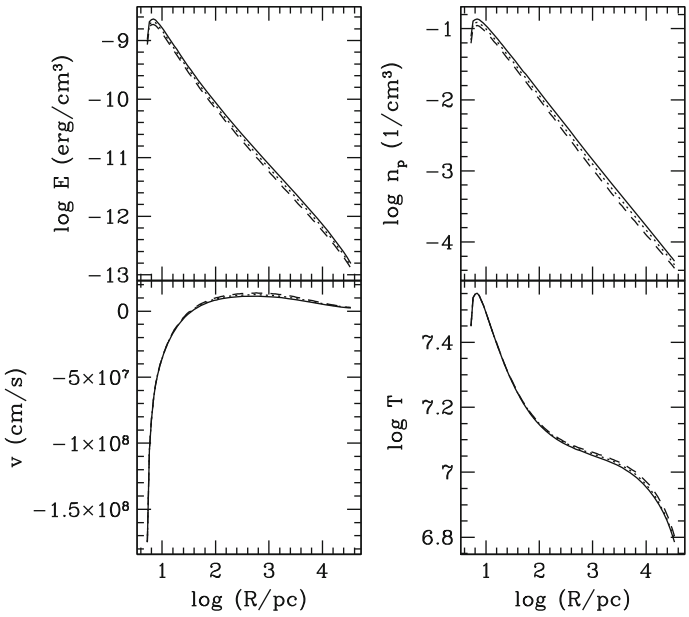

Fig. 4.8 The end of the evolution of model $B3_{02}$. The *lines* (in order *solid, dotted and dashed*) are separated by 500 Myr. The galaxy is in the low-luminosity, high-temperature and low-density stationary accretion phase in the inner parts and, in its outer parts a $\simeq$ 100 km s^{-1} wind is carrying out most of the late recycled gas. (Adapted from Ciotti and Ostriker 2007 by permission of the AAS)

the simulations, namely the confining effect of the ICM and the energy deposition due to a jet.

Before concluding, we recall an important feature of the radial distribution of feedback in combined models (see Ciotti et al. 2010): we found that while after and before the burst the radiative feedback affects all the galaxy volume (due to the low opacity of the hot ISM), and the mechanical feedback is concentrated in the central kpc region, during the burst almost all the AGN radiation is absorbed (and reprocessed in the IR) by the cold and optically thick collapsing shell. This means that, during the burst, mechanical feedback (even with a mechanical efficiency at or below $3\,10^{-4}$, at least a factor of ten lower than commonly assumed) plays a major role in the model evolution (e.g., see also Proga et al. 2008, Kurosawa and Proga 2009, Kurosawa et al. 2009).

4.5 Conclusions

In this review we have summarized the main results of combined (radiative and mechanical, i.e., produced by direct interaction of a nuclear wind/jet with the ISM) AGN feedback in elliptical galaxies, obtained with the aid of high-resolution

1D hydrodynamical simulations with a physically based feedback description. We presented for the first time a comparison of feedback effects on galaxy models of different mass. For completeness, we recall the main secure points on which our framework is based.

First, it is known from stellar evolution theory, and supported by observations, that the recycled gas from dying stars, available *independently of external phenomena such as galaxy merging*, sums up to 20–30% of the total mass in stars, and it is released over the cosmic epoch. Therefore, recycled gas is an important source of fuel for the central SMBH, with a total mass $\approx$ 2 orders of magnitude larger than the mass measured in SMBHs in the local universe.

Second, the metal rich recycled gas, if not removed from the parent galaxy (by SNe Ia heating, ram-pressure, or tidal stripping), is necessarily a subject of a classical radiative cooling instability, leading to a collapse towards the center. This is the idea behind the well known (and much debated) "cooling flow" scenario.

Third, as the cooling gas cannot disappear, a star-burst must occur and also the central SMBH must be fed. The details of how much is accreted on the central SMBH vs. consumed in stars vs. ejected from the center by energy input from the starburst and the AGN are uncertain. But the observed mass of central SMBHs, and the mass of the X-ray emitting hot gas, force to conclude that the bulk is transformed into stars or blown out as a galactic wind, with less than 1% going into the central SMBH.

Fourth, since at the end of a major outburst a hot bubble remains at the galaxy center, feedback processes shut themselves off, with a recurrence time determined by stellar evolution and ISM cooling time. Steady accretion on SMBHs is only possible at very low Eddington ratios, and no steady flow appears to be possible for Eddington ratios above $\simeq$ 0.01. Whenever the luminosity is significantly above this limit, both the accretion and the output luminosity is in burst mode.

Fifth, during the bursting phase the galaxy center would be optically thick to dust, so one would observe a largely obscured starburst and a largely obscured AGN, with most radiation in the far IR. As gas and dust are consumed, the central source becomes visible. Much of the AGN output occurs during obscured phases; then there is a brief interval when one sees a "normal" quasar, and finally one would see a low X-ray luminosity and E+A spectrum galaxy, in the central several hundred pc, for 10^{7-8} years (e.g., Goto 2007).

All the simulations performed so far confirmed these expectations, and the general results can be summarized as follows:

1. Radiative heating and radiation pressure on the ISM by photons emitted by the central AGN and by the starburst, without any mechanical input, greatly reduces the "cooling flow catastrophe" problem, but leads to a central SMBH that would be too bright and too massive, and the galaxy would be too blue, due to repeated bursts of central star formation.

2a. In absence of radiative feedback, mechanical energy from an AGN wind with fixed efficiency also does not give a solution that in detail satisfies the observations. For large efficiencies a giant burst and an explosive degassing of the galaxy occurs (e.g., Di Matteo et al. 2005, Johansson et al. 2008). The gas content of the galaxy

drops to levels below what is observed in real elliptical galaxies and the systems would have coronal X-ray luminosities orders of magnitude lower than those typically seen in nearby ellipticals. Also, the computed AGN duty cycle is too small. If the fixed efficiency is made low enough to avoid these problems, then one reverts to the classical cooling flow picture.

2b. Models with mechanical energy efficiency proportional to the accretion luminosity, as indicated both by observations and detailed 2D hydrodynamical simulations for radiatively driven winds (e.g., see Kurosawa and Proga 2008, 2009, Kurosawa et al. 2009) perform better, but are still inadequate. We thus conclude that mechanical energy input – by itself – is unable to provide appropriate levels of feedback that would leave ellipticals at the current epoch with the properties that they are observed to have.

3. The combined models, in which both radiative and mechanical feedback are allowed (as supported by observations, e.g., Alexander et al. 2010), are the most satisfactorily. This family of models, with mechanical energy efficiency proportional to the luminosity, when combined with a physically based treatment of the radiative effects, does seem to be consistent with all observations for a range of realistic efficiencies ϵ_w (e.g., see Sijacki et al. 2008). Radiative and mechanical feedback affect different regions of the galaxy at different evolutionary stages. During the "quiescent", optically thin phases, radiative heating is distributed over all the galaxy body, while the mechanical feedback is deposited in a region of a kpc scale radius. During the bursts, the collapsing cold shells are optically thick, and most of the radiation is intercepted and re-radiated in the IR; mechanical feedback plays a major role in controlling accretion.

4. In combined models, radiative feedback from the central SMBH (primarily the X-ray component) and the young star feedback consequent to central star bursts (e.g., see Thompson et al. 2005) can balance and consume the cooling flow gas over the 10^2–10^3 pc scale, but they will not sufficiently limit the growth of the central SMBHs. Mechanical feedback from the central SMBH on the 10–10^2 pc scale, mediated by the Broad Line Region winds (e.g., see Binney and Tabor 1995, Begelman and Nath 2005, Begelman and Ruszkowski 2005, Di Matteo et al. 2005), is efficient in limiting the growth of the SMBH, but, absent the radiative feedback, would leave elliptical galaxies with more central star formation than observed.

From cosmological point of view, one of the main results of our study is that *the evolution of an isolated galaxy, subject to internal evolution only, naturally leads to significant AGN and starburst activity, even in absence of external phenomena such as galaxy merging*. This conclusion is gaining more and more observational support (e.g., see Pierce et al. 2007, Li et al. 2008, Kauffmann and Heckman 2009, Tal et al. 2009, Cisternas et al. 2011).

4.5.1 Open Questions and Future Developments

The investigation conducted so far, and summarized in the previous Sections, suffers from a few weak points, namely: (1) the newly formed stars are placed in the galaxy

where they form; (2) the modifications of the galaxy structure, gravitational field and velocity dispersion profile, due to the stellar mass losses, galactic wind, and star formation, are ignored; (3) the simulations are spherically symmetric, so that Rayleigh–Taylor and Kelvin–Helmolthz unstable configurations of the ISM (such as the formation of the cold shells, and the nuclear wind and jet propagation), cannot be followed in detail.

The first two points will be addressed in future works. Instead, we already started the exploration of 2D models, with very encouraging and interesting results (Novak et al. 2011). Additional lines that have been or will be studied are, for example, the properties expected for the starburst population (such as spatial distribution, spectral properties, etc.), the X-ray properties of the perturbed ISM as a function of the combined effect of SNe Ia and central feedback (Pellegrini et al. 2009, 2011), and the cosmic rays emission following a central burst (Jang et al. 2010). Other obvious issues are the effects of environment, as for a cD galaxy in a cluster, the stripping effects (Shin et al. 2010b), and the impact of combined feedback models on the ICM (extending the preliminary investigation Ciotti 2004, see also Pope et al. 2007). We finally mention another observational riddle that could be solved by the present models (with some additional work in the physical modelization of feedback in the very sub-Eddington accretion regime), i.e., that of the apparent "underluminosity" of SMBHs in the local universe (e.g., see Fabian and Canizares 1988, Pellegrini 2005). In fact, the simulations show clear evidence that an additional form of feedback is needed during the quiescent, low-luminosity accretion phases (in particular at late epochs). Of course, standard radiative feedback is not effective during such phases, and presumably the further reduction is provided by nuclear jets and/or thermally driven winds (e.g., see Allen et al. 2006, Merloni and Heinz 2007).

Acknowledgements We thank Ena Choi, Janfey Jang, Greg Novak, Silvia Pellegrini, Daniel Proga, Sergei Sazonov, Min-Su Shin, Anatoly Spitkovski, Rashid Sunyaev for their precious collaboration in the research effort described in this paper. We also thank Dong-Woo Kim and Silvia Pellegrini for organizing the Joint Discussion at the IAU General Assembly in Rio, and for editing this volume. L.C. is supported by the MIUR Prin2008.

References

D.M. Alexander, A.M. Swinbank, I. Smail, R. McDermid, N.P.H. Nesvadba, MNRAS **402**, 2211 (2010)
S.W. Allen, R.J.H. Dunn, A.C. Fabian, G.B. Taylor, C.S. Reynolds, MNRAS **372**, 21 (2006)
V. Antonuccio-Delogu, J. Silk, MNRAS **389**, 1750 (2008)
M.C. Begelman, B.B. Nath, MNRAS **361**, 1387 (2005)
M.C. Begelman, M. Ruszkowski, Phil. Trans. Roy.Soc., part A **363**(1828), 655 (2005)
G. Bertin et al., A&A **292**, 381 (1994)
J. Binney, in *Particles and Fields in Radio Galaxies Conference*, ed. by R.A. Laing, K.M. Blundell. ASP Conference Proceedings, vol. 250, p. 481 (2001)
J. Binney, N.W. Evans, MNRAS **327**, L27 (2001)

J. Binney, G. Tabor, MNRAS **276**, 663 (1995)
A.J. Blustin, G.A. Kriss, T. Holczer, E. Behar, J.S. Kaastra, M.J. Page, S. Kaspi, G. Branduardi-Raymont, K.C. Steenbrugge, A&A **466**, 107 (2007)
M. Brüggen, C.R. Kaiser, Nature **418**, 301 (2002)
M. Brusa, F. Fiore, P. Santini, A. Grazian, A. Comastri, G. Zamorani, G. Hasinger, A. Merloni, F. Civano, A. Fontana, V. Mainieri, A&A **507**, 1277 (2009)
A. Burkert, J. Silk, ApJ **554**, L151 (2001)
C.R. Canizares, G. Fabbiano, G. Trinchieri, ApJ **312**, 503 (1987)
M. Cappellari et al., MNRAS **366**, 1126 (2006)
E. Cappellaro, R. Evans, M. Turatto, A&A **351**, 459 (1999)
A. Cattaneo et al., Nature **460**, 213 (2009)
A. Cavaliere, V. Vittorini, ApJ **570**, 114 (2002)
R. Cen, J.P. Ostriker, ApJ **650**, 560 (2006)
S. Chandrasekhar, *Radiative Transfer* (Dover, New York, 1960)
G. Chartas, W.N. Brandt, S.C. Gallagher, D. Proga, ApJ **133**, 1849 (2007)
I. Chilingarian, S. De Rijcke, P. Buyle, ApJ **697**, L111 (2009)
E. Churazov, S. Sazonov, R. Sunyaev, W. Forman, C. Jones, H. Böhringer, MNRAS **363**, L91 (2005)
L. Ciotti, ApJ **471**, 68 (1996)
L. Ciotti, La Rivista del Nuovo Cimento **32**, 1 (2009a)
L. Ciotti, Nature **460**, 333, (2009b)
L. Ciotti, G. Bertin, A&A **352**, 447 (1999)
L. Ciotti, J.P. Ostriker, ApJ **487**, L105 (1997)
L. Ciotti, J.P. Ostriker, ApJ **551**, 131 (2001)
L. Ciotti, J.P. Ostriker, ApJ **665**, 1038 (2007)
L. Ciotti, A. D'Ercole, S. Pellegrini, A. Renzini, ApJ **376**, 380 (1991)
L. Ciotti, L. Morganti, P.T. de Zeeuw, MNRAS **393**, 491 (2009)
L. Ciotti, J.P. Ostriker, D. Proga, ApJ **699**, 89 (2009)
L. Ciotti, J.P. Ostriker, D. Proga, ApJ **717**, 708 (2010)
L. Ciotti, J.P. Ostriker, S. Pellegrini, in *The Proceedings of the international symposium*, ed. by G. Bertin, D. Farina, R. Pozzoli. Plasmas in the Laboratory and in the Universe: New Insights and New Challenges, vol. 703, p. 367 (AIPCS, 2004)
M. Cisternas et al., ApJ **726**, 57 (2011)
L.L. Cowie, J. Binney, ApJ **215**, 723 (1977)
L.L. Cowie, J.P. Ostriker, A.A. Stark, ApJ **226**, 1041 (1978)
D.M. Crenshaw, S.B. Kraemer, I.M. George, ARAA **41**, 117 (2003)
D.J. Croton et al., MNRAS **365**, 11 (2006)
O. Czoske, M. Barnabé, L.E.V. Koopmans, T. Treu, A.S. Bolton, ApJ **384**, 987 (2008)
A. D'Ercole, A. Renzini, L. Ciotti, S. Pellegrini, ApJ **341**, L9 (1989)
L.P. David, W. Forman, C. Jones, ApJ **359**, 29 (1990)
R.I. Davies, F. Mueller Sánchez, R. Genzel, L. Tacconi, E. Hicks, S. Friedrich, A. Sternberg, ApJ **671**, 1388 (2007)
P.T. de Zeeuw, in *Proceedings of the ESO Workshop 1999*, ed. by L. Kaper, E.P.J. van den Heuvel, P.A. Woudt, p.78 (2001)
T. Di Matteo, V. Springel, L. Hernquist, Nature **433**, 604 (2005)
S. Diehl, T.S. Statler, ApJ **680**, 897 (2008)
A. Dorodnitsyn, T. Kallman, D. Proga, ApJl **675**, 5 (2008)
J. Dubinski, R.G. Carlberg, ApJ **378**, 496 (1991)
S. Dye, N.W. Evans, V. Belokurow, S.J. Warren, P. Hewett, MNRAS **388**, 384 (2008)
A.C. Fabian, MNRAS **308**, L39 (1999)
A.C. Fabian, P.E.J. Nulsen, MNRAS **180**, 479 (1977)
A.C. Fabian, C.R. Canizares, Nature **333**, 829 (1988)
A.C. Fabian, A. Celotti, M.C. Erlund, MNRAS **373**, L16 (2006)
A.C. Fabian, P.A. Thomas, S.M. Fall, R.E. White III, MNRAS **221**, 1049 (1986)

S.M. Faber et al., AJ **114**, 1771 (1997)
L. Ferrarese, H. Ford, Space Sci. Rev. **116**, 523 (2005)
L. Ferrarese, D. Merritt, ApJ **539**, L9 (2000)
W. Forman et al., ApJ **665**, 1057 (2007)
M. Fukugita, O. Nakamura, E.L. Turner, J. Helmboldt, R.C. Nichol, ApJ **601**, L127 (2004)
T. Fukushige, J. Makino, ApJ **477**, L9 (1997)
E. Gallo, T. Treu, P.J. Marshall, J.-H. Woo, C. Leipski, R. Antonucci, ApJ **680**, 154 (2010)
R. Ganguly, M.S. Brotherton, ApJ **672**, 102 (2008)
M. Gaspari, C. Melioli, F. Brighenti, A. D'Ercole, MNRAS **411**, 349 (2011)
K. Gebhardt et al., ApJ **539**, L13 (2000)
T.S. Goncalves, C.C. Steidel, M. Pettini, ApJ **676**, 816 (2008)
T. Goto, MNRAS **381**, 187 (2007)
A.W. Graham, ApJ **613**, L33 (2004)
A.W. Graham, S.P. Driver, PASA **22**, 118 (2005)
A.W. Graham, P. Erwin, N. Caon, I. Trujillo, Rev.Mex.A.A. **17**, 196 (2003)
G.L. Granato, G. De Zotti, L. Silva, A. Bressan, L. Danese, ApJ **600**, 580 (2004)
J.E. Greene, L.C. Ho, ApJ **670**, 92 (2007)
L. Greggio, A&A **441**, 1055 (2005)
Z. Haiman, L. Ciotti, J.P. Ostriker, ApJ **606**, 204 (2004)
F. Hamann, K.F. Kaplan, P. Rodriguez Hidalgo, J.X. Prochaska, S. Herbert-Fort, MNRAS **391**, L39 (2008)
T.M. Heckman, G. Kauffmann, J. Brinchmann, S. Charlot, C. Tremonti, S.D.M. White, ApJ **613**, 109 (2004)
J.F. Helmboldt, R.A.M. Walterbos, T. Goto, MNRAS **387**, 1537 (2008)
L. Hernquist, ApJ **356**, 359 (1990)
L.C. Ho, ARAA **46**, 475 (2008)
L.C. Ho, ApJ **699**, 626 (2009)
J. Holt, C.N. Tadhunter, R. Morganti, MNRAS **387**, 639 (2008)
P.F. Hopkins, L. Hernquist, ApJ **698**, 1550 (2009)
P.F. Hopkins, L. Hernquist, T.J. Cox, B. Robertson, T. Di Matteo, V. Springel, ApJ **639**, 700 (2006)
P.F. Hopkins, R. Narayan, L. Hernquist, ApJ **643**, 641 (2006)
P.F. Hopkins, L. Hernquist, T.J. Cox, D. Keres, S. Wuyts, ApJ **691**, 1424 (2009)
P. Kroupa, MNRAS **322**, 231 (2001)
W. Jaffe, MNRAS **202**, 995 (1983)
W. Jaffe, H.C. Ford, R.W. O'Connell, F.C. van den Bosch, L. Ferrarese, AJ **108**, 1567, (1994)
Y.-F. Jang, L. Ciotti, J.P. Ostriker, A. Spitkovsky, ApJ **711**, 125 (2010)
P.H. Johansson, T. Naab, A. Burkert, Astron.Nachr. **329**, 956 (2008)
C. Jones, W. Forman, A. Vikhlinin, M. Markevitch, L. David, A. Warmflash, S. Murray, P.E.J. Nulsen, ApJ **567**, L115 (2002)
G. Kauffmann, T.M. Heckman, MNRAS **397**, 135 (2009)
A.R. King, ApJ **596**, L27 (2003)
A. King, MNRAS **402**, 1516 (2010)
I.R King, ApJ **174**, L123 (1972)
J. Kormendy, D. Richstone, ARAA **33**, 581 (1995)
J. Kormendy, D.B. Fisher, M.E. Cornell, R. Bender, ApJs **182**, 216 (2009)
E. Krügel, A.V. Tutukov, A&A **275**, 416 (1993)
R. Kurosawa, D. Proga, ApJ **674**, 97 (2008)
R. Kurosawa, D. Proga, MNRAS **397**, 1791 (2009)
R. Kurosawa, D. Proga, K. Nagamine, ApJ **707**, 823 (2009)
J.H. Lee, M.G. Lee, C. Park, Y.-Y. Choi, MNRAS **401**, 1804 (2010)
T.R. Lauer et al., AJ **129**, 2138 (2005)
C. Li, G. Kauffmann, T.M. Heckman, S.D.M. White, Y.P. Jing, MNRAS **385**, 1915 (2008)
M. Loewenstein, W.G. Mathews, ApJ **319**, 614 (1987)
E. Lusso, L. Ciotti, A&A **525**, 115 (2010)

J. Magorrian et al., AJ **115**, 2285 (1998)
F. Mannucci, M. Della Valle, N. Panagia, E. Cappellaro, G. Cresci, R. Maiolino, A. Petrosian, M. Turatto, A&A **433**, 807 (2005)
C. Maraston, MNRAS **362**, 799 (2005)
A. Marconi, L.K. Hunt, ApJ **589**, L21 (2003)
P. Martini, in *Coevolution of Black Holes and Galaxies, Carnegie Observatories Centennial Symposia*, ed. by L.C. Ho. vol. 169 (Cambridge University Press, Cambridge, 2004)
W.G. Mathews, F. Brighenti, ARA&A **41**, 191 (2003)
F. Matteucci, N. Panagia, A. Pipino, F. Mannucci, S. Recchi, M. Della Valle, MNRAS **372**, 265 (2006)
R.J. McLure, J.S. Dunlop, MNRAS **331**, 795 (2002)
A. Merloni, S. Heinz, MNRAS **381**, 589 (2007)
M. Milosavljevic, S.M. Couch, V. Bromm, ApJ **696**, L146 (2009)
C.W. Morgan, C.S. Kochanek, N.D. Morgan, E.M. Falco, ApJ **712**, 1129 (2010)
N. Murray, E. Quataert, T.A. Thompson, ApJ **618**, 569 (2005)
S. Nayakshin, R. Sunyaev, MNRAS **364**, L23 (2005)
R. Narayan, I. Yi, ApJ **428**, L13 (1994)
E. Nardini, G. Risaliti, Y. Watabe, M. Salvati, E. Sani, MNRAS **405**, 2505 (2010)
J.F. Navarro, C.S. Frenk, S.D.M. White, ApJ **490**, 493 (1997)
S.C. Noble, J.H. Krolik, J.F. Hawley, ApJ **692**, 411 (2009)
L.A. Nolan, S. Raychaudhury, A. Kabán, MNRAS **375**, 381 (2007)
G.S. Novak, J.P. Ostriker, L. Ciotti, ApJ **737**, 26 (2011)
E. O'Sullivan, T.J. Ponman, R.S. Collins, MNRAS **340**, 1375 (2003)
E. O'Sullivan, J.M. Vrtilek, J.C. Kempner, ApJ **624**, L77 (2005)
H. Omma, J. Binney, G. Bryan, A. Slyz, MNRAS **348**, 1105 (2004)
J.P. Ostriker, L. Ciotti, Phil. Trans. Roy. Soc., Part A **363**(1828), 667 (2005)
J.P. Ostriker, R. Weaver, A. Yahil, R. McCray, ApJ **208**, L61 (1976)
J.P. Ostriker, E. Choi, L. Ciotti, G.S. Novak, D. Proga, ApJ (2010)
J.R. Parriott, J.N. Bregman, ApJ **681**, 1215 (2008)
S. Pellegrini, ApJ **624**, 155 (2005)
S. Pellegrini, ApJ **717**, 640 (2010)
S. Pellegrini, L. Ciotti, A&A **333**, 433 (1998)
S. Pellegrini, L. Ciotti, J.P. Ostriker, Adv. Space Res. **44**, 340 (2009)
S. Pellegrini, L. Ciotti, J.P. Ostriker, ApJ in press (arXiv:1107.3675) (2011)
C.M. Pierce et al., ApJ **660**, L19 (2007)
A. Pipino, J. Silk, F. Matteucci, MNRAS **392**, 475 (2009)
A. Pipino, S. Kaviraj, C. Bildfell, H. Hoekstra, A. Babul, J. Silk, MNRAS **395**, 462 (2009)
A. Pope et al., MNRAS **370**, 1185 (2006)
E.C.D. Pope, G. Pavlosvski, C.R. Kaiser, H. Fangohr, MNRAS **367**, 732 (2007)
D. Proga, MNRAS **304**, 938 (1999)
D. Proga, J.M. Stone, J.E. Drew, MNRAS **295**, 595 (1998)
D. Proga, J.M. Stone, T. Kallman, ApJ **543**, 686 (2000)
D. Proga, T. Kallman, ApJ **565**, 455 (2002)
D. Proga, T. Kallman, ApJ **616**, 688 (2004)
D. Proga, J.P. Ostriker, R. Kurosawa, ApJ **676**, 101 (2008)
S.W. Randall, C.L. Sarazin, J.A. Irwin, ApJ **600**, 729 (2004)
S. Recchi, A. D'Ercole, L. Ciotti, ApJ **533**, 799 (2000)
A. Renzini, L. Ciotti, ApJ **416**, L49 (1993)
A. Renzini, L. Ciotti, A. D'Ercole, S. Pellegrini, ApJ **419**, 52 (1993)
A. Riciputi, B. Lanzoni, S. Bonoli, L. Ciotti, A&A **443**, 133 (2005)
G. Rodighiero et al., MNRAS **376**, 416 (2007)
D. Rusin, C.S. Kochanek, ApJ **623**, 666 (2005)
R.P. Saglia et al., A&A **403**, 567 (1993)
C.L. Sarazin, R.E. White, ApJ **320**, 32 (1987)

S.Yu. Sazonov, J.P. Ostriker, R. Sunyaev, MNRAS **347**, 144 (2004)
S.Yu. Sazonov, J.P. Ostriker, L. Ciotti, R.A. Sunyaev, MNRAS **358**, 168 (2005)
S.Yu. Sazonov, M. Revnivtsev, R. Krivonos, E. Churazov, R.A. Sunyaev, A&A **462**, 57 (2007)
S.Yu. Sazonov, R. Krivonos, M. Revnivtsev, E. Churazov, R.A. Sunyaev, A&A **482**, 517 (2008)
J.L. Sersic, Atlas de galaxias australes. Obs. Astr., Cordoba (1968)
N.I. Shakura, R.A. Sunyaev, A&A **24**, 337 (1973)
K.L. Shapiro et al., MNRAS **402**, 2140 (2010)
J. Shi, J. Krolik, ApJ **679**, 1018 (2008)
M.S. Shin, J.P. Ostriker, L. Ciotti, ApJ **711**, 268 (2010a)
M.S. Shin, J.P. Ostriker, L. Ciotti, submitted to ApJ (arXiv:1003:1108) (2010b)
D. Sijacki, C. Pfrommer, V. Springel, T.A. Ensslin, MNRAS **387**, 1403 (2008)
J. Silk, M.J. Rees, A&A **331**, L1 (1998)
R.S. Somerville, in *Panoramic Views of Galaxy Formation and Evolution, ASP Conference Series*, ed. by T. Kodama, T. Yamada, K. Aoki, vol. 399, p. 391 (2008)
V. Springel, T. Di Matteo, L. Hernquist, MNRAS **361**, 776 (2005)
G. Tabor, J. Binney, MNRAS **263**, 323 (1993)
T. Tal, P.G. van Dokkum, J. Nelan, R. Bezanson, AJ **138**, 1417 (2009)
Y. Tang, Q.-S. Gu, J.-S. Huang, Y.-P. Wang, MNRAS **397**, 1966 (2009)
T.A. Thompson, E. Quataert, N. Murray, ApJ **630**, 167 (2005)
S.C. Trager, S.M. Faber, A. Dressler, MNRAS **386**, 715 (2008)
T. Treu, L.V.E. Koopmans, ApJ **575**, 87 (2002)
T. Treu, L.V.E. Koopmans, ApJ **611**, 739 (2004)
J.C. Vernaleo, C.S. Reynolds, ApJ **645**, 83 (2006)
Y. Watabe, N. Kawakatu, M. Imanishi, ApJ **677**, 895 (2008)
V. Wild, T. Heckman, S. Charlot, MNRAS **405**, 933 (2010)
J.S.B. Wyithe, A. Loeb, ApJ **595**, 614 (2003)
J.M. Wrobel, Y. Terashima, L.C. Ho, ApJ **675**, 1041 (2008)
Q. Yu, S. Tremaine, MNRAS **335**, 965 (2002)

Chapter 5
Metal Abundances in the Hot ISM of Elliptical Galaxies

Dong-Woo Kim

Abstract X-ray spectroscopy provides a powerful tool to measure various elemental abundances in the hot ISM and the measured abundances in turn can be compared with galaxy chemical evolution models to constrain important astrophysical quantities and to help our understanding of the formation and evolution of elliptical galaxies and their ISM. In this chapter, I will address various technical issues involved in X-ray spectral fitting and review observational results of metal abundances in the hot ISM of elliptical galaxies.

5.1 Introduction

Heavy elements in the hot halos of elliptical galaxies are the relics of stellar evolution. Determining their abundance is key to our understanding of the formation and evolution of these galaxies. In particular, since metal abundances are directly related to the stellar mass loss and supernova (SN) ejecta, they can provide an important clue on the star formation history and constrain the SN rate and the initial mass function (IMF) of the stellar population. In addition to the absolute abundances, the relative abundance ratio, particularly the ratio of Fe to α-element, carries important information on the metal enrichment history of the ISM. Since Fe is primarily produced in SN Type Ia (exploding white dwarfs by mass transfer in close binary systems) and α-elements are produced in SN Type II (core-collapsed massive stars), the abundance ratio directly provides the relative importance of the two types of SNe (see Table 5.3 for SN yields of several important elements). Moreover, spatially resolved thermal and chemical structures are important in understanding the evolution of the hot interstellar medium (ISM) via AGN and

D.-W. Kim (✉)
Harvard-Smithsonian Center for Astrophysics, 60 Garden Street, Cambridge, MA 02138, USA
e-mail: kim@cfa.harvard.edu

D.-W. Kim and S. Pellegrini (eds.), *Hot Interstellar Matter in Elliptical Galaxies*,
Astrophysics and Space Science Library 378, DOI 10.1007/978-1-4614-0580-1_5,
© Smithsonian Institution 2012

SN feedback, which may cause global (e.g., onset of galactic winds) and local (e.g., buoyantly uplifted cavities) structural variation throughout the ISM evolution. Yet these abundance measurements are difficult, and the results have often been controversial.

Following the standard stellar evolution models of passively evolving elliptical galaxies where heavy elements come out of stellar mass loss and additional SN Ia ejecta, we would expect that the metallicity in the hot ISM is higher than or at least as high as that observed in the stellar system, i.e., super-solar metal abundance (Arimoto et al. 1997). While recent results with Chandra and XMM-Newton data suggest that the extremely low Fe abundances (often reported in earlier missions) can be statistically rejected in X-ray bright, gas-rich elliptical galaxies, the observed Fe abundance is still lower than expected (see Sect. 5.4). Furthermore, for X-ray faint early type galaxies which contain only a small amount of the hot ISM, the metal abundance is controversial and very low abundances are still reported, even with the Chandra and XMM-Newton data. It is critical to accurately assess all uncertainties associated in the abundance measurement.

In this chapter, I will first summarize in Sect. 5.2 the basic ISM properties which are most relevant to the metal abundance (see also Fabbiano in this book and Statler in this book for more details). In Sect. 5.3, I will discuss technical issues and related uncertainties involved in abundance determination by fitting X-ray spectra. In Sect. 5.4, I will review in detail observational results of metal abundances and the abundance ratios and their implications (see also Pipino in this book for theoretical results).

5.2 The Hot ISM

Before we address the metal abundance in the hot ISM, it is necessary to understand the basic properties of the hot ISM, i.e., how much gas is in elliptical galaxies and how the gas is spatially distributed. In particular, these gas properties are important in selecting the most appropriate X-ray emission model to accurately analyze the X-ray spectra. As shown in Sect. 5.3.1, the resulting metal abundance critically depends on the adopted model.

5.2.1 Amount of the Hot ISM

One of the long standing puzzles in the X-ray study of early type galaxies is the two orders of magnitude spread in L_X(total) for a given optical luminosity (e.g., Fabbiano 1989; White and Sarazin 1991; Eskridge et al. 1995; O'Sullivan et al. 2001; Ellis and O'Sullivan 2006). L_X(total) was used as a proxy for the hot gas content of the galaxies and L_B (now L_K is preferred) was used, as a proxy of the stellar luminosity. Several mechanisms have been proposed to account

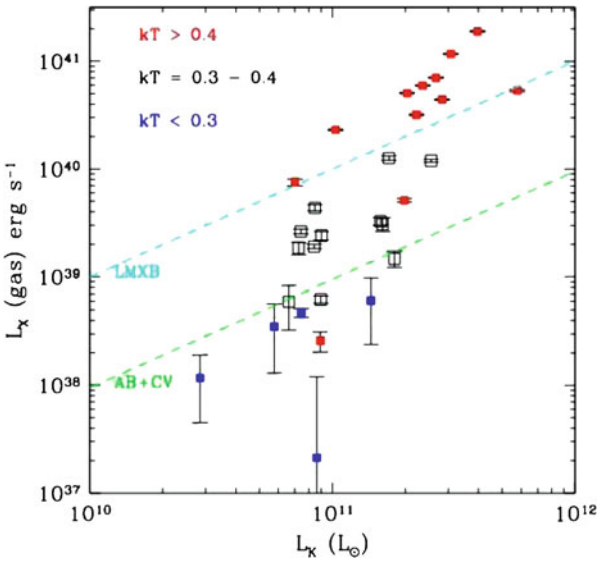

Fig. 5.1 X-ray luminosity of the hot gas is plotted against L_K. Three sub-groups in different kT bins are marked differently (*red, black, blue* in order of decreasing kT). The L_X/L_K ratios corresponding to LMXBs and ABs+CVs are marked by two diagonal lines. Taken from Boroson et al. (2011), reproduced by permission of the AAS

for this spread, including internal (e.g., dark matter, outflow/winds) and external (e.g., ram pressure stripping, infall) effects, but the proper physical process is yet to be explained (e.g., Fabbiano 1989; White and Sarazin 1991). The large $L_X(\text{total})/L_B$ scatter was partly attributed to giant cD-type galaxies filling the high L_X space in the $L_X - L_B$ plane. Since the hot gas dominates the X-ray emission in the gas-rich galaxies with $L_X(\text{gas}) = 10^{41}$–$10^{42}\text{erg s}^{-1}$, $L_X(\text{gas})$ is comparable to $L_X(\text{total})$. However, in gas-poor galaxies, $L_X(\text{total})$ may still be 10^{40}–10^{41}erg s^{-1} because of the stellar contribution, but $L_X(\text{gas})$ is considerably lower than $L_X(\text{total})$: $L_X(\text{gas}) = 10^{38}$–$10^{40}\,\text{erg s}^{-1}$. Therefore the true spread in the $L_X(\text{gas})$–L_K relation is even larger than that of the $L_X(\text{total})$–L_K.

Using a sample of X-ray- (with Chandra observations) and optically- (with optical line measurements) selected elliptical galaxies, Boroson et al. (2011) estimated X-ray luminosities of the hot ISM after properly excluding other emission components, including the nucleus, low-mass X-ray binaries (LMXB), active binaries (AB) and cataclysmic variables (CV). The $L_X(\text{gas})$–L_K diagram is shown in Fig. 5.1. To better represent normal galaxies, their sample does not include a small number of gas-rich cD-type cluster/group dominating galaxies which would reside on the top-right corner (or beyond the range toward the higher L_X) of this plot. The average L_X/L_K relations of a population of LMXBs ($L_X/L_K = 10^{29}\text{erg s}^{-1}\text{L}_{K\odot}^{-1}$; see Sect. 5.3.3.1) and ABs + CVs($L_X/L_K = 9.5 \times 10^{27}\text{erg s}^{-1}\text{L}_{K\odot}^{-1}$; see Sect. 5.3.3.2) are marked by two diagonal lines in this figure which divide the diagram in three

regions. The number of galaxies in these three regions are roughly the same in this sample which covers a large range in L_X(gas) and L_X(gas)/L_K including both gas-rich, intermediate, and gas-poor galaxies. As seen in Fig. 5.1, the spread is more than 2 orders of magnitude in L_X(gas) for a given L_K($\sim 10^{11} L_{K\odot}$). If we include gas-rich cD galaxies with L_X(gas) $\sim 10^{42}$erg s^{-1} in our sample, the spread in the L_X(gas)–L_K relation would be even larger up to $\sim$3 orders of magnitude. This figure clearly illustrates that there are a number of gas-poor galaxies with a very small amount of the hot ISM, i.e., L_X(gas) is often less than L_X(LMXB) and L_X(gas) may even be less than L_X(AB + CV) in extremely gas-poor galaxies. This also indicates the importance of accurately accounting for the amount of stellar emission (from undetected LMXBs, ABs and CVs as described in Sect. 5.3.3) to determine the gas properties of gas-poor galaxies.

5.2.2 Spatial Distribution of the Hot ISM

Although some spatially resolved features of the hot ISM have been reported in earlier X-ray missions, e.g., X-ray cavity in NGC 1316 (Kim et al. 1998) and X-ray tails in NGC 4406 (Rangarajan et al. 1995), NGC 4472 (Irwin and Sarazin 1996), and NGC 7619 (Trinchieri et al. 1997), it is Chandra which provides unprecedented fine details of morphological and thermal sub-structures of the hot ISM. An excellent example is the multi-phase gas seen in M87, the central galaxy in the Virgo cluster. Million et al. (2010) and Werner et al. (2010) analyzed deep Chandra observations and showed in-depth spatial (see Fig. 5.2) and spectral (see Fig. 5.9 in Sect. 5.4) features. The most striking features are two X-ray arms, which are cooler and have lower entropy (kT $n_e^{-2/3}$) than the surrounding region, and are spatially correlated with the radio emission, strongly indicating that they are likely driven outward by the central AGN. Werner et al. (2010) show that the X-ray arms consist of multiphase medium with gas as cool as 0.5 keV, which spatially coincides with the Hα emission region. Additionally, Million et al. (2010) identified the presence of a thick ($\sim$3 kpc) ring of high pressure gas at a radius of $\sim$14 kpc from the central AGN, which is consistent with an AGN driven shock propagating through the ICM. Several other cavities, shocks, and edges are also seen in the central region (Werner et al. 2010).

Other examples of AGN-related ISM features can be found in cD galaxies, (NGC 5044 by David et al. 2010; NGC 5813 by Randall et al. 2010) and non-cD galaxies (NGC 1316 by Kim and Fabbiano 2003, NGC 4374 by Finoguenov et al. 2008; NGC 4552 by Machacek et al. 2006; NGC 4636 Baldi et al. 2009).

Another type of ISM sub-structures (and not AGN-related) is X-ray tails which are likely being stripped by ram pressure. Clear examples are NGC 4406 (Randall et al. 2008), NGC 4472 (Biller et al. 2004) and NGC 7619 (Kim et al. 2008). In Fig. 5.3, we show the hot gas distribution in NGC 7619, where a long X-ray tail is extended toward the SW. A sharp discontinuity in the opposite direction (NE)

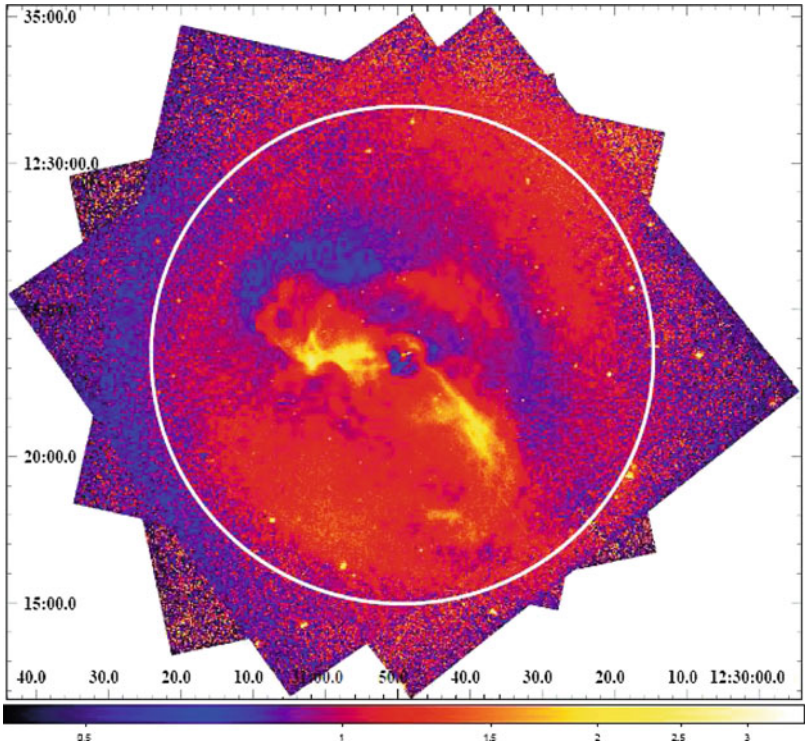

Fig. 5.2 High resolution Chandra image of the central region ($r = 8.6'$ or 40 kpc) of the Virgo cluster, M87. This smoothed surface brightness map was exposure-corrected, flat-fielded and divided by the azimuthally-symmetric double-β model to optimally reveal fine structural details. Taken from Million et al. (2010), reproduced by permission of the RAS

indicates that the galaxy is moving at $\sim$500 km s^{-1} (a Mach number $\sim$1) relative to the surrounding hot gas. Spectral analysis of these data shows that the iron abundance of the hot gaseous medium is much higher (1–2 solar) near the center of NGC 7619 and in the tail extending from the core than in the surrounding regions ($<1/2$ solar), indicating that the gas in the tail originated from the galaxy.

High resolution Chandra observations clearly illustrate complex morphological, thermal and chemical sub-structures of the hot ISM in virtually all gas-rich elliptical galaxies which are either bright enough or close enough for a given Chandra exposure (see by Diehl and Statler 2007, 2008a, b and Statler in this book). As noted above, only a fraction of elliptical galaxies contain a large amount of the hot ISM and were extensively studied for gas sub-structures. If they had been observed in a lower spatial resolution and/or for a shallow exposure, most fine structures might have been missed. If a simplified gas model is applied in X-ray spectral fitting, the measured gas properties could be grossly incorrect, as described below (Sect. 5.3.1).

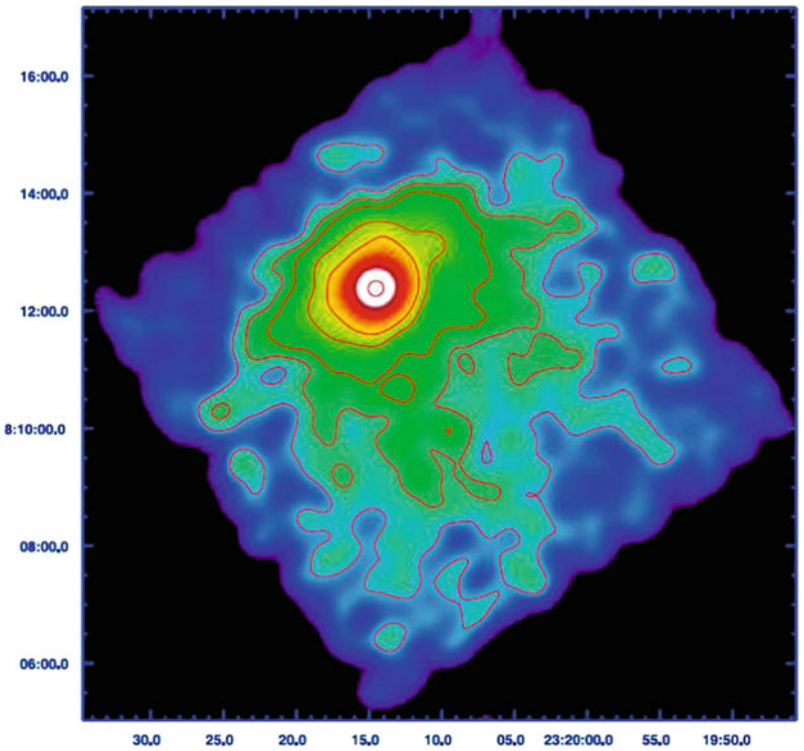

Fig. 5.3 Exposure-corrected, point-source-excluded, Gaussian-smoothed, narrow-band (0.7–1.2 keV) Chandra image of NGC 7619. The X-ray tail extended toward the south-west and the sharp discontinuity in the opposite side are clearly seen. Taken from Kim et al. (2008), reproduced by permission of the AAS

5.3 X-ray Spectral Fitting and Related Issues in Abundance Measurement

Typical X-ray spectra from the gas-rich elliptical galaxies obtained in the current missions are shown in Fig. 5.5 (XMM-Newton MOS), Fig. 5.6 (Chandra ACIS) and Fig. 5.10 (XMM-Newton RGS). As marked in Fig. 5.5, strong emission features from various metal elements are clearly seen in the imaging spectroscopy obtained by the CCD-type instrument.

The emission features consist of multiple emission lines from various transitions. Individual emission lines can be further resolved in the grating spectra, as seen in Fig. 5.10 (see Sect. 5.4.3 for more discussions on grating spectroscopy). Given that the gas temperature in elliptical galaxies ranges from 0.3 keV to 1.2 keV, the strong emission lines are typically from O, Ne, Mg, Si, S and Fe in various ionization stages. In Table 5.1, we list important emission lines from different elements

Table 5.1 X-ray emission lines and peak temperature

Z	Ionization	Stage	E (keV)	λ (Å)	Upper level	Lower level	T_{peak} (keV)
8	O VII	He-like	0.56	22.1	1s2s	$1s^2$	0.2
8	O VII	He-like	0.57	21.6	1s2p	$1s^2$	0.2
8	O VIII	H-like	0.65	19.0	2p	1s	0.3
8	O VIII	H-like	0.78	16.0	3p	1s	0.3
10	Ne IX	He-like	0.91	13.7	1s2s	$1s^2$	0.3
10	Ne IX	He-like	0.92	13.4	1s2p	$1s^2$	0.3
10	Ne X	H-like	1.0	12.1	2P	1s	0.5
12	Mg XI	He-like	1.3	9.3	1s2s	$1s^2$	0.5
12	Mg XI	He-like	1.4	9.2	1s2p	$1s^2$	0.5
12	Mg XII	H-like	1.5	8.4	2p	1s	0.9
14	Si XIII	He-like	1.8	6.7	1s2s	$1s^2$	0.9
14	Si XIII	He-like	1.9	6.6	1s2p	$1s^2$	0.9
14	Si XIV	H-like	2.0	6.2	2p	1s	1.4
16	S XV	He-like	2.4	5.1	1s2s	$1s^2$	1.4
16	S XV	He-like	2.5	5.0	1s2p	$1s^2$	1.4
16	S XVI	H-like	2.6	4.7	2p	1s	2.2
18	Ar XVII	He-like	3.1	4.0	1s2s	$1s^2$	1.7
18	Ar XVII	He-like	3.1	4.0	1s2p	$1s^2$	1.7
18	Ar XVIII	H-like	3.3	3.7	2p	1s	3.4
20	Ca XIX	He-like	3.9	3.2	1s2s	$1s^2$	2.7
20	Ca XIX	He-like	3.9	3.2	1s2p	$1s^2$	2.7
20	Ca XX	H-like	4.1	3.0	2p	1s	4.3
26	Fe XVII	Ne-like	0.73	17.0	$2s^22p^53s$	$2s^22p^6$	0.4
26	Fe XVII	Ne-like	0.83	15.0	$2s^22p^53d$	$2s^22p^6$	0.4
26	Fe XVIII	F-like	0.77	16.0	$2s^22p^43s$	$2s^22p^5$	0.5
26	Fe XVIII	F-like	0.87	14.2	$2s^22p^43d$	$2s^22p^5$	0.7
26	Fe XIX	O-like	0.92	13.5	$2s^22p^33d$	$2s^22p^4$	0.7
26	Fe XX	N-like	0.96	12.8	$2s^22p^23d$	$2s^22p^3$	0.9
26	Fe XXI	C-like	1.0	12.3	$2s^22p3d$	$2s^22p^2$	0.9
28	Ni XIX	Ne-like	0.88	14.1	$2s^22p^53s$	$2s^22p^6$	0.5
28	Ni XIX	Ne-like	1.0	12.4	$2s^22p^53d$	$2s^22p^6$	0.7
28	Ni XX	F-like	0.93	13.3	$2s^22p^43s$	$2s^22p^5$	0.7
28	Ni XX	F-like	1.0	11.8	$2s^22p^43d$	$2s^22p^5$	0.9
28	Ni XXI	O-like	1.0	12.4	$2s^22p^33d$	$2s^22p^4$	0.9
28	Ni XXII	N-like	1.1	11.2	$2s^22p^23d$	$2s^22p^3$	0.9
28	Ni XXIII	C-like	1.2	10.7	$2s^22p3d$	$2s^22p^2$	1.1

in different ionization stages. Also listed are the upper and lower levels (in an abbreviated form without spin and total angular momentum states) and the peak plasma temperatures where a given emission line is strongest. For detail atomic data and line specifications, we refer to the ATOMDB in http://cxc.harvard.edu/atomdb/WebGUIDE) and ASD (atomic spectra database) in http://www.nist.gov/pml/data/asd.cfm.

The strongest feature in the X-ray spectra of the hot ISM is from Fe. The Fe emission features at E = 0.7–1.0 keV (or $\lambda = 12$–17Å) originate from various ionization stages, ranging from Ne-like (with 10 electrons) Fe XVII at low temperatures (kT ∼0.5 keV) to C-like (with 6 electrons) Fe XXI in high temperatures (kT ∼1 keV). The emission features are progressively shifted toward shorter wavelengths (higher energies), as the dominant ionization stages change with increasing temperature (e.g., see Fig. 9.3 in Seward 2000). The ∼7 keV Fe K-shell lines from H-like (with 1 electron) and He-like (with 2 electrons) Fe ions, which are often observed in the hotter ICM (kT = 5–10 keV), are not easily seen in the ISM. The Ne and Ni emission lines are also located at E ∼1 keV and often mixed with stronger Fe emission features. At lower energies (E = 0.5–0.7 keV below Fe features), the O VIII emission lines are strongest and more or less isolated. In contrast, O VII lines, which originate from relatively cooler gas (<0.3 keV), are rarely seen and often used to prove the absence of the cooler gas in cooling flows (see Sect. 5.4.3). The emission features of H-like and He-like Mg, Si, S, Ar and Ca ions are located in a clean part of the X-ray spectrum at E ∼1.5 keV. ∼2 keV, ∼2.5 keV, ∼3 keV and ∼4 keV, respectively (see Fig. 5.5). With increasing ionization potentials (from Mg to Ca), they come from progressively hotter gas.

Ideally, the metal abundances can be measured by fitting proper models to the observed X-ray spectra and the related uncertainties can be constrained by applying proper statistics. Practically, however, there are various systematic effects and simplified assumptions which affect the results but are not easy to fully take into account. In this section, I will review those technical issues and their effects on the measured metal abundances.

5.3.1 Emission Models of Hot Plasma

One of the fundamental problems in abundance measurement is how to select the most appropriate gas emission model. Even though the measured abundances critically depend on the adopted emission model, X-ray spectral fitting often does not statistically require a complex, but realistic model. In this case, investigators tend to stop as soon as the fitting returns reasonable statistics (e.g., χ^2 per degree of freedom ∼1). However, spectral fitting results (particularly the best-fit Fe abundance) can be significantly different when determined, for example, by applying a single-temperature model or a multiple-temperature model. The X-ray spectra of typical hot gas in elliptical galaxies (at kT = 0.3–1.2 keV) peak at E ∼1 keV, mainly by the Fe-L emission feature (see Figs. 5.5 and 5.6; Table 5.1). The peak at E ∼1 keV from mixed gas with two different temperatures (for example, 0.75 keV and 1.5 keV) will be broader than that from isothermal gas at the emission-weighted average temperature (∼1 keV). If the X-ray spectrum from the multi-T gas is fitted with a single-T model, the best fit Fe abundance would be underestimated to reproduce the broad peak (see Fig. 5.4, taken from Buote 2000). This problem is known as *Fe bias* (Buote and Canizares 1994; Trinchieri et al. 1994, 1997; Fabbiano

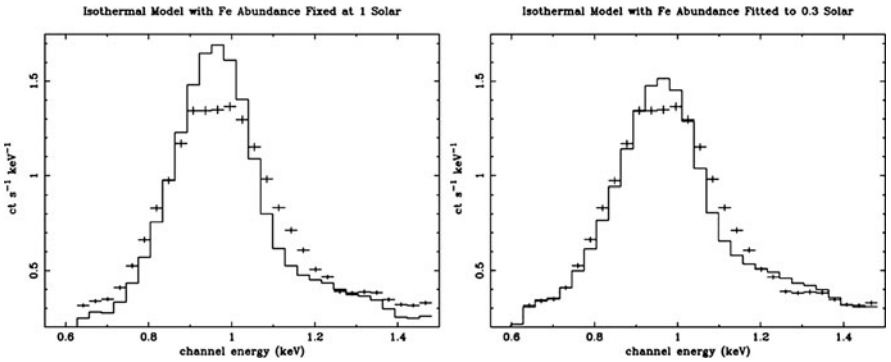

Fig. 5.4 Simulated spectrum (*crosses*) of a two-temperature plasma (0.75 keV and 1.5 keV) with $Z_{\rm Fe} = 1\,{\rm Z}_{\odot}$, and the best-fitting single-temperature model with (*left*) $Z_{\rm Fe}$ fixed at $1\,{\rm Z}_{\odot}$ and (*right*) $Z_{\rm Fe}$ allowed to vary (in this case, the best-fit $Z_{\rm Fe} = 0.3\,{\rm Z}_{\odot}$). Taken from Buote (2000), reproduced by permission of the AAS

et al. 1994; Kim et al. 1996; Buote and Fabian 1998). See more discussion in Sect. 5.4.1.

As described in Sect. 5.2, the hot ISM is likely in multi-phases with multiple temperatures. The multi-phase nature may be caused by a projection effect when the gas temperature distribution is azimuthally symmetric, but has a non-zero radial gradient (see Sect. 5.3.4) or by incomplete mixing of different temperature gas even at the similar radii. A spherically symmetric ISM embedded in spherically symmetric ICM is an example of the former, while mixed gas driven by AGN/SN feedback or by recent mergers may be an example of the latter. The real situation is likely a combination of both effects as in M87 (see Fig. 5.2). It is also important to note the possibility that different phases of ISM may have different metal abundances, but this has not been properly taken into account yet. We will further discuss this problem later.

One of the best examples of multiphase gas is in M87 where Chandra X-ray spectra can be extracted in a small region and analyzed individually due to its high luminosity and proximity (see Fig. 5.2). This spatially resolved spectroscopy reveals the complex spatial distribution of gas temperature and metallicity, related to the AGN activities and mixture of the high metallicity, low temperature ISM and the low metallicity, high temperatures ICM (see Fig. 5.9 in Sect. 5.4 taken from Million et al. 2010; see also Werner et al. 2010). Similarly complex temperature and abundance maps were also reported in NGC 5044 (David et al. 2010). However, this level of spatially resolved spectroscopy is only available in a few gas-rich cD-type galaxies with deep Chandra observations.

Most Chandra and XMM-Newton observations of external galaxies are typically done for a relatively short exposure 20–40 ks. This may still be deep enough for gas-rich galaxies to statistically require a multi-T model. In this case, the Fe abundance is usually close to solar or super-solar (see Sect. 5.4.2). However, for X-ray faint

galaxies with a small amount of hot ISM, the observational data may not statistically require more realistic complex emission models. In this case, a simple 1-temperature thermal plasma model is often applied and, the measured Fe abundance is usually very low (see Sects. 5.4.1 and 5.4.2.3). Ideally, the gas properties can be best measured by spatially resolved spectra. If they are not available, the temperature can still be measured with moderate accuracy from the integrated emission and will be close to the emission-weighted average. However, the abundance cannot be measured that way, because fitting the X-ray spectra from the multi-phase gas with a single temperature model will always return a lower abundance. Therefore, the measured abundance should not be interpreted as an average, e.g., emission-weighted average (for various definitions of average abundances see e.g., Ciotti and Pellegrini 2008; Tang and Wang 2010).

Commonly used hot plasma models are MEKAL (Mewe-Kaastra-Liedahl) and APEC (Astrophysical Plasma Emission Code; Smith et al. 2001). The MEKAL code is based on the model by Mewe et al. (1985, 1986) and Kaastra (1992), and then modified for Fe-L lines by Liedahl et al. (1995). The APEC with atomic database (ATOMDB) provides improved spectral modeling through additional emission lines, accurate wavelengths and new density-dependent calculations. As shown in Sect. 5.3.6, APEC seems to fit the observed spectra better than MEKAL. The detailed comparisons between APEC and MEKAL (e.g., different predictions of O VIII and Fe XVII lines) can be found in the Chandra X-ray Center web site, http://cxc.harvard.edu/atomdb/issues_comparisons.html.

5.3.2 Absorption Models

Elliptical galaxies do not contain a large amount of cold gas and dust, as seen in far-IR (e.g., Knapp et al. 1989) and H I observations (e.g., Knapp et al. 1985). With a typical Galactic $N_H(1–5 \times 10^{20}\,cm^{-2}$, away from the Galactic plane), any measureable excess $N_H(> 5 \times 10^{20}\,cm^{-2})$, intrinsic to the target galaxy, corresponds to $M_{HI} \sim 10^9–10^{10} M_\odot$, which is much higher than observed (Knapp et al. 1985). Most recent results obtained with Chandra and XMM-Newton data consistently indicate no extra absorption above the Galactic line of sight H column density (e.g., Kim and Fabbiano 2004; Humphrey and Buote 2006; Ji et al. 2009), although some earlier results with ROSAT and ASCA data did claim intrinsic absorption as much as $N_H \sim 10^{21}\,cm^{-2}$.

If N_H is overestimated, the Fe abundance could be underestimated, by overestimating the continuum level at low energies (e.g., Kim and Fabbiano 2004; Humphrey and Buote 2006). This may also be accompanied by underestimating the hard component from undetected LMXBs (which has the same effect as overestimating the continuum), when fitted with both N_H and the hard component normalization allowed to vary freely. This in turn would affect the continuum both at low ($E < 0:7\,keV$) and high energies ($E > 2\,keV$), reducing the required strength

of the Fe peak at ∼1 keV. This effect was partly responsible for earlier reports of low abundances measured by ASCA and ROSAT data (see Sect. 5.4.1).

Most common absorption models used in the literature are (1) photoelelctric absorption with Wisconsin cross-section (wabs; Morrison and McCammon 1983), (2) photoelectric absorption with a revised cross-section (phabs; Balucinska-Church and McCammon 1992), and (3) Tuebingen-Boulder ISM absorption (tbabs; Wilms et al. 2000) which considers absorption due to the gas, the dust grain and the H_2 molecules. The new version of tbabs (improved in the O K-edge and Fe L-edge) is also available in http://pulsar.sternwarte.uni-erlangen.de/wilms/research/tbabs/. Given that the intrinsic absorption is negligible and that the Galactic line-of-sight N_H is relatively small (a few x 10^{20} cms^{-1}), different absorption models in analyzing CCD spectra do not affect the Fe abundance in any significant manner, as long as the emission and absorption components are properly considered. In general, it is recommended to use tbas with high resolution spectra (e.g., grating data).

5.3.3 Subtraction of Other X-ray Sources

As the metal abundances are basically determined by the line to continuum ratios, it is critical to accurately subtract all non-gas X-ray emission to properly account for the gaseous emission. Incorrect subtraction could affect the continuum level and, in turn, introduce an error in the metal abundance.

5.3.3.1 Low Mass X-ray Binary (LMXB)

Prior to the Chandra mission, individual LMXBs were not easily detected in typical galaxies, mainly due to a poor spatial resolution in the previous missions. The X-ray emission of LMXBs is significantly harder than that of the hot ISM (kT = 0.3–1.0 keV) and well represented either by a Bremsstrahlung model with kT ∼7 keV, or a power-law model with a photon index of Γ ∼1.7 (e.g., Kim et al. 1992; Irwin et al. 2003; Boroson et al. 2011). Because of their harder spectra, the existence of a population of LMXBs could be identified by fitting unresolved spectra, particularly in X-ray faint (gas-poor, LMXB-dominating) galaxies (e.g., Kim et al. 1992), although in some previous studies, the entire X-ray emission was mistakenly attributed to the hot ISM (see Sect. 5.4.1).

With high resolution Chandra observations, most bright LMXBs can be detected and excluded from the diffuse emission. While the problem is generally less critical than before, the remaining population of undetected fainter LMXBs is still important in estimating the gas properties (luminosity, temperature, and metal abundances), particularly for gas-poor galaxies.

5.3.3.2 Active Binary (AB) and Cataclysmic Variable (CV)

Analogous (though less luminous) to LMXBs, active binaries (ABs) and cataclysmic variables (CVs), as seen in the Milky Way (e.g., Charles and Seward 1995), must be properly excluded. The integrated contribution from these sources was identified in M32 and the Galactic bulge (Revnivtsev et al. 2007, 2009), although they cannot be individually detected even with Chandra. They are often ignored because of their relatively small contribution to the total X-ray luminosity, as first estimated by Pellegrini and Fabbiano (1994). However, their contribution to the unresolved emission of the gas-poor galaxies is not negligible, once most bright LMXBs are excluded.

Boroson et al. (2011) characterized the X-ray spectra of a population of ABs and CVs. Their results are similar to those of Revnivtsev et al. (2007), but improved with smaller errors by jointly fitting the Chandra spectra of M31 and M32 with a combination of APEC and power-law (PL) models. They determine the spectral parameters: $kT = 0.48(-0.05, +0.07)$ keV for AP and $\Gamma = 1.76 \pm 0.37$ for PL. The X-ray to K-band luminosity ratio in 0.3 – 8 keV is $L_X/L_K = 9.5^{+2.1}_{-1.1} \times 10^{27}$ erg s^{-1} $L_{K\odot}$ As shown in Fig. 5.1, in extremely gas-poor galaxies (almost 1/3 of their sample), L_X(gas) is less than L_X(AB + CV).

Similar to undetected LMXBs, improper subtraction of the X-ray emission from ABs and CVs would result in incorrect measurements of the hot gas properties. As for the accuracy of metal abundances, the stellar coronal emission (mostly from ABs) will be mixed with the thermal gas emission and the hard emission (mostly from CVs) will affect the continuum level. The previously reported abundance measurements in gas-poor galaxies, if measured without proper consideration of the stellar contribution, need extra cautions (see Sect. 5.4.2.3). In this case, the hard PL component could have been subtracted as a part of a hard LMXB component (although the LMXB emission would have been slightly overestimated), but the soft component would have mistakenly added to the gas emission.

5.3.3.3 Nucleus

In normal early type galaxies, most nuclei are generally weak (so called low-luminosity AGN), when compared to typical AGNs (e.g., Pellegrini 2010), hence the nuclear emission can be isolated and separated from the gaseous emission, as long as the central source is properly excluded in Chandra observations. However, in case of moderately luminous nuclei in some LINERs (e.g., NGC 1052 and NGC 4261; Gonzalez-Martin et al. 2009), extra caution is necessary, because the PSF wing from the nucleus can still affect the emission from the neighboring region and the nuclear emission is often more complex than a simple power-law. Also the AGN may flare up, as seen in NGC 4278 (Cardullo et al. 2009). In this case, the AGN must be fully accounted for to analyze the gas emission in the central region.

5.3.3.4 X-ray Background

The X-ray background consists of the cosmic X-ray background (CXB) and the particle-induced background. The former consists of Galactic diffuse emission, heliospheric and geocoronal diffuse emission and distant AGNs (and possibly warm-hot intergalacitc medium – WHIM). The latter comes from charged/neutral particles (and photons) interacting with detector structures and depositing energy in the instrument. For the nature of the background, we refer to the detailed analyses of the Chandra and XMM-Newton background in http://cxc.harvard.edu/cal/Links/Acis/acis/Cal_prods/bkgrnd/current/ and http://xmm.vilspa.esa.es/external/xmm_sw_cal/background/index.shtml. Here we present how to effectively remove the background emission.

While the background uncertainty has little or no effect for a source which is strong and/or localized in a small region, the accurate background subtraction is critical to analyze an extended diffuse source, like the hot ISM. Ideally, the best way to subtract the background emission from the source emission is to take both at the same detector position at the same time. But this is not feasible in most X-ray observations. Instead, the background is obtained at the source-free region in the same detector (local background), or estimated by properly scaling the pre-made blank sky background template (sky background) which was generated by combining many observations after excluding X-ray sources. Whenever possible, the local background is preferred if the energy-dependent telescope vignetting (decreasing effective area with increasing off-axis angle) is properly corrected.

When the extended source fills up the field of view of the detector, the sky background is the only option. In this case, the background spectra can be extracted from the same detector region as the source spectra. However, the temporal and spatial variations of the background spectra and fluxes need to be corrected. This is often done by screening for background flares and matching source and background count rates at high energies ($>$5–10 keV), where the cosmic background emission dominates over the source emission. This is applicable when the background spectrum does not vary. However, the background may vary in time and space. Furthermore, background X-rays and non-X-ray particles behave differently, e.g., no vignetting for the particle background.

To properly subtract both X-ray and non-X-ray background emission, one may apply more sophisticated, self-consistent method, like the double background subtraction technique described by Arnaud et al. (2002). See also Humphrey and Buote (2006) for a similar technique. After screening the background for flares using the same criteria (i.e., the same count rate at the same energy band) as in the source spectra, applying vignetting correction photon by photon to both the observations and the blank sky background, and scaling the background by the ratio of count rates determined at high energies (e.g., $>$10 keV), the sky background is first subtracted. Then the residual background determined at the source free-region at the edge of the detector is subtracted.

5.3.4 Projection Effect: Spectral Fitting Case 1

To properly extract 3D properties from projected 2D observational data, an onion skin peeling technique is commonly applied. The hot ISM is assumed to be spherically symmetric. This method may be still applicable if the symmetry holds at least within a pie section. In that case, the de-projection can be done within the pie region.

For spectral fitting purposes, it is easier to project the 3D model to the sky plane and then compare with observed spectra extracted from the projected data, rather than de-project the observed spectra. This can be done for example by using a *projct* tool available in the XSPEC package (http://heasarc.gsfc.nasa.gov/docs/xanadu/xspec/), or a *deproject* tool available in the CIAO contributed software (in http://cxc.harvard.edu/contrib/deproject/).

The de-projection effect is most obvious, when the radial gradient is significant, as it also mitigate the problem of the multiphase gas (e.g., Buote 2000; Kim and Fabbiano 2004). Figure 5.5 shows an example of NGC 507 where the gas temperature increases with increasing galacto-centric distance, partly because the cooler (∼0.8 keV) ISM is embedded in a hotter (∼1.4 keV) ambient (ICM) gas (see Sect. 5.4.2 for more details). Because of the temperature gradient, the 3D fitting (upper panels in Fig. 5.5) significantly improves χ^2 statistics over the 2D fitting (lower panels in Fig. 5.5). Also noticeable is the localized deviation in $\Delta\chi$ (excess – deficit – excess around ∼1 keV at the lower panels). This $\Delta\chi$ pattern is likely due to incorrect lines from the same element but in different ionization stages in different temperatures, as described above (see Table 5.1). By properly correcting the projection effect (in the upper panels), not only the overall χ^2 is reduced, but also the local $\Delta\chi$ pattern disappears.

5.3.5 Standard Solar Elemental Abundances

In the last two decades, there have been several different measurements of the solar elemental abundances. They are based on either mass spectroscopy of meteorites or modeling solar photospheric spectral lines, and the results have been significantly different for many key elements (e.g., Fe, O). With considerable improvements in atomic and molecular data as well as in modeling with a realistic time-dependent 3D hydrodynamic model, the photospheric and meteoric abundances seem to converge at least for non-volatile elements (see recent review and redetermination by Asplund et al. 2009). Since volatile elements (H, He, C, N, O, Ne) are depleted in meteorites, they cannot be reliably measured with meteorites.

In Table 5.2, we present three solar standards: two commonly used (ANGR and GRSA) and the most up-to-date (ASPL) standards. Several key elements are listed by number relative to H and Fe. Often in the literature, it is also written in a logarithmic form: for an element X, $\log \varepsilon_X = \log(N_X/N_H) + 12$, where N_X and N_H are the

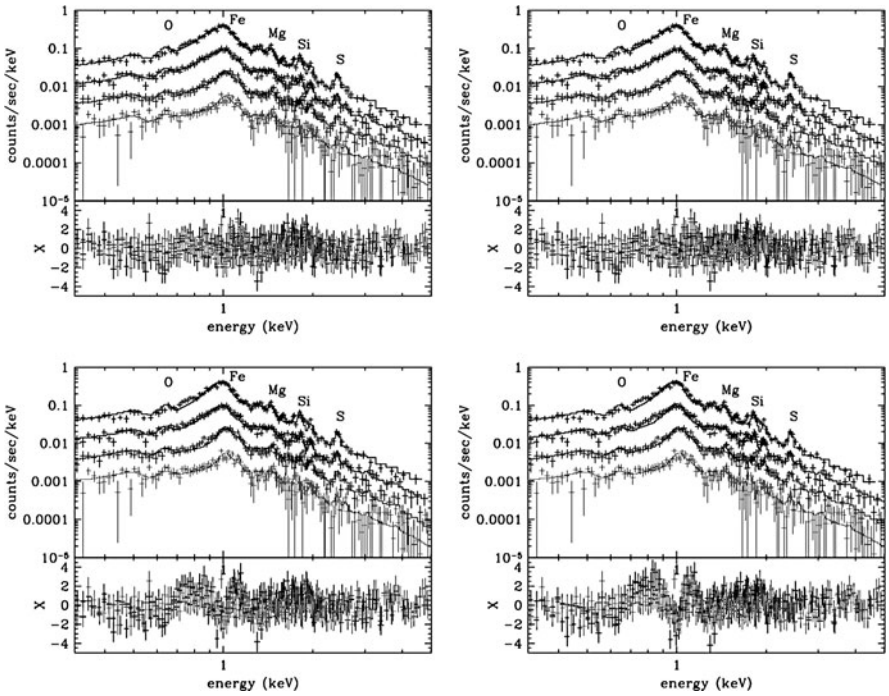

Fig. 5.5 Comparison of spectral fitting in 3D (*top*) and 2D (*bottom*). The *left and right* panels are for 3-component models and 2-component models, respectively. In each figure, the X-ray spectra extracted from r = 0–1′, 1′–2′, 2′–3′ and 3′–5′ are shown from top to bottom. Except for the first spectrum, they are vertically displaced for visibility. Also marked are strong emission features from O, Fe, Mg, Si, and S. The bottom panel indicates the goodness of the fit by $\Delta\chi =$ (observation-model)/error. Note the progressively worse $\Delta\chi$ from the top-left to the bottom-right. Taken from Kim and Fabbiano (2004), reproduced by permission of the AAS

number densities of elements X and H, respectively. For example, $\log \varepsilon_{\rm H} = 12$ and $\log \varepsilon_{\rm Fe} = 7.5$ in ASPL. Another alternative form is [X/H] which is normalized by the solar ratio: for an element X, $[{\rm X/H}] = \log({\rm N_X/N_H}) - \log({\rm N_{X,\odot}/N_{H,\odot}})$. It can be also written in mass: $[{\rm X/H}] = \log({\rm M_X/M_H}) - \log({\rm M_{X,\odot}/M_{H,\odot}})$. In this form, $[{\rm X/H}] = 0.0$ indicates the solar abundance.

Most notably, the Fe abundance was reduced from 4.7×10^{-5} in ANGR (Anders and Grevesse 1989) to 3.16×10^{-5} in GRSA (Grevesse and Sauval 1998) and in ASPL (Asplund et al. 2009). The decrease of the solar Fe abundance by a factor of $\sim$1.5 has somewhat relaxed the Fe discrepancy (described in Sect. 5.4.1). Another notable change is that O, Ne and Ar are significantly reduced. For example, the O abundance decreases from 8.5×10^{-4} in ANGR to 6.8×10^{-4} in GRSA and further decreases to 4.9×10^{-4} in ASPL. Similar to Fe, the change in the O abundance by a factor of 1.7 considerably mitigates the missing O problem (see Sect. 5.4.4.2), although it is still unsolved. The other elements remain almost unchanged.

Table 5.2 Solar element abundances

	By number relative to H			By number relative to Fe		
	ANGR	GRSA	ASPL	ANGR	GRSA	ASPL
O	8.51e-04	6.76e-04	4.90e-04	18.184	21.392	15.506
Ne	1.23e-04	1.20e-04	8.51e-05	2.628	3.797	2.693
Mg	3.80e-05	3.80e-05	3.98e-05	0.812	1.203	1.259
Si	3.55e-05	3.35e-05	3.24e-05	0.759	1.060	1.025
S	1.62e-05	2.14e-05	1.32e-05	0.346	0.677	0.418
Ar	3.63e-06	2.51e-06	2.51e-06	0.078	0.079	0.079
Ca	2.29e-06	2.29e-06	2.19e-06	0.049	0.072	0.069
Fe	4.68e-05	3.16e-05	3.16e-05	1	1	1
Ni	1.78e-06	1.78e-06	1.66e-06	0.038	0.056	0.053

ANGR Anders and Grevesse (1989), *GRSA* Grevesse and Sauval (1998), *ASPL* Asplund et al. (2009)

When comparing abundances reported previously in the literature, it is necessary to rescale for the same solar standard. Note that if O and Fe abundances were solar in ANGR, they would be 1.7 and 1.5 solar in ASPL. The solar O/Fe ratio in ANGR would be non-solar (slightly super-solar) in ASPL. It is also important to note that even after this adjustment the measured abundances may be still affected if different elements are tied in spectral fitting following different solar standards (see Sect. 5.3.6).

While the accuracy in the standard solar elemental abundances has been significantly improved, we should keep in mind that the uncertainties are still far from negligible (see Asplund et al. 2009).

5.3.6 Non-solar Ratios Between Elements: Spectral Fitting Case 2

Another important problem in X-ray spectral fitting is that various element abundances relative to Fe are often fixed at the solar ratio. This practice has been customary mainly because the observed spectra do not have enough statistics to allow variable individual elements. However, some elements are expected to deviate from the solar abundance. For example, the α-element to Fe ratio both in stars and in gas is expected to vary depending on the relative contribution from SN Ia and SN II (see Sect. 5.4.4.1). Also known is the low O abundance (see Sect. 5.4.4.2) relative to Fe and even relative to the same SN II products, Mg (Buote et al. 2003; Kim and Fabbiano 2004; Humphrey and Buote 2006). It is important to note that the measured Fe abundance depends on how other elements are tied. For example, Matsushita et al. (2000) pointed out that the Fe abundance is significantly different when measured with solar and non-solar α-element to Fe ratios. David et al. (2010)

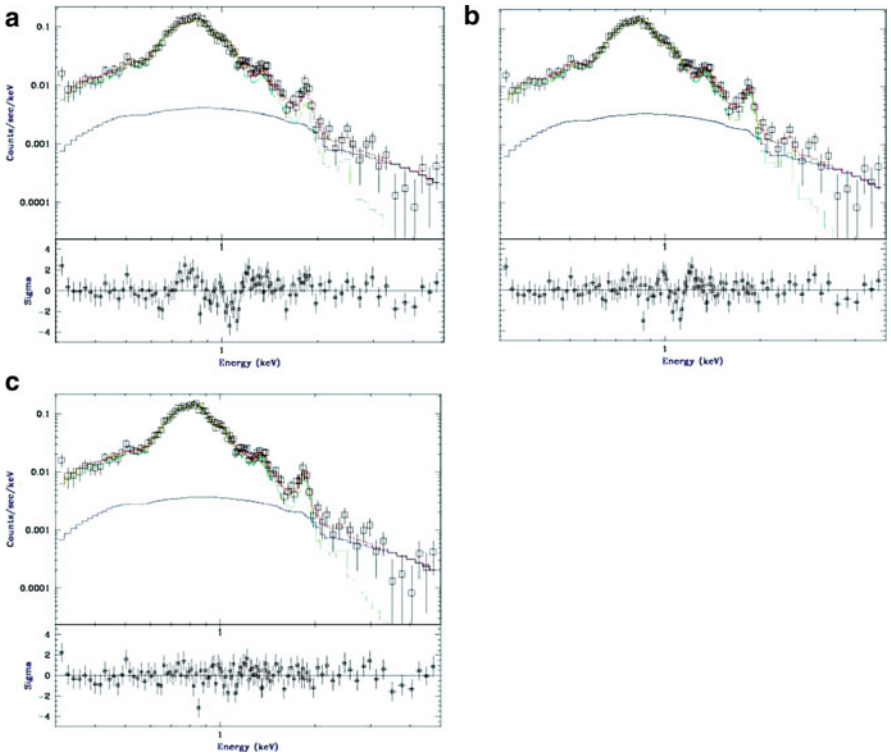

Fig. 5.6 Spectral fitting of Chandra X-ray spectrum extracted from the central ($r < 30''$) region of NGC 720 with (**a**) MEKAL (all elements tied at the solar ratio), (**b**) VMEKAL (all elements allowed to vary independently) and (**c**) VAPEC (all elements allowed to vary independently). Note that the overall $\Delta\chi^2$ (as well as local deviation) is progressively reduced from (**a**) to (**c**), see the electronic version for a color version of this figure

further demonstrated (see their Fig. 5.7) that tying O to Fe results in an incorrect Fe abundance by artificially altering the continuum level at low energies ($\sim$0.5 keV).

To illustrate the effect of tying elements, we compare the spectral fitting results in Fig. 5.6, using deep Chandra observations of NGC 720 (Kim 2010; Kim et al. in preparation). While the hot gas in NGC 720 is extended to $\sim 5'$, the X-ray spectrum was extracted only from the central region ($r < 0.5'$), by separating the outer region which could be in a different temperature and metallicity. This ensures that the simplest emission model (i.e., a single phase gas model) is applicable (Sect. 5.3.1) and that the projection effect is not significant (Sect. 5.3.4) so that the effect of non-solar abundance ratios is best illustrated. Another advantage of using a small region is that the uncertainty in background subtraction is less important (Sect. 5.3.3.4). All detected LMXBs are excluded and a hard component is added for the remaining undetected LMXBs (Sect. 5.3.3.1). Also excluded is an AGN which is relatively weak and its PSF wing does not affect the gas emission (Sect. 5.3.3.3). The X-ray emission from ABs and CVs is negligible in this small region (Sect. 5.3.3.2).

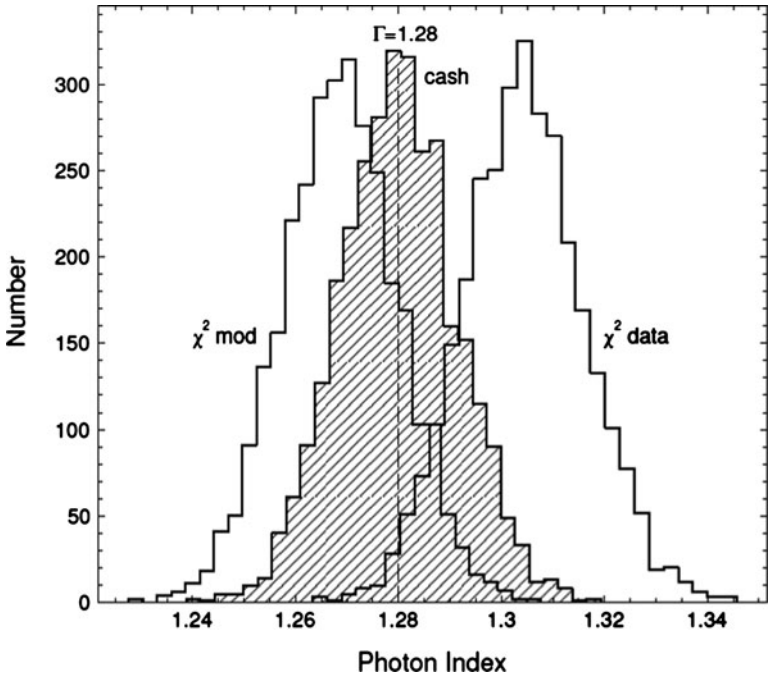

Fig. 5.7 Distributions of a photon index Γ obtained by fitting simulated X-ray spectra with 60,000 counts and using the three different statistics: χ^2 with model variance, χ^2 with data variance and Cash statistics (taken from Siemiginowska 2011)

We fit the X-ray spectrum from the hot ISM in the center of NGC 720 (a) with a 2-component model consisting of MEKAL (all elements relative Fe are fixed at the solar ratio) for the hot gas and 7 keV Bremsstrahlung for undetected LMXBs, (b) by using VMEKAL (instead of MEKAL) with all elements allowed to vary independently and (c) using VAPEC instead of VMEKAL. When all elements are tied (Fig. 5.6a), the metal abundance is statistically constrained at 0.70 (–0.13 +0.19) solar. But the fit is formally unacceptable with the reduced χ^2 of 1.29 for 108 degrees of freedom (dof). A probability that one would observe χ^2 or a larger value is only 0.02. In addition to the poor overall χ^2 statistic, the localized deviations in $\Delta\chi$ (the bottom panel in Fig. 5.6a) are clearly visible near emission features, e.g., excess at 0.5 keV (O), excess at 0.7–0.9 keV (Fe and Ne), deficit at 1.2 keV (Fe), excess at 1.3–1.5 keV (Mg) and excess at 1.8–2.0 keV (Si). This pattern of excess followed by deficit (or deficit followed excess) is similar to that in the lower panel of Fig. 5.5, where the temperature gradient is not properly considered. Since the temperature is relatively well determined and the radial gradient is not important in the small central region, the temperature gradient is not an issue in the center of NGC 720. The problem is likely (1) incorrect individual elemental abundances by arbitrarily tying with other elements, and (2) inaccurate emission models (e.g., in MEKAL and APEC).

When all elements are allowed to vary independently in VMEKAL (Fig. 5.6b), the reduced χ^2 is significantly improved to 1.01 with 96 dof. The fit is formally acceptable with a probability of 0.45. The Fe abundance increases to 1.48 (–0.39 +0.31) solar which is inconsistent ($\sim 2\sigma$ significance) with the first result (0.7 solar). The Si abundance is 2.5 (−0.52 + 0.48) solar which is also inconsistent ($\sim 3\sigma$ significance) with the first results (0.7 solar). While the overall χ^2 was improved to an acceptable level, the localized deviations in $\Delta\chi$ are still visible, most prominently at 0.9–1.3 keV (excess, deficit, then excess).

When VAPEC is used instead of VMEKAL (Fig. 5.6c), the reduced χ^2 is further improved to 0.80 with 97 degrees of freedom, corresponding to a probability of 0.93. Furthermore, no prominent localized deviation in $\Delta\chi^2$ is visible in the entire energy range. Given that the overall statistics and the local deviations significantly improved, VAPEC seems to better represent the hot plasma emission than VMEKAL, as APEC is known to use more accurate plasma emission data (Smith et al. 2001). The Fe and Si abundances are 0.80 (–0.71 + 0.27) and 1.37 (–0.28 + 0.31) solar, respectively. The Si/Fe abundance ratio is 1.71 solar. The Fe and Si abundances are again inconsistent with the MEKAL results ($1–2\sigma$ significance), and also with the VMEKAL results ($1.5–2\sigma$ significance). It is clear that the Fe abundance significantly varies, depending on the way how elements are tied and the adopted plasma model. It is also interesting to note that while the Fe abundance is quite different (1.48 and 0.8 solar in VMEKAL and VAPEC, respectively), the Si/Fe abundance ratio is very similar (1.7 solar in both cases). The relative abundance ratio is often more reliable than the absolute abundance (see Sect. 5.4.4).

5.3.7 Optical Depth for Strong Emission Lines

The ISM is, in general, optically thin and its X-ray spectrum is well represented by an optically thin hot plasma model (e.g., APEC). However, the resonance scattering of the strongest line may not be negligible in a high density environment. In that case, the ISM is no longer optically thin for that line. The resonance scattering can also provide important information about the turbulent velocity in the hot plasma, as it depends on the small scale gas motion (Werner et al. 2009).

The resonance scattering was identified for a strong Fe XVII line at 15Å (see Table 5.1) in the core of NGC 4636 by Xu et al. (2002) and confirmed by Werner et al. (2009). Analyzing the RGS spectra of NGC 4636, Xu et al. (2002) showed that the ratio of the weaker Fe XVII 17Å line to the stronger 15Å line (see Table 5.1) peaks at the center of the galaxy and decreases with increasing projected distance, as expected when the strong Fe line at 15 Å is being suppressed at the center by resonant scattering. Werner et al. (2009) further studied five gas-rich elliptical galaxies and found the resonant scattering effect in the cores of four galaxies (NGC 1404, 4472, 4636, 5813) and estimated that correcting for this optical depth effect increases Fe and O abundances by 10–20%. By excluding the problematic line at

15Å in their spectral fitting, Ji et al. (2009) found that the correction of resonant scattering increases the Fe abundance by 20–30% in NGC 4636. However, they found no change in other gas-rich galaxies including NGC 4472 where Werner et al. (2009) found the suppressed Fe XVII line at 15.01Å.

5.3.8 Helium Sedimentation

The Helium abundance cannot be determined by X-ray spectral fitting and is usually assumed to be solar. However, if the He abundance is enhanced, other element abundances will be reduced due to over-estimating Bremsstrahlung continuum emission. The enhanced He abundance could occur due to the diffusion under the gravitational potential at the center, known as helium sedimentation (e.g., Fabian and Pringle 1977; Gilfanov and Syunyaev 1984). Considering relaxed galaxy clusters, Ettori and Fabian (2006) showed that a He enhancement by a factor of a few with respect to the solar value could reduce by ∼50% the metallicity measured in the center of the ICM (while it does not change the gas temperature) and might explain the metallicity drop reported in the inner (∼20 kpc) regions of nearby bright galaxy clusters (e.g. Centaurus et al. 2002; A2199, Johnstone et al. 2002). The metallicity drop was also seen in galaxy groups with gas in a lower temperature (1–2 keV) (e.g., Rasmussen and Ponman 2009) which, if proved, may be caused by the same effect (however, there may be a problem in this measurement, as described in Sect. 5.4.5). Additionally, the enhanced Far UV flux (called UV upturn) often found in the bright cluster galaxies may be explained by the helium sedimentation due to He-enhanced core-He burning HB (horizontal branch) stars (Peng and Nagai 2009). However, the sedimentation rate could be significantly reduced by the presence of magnetic fields, which is not well understood. The effect of the He sedimentation on reducing measured metal abundances may be somewhat different in the ISM at a lower temperature (∼1 keV or less) and a lower density, as the drift velocity depends on them, $v_D \sim T^{3/2}\, n^{-1}$ (Fabian and Pringle 1977). It is necessary to properly calculate the amount and time scale of the He diffusion under the galaxy environment.

5.3.9 Calibration Uncertainty

The relative calibration uncertainties between different instruments can be measured and possibly corrected by comparing data taken by multiple instruments. However, most cross-calibration studies indicate that systematic differences still remain between different missions and even between different instruments onboard the same observatory.

Recently, led by the international working group, IACHEC (International Astronomical Consortium for High Energy Calibration, see http://www.iachec.org/), a

cross-calibration study has been initiated for most current X-ray observatories, including Chandra, XMM-Newton and Suzaku. A few initial results with well known targets (e.g., supernova remnants and clusters of galaxies) have been reported (Plucinski et al. 2008; Nevalainen et al. 2010; Tsujimoto et al. 2010). They identified systematic differences in the best-fit parameter values which cannot be attributable to the statistical scatter of the data alone.

Plucinski et al. (2008) investigated a supernova remnant in SMC, 1E0102.2–7219 to compare O lines (0.57 and 0.65 keV) and Ne lines (0.92 and 1.0 keV – see Table 5.1). They found the maximum discrepancies as high as 13–24% among Chandra, XMM-Newton and Suzaku instruments. Tsujimoto et al. (2010) used another supernova remnant, G21.5–0.9 (also called Pulsar wind nebula) and found that the differences can be as large as 20% and 9% for the 2–8 keV band flux and power-law index, respectively, but could not study softer energies (<2 keV) due to very high absorption.

Nevalainen et al. (2010) used a sample of 11 relaxed clusters of galaxies whose X-ray emission is dominated by optically thin ionized plasma emission at kT = 2.5–9 keV. They measured the energy dependent effective area by comparing the temperature measured with different instruments and the normalization of the effective area by comparing the flux. While the temperatures agree well when determined in the hard band (2–7 keV), they disagree when measured in the soft band (0.5–2 keV), the ACIS temperature being ∼18% higher than the PN temperature. In the full band (0.5–7.0 keV), the temperatures measured with the EPIC or ACIS data are uncertain by ∼10–15% on average. While the fluxes agree relatively well in the soft band, there is a significant systematic difference in the hard band, the ACIS flux being ∼ 11% higher than the PN flux.

In addition to the cross-calibration uncertainties between observatories, there are important calibration issues related to the time-dependent instrument responses in the same observatory. For example, the Chandra ACIS instrument is known to suffer from molecular contamination which has been building up on the optical blocking filters (see http://cxc.harvard.edu/cal/memos/contam_memo.pdf). This causes the ACIS QE (quantum efficiency), hence ARF (auxiliary response function), to vary in time (also in energy, and detector position). Therefore, it is necessary to take into account the QE difference when compare two ACIS observations taken in different times.

The cross-calibration uncertainties are on the order of 10–20%. However, it is not straightforward to translate these results to the uncertainties relevant to metal abundances in the hot ISM. The most critical factor for the ISM abundance is the uncertainty of the energy dependent effective area in the soft band (0.5–2 keV) where most important emission features reside and where the characteristics of CCD-based instruments (e.g., QE and spectral resolution) are rapidly changing. This could selectively affect some elements due to localized uncertainties, e.g., calibration uncertainties at the C and Si edges. This could also affect the continuum level determined in different energies (e.g., hard emission from undetected LMXBs determined at higher energies) or in different instruments (e.g., when imaging data are used to analyze grating data in Sect. 5.4.3). It will be necessary to perform

an extensive study with a sample of elliptical galaxies to fully understand the calibration effect on the metal abundance measurement.

5.3.10 Statistics: χ^2 vs. Cash Statistic

Two commonly used statistics are χ^2 and cash (or C-stat). The χ^2 method, most widely used in the literature, can determine both a confidence interval of each parameter and a goodness-of-fit. In this method, the X-ray spectra need to be binned with at least 20–30 counts in each bin to properly apply the Gaussian approximation. On the other hand, the cash statistic (Cash 1979) can be applied regardless of the number in each bin. However, a goodness-of-fit measure is not assigned to a given value of the cash statistic and Monte Carlo simulations are required.

In the χ^2 statistic, the variance is calculated from the data (called data variance) by simply taking $\sqrt{N}$, where N is the number of observed counts in a given bin. Alternatively, the variance can be calculated from the model amplitude (called model variance). With a finite number of observed counts, both data and model variances could be biased, called χ^2 *bias* (Siemiginowska 2011; see also Humphrey et al. 2009). This bias is illustrated in Fig. 5.7, taken from Siemiginowska (2011). X-ray spectra of a single power-law model were simulated with Chandra calibration response files and the Poisson noise was added. Then the simulated spectra were fitted with the same model to determine the best fit parameter. The simulation results show that the model-variance χ^2 statistic underestimates the power-law index and the data-variance χ^2 statistic overestimates. Conversely, the cash statistic returns more reliable results (see also Humphrey et al. 2009). Another alternative is to use Gehrels variance function, $1 + \sqrt{N+0.75}$ (Gehrels 1986) to better approximate in the low-counts regime. However, this approximation is too conservative and may overestimate the size of the confidence range for a given significance.

In most practical cases of the hot ISM, the statistical error is larger, and the emission model is more complex than depicted in Fig. 5.7 and additionally various non-negligible systematic errors are complex as described in Sect. 5.3.1–5.3.9. Therefore, this χ^2 bias might not cause a problem in any significant manner in the published results. However, it is important to take into account this bias in analyzing high s/n spectra and also in future missions.

5.4 Observed Metal Abundances in the Hot ISM of Elliptical Galaxies

5.4.1 Before Chandra and XMM-Newton

In early X-ray missions, the observationally measured Fe abundance was often sub-solar and considerably lower than expected. This problem is often referred to as the

Fe discrepancy (e.g., Arimoto et al. 1997; Pipino in this book). It was most serious when poor (spectral and spatial) resolution spectra (like ROSAT and ASCA data) were analyzed by fitting a simplified emission model, e.g., a single temperature (1T) thermal plasma model (sometimes with an additional hard component to take into account LMXBs). As described in Sect. 5.3.1, the reported Fe abundances were always lower than 0.5 solar and quite often as low as 0.1 solar (e.g., Awaki et al. 1994; Loewenstein et al. 1994; Davis and White 1996; Matsumoto et al. 1997). Furthermore, the associated statistical errors (taken directly from the spectral fitting) were usually very small.

It is interesting to note that the metal abundances measured using the X-ray (mostly ASCA) spectra from stellar coronae had suffered from the similar problem of anomalously low metal abundances, Fe abundances as low as 10–30% of the solar value were regularly reported (e.g., see a review by Gudel 2004).

As described in Sect. 5.3.1, the observationally measured Fe abundance critically depends on the adopted model. Analyzing ROSAT data, several investigators (Buote and Canizares 1994; Trinchieri et al. 1994, 1997; Fabbiano et al. 1994; Kim and Fabbiano 1995) recognized that the observed spectra could allow not only a 1-T gas model with very low Z_{Fe}, but also a 2-T gas model with roughly solar Z_{Fe}, although they could not distinguish the two possibilities due to the limited spectral resolution. Kim et al. (1996), using additional ASCA data, could reject the very low abundance 1-T model in NGC 4382. Buote and Fabian (1998) further analyzed ASCA data of 20 gas-rich early type galaxies and confirmed that the extremely low abundance is not required. They found that the Fe abundance is close to solar, when fitted with a 2-T model and that in a few very high S/N galaxies, an even more complex, 3-T model is preferred.

Buote (2000) also pointed the importance of the projection effect to correctly account for the temperature and abundance gradient (see Sect. 5.3.4). Analyzing ROSAT data of 10 galaxies and groups, he found that the Fe abundance decreases with increasing radius: from $Z_{Fe} \sim$ 1- several $Z_\odot$ within the central radial bin ($r <$ 10 kpc) to $Z_{Fe} \sim 0.5 Z_\odot$ at the largest radii examined ($r \sim$50–100 kpc). The negative gradient of the Fe profile was reported earlier, e.g., in NGC 4636 by Mushotzky et al. (1994), but the absolute abundance was less accurate (sub-solar) in the entire radius range.

Reanalyzing ASCA data of 27 elliptical galaxies, Matsushita et al. (2000) pointed out the effect of coupling among different elements. As discussed in Sect. 5.3.6, the allowed abundances of two elements (e.g., Fe and α–elements) are often strongly coupled such that the confidence contours of two interesting elements are diagonally elongated. Because the continuum level might be raised or lowered by incorrectly tying different elements, the measured Fe abundance would change with non-solar Fe to α ratios. Matsushita et al. (2000) found that the metallicity becomes significantly higher with a non-solar α to Fe ratio than with the fixed solar ratio (also by adding a systematic error of ∼20%) and becomes close to $\sim 1 Z_\odot$ within a factor 2.

5.4.2 The Chandra and XMM-Newton Era

5.4.2.1 Gas-Rich cD Galaxies

Taking advantage of high spatial resolution in Chandra and a large effective area in XMM-Newton, many investigators have revisited the low metal abundance problem. The new results generally suggest that extremely low, sub-solar, Fe abundances can be statistically rejected at least in X-ray bright elliptical galaxies (this section and Sect. 5.4.2.2), although it is still not clear in the X-ray faint, gas-poor galaxies (see Sect. 5.4.2.3 below).

Analyzing XMM-Newton data of NGC 1399, the brightest elliptical galaxy in the Fornax group, Buote (2002) reported that the hot gas is best represented by a two-phase model with T $\sim$ 0.9 keV and $\sim$ 1.5 keV. The lower temperature is comparable to the stellar kinetic temperature and the higher temperature corresponds to a larger scale gravitational mass of $10^{13} M_{\odot}$ associated with the group. The two-phase model returns $Z_{Fe} = 1.5$–$2\ Z_{\odot}$ in the central region ($r < 20$ kpc). At larger radii, the iron abundance drops to $Z_{Fe} \sim 0.5 Z_{\odot}$ at $r \sim 50$ kpc. Similarly analyzing Chandra and XMM-Newton data of NGC 5044, another dominant galaxy in a small group, Buote et al. (2003a, b) reported that the hot gas is well fitted by a two-temperature model with 0.7 keV and 1.4 keV. In this model, $Z_{Fe} \sim 1 Z_{\odot}$ in the central region ($r < 50$ kpc) and $Z_{Fe} \sim 0.4 Z_{\odot}$ at $r = 100$ kpc.

Kim and Fabbiano (2004) analyzed XMM-Newton data of NGC 507, another X-ray bright, dominant elliptical galaxy in a galaxy group. Taking into account various possible systematic effects in their measurement, they clearly reported super-solar Fe (and super-solar α-element) abundance: $Z_{Fe} = 2$–$3 Z_{\odot}$ inside the D_{25} ellipse of NGC 507 (see Fig. 5.8), the highest Z_{Fe} reported for the hot halo of an elliptical galaxy. This high Fe abundance may be still lower than expected, but much closer to the predictions of standard stellar evolution models with the contributions from both SN Ia and SN II.

Similar to NGC 1399 and NGC 5044, the hot ISM of NGC 507 has temperatures ranging from 0.6 to 1.4 keV (within each concentric shell). All three galaxies clearly demonstrate that abundance measurements are critically dependent on the selection of the proper emission model (Sect. 5.3.1). The XMM-Newton and Chandra spectra provide enough statistics to formally require at least three emission components in each concentric shell. In addition to a harder component for the integrated output of LMXBs, two soft thermal components (with relative contribution varying at different radii) are necessary to represent a range of temperatures in the hot ISM. It is important to note that the 3-component model is still an approximation, unless the multiple gas phases are fully resolved (e.g., as in M87 as described below). With a single-phase gas model (with or without the LMXB component) customarily used in the past, both studies (Buote et al. and Kim and Fabbiano) could reproduce a much lower Z_{Fe}, consistent with previous reports of sub-solar metal abundances, but with a large χ^2 value (i.e., statistically unacceptable).

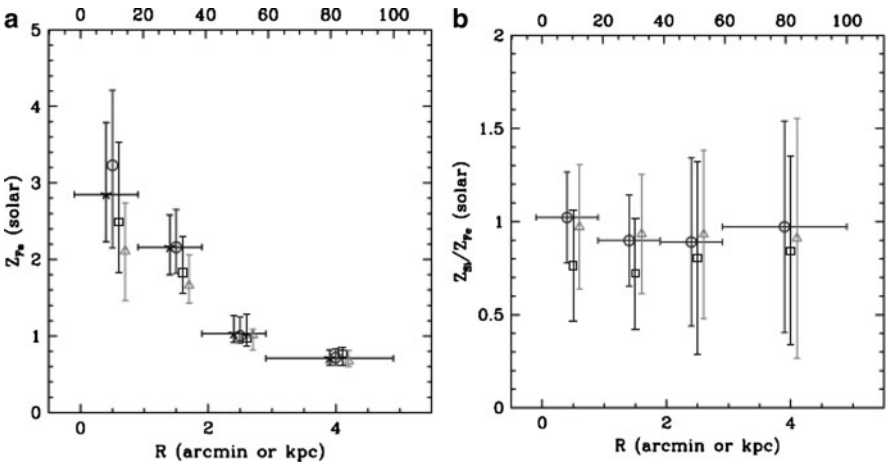

Fig. 5.8 Radial distributions of (**a**) Fe abundances and (**b**) Si-to-Fe abundance ratios measured with Chandra data of NGC 507. Different symbols indicate different ways of tying elements. Taken from Kim and Fabbiano (2004), reproduced by permission of the AAS

The α element abundances (mainly determined by Si) are also close to solar in all 3 galaxies: $Z_{\rm Si}/Z_{\rm Fe} \sim 0.8$ in NGC 1399, $Z_{\rm Si}/Z_{\rm Fe} \sim 0.83 \pm 0.1$ in NGC 5044 and $Z_{\rm Si}/Z_{\rm Fe} \sim 0.8$–1.1 in NGC 507 (see Fig. 5.8). These Fe to Si abundance ratios imply that ∼70% of the Fe mass originates from SN Ia (see Sect. 5.4.4). While the Fe and α-element abundances decrease with increasing radius, their ratio remains constant at the solar ratio over the entire region (out to 100 kpc), indicating that SN II and SN Ia ejecta are well mixed on a scale much larger than the extent of the stellar body (see Sect. 5.4.5).

Recently, spatially resolved high quality spectra are obtained for a few X-ray bright, nearby cD galaxies with ultra deep Chandra observations. Figure 5.2 shows an ultra deep Chandra observation of M87 (total exposure of ∼570 ks). Million et al. (2010) extracted X-ray spectra applying a contour binning method from a small region consisting of neighboring pixels of similar surface brightness, but with enough counts for proper spectral fitting (∼2,500 counts on average in ∼6,000 regions). The spatially resolved spectroscopy reveals in detail the complex spatial distribution of gas temperature and metallicity (see Fig. 5.9 taken from Million et al. 2010; see also Werner et al. 2010). The gas temperature ranges from 0.8 to 3 keV, generally cooler inside (and in the X-ray arms) and hotter in the outskirts, as the ICM contributes progressively more with increasing distance from the center. The metallicity ranges from 0.4 solar to 2 solar, generally higher in the inner region and lower in the outskirts, again by more contribution from the low-metallicity ICM with increasing distance. In addition to the global radial variation, multi-phase gas (with different temperature and metallicity) co-exists locally. Furthermore, in Fig. 5.9, various thermal and chemical sub-structures are seen, e.g., a high metallicity structure is observed at a radius of r ∼4.5 arcmin to the west of the central

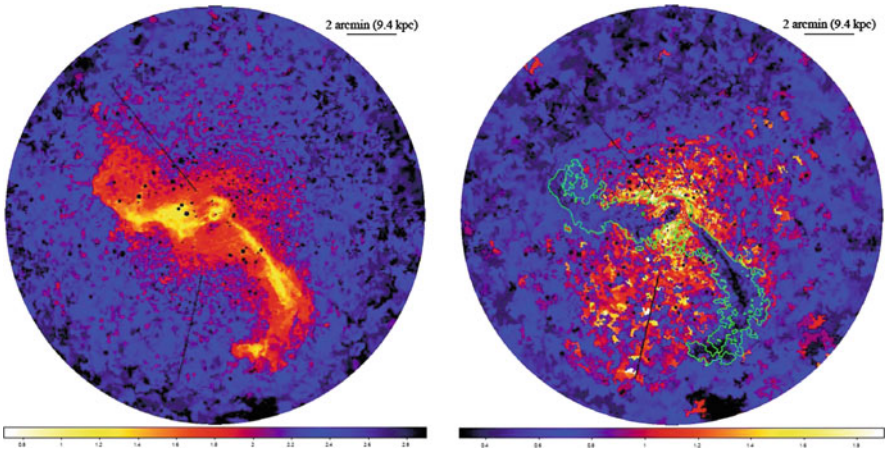

Fig. 5.9 (*top*) Temperature map of the central region of the Virgo cluster (in units of keV). Point sources and readout errors have been excluded (*black holes*). (*bottom*) Metallicity map in solar units. Regions inside the green contours cannot be modeled by a single-temperature plasma and the abundance is significantly underestimated. Taken from Million et al. (2010), reproduced by permission of the RAS, see the electronic version for a color version of this figure

AGN. This ridge connects with the high metallicity extension to the northwest of the core at a radius of r ∼3.3 arcmin. This structure is likely due to the uplift of cool, metal-rich gas in the wake of buoyantly rising, radio-emitting plasma (see Roediger et al. 2007 for numerical simulations of mixing metal by buoyant bubbles). Also noticeable is an asymmetric feature: the southern region is more metal rich than the north.

David et al. (2009, 2010) reported similarly complex features in NGC 5044, with spatially varying amounts of multiphase gas, by analyzing spatially resolved spectra extracted from deep Chandra observations.

While it is clear that the high spatial-resolution spectroscopy is most desirable to properly identify the fine details of the ISM and to measure the gas properties (including metal abundances), this level of detail observational information is only available in a small number of gas-rich nearby cD-type galaxies with deep Chandra observations.

5.4.2.2 Gas-Rich Normal (Non-cD) Galaxies

Humphrey and Buote (2006) re-analyzed archival Chandra data of 28 early-type galaxies, covering a wide range in the X-ray luminosity. In a high-L_X sub-sample ($L_X = 10^{41.5–43}$ erg s^{-1}, including some cD galaxies), the measured Fe abundance is $Z_{Fe} = 0.4–3.0Z_\odot$, while in a moderate-L_X sub-sample ($L_X = 10^{40.5–41.5}$ erg s^{-1}, all non-cD galaxy), $Z_{Fe} = 0.2–5Z_\odot$. In their sample, even if the best fit Z_{Fe} is very low, the corresponding error is large such that $Z_{Fe} \sim 1Z_\odot$ is usually allowed within

the error. They also found no clear difference in Z_{Fe} between high and moderate L_X sub-samples. More specifically, there is no correlation between Z_{Fe} and L_X, possibly indicating that the solar or super-solar Z_{Fe} found in cD galaxies still holds in non-cD normal galaxies with lower L_X.

Ji et al. (2009) re-analyzed archival XMM-Newton EPIC and RGS data for 10 nearby X-ray bright galaxies including two cD galaxies. In their two-phase model fitting, they found $Z_{Fe} = 0.5$–$1.8 Z_\odot$ with a median Fe abundance of $0.86\ Z_\odot$. Again, there is no Z_{Fe} dependency on the X-ray luminosity.

Both studies indicate that the Fe abundance is generally close to solar in most gas-rich elliptical galaxies and the very sub-solar Fe abundance reported earlier (in Sect. 5.4.1) is statistically rejected. In this regard, cD and non-cD elliptical galaxies do not differ, except that cD galaxies are more luminous and can be investigated in detail.

While the above general trend is obvious, the individual abundance in each galaxy still varies from one measurement to another, often by more than the statistical error. For example, two (NGC 1399 and NGC 4552) of five galaxies which are common in Humphrey and Buote (2006) and Ji et al. (2009) samples have quite different Fe abundances. The reported abundances are sometimes different even when measured by the same instrument and the same model, e.g., with XMM-Newton EPIC data of NGC 4649 (a gas-rich Virgo elliptical galaxy), $Z_{Fe} = 1.4$–$1.6 Z_\odot$ (for 1T) and 1.6–1.7 $Z_\odot$ (for 2T) by Ji et al. (2009) while $Z_{Fe} = 0.7 Z_\odot$(for 1T) and 1.1 $Z_\odot$(for 2T with all elements tied) by Randall et al. (2006). The quoted error is relatively small ($\sim$0.1 $Z_\odot$). Also note that a low Fe abundance is reported for a gas-rich galaxy even recently, although rare, e.g., in NGC 6251 with 1T gas + power-law (Sambruna et al. 2004). While the sample-averaged metal abundance seems to be reliable, an individual abundance measurement should be taken with caution.

5.4.2.3 Gas-Poor Galaxies

While extremely low, sub-solar, Fe abundances can be statistically rejected in X-ray bright elliptical galaxies (with the best fit Fe abundance close to solar or even super-solar), the measured abundances in X-ray faint, gas-poor, galaxies are still controversial. Very low abundances ($Z_{Fe} < 0.1\ Z_\odot$) are reported from the XMM-Newton data analysis of X-ray faint early type galaxies, for example NGC 3585, NGC 4494, and NGC 5322 by O'Sullivan and Ponman (2004a). Similar low (sub-solar) metal abundances (but with a large uncertainty) were also reported from the analysis of the Chandra data of NGC 4697 (Sarazin et al. 2001), NGC 1553 (Blanton et al. 2001), NGC 1291 (Irwin et al. 2002), NGC 4365 and NGC 4382 (Sivakoff et al. 2003), and NGC 4555 (O'Sullivan and Ponman 2004b).

Is this because the gas metallicity is really lower in gas-poor galaxies than in gas-rich galaxies? Given that the ISM in gas-poor and gas-rich galaxies will be in different dynamical states, outflow/wind vs. inflow (e.g., Ciotti et al. 1991; Loewenstein and Mathews 1991; see also Pellegrini in this book), the metallicity

may be also different. However, it is expected that the ISM metallicity is at least as high as the stellar metallicity. We refer to Pipino (in this book) for possible solutions of this issue. In particular, the incomplete mixing of the SN Ia ejecta suggested by Tang and Wang (2010) may be more effective in the gas-poor galaxies with the lower density outflow/wind state than the gas-rich (higher density) galaxies. Or is this because we do not see the complexity due to a low s/n ratio of gas-poor galaxies? If so, the problem would be similar to the early results of extremely low metallicity reported in the pre-Chandra missions (Sect. 5.4.1). Due to the model-dependency, the measured metal abundance would be lower with a very small error if the adopted model is too simple. Most XMM-Newton and Chandra observations of the X-ray faint galaxies for typically short exposures of 20–40 ks do not statistically require complex emission models. Once again, the measured abundance is model-dependent, 1T with low-abundances or 2-T with abundances close to solar abundance. For example, Kim and Fabbiano (2003) find metal abundances in NGC 1316 consistent with solar, but with a large uncertainty (0.25–1.3 $Z_\odot$) by applying a 3-component model to the Chandra data. They noted that $Z_{Fe} \sim 0.1 Z_\odot$ if a 1T model was applied. Among the gas-poor galaxies ($L_X < 10^{40.5}$ erg s^{-1}) studies by Humphrey and Buote (2006), the best fit value of Z_{Fe} appears to be sub-solar, but because the error is poorly constrained, Z_{Fe} comparable to those in gas-rich galaxies is always allowed.

It is also important to note that the contribution from ABs and CVs must be properly considered in gas-poor galaxies. As described in Sects. 5.2.1 and 5.3.3.2, the X-ray luminosity from the entire ISM can be even lower than that of the population of ABs and CVs in a number of gas-poor elliptical galaxies. For example, NGC 3585 and NGC 4697 (among those listed above) have a relatively low L_X(gas), comparable to their L_X(ABs+CVs). As shown by Revnivtsev et al. (2007) and Boroson et al. (2011), the spectra of ABs and CVs can be modeled by 2-components: soft (APEC with kT ~0.5 keV) and hard (power-law with a photon index of 1.7). Since the hard component is similar to the LMXB spectrum, even if ignored, it might have been subtracted as a part of the LMXB component with no effect on abundance measurement. However, it is the soft thermal component which affects not only the amount of the ISM, but also the metal abundance, because this additional component must be added in the spectral fitting. Up to now, this has not been done properly.

5.4.3 High Spectral Resolution Grating Observations

The XMM-Newton reflecting grating spectrometer (RGS) provides significantly higher spectral resolution ($E/\Delta E = 100$–500 in FWHM) than that available by CCD imaging spectrographs (e.g., $E/\Delta E = 20$–50 in XMM-Newton MOS). Compare EPIC MOS spectra in Fig. 5.5 and Chandra ACIS spectra in Fig. 5.6 with the RGS spectrum in Fig. 5.10. Given that Chandra transmission grating instruments (LETG and HETG) are not suitable for extended sources, RGS is a unique high resolution

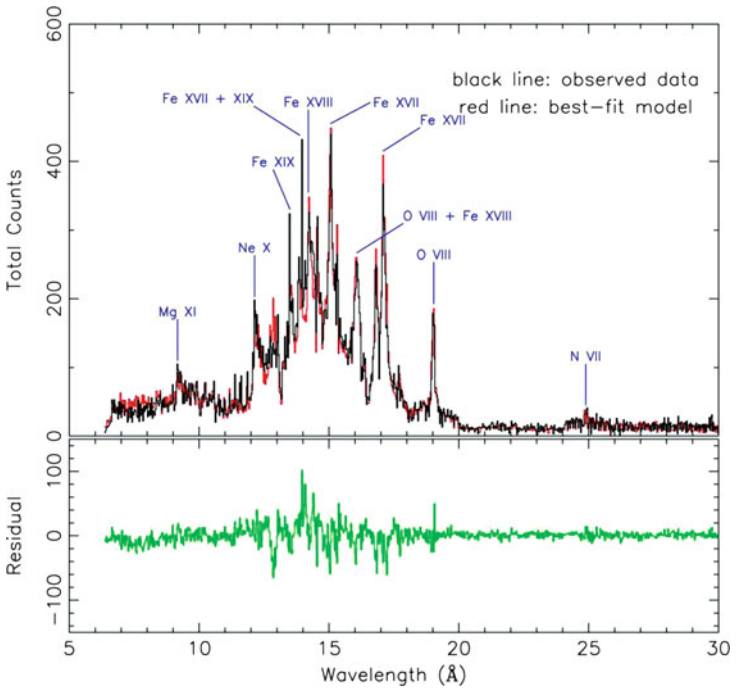

Fig. 5.10 RGS spectrum of NGC 4636 taken from Xu et al. (2002). Both 1st and 2nd order from RGS1 and RGS2 have been added together. Important emission lines from Fe, O, Mg, Ne and N are marked. Reproduced by permission of the AAS, see the electronic version for a color version of this figure

spectrometer which is currently available for X-ray bright galaxies (s/n is too low for X-ray faint galaxies). Analyzing the RGS data of NGC 4636, Xu et al. (2002) showed strong individual lines, such as O VIII, Fe XVII, and Fe XVIII from the hot ISM (Fig. 5.10). See also Ji et al. (2009). Furthermore, Xu et al. (2002) addressed the usefulness of key diagnostic line ratios, such as a temperature-sensitive Fe XVII to Fe XVIII line ratio, which resembles optical line diagnostics often used in the HII region (e.g., Osterbrock and Ferland 2006).

One of the most significant contributions of the RGS data is to confirm the absence of O VII triplet (21–22 Å) in a few gas-rich elliptical galaxies (e.g., NGC 4472 and NGC 4636). Since they must be present in the X-ray spectra from the relatively cool gas (see Table 5.1), this strongly indicates that there is very little contribution from the gas below kT < 0.5 keV. A similar result was also reported in the cluster of galaxies and used to argue against the earlier cooling flow model predictions (e.g., Fabian et al. 2000; Sanders and Fabian 2010).

One may expect that the RGS spectra could provide the definite answer for the metal abundance problem, since individual lines can be resolved. However, the results obtained by analyzing RGS spectra suffer from a number of serious

limitations for an extended source. The main drawback of X-ray grating instruments is that there is no slit to isolate a spatial region of interest when the X-ray emission is extended as in the hot ISM of gas-rich elliptical galaxies (gas-poor galaxies do not provide enough s/n). The field of view of RGS is 1° in the dispersion direction and 5′ in the cross-dispersion direction. Therefore, it is quite a challenge to separate the space and energy both of which disperse X-rays along the dispersion direction. In other words, the line spread function critically depends on the spatial distribution of the X-ray emission, such that even if different emission lines can be separated, they are considerably broadened. To overcome this problem, Xu et al. (2002) performed extensive Monte Carlo simulations by assuming a 3-D β model for the electron density, $n_e \sim [1 + (r/rc)^2]^{-3\beta/2}$ and by allowing the gas temperature to monotonically increase with increasing radius near the center. Ji et al. (2009) assumed a 2-D β model for the azimuthally averaged surface brightness, $[1 + (r/rc)^2]^{-3\beta+1/2}$ and determined the parameters by using corresponding MOS images.

Another challenge in measuring abundances with RGS data is that the continuum level is hard to determine. While this can be a problem in analyzing CCD spectra (see Sect. 5.3), it is more serious with the RGS grating data, because the limited energy range (0.3–2.5 keV) of RGS does not allow for proper measurement of the hard emission from LMXBs and AGN (also possibly from the cosmic background). The contribution from the hard component must be provided independently, e.g., Ji et al. (2009) used MOS/PN data, but source extraction regions are not the same. A less serious, but still important problem in the continuum level is that the background cannot be determined locally in the same detector for most gas-rich galaxies (e.g., Ji et al. applied the template background). Therefore, the absolute abundances measured with the RGS data should be taken with caution. As described in Sect. 5.4.4 below, the relative abundance ratio is less seriously affected by the uncertainty in the continuum level.

5.4.4 Abundance Pattern

In addition to the absolute metallicity, the relative abundance ratio (see Fig. 5.11) is very useful to constrain the metal enrichment history by directly comparing with the chemical evolution models. In particular, the ratio of α-elements to *Fe* has been widely used to measure the relative importance of SN Ia and SN II, because of their different production yields in different timescales. See Nomoto et al. (1997a) and Iwamoto et al. (1999) for SN Ia yields and Woosley and Weaver (1995), Thielemann (1996), Nomoto et al. (1997b, 2006), and Kobayashi et al. (2006) for SN II yields (for more details see Pipino in this book.) In Table 5.3, the SN yields in units of $M_\odot$ (taken from Iwamoto et al. 1999) are listed in column 2 for SN II and in columns 3–4 for two commonly used SN Ia explosion models, slow deflagration (W7) and delayed detonation explosion (WDD1). Also listed in columns 5–7 are individual elements in number relative to Fe from SN II for convenient comparison with observationally measured abundance ratios. The Fe peak elements (e.g., Fe, Ni)

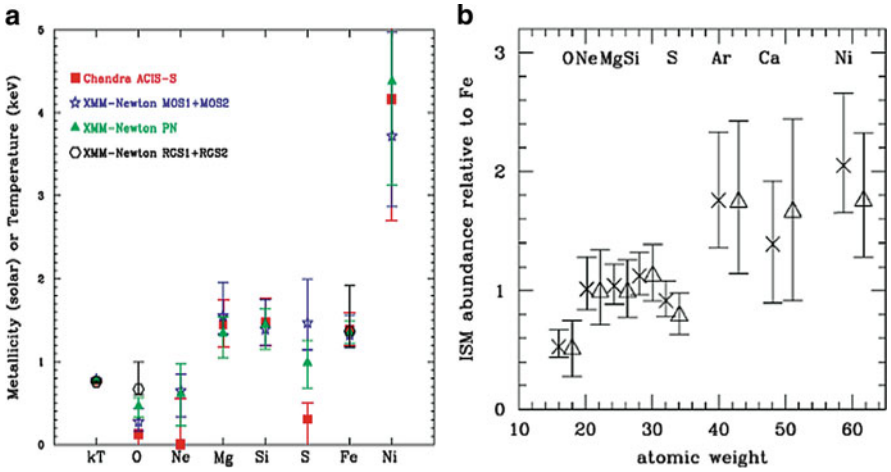

Fig. 5.11 (**a**) Abundances measured with the *XMM-Newton* and the *Chandra* observations of the central region ($r < 1'$) of NGC 4649 (top, taken from Ji et al. 2009). Elements heavier than Ne are modestly super-solar, while the two lighter metals, O and Ne, have abundances about a factor of 2 lower. (**b**) ISM abundance pattern (relative to Fe) in the inner (0–4′; *crosses*) and outer region (4′–8′; *triangles*) of NGC 4472, determined with Suzaku observations (Taken from Loewenstein and Davis 2010). Reproduced by permission of the AAS, see the electronic version for a color version of this figure

Table 5.3 SN yields

	In mass ($M_\odot$)			In relative number		
	SN II	SN Ia		SN II	SN Ia	
	10–50 $M_\odot$	W7	WDD1	10–50 $M_\odot$	W7	WDD1
O	1.80	1.43E-01	8.82E-02	69.521	5.511	3.399
Ne	2.31E-01	4.52E-03	1.45E-03	7.080	0.132	0.044
Mg	1.23E-01	8.57E-03	7.69E-03	3.100	0.220	0.197
Si	1.22E-01	1.57E-01	2.74E-01	2.669	3.445	6.022
S	4.12E-02	8.70E-02	1.63E-01	0.791	1.674	3.138
Ar	7.99E-03	1.57E-02	3.23E-02	0.136	0.267	0.553
Ca	5.87E-03	1.19E-02	3.10E-02	0.090	0.184	0.479
Fe	9.07E-02	7.49E-01	6.72E-01	1	8.280	7.422
Ni	5.97E-03	1.26E-01	3.81E-02	0.062	1.330	0.403

are mostly produced from SN Ia. Some α-elements (O, Ne, Mg) are predominantly produced from SN II and other α-elements (Si, S) are produced by both types in comparable proportions. Kobayashi et al. (2006) also considered hypernovae (HNe) which have significantly higher explosion energies than normal SNe II and have different yields for some heavy elements (e.g., Zn, Co, Mn). However, adding HNe to nomal SNe II does not significantly affect the abundance of those elements of interest (relative to Fe) listed in Table 5.3 (see also Nomoto et al. 2006).

It is important to note that the SN II yields significantly vary among different studies and that the uncertainties are not fully understood, e.g., the effect of mass loss and rotation in initially massive stars (see Gibson et al. 1997; Romano et al. 2010). The SN II yields can also vary, depending on the adopted IMF and progenitor pre-enrichment levels. For more details, see the above references. For SN Ia yields, the two SN Ia models predict quite different yields in most elements, except Fe. The differences for O, Ne and Mg are not important, because they are primarily produced in SNe II. Most notable are (1) the delayed detonation model produces higher yields for Si, S, Ar and Ca by a factor of ∼2 (see Sect. 5.4.5) and (2) the deflagration model produces higher yields for Ni by a factor of ∼3 (see 4.4.5). It seems that different observational data exclusively support the deflagration or delayed detonation model (Sects. 5.4.4.5 and 5.4.4.7). Among the delayed detonation models, WDD1, WDD2 and WDD3 in order of increasing density at DDT (deflagration to detonation transition) produce progressively less Si and S, but more Fe and Ni (see Iwamoto et al. 1999). In this chapter, we use two representative modes, W7 and WDD1.

Following the solar standard in Table 5.2, we convert the SN yields to abundance ratios relative to Fe in solar units in Table 5.4. They provide the abundance ratios when only one type of SNe dominates. We list the abundance pattern under three solar standards so that the reported results measured with different solar standards can be compared. In Table 5.5, we list an example set of the ISM abundance pattern in solar units, when individual elements from the SN Ia and SN II ejecta are linearly combined, assuming the number ratio of two types of SNe, N(SN Ia)/N(SN II) = 1/3. This ratio is selected to reproduce the solar Si/Fe abundance ratio, if we take the ASPL standard and the W7 SN II model. As described in Sect. 5.4.2 (and Sect. 5.4.4.1 below), the Si/Fe ratio is close to solar in typical giant gas-rich elliptical galaxies.

The real ISM abundance pattern may be more complex than expressed by the linear combination of two sets of SN yields due to mass loss from evolved stars with non-solar (α-element enhanced) abundances and various metal transport mechanisms throughout the ISM evolution which could add, remove and/or mix various chemical elements in different scales in different locations, e.g., by

Table 5.4 Abundance ratio (X/Fe) in solar units

	II only			Ia only					
	ANGR	GRSA	ASPL	ANGR		GRSA		ASPL	
				W7	WDD1	W7	WDD1	W7	WDD1
O	3.82	3.25	4.48	0.04	0.03	0.03	0.02	0.04	0.03
Ne	2.69	1.86	2.63	0.006	0.002	0.004	0.002	0.006	0.002
Mg	3.82	2.58	2.46	0.03	0.03	0.02	0.02	0.02	0.02
Si	3.52	2.52	2.60	0.55	1.07	0.39	0.77	0.41	0.79
S	2.29	1.17	1.89	0.58	1.22	0.30	0.62	0.48	1.01
Ar	1.74	1.72	1.72	0.41	0.96	0.41	0.94	0.41	0.94
Ca	1.84	1.25	1.30	0.45	1.32	0.31	0.90	0.32	0.94
Ni	1.63	1.11	1.17	4.23	1.43	2.87	0.97	3.03	1.02

Table 5.5 Abundance ratio (X/Fe) in solar units in case N(SNe Ia)/N(SNe II) = 1/3 by number

	ANGR		GRSA		ASPL	
	W7	WDD1	W7	WDD1	W7	WDD1
O	1.06	1.14	0.90	0.97	1.24	1.33
Ne	0.73	0.79	0.51	0.55	0.72	0.77
Mg	1.06	1.14	0.71	0.77	0.68	0.74
Si	1.35	1.79	0.97	1.28	1.00	1.32
S	1.04	1.53	0.53	0.78	0.86	1.27
Ar	0.77	1.19	0.76	1.17	0.76	1.17
Ca	0.83	1.47	0.56	1.00	0.59	1.04
Ni	3.53	1.49	2.39	1.01	2.53	1.07

partial/full winds, AGN-driven buoyant bubbles, infall (dilution by ICM), mergers, ram-pressure stripping, tidal stripping, metal depletion (in different degrees for different elements) etc. Nevertheless, all elements which we are discussing in this chapter had been formed in SNe, regardless of how they were recycled. Therefore, to the first approximation, Tables 5.4 and 5.5 provide a useful guideline to compare and interpret the observed abundance pattern. We refer readers to Pipino (in this book) for more complex mixing of elements, depending on galaxy evolution models.

It is also important to note that while the absolute abundance is seriously affected by the uncertainty of the continuum level, the relative abundance (or abundance ratio of two elements) is less affected by this problem. This can be understood by a correlation between errors in individual elements. In other words, the 2D confidence contours of two interesting parameters (e.g., Fe and Si) are often elongated diagonally. Because the abundance is determined by the line to continuum ratio, the uncertainties in the continuum level will affect both elements in the same manner, i.e., if one element is over-estimated, the other element is also overestimated and vice versa. The continuum may be affected by incorrect absorption (Sect. 5.3.2), incorrect subtraction of non-gas X-ray emission, such as LMXBs, ABs, CVs, AGNs and background (see Sect. 5.3.3), tying elements at incorrect solar ratios (Sect. 5.3.6), and helium sedimentation (3.10). Partly because of this, even if the absolute abundance is different in different studies, the relative abundance may be still consistent (e.g., compare Fig. 5.11a, b). Also the Si to Fe ratio is close to solar even if the absolute abundance is quite low in the early report (Sect. 5.4.1; also see Fig. 5.6a in Sect. 5.3.6).

Given that the measurement of elements other than Fe requires high s/n spectra, the abundance pattern is not easily measured in gas-poor elliptical galaxies. Therefore, the following results and related discussions are mainly for gas-rich galaxies.

5.4.4.1 Silicon

Among α-elements, Si is most useful and best measured, because of its strong, isolated emission features. The theoretical yield of Si is also the best determined,

with the least amount of scatter between model predictions (e.g., Gibson et al. 1997; Nagataki and Sato 1998). As shown in Table 5.4, it is expected that the Si/Fe abundance ratio is ∼2.5 solar, if heavy elements were mainly synthesized in SN II.

For example, significantly enhanced alpha to Fe ratios are seen in metal poor Galactic halo stars and local group dwarf galaxies with low Fe/H ratios which basically represent pure SN II products (e.g., see Pagel 2009). This ratio would decrease with increasing contributions from SN Ia. If the SN Ia contributed most of the hot ISM metals, the Si/Fe abundance ratio would be ∼0.5 solar (for W7). Typical giant elliptical galaxies have Si/Fe close to solar (see Fig. 5.11). Examples are NGC 1399 (Buote 2002), NGC 5044 (Buote et al. 2003), NGC 507 (Kim and Fabbiano 2004), NGC 7619 (Kim et al. 2008) and NGC 4472 (Loewenstein and Davis 2010). More examples can be found in the Chandra and XMM-Newton archival studies by Humphrey and Buote (2006) and Ji et al. (2009). The solar Si/Fe ratio indicates that the ejecta from both SNe II (from early star formation) and SNe Ia (continuously added later) are well mixed in these elliptical galaxies. With SN yields in Table 5.3, the measured solar abundance ratio of Si to Fe indicates that ∼70% of the detected iron mass was produced by SN Ia.

In contrast with the typical old elliptical galaxies, α-elements are significantly enriched in the ISM of merging galaxies where new stars are actively forming (e.g., in the Antennae, Fabbiano et al. 2004; Baldi et al. 2006). Kim (2010) found a signature of enhanced Si relative to Fe (i.e., super-solar Si/Fe ratio) in two young elliptical galaxies, NGC 720 and NGC 3923 by using deep Chandra observations and isolating the X-ray emission from the central 30". Figure 5.6 shows the relatively strong Si feature (at E ∼ 2 keV) from the central region of NGC 720 which can be compared with Fig. 5.5 for a typical case of the solar Si/Fe ratio (the 2 keV Si emission feature is less strong). This may indicate that the enhanced α-elements in young elliptical galaxies reflect the second generation star formation and additional SN II associated with recent major/minor mergers. However, other studies for the same galaxies, but with spectra extracted from a larger spatial region with XMM-Newton and Suzaku observations do not show this trend of enhanced α-elements (Ji et al. 2009; Tawara et al. 2008). Due to the low spatial resolution of XMM-Newton and Suzaku observations, multi-phase gas may be mixed in their spectra. This age effect needs to be confirmed with deep Chandra observations with a bigger sample of young elliptical galaxies.

5.4.4.2 Oxygen

The low O abundance (sub-solar O abundance as well as sub-solar O/Fe and O/Mg ratios) is unequivocally reported. The O to Fe ratio is ∼ 0.3 solar in NGC 5044, (Buote et al. 2003; David et al. 2010), 0.3–0.5 solar in NGC 507 (Kim and Fabbiano 2004) while the Mg to Fe ratio is only slightly lower than solar (0.8–0.9 solar) in both galaxies. Recent studies with the Chandra and XMM-Newton archival data by Humphrey and Buote (2006) and Ji et al. (2009) and with Suzaku data of NGC 4472 by Loewenstein and Davis (2010) also show the same trend: the O/Fe

ratio is ∼0.5 solar, while the Mg/Fe ratio is close to solar, resulting in the O/Mg ratio ∼0.5 solar (see Fig. 5.11). The above observed ratios were based on GRSA, except Humphrey and Buote (2006) who adopted an older version of ASPL. Both ratios would be higher by a factor of 1.4 when converted from GRSA to ASPL due to the lower O abundance in ASPL (see Table 5.2).

With a simple combination of SN II and SN Ia, for example, if the Si/Fe ratio is close to solar (Table 5.5), the O/Fe ratio would be 0.9–1.3 solar depending on the solar standard. Since both O and Mg are mainly produced by SN II, the O/Mg ratio does not depend on the SN Ia rate. Based on the SN II yield alone, the O/Mg ratio should be close to solar in ANGR and GRSA, or super-solar (1.8 solar) in ASPL, regardless of the Si/Fe ratio. Therefore, the observed ratios of O/Fe and O/Mg are clearly inconsistent with those expected from the SN yields. Possible explanations for this unexpected low O abundance include a warm absorber (Buote et al. 2003), Population III hypernovae (Humphrey and Buote 2006) and incorrect standard core collapse nucleosynthesis models which simply overproduce O by ∼2 (Ji et al. 2009; Loewenstein and Davis 2010).

The O abundance is also measured in the warm (∼10000 K) ionized gas by measuring the line ratios of O II and O III emission lines to H Balmer lines (Athey and Bregman 2009; Annibali et al. 2010). In general, early type galaxies contain only a small amount of the warm ISM (e.g., Kim 1989; Sarzi et al. 2007), if any, and those emission line galaxies are mostly LINERs. Using a small sample (mainly consisting of LINERs), Athey and Bregman (2009) and Annibali et al. (2010) reported that the O abundance in the warm ISM is close to or slightly lower than solar. Annibali et al. (2010) further reported that the gas O abundance is lower (by 0.2 dex) than that of stars and suggested the possibility of the incorrect O yield from SN II. However, note that the O abundance in the warm ISM depends on the ionization mechanism which is not fully understood yet for LINERs.

5.4.4.3 Neon

Similar to O and Mg, Ne is also primarily produced by SN II (Table 5.3) and the Ne to Mg ratio is expected to be close to solar, 0.7 solar in ANGR and GRSA, and 1.1 solar in ASPL (Tables 5.4 and 5.5). The reported Ne/Mg ratios vary from one galaxy to another. It is about a half solar in NGC 4649 and NGC 5044 (Ji et al. 2009), while close to solar in NGC 4636 (Xu et al. 2002; Ji et al. 2009) and NGC 4472 (Loewenstein and Davis 2010). See the contrast in Fig. 5.11a, b. Given the associated uncertainties, the Ne/Mg ratio may still be close to solar.

5.4.4.4 Magnesium

As described above, Mg is primarily produced by SN II (Table 5.3). The observed Mg to Fe ratio is close to solar in most galaxies (see Fig. 5.11). For example, the Mg/Fe ratios measured in 20 galaxies by Humphrey and Buote (2006) are all

consistent with solar. Combining SN II and SN Ia yields in Table 5.5, the Mg/Fe ratio would be 0.7–1.1 solar depending on the solar standard.

5.4.4.5 Nickel

The Ni/Fe ratio may be super-solar (1.5–3 solar) in NGC 1399, 4472, 4649 and 5044 (Ji et al. 2009; Loewenstein and Davis 2010). A similarly high Ni/Fe ratio is also found in the gas-rich galaxies by Humphrey and Buote (2006). Because both Ni and Fe are primarily produced in SN Ia (Table 5.3), the Ni/Fe ratio is useful to constrain the SN Ia model. In particular, the two SN Ia explosion models (deflagration and delayed detonation explosion) predict quite different Ni/Fe ratios. In the former model the Ni/Fe ratio ∼3 solar, while in the latter model the Ni/Fe ratio ∼1 solar (see Tables 5.4 and 5.5). The measured super solar Ni/Fe ratio seems to prefer the W7 model rather than WDD1 (see also Dupke and White 2000).

5.4.4.6 Other Elements (Sulfur, Argon, Calcium)

In term of SN yields, S, Ar and Ca are more or less similar to Si. The yields of the SN Ia deflagration model (W7 in Table 5.3) are higher by a factor of ∼2 than those of SNe II and the yields of the delayed detonation model (WDD1 in Table 5.2) are higher by another factor of ∼2 than the deflagration model. Taking the number ratio of two types of SNe, N(SN Ia)/N(SN II) = 1/3 (in Table 5.5), they are produced by both types of SNe in similar proportions. As expected, the S abundance measured in a few gas-rich galaxies with relatively hotter gas is more or less similar to the Si abundance, i.e., S/Fe ∼ solar (Fig. 5.11; see also Humphrey and Buote 2006; Ji et al. 2009). However, its error is large because the S emission lines are at higher energies and their peak temperature (1.5–2 keV in Table 5.1) is higher than the typical ISM temperature. Also note that the S lines are not observed by the RGS.

Ar and Ca are harder to measure, because they originate from even higher temperature gas (peak temperature = 2–4 keV in Table 5.1). Analyzing Suzaku X-ray spectra of NGC 4472 (Fig. 5.11b), Loewenstein and Davis (2010) found that the Ar and Ca abundances are similar (and super-solar), but with a large error. It is interesting to note that analyzing XMM-Newton data of a sample of 22 clusters of galaxies where Ar and Ca can be measured more reliably, de Plaa et al. (2007) found sub-solar Ar/Ca ratios in the central region ($0.2 \times R_{500} = 200$–400 kpc). They further discussed the quality of type Ia models and proposed a modified delayed detonation model based on Tycho SNR.

5.4.4.7 Comparison with Models

While the observed abundance pattern of the ISM and ICM has been extensively compared with model predictions, there is no simple combination of SNe yields

which can reproduce the observation abundance pattern (e.g., Gibson et al. 1997, 2007; Nagataki and Sato 1998; Pipino et al. 2005; for more discussions see also Pipino in this book). Loewenstein and Davis (2010) further compared the observed elemental abundance pattern with those predicted by simple chemical evolution models. In NGC 4472 (see Fig. 5.11b), they found that the best-fit temperatures in a 2-T model are 0.8 keV and 1.4 keV in $r < 2.5'$ and increase with increasing galactocentric distance (1 keV and 1.6 keV at $r = 5'$). As discussed in Sect. 5.4.2.1, the two temperatures are similar to those of NGC 507 and NGC 1399. The two phases likely represent the stellar system (the cooler one) and the group/cluster potential (the hotter one). It is likely that two phases of the ISM have different absolute and relative abundances. However, it is difficult to model two sets of abundance patterns, because they are not easily separated. They attempted to reproduce the observed abundance patterns with α-element enhanced stellar mass loss and a reduced SN Ia rate (by a factor of 4–6). Most elements could be reproduced, but still failed to match the entire observed pattern; for example, Ca and Ar (under-predicted) and O (over-predicted). With WDD1 yields (delayed detonation) instead of standard W7 yields, the observed pattern of Ca and Ar can be reproduced, but then S and Ni are over-predicted and under-predicted, respectively.

5.4.5 Spatial Variation of Metal Abundances

The radial profiles of elemental abundances and abundance ratios have direct implications on metal enrichment history by two types of SNe and metal transport mechanisms, e.g., by SN-driven global/partial winds and AGN-driven buoyant bubbles. Consequently, the radial abundance profiles have been extensively studied for clusters of galaxies (e.g., Mushotzky et al. 1978; Finoguenov et al. 2002; Tamura et al. 2004; Simionescu et al. 2009; see also a recent review by Bohringer and Werner 2010). However, this study in elliptical galaxies is limited only to gas-rich, cD type group dominant galaxies listed in Sect. 5.4.2.1, and the measurement error is still large at large radii due to the limited statistics.

As described in Sect. 5.4.2 (e.g., Fig. 5.8a), the Fe abundance generally decreases with increasing galacto-centric distance in gas-rich elliptical galaxies, e.g., NGC 507 (Kim and Fabbiano 2004) and NGC 1399 (Buote 2002). See also Buote (2000) for earlier ROSAT results. When azimuthally averaged, the Fe abundance is super-solar at the center and sub-solar (0.3–0.5 solar) at the outskirts. The latter is generally consistent with the typical ICM metal abundance (e.g., Mushotzky et al. 1978, 1996; Edge and Stewart 1991). Rasmussen and Ponman (2007) found a similar abundance gradient in a sample of galaxy groups. Johnson et al. (2009) also found a radial gradient in a gas-rich Virgo elliptical galaxy, NGC 4636. They further pointed out the effect of the abundance gradient on the mass measurement, because allowing the abundance gradient would result in a flat density profile and potentially reduce the gravitational mass.

While the Fe and Si abundances show radial variations, the Si to Fe abundance ratio appears to be constant, although a mild radial gradient, either positive or negative, cannot be ruled out due to the error at large radii (e.g., Fig. 5.8b). This roughly uniform Si/Fe ratio suggests that SN II and SN Ia ejecta are well mixed on a larger scale (∼100 kpc) than the optical galaxy (∼40 kpc). A similarly flat radial profile of the Si/Fe ratio has been found even in a larger scale (∼500 kpc) in galaxy clusters (e.g., Finoguenov et al. 2002; Tamura et al. 2004).

In contrast to Fe and Si, O is more or less uniformly distributed over the ICM, i.e., the O/Fe ratio has a positive radial gradient (e.g., Tamura et al. 2004). Although it is less clear in the ISM, because of a large error at the large radii (e.g., Buote et al. 2003; Kim and Fabbiano 2004; David et al. 2010), the under-abundant O (i.e., sub-solar O/Fe and O/Mg ratios) near the center of gas-rich elliptical galaxies (Sect. 5.4.4.2) is consistent with being flatter than Fe as in galaxy clusters.

As explained in Sect. 5.4.4, while Fe and O are exclusively produced by SN Ia and SN II respectively, Si is produced by both types of SNe. Through the early star formation episode in elliptical galaxies, the ISM would be primarily enriched by SN II and then ejected from host galaxies by SN-driven galactic winds. The SN II ejecta (e.g., O) would be distributed to large radii from the galaxy center and/or accumulated in the ICM. After the early star formation ended, the ISM in the passively evolving elliptical galaxies would be enriched by SN Ia ejecta, e.g., Fe which would be centrally peaked with a negative radial gradient. In this simple picture, the radial profile of Si (produced by both types of SNe) is expected to be flatter than that of Fe, but steeper than that of O. The Si/Fe ratio would increase with increasing distance up to ∼2 solar (close to the ratio given by SN II – Table 5.4) at large radii (e.g., Mushotzky et al. 1996). However, the observed radial profiles do not fit this simple picture. The flat Si/Fe profile may suggest the diversity of SNe Ia, i.e., both deflagration (producing lower Si yields, dominating earlier) and delayed detonation (producing higher Si yield, dominating later) scenarios are required (Finoguenov et al. 2002). Studying 6 clusters of galaxies, Simionescu et al. (2009) found that O is also centrally peaked, although less steep than Fe (still a positive O/Fe gradient), suggesting that the initial enrichment by SNe II in the early phase is not well mixed on large scales as previously thought.

It has been reported that while the metallicity decreases with increasing radius in a large scale, there may be a metallicity deficit in the very center of gas-rich galaxies (mostly cD-type galaxies). If real, this seems to be in contrast to what we expect by the metal enrichment from stellar ejecta. Examples are M87 (Gastaldello and Molendi 2002), the core of the Centaurus cluster (Sanders and Fabian 2002), NGC 5044 (Buote et al. 2003b) and a sample of galaxy groups (Rasmussen and Ponman 2007). Furthermore, using 3-D hydrodynamic simulations of hot gas in an intermediate mass galaxy, Tang and Wang (2010) showed that the positive metallicity gradient at the very center may be a natural consequence of a high outward velocity of hot SN ejecta due to the large buoyancy. If real, the resonance scattering (Sect. 5.3.7), the He sedimentation (Sect. 5.3.8), and the AGN feedback may also play a role. However, given that the central region is the most complex in thermal and chemical structures of the multi-phase hot ISM, this observational result may be caused by incorrect analysis, interpretation, and/or modeling. For example,

Buote et al. (2003b) showed that the abundance dip in the center of NGC 5044 disappeared when the abundances in each component of a 2T model are allowed to vary independently. With deep Chandra observations of the same galaxy, NGC 5044, David et al. (2010) showed that while the Fe abundance dip appears at the center ($r < 10$ kpc) if all elements are tied to Fe, it disappears if O is allowed to vary independently of Fe.

5.5 Summary

The morphological and thermal structures of the hot ISM in gas-rich elliptical galaxies are quite complex as seen in a few ultra deep Chandra observations (e.g., M87, NGC 5044). The hot ISM consists of multi-phases with various sub-structures related to AGN activities and interactions with the ambient medium. Consequently, the chemical structure of the hot ISM is also complex, when measured with spatially resolved spectroscopy, using a high spatial-resolution spectroscopic data.

In the gas-rich (cD and non-cD) galaxies, the Fe abundance is close to solar, or slightly super-solar in the central region. The early controversial report of the extremely sub-solar Fe abundance is now statistically excluded. The Si/Fe ratio is close to solar in typical giant old galaxies, as expected from a mixture of SN Ia and SN II ejecta. While the Mg/Fe ratio is close to solar, the O/Fe ratio is sub-solar, resulting in a sub-solar O/Mg ratio. Since both O and Mg are produced by SNe II, the observed O/Mg ratio is lower than expected. The solution of this problem is still unknown. Ni/Fe may be super-solar, favoring the deflagration model for SN Ia (however, other observational results prefer the delayed detonation model or mixture of both models). The entire abundance pattern is not reproduced by a simple combination of two SNe yields, or by a simple model with mass loss from stars with non-solar (α-element enhanced) abundances.

While gas-poor elliptical galaxies are more common than gas-rich elliptical galaxies, low s/n spectra result in large uncertainties in the ISM metal abundances in these galaxies, Consequently, the results are still controversial and the Fe abundance could be either sub-solar or close to solar. While the Fe abundance is expected to be close to solar as in gas-rich galaxies (at least similar to the stellar metallicity), the current observational data cannot fully reject the lower Fe abundance. The future generation of X-ray missions with high spatial and spectral resolution, e.g., Chandra spatial resolution combined with calorimeter spectral resolution, is critically required for the most accurate measurement of the metal abundances in the hot ISM in elliptical galaxies.

References

E. Anders, N. Grevesse, Geochimica et Cosmochimica Acta **53**, 197 (1989)
F. Annibali et al. 2010, A&A, **519**, A40
N. Arimoto et al., ApJ **477**, 128 (1997)

M. Arnaud, S. Majerowicz, D. Lumb et al., A&A **390**, 27 (2002)
M. Asplund, N. Grevesse, A.J. Sauval, P. Scott, ARA&A **47**, 481 (2009)
A.E. Athey, J.B. Bregman, ApJ **696**, 681 (2009)
H. Awaki et al., PASJ **46**, L65 (1994)
A. Baldi et al., ApJ **636**, 158 (2006)
A. Baldi et al., ApJ **707**, 1034 (2009)
M. Balucinska-Church, D. McCammon, ApJ **400**, 699 (1992)
B.A. Biller, C. Jones, W.R. Forman, R. Kraft, T. Ensslin, ApJ **613**, 238 (2004)
E.L. Blanton, C.L. Sarazin, J.A. Irwin, ApJ **552**, 106 (2001)
H. Bohringer, N. Werner, A&A Rev. **18**, 127 (2010)
B. Boroson, D.W. Kim, G. Fabbiano, 2011, ApJ, **729**, 12
D.A. Buote, C.R. Canizares, ApJ **427**, 86 (1994)
D.A. Buote, A.C. Fabian, MN **296**, 977 (1998)
D.A. Buote, ApJ **539**, 172 (2000)
D.A. Buote, ApJ **574**, L135 (2002)
D.A. Buote, A.D. Lewis, F. Brighenti, W.G. Mathews, ApJ **595**, 151 (2003a)
D.A. Buote, A.D. Lewis, F. Brighenti, W.G. Mathews, ApJ **594**, 741 (2003b)
A. Cardullo et al., A&A (2009)
Cash, ApJ **228**, 939 (1979)
P.A. Charles, F.D. Seward, *Exploring the X-ray Universe* (Cambridge University Press, Cambridge, 1995)
L. Ciotti, S. Pellegrini, A. Renzini, A. D'Ercole, ApJ **376**, 380 (1991)
L. Ciotti, S. Pellegrini, MNRAS **387**, 902 (2008)
L. David, C. Jones, W. Forman, P. Nulsen, J. Vrtilek, E. O'Sullivan, S. Giacintucci, S. Raychaudhury, ApJ **705**, 624 (2009)
L.P. David et al., 2011, ApJ, **728**, 162
D.S. Davis, R.E. White, ApJ **470**, L35 (1996)
J. de Plaa et al., A&A **465**, 345 (2007)
S. Diehl, T.S. Statler, ApJ **668**, 150 (2007)
S. Diehl, T.S. Statler, ApJ **687**, 986 (2008a)
S. Diehl, T.S. Statler, ApJ **680**, 897 (2008b)
R.A. Dupke, R.E. White III, ApJ **528**, 139 (2000)
A.C. Edge, G.C. Stewart, MNRAS **252**, 414 (1991)
S.C. Ellis, E. O'Sullivan, MNRAS **367**, 627 (2006)
S. Ettori & A.C. Fabian, MNRAS **369**, L42 (2006)
P. Eskridge, G. Fabbiano, D.W. Kim, ApJS **97**, 141 (1995)
G. Fabbiano, ARA&A **27**, 87 (1989)
Fabbiano et al., ApJ **605**, L21 (2004)
G. Fabbiano, D.W. Kim, G. Trinchieri, ApJ **429**, 94 (1994)
A.C. Fabian, J.E. Pringle, MNRAS **181**, 5 (1977)
A.C. Fabian et al., MNRAS **318**, L65 (2000)
A. Finoguenov, A. Matsushita, H. Bohringer, Y. Ikebe, M. Arnaud, A&A **381**, 21 (2002)
A. Finoguenov et al., ApJ **686**, 911 (2008)
F. Gastaldello, S. Molendi, ApJ **572**, 160 (2002)
N. Gehrels, ApJ **303**, 336 (1986)
B.K. Gibson, M. Loewenstein, R.F. Mushotzky, MN **290**, 623 (1997)
B.K. Gibson, P. S'anchez-Bl'azquez, , S. Courty, D. Kawata, in *Chemodynamics: From First Stars to Local Galaxies*, ed. by E. Emsellem et al. EAS Publications Series, vol. 24, p. 133 (also in astro-ph/061108, 2007)
M.R. Gilfanov, R.A. Syunyaev, Soviet Astron. Lett. **10**, 137 (1984)
O. Gonzalez-Martin et al., A&A **506**, 1107 (2009)
N. Grevesse, A.J. Sauval, Space Sci. Rev. **85**, 161 (1998)
M. Gudel, A&A Rev. **12**, 71 (2004)
P.J. Humphrey, D.A. Buote, ApJ **639**, 136 (2006)

P.J. Humphrey et al., ApJ **693**, 822–829 (2009)
J.A. Irwin, C.L. Sarazin, ApJ **471**, 683 (1996)
J.A. Irwin, C.L. Sarazin, J.N. Bregman, ApJ **570**, 152 (2002)
J.A. Irwin, A.E. Athey, J.N. Bregman, ApJ **587**, 356 (2003)
K. Iwamoto et al., ApJS **125**, 439–462 (1999)
J. Ji et al., 2009, ApJ **696** 2252
R. Johnson, D. Chakrabarty, E. O'Sullivan, S. Raychaudhury, ApJ **706**, 980 (2009)
J.S. Kaastra, *An X-Ray Spectral Code for Optically Thin Plasmas* (Internal SRON-Leiden Report, updated version 2.0) (1992)
D.W. Kim, ApJ **346**, 653 (1989)
D.W. Kim, Highlights Astron. **15**, 285 (2010)
D.W. Kim, G. Fabbiano, G. Trinchieri, ApJ **393**, 134 (1992)
D.W. Kim, G. Fabbiano, ApJ **441**, 182 (1995)
D.W. Kim, G. Fabbiano, H. Matsumoto, K. Koyama, G. Trinchieri, ApJ **468**, 175 (1996)
D.W. Kim, G. Fabbiano, G. Mackie, ApJ **497**, 699 (1998)
D.W. Kim, G. Fabbiano, ApJ **586**, 826 (2003)
D.W. Kim, G. Fabbiano, ApJ **613**, 93 (2004)
D.W. Kim, E. Kim, G. Fabbiano, G. Trinchieri, ApJ **688**, 931 (2008)
G.R. Knapp, E.L. Turner, P.E. Cunnifee, AJ **90**, 454 (1985)
G.R. Knapp, P. Guhathakurta, D.W. Kim, M. Jura, ApJS **70**, 329 (1989)
C. Kobayashi et al., ApJ **653**, 1145 (2006)
D.A. Liedahl, A.L. Osterheld, W.H. Goldstein, ApJL **438**, 115 (1995)
M. Loewenstein, W.G. Mathews, ApJ **373**, 445 (1991)
M. Loewenstein et al., ApJ **436**, L75 (1994)
M. Loewenstein, D.S. Davis, ApJ **716**, 384 (2010)
M. Machacek, C. Jones, W.R. Forman, P. Nulsen, ApJ **648**, 947 (2006)
H. Matsumoto et al., ApJ **482**, 133 (1997)
K. Matsushita, T. Ohashi, K. Makishima, PASJ **52**, 685 (2000)
R. Mewe, E.H.B.M. Gronenschild, G.H.J. van den Oord, A&AS **62**, 197 (1985)
R. Mewe, J.R. Lemen, G.H.J. van den Oord, A&AS **65**, 511 (1986)
E.T. Million et al., MNRAS **407**, 2046 (2010)
R. Morrison, D. McCammon, ApJ **270**, 119 (1983)
R.F. Mushotzky et al., ApJ **225**, 21 (1978)
R.F. Mushotzky et al., ApJ **436**, L79 (1994)
R.F. Mushotzky et al., ApJ **466**, 686 (1996)
S. Nagataki, K. Sato, ApJ **504**, 629 (1998)
J. Nevalainen L. David, M. Guainazzi, A&A (astro-ph/1008.2102) (2010)
K. Nomoto et al., Nuphy **621**, 467 (1997a)
K. Nomoto et al., Nuphy **616**, 79 (1997b)
K. Nomoto et al., Nuphy, **777**, 424 (2006)
D.E. Osterbrock, G.J. Ferland, *Astrophysics of Gaseous Nebulae and Active Galactic Nuclei* (University Science Books: Mill Valley, CA, 2006)
E. O'Sullivan, D.A. Forbes, T.J. Ponman, MNRAS **328**, 461 (2001)
E. O'Sullivan, T.J. Ponman, MNRAS **349**, 535 (2004a)
E. O'Sullivan, T.J. Ponman, MNRSA **354**, 935 (2004b)
B.E.J. Pagel, *Nucleosynthesis and Chemical Evolution of Galaxies* (Cambridge University Press, Cambridge UK, 2009)
S. Pellegrini, ApJ **717**, 640 (2010)
S. Pellegrini, G. Fabbiano, ApJ **429**, 105 (1994)
F. Peng, D. Nagai, ApJ **705**, L58 (2009)
A. Pipino, D. Kawata, B.K. Gibson, F. Matteucci, A&A **434**, 553 (2005)
P.P. Plucinski et al., in *SPIE Conference Series Vol. 7011: Space Telescopes and Instrumentation II: Ultraviolet to Gamma Ray* (2008)
F.V.N. Rangarajan, MNRAS **277**, 1047 (1995)

S.W. Randall, P. Nulsen, W.R. Forman et al., ApJ **688**, 208 (2008)
S.W. Randall et al., 2011, ApJ, 726, 86
J. Rasmussen, T. Ponman, J. MNRAS **380**, 1554 (2007)
J. Rasmussen, T. Ponman, J. MNRAS **399**, 239 (2009)
M. Revnivtsev, E. Churazov, S. Sazonov, W. Forman, C. Jones, A&A **473**, 783 (2007)
M. Revnivtsev, S. Sazonov, E. Churazov et al., Nature **458**, 1142 (2009)
E. Roediger, M. Bruggen, P. Rebusco, H. Bohringer, E. Churazov, MNRAS **375**, 15 (2007)
D. Romano, A.I. Karakas, M. Tosi, F. Matteucci, A&A, **522**, 32 (2010)
R.M. Sambruna, M. Gliozzi, D. Donato, F. Tavecchio, C.C. Cheung, R.F. Mushotzky, A&A, **414**, 885 (2004)
J.S. Sanders, A.C. Fabian, MNRAS submitted astro-ph/1012.0235 (2010)
C.L. Sarazin, J.A. Irwin, J.N. Bregman, ApJ **556**, 533 (2001)
M. Sarzi et al., NewAR **51**, 18 (2007)
F. Seward, in *Astrophysical Quantities* 4th edn., ed. by Cox. (AIP Press, New York, 2000)
A. Siemiginowska, *X-ray Astronomy Handbook*, ed. by K. Arnaud, R. Smith, A. Siemiginowska (Cambridge University Press, Cambridge, UK, 2011)
A. Simionescu, N. Werner, H. Böhringer, J.S. Kaastra, A. Finoguenov, M. Brüggen, P.E.J. Nulsen, A&A **493**, 409 (2009)
G.R. Sivakoff, C.L. Sarazin, J.A. Irwin, ApJ **599**, 218 (2003)
R.K. Smith, N.S. Brickhouse, D.A. Liedahl, J.C. Raymond, in *Spectroscopic Challenges of Photoionized Plasmas, ASP Conference Series*, ed. by G. Ferland, D.W. Savin, vol. 247 (Astronomical Society of the Pacific, San Francisco, 2001), p. 159
T. Tamura, J.S. Kaastra, J.W.A. den Herder, J.A.M. Bleeker, J.R. Peterson, A&A **420**, 135 (2004)
S. Tang, Q.D. Wang, MNRAS **408**, 1011 (2010)
Y. Tawara et al., PASJ **60**, 307 (2008)
F.K. Thielemann, , ApJ **460**, 408 (1996)
G. Trinchieri, D.W. Kim, G. Fabbiano, C.R. Canizares, ApJ **428**, 555 (1994)
G. Trinchieri, G. Fabbiano, D.W. Kim, A&A **318**, 361 (1997)
M. Tsujimoto et al., 2011, A&A, **525**, 25
N. Werner et al., MNRAS **398**, 23 (2009)
N. Werner et al., MMRAS **40**, 2063 (2010)
R.E. White III, C.L. Sarazin, ApJ **367**, 476 (1991)
J. Wilms, A. Allen, R. McCray, ApJ **542**, 914 (2000)
S.E. Woosley, T.A. Weaver, ApJS **101**, 181 (1995)
H. Xu et al., ApJ **579**, 699 (2002)

Chapter 6
Abundances and Abundance Ratios in Stars and Hot Gas in Elliptical Galaxies

Antonio Pipino

Abstract Elliptical galaxies have well-studied stellar chemical properties by means of colours and absorption lines taken mostly in the optical part of the spectrum; it is natural to consider whether the theoretical interpretation of these observables can simultaneously provide a satisfactory explanation for the properties of their hot gas. X-ray spectra provide unique tools to study these reservoirs of gas in which evidence of the role played by recent SNe Ia activity and mass loss, due to stellar winds, can be found, as opposed to stars, whose chemical abundances mirror those at the time of the formation of the galaxy, 8-10 Gyr earlier. In this Chapter I, first briefly review the galaxy formation process as inferred from the analysis of the optical/chemical properties. I then introduce some basic tools to study the chemical evolution in the stars and in the gas of elliptical galaxies. Finally, I discuss the evolution of the abundances and the abundance ratios in such galactic components.

6.1 A Brief Overview on the Formation of Elliptical Galaxies

Several models for the formation and evolution of galaxies have been put forth in the last three decades. Any model of galaxy evolution presented so far had to overcome the strong challenge represented by the observational fact that elliptical galaxies show a remarkable uniformity in their photometric and chemical properties. The first proposed scenario of elliptical formation was the so-called monolithic collapse (Larson 1974; Matteucci and Tornambé 1987; Arimoto and Yoshii 1987; Chiosi and Carraro 2002). In this framework, ellipticals are assumed to have formed at high redshift as a result of a rapid collapse of a gas cloud. This gas is then rapidly

A. Pipino (✉)
Dip. di Fisica, sez. Astronomia, Universita'di Trieste, via G.B. Tiepolo 11, 34100 Trieste, Italy

ETH Zurich, Wolfgang-Pauli-Str. 27, 8093 Zurich, Switzerland
e-mail: pipino@oats.inaf.it; antonio.pipino@phys.ethz.ch

D.-W. Kim and S. Pellegrini (eds.), *Hot Interstellar Matter in Elliptical Galaxies*,
Astrophysics and Space Science Library 378, DOI 10.1007/978-1-4614-0580-1_6,
© Springer Science+Business Media, LLC 2012

converted into stars by means of a very strong burst, followed by a *galactic wind* powered by the energy injected into the interstellar medium (ISM) by supernovae (SN) and stellar winds. The wind carries out the residual gas from the galaxies, thus inhibiting further star formation. Late time mass loss from stars and Type Ia SN (SN Ia) may then rebuild a hot diffuse medium that we observe in the X-rays.

Indeed, many observations (see Peebles 2002, for a review) suggest that ellipticals could already be in place at $z \sim 2-3$, with their stars formed at high redshift ($z > 3$) in a well synchronized epoch, and then evolved quiescently. For the purposes of our discussion it is important to recall that the high redshift formation of ellipticals is supported by spectroscopic evidence and by the red colours of the stars. Moreover, observations show an increase in the strength of the metal absorption lines (mass-metallicity relation, e.g. Carollo et al. 1993; Gonzalez 1993; Davies et al. 1993; Trager et al. 1998, 2000) and a reddening of the stellar light (color-magnitude relation; Bower et al. 1992) with the velocity dispersion of the galaxies: the most massive ellipticals are also the most metal rich. In particular, the higher the mass of the galaxy, the longer is the chemical enrichment process, the redder are the colors. However, the galactic wind scenario has been revised in the last years, owing to the observed [Mg/Fe][1] ratio in the central parts of ellipticals (e.g. Faber et al. 1992; Worthey et al. 1992). As we will see, an overabundance of Mg relative to Fe is the clear sign that galaxy formation was a rapid and intense process. In addition, the [Mg/Fe] ratio in the cores of ellipticals increases with galactic mass (Worthey et al. 1992; Weiss et al. 1995, Kuntschner 2000; Kuntschner et al. 2001; Graves et al. 2007) indicating, among the possible solutions, that the star formation lasted for a shorter period in the more massive systems (Matteucci 1994).

On the other hand, thanks to the success of the cold dark matter theory in reproducing the large scale structure of the Universe, an alternative picture of galaxy formation based on the Hierarchical Clustering scenario for the formation of dark matter halos was proposed (see Benson 2010, for a recent review). Hierarchical models predict that ellipticals are formed by several merging episodes which trigger star-bursts and regulate the chemical enrichment of the system (White and Rees 1978). In this picture the baryons share the same destiny of their host dark haloes and massive ellipticals form at relatively low redshifts through major mergers between spiral galaxies (e.g. Kauffmann and White 1993; Kauffmann and Charlot 1998). The main process responsible for the formation of elliptical galaxies in the framework of the hierarchical clustering scenario, namely of a major merger involving two spirals at late times (e.g., Kauffmann and White 1993), has been questioned several times (e.g., Ostriker 1980) since its original formulation. Indeed, to reconcile at the same time the anti-hierarchical behavior of Active Galactic Nuclei (AGNs, e.g., Hasinger et al. 2005), the evolution of the luminosity function with redshift (e.g., Bundy

[1] In the following I will use the notation [X/Y]=log(X/Y)−log(X/Y)$_\odot$ to express the relative abundance ratio of any two elements X and Y with respect to that measured in the Sun. In such a notation [X/Y]=0 implies that the X/Y abundance ratio is the same as in the Sun. The reader interested in the details of the solar abundance pattern should refer to Anders and Grevesse (1998), Grevesse and Sauval (1998), Lodders (2003), Asplund et al. (2005). See also Sect. 3.5 in Kim, this book.

et al. 2005), as well as the evidence from the analysis of the stellar populations inhabiting ellipticals, a substantial modification of baryons' behavior, with respect to the behavior of the Dark Matter, seems to be required. In particular, more massive ellipticals must be older and form faster with respect to smaller objects (Thomas et al. 2005), a trend now popular with the term of *downsizing* (Cowie et al. 1996). The latest hierarchical models have been refined in the attempt to account for downsizing. In practice, the mass assembly still occurs at late times, but most of the stars have been formed at high redshift in small subunits. The preferred mechanism for the assembly of massive spheroids is a sequence of dry mergers[2] (e.g., Khochfar and Burkert 2003; De Lucia et al. 2006). However, if we restrict ourselves to the most massive elliptical galaxies ($L > L_*$), they seem to be in place and do not show any signs of significant evolution in mass since $z \sim 1$ (Scarlata et al. 2007). Moreover, despite the emphasis on dry-mergers, models based on the hierarchical picture still do not reproduce the [Mg/Fe]-mass relation in elliptical galaxies.

Peebles (2002) critically reviewed the standing problems and the differences between these two competing scenarios for galaxy formation, pointing out that the best way to explain the whole set of observables within a cosmological framework would require both scenarios to converge. The switching of emphasis on an early star formation as opposed to late time wet mergers in hierarchical models, being an example.

Many theoretical works and simulations which have focused on the hot ISM in elliptical galaxies assumed that the star formation period was an episode occurring in a somewhat distant past, without further details on its nature (i.e. monolithic vs. merger-driven). Namely, for all practical purposes, the stars of the galaxy under study were formed much earlier in time. Following these lines of thought, and considering that it is the best phenomenological model that we have to explain the photo-chemical properties of elliptical galaxies, the framework that I will adopt in the rest of this Chapter will be that of "monolithic" formation. I will discuss the results of chemical evolution model: the most important results can be easily understood if the star formation process occurred in *monolithic* fashion, namely in a limited region of space within a limited time, without losing generality. When this ability to understand the origin and the evolution of the abundance ratios is mastered, it will be easy to understand the consequences of more complicated star formation and assembly histories.

6.2 How to Model Chemical Evolution: Role of SNe Ia vs. SNe II

Before going into the detailed chemical evolution history of a typical elliptical galaxy, it is necessary to understand how to model, in general, galactic chemical evolution. The most important ingredients to build a model of galactic chemical

[2]Here *dry-merger* means a pure dissipationless merger of stellar systems, i.e., without any gas and star formation. The original suggested mechanism for the formation of elliptical galaxies, namely the merger of gas rich disk that induced star formation, is often referred to as *wet mergers*.

evolution that I will review are: i) the stellar birthrate function (the rate at which stars are formed from the gas, and their mass spectrum); ii) the stellar yields and the SN rate (how elements are produced in stars and restored into the interstellar medium). I refer the reader to Matteucci (2001) for a more extended review and historical perspective.

6.2.1 Birthrate Function

The birthrate function, $B(M,t) = \psi(t)\varphi(m)$, is the product of the quantity $\psi(t)$ (the star formation rate – SFR – namely the rate at which the gas is turned into stars), and the quantity $\varphi(m)$ (the initial mass function – IMF – namely the mass distribution of the stars at birth). The most common parameterization of the SFR is the Schmidt (1959) law:

$$\psi(t) = \nu\sigma_{gas}^{k}, \tag{6.1}$$

where k = 1 − 2 and ν is a parameter describing the star formation efficiency. ν has the dimensions of inverse time.

The most common parameterization of the IMF is either a one-slope (Salpeter 1955) or multi-slope (Scalo 1986; Kroupa et al. 1993) power law. The simplest example of a one-slope power law is:

$$\varphi(m) = am^{-(1+x)}, \tag{6.2}$$

generally defined in the mass range of 0.1-100 $M_{\odot}$, where a is the normalization constant derived by imposing that $\int_{0.1}^{100} m\varphi(m)dm = 1$.

For the sake of clarity, all the discussion in this Chapter will assume a Salpeter (1955) IMF with $x = 1.35$, constant in time and space. Such an assumption allows a comparison with previous work and with stellar elemental abundances inferred from observations. However, some other observational studies seem to require a slight modification below $1M_{\odot}$ (e.g., Renzini 2005). For the reader interested in a recent review on the IMF, I refer to Bastian et al. (2010). The smaller x, the higher the fraction of massive stars relative to low mass stars in a given population.

6.2.2 Stellar Yields

As we will see, SN Ia, SN II, and single low-mass stars that died during the active star forming phase of ellipticals, are important in setting the abundance ratios in the stars of ellipticals. The first two channels also provide negative feedback that will eventually halt the star formation. Present-day ellipticals seem to have been passively evolving in the last 8-10 Gyr. Indeed, only SNe Ia explosions are observed. Therefore, as far as the hot X-ray gas around present-day ellipticals is concerned,

it can only be enriched by long-living, hence low-mass, stars (including SNe Ia). Single low-mass stars do not produce the heavy elements that we observe in the hot medium today, they can only "recycle" the chemical species that were locked up at the time of their formation, and I will not discuss them further. SNe Ia, instead, are a continuous source of (mostly) Fe. Here I briefly summarize the main aspects of the nucleosynthesis of massive stars and SNe Ia.

6.2.2.1 Massive Stars

Stars with mass $> 10\ M_{\odot}$ end their life as SNe II and explode by core-collapse; they produce mainly α-elements (O, Ne, Mg, Si, S, Ca), some Fe-peak elements, s-process elements and r-process elements. Their lifetimes are below 30 Myr. Available calculations are from Woosley and Weaver (1995), Thielemann et al. (1996), Meynet and Maeder (2002), Nomoto et al. (1997), among others. As an example, in Fig. 6.1 the average yields by Kobayashi et al. (2006) as a function of the SNe II progenitor metallicity are shown as solid lines. In practice, this figure shows the ratios of the ejecta integrated over the IMF, namely the contribution of the massive stars in a stellar population of a given initial metallicity. The yields are shown in terms of the ratio of the ejected mass with respect to Fe using the Anders and Grevesse (1998) standard. It is worth noting that the ejecta of the α

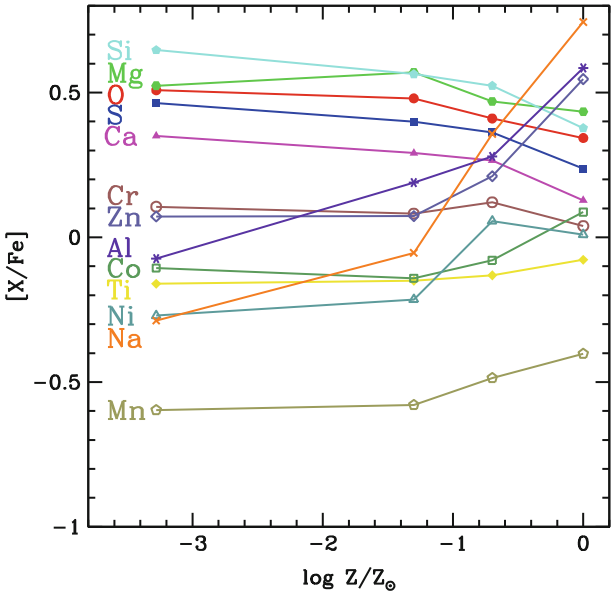

Fig. 6.1 IMF-weighted abundance ratios as a function of the metallicity in solar units (Anders and Grevesse 1998). Figure from Kobayashi et al. (2006). Reproduced by permission of the AAS

elements have a different degree of enhancement with respect to the solar value. The implication of these differences will become clearer from Sect. 3 onward.

6.2.2.2 SNe Ia Progenitors

There is a general consensus about the fact that SNe Ia originate from C-deflagration in C-O white dwarfs (WD) in binary systems, but several evolutionary paths can lead to such an event. The C-deflagration produces $\sim 0.6 - 0.7 M_{\odot}$ of Fe plus traces of other elements from C to Si, as observed in the spectra of SNe Ia. Two main evolutionary scenarios for the progenitors of SNe Ia have been proposed:

Single Degenerate (SD) scenario: the classical scenario of Whelan and Iben (1973), recently revised by Han and Podsiadlowski (2004), namely C-deflagration in a C-O WD reaching the Chandrasekhar mass $M_{Ch} \sim 1.44 M_{\odot}$ after accreting material from a red giant companion. One of the limitations of this scenario is that the accretion rate should be defined in a quite narrow range of values.

The clock to the explosion is given by the lifetime of the secondary star in the binary system, where the WD is the primary (the originally more massive one). The largest mass for a secondary is $8 M_{\odot}$, which is also the maximum mass for the formation of a C-O WD. As a consequence, the minimum timescale for the occurrence of SNe Ia is $\sim$30 Myr (i.e. the lifetime of a $8 M_{\odot}$) after the beginning of star formation. The minimum mass for the secondary is $0.8 M_{\odot}$, which is the star with lifetime equal to the age of the Universe. Stars with masses below this limit are obviously not considered.

Double Degenerate (DD) scenario: the merging of two C-O white dwarfs, due to loss of angular momentum caused by gravitational wave radiation, which explode by C-deflagration when M_{Ch} is reached (Iben and Tutukov 1984). In this scenario, the two C-O WDs should be of $\sim 0.7 M_{\odot}$ in order to give rise to a Chandrasekhar mass after they merge, therefore their progenitors should be in the range 5–8 $M_{\odot}$. The clock to the explosion here is given by the lifetime of the secondary star plus the gravitational time delay which depends on the original separation of the two WDs. The minimum timescale for the appearance of the first SNe Ia in this scenario is one million years more than in the SD scenario (e.g. Greggio 2005, and references therein). At the same time, the maximum gravitational time delay can be as long as a Hubble time.

A way of defining the typical SNe Ia timescale is to assume it as the time when the maximum in the SNe Ia rate is reached (Matteucci and Recchi 2001). *This timescale varies according to the chosen progenitor model and to the assumed star formation history, which varies from galaxy to galaxy.* For the solar vicinity, this timescale is at least 1 Gyr, if the SD scenario is assumed, whereas for elliptical galaxies, where the stars formed much more quickly, this timescale is only 0.5 Gyr (Matteucci and Greggio 1986; Matteucci and Recchi 2001). The normalized SNe Ia rate for a stellar population formed during an instantaneous starburst is defined as the delay time distribution (DTD). The convolution of this DTD with ψ over the galactic volume gives the total SNe Ia rate (see Greggio 2005). Each SNe Ia progenitor

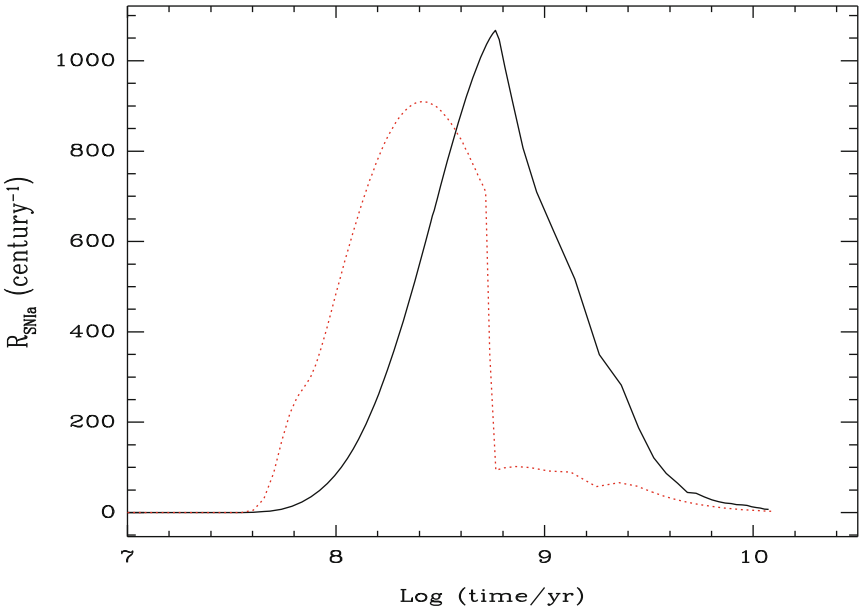

Fig. 6.2 The computed SNe Ia rate in the standard (*solid*) and Mannucci et al. (2006, *dotted*) DTD formulation for a typical elliptical galaxy of $10^{11} M_{\odot}$ of initial luminous mass. From Matteucci et al. (2006), see the electronic version for a color version of this figure

scenario will have its distinctive DTD. I refer the reader to Greggio (2005) and Valiante et al. (2009) for a thorough discussion of the expected SNe Ia rates for differing progenitors and for the specific case in which star formation histories of typical elliptical galaxies are adopted, respectively.

In Fig. 6.2, I show the computed SNe Ia rates for a typical elliptical of $10^{11} M_{\odot}$ of initial luminous mass for both the standard SD and a recent empirical (Mannucci et al. 2006) formulation of the DTD.

From Fig. 6.2 we can infer that the late time (i.e. after a few Gyr) SNe Ia rate can be approximated as a power-law function of time and this is a common assumption when modelling the ISM properties after the major epoch of star formation (see Pellegrini, this book). Here I mention that very recent SNe Ia rate measurements in galaxy clusters at different redshifts seem to favor $R_{SNe\ Ia} \propto t^{-1.1}$ (Maoz et al. 2010), which is in qualitative agreement with the predictions of the standard single degenerate scenario depicted in Fig. 6.2 (solid line). However, such an assumption does not hold true during the star formation period.

While SNe Ia produce mostly Fe, the reader should also note that the mass of O and Mg produced by a single SNe Ia event is not 0 (see Tables 3 and 4 in Kim, this book). Indeed, they should be taken into account when studying the hot ISM (see Sect. 4.2).

6.2.3 The Equation of the Chemical Evolution

Once the yields – as well the stellar lifetimes – are chosen, the IMF fixed, and the star formation efficiency and infall history specified, one can build an equation to follow the evolution of a single chemical species, accounting it being produced by stars in a suitable mass range, over some timescale. One also has to account for the fact that atoms of this element will be incorporated in future generation of stars and released again into the ISM on possibly even longer timescales. The equation of chemical evolution for a single element i takes the following form:

$$\begin{aligned}\frac{dG_i(t)}{dt} &= -\psi(t)X_i(t) + \int_{M_L}^{M_{Bm}} \psi(t-\tau_m)Q_{\rm mi}(t-\tau_m)\varphi(m)dm \\ &+A\int_{M_{Bm}}^{M_{BM}} \varphi(m)\left[\int_{\mu_{\rm min}}^{0.5} f(\mu)Q_{\rm mi}(t-\tau_{\rm m_2})\psi(t-\tau_{\rm m_2})d\mu\right]dm \\ &+(1-A)\int_{\rm M_{Bm}}^{M_{\rm B_M}} \psi(t-\tau_m)Q_{\rm mi}(t-\tau_m)\varphi(m)dm \\ &+\int_{\rm M_{B_M}}^{M_U} \psi(t-\tau_m)Q_{\rm mi}(t-\tau_m)\varphi(m)dm \\ &+\left(\frac{dG_i(t)}{dt}\right)_{\rm infall} - W(t)X_i(t) + \left(\frac{dG_i(t)}{dt}\right)_{\rm acc}, \end{aligned} \tag{6.3}$$

where $G_i(t)$ is the normalized mass density of the element i at the time t in the ISM (see also Matteucci and Greggio 1986; Gibson 1997, and Pipino and Matteucci 2004, and references therein, for a comprehensive discussion of this equation).

The total ISM normalized gas mass density at each time step is then simply $G(t) = \Sigma_i G_i(t)$. The term $-\psi(t)X_i(t)$ gives the rate at which the element i is subtracted from the ISM owing to the star formation process, whereas the integrals in the right-hand side of the equation give the rate at which the element i is restored into the interstellar medium an unprocessed or newly-synthesized element by low- and intermediate-mass stars, and/or SNe Ia and SNe II. Also, I explicitly take into account a possible mass flow due to the galactic wind ($W(t)$) and a possible secondary episode of gas accretion. Equation (6.3) cannot be solved analytically, therefore one needs a suitable computational algorithm that is iterated until convergence is attained. The reader interested in more details on the solution of (6.3) should refer to Talbot and Arnett (1971). A chemical evolution model is hence a code which solves (6.3) for a given set of nucleosynthetic yields and for different galaxy formation histories. These are specified by the infall and outflow terms as well as by the star formation efficiency. Each of these factors might depend on the galaxy (stellar) mass in order to reproduce the observed properties. Such an equation can also be implemented in either dynamical codes or in semi-analytic models. However, here I focus on the formation mechanism of a single galaxy in a

monolithic fashion. Before I fully exploit the power of such formalism, it is useful to remind that, in the so-called Simple Model with the instantaneous recycling approximation (I.R.A.), the chemical evolution equations can be simplified (e.g. Searle and Sargent 1972; Audouze and Tinsley 1976). This approximation allows us to ignore the stellar lifetimes and therefore the delay with which some of the chemical elements are produced and restored into the ISM. In other words, all the elements are produced instantaneously by massive stars, whereas low mass stars (including SNe Ia) never die.

In this case,

$$\frac{X_i}{X_j} = \frac{y_i}{y_j} \tag{6.4}$$

namely, the ratio of two abundances is directly the ratio of the two "yields" per stellar generation:

$$y_i = \frac{1}{(1-R)} \int_{1M_\odot}^{\infty} m p_{im} \varphi(m) dm \tag{6.5}$$

which depends on the IMF $\varphi(m)$ and the stellar yield p_{im}, namely the fraction of the stellar mass ejected as the newly created element i by a star of mass m to the mass locked-up in low mass stars $1 - R$.

6.3 The Abundances and Abundance Ratios in the Stars

6.3.1 The Time-Delay Model

The full solution of the chemical evolution equations allows for the understanding of the behavior of several abundance ratios that is not allowed under the I.R.A.. I take as an example the models developed by Pipino and Matteucci (2004), Pipino et al. (2005) and Pipino et al. (2009a), where the formation of elliptical galaxies is followed in space and time under a version of the monolithic collapse scenario that has been *revised* in order to account for the [Mg/Fe]-mass relation as well as other observed properties like metallicity gradients. In particular I refer to the Pipino and Matteucci (2004) Model II predictions. This model is characterized by an increasing star formation efficiency and decreasing infall timescale with galactic mass in order to reproduce the abundance pattern in the stars as explained in the next sections. The models by Pipino et al. (2005) strictly follow these prescriptions. The main input parameters as well as the times of the wind onset (t_{gw}) and end (t_{stop}) are summarized in Table 6.1. In particular, $R_{\rm eff}$ is the optical effective radius, ν is star formation efficiency that enters (6.1), τ is the timescale of the infall term in (6.3). The SN feedback is parameterized through the efficiencies $\epsilon_{\rm SNe\ II}$ and $\epsilon_{\rm SNe\ Ia}$. For further literature of monolithic formation models the reader should refer to Arimoto and Yoshii (1987), Matteucci and Tornambé (1987), Matteucci (1994), Tantalo et al. (1998), Chiosi and Carraro (2002), among others.

Table 6.1 Pipino and Matteucci (2004)/Pipino et al. (2005) model parameters

Model	$M_{\rm lum}$ ($M_\odot$)	$R_{\rm eff}$ (kpc)	ν (Gyr^{-1})	τ (Gyr)	$\epsilon_{\rm SNe\ II}$	$\epsilon_{\rm SNe\ Ia}$ ($t \leq t_{\rm gw}$)	$\epsilon_{\rm SNe\ Ia}$ ($t > t_{\rm gw}$)	$t_{\rm gw}$ (Gyr)	t_{stop} (Gyr)
La1	10^{11}	3	15	0.3	0.10	0.10	0.50	0.82	7.8
Ha1	10^{12}	10	25	0.2	0.10	0.10	0.70	0.49	3.7

Pipino et al. (2005) Model La1 is the equivalent of the $10^{11} M_\odot$ case for Pipino and Matteucci (2004)'s Model II. Similarly model Ha1 is the highest mass model. Adapted from Pipino et al. (2005) A&A, 434, 553, reproduced with permission ©ESO

In order to understand the metallicity and the abundance ratios in the stars, it is important to study the evolution of the chemical species in the gas during the star forming phase. The so-called time-delay model is the interpretation of the behavior of abundance ratios such [α/Fe] versus [Fe/H]. The time-delay refers to the delay with which Fe is ejected into the ISM by SNe Ia relative to the fast production of α-elements by core-collapse SNe. Tinsley (1979) first suggested that this time delay would have produced a typical signature in the [α/Fe] vs. [Fe/H] diagram. Matteucci and Greggio (1986) – see also Greggio and Renzini (1983a) included for the first time the SNe Ia rate formulated by Greggio and Renzini (1983a) in a detailed numerical model for the chemical evolution of the Milky Way. The effect of the delayed Fe production is to create an overabundance of O relative to Fe ([O/Fe]$>$ 0) at low [Fe/H] values, and a continuous decline of the [O/Fe] ratio until the solar value ([O/Fe]$_\odot = 0.0$) is reached for [Fe/H]> -1.0 dex (Fig. 6.3, left panel, solar neighborhood (SN) model, Chiappini et al. 1997). This is also what is observed in the Milky Way. Elliptical galaxies, in which the star formation proceeds faster than in spirals, exhibit higher [O/Fe] ratios, and the [O/Fe] $= 0$ is attained later (i.e. at [Fe/H] > 0) than the Milky Way case. A flatter IMF would have the effect of systematically shifting upward the diagram.

In the right panel of Fig. 6.3, I plot the predicted curves for the [α/Fe] abundance ratios versus [Fe/H] in the ISM of what will be our reference $10^{11} M_\odot$ model galaxy. The α-elements exhibit different degrees of enhancement with respect to Fe. This is due, from a theoretical point of view, to the different degree of production of each element in SNe Ia and SNe II. In particular, Si and Ca show a lower overabundance relative to Fe than O and Mg. It is very important to keep this fact in mind when one wants to infer the relative role of SNe Ia and SNe II in enriching the hot ISM by using (6.4) and the only available information is for just one α element. The results presented in Fig. 6.3 will be recast in terms of abundance ratios versus time in Fig. 6.13 with greater emphasis on the post galactic wind (i.e. $t > 2$Gyr) evolution. The full temporal evolution of the Fe abundance in the ISM for this model will be shown in Fig. 6.7. The reader should note that, while the chemical abundances in the gas at $t < t_{gw}$ are affected by the continuous birth and death of stars, those at $t >> t_{gw}$ will be the results of the interplay between the pollution by low-mass stars (including SNe Ia), the gas ejection during the wind – that somewhat makes the gas *lose the memory* of what happened until $t \sim t_{gw}$ – and possible gas inflows.

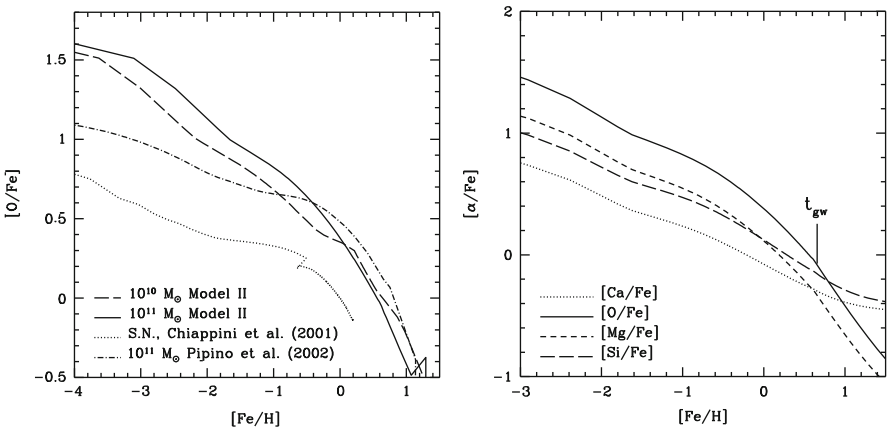

Fig. 6.3 *Left panel*: Theoretical [O/Fe] abundance ratio in the ISM as a function of [Fe/H] from two mass cases by Pipino and Matteucci (2004)'s Model II (see text) for elliptical galaxies compared to a model for the Milky Way (Chiappini et al. 1997). Adapted from Pipino and Matteucci (2004). *Right panel*: Theoretical [O, Mg, Si, Ca/Fe] abundance ratios in the ISM as functions of [Fe/H] predicted for a $10^{11} M_{\odot}$ galaxy in Pipino and Matteucci (2004). Solar value for O by Holweger (2001, namely 0.2 dex lower than Anders and Grevesse 1998). The [Fe/H] that corresponds to the time for the occurrence of the galactic wind, t_{gw}, is indicated. Figure from Pipino and Matteucci (2004)

Therefore, the results of this sections are strictly valid for the star forming phase only.

6.3.2 The Stellar Metallicity

Once the evolution of both the metallicity and the abundances ratios in the gas are known, I can couple this information to the star formation history to predict the stellar metallicity distribution function, namely the number of stars per metallicity[3] bin. Figure 6.4 gives an example of a predicted stellar metallicity distribution for the low-mass stars that survive today in a model elliptical galaxy. Let us first derive some general considerations. I can explain the slow rise in the [Z/H]-distribution as the effect of the infall,[4] whereas the sharp truncation at high metallicities is due to a sudden and strong wind which stopped the star formation.

[3] Similar distributions can be constructed for any given abundance or abundance ratio.

[4] The presence of the infall reduces the fraction of low metallicity stars with respect to the case in which all the gas is already in place at the beginning of the star formation process as requested by observations (Bressan et al. 1994).

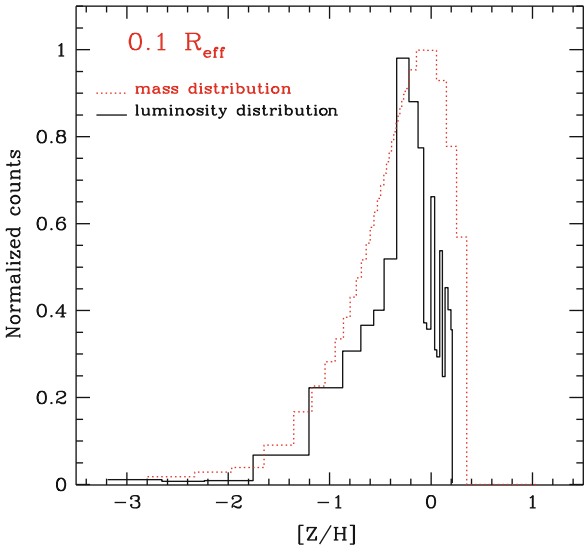

Fig. 6.4 The predicted stellar metallicity distributions. In particular, I show the total mass in long-living stars per bin of [Z/H] (*dotted line*) as well as total B-band luminosity per metallicity bin (*solid line*). Adapted from Pipino et al. (2006). Reproduced by permission of the AAS, see the electronic version for a color version of this figure

Both the peak and the median of the predicted distribution shift to higher metallicities as the galactic mass increases: this is what we then observe as the mass-metallicity relation. The reader should note that the mean metallicity in stars reflects the average chemical enrichment of the galaxy, whereas the abundance in the gas is closer to the composition of the youngest stellar population formed, thus being more indicative of the most recent period of star formation. Hence, measuring abundance ratios in both galactic components gives tighter constraints to the models.

Unfortunately, we cannot resolve the stars in elliptical galaxies, given their distances. Therefore, there are no observed stellar metallicity distributions' available.[5] Instead we can measure their chemical abundance pattern from the integrated light; namely, from the spectrum, in which the contribution of all the single stellar spectra somehow add up together. Hence we should resort to a suitable indicator of an average metallicity (or abundance ratio). The standard has been set by the so-called Lick/IDS (Faber et al. 1985) system. In these low resolution spectra, the absorption lines of several elements may contribute to the measured absorption 'feature', whose equivalent width defines an index. Such an equivalent width is measured with respect to a pseudo continuum level defined by two flanking bands on either side of the 'feature'. Given their nature, the Lick indices are also sensitive to the age and the IMF of the stellar population.

[5]However, I mention that from the comparison with outer fields taken by Harris and Harris (2002) in the elliptical galaxy NGC 5128, the qualitative agreement of the model predictions is remarkable.

One possibility to mimic the observational process is to make use of the mass-weighted mean stellar metallicity as defined by Pagel and Patchett (1975, see also Matteucci 1994):

$$< Z >= \frac{1}{S_f} \int_0^{S_f} Z(S)\, dS\,, \tag{6.6}$$

where S_f is the total mass of stars ever born contributing to the light at the present time and Z is the metal abundance (by mass) in the gas out of which an amount of stars S formed. In practice, I make use of the stellar mass distribution as a function of Z in order to derive the mean metallicity in stars.

One can further adapt (6.6) in order to calculate, e.g., the mean O/Fe ratio in stars. In this case, however, I should make use of the stellar mass distribution as a function of O/Fe.

Another way to estimate the average composition of a composite stellar population which is closer to the actual observational value is to use the luminosity weighted abundances. Generally the mass averaged [Fe/H] and [Z/H] are slightly larger than the luminosity averaged ones, except for large galaxies (see Yoshii and Arimoto 1987; Matteucci et al. 1998).

On the observational side, when the indices are measured, they are converted into a single value for the vector (age, metallicity,[α/Fe]) by comparing them with stellar libraries, where the indices are predicted for a true SSP[6] as a function of t, [Z/H], [α/Fe] and a given IMF. Since luminosity-weighted quantities are strongly affected by the presence of a small fraction of young stars, they do not always reflect the mean age and composition of the bulk of the population. Indeed they might be biased by the youngest and most luminous component even if its contribution to the total mass is a few percent (e.g. Serra and Trager 2007). Moreover, different values for age, metallicity and [α/Fe] ratios are obtained by using differing set of indices to calculate them.

In summary, to have a fair comparison between theory and observations, the model predictions must be collapsed into suitable average quantities, whereas the information contained in the spectrum must be converted into the age, metallicity and abundance ratios of a SSP that exhibits the same values of the observed indices. Such a procedure is definitely more involved than the derivation of the abundance ratios in the hot ISM (see Kim, this book), and leaves room for uncertainties.

6.3.3 [α/Fe]-Mass Relation in the Stars

With the caveat of the previous section in mind, I can study the inferred abundance ratios in the stars of elliptical galaxies and their relation with the stellar mass.

[6] A simple stellar population (SSP) is stellar population uniquely characterized by age, IMF and chemical abundances.

A particular emphasis should be given to the observed increase in the enhancement of α elements with respect to Fe with mass in ellipticals (e.g. Worthey et al. 1992; Matteucci 1994; Thomas et al. 2002) as it represents a very strong constraint on their star formation history. I will often refer to it by its proxy [Mg/Fe] ratio, since Mg dominates most of the absorption features in the spectra from which the α-enhancement is derived.

One can envisage several possibilities to account for the [Mg/Fe]-mass trend: a shorter timescale of star formation which can be obtained by increasing the star formation efficiency with galactic mass. This, in turn, induces the occurrence of galactic winds, with consequent loss of the residual gas, earlier in the most massive objects (inverse wind picture, see Matteucci 1994). Another possibility is to assume that the IMF varies from galaxy to galaxy becoming flatter with increasing galactic mass. Finally, a decreasing amount of dark matter with increasing luminous mass or a selective loss of metals could be the cause for the increase of [Mg/Fe].

Here I will focus on the first of these interpretations and refer to Matteucci (1994) for an extensive discussion. First of all, I recall that in galaxies undergoing a strong burst of star formation, the [Mg/Fe] in the gas out of which stars form is oversolar for most of the evolution (Fig. 6.3). What observations tell us is that there is a further difference in elliptical galaxies of differing mass, such that the largest have even higher [Mg/Fe] than the smallest. For the lowest mass systems, [Mg/Fe]$\sim$0 is observed, therefore a star formation efficiency not much different from the one that characterizes the Milky Way might be expected. To be more quantitative, in the lower panel of Fig. 6.5 I show the predictions (solid line) from the fiducial chemical evolution model (the Model II case) for elliptical galaxies in which the star formation efficiency increases with mass and leads to the star formation histories portrayed in the upper panel of Fig. 6.5 (solid lines) and whose input parameters are summarized in Table 6.1. The observed [Mg/Fe]-mass trend (along with its 1σ scatter) is given by the shaded area. The scatter can be understood by the fact that the star formation history is not the same for all the galaxies of a given mass. For instance, small variations in either the mean feedback efficiency (dashed lines, lower panel of Fig. 6.5) or the star formation efficiency (dashed lines, upper panel of Fig. 6.5) can produce the necessary variation. When discussing the abundances in the hot ISM later in this Chapter, we will take into account that the late time mass loss (with the suitable abundance pattern) from single low-mass stars and the SNe Ia rate are those predicted by a monolithic collapse/galactic wind model which fulfills the [Mg/Fe]-mass relation in stars, according to the scenario above. It is interesting to note that some dry-mergers can be accommodated in such a scenario. Indeed, Pipino and Matteucci (2008) show that, given the scatter in the observed [Mg/Fe]-mass relation, galaxies already fulfilling it could not have had more than $\sim$3 equal mass dry-mergers. This is because a dry merger of galaxies that already fulfill the [Mg/Fe]-mass relation[7] would move the *daughter* galaxy to higher masses with

[7]For simplicity I assume that the galaxies have the same mass and the same [Mg/Fe] in order to make the example clearer.

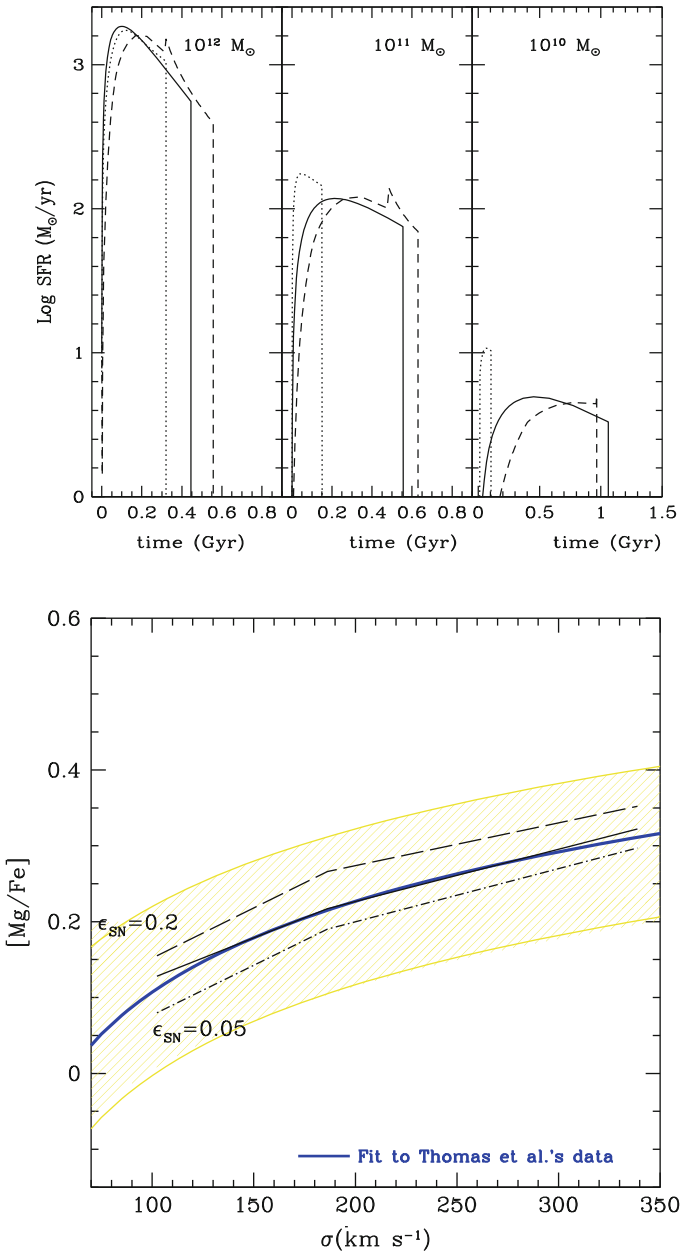

Fig. 6.5 *Upper panel*: The time evolution of the star formation rate for different mass models as reported in each panel. *Solid line*: Example of downsizing in the star formation efficiency following the prescriptions by Pipino and Matteucci (2004). *Lower panel*: Predicted [Mg/Fe] in the stars as a function of galactic velocity dispersion for three supernova feedback efficiencies, compared to the data by Thomas et al. (2007, *shaded area* and *thick solid line*). Figures from Pipino et al. (2009c), see the electronic version for a color version of this figure

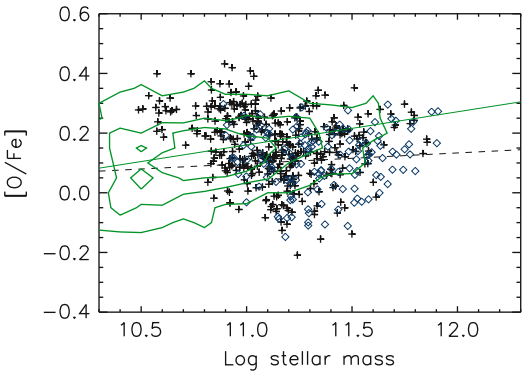

Fig. 6.6 The stellar [α/Fe]-mass relation as predicted by the hierarchical models by Pipino et al. (2009b) for the whole sample of ellipticals (points). Contours: observations by Thomas et al. (2007) along with a linear fit to them (*solid line*). Satellite galaxies (*crosses*) and central galaxies (*diamonds*) are marked. A linear fit to the relation for central galaxies is represented by a *dashed line*. Figure from Pipino et al. (2009b) A&A, 505, 1075, reproduced with permission ©ESO, see the electronic version for a color version of this figure

respect to their *parents* without changing the [Mg/Fe]. After several such mergers, the *daughter* will be below the mean [Mg/Fe] for its mass.

Hierarchical models have been revised as well, in order to reproduce the observed [Mg/Fe]-mass relation, with a great emphasis on an early formation of the stars and a later assembly of the galaxy as a unique entity. Unfortunately, for the above argument, several dry-mergers are not enough to match the observations. This can be seen in Fig. 6.6, where the results of a hierarchical semi-analytical model (Pipino et al. 2009b) are shown as points (in particular, crosses refer to satellite galaxies, whereas diamonds represent central galaxies) and observations (from Thomas et al. 2007) as contours. I also show a fit to the Thomas et al. data by means of a solid line to help the visualization of the mean [α/Fe] at a given mass. I note that the most massive galaxies attain a typical level of α-enhancement that is only 1σ deviant from (below) the value suggested by the observations at a given mass. This is an improvement with respect to earlier hierarchical models (e.g. Thomas 1999; Pipino and Matteucci 2006) and a fundamental ingredient is the fact that these galaxies assemble through dry mergers of building blocks that formed very fast. Indeed, the former condition ensures that the pollution from SNe Ia is kept at a low level after the main star forming phase and, hence, that they maintain a super-solar [α/Fe] ratio in their stars. The drawback is that an increasing trend of [Mg/Fe] with mass cannot be created. Therefore, when discussing the predictions on the hot ISM by hierarchical models, the reader should keep in mind that state of the art simulations are not capable of reproducing the abundances in stars, and this might have consequences on the chemical abundance pattern of the late ISM evolution.

As for the other possibilities, I mention that other works (e.g. Nagashima et al. 2005) showed that a change in the IMF with mass is not enough to produce the required variation in [Mg/Fe].

Unfortunately, O absorption lines cannot be observed in the optical region of the spectrum. As shown above, however, I expect this element to share with Mg a similar average enhancement with respect to Fe. Other α-elements exhibit different degrees of enhancement with respect to Fe. For instance, the observations show that, although Ca belongs to the α elements, the strength of the observed lines follows very closely [Fe/H] instead of [Mg/H] (Worthey et al. 1992; Trager et al. 1998). In particular, observational results by Thomas et al. (2003) suggested [Ca/Mg] $= -0.16$ and there was a claim of Ca depletion. This is a common example of misinterpretation of the '[X/Y]' notation and of the class of α-elements. A closer look to the SNe II yields (Fig. 6.1, c.f. Tables 3 and 4, Kim, this book) tells us [Ca/Mg]< 0 can be explained simply in terms of SNe II nucleosynthesis. The fact that [Ca/Fe] slowly changes with the galactic mass stems from the fact that Ca is produced in a non-negligible amount by SNe Ia (Pipino et al. 2009a). Hence, the [Ca/Fe]-mass relation is naturally explained by the standard chemical evolution model introduced above without any further assumption needed. In fact, calculations based on the chemical evolution model discussed above suggest [Ca/Mg] $= -0.152$ and [Ca/Fe] $= -0.03$ in the stars. Silicon, for the same reason of Ca, presents a very similar behavior and a clear evidence of these departures from the α element abundance pattern (represented by O and Mg) at high [Fe/H], as can be be seen in Fig. 6.3.

6.4 Metals in the Hot ISM

When the energy support from SNe Ia tapers off, the wind slowly comes to a stop and a sizable ISM can then be re-built. Concerning the study of the chemical composition of the ISM, I first analyze the iron abundance, which is the best determined among all the metals. I will first review the predictions by monolithic collapse/galactic wind models, as they are the most widely discussed in the literature. I will then present the results from some *hierarchical* models and compare the predictions in these two differing scenario with observations.

6.4.1 The Fe Abundance in the ISM

6.4.1.1 Fe Abundance as Predicted by *Monolithic-Collapse* Models

The galactic wind, occurring at about 0.5-1 Gyr from the beginning of the simulations, halts further star formation. During the galactic wind phase, most of the gas (and hence the metals) is ejected from the galaxy and pollutes the Intracluster/Intergalactic Medium (ICM/IGM). In Fig. 6.7 (left panel) I show an example of the temporal behavior of both mass and energy flow rate from a fiducial

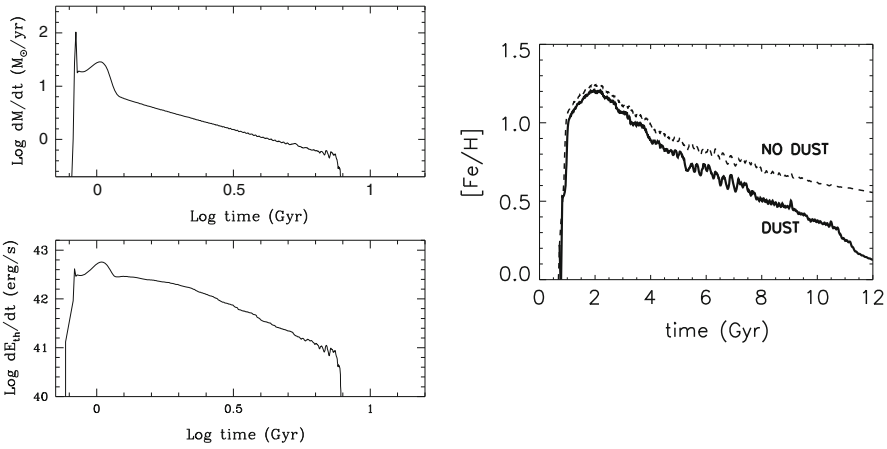

Fig. 6.7 *Left*: Mass and energy flow rate versus time during the galactic wind for a model galaxy. From Pipino et al. (2005) A&A, 434, 553, reproduced with permission ©ESO. *Right*: Evolution of the Fe abundance in the hot phase of an elliptical galaxy with and without (maximal) creation of dust (adapted from Pipino 2011, in preparation)

model of a medium sized elliptical, that is the model La1 in Pipino et al. (2005).[8] After a very short period in which they exhibit quite high values, most of the wind phase is governed by their slow decrease as a consequence of the secular decline of SNe Ia. The mass flow rate has the same order of magnitude (in general within a factor of 2) of the value taken by the star formation rate just before the galactic wind, and this result is in agreement with the observations of starburst galaxies (e.g. Heckman 2002). The luminosity of the wind after the very first intense blow-out is $\sim 10^{41}$ erg s^{-1}, giving a wind speed $v \sim (2\,dE/dM)^{1/2} \simeq 200$ km s^{-1}, again in agreement with the the typical estimates for starbursts (Heckman 2002). SNe Ia-driven winds can last for a long period and inject into the ICM a suitable amount of iron, even if the SN thermalization efficiency is less than 100%. After the wind has stopped (and 5-8 Gyr have elapsed since the galactic wind onset) the chemical abundance pattern is very different: most of the H present during the star forming phase has been ejected and only a minor fraction is restored by the dying stars ($<$1.5-2 M$_\odot$).

The natural predictions in a monolithic collapse + galactic wind model for the Fe abundance are shown in Fig. 6.7 (right panel, dashed line). In particular from Fig. 6.7, we see the early phase – lasting less than 1 Gyr – in which the star formation is active and the ISM quickly attains a solar Fe abundance. [Fe/H]$>$1

[8]For all the purposes of the following discussion the Pipino et al. (2005) model La1 is identical to the $10^{11} M_\odot$ mass case by Pipino and Matteucci (2004, their Model II) and I recall that the main input parameters (effective radius, star formation efficiency, infall timescale, SN feedback efficiency) as well as the times of the wind onset and end are summarized in Table 6.1. I keep the names of the models as in the original papers for the reader interested in more details.

is the likely composition of the wind as soon as it starts, out to an intermediate phase, namely when most of the H in the galaxy has already been expelled. This means that at each timestep, the ejecta from SNe Ia dominate the composition of the ISM. Indeed, we expect the ISM of the galaxy to be heavily polluted by SNe Ia also at times slightly before the wind starts. However, most of the ISM has already been used to form stars, therefore the effect on the stellar metallicity is just to create a small (if any) high metallicity tail in the stellar metallicity distribution. Most of this Fe will be ejected during the wind and contribute to the enrichment of the IGM/ICM. At very late times, when the ISM has been built-up again, the Fe abundance decreases because of both the dilution by low mass stars and the decline in the SNe Ia rate. However, the predicted final Fe abundance will be still over-solar. Such a high abundance is a clear consequence of the simplest possible model, where all the iron produced after the wind has stopped is retained by the galaxies, whereas observations (Fig. 6.8) tell us that on average the Fe abundance in the ISM should be similar to the mean stellar Fe abundance. We will refer to this as the *theoretical Fe discrepancy.*

Let us qualitatively analyze this issue. A typical model predicts the [Fe/H] in the ISM to be at least a factor of three higher than the average Fe abundance in stars. During the star forming phase, the abundance of a given element in the gas is similar to that in the latest stellar population formed and certainly higher than the average abundance in the stars. As we have seen in Sect. 3.2, the typical star

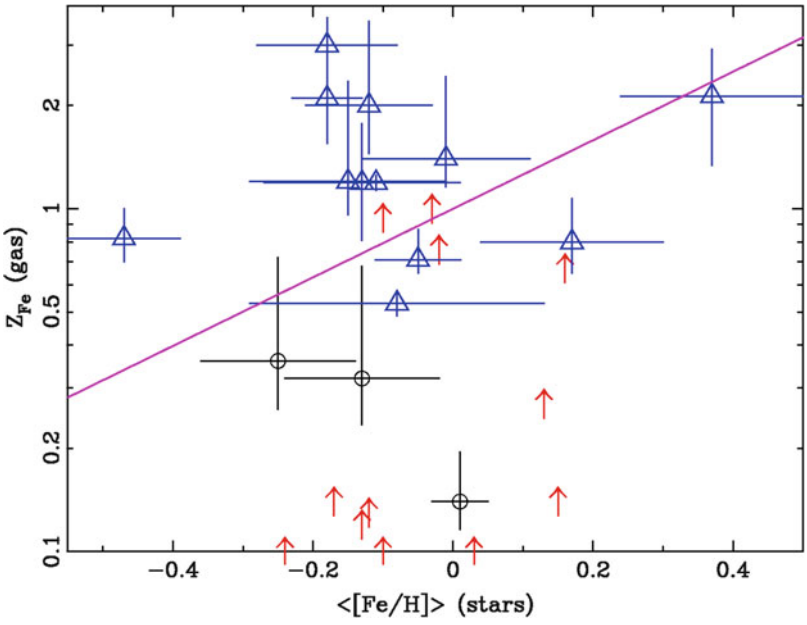

Fig. 6.8 A comparison between gaseous and stellar Fe abundance in a sample of elliptical galaxies. Figure from Humphrey and Buote (2006). Reproduced by permission of the AAS, see the electronic version for a color version of this figure

formation history in a massive elliptical galaxy is such that the stellar metallicity distribution function is skewed in such a way that there is only a negligible fraction of stars at [Fe/H]< -1, with the average [Fe/H] being about solar. The late phase is governed by SNe Ia. Therefore, there is no reason to expect the abundance in the hot ISM to be similar to that in the stars. However, this is what is observed (e.g. Humphrey and Buote 2006). Here we mention that the Fe abundance inferred from stellar absorption lines is dependent on the adopted synthetic SSP[9] and sometimes it is confused with the average metallicity ([Z/H]) in stars. Finally, average abundances derived from stars are not entirely reliable in an absolute sense. These factors render the comparison between the ratios in the stars to those in the gas uncertain.

In principle, the [Fe/H] in the hot ISM can also be used as an age indicator, as can be seen from its strong evolution with time (Fig. 6.7). Therefore, galaxies with similar mass but different [Fe/H] and L_X (that roughly tracks the hot gas mass) may just be in different stages of the hot ISM build-up.

After these general considerations, let us take a more detailed look at the model predictions. At $z \sim 0$, i.e. after 12 Gyr of evolution, these models predict a still very high (>0.5 dex) [Fe/H], as expected from the continuous Fe production by SNe Ia.[10] Again, this is at variance with observations, even if I compare our results with recent iron abundance determination, namely $\sim 1 - 3\,\mathrm{Fe}_\odot$ (Kim, this book). However, as opposed to earlier models where the predicted Fe abundance was offset by the observed values by a factor of 3 or more, the latest model predictions are only within a factor of 2 of the observations. One reason is the fact that updated versions of the SNe Ia W7 model produce $\sim 0.6 M_\odot$ of Fe instead of the classically used mass of $\sim 0.74 M_\odot$. This change alone accounts for a 0.1 dex decrease in the predicted [Fe/H]. As I will discuss below, changes in the observed present-day SNe Ia rate and its past evolution lead to changes in the final Fe abundance. Also, models differing in the duration of the wind and its mass-loading will have slightly different final [Fe/H] in the gas. Overall, one can estimate that the contribution of SNe Ia to the metal enrichment of the hot ISM is quite important, probably more than 60% (e.g. Humphrey and Buote 2006).

The above results have been presented by the Pipino et al. (2005) model in order to allow a self-consistent comparison with the analysis of the stellar abundances and abundance ratios presented in Sect. 3. However, the main conclusions are shared among other models.[11] Basically, since the earlier attempts by Loewenstein and Mathews (1991, see also Renzini et al. 1993), all the models agree in predicting quite high abundances, a factor of 2-3 higher than the latest observational measurements.

[9]For instance, in the widely used models by Thomas et al. (2003) [Fe/H] is not an independent quantity, but it is derived after the total metallicity and α-enhancement are measured, see the discussion in Pipino et al. (2006).

[10]Whose explosion rate is constrained by observations (e.g. Mannucci et al. 2008).

[11]It is worth reminding that most of the galactic wind models did not study the formation of the galaxy, nor did they make predictions on the stellar abundance. In most cases the simulation starts after the galaxy has been assembled.

Therefore, either some modifications to the simple galactic wind scheme are required or a completely different galaxy formation scenario should be adopted. Below I will highlight the contribution of single models, other than the Pipino et al. (2005), to this investigation. I stress that, while the Pipino et al. (2005) model is a pure chemical evolution model with an accurate treatment of stellar nucleosynthesis and SNe Ia where the treatment of the ISM energetics is simplified, most of the models that I will discuss below solve the hydrodynamical equations but track the metal production is a simplified way. A discussion on the development of the wind, the build-up of the hot ISM, as well as the cooling of the gas and the radial flows within the gas that these models feature is beyond the scope of this Chapter and can be found elsewhere in this book. Here I will use them as tools to explore the fate of the Fe in galactic wind models which complement those by Pipino et al. (2005).

6.4.1.2 Solutions to the Theoretical Fe Discrepancy in Wind Models

The possible physical mechanisms invoked to solve the discrepancy between the predicted (theoretical) Fe abundances and the observed ones (see also Renzini et al. 1993; Arimoto et al. 1997, for earlier studies), can be roughly grouped in several classes: (1) differential ejection of Fe, (2) iron hidden in a colder phase (warm gas or dust), (3) a significant dilution from freshly accreted gas with primordial abundances, and (4) the SNe Ia rate. Namely, some other physical processes must be added to the basic wind model.

1. Differential ejection of Fe. According to explanation (1), although the galaxies stop the *global* wind phase, SNe Ia ejecta might be still able to escape the galactic potential well, thus lowering the iron abundance in the ISM, or move further out, thus decreasing the Fe abundance in the central regions. Indeed, very recent simulations by Tang and Wang (2010) show that the hot and low-density SNe Ia bubbles move outward faster than the surrounding medium.[12] Such a differential motion is more evident in the inner galactic regions due to the stronger buoyancy force and reduces [Fe/H] by > 0.2 dex (see Fig. 6.9, solid line) with respect to the case in which the Fe is immediately mixed with the ambient gas (horizontal light dash-dotted line). Moreover, because of the high temperature and low density inside the bubbles, the contribution of such Fe-rich gas to the total X-ray emission is negligible, hence the "emission weighted" abundance that we infer from observations mirrors the metallicity of the dense (and relatively less Fe enriched) shells swept by the SNe Ia remnants. Therefore, the measured metallicity is even lower (Fig. 6.9, dashed and dotted lines) than the actual mass-weighted one. These two effects combined can easily reconcile galactic wind model predictions with observations and, indeed, it is worth noting that these results have been obtained by 3D simulations that can handle such physical processes, whereas most of the

[12]The simulation set-up is such that the model galaxy is still experiencing a wind/outflow.

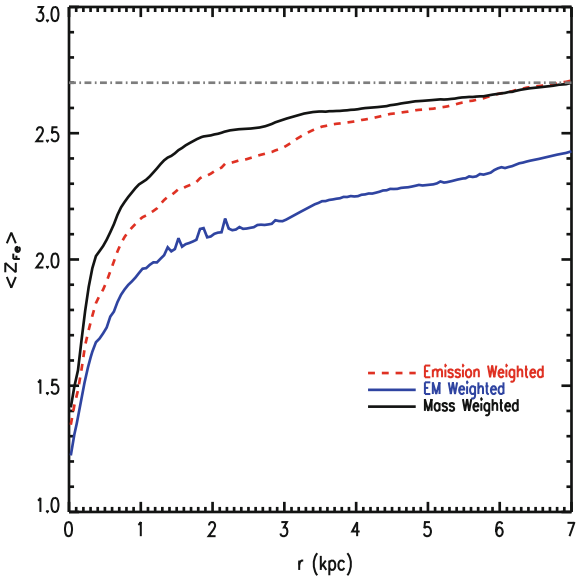

Fig. 6.9 Average radial iron abundance profiles taken from Tang and Wang (2010). The metallicity profiles weighted by mass, emission, and emission measure are plotted separately as labeled. The *horizontal dash-dot line* denotes the expected abundance if iron ejecta is uniformly mixed with stellar mass loss materials, see the electronic version for a color version of this figure

simulations used a lower dimensionality. Also, recent observations show that both the X-ray haloes and the region of the ICM very close to the central galaxy, are not uniform and that the presence of X-ray cavities, bubbles with relativistic gas that pushes away the 'thermal' gas, could be related to the AGN activity (Churazov et al. 2001, see Ciotti and Ostriker, Statler, this book). As shown by Mathews et al. (2004), circulation flows in which Fe rich bubbles are heated and flow in the outer regions where they mix with the inflowing gas give [Fe/H] values below solar, even in the central regions, that cannot be attained with classic cooling flow models. Finally, we note that heating the gas is a way to lower the emission weighted Fe abundance.

2a. Fe hidden in a colder gas phase. The second possibility, on the other hand, explains the low observed [Fe/H] by means of condensation in a colder gas phase. Considering evolution after the galaxy formed, using a multi-phase chemical evolution model, Fujita et al. (1996, 1997) suggested that X-ray-emitting hot gas is hardly enriched, because the enriched gas cools more easily and drops out of the hot gas phase. Figure 6.10 shows some results from these simulations. Models A1 and A3 have a lower present-day SNe Ia rate than observed (see Case 4 below) and predict solar Fe abundance, whereas the natural outcome of the only model (A2) with the correct present-day SNe Ia rate is an Fe abundance an order of magnitude higher than the solar value. Model A1 incorporates an average mass loss from low-mass stars, whose assumed metallicity has the solar value at one half-light radius and the radial profile given by the long dashed line in Fig. 6.10. Model A3 has

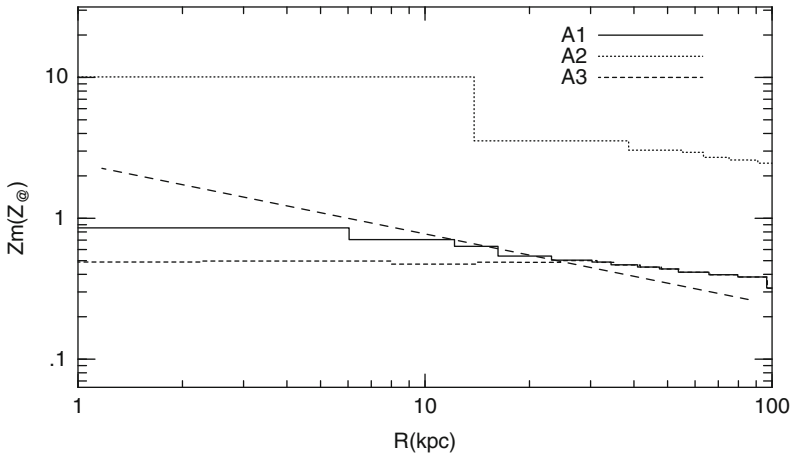

Fig. 6.10 Metallicity gradient in the gas (*solid*) as predicted by different models (see text for details). The *diagonal long dashed line* shows the Fe abundance in the stellar ejecta in the same simulations. Figure from Fujita et al. (1997). Reproduced by permission of the AAS

two mass loss regimes ("phases"), one with metallicity 0.2 times the solar value and the other with a metallicity of 1.8 times the solar value. Fujita et al.'s result is that the metal abundance in model A3 is smaller than those in model A1, because the mass-loss phase with higher metal abundance cools faster than that with lower metal abundance, therefore only the latter adds up to the hot ISM metallicity that we would observe.

According to Brighenti and Mathews (2005), Fe-rich ejecta may cool faster than the ambient medium because of its large radiative emissivity. Finally, we mention that Mathews and Brighenti (2003) put forward that a sizable fraction of metals never enter in the hot phase due to dust-assisted cooling. In practice, the presence of dust (see below) could greatly reduce the cooling time with respect to the dust-free case. While this process has been invoked mainly for the relatively Fe-poor stellar ejecta, it is not unlikely that it can help in lowering the total mass of Fe in the ISM. However, Tang and Wang (2010) do not observe such a selective cooling in their (more sophisticated) simulations and conclude that it is not significant, at least in low- and intermediate-mass elliptical galaxies. The problem with this broad scenario is that the observed lines at $\sim 10^6$K strongly constrain the amount of metals that can cool (e.g. Xu et al. 2002). However, warm ISM is observed in ellipticals and its metallicity is nearly solar (e.g. Athey and Bregman 2009), hence consistent with the measurements in both stars and hot ISM.

2b. Fe hidden in dust. Another solution in the broad context of the possibility (2) is to hide Fe directly in dust. Indeed, Fe is a refractory element (e.g. Lodders 2003) and there is evidence of Fe locked-up in dust grains from the abundance pattern of our own Galaxy, as well as that in high redshift progenitors of present-day ellipticals. We refer the interested reader to a thorough discussion on chemical

evolution models that take the dust into account and their comparison to both present-day ellipticals and high redshift progenitors to Calura et al. (2008) and references therein, and Pipino et al. (2011). Here, we note that dust may be created in the atmosphere of low mass stars during the Asymptotic Giant Branch phase, as well in the ejecta of SNe Ia and SNe II. Moreover, dust grains can accrete a mantle and, thus, grow in size. The main sources of grain destruction are SN blast waves and sputtering in the hot gas. According to Itoh (1989), the density and temperature of the hot ISM in ellipticals are such that the lifetime of a Fe dust grain can be as short as $\sim 10^{6-7} yr$, therefore Arimoto et al. (1997) argued that it is unlikely to store a large amount of Fe in dust. Such an argument was supported by relatively small mass of dust that could be observed in lanes and clouds. Recent observations, however, claim that the dust mass in ellipticals could be $\sim 10^{6-7} M_{\odot}$, (e.g. Temi et al. 2004). This dust is present under a diffuse component and exceeds in mass by two orders of magnitude the dust present in lanes and clouds in the galactic core. Since the dust production in SN and stars is constrained by independent measurements, such an observational result seems at variance with the classical argument that the dust lifetime is short owing to the interaction with the hot ISM via sputtering, and therefore it might represent a viable solution to hide huge amounts of iron for a long period. Recent simulations by Parriott and Bregman (2008) show that a fraction of the dust that condenses in evolved stars may not immediately be injected into the hot ISM. Moreover, the dust production rate is higher than the destruction rate and could account for the observed mass. Preliminary simulations have been conducted implementing a dust-chemical evolution scheme in the models by Pipino et al. (2005) discussed above. In Fig. 6.7 (right panel), I show the predicted evolution of the Fe abundance in the hot phase of an elliptical galaxy without dust (solid line) and with dust (dotted line) with a factor of 3 difference at 12 Gyr. In this latter case I assume that no sputtering from the hot ISM is occurring and that as much as 80% of SNe Ia ejecta may condense into dust. While such a model may not be realistic, it represent a case in which the galaxy features a $z \sim 0$ dust mass comparable to the upper limit set by the most recent observations. Models with lower dust production by SNe Ia and/or stronger grain destruction do not meet such requirement. Comparing the two curves in the right panel of Fig. 6.7, one can notice that the models diverge at $\sim$8 Gyr, namely when the wind stops and accumulation of Fe (and dust) in the hot ISM becomes more and more important. Less extreme and more realistic cases may lower the predicted [Fe/H] by $\sim$0.1 dex. This is not enough to solve the theoretical Fe discrepancy, although it is likely that the combined effect of dust and the other processes discussed in this section can succeed.

3. Dilution by external pristine gas. When a significant amount of gas with primordial composition is accreted, a substantial dilution of the abundances is expected. For instance, if I allow for the excess mass of iron to be replaced by primordial gas, in such a way that models do not change their ISM gas mass, thus roughly preserving their L_X, the iron abundance may be reduced to the observed values. For example, in the simplistic case in which the metallicity is composed only of iron, if I assume mixing to take place from the time at which the galactic wind stopped until the present day, and I want to remove the iron mass in excess

($\sim M_{\rm Fe}^{ISM}$) in order to end up with [Fe/H] = 0 in the ISM, the rate of mass exchange is $\sim M_{\rm Fe}^{ISM}/5\,Gyr \sim 0.5 {\rm M}_{\odot}{\rm yr}^{-1}$. When applied to model La1 and to a higher mass model (empty triangles in Fig. 6.11, upper panel) such a mixing process will reconcile the model predictions with the observations. In the case of mixing involving non-primordial gas (e.g. [Fe/H]~ -0.5 in the ICM), instead, it should be either more extended in time or require a slightly higher rate of mass exchange. The previously discussed model La1 by Pipino et al. (2005) has a small late time infall of mass, amount to less than 1% of the total stellar mass. Such an infall is not enough to dilute the Fe from SNe Ia to bring it in agreement with observations. When higher (10% of the total stellar mass) dilutions are adopted, the density increases, hence the cooling is faster and the wind stops earlier. Thus Pipino et al. (2005) find the counter-intuitive result that there is more time for the Fe to be accumulated in the hot ISM and the predicted [Fe/H] is higher than in the case with lower accretion. While this latter result may stem out of the 1D (spherically symmetrical) nature of the simulation, some fine tuning might be required in the models, with the exact details differing from galaxy to galaxy (c.f., Brighenti et al. 2009).

4. The SNe Ia rate. Finally, let us examine different possibilities grouped under the broad case (4). In the first place, galaxy models are constrained to reproduce the mean observed present-day SNe Ia rate as a function of the galactic mass. A relatively good estimate of the late time Fe abundance in the ISM might be obtained by (Ciotti et al. 1991):

$$X_{Fe,ISM} \simeq < X_{Fe,*} > + \frac{M_{Fe,SNe\,Ia} \cdot R_{SNe\,Ia}}{\dot{M}_*} \tag{6.7}$$

where $< X_{Fe,*} >$ is the average Fe abundance returned by single low mass stars, $M_{Fe,SNe\,Ia}$ and $R_{SNe\,Ia}$ are the SNe Ia Fe yield and rate, respectively. Finally, $\dot{M}_*$ is the stellar mass loss. For the standard W7 yields, and knowing that the Fe abundance in stars is roughly solar, (6.7) can be recast as:

$$X_{Fe,ISM}/X_{Fe,\odot} \simeq 1 + 5\theta_{SNe\,Ia} \tag{6.8}$$

where $\theta_{SNe\,Ia}$ is the present-day SNe Ia rate in units of the observed one.[13] As expected from the previous discussion based on more complicated models, such an equation shows how sensitive the predicted Fe abundance is to the current SNe Ia rate and that if $\theta_{SNe\ Ia} = 1$, the predicted $X_{Fe,ISM}/X_{Fe,\odot} = 6$ (i.e. [Fe/H]$\sim$0.8 dex). By means of this equation, early works by Renzini et al. (1993) and Arimoto and Yoshii (1987 – see also Loewenstein and Mathews 1991, for an earlier study of the effect of rescaling the SNe Ia rate) claimed that the actual SNe Ia rate in ellipticals is at most 1/4 of the observationally derived one, but no study offered a clear explanation of the reason. Equation (6.8) can be further extended in time by using $R_{SNe\,Ia} \propto \theta_{SNe\,Ia} \cdot t^{-s}$, namely adopting a power-law late time SNe Ia rate as discussed in Sect. 2.2.2.

[13] 0.16 ± 0.06 SNu, i.e. in units of $(10^{10} L_{B,\odot} century)^{-1}$, Cappellaro et al. (1999).

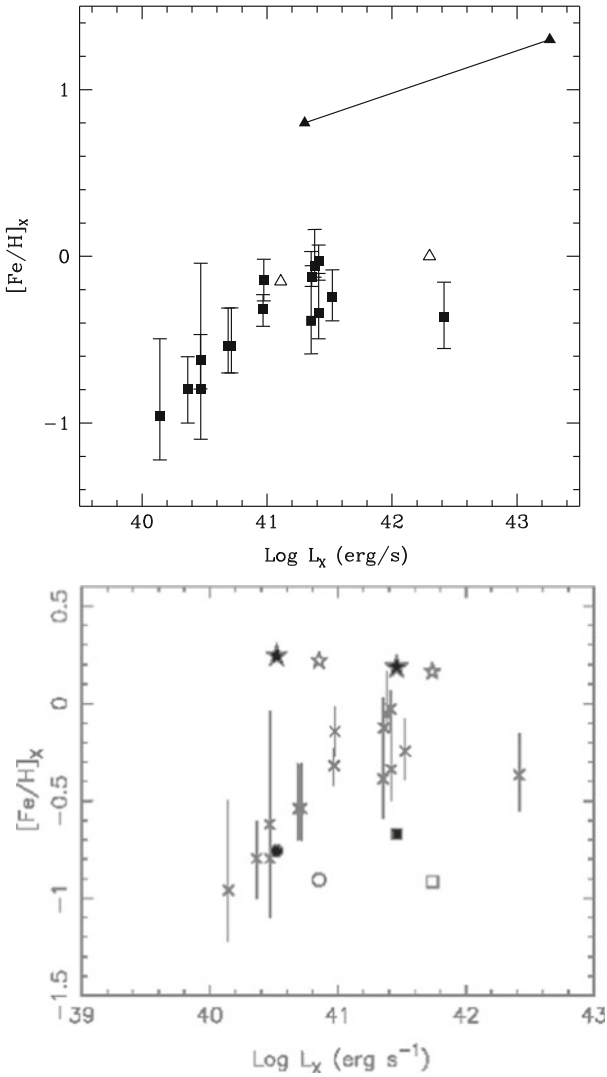

Fig. 6.11 *Upper panel*: Predictions for $L_X - [\mathrm{Fe/H}]_X$ relation (*full triangles*) for models by Pipino et al. (2005) compared to the data of Matsushita et al. (2000, *squares*). From Pipino et al. (2005) A&A, 434, 553, reproduced with permission ©ESO. *Empty triangles* refer to models Ha1 and La1 with the same L_X, but with [Fe/H]∼0. *Lower panel*: Hierarchical model predictions (*open square and circle*) by Kawata and Gibson (2003) compared to the same set of observed galaxies presented in the left panel. The *stars* show the predicted Fe abundance in the stars of the model galaxies. Figure from Kawata and Gibson (2003)

In principle, galaxies have different star formation histories, hence slightly different SNe Ia rates. Those with a higher average SNe Ia rate in the recent past may have undergone a galactic wind till later times and perhaps they have not yet built

enough gas mass to be detectable in the X-rays. There are some recent suggestions that the present-day SNe Ia rate correlates with the colour of the galaxy, even among ellipticals, and with the presence of a radio-loud AGN (see Mannucci et al. 2005). As we have seen in Sect. 2.2.2, a different DTD (i.e. different progenitor systems) changes the SNe Ia rate. Even if the total number of SNe Ia ever exploded and the present-day SNe Ia rate are the same, the distribution in time of the SNe Ia events changes. This affects the fraction of Fe ejected in the wind as opposed to the Fe trapped in the hot ISM. Again, it is the average SNe Ia rate in the recent past that varies, leading to a likely reduction in the [Fe/H] abundance by a few tenths of a dex. A change in $\theta_{SNe\ Ia}$ and the role of the SNe Ia progenitors might be interesting solutions, however they deserve more careful modelling by means of full chemical evolution simulations and comparison to the latest observations, which can likely rule out several combinations of $\theta_{SNe\ Ia}$ and s.

6.4.1.3 Fe Abundance as Predicted by *Hierarchical* Models

As far as models that involve mergers are concerned, there are some studies following the chemodynamical evolution of elliptical galaxies from the epoch of their complex hierarchical formation. Here we briefly summarize their findings.

Using a chemodynamical evolution simulation of merging disks, Bekki (1998) showed that the metallicity of the ISM (especially in the outer regions) becomes lower than that of the stellar component in elliptical galaxies formed by gas-rich disk-disk galaxy mergers. In particular, elliptical galaxies formed by multiple mergers are more likely to have metal-poor gaseous halo components and steep gaseous metallicity gradients than those formed by pair mergers. Unfortunately, these simulations were aimed at reproducing old ASCA data that yielded a much lower observed Fe abundance in the ISM (see Kim, this book), therefore they are not meant to explain the most recent data.

More recent simulations by Cox et al. (2006), examine the hot X-ray emitting gas outcome of merging disk of equal mass. These simulations require the presence of black hole feedback that eject metals in the hot phase to attain a metallicity that is nearly solar. Moreover, these simulations deal with the "birth" of the galaxy and leave the creation of the extended and hot ISM that we observed today to the same mechanism (i.e. stellar mass loss) which occurred in the standard galactic wind models discussed above. Therefore, the simulations by Cox et al. (2006) are not directly comparable to observation.

Finally, Kawata and Gibson (2003) simulated single galaxies from cosmological initial condition. Such a model predicts quite low [Fe/H] ratios (see Fig. 6.11, lower panel), even lower than the observations available at that time, mostly because Fe cools rapidly and enriches the cold gas as opposed to the hot gas. The cold gas, then, feeds late time star formation that makes the Kawata and Gibson (2003) model galaxy too blue in the optical.

Future theoretical efforts should aim to either "fix" the shortcomings of the Kawata and Gibson (2003) simulations or to implement detailed stellar mass loss

and SNe Ia in simulations like those by Cox et al. (2006). Another improvement could be to follow the evolution for, say, 10 Gyr after the merger.

6.4.1.4 Final Remarks on the Fe Abundance

Figure 6.11 captures the differences between the monolithic/galactic wind model and hierarchical model predictions. In particular, Fig. 6.11 (upper panel) displays the models taken from Pipino et al. (2005, filled triangles joined by a solid line): the La1 model previously discussed (but with older SNe Ia yields), and a higher mass model (Ha1) that has a qualitative evolution similar to the La1 case, but for the more intense and shorter star formation period and a slightly shorter duration of the wind. In particular, the predicted Fe abundance is shown as a function of the X-ray luminosity L_X. The reader should note that such models are applicable only to gas rich massive ellipticals, where the contribution to the X-ray flux from the hot ISM exceeds that from low-mass X-ray binaries. The lower panel of Fig. 6.11 displays the same relation for models based on the hierarchical paradigm that underpredicts the Fe abundance in the ISM. In the former scenario, a long phase of passive evolution makes the gas highly enriched in SNe Ia ejecta. Therefore, the predicted [Fe/H] is higher than the observed one. Several solutions have been proposed that give remarkably similar answers and it may seem difficult to find the dominant[14] one. In the next sections we will see how to use the abundance ratios to put some more constraints on them. Here I note that these solutions probably are a warning signal telling us that more physics must be added to the simple picture of the galactic wind in which SNe Ia ejecta and ambient medium instantaneously mix. Such a requirement might imply the need of 3D simulation to fully assess the problem.

Before concluding I note that the observed SNe Ia present-day explosion rate is shown to have little dependence on the galactic mass (e.g. Mannucci et al. 2008), hence on the luminosity. Therefore one can naively expect a mild (if any) correlation between the Fe abundance in the hot ISM and the galaxy mass. That is, while the stellar abundances conform to a very tight galactic mass-metallicity relationship, this is not true as far as the hot gas abundances are concerned. This is indeed what is observed by Humphrey and Buote (2006) and what is predicted by the wind models (Fig. 6.11). On the other hand, hierarchical models still have problems in reproducing both the stellar and the hot ISM abundances and abundance ratios. Nevertheless, the predicted mass-gaseous metallicity relation is as flat as in the galactic wind models.

6.4.2 The Abundance Pattern in the Hot ISM

Let us first have some general remarks before undertaking the study of single abundance ratios in the ISM and comparing them to those in the stars. In order to do

[14] It is quite likely that several of them should be included in modelling.

so, I make use of the recent results by Loewenstein and Davis (2010). Their models make use of analytic approximations of the chemical evolution which take into account the recycling of chemical species, without the full solution of the chemical evolution equation. Broadly speaking they are a generalization of (6.7) applied to several elements and allow to quickly check the impact of changing the composition of the stellar ejecta, their mixing with the SNe Ia ejecta, as well as the SNe Ia rate. Figure 6.12 compares models by Loewenstein and Davis (2010) to the abundance pattern of the galaxy NGC 4472 for different combinations of yields. The figure illustrates the fact that in order to reproduce the abundance ratios of many elements it is important to have an α-enhanced gas ejected (recycled) by single low-mass stars. That is, the abundance ratios cannot be interpreted in terms of the ratio of the stellar yields, even if they involve α-elements, namely elements that one naively expects

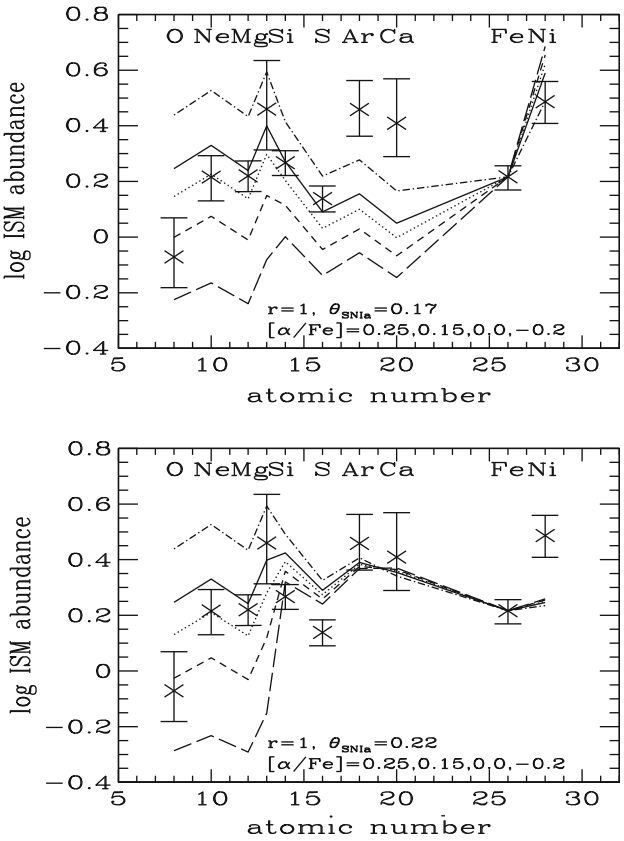

Fig. 6.12 *Crosses*: abundance pattern (with respect to Fe) in the elliptical galaxy NGC 4472, adapted from Loewenstein and Davis (2010). *Lines*: abundance pattern predicted by the Loewenstein and Davis model for different yields (upper panel: Nomoto et al. (1997) and W7, *lower panel*: Nomoto et al. (1997) and WDD1) and different composition of the single low-mass stars ejecta ([α/Fe]=0.45,0.25,0.15,0,-0.2 from top to bottom). Reproduced by permission of the AAS

to be produced on the same (short) timescale. It is important to note, however, that neither a single model (lines in Fig. 6.12) by Loewenstein and Davis (2010) nor a single set of SNe Ia yields can reproduce the entire abundance pattern and that an effective SNe Ia rate lower than the observed one is required as well. In other words, the theoretical Fe discrepancy affects the [element/Fe] ratios too, hence the predictions will exhibit – in general – lower abundance ratios than the observations. The reader should note that most of the models discussed in the previous sections do not attempt to track the evolution of species other than Fe, therefore they cannot be thoroughly tested against the ISM abundance pattern. However, the results obtained by Loewenstein and Davis (2010) are quite general and closely track those that can be obtained with a full chemical evolution model. Therefore, I consider that Fig. 6.12 depicts a rather general situation.

Both the simplified model by Loewenstein and Davis and the chemical evolution/galactic wind model agree on the fact that the predicted α/Fe ratios in the ISM are under-solar and, hence, lower than the observational values because of the excess in the predicted Fe abundance. Also, models predict [Mg/O]$\sim$0, whereas observations hint for [Mg/O]$\sim$0.3 (Ji et al. 2009, Loewenstein and Davis 2010), namely the O should be under-produced (or the Mg over-produced) by a factor of 2. Indeed, the Mg and the O abundance are best fit by two different lines (the one for Mg requiring more αs stored in low-mass stars) by the simple models shown in Fig. 6.12. [Mg/O]$\sim$0 should be naively expected since both O and Mg are produced during the hydrostatic nuclear burning in massive stars. However, as can be inferred from Tables 3 and 4 by Kim (this book), SNe Ia ejecta may feature [Mg/O]>0 (especially in the WDD1 model), and even some recent SNe II yields like the ones by Kobayashi et al. (2006) have a mild (0.1 dex) Mg overabundance with respect to O. Moreover, stars suffer from mass loss that increases with increasing metallicity.[15] The larger the mass loss, the smaller the He and C cores and, hence, the O production. Therefore, when the effect of the mass loss is accounted for, the predicted [O/Mg] ratio in the gas decreases with metallicity during the star forming phase. This process seem to be relevant in the Milky Way (McWilliam et al. 2008; Cescutti et al. 2009). Therefore, we may expect that some of the gas locked in low-mass metal-rich stars is indeed O-depleted. When these stars expel their envelopes in the planetary nebula phase they may lower the O/Mg ratio in the ISM. Such an effect, however, is still probably within the uncertainty in the observed O/Mg ratio in the hot ISM.

Another possibility is that a modification to the Mg yields is required. As an example, I show in Fig. 6.13 the prediction for the [Mg/Fe] abundance ratio by (a) a "standard" model like the La1 by Pipino et al. (2005) that has been discussed above, (b) a model (F04) in which modifications to both the SNe Ia and SNe II nucleosynthesis[16] suggested by François et al. (2004) have been applied and (c) this

[15] In the gas out of which the star formed.

[16] François et al. (2004) compare the predictions by a state-of-the-art chemical evolution model with different sets of yields to a large set of observed abundance ratios in the Milky Way by means

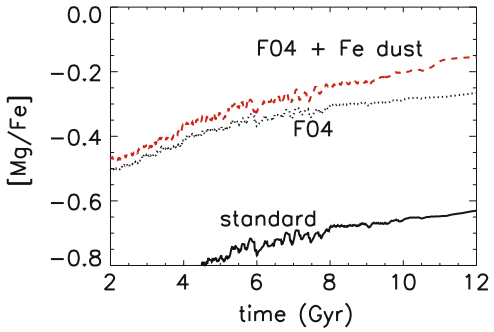

Fig. 6.13 Pipino et al. (2005) *standard* model predictions for the temporal evolution of the [Mg/Fe] ratio in the ISM compared to a model in which the SNe Ia Mg yield has been modified according to François et al. (2004, label F04) and a case in which also Fe dust is allowed. From Pipino et al. (2011, in preparation). Note the rising trend of $[\alpha/Fe]$ ratios with time in both panels due to the decrease in the SNe Ia rate and the recycling of α-rich gas from low mass single stars, see the electronic version for a color version of this figure

last model plus dust/cool phase depletion (only Fe in this specific toy model). These processes act in the same direction and the net effect is to reconcile models with observations that require [Mg/Fe] closer to the solar value.

In this context, it is worth noting that some solutions to the theoretical Fe discrepancy put forward in Sect. 6.4.1.2 lead to specific changes in the predicted abundance ratios and could mitigate the disagreement with observations. A dilution with pristine gas (infall from the IGM/ICM), instead, would not affect the abundance ratios. As far as the dust is concerned, it is worth noting that Fe and O have different condensation temperatures, being Fe a "refractory" element, hence more easily prone to dust depletion than O. Mg, instead, has nearly the same condensation temperature of Fe (Lodders 2003). Therefore, the two possibilities in the scenario (2) described in Sect. 6.4.1.2 may in principle lead to different predictions for the [Mg/Fe] and the [O/Fe] in the ISM. If we include the dust in the models (and assume that the Fe that we observe is only a fraction of the total Fe in the ISM), we expect that the predicted [O/Fe] ratio in the gas will increase because part of the Fe in the model will be locked into dust too. This will improve the agreement with observations. On the other hand, the expected increase in the [O/Mg] would be at variance with observations. Unfortunately, the condensation temperatures of Mg and Fe are very similar, hence the predicted [Mg/Fe] will remain basically the same, thus still below the observed value. If only Fe preferentially cools, depletes into dust (e.g. Vladilo 2002; Calura et al. 2003, Pipino et al. 2011) or is more easily ejected than

of [X/Fe]-[Fe/H] diagrams. While the agreement is generally good, both the SNe Ia and the SNe II yields of some elements require an "ad hoc" modification to best fit the data. For our discussion it is important to note that the Mg production in SNe Ia must increase by a factor of 5, whereas the O and Fe production should not change.

other elements, we expect the theoretical predictions for the [Mg/Fe] and [O/Fe] ratios in the hot ISM to increase in lock step. Therefore we would still predict [Mg/O]∼0 and we would still need a change in, e.g., the Mg yields to account for the observed ratio. Most of the simulations made in the hierarchical scenario do not make predictions on the abundance ratios. I note that the Kawata and Gibson (2003) models predict [O/Fe]∼-0.7 and [Si/Fe]∼-0.3 in the hot gas, perhaps in marginal (3σ) agreement with data, and [O/Fe]∼0 in the stars, at variance with observations. The latter abundance ratio is so low because of continuous star formation.

As expected from Fig. 4 and Tables 3 and 4 (Kim, this book), [Ca/Fe] and [Si/Fe] ratios are predicted to be solar or higher. Indeed, Figure 6.12 shows that only the WDD1 model (right panel) yields enough Ca (as well as Si and Ar) to reproduce the data, at the expenses of worsening the agreement for Ni. The opposite happens when the SNe Ia model W7 is adopted. Similar claims have been made by other authors (e.g. Finoguenov et al. 2002), but their quantitative conclusions are less certain, since they are based on a direct comparison to the tabulated yields without taking into account the recycling of the metals.

In summary, there does not seem to be any combination of nucleosynthetic yields from both SNe II and SNe Ia that produces the observed abundance pattern in the hot ISM, with the caveat of the large observational uncertainty affecting the Ca abundance. As mentioned earlier, I cannot constrain the O, Si, Ar, Ni abundances by means of the integrated stellar spectra.

I briefly mention that a larger contribution from SNe II may be invoked to explain the observed abundance pattern. This can easily be done by requiring a flatter IMF than the Salpeter one. However, if a flat IMF is kept for the entire galactic evolution, the larger amount of metals promptly released by SNe II, will make the stars of the galaxies too metal-rich at variance with observations. Also, as discussed in Sect. 3.3, a flatter IMF does not help in reproducing the observed trend of the stellar [Mg/Fe] with galactic mass.

If the flat IMF is confined were to the very early phases in which the so-called Pop III (metal-free) stars were formed, such a regime is so short in time that very few stars are created, compared to the total, therefore their impact should be minimal (e.g. Matteucci and Pipino 2005).

6.4.3 On the Use of Abundance Ratios

Before concluding, some words of caution must be spent, especially if one wants to constrain the history of galaxy formation by just comparing the observed abundance ratios to their (stellar) yields. Matteucci and Chiappini (2005) discuss the evolution of the ratio of a typical α-element such as O relative to Fe as a function of time, as predicted in models which are basically the same of those in Pipino et al. (2005). Matteucci and Chiappini show that the final O/Fe ratios contributed by galaxies of different luminous masses are different and the difference depends on the duration of the star formation period in each galaxy (see Sect. 3.2.2). As pointed out by

Matteucci and Chiappini (2005), the difference, $\Delta log(O/Fe) \sim 0.3$, is comparable to the differences among production ratios obtained by adopting different sets of yields (c.f. Tables 3 and 4, Kim, this book).

A common *mistake* is to over emphasize the discrimination above/below the 'solar ratio', i.e. when the abundance ratio of a generic element X with respect to Fe is [X/Fe] = 0. While it is true that from [X/Fe] = 0 I may infer that the relative contribution of SNe Ia and SNe II has proportions similar to those in the solar vicinity, the actual percentages depend on other important factors such as the differences in the star formation history, in the IMF, and in the recycling history of matter in low-mass stars. Even if all these quantities are the similar to, say, those in the Milky Way, the reader should not forget that the hot ISM is possibly rebuilt after a galactic wind phase, which may *erase* the previous chemical enrichment history. The above statement has other consequences. For instance, if one of the possibilities grouped under the cases (1) or (2) described in Sect. 6.4.1.2 to address the theoretical Fe discrepancy is true, it implies that I cannot infer the present-day SNe Ia rate by means of the Fe abundance in the hot ISM and vice-versa. Therefore one can only qualitatively say that the SNe Ia production is dominant over the SNe II one, or vice-versa. One also has to keep in mind that, while in the solar neighborhood SNe II continue to explode, all the metals produced by SNe II in elliptical galaxies have been either released a long time ago or they have been locked-up and the restored by low-mass stars. Moreover, the observationally inferred solar abundance of O changed in the last decade by a factor of ∼2 (e.g. compare the Grevesse and Sauval 1998, abundance ratios to the Lodders 2003, to Asplund et al. 2005) and several groups did not reach an agreement yet. This means that if the measured O abundance X_O implies $[X_O/\text{Fe}] = -0.3$ in the Grevesse and Sauval (1998) solar scale, it will be nearly solar in the Asplund et al. (2005) scale. Therefore a careful comparison between theoretical expectations and observations must always start from setting all the ratios in the same scale.

It is important to stress that many of the results presented above are still the topic of ongoing investigation. Therefore, even if they seem to represent reliable ways to explain the observed abundances and abundance ratios, more study is needed. On the other hand, the examples in Sect. 6.4.1.2 show how a good knowledge of what happens during the star forming phase is not enough to predict the *details* of the evolution of the abundance ratios 10 Gyr later. The positive aspect of this fact is that (thankfully!) the observed abundance ratios in the ISM represent independent constraints to the galaxy formation process and its key elements, namely stellar yields, star formation history and IMF.

6.5 Abundance and Abundance Ratio Gradients

Until this point I discussed the metallicity and the abundance ratios in both the stars and the hot gas as if they were uniform along the radius. While this approximation holds as long as one wants to study general properties of galaxy at the 0-th order

level, gradients become important when the study goes into further detail, such that the distance from the centre matters.

6.5.1 Gradients in the Stars

Elliptical galaxies do exhibit metallicity gradients in their stars out to (at least) 1 R_{eff}. In general, observations show that the majority of ellipticals have a typical decrease in metallicity of 0.2–0.3 dex per decade in radius (e.g. Carollo et al. 1993; Davies et al. 1993). However, a large scatter in the gradient slope at a given galactic mass is also observed. Below I give a brief historical perspective for what concerns the relation between gradient slope and mass. I refer the reader to other works (e.g. Sanchez-Blazquez et al. 2006) for a review about the debate on the observations in the literature.

Indeed, a positive correlation of the metallicity gradient slope with the galactic mass – namely gradients becoming steeper at higher galactic masses – (in agreement with the Larson 1974, predictions), has been reported by Carollo et al. (1993), but only for masses lower than $10^{11} M_{\odot}$. In fact, Carollo et al. (1993) found a flattening of the observed gradients in the most massive galaxies of their sample and ascribed this fact to: i) an increase in the importance of mergers; or ii) a less important role of dissipation in the formation of the most massive galaxies. In more recent years, a positive correlation of gradient slope with mass has been suggested again by Forbes et al. (2005), Sanchez-Blazquez et al. (2007), for the entire mass range of elliptical galaxies. Ogando et al. (2005), rather than a clear trend, noticed an increasing number of elliptical galaxies harboring steep gradients with increasing velocity dispersion.

From the theoretical point of view, steep metallicity gradients are expected from classical dissipative collapse models (e.g. Larson 1974; Chiosi and Carraro 2002) and their (*revised*) up-to-date versions (e.g. Kawata 2001; Kobayashi 2004, Pipino et al. 2008). The abundance gradient arises because the stars form everywhere in a collapsing cloud and then remain in orbit with a little inward motion,[17] whereas the gas sinks further in because of dissipation. This sinking gas contains the new metals ejected by evolving, stars so that an abundance gradient develops in the gas. As stars continue to form their composition reflect the gaseous abundance gradient. The original dissipative models predict a steepening of the gradient as the galactic mass increases, mainly because the *central* metallicity is quickly increasing with mass,[18] whereas the *global* one has a milder variation (Carlberg 1984). On the other hand, the few attempts to study the gradients in the merger-based models hint for very shallow (if any) gradient (Bekki and Shioya 1999), less steep than the mean

[17] Stars will spend most of their time near the apocentre of their orbit.

[18] The fit of the mass-metallicity relation, namely the increase of the mean metal content in the stars as a function of galactic mass (O'Connell 1976), was the main success of these original models.

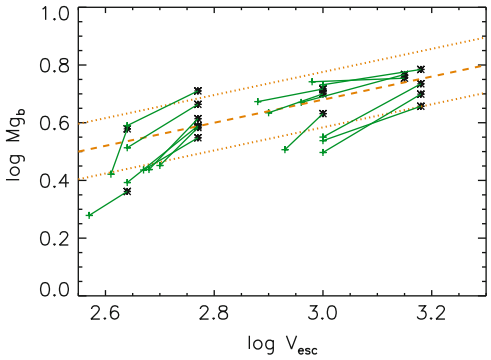

Fig. 6.14 Metallicity – in terms of the line-strength index Mg_b – versus v_{esc} gradient slope for our models. The central Mg_b value for each model galaxy is given by an asterisk, whereas the value at 1 R_{eff} by a cross. Each couple of points connected by a line represents a galaxy. The *dashed line* is the observational mean trend reported by Scott et al. (2009) along with the 3σ dispersion (*dotted lines*). Reproduced from Pipino et al. (2010), see the electronic version for a color version of this figure

observational values and than the predictions from monolithic collapse models. Moreover, dry mergers flatten pre-existing gradients (Di Matteo et al. 2009). Indeed, when the two scenarios (monolithic collapse and mergers) are considered as two possible channels working at the same time, the scatter in the predicted gradients for such a population of galaxies seem to be in agreement with observations (Kobayashi 2004).

The galactic wind occurs externally first, then internally, because the work to extract the gas from the outskirts is less than the work to extract the gas from the center of the galaxy. This implies that the stellar metallicity is a function of the local escape velocity v_{esc} for all the galaxies (see Martinelli et al. 1998). Such a relation has been originally suggested by several authors (e.g. Davies et al. 1993; Peletier et al. 1990) and now confirmed by Scott et al. (2009). In Fig. 6.14, I show that models very similar to the La1 and Ha1 cases previously discussed reproduce the observed trend (solid line) within the observed scatter (dotted lines). It is interesting that the *local* index-v_{esc} trend matches the *global* scaling,[19] again reinforcing the idea that a uniform process very close to a monolithic collapse explains the formation of the gradients.

More recently, observations showed that successful models for elliptical galaxies should also reproduce gradients in the [α/Fe] ratios (e.g. Mehlert et al. 2003; Sanchez-Blazquez et al. 2007). Indeed, these observations show that the slope in the [α/Fe] gradient has a typical value close to zero and does not correlate with mass. These observations have been interpreted by Pipino et al. (2008) as the fact that the suggested outside-in mechanism for the formation of the ellipticals is not the only

[19]Namely another way of looking at the mass-metallicity relation.

process responsible for the formation of gradients in the abundance ratios. Other processes should be considered such as the interplay between the star formation timescale and gas flows. While such an interplay flattens the [α/Fe] gradient to the value required by observations, it still enables galaxies to harbor gradients in the stellar [Fe/H] and [Z/H] in agreement with the most recent observations.

6.5.2 Gradients in the Hot Gas

Abundance gradients are detected also in the hot ISM (c.f. Fig.8 in Kim, this book). The gradients are such that the [α/Fe] ratio is approximately constant with radius. These facts offer an intriguing analogy to what happens in the stars. However, I first note that the scale-lengths are different. A factor of 2 decrease in the metallicity in the stars occurs with 1 R_{eff}, that is within $\sim$10 kpc (or a slightly bigger radius if the galaxy is also a cD), whereas the changes in the hot ISM are on larger scales.

Secondly, the gradient in the stars is virtually unaffected after the passive evolution. The only variation is due to the effect of the aging stellar populations in the shape of the spectra. On the other hand, the gradients in the hot gas may well be erased during the galactic wind and hence they may not have *memory*.

In the literature, however, stellar metallicity gradients, along with the long-term chemical evolution of the ISM driven by stellar mass loss or SNe Ia, and the dilution of metal-enriched ISM by external metal-poor gas are considered to be likely explanations for the origin of gaseous metallicity gradients (e.g., Mushotzky et al. 1994; Matsushita et al. 1997). For instance, the gradients predicted in the multi-phase chemical evolution model by Fujita et al. (1997) are shown in Fig. 6.10. Figure 6.15 shows the metallicity gradient in the stars (dashed), and gas (solid), as predicted by Brighenti et al. (2009)'s wind/cooling flow model compared to data for NGC4649 (Humphrey et al. 2006). The lowest solid line is the fiducial model, in which the Fe injected by SNe Ia is diluted by the inflow of pristine case. The upper line shows the gradient in the case in which non dilution occurs. The inflow of gas seem to contribute to the gaseous gradient slope.

In conclusion, I note that the theoretical Fe discrepancy disappears if only a "central" Fe abundance is taken into account. Indeed, on small scales, the measured [Fe/H] in the hot gas can reach values as high as 0.6 dex (e.g. in NGC 507, Kim and Fabbiano 2004). Finally, the study of the gradients in the abundance ratios in M87 (Finoguenov et al. 2002) has been also used to infer a radial variation in the SNe Ia channels (e.g. W7 versus WDD1).

As far as the hierarchical models are concerned, metallicity gradients in the gas have been studied by Kawata and Gibson (2003, see Fig. 6.16). Their models differ by feedback strength and the predicted properties are used to create mock observations that are then studied with the same techniques used for real observations. From Fig. 6.16, I note that there is a clear negative gradient in [Fe/H], which is consistent with the observational trends of some bright elliptical galaxies. Kawata and Gibson (2003) argue that this is because stars, which are the source of the iron, stay within the central region corresponding to the inner most bin.

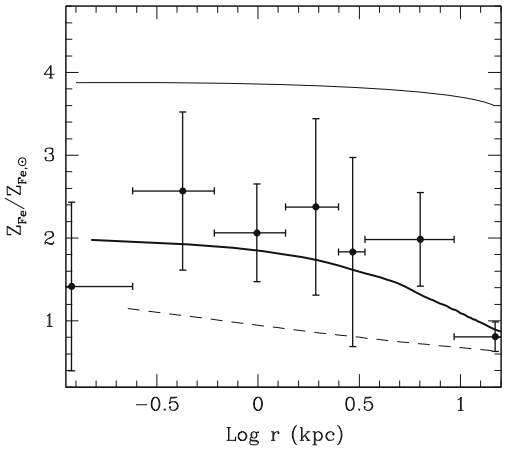

Fig. 6.15 Metallicity gradient in the stars (*dashed*) and gas (*solid*) as predicted by Brighenti et al. (2009)'s cooling flow model compared to data for NGC4649 (Humphrey et al. 2006). The *lowest solid line* is the fiducial model in which the Fe injected by SNe Ia is diluted by the inflow of pristine case. The *upper line* shows the gradient in the case in which non dilution occurs. Figure from Brighenti et al. (2009). Reproduced by permission of the AAS

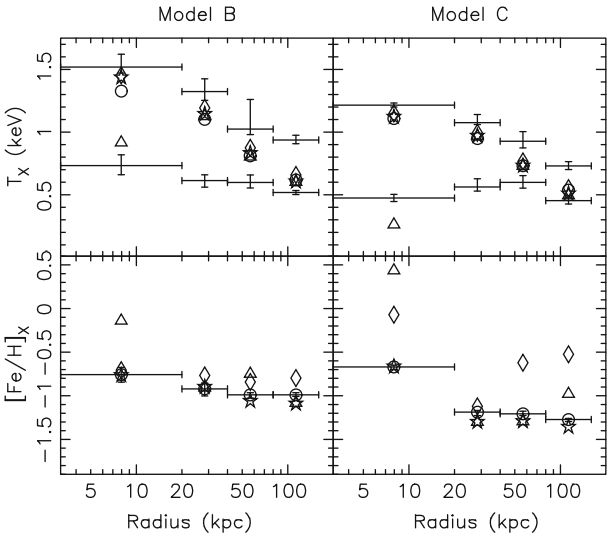

Fig. 6.16 Predicted temperature and metallicity gradients from Kawata and Gibson (2003). Different symbols correspond to the values derived by the different methods, such as spectrum fitting (*circles*), X-ray luminosity (0.5−4 keV) weighted mean values (*diamonds*), $\rho^2 T^{1/2}$ weighted mean values for the gas with $T > 12000$ K (*triangles*), and $\rho^2 T^{1/2}$ weighted mean values for the gas with $T > 10^6$ K (*stars*)

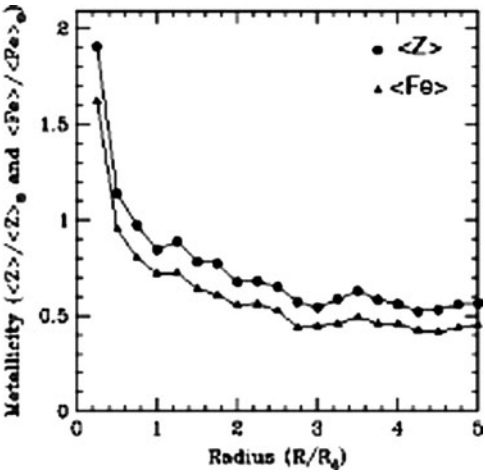

Fig. 6.17 Metallicity gradient in the gas. Figure from Bekki (1998). Reproduced by permission of the AAS

On the other hand, Bekki (1998) argues the ISM metallicity gradients may be closely associated with processes occurring at the epoch of elliptical formation. Bekki (1998) found that elliptical galaxies formed by gas-rich mergers show steep negative metallicity gradients in the ISM, especially in the outer parts of galaxies. In particular, the radial inflow of metal-enriched ISM during dissipative galaxy merging act in a way that metal enrichment of the ISM is more efficient in the central regions. According to Bekki (1998), the metal enrichment is less efficient in the outer parts, because a large amount of metal-rich ISM is tidally stripped away. The metallicity gradients in the hot ISM for these models is shown in Fig. 6.17 for both the total metallicity Z and the Fe abundance at different radii (in units of the progenitor radii). Unfortunately, the metallicity gradients predicted in the stars by these model galaxies are too flat compared to observations (Bekki and Shioya 1999). Moreover, negative metallicity gradients derived by Bekki (1998) are only true for ellipticals of a few Gyr age.

6.6 Summary

Table 6.2 displays a quick comparison between observed abundances and abundance ratios in stars and those in the hot ISM, as well the predicted values by both monolithic collapse/galactic wind (GW) and hierarchical (H) models. The predicted values for the hot ISM do not take into account processes (e.g. dust, inefficient mixing or rapid cooling of SNe Ia ejecta) that *hide* Fe. Moreover, the entries in the Table are meant to give a qualitative summary of what I discussed above in the Chapter. Differences between models in the same scenario are not highlighted. As far as the O and Si are concerned, we have no direct way to measure them in the

Table 6.2 Comparison between stellar and hot ISM abundance ratios in massive ellipticals

	Observed	Average in stars *Predicted* GW models	H models	*Observed*	Hot ISM *Predicted* GW models	H models[a]
Fe/H	Solar	0 − 0.1dex	0 − 0.1dex	Solar to over-solar	0.3–0.5 dex	Under-solar
Mg/Fe	>0.2dex	0.3dex	0.2dex	Close to solar	Under-solar	–
O/Fe	Unknown	>0.3dex	∼ 0dex	Under-solar	Strongly under-solar	Strongly under-solar
Ca/Fe	Solar	Solar	–	Over-solar	Mildly over-solar	–
Si/Fe	Unknown	Solar	–	Close to solar	Close to solar	Under-solar

[a]The reader should note that H models were either aimed at reproducing old ASCA data or young merger systems, hence they are not directly comparable to present-day observations (see text)

integrated optical spectra. However, in the MW bulge, that is the closest example of an old spheroid, the O abundance tracks the Mg abundance, but for the highest metallicities. Therefore we may expect that, at least in the stars, [O/Fe] is over-solar. The reported ISM [Fe/H] observational value refers mostly to gas-rich X-ray bright ellipticals.

On the observational side, there is a clear asymmetry (Renzini et al. 1993) between α-enhanced stars, and Fe-enhanced hot ISM. This is well understood in terms of SNe II which dominate the early phases in the evolution, when the stars are formed, and SNe Ia, which dominate the late time ISM abundance pattern. However the situation is not so clear-cut that all the α-elements have the same degree of enhancement (depletion) in the stars (hot ISM). The yields for each given element, as well as the recycling by low-mass single stars do play a role is shaping the abundance pattern. On the theoretical side, the GW models well reproduce the pattern in stars, whereas they predict too much Fe to be released in the hot ISM by SNe Ia. Several solutions have been put forth, and they basically tell us that what happens after the galactic wind phase is a rather complicated mixture of processes that, perhaps, cannot be captured with 1D symmetrical simulations. Hierarchical models, on the other hand, do not give satisfactory answers for the opposite problem, namely too low a predicted Fe abundance. We note here that most of these models are built on simulations in which equal mass disks mergers are not followed until a hot halo is built, or they were tuned to reproduce old ASCA data. Unfortunately nobody carried out simulations of equal mass elliptical dry-mergers aimed at studying the hot ISM. We have seen that such a mode of galaxy assembly improves the agreement between hierarchical model predictions and the observations of the [α/Fe] ratio in the stars. It would be interesting to pursue this scenario and test whether this is the case also for the predicted abundances in the hot ISM. Indeed, given the fact that observations are now mature, we call for new and more detailed modelling (in both scenarios) which feature a detailed and self-consistent chemical evolution scheme, in order not to focus on the Fe discrepancy only and fully constrain the model parameters. The examples given through this Chapter show how powerful multiple abundance ratios are to disentangle the degeneracies between model parameters, or to rule out scenarios that give similar answers to a problem. As far as the hot ISM in ellipticals is concerned, we have seen that the problem is the high predicted Fe abundance, but it might well be the galaxy formation process as a whole. For instance, both earlier monolithic and galaxy formation models were built to reproduce the mass-metallicity relation; both failed when abundance ratio ([Mg/Fe]) constraints came along. In the context of the former scenario, it was relatively easy to devise a way out, whereas in the latter scenario, even after modifications with respect to the original paradigm, the problem remains. Nonetheless it triggered a substantial revision of the assembly in the baryonic structures.

Acknowledgements This work was partially supported by the Italian Space Agency through contract ASI-INAF I/016/07/0. AP warmly thanks E.Cameron, K.Kornei for a careful reading of the manuscript, and C.Kobayashi for useful comments.

References

E. Anders, N. Grevesse, Geochim. Cosmochim. Acta **53**, 197 (1998)
N. Arimoto, K. Matsushita, Y. Ishimaru, T. Ohashi, A. Renzini, ApJ **477**, 128 (1997)
N. Arimoto, Y. Yoshii, A&A **173**, 23 1987
M. Asplund, N. Grevesse, A.J. Sauval, ASPC **336**, 25 (2005)
A.E. Athey, J.N. Bregman, ApJ **696**, 681 (2009)
J. Audouze, B.M. Tinsley, ARA&A **14**, 43 (1976)
N. Bastian, K.R. Covey, M.R. Meyer, ARA&A **48**, 339 (2010)
K. Bekki, ApJ **504**, 50 1998
K. Bekki, Y. Shioya, ApJ **513**, 108 (1999)
A.J. Benson, PhR **495**, 33 (2010)
R.G. Bower, J.R. Lucey, R.S. Ellis, MNRAS **254**, 589 (1992)
A. Bressan, C. Chiosi, F. Fagotto, ApJs **94**, 63 (1994)
F. Brighenti, W.G. Mathews, ApJ **630**, 864 (2005)
F. Brighenti, W.G. Mathews, P.J. Humphrey, D.A. Buote, ApJ **705**, 1672 (2009)
K. Bundy, S. Ellis Richard, J. Conselice, Christopher, ApJ, **625**, 621 (2005)
F. Calura, F. Matteucci, G. Vladilo, MNRAS **340**, 59 (2003)
F. Calura, A. Pipino, F. Matteucci, A&A **479**, 669 (2008)
E. Cappellaro, R. Evans, M. Turatto, A&A **351**, 459 1999
R.G. Carlberg, ApJ **286**, 403 (1984)
C.M. Carollo, I.J. Danziger, L. Buson, MNRAS, **265**, 553 (1993)
G. Cescutti, F. Matteucci, A. McWilliam, C. Chiappini, A&A **505**, 605 (2009)
C. Chiappini, F. Matteucci, R. Gratton, ApJ **477**, 765 (1997)
C. Chiosi, G. Carraro, MNRAS **335**, 335 (2002)
E. Churazov, M. Bruggen, C.R. Kaiser, H. Bohringer, W. Forman, ApJ, **554**, 261 (2001)
L. Ciotti, A. D'Ercole, S. Pellegrini, A. Renzini, ApJ **376**, 380 (1991)
L.L. Cowie, A. Songaila, E.M. Hu, J.G. Cohen, AJ **112**, 839 (1996)
T.J. Cox, T. Di Matteo, L. Hernquist, P.F. Hopkins, B. Robertson, V. Springel, ApJ **643**, 692 (2006)
R.L. Davies, E.M. Sadler, R.F. Peletier, MNRAS, **262**, 650 (1993)
G. De Lucia, V. Springel, S.D.M. White, D. Croton, G. Kauffmann, MNRAS **366**, 499 (2006)
P. Di Matteo, A. Pipino, M.D. Lehnert, F. Combes, B. Semelin, A&A **499**, 427 (2009)
S.M. Faber, E.D. Friel, D. Burstein, C.M. Gaskell, ApJS **57**, 711 (1985)
S.M. Faber, G. Worthey, J.J. Gonzalez, in IAU Symp. n.149, eds. B. Barbuy, A. Renzini, p. 255 (1992)
A. Finoguenov, K. Matsushita, H. Bohringer, Y. Ikebe, M. Arnaud, A&A **381**, 21 (2002)
D.A. Forbes, P. Sanchez-Blazquez, R. Proctor, MNRAS **361**, 6 (2005)
P. François, F. Matteucci, R. Cayrel, M. Spite, F. Spite, C. Chiappini, A&A **421**, 613 (2004)
Y. Fujita, J. Fukumoto, K. Okoshi, ApJ, **470**, 762 1996
Y. Fujita, J. Fukumoto, K. Okoshi, ApJ **488**, 585 (1997)
B.K. Gibson, MNRAS **290**, 471 1997
J.J. Gonzalez, PhD thesis, Univ. of California (1993)
G.J. Graves, S.M. Faber, R.P. Schiavon, R. Yan, ApJ **671**, 243 (2007)
L. Greggio, A&A **441**, 1055 (2005)
L. Greggio, A. Renzini, A&A **118**, 217 (1983a)
L. Greggio, A. Renzini, MmSAI **54**, 311 (1983b)
N. Grevesse, A.J. Sauval, Space Sci. Rev. **85**, 161 (1998)
Z. Han, Ph. Podsiadlowski, MNRAS **350**, 1301 (2004)
W.E. Harris, G.L.H. Harris, AJ **123**, 3108 (2002)
G. Hasinger, T. Miyaji, M. Schmidt, A&A **441**, 417 (2005)
T.M. Heckman, Extragalactic Gas at Low Redshift, ASP Conference Proceedings Vol. 254. Eds. J.S. Mulchaey & J. Stocke. San Francisco: Astronomical Society of the Pacific, p. 292 (2002)
H. Holweger, in Solar and Galactic Composition, ed. R.F. Wimmer-Schweingruber (2001)

P.J. Humphrey, D.A. Buote, ApJ **639**, 136 (2006)
P.J. Humphrey, D.A. Buote, F. Gastaldello, L. Zappacosta, J.S. Bullock, F. Brighenti, W.G. Mathews, ApJ, **646**, 899 (2006)
I. Iben Jr., A.V. Tutukov, ApJ, **284**, 719 (1984)
I. Itoh, PASJ **41**, 853 (1989)
J. Ji et al., 2009, ApJ **696**, 2252
J. Jun, A.I. Jimmy, A. Alex, N.B. Joel, J.L.-D. Edward, ApJ **696**, 2252 (2009)
G. Kauffmann, S. Charlot, MNRAS **294**, 705 (1998)
G. Kauffmann, S.D.M. White, MNRAS **261**, 921 (1993)
D. Kawata, ApJ, **558**, 598 (2001)
D. Kawata, B.K. Gibson, MNRAS **346**, 135 (2003)
S. Khochfar, A. Burkert, ApJ **597L**, 117 (2003)
D.-W. Kim, G. Fabbiano, ApJ **613**, 933 (2004)
C. Kobayashi, MNRAS **347**, 740 (2004)
C. Kobayashi, H. Umeda, K. Nomoto, N. Tominaga, T. Ohkubo, ApJ **653**, 1145 (2006)
P. Kroupa, C.A. Tout, G. Gilmore, MNRAS **262**, 545 (1993)
H. Kuntschner, MNRAS **315**, 184 (2000)
H. Kuntschner, J.R. Lucey, R.J. Smith, M.J. Hudson, R.L. Davies, MNRAS **323**, 615 (2001)
R.B. Larson, MNRAS **166**, 585 (1974)
K. Lodders, ApJ **591**, 1220 (2003)
M. Loewenstein, ApJ, **557**, 573L (2001)
M. Loewenstein, D.S. Davis, ApJ **716**, 384 (2010)
M. Loewenstein, W.G. Mathews, Proceedings of the Eighth Santa Cruz Summer Workshop in Astronomy and Astrophysics, Santa Cruz, CA. (New York, Springer, 1987), p. 96
M. Loewenstein, W.G. Mathews, ApJ **373**, 445 (1991)
F. Mannucci, M. Della Valle, N. Panagia, MNRAS **370**, 773 (2006)
F. Mannucci, M. Della Valle, N. Panagia, E. Cappellaro, G. Cresci, R. Maiolino, A. Petrosian, M. Turatto, A&A **433**, 807 (2005)
F. Mannucci, D. Maoz, K. Sharon, M.T. Botticella, M. Della Valle, A. Gal-Yam, N. Panagia, MNRAS **383**, 1121 (2008)
D. Maoz, F. Mannucci, W. Li, A.V. Filippenko, M. Della Valle, N. Panagia, MNRAS, in press., arXiv1002.3056 (2010)
A. Martinelli, F. Matteucci, S. Colafrancesco, MNRAS **298**, 42 (1998)
W.G. Mathews, F. Brighenti, ARA&A **41**, 191 (2003)
W.G. Mathews, F. Brighenti, D.A. Buote, ApJ **615**, 662 (2004)
K. Matsushita, K. Makishima, Y. Ikebe, E. Rokutanda, N. Yamasaki, T. Ohashi, ApJ **499**, L13 (1998)
K. Matsushita, K. Makishima, E. Rokutanda, N.Y. Yamasaki, T. Ohashi, ApJ **488**, L125 (1997)
K. Matsushita, T. Ohashi, K. Makishima, PASJ **52**, 685 (2000)
F. Matteucci, A&A **288**, 57 (1994)
F. Matteucci, The chemical evolution of the Galaxy, Kluwer Academic Publishers, Dordrecht (2001)
F. Matteucci, C. Chiappini, PASA **22**, 49 (2005)
F. Matteucci, L. Greggio, A&A **154**, 279 (1986)
F. Matteucci, N. Panagia, A. Pipino, F. Mannucci, S. Recchi, M. Della Valle, MNRAS **372**, 265 (2006)
F. Matteucci, A. Pipino, MNRAS **357**, 489 (2005)
F. Matteucci, R. Ponzone, B.K. Gibson, A&A **335**, 855 (1998)
F. Matteucci, S. Recchi, ApJ **558**, 351 (2001)
F. Matteucci, A. Tornambé, A&A **185**, 51 (1987)
A. McWilliam, F. Matteucci, S. Ballero, R.M. Rich, J.P. Fulbright, G. Cescutti, AJ **136**, 367 (2008)
D. Mehlert, D. Thomas, R.P. Saglia, R. Bender, G. Wegner, A&A **407**, 423 (2003)
G. Meynet, A. Maeder, A&A **381**, 25 (2002)
R.F. Mushotzky, M. Loewenstein, H. Awaki, K. Makishima, K. Matsushita, H. Matsumoto, ApJ **436**, 79 (1994)

M. Nagashima, C.G. Lacey, T. Okamoto, C.M. Baugh, C.S. Frenk, S. Cole, MNRAS **363**, L31 (2005)
K. Nomoto, M. Hashimoto, T. Tsujimoto, F.K. Thielemann, N. Kishimoto, Y. Kubo, N. Nakasato, Nuclear Physics A **A621**, 467 (1997)
R.W. O'Connell, ApJ, **206**, 370 (1976)
R.L.C. Ogando, M.A.G. Maia, C. Chiappini, P.S. Pellegrini, R.P. Schiavon, L.N. da Costa, ApJ **632**, 61 (2005)
J. Ostriker, ComAp **8**, 177 (1980)
B.E.J. Pagel, B.E. Patchett, MNRAS **172**, 13 (1975)
J.R. Parriott, J.N. Bregman, ApJ **681**, 1215 (2008)
P.J.E. Peebles, in A New Era in Cosmology, ASP Conference Series, eds. N. Metcalfe, T. Shanks, San Francisco: (Astronomical Society of the Pacific, 2002), p. 351
R.F. Peletier, R.L. Davies, G.D. Illingworth, L.E. Davis, M. Cawson, AJ **100**, 1091 (1990)
A. Pipino, C. Chiappini, G. Graves, F. Matteucci, MNRAS **396**, 1151 (2009a)
A. Pipino, A. D'Ercole, C. Chiappini, F. Matteucci, MNRAS **407**, 1347 (2010)
A. Pipino, A. D'Ercole, F. Matteucci, A&A **484**, 679 (2008)
A. Pipino, J.E.G. Devriendt, D. Thomas, J. Silk, S. Kaviraj, A&A **505**, 1075 (2009b)
A. Pipino, X.L. Fan, F. Matteucci, F. Calura, L. Silva, G. Granato, R. Maiolino, A&A **525**, 61 (2011)
A. Pipino, D. Kawata, B.K. Gibson, F. Matteucci, A&A **434**, 553 (2005)
A. Pipino, F. Matteucci, MNRAS **347**, 968 (2004)
A. Pipino, F. Matteucci, MNRAS, **365**, 1114 (2006)
A. Pipino, F. Matteucci, A&A **486**, 763 (2008)
A. Pipino, F. Matteucci, C. Chiappini, ApJ **638**, 739 (2006)
A. Pipino, J. Silk, F. Matteucci, MNRAS **392**, 475 (2009c)
A. Renzini, L. Ciotti, A. D'Ercole, S. Pellegrini, ApJ **419**, 52 (1993)
A. Renzini, ASSL **327**, 221 (2005)
E.E. Salpeter, ApJ **121**, 161 (1955)
P. Sanchez-Blazquez, D.A. Forbes, J. Strader, J. Brodie, R. Proctor, **377**, 759 (2007)
P. Sanchez-Blazquez, J. Gorgas, N. Cardiel, A&A **457**, 82 (2006)
J.M. Scalo, IAUS **116**, 451 (1986)
C. Scarlata et al., ApJS **172**, 494 (2007)
M. Schmidt, ApJ **129**, 243 (1959)
N. Scott et al., MNRAS **398**, 1835 (2009)
L. Searle, W.L.W. Sargent, ApJ **173**, 25 (1972)
P. Serra, S.C. Trager, MNRAS **374**, 769 (2007)
T. Shikui, W.Q. Daniel, MNRAS **408**, 1011 (2010)
R.J. Talbot Jr., W.D. Arnett, ApJ **170**, 409 (1971)
S. Tang, Q.D. Wang, MNRAS **408**, 1011 (2010)
R. Tantalo, A. Bressan, C. Chiosi, A&A **333**, 419 (1998)
P. Temi, F. Brighenti, W.G. Mathews, J.D. Bregman, ApJS **151**, 237 (2004)
F.K. Thielemann, K. Nomoto, M. Hashimoto, ApJ **460**, 408 (1996)
D. Thomas MNRAS **306**, 655 (1999)
D. Thomas, C. Maraston, R. Bender, Ap&SS **281**, 371 (2002)
D. Thomas, C. Maraston, R. Bender, MNRAS **339**, 897 (2003)
D. Thomas, C. Maraston, R. Bender, C. Mendes de Oliveira, ApJ **621**, 673 (2005)
D. Thomas, C. Maraston, K. Schawinski, M. Sarzi, S.-J. Joo, S. Kaviraj, S.K. Yi, IAUS **241**, 546 (2007)
B.M. Tinsley, ApJ **229**, 1046 (1979)
B.M. Tinsley, R.B. Larson, MNRAS **186**, 503 (1979)
S.C. Trager, S.M. Faber, G. Worthey, J.J. Gonzalez, AJ **119**, 1654 (2000)
S.C. Trager, G. Worthey, S.M. Faber, D. Burstein, J.J. Gonzalez, ApJS **116**, 1 (1998)
R. Valiante, F. Matteucci, S. Recchi, F. Calura, NewA **14**, 638 (2009)
G. Vladilo, A&A **391**, 407 (2002)

A. Weiss, R.F. Peletier, F. Matteucci, A&A **296**, 73 (1995)
J. Whelan, I. Iben Jr., ApJ **186**, 1007 (1973)
S.D.M. White, M.J. Rees, MNRAS **183**, 341 (1978)
S.E. Woosley, T.A. Weaver, ApJS **101**, 181 (WW95) (1995)
G. Worthey, S.M. Faber, J.J. Gonzalez, ApJ **398**, 69 (1992)
H. Xu, S.M. Kahn, J.R. Peterson, E. Behar, F.B.S. Paerels, R.F. Mushotzky et al., ApJ **579**, 600 (2002)
Y. Yoshii, N. Arimoto, A&A **188**, 13 (1987)

Chapter 7
Hot Gas Morphology, Thermal Structure, and the AGN Connection in Normal Elliptical Galaxies*

Thomas S. Statler

Abstract Quantitative morphological studies of the hot ISM in normal elliptical galaxies are in their early explorative stages. Such studies have the potential to reveal much about the mass distributions in these systems and the roles of active galactic nuclei and environmental interactions in their evolution. If the hot ISM were precisely in hydrostatic equilibrium, measurements of gas temperature, density, and morphology could reveal not only a galaxy's radial mass profile, but the shape of the total gravitating mass. However, the available evidence from *Chandra* observations indicates that this precise degree of equilibrium is not a characteristic of the general population of ellipticals. Instead, gas morphologies are seen to be nearly always disturbed; the degree of disturbance is correlated with indicators of nuclear activity and with signs of interaction with the intergalactic medium. The systems with more nuclear activity are also characterized by temperature profiles that increase outward in the main stellar bodies, at moderate radii. These correlations indicate an important, but still ambiguous, role for active galactic nuclei in determining both the thermal properties and the morphologies of the hot gas. Future progress in understanding and interpreting gas morphology will require the development of more sophisticated, and more stringently tested, quantitative measures of shape and asymmetry.

7.1 The Potential of Hot Gas Morphology

The modern generation of X-ray telescopes has given us the ability, for the first time, to resolve the distribution of X-ray sources in normal galaxies, and to begin to reveal the detailed morphology of the hot ionized interstellar plasma. To put our

*Editor's note. The next chapter by Buote and Humphrey presents a different viewpoint on the issue of hydrostatic equilibrium. We ask readers to carefully consider the two different positions.

T.S. Statler (✉)
Astrophysical Institute, Ohio University, Athens, OH, 45701, USA
e-mail: statler@ohio.edu

D.-W. Kim and S. Pellegrini (eds.), *Hot Interstellar Matter in Elliptical Galaxies*,
Astrophysics and Space Science Library 378, DOI 10.1007/978-1-4614-0580-1_7,
© Springer Science+Business Media, LLC 2012

present state of knowledge in context, some historical perspective is in order. Optical studies of elliptical galaxies began in the 1920s with Hubble (1926) classification of "extragalactic nebulae" from images on photographic plates. In the following decades, photographic surface photometry yielded not only the famous "$r^{1/4}$ law", but the first isophotal shape profiles, which confirmed the visual impression that elliptical galaxies are, in fact, quite precisely elliptical. With the advent of CCDs in the 1980s, precision isophotal analyses became possible. Several groundbreaking studies (for example, Lauer 1985b,a; Jedrzejewski 1987) probed the detailed surface brightness profiles at small and large radii, as well as the deviations from exact isophotal ellipticity. These isophotal deviations were seen to correlate systematically with luminosity and with dynamical properties – most notably the degree of rotational support, v/σ (Bender et al. 1989). After substantial theoretical and numerical follow-up, we now understand that the detailed morphological properties of the starlight in normal ellipticals can actually be indicators of formation and evolution, particularly of these systems' recent merger histories (Naab et al. 1999).

In this context, it is good to remember that a 50 ks *Chandra* observation of a normal elliptical results in roughly the same signal-to-noise ratio as a 10 s V-band exposure on a 1-m optical telescope with a 1970s-era photographic plate. Quantitative morphological studies of the hot ISM still have a long way to go to reach maturity, and the physical interpretation is far from clear-cut. We have just begun to see that in X-rays, elliptical galaxies are often *not* elliptical; the asymmetrical deviations are frequently not small. And we have only the initial clues as to what the substantial differences between X-ray and optical morphology may be telling us.

The implications of gas morphology would be clearest if the gas were in hydrostatic equilibrium. In this case, the gas density ρ, pressure P, and the total gravitational potential Φ would be connected by the relation

$$\nabla P + \rho \nabla \Phi = 0, \tag{7.1}$$

providing a means to convert observational determinations of gas density and pressure into constraints on the potential, and thereby also on the mass distribution in the galaxy. The seeming cleanliness of this route to mass measurement is too attractive to ignore, especially in comparison with stellar dynamics approaches, where systematic effects due to anisotropy in the stellar velocity distribution are difficult to overcome.

There is good physical reason to expect that the gas in most normal galaxies is not very far from hydrostatic. Since the gas is observed to be close to the virial temperature, the sound speed is on the same order of magnitude as the stellar velocity dispersion. If the gas were significantly over- or under-pressured, one would expect it to expand or contract and find a new equilibrium on roughly the sound crossing time, which is of order the dynamical time. The fact that the stellar component of most ellipticals is not severely disturbed implies that any global perturbations are more than several dynamical times old, and that the gas, responding on the same time scale as the stars, should be comparably relaxed.

This simple argument neglects the important possibility that local perturbations – for example, from AGN – could influence the gas over shorter time scales; nonetheless it encourages optimism that masses obtained from X-ray data may be reasonably accurate. A standard approach is to average observations over radial bins and analyze the system as if it were spherically symmetric, in the hope that this strategy will reduce the influence of small-scale hydrodynamic disturbances.

If one assumes a spherical, hydrostatic galaxy, in which the gas is supported entirely by thermal pressure, one can ignore the vector (actually, tensor) nature of equation (7.1). Under this assumption, $\nabla P = dP/dr$ and $\nabla \Phi = GM(r)/r^2$, where $M(r)$ is the total gravitating mass enclosed with a distance r of the galaxy center. In normal galaxies (unlike in galaxy clusters), the hot plasma makes an insignificant contribution to the total mass, so in principle the mass profile could be obtained from the deceptively simple prescription

$$M(r) = -\frac{r^2}{G\rho}\frac{dP}{dr}. \tag{7.2}$$

In practice the density and temperature can be obtained from fits to the observed spectrum, deprojecting the emissivity assuming spherical symmetry, and adopting a cooling function $\Lambda(Z, T)$ that depends on metallicity Z and temperature. If the pressure is entirely thermal, then $P = \rho kT/\mu m_p$ (where μ is the mean particle mass in units of the proton mass m_p), and one has everything one needs to solve for $M(r)$ directly. The obstacle to doing so is that differentiating any realistic data set to obtain dP/dr is bound to amplify observational errors and produce an unphysical mass profile. As a result, a wide range of strategies have evolved to fit spherical mass models to X-ray data; these techniques and the results obtained from them are reviewed in detail in the chapter by Buote and Humphrey in this volume.

If one knew that *all* hydrodynamic disturbances were absent and that the gas were truly hydrostatic, then one could go substantially further, as shown by Buote and Canizares (1994). Equation (7.1) says that in this case the gradients of P and Φ would be everywhere antiparallel to each other, implying that the surfaces of constant P would also be surfaces of constant Φ. Taking the curl of the equation yields $\nabla\rho \times \nabla\Phi = 0$, which similary implies that surfaces of constant Φ would be surfaces of constant ρ. Thus P would have to be expressible as a function of $\rho, P = P(\rho)$. This, along with the ideal gas law, would guarantee that $T = T(\rho)$. For a given metallicity, the volume emissivity is a function of density and temperature, and therefore the X-ray emissivity would be stratified on surfaces of constant gravitational potential. This potentially powerful result[1] suggests that the projected shape of the total mass distribution could be inferred from the shapes of the X-ray isophotes, *if* the metallicity could be described by $Z = Z(\rho)$, a function of density alone, and *if* precise hydrostatic equilibrium held.

Clearly, the degree to which the hot ISM is genuinely hydrostatic is key to our ability to tease the detailed distribution of mass from X-ray observations.

[1] Pun unavoidable.

Though there are good reasons to think that most systems are not very far from hydrostatic, there are equally good reasons to expect that they are not terribly close to hydrostatic, either. This stems from the array of physical processes known to be playing a role in early-type galaxies, including:

- *Galaxy interactions.* Nearly all normal ellipticals are in group or cluster environments. Even in the absense of mergers, the episodic time-varying gravitational perturbations produced by passing systems ("galaxy harassment") can keep a system out of equilibrium when the characteristic time between interactions is not much larger than the sound crossing time.
- *Ram pressure.* Motion of a galaxy, at speed v, through an ambient intergalactic medium (IGM) of density ρ generates a ram pressure at the leading face on the order of ρv^2. In a rich cluster where the velocity dispersion of cluster members may be an order of magnitude higher than their internal stellar dispersions, ram pressure can rival thermal pressure even where the ISM density is 2 orders of magnitude above that of the IGM.
- *AGN outbursts.* Powerful AGN clearly create disturbances in, and may dominate the heating of, the hot IGM in galaxy clusters. There are compelling indications, as we will see below, in individual galaxies of interaction between AGN-created radio jets and the X-ray emitting plasma. Given the much larger abundance of lower luminosity AGN compared to higher, we should expect a substantial population of systems that are only mildly disturbed, below the observational threshold where the disturbances are conspicuous.

Thus, the physically motivated suspicion that internal and/or external influences may cause a certain degree of disequilibrium in normal galaxies should motivate us to look for ways of verifying whether these systems are precisely hydrostatic. We will see in this chapter that, according to the available tests, the general population of normal ellipticals is not – even though some individual systems may be close. If this is so, the natural next question is how hot gas morphology may be used, not as a probe of the mass distribution, but rather as a probe of galaxy environments and AGN physics.

7.2 Hot Gas Morphology in the Pre-Chandra Era

Genuine morphological studies were all but impossible with the *Uhuru* satellite. While a trailblazing project for X-ray astronomy, *Uhuru* was a scanning (as opposed to imaging) observatory with an angular resolution limited to only half a degree, and could only marginally resolve the largest galaxies in the Virgo Cluster (Kellogg et al. 1971). Its successor, the *Einstein* observatory, carried two primary instruments useful for extended sources: the Imaging Proportional Counter had an angular resolution of $\sim$ 1 arcminute; the High Resolution imager had an angular resolution some 30 times better, but an effective area one-tenth as large. Naturally, more was learned about the radial profiles of the X-ray emission at larger radii than about

detailed morphologies. Strong indications of environmental effects began to appear, both in galaxy groups within rich clusters, and in individual systems. One of the clearer examples was the observation of NGC 4472 by Trinchieri et al. (1986). The authors noted "significant asymmetry in the X-ray map [that is] totally uncorrelated with the stellar distribution." Later observations with *ROSAT* and *Chandra* would show this to be a frequent characteristic of elliptical galaxies. The fact that, in NGC 4472, the mismatch in the X-ray and optical morphologies appeared at large radii suggested to the authors that the former "could be explained if the galaxy is moving with respect to the intergalactic gas." Galaxy environment was clearly seen as being an important influence on morphology a quarter-century ago, and it was obvious, at least in this luminous galaxy, that "present X-ray data do not warrant [an assumption of] hydrostatic equilibrium at large radii." (Trinchieri et al. 1986)

One of the more enduring legacies of the *Einstein* era was the popularization of the *beta model*. This model has been so widely used for fitting the radial surface brightness profiles of both galaxies and galaxy clusters that a quick review of its origin and meaning are in order. In its original form (which actually predated the launch of *Einstein*), the beta model (Gorenstein et al. 1978) was founded on one ad-hoc theoretical assumption and one empirical observational fact. The assumption was that, in a spherical cluster of galaxies, the gas and galaxies could each be considered isothermal, in which case the volume density of the gas and of the galaxies would each be an exponential function of the potential:

$$\rho_{\rm gas} \propto e^{-\Phi/(kT/\mu m_p)}, \qquad \rho_{\rm gal} \propto e^{-\Phi/\sigma^2}, \tag{7.3}$$

where σ is the 1-dimensional velocity dispersion of the galaxies. The empirical fact was that galaxy counts in Coma could (at the time) be adequately fitted by the simple model

$$\rho_{\rm gal} \propto \left[1 + \left(r^2/r_c^2\right)\right]^{-3/2}, \tag{7.4}$$

where r_c is the "core radius" of the cluster. As a result one can immediately write

$$\rho_{\rm gas} \propto \left[1 + \left(r^2/r_c^2\right)\right]^{-3\beta/2}, \tag{7.5}$$

where $\beta \equiv \sigma^2 \mu m_p / kT$ is the ratio of the dynamical temperatures of the galaxies and the gas. Since the X-ray volume emissivity is proportional to the square of the density, one can quickly project this model and obtain the surface brightness S as a function of projected distance R from the center,

$$S(R) \propto \left[1 + \left(R^2/r_c^2\right)\right]^{-3\beta+1/2}. \tag{7.6}$$

By modern (which is to say, current) standards, this derivation is a bit of a cheat because it completely sidesteps the nature of the potential, in which both galaxies and gas are presumed to be confined. One way to give the beta model a more

physical basis[2] is to postulate a logarithmic potential with a core:

$$\Phi = \left(V_c^2/2\right) \ln\left[1 + \left(r^2/r_c^2\right)\right], \tag{7.7}$$

where V_c is the asymptotic circular velocity. Hydrostatic, isothermal gas in this potential takes on the density profile of equation (7.5) if one defines $\beta \equiv V_c^2 \mu m_p / 3\,kT$. Now, β expresses the ratio of the dark matter temperature ($\sigma_{\rm DM}^2 = V_c^2/2$) to the gas temperature. The two formulations of the model are equivalent if $\sigma_{\rm gal} = (2/3)^{1/2}\sigma_{\rm DM}$ – reasonable, since we expect the galaxies, which formed through dissipative processes, to be colder than the collisionless dark matter.

The *ROSAT* observatory exceeded *Einstein* in sensitivity by a factor of roughly two. With an angular resolution slightly under 5″ on-axis, X-ray morphology in the vicinity of, and beyond, the optical effective radius could finally be revealed for some of the more luminous systems, and surface brightness profile fits for a large number of ordinary galaxies could be derived. Values of β obtained from profile fits were found to be typically in the vicinity of 0.5–1.0 (O'Sullivan et al. 2003), indicating asymptotic gas density profiles between $r^{-3/4}$ and $r^{-3/2}$. Note that these gas profiles are typically (thought not always) much shallower than stellar density profiles, which fall generally between r^{-3} and r^{-4} at large radii. In fact, fitted beta models are often asymptotically divergent, formally (and, of course, unrealistically) implying infinite gas masses at large radii. This difference indicates that the gas, if approximately hydrostatic, is dynamically hotter than the stars. Purely dynamical heating of gas lost by ordinary stellar evolution (e.g., by colliding stellar winds) is not sufficient to explain the extended gas distribution.

7.3 Glimpses of Morphology in the Early Days of Chandra

Some of the earliest normal ellipticals observed by *Chandra* were, not surprisingly, already well-studied systems that were known from earlier *Einstein* and *ROSAT* studies to be "interesting." These observations were reported in several "one-off," detailed examinations of individual X-ray-luminous systems. Two of these studies, in particular, had a major impact on the field, alerting many to the importance of interactions between radio sources and the hot ISM, and of disequilibrium in the latter. The most conspicuous of these interactions is in NGC 4374 (Fig. 7.1a). Based on the spatial correspondence between the radio lobes and local minima in the X-ray emission, Finoguenov and Jones (2001) reasonably conjectured that "expansion of the radio lobes has caused the hot gas to have the H-shaped structure." Estimating the pressure inside and outside the lobes, they concluded that the lobes are in approximate pressure equilibrium with their surroundings and therefore the morphological disturbances seen in X-rays are not the result of strong shocks being

[2]For a more sophisticated approach, see Capelo et al. (2010).

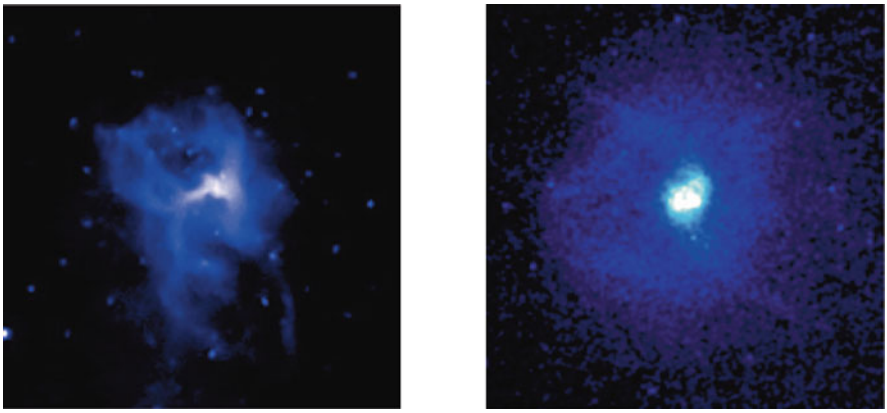

Fig. 7.1 (**a**) (*left*): *Chandra* image of NGC 4374 (Finoguenov and Jones 2001) showing prominent cavities in the diffuse X-ray emission that are filled by, and in pressure equilibrium with, radio lobes. (Image credit: NASA/CXC/MPE/A. Finoguenov et al.) (**b**) (*right*): *Chandra* image of NGC 4636 (Jones et al. 2002) showing sharp-edged structure consistent with shock models. (Image credit: NASA/SAO/CXC/C. Jones et al.), see the electronic version for a color version of this figure

driven into the ISM. A contrasting view of a radio source-ISM interaction is seen in the observations of NGC 4636 (Jones et al. 2002) which show a curious S-shaped structure (Fig. 7.1b). Because of the sharp edges of these features and the elevated temperatures measured in the brighter part of the S, the authors concluded that the structure is produced by shocks, and suggested a history of symmetric but off-center outbursts from an AGN. They speculate that this phase is "part of a cycle in which the cooling gas... fueled a nuclear outburst... reheating the cooling gas and... temporarily starving the central AGN."

However, these observations were of X-ray luminous systems with comparatively powerful central radio sources. It was well known by this time, primarily from *ROSAT* surveys, that most normal ellipticals are not as luminous. Since the days of *Einstein*, a great deal of effort had focused on the $L_X - L_B$ diagram (see the chapter by Fabbiano in this volume) and the origin of the large scatter exhibited by normal galaxies. One expression of this scatter is that the optical luminosity of a galaxy is not a good predictor of its X-ray luminosity – a fact that we will see echoed in optical and X-ray morphologies. In addition to the scatter, there is a change in the slope of the mean trend, occurring around $L_X \sim 10^{40}\,\mathrm{erg\,s^{-1}}$, which has long been suspected of marking the transition from hot-gas-dominated systems to stellar-source-dominated systems.

In this context, the *Chandra* observation of the rather unremarkable – but nearby – galaxy NGC 4697 (Sarazin et al. 2000, 2001) was a watershed. The unprecedented angular resolution of *Chandra* permitted some 80 low-mass X-ray binaries (LMXBs) to be resolved, conclusively demonstrating that the majority of the X-ray emission from X-ray-faint ellipticals comes from these stellar objects and not from the diffuse ISM. Later studies (Diehl and Statler 2007) confirmed that the

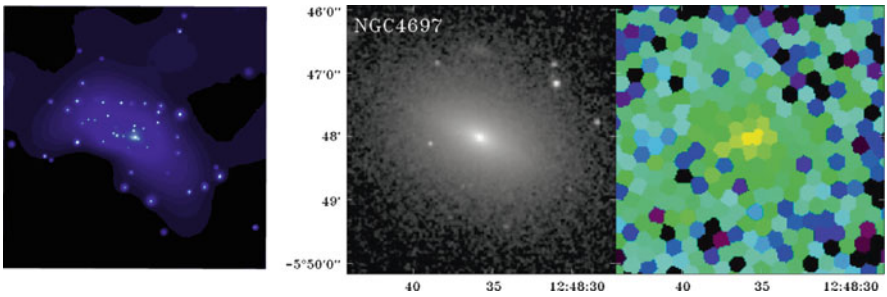

Fig. 7.2 (**a**) (*left*): Adaptively smoothed *Chandra* image of NGC 4697 (Sarazin et al. 2000) showing a suggestive "L-shaped" morphology in the diffuse emission at large radii. (Image credit: NASA/CXC/UVa/C. Sarazin et al.) (**b**) (*right*): Near-infrared 2MASS (*left*) and adaptively-binned *Chandra* (*right*) gas-only image of NGC 4697, on the same scale, reproduced from (Diehl and Statler 2007). After removal of both resolved and unresolved LMXB contributions, the L shape is no longer statistically significant

fraction of the X-ray emission in X-ray faint ellipticals coming from LMXBs can be as large as 100%. In NGC 4697, the morphology of the residual diffuse emission was examined qualitatively by Sarazin et al. (2001) from adaptively smoothed images. Their conclusion was that the emission attributed to gas is generally rounder than the optical starlight, but takes on an "L-shaped" appearance at larger radii (Fig. 7.2a). They speculated that this latter morphology might be due to ram-pressure effects, but were not able to assess the statistical significance of the L shape itself.

The relative flattenings of the optical and X-ray isophotes are of prime importance if one believes that – or wants to test whether – the X-ray emissivity can trace the shape of the gravitational potential. This important possibility had been raised initially by Buote and Canizares (1994) in the case of NGC 720, using *ROSAT* data. These authors argued that, even though the X-ray emission in this system is rounder than the stellar light, it is flatter than the potential that would be generated by the stellar mass, implying the existence of a highly flattened dark halo which makes the total potential as flat as the observed X-ray isophotes. The inital conclusion was relaxed somewhat with the later addition of *ASCA* and *Chandra* data, which permitted correction for unresolved stellar sources (see below, Buote et al. 2002). Nonetheless, as the implications for dark matter physics could be cosmologically game-changing, verifying whether the "geometrical test for dark matter" is reliable for this and other systems is clearly important.

A counterargument was made by Statler and McNamara (2002) in the case of NGC 1700. Here the maximum measured X-ray ellipticity ($\epsilon_X = 0.65$) exceeds not only that of the starlight, but that of any potential generated by any astrophysically realistic mass distribution. The authors conjectured that this difference could signal a dynamically significant rotation in the hot ISM. As in the case of NGC 720, the initial conclusion was subsequently softened after a more sophisticated analysis (Diehl and Statler 2007); but the result again highlighted the urgent need for a careful examination of whether the exact hydrostatic equilibrium needed for the "geometrical test" actually holds in the general population.

7.4 Results from Chandra Archival Studies

A major obstacle in studying the hot ISM in normal ellipticals is that only a fraction – sometimes a small fraction – of the X-ray emission comes from hot plasma, and so revealing its morphology requires separating this emission from that due to stellar sources. This is quite unlike the situation in galaxy clusters, where the gas emission completely overwhelms stellar sources because gas masses exceed stellar masses by orders of magnitude. In normal ellipticals, the observable gas typically amounts to only a few percent of the stellar mass. The *Chandra* observations of NGC 4697 demonstrated that some of the stellar emission can be resolved into discrete sources. But these resolved sources represent only the bright end of a broad luminosity function. Unresolved sources blend into the diffuse emission and masquerade as gas. If not corrected, this will tend to make the gas distribution more closely resemble the stellar distribution.

The key to making this separation is that the spectrum of the hot ISM and the spectrum of stellar sources are not the same. Observations of resolved LMXBs (Irwin et al. 2003; Diehl and Statler 2007) indicate a "universal" power-law with a photon spectral index around 1.6. Naturally, this is known only for the bright end of the luminosity function, but there is no evidence for a strong variation of the spectrum with source luminosity. *ASCA* spectra of NGC 720 allowed Buote et al. (2002) to perform a two-component spectral fit, and estimate the overall contribution from gas and LMXBs. These authors then assumed that the LMXB distribution followed that of the overall starlight, and subtracted from the diffuse *ROSAT* image an appropriately scaled model for the unresolved stellar sources. The resulting gas-only image was isophotally rounder than the uncorrected image (since the stellar isophotes are flatter than the X-rays), somewhat weakening the earlier halo flatness estimate (Buote and Canizares 1994).

A more general, and less model-dependent, approach to obtaining the gas-only morphology was developed by Diehl and Statler (2007). This approach exploits the ability of X-ray imagers to record individual photon energies, which permits the construction of arbitrary-bandpass images in the reduction stage. To understand the basics, assume that one has already extracted a hard-band image, H, and a soft-band image, S, of the galaxy, calibrated both of them, and removed the resolved sources by standard techniques. The full-band image (the union of the soft and hard bands) is composed of a contribution from gas, G, and a contribution from unresolved stellar sources, U. Because the spectra of the two contributions differ, the soft- and hard-band images are different linear combinations of G and U:

$$S = \gamma U + \delta G, \tag{7.8}$$

$$H = (1-\gamma)U + (1-\delta)G, \tag{7.9}$$

where γ and δ are the *softness ratios* (soft band to total band) of the unresolved sources and gas, respectively. Equation (7.8) is a linear system which is trivially solved for the gas contribution:

$$G = \frac{1-\gamma}{\delta-\gamma}\left(S - \frac{\gamma}{1-\gamma}H\right). \tag{7.10}$$

Thus a gas-only image can be constructed from a suitably scaled difference of the hard and soft images. In its simplest form, this approach assumes that γ and δ are spatially constant. Strictly speaking this is not true because gas temperatures are not uniform, and the stellar source population could vary, say, with galactocentric distance; but in practice, the resulting morphologies are not affected by typical variations in these ratios. This approach is less model-dependent than the strategy of Buote et al. (2002) in that there is no need to assume that the unresolved sources follow the starlight. There is evidence that higher luminosity LMXBs are found preferentially in globular clusters, whose distributions are more extended than the main stellar bodies of the galaxies (Kim et al. 2009, and references therein), although whether the overall LMXB contribution may still follow the stellar halo light is still an open issue (Kim et al. 2006).

This separation technique was used by Diehl and Statler (2007) to produce a "gas gallery" of 54 normal ellipticals from data in the *Chandra* archive. Representative results are shown in Fig. 7.3, ordered by decreasing optical luminosity, top to bottom. The gas images are *adaptively binned* rather than smoothed, using the Weighted Voronoi Tesselation (WVT) algorithm (Diehl and Statler 2006) described in Sect. 7.5 below. The WVT algorithm guarantees bins that are always convex (or nearly so) and not linked to a coordinate system – an advantage in interpretation since the bin geometry does not lead the eye. The images have a uniform signal-to-noise ratio of 4 per bin, except in the outer regions where a maximum bin size is imposed. It is obvious by inspection that not only is optical luminosity a poor predictor of X-ray gas luminosity, optical morphology is an even *worse* predictor of X-ray morphology!

It can, at first glance, seem disappointing that gas-only images tend to have lower signal-to-noise ratio than simple, adaptively smoothed, broad-band images, which have often been used to infer gas morphologies (for example, Fig. 7.2a). But this is a predictable statistical consequence of removing the contamination of unresolved sources. A high S/N image is hardly informative if, say, 70% of the signal is not from gas. The effect on what one can infer about gas morphology can be significant, as can be seen in the adaptively binned gas-only image of NGC 4697 (Fig. 7.2b, right). After removing the unresolved source contribution, the putative "L-shape" becomes statistically insignificant. Nonetheless, the separation approach is limited. When gas temperatures approach 1.5 keV, the softness ratio (in the optimal *Chandra* bands) matches that of the LMXBs, and a two-band separation fails. Fortunately, most normal galaxies are cooler than this. The approach also does not account for other stellar sources, such as chromospherically active binaries and catalysmic variables, whose spectra may be very similar to that of the diffuse gas, and whose contribution may be important in extremely gas-poor systems (Boroson et al. 2010).

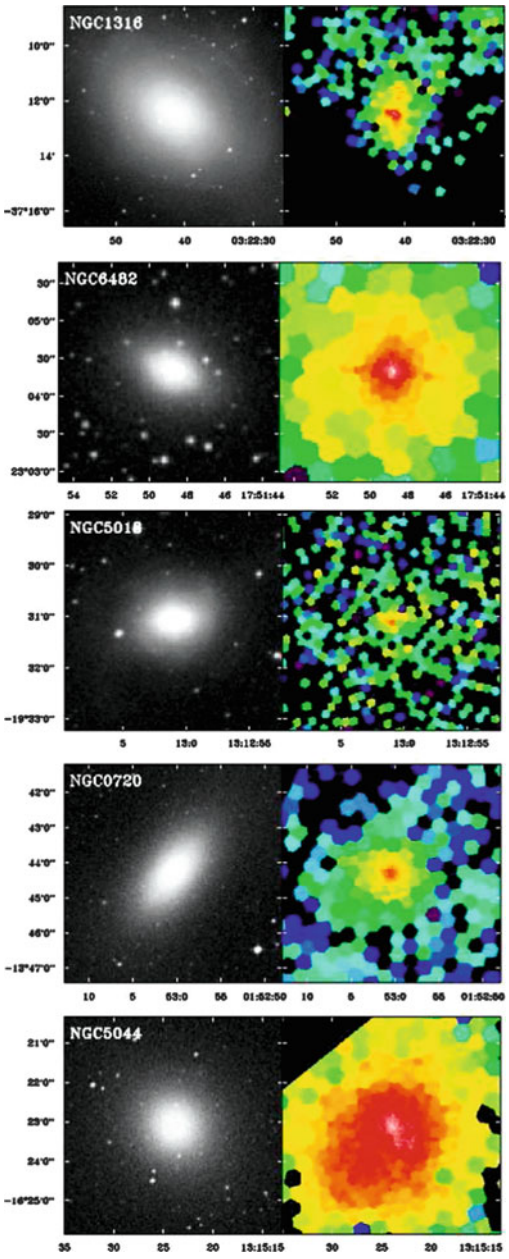

Fig. 7.3 Optical DSS (*left*) and X-ray gas-only (*right*) images of representative normal ellipticals from the *Chandra* archive sample of Diehl and Statler (2007). Each image has a physical width of 50 kpc. Systems are ordered from top to bottom by decreasing optical luminosity, spanning a factor of 3. Note the wide range in gas luminosities at comparable optical luminosities, and the dissimilarity in stellar and gas morphologies. (Figures reproduced from Diehl and Statler (2007))

7.4.1 How Exact is Hydrostatic Equilibrium?

Chandra's combination of angular resolution and effective area made it possible for the first time to quantitatively study the gas morphology *well within the main stellar bodies* of many normal galaxies. This is critical because extensive stellar dynamical as well as gas dynamical modeling have established that the mass-to-light ratios in these regions are only of order a few, in solar units, implying that the mass is strongly stellar dominated and dark matter contributes little to the local potential (Mamon and Lokas 2005; Humphrey et al. 2006, and references therein). Since the bulk of the mass is visible, comparison of X-ray and optical isophotes at the same radii could finally provide a statistical test for whether the precise degree of equilibrium needed to be able to infer dark halo shapes from the X-ray isophotes is a general property normal ellipticals.

Though complex in practice, the test is simple intuitively. If the population is characterized by precisely hydrostatic gas, the isophotal ellipticities of the gas emission and the starlight should be correlated. The logical contrapositive is that if there is no such correlation, then precise hydrostatic equilibrium is not a characteristic of the population. In practice, one must model projection and orientation effects and assess the effects of different plausible dark halo models; but the logic remains the same.

Measuring the isophotal ellipticities, ϵ_X, of the gas X-ray emission is far from trivial; but we will ask the reader to accept for the moment that it is possible, and defer discussion of the important technical details to Sect. 7.5. To effect the test, profiles of ϵ_X were measured by Diehl and Statler (2007) for 24 galaxies in their archive sample with enough detected photons to permit the analysis, and compared with optical ellipticities $\epsilon_{\rm opt}$ from the literature. Both quantities were averaged over a radial range extending between 0.6 and 0.9 of the J band effective radius; this range was chosen based on the extent of the data, in order to include the largest possible number of galaxies in the analysis. The result of this comparison is shown in Fig. 7.4. Very roughly, from simple models one would expect to see a linear correlation with a slope around $1/3$ if the gas were always hydrostatic in the stellar potential. Instead, ϵ_X and $\epsilon_{\rm opt}$ are *uncorrelated.* To assess the dynamical implications, Diehl and Statler (2007) constructed several thousand 24-object samples composed of simulated systems containing hydrostatic gas, incorporating a wide variety of dark halo models, and calculated the probability of obtaining a correlation as weak as, and a mean ϵ_X as large as, those seen in the real data. The conclusion was that nearly all hydrostatic models are ruled out at $> 99\%$ confidence. Those that are not are models in which the shape of the halo has nothing whatsoever to do with the shape of the luminous galaxy, *and* in which the halo either strongly dominates the stellar mass inside the effective radius or is prominently cigar-shaped; all of these alternatives are in conflict with well established observational or theoretical results.

Thus, even though the gas in normal ellipticals may be, on average, close enough to hydrostatic that reasonable radial mass profiles can be derived under

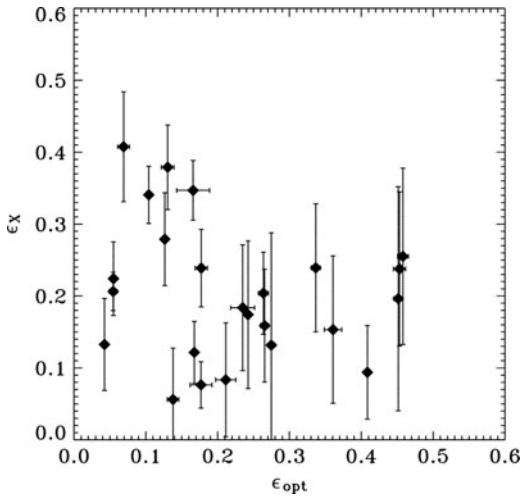

Fig. 7.4 Isophotal ellipticity of the X-ray gas, ϵ_X, vs. that of the stars, $\epsilon_{\rm opt}$, for 24 ellipticals in the *Chandra* archive, reproduced from Diehl and Statler (2007). Note the absence of any correlation, contrary to what would be expected if precise hydrostatic equilibrium in the stellar potential were a general property of the population

the assumption of equilibrium, the available evidence does *not* indicate that exact hydrostatic equilibrium is a general property of the population. Some systems may be truly hydrostatic, but we have no objective test that will identify them a priori.[3]

It is critically important to clearly understand the logical basis and statistical meaning of this conclusion. To reiterate the earlier point, we know that *if* the population is characterized by precisely hydrostatic gas, the stellar and X-ray gas isophotal ellipticities should be correlated. Given now the observational absence of such a correlation, the proper conclusion is that *precise hydrostatic equilibrium is not a characteristic of the population.* It is tremendously tempting to try to salvage, perhaps, a precisely hydrostatic sub-population from the data. Indeed, if one simply removed the galaxies in Fig. 7.4 with low $\epsilon_{\rm opt}$ and high ϵ_X and labeled them as "unusual," one could easily manufacture a sub-population having the desired correlation, which one could then label as precisely hydrostatic – couldn't one? But this would be a logical fallacy and a gross misuse of the data. Consider this toy analogy to illustrate the point: a school teacher, Ms. Smith, is accused by a parent of giving extra help to taller children. As a test, the principal checks for a correlation between students' test scores and their heights. She finds no correlation, and correctly concludes that the data do not support the charge of height bias. The parent, however, is unconvinced, and argues, "My child is short and gets bad grades, and my neighbor's child is tall and gets good grades." The principal points out that there are short students who are getting high scores and tall students who are getting low scores in Ms. Smith's class, but the parent is still not satisfied. "Those children are obviously special cases. If you leave them out there is clearly

[3] Buote and collaborators have inaccurately represented the results described in this section and in Sect. 7.4.5, both in refereed papers and in their chapter in this volume. Readers should consult the original sources and treat *straw man* arguments appropriately.

a correlation, which proves that my child has been discriminated against!" The parent's unfortunate mistake is that he is "cherry-picking" the data to show a desired result, and to suggest a causality that is not supported by the whole sample. This is wrong. In the same sense, one cannot pick a subset of galaxies chosen to follow a desired correlation which is not present in the full sample, and then claim that the existence of such a subset proves that the correlation is real and that these chosen systems have physical properties that would have been implied had the correlation actually existed. This does *not* mean that there are no truly hydrostatic galaxies. It means that whether a particular galaxy is or is not hydrostatic cannot be judged solely by a comparison of its X-ray and optical isophotes, in the same way it cannot be judged whether a particular child in Ms. Smith's class was or was not discriminated against based solely on a comparison of his height and test scores. One cannot draw conclusions as to the nature of individual objects based on their distance from an expected mean trend that is not there.

In one way, this is a disappointing outcome, since it closes off the geometrical route to dark halo shapes – at least until such as time as we have an objective test that will identify genuinely hydrostatic systems. But in the meantime, it opens the door to deeper discussion. If gas morphology is *not* determined solely by the potential, what else is responsible?

One option is net rotation in the gas. This possibility was raised by Statler and McNamara (2002) specifically in connection with NGC 1700. Earlier, however, Hanlan and Bregman (2000) had examined this issue in a different context. A large fraction of the X-ray emitting gas is thought to come from ordinary stellar mass loss, and should therefore retain the angular momentum of the stars. In a standard scenario in which gas gradually cools and settles to smaller radii, conservation of angular momentum should lead to the formation of a rotationally flattened "thick disk" of hot gas at small radii (Brighenti and Mathews 1996). Using a small *ROSAT* and *Einstein* sample, Hanlan and Bregman (2000) found no evidence for a systematic inward flattening. This result was confirmed by Diehl and Statler (2007), who also looked for a correlation between ϵ_X and stellar v/σ (the ratio of mean rotation velocity to velocity dispersion) and found none. So it seems unlikely that rotation is responsible for the large dispersion in ϵ_X seen in Fig. 7.4.

7.4.2 The Morphology-AGN Connection

Isophotal ellipticities are by no means the only, or most important, morphological property that can be quantified. Remember that tremendous insight was gained by detailed study of optical isophotes and their deviations from perfect ellipses. In the X-ray, we see that distortions in the gas isophotes are often asymmetric at both the small and large scales (Figs. 7.1 and 7.3). We fully expect that interactions with the IGM or with neighboring systems could produce large-scale asymmetry. We also anticipate that many normal galaxies may contain "bubbles" or "cavities," similar to those seen in galaxy clusters, but of sufficiently low contrast that they are simply

not discernable in the low signal-to-noise conditions that we are forced to confront in typical observations.

Recognizing that the problem of detecting substructure under these conditions is a statistical one, Diehl and Statler (2008b) defined an *asymmetry index*, η (for details see Sect. 7.5) that measures the mean square fractional deviation from the best fit symmetric, elliptical-isophote model, in excess of what would be expected from statistical fluctuations. They showed through tests with simulated images containing low-contrast cavities that η measures gas asymmetry in an unbiased way, and is relatively unaffected by non-morphological properties (signal-to-noise, resolution, binning, etc.) of the data. This quantity was measured for 34 objects with sufficient signal for isophotal fits to be done. Diehl and Statler (2008b) then searched for significant correlations of η with other galaxy properties. No correlation was found with any of the usual optical or stellar kinematic properties, nor with X-ray luminosity. A weak, marginally significant correlation was found with the number density of neighboring galaxies. But the most significant correlations were found with two independent measures of AGN luminosity – the 20 cm radio continuum luminosity and the X-ray luminosity of the central point source – and with the logarithmic gas temperature gradient measured at large radii, between 2 and 4 optical effective radii.

This remarkable result is illustrated in Fig. 7.5. The plot on the left shows the correlation with radio power, a proxy for AGN luminosity. Note that this correlation is not caused merely by a few highly disturbed systems with conspicuous AGN, but is really a continuous trend, extending all the way down to the faintest radio sources detected in the NVSS survey.[4] The plot on the right shows the correlation with the outer logarithmic gas temperature gradient. In each case, points are colored according to the value of the unplotted third variable, with which the residuals are correlated in roughly equal measure.

The interpetation is that the gas morphology tends to be more asymmetrically disturbed when (1) the central radio source is more powerful or (2) when the gas temperature is rising at large radii. The first is clear indication of local, internal effects, specifically from an AGN. Since the same correlation is seen with the central X-ray source luminosity, black hole accretion is the probable power source. The second is clear indication of an environmental effect – though not of galaxy–galaxy interactions specifically, as only weak correlation is seen with the density of neighboring systems. A rising gas temperature at large radii is suggestive of a transition to an intracluster or intragroup medium, and so the correlation between asymmetry and outer gradient most likely indicates distortions caused by ram pressure.

[4]The most powerful radio sources in Fig. 7.5a are comparable in luminosity to the *median* Fanaroff-Riley class I sources in the Combined NVSS-FIRST Galaxies (CoNFIG) survey (Gendre et al. 2010).

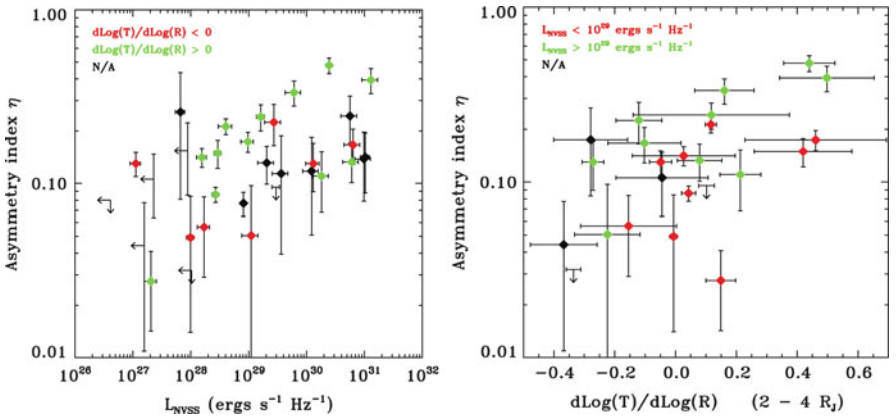

Fig. 7.5 *Left*: Correlation between asymmetry index η and radio luminosity $L_{\rm NVSS}$. *Red and green* points respectively indicate negative (outwardly falling) and positive (outwardly rising) outer logarithmic gas temperature gradients, α_{24}, measured between 2 and 4 optical effective radii. *Right*: Correlation between η and the outer logarithmic gas temperature gradient, α_{24}. *Red* points indicate lower, and *green* points higher, radio luminosity. In both plots, residuals from the mean relation are correlated with the third variable (Figures reproduced from Diehl and Statler (2008b))

7.4.3 Thermal Structure

With more than a quarter-century of resolved X-ray observations of galaxy clusters with "cool cores" – formerly called "cooling flows" – we are accustomed to seeing the characteristic, outwardly rising temperature profile of these massive systems. Positive radial temperature gradients are nearly ubiquitous in galaxy clusters, X-ray groups, and massive ellipticals, and are generally understood as resulting from efficient radiative cooling in the dense central regions, where cooling times can drop well below 100 Myr. By contrast, the recognition that the thermal structure of lower-mass normal galaxies is often *not* like that of clusters or groups is more recent. The existence of galaxies with outwardly falling temperature profiles was noted only midway through the previous decade (Khosroshahi et al. 2004, Randall et al. 2006, Fukazawa et al. 2006, Humphrey et al. 2006). These objects present a puzzle because their central cooling times are comparably short to those in their much larger cousins. It was suggested by Fukazawa et al. (2006) that the gradients reflect the environment, with positive gradients revealing the hotter intracluster or intragroup gas surrounding the galaxy. On the other hand, (Humphrey et al. 2006) proposed a bimodal distribution of temperature gradients, determined by the total system mass and separated at a mass scale ($\sim 10^{13}\,M_\odot$) that implies a distinction between normal galaxies and groups.

The variety of temperature gradients was examined by Diehl and Statler (2008a), in the context of the morphological studies described above. These authors made an important distinction in separating the logarithmic gradient, $\alpha \equiv d \ln T / d \ln R$, measured in the stellar main body of the galaxy from that measured at larger radii.

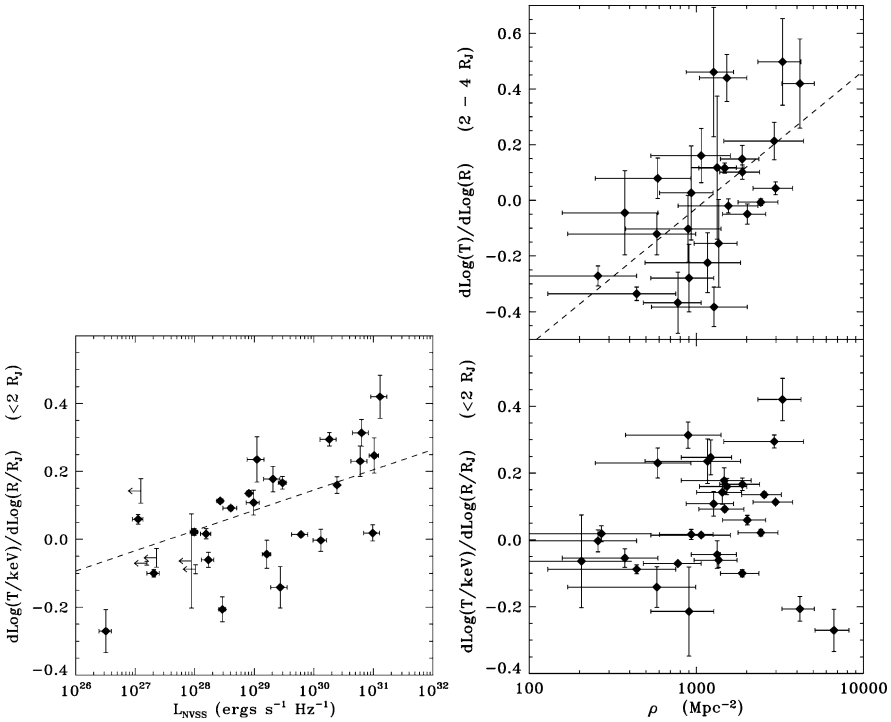

Fig. 7.6 *Left*: Inner gas temperature gradient α_{02} plotted against 1.4 GHz radio luminosity obtained from the NVSS survey. *Dashed line* indicates the best-fit mean relation. (The slope may appear not to match the plotted points because upper limits are included in the fit.) *Right, top*: Outer temperature gradient α_{24} plotted against the surface density of neighboring galaxies obtained from the 2MASS catalog. *Dashed line* indicates the best-fit mean trend. *Right, bottom*: Outer gradient plotted against 1.4 GHz luminosity; there is no significant correlation. (Figures reproduced from Diehl and Statler (2008a))

The mean values of these two gradients, α_{02}, measured between 0 and 2 effective radii, and α_{24}, measured between 2 and 4 effective radii, are found to correlate quite differently with nuclear and environmental properties. This is illustrated in Fig. 7.6. The lower left frame shows the inner gradient, α_{02}, plotted against radio luminosity. The correlation is significant at $> 3\sigma$ level, indicating a connection between the temperature structure in the main body of the galaxy and nuclear activity. The upper right frame shows the outer gradient, α_{24}, plotted against the projected surface density of neighboring galaxies. This correlation is significant at $> 4\sigma$ level, indicating a connection between the temperature structure at large radii and the local environment. The lower right plot, however, shows that environmental effects evidently do not penetrate into the main bodies of the galaxies; there is no correlation between neighbor density and the inner gradient ($< 1\sigma$ significance). Similarly, there is no indication that nuclear activity strongly influences the gas at large radii.

Thus the situation not as simple as the suggestions of either Fukazawa et al. (2006) or Humphrey et al. (2006). While temperature gradients are correlated with stellar velocity dispersion and optical luminosity (proxies for mass), there is no bimodality in the larger sample of Diehl and Statler (2008a) indicating a special mass scale. Environment does play an important role, but mostly at large radii. Within their main bodies, the hot ISM in normal ellipticals shows every indication of being primarily controlled – or at least modulated – by nuclear activity.

7.4.4 Implications for Galaxy Evolution

It was emphasized earlier in this chapter that normal elliptical galaxies are not like galaxy clusters. The hot IGM in clusters dominates the stellar mass in galaxies by more than an order of magnitude, and still contains most of the baryons that were ever bound in the cluster halo. The hot ISM in normal ellipticals makes up only a few percent of the baryonic mass, and is only a tenuous relic of its former self. Much of the original ISM and most of the gas returned by stars over these galaxies' lifetimes have probably been driven out of the systems and rendered unobservable, either becoming gravitationally unbound or simply lingering at large radii, at sufficiently low density that radiative cooling has little effect. The remaining gas is stirred up to varying degrees, showing morphologies and thermal profiles that are evidently related to the current power of the central sources. This, again, is unlike the situation in clusters. There, the mechanical heating attributed to rising bubbles is not correlated with current AGN luminosity; the standard interpretation is that the "ghost cavity" buoyancy timescales are much longer than the durations of AGN outbursts. But the galactic length scale is some two orders of magnitude smaller than the cluster scale, and the fact that correlations with current nuclear activity are seen may be an indication that AGN recurrence timescales, heating and cooling timescales, and hydrodynamic timescales are all comparable.

Still, we are not yet close to a physical understanding of these relationships, or even of the underlying difference between galaxies with radially falling temperatures and those with radially rising temperatures within their main bodies. Three alternative scenarios were offered speculatively by Diehl and Statler (2008a) to qualitatively explain the differing roles of AGN in the less disturbed galaxies with negative inner gradients and the more disturbed ones with positive inner gradients:

1. Low-power AGN with small black holes heat the ISM locally; higher-power sources with larger black holes distribute the heat globally by feeding jets that blow large cavities into the ISM. In this scenario, negative temperature gradients reflect very localized heating by the AGN. All AGN disturb the gas, but the weakest sources do so on a scale and at a surface brightness level that is less detectable, resulting in a lower observed asymmetry.
2. AGN dominate global heating of the ISM only in the X-ray-bright galaxies with positive temperature gradients. In this scenario, the onset of negative

gradients marks the point where AGN heating becomes unimportant, relative to other sources. One possibility is supernovae; an order-of-magnitude calculation reveals that, for a typical SN Ia rate, the supernova energy input rate exceeds the gas X-ray luminosity for total stellar luminosities below that where inner temperature gradients change sign. A second is compressional heating; if the gas is relatively cool, and radiatively inefficient, compressional heating can exceed radiative cooling in steep gravitational potentials, resulting in a "cooling flow" that actually becomes hotter, forming a negative gradient (Mathews and Brighenti 2003).

3. The observed temperature gradients represent snapshots of a time-dependent flow (Ciotti and Ostriker 2007), in which the temperature gradient is cyclically reversed. In this scenario, heating and cooling conspire to maintain central temperatures around the observed 0.6 keV, while AGN jets and radiative processes reverse the temperature gradient by heating or cooling predominantly at large radii. This may require galaxies to cycle through wind and inflow phases, probably correlated with the fueling of the central black hole.

7.4.5 Are X-Ray-Derived Mass Profiles Reliable?

The discussion of hydrostatic equilibrium in this chapter might well leave one concerned as to whether radial mass profiles derived from X-ray data can be believed. But to recapitulate an earlier argument, even though the detailed evidence indicates that *precise* equilibrium is not characteristic of the general population, most systems are probably close to hydrostatic simply because, were they not, they would readjust and find an equilibrium in a few dynamical times. Still, order-unity disturbances in gas density are apparent in many *Chandra* observations. A back-of-the-envelope estimate of how these might affect mass estimates was given by Diehl and Statler (2007), who argued as follows: Consider a region temporarily overpressured by a factor of q. If it expands adiabatically to recover its nominal pressure, it will grow by a factor of $q^{1/5}$. Requiring that this expansion be sufficient to move material a distance comparable to the size of the region itself (an order unity disturbance) then implies $q \sim 10$. If the entire galaxy were overpressured by this amount, hydrostatic models would yield a mass too large by a factor of q. However, in practice one observes a superposition of overpressured and underpressured regions in various states of expansion or contraction. Averaging over N such regions in a standard radial analysis would dillute the effect by a factor $\sim 1/2N^{1/2}$, resulting in a local mass estimate no more than a factor of 2 or 3 high or low.[5]

[5]The argument in Diehl and Statler (2007) neglected the fact that overpressured regions will, on average, be observed half-expanded, and so obtained a dilution factor of $1/N^{1/2}$.

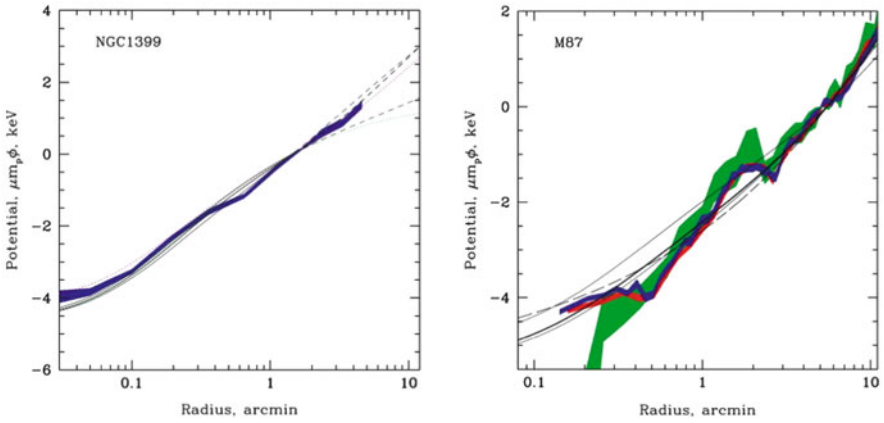

Fig. 7.7 Comparison of gravitational potentials derived from X-ray data assuming hydrostatic equilibrium (*colored bands*) and from stellar dynamical methods (*lines*). *Left*: NGC 1399; *right*: M87. Differences in the local slope correspond to factor ∼2 differences in enclosed mass, roughly consistent with expectations from local departures from hydrostatic equilibrium. (Figures reproduced from Churazov et al. (2008)), see the electronic version for a color version of this figure

This is exactly the level of the irregularities seen in recent results. Figure 7.7 shows detailed comparisons of gravitational potentials derived from X-ray and stellar dynamical analyses, for NGC 1399 and M87 (Churazov et al. 2008). In NGC 1399, the difference in the potential slopes between 0.3 and 0.7 arcminutes corresponds to a factor 2 difference in enclosed mass in that radial bin, obtained by the two methods. For M87, the difference in slopes between 0.5 and 2.0 arcminutes again represents a factor of 2 in mass, and between 2 and 3 arcminutes the X-ray analysis implies an unphysical negative enclosed mass. This in no way reduces the value of the X-ray results, which in broad terms are consistent with stellar dynamics and indicate that on a global scale X-ray mass profiles are reliable. But local irregularities in these profiles are also consistent with what one should expect from local departures from hydrostatic equilibrium.[6]

7.5 Methods (and Pitfalls) of Quantitative Morphology

Robust scientific conclusions nearly always require statistical results, obtained from homogeneous measurements performed on a well defined sample of test objects. Anecdotal or subjective results can be suggestive, but never definitive. As in the case of the pioneering optical studies of elliptical galaxy morphology nearly 30 years ago, morphological studies of the hot ISM require well tested quantitative methods that

[6]The estimate of the effect by Diehl and Statler (2007) was criticized as "too pessimistic" by Churazov et al. (2008); however, the reader can see that there is no real quantitative disagreement, and so the point of contention is purely a rhetorical one.

are able to produce statistically reliable results in the low signal-to-noise regimes that characterize the available data.

7.5.1 Adaptive Binning and Smoothing

Inevitably, with small numbers of counted X-ray photons per pixel, one is compelled to sacrifice resolution to boost the signal-to-noise ratio to the point where putative features are statistically significant. Photon counts can be collected into larger resolution elements by either *binning* or *smoothing*. In the former, counts are collected into independent bins. Each pixel in the original image affects one bin; hence the statistical errors are independent in each bin. In the latter, counts are collected from, or distributed into, neighboring pixels in varying proportions. Each pixel in the original image may affect many pixels in the smoothed image, and therefore the errors are spatially correlated. When the original signal-to-noise ratio is spatially variable (which is, basically, all the time in astronomical observations), binning or smoothing by differing degrees in different parts of the data may be necessary; this need gives rise to *adaptive smoothing* and *adaptive binning* methods, which have been widely used with X-ray data. Each approach has advantages and disadvantages, and neither is guaranteed to provide the ideal view of the data. Adaptive binning has the virtue of always producing statistically independent bins, and the binning scale is immediately visible to the eye; on the other hand, the bin boundaries are also visible, and in some circumstances can lead the eye and impose the impression of a regular geometry onto the data. Adaptive smoothing produces an image that is, arguably, more pleasing to the eye, but one that is much harder to interpret statistically, since the smoothing scale is not readily visible and neighboring regions in the image have correlated errors.

Various adaptive binning and smoothing techniques were reviewed by Diehl and Statler (2006), in their exposition of the Weighted Voronoi Tesselation (WVT) binning algorithm.[7] WVT binning can produce adaptively binned images of arbitrary data (e.g., intensity, hardness ratios, temperatures) with a uniform signal-to-noise ratio per bin. The bins are compact and are not linked to any coordinate system (except the original pixel coordinates), minimizing the eye-leading effects of coordinate-based methods. WVT binning out-performs other adaptive binning techniques in signal-to-noise uniformity and bin compactness.

A comparison of adaptive binning and smoothing is shown in Fig. 7.8. The original image is a random realization of a featureless gray field, with a top-to-bottom gradient in signal-to-noise ratio. This image contains no real features; everything is Poisson noise. On the left, the image has been adaptively smoothed using the *asmooth* algorithm in the XMMSAS package, to a target $S/N = 5$. On the right, the image has been binned to the same S/N by the WVT algorithm.

[7] WVT binning is a generalization of the Voronoi binning method of Cappellari and Copin (2003).

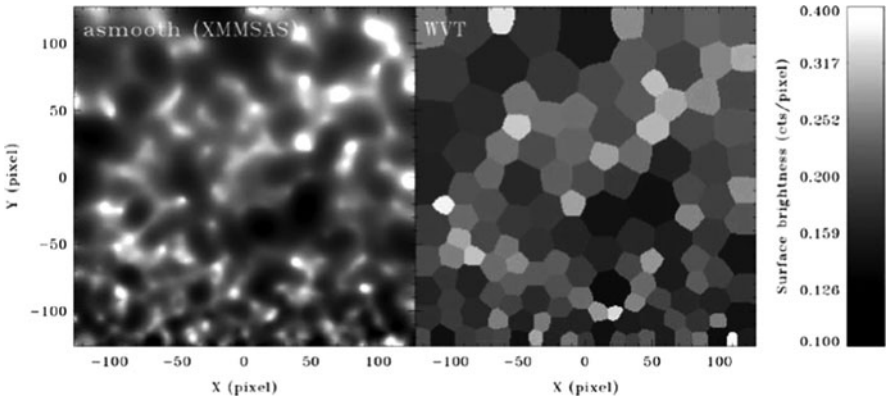

Fig. 7.8 Comparison of adaptive binning and smoothing methods. The underlying image is a random realization of a featureless gray field with a vertical gradient in signal-to-noise ratio. *Left*: adaptively smoothed image computed using the XMMSAS "asmooth" task; *Right*: adaptively binned image computed using the WVT technique. Note the spurious impression of thin, quasi-linear features and round cavities in the adaptively smoothed image. (Figure reproduced from Diehl and Statler (2006))

The binned image is clearly featureless, and the educated eye can see that the distribution of bin brightnesses is Poisson-like. One can clearly see the distribution of binning scales. But one may feel that the bins themselves are distracting, and, in a different random realization of the same data, might have been laid down in different positions. The smoothed image, while "prettier," is harder to interpret. It gives a strong impression of a network of thin walls or filaments and round cavities, none of which is real. These spurious features all appear just below the smoothing scale. In this example, one can infer the smoothing scale from the adaptively binned image. But typically one may not have this information because smoothing scale maps are often not published.

Adaptive binning and smoothing both have the property that local gradients are not preserved on scales smaller than the smoothing/binning scale; this is unavoidable. Adaptive smoothing has an additional tendency to create quasi-linear structures between local peaks in S/N. This is a concern because of the widespread use of adaptively smoothed images for qualitative morphology – for instance, the identification of bubbles or shocks. At minimum, if adaptive techniques are to be used to study diffuse morphology, *it is absolutely essential that the images of resolved sources be modeled and removed first*, so that the PSF tails do not contaminate the actual diffuse emission. One should exercise extreme caution in interpreting images in which this has not been done, especially when adaptive smoothing has been used, because of its tendency to create linear features between sources (Allen et al. 2006; Shurkin et al. 2008).

7.5.2 *Ellipticity Measures and Isophotes*

The ellipticity ϵ is the first quantitative measure of morphology beyond the ubiquitous radial surface brightness profile. Determining the ellipticity nearly always involves calculating the second moments of some region of the brightness distribution $I(x_i, y_i)$, which is known over a set of pixels i. The matrix representation of the second moment tensor is

$$\mathbf{I} = \begin{bmatrix} \sum_i I(x_i, y_i) x_i^2 & \sum_i I(x_i, y_i) x_i y_i \\ \sum_i I(x_i, y_i) x_i y_i & \sum_i I(x_i, y_i) y_i^2 \end{bmatrix}, \tag{7.11}$$

where the sum is over the pixels in the region of interest. The principal axes of the brightness distribution are located by diagonalizing the matrix; the resulting diagonal elements (eigenvalues) I_1 and I_2 are the principal moments. If one chooses the diagonalization so that $I_1 > I_2$, then the 1 and 2 axes are the major and minor axes respectively. In the simple case where the brightness distribution is everywhere stratified on concentric, axially aligned ellipses with constant axis ratio q, then the ratio of eigenvalues I_2/I_1 will be equal to $q^2 = (1-\epsilon)^2$, *if* the region included in the sum is bounded by isophotes. Since the isophotes are not known a priori, calculating ϵ necessarily involves some iteration. A common expedient is to instead calculate moments inside a circular region or annulus; but in this case, the relation between the eigenvalue ratio and the ellipticity depends sensitively on the radial surface brightness profile.

If one desires only a mean ellipticity over the entire image, is it straightforward to apply the second-moment approach to the entire part of the image above some signal-to-noise threshold. An alternative is to fit the entire image with a smooth model having fixed isophotal ellipticity (Hanlan and Bregman 2000). To obtain ellipticity and position angle *profiles* as functions of radius, one approach in use is to compute the principal moment ratio for *all* of the emission inside a sequence of progressively larger ellipses (Buote et al. 2002). If one chooses this route, one needs to be fully aware that the result is *not* an isophotal ellipticity profile, but rather a sequence of mean enclosed ellipticities that asymptotically approaches a global average. This technique has the pleasant property that it is virtually guaranteed to produce a radially smooth profile. However, this smoothness may be deceptive because all of the statistical errors are strongly correlated. In addition, one may be given a false impression of a robustly determined ellipticity at very large radii, where progressively larger outer boundaries enclose the same signal but encompass ever larger amounts of noise. Tests of how this enclosed-moment approach performs on realistic simulated images with ellipticity and position angle gradients have not been published.

A method for computing true isophotes (at least at the level allowed by the data) was developed by Diehl and Statler (2007), making use of their WVT-binned, gas-only images and the noise images generated in the same procedure. In their method, the original data are replaced in each bin by a set of randomly-placed particles

(pseudo-counts). The number of particles is chosen so that the pure Poisson ($\sqrt{N}$) noise approximately matches the actual value in the noise image; the brightness of each particle is scaled so that the total brightness matches the actual counts in the bin. Ellipticities are then calculated iteratively in narrow annular rings bounded by similar, aligned ellipses, adjusting the ellipticity of the ring so that the eigenvalues of the second-moment tensor of the particles in the ring match those for a constant-density ring of the same shape. It is demonstrated in Diehl and Statler (2007) that this method is able to accurately recover radially varying profiles in ellipticity and isophotal position angle in typically sparse data, even in the presence of contamination by unresolved sources.

7.5.3 Quantifying Asymmetry

In the optical, visual inspection of residual maps, obtained by subtracting smooth elliptical models from the observed images of elliptical galaxies, showed early on that the largest deviations from perfect ellipticity occur in the $m = 4$ component of the azimuthal Fourier expansion of the surface brightness. This harmonic corresponds to actual dynamical components of galaxies, namely disks and boxy spheroids, and therefore the so-called A_4 parameter is a useful measure of isophotal distortion that is linked to physics. For the X-ray gas, the situation is far less clear. As emphasized throughout this chapter, morphological studies are still in their adolescence, and we are, in effect, groping about looking for the best physically meaningful ways to quantify morphology. With this situation in mind, Diehl and Statler (2008b) defined their asymmetry index η as a catch-all measure of all structure that is not elliptically symmetric. They first create a smooth elliptical model of the gas emission by fitting low-order polynomials to the isophotal ellipticity and position angle profiles, cast as functions of log-radius. The model is binned using the adaptively binned gas-only image, and the difference between the binned gas image G and the binned model M is calculated. The asymmetry index is then computed according to

$$\eta = \frac{1}{N} \sum_{i=1}^{N} \left[\left(\frac{G_i - M_i}{M_i} \right)^2 - \left(\frac{\sigma_{G,i}}{M_i} \right)^2 \right], \tag{7.12}$$

where σ_G is the binned noise image and the sum is over pixels i. The asymmetry index is thus the mean square deviation from the model, over and above what one would expect from statistical fluctuations. This quantity has been shown to be useful in revealing the influence of AGN and environment on gas morphology. But it is far from clear that η is the best physically useful measure of asymmetry. Alternative measures should be developed, and may prove to be more useful in isolating the dominant physical processes.

7.6 Future Directions and Complications

We have, at best, only a partial view of the processes at work in elliptical galaxies that influence the hot ISM. Whether the range of morphological disturbances observed reflects true differences in the long-term properties of galaxies, or are merely snapshots of intrinsically similar systems in different phases of a recurring cycle of AGN activity, is unknown.

In either case, it may prove to be challenging to explain the very tight correlation in average gas properties known as the X-ray Gas Fundamental Plane (XGFP) (Diehl and Statler 2005). The XGFP is a relation between the X-ray gas mean temperature T_X, half-light radius R_X, and mean surface brightness I_X that takes the form $T_X \propto R_X^{0.28} I_X^{0.22}$. Galaxies thus lie on a plane in $(\log T_X, \log R_X, \log I_X)$ space (Fig. 7.9). This is reminiscent of, but distinct from, the stellar Fundamental Plane, which connects the velocity dispersion σ, effective radius R_e, and effective surface brightness I_e according to the relation $\sigma^2 \propto R_e^{1.42} I_e^{1.24}$. While the stellar FP is primarily an expression of the virial theorem, the XGFP is not, because the gas is not self-gravitating. The XGFP says that gas that is warmer, on average, tends to be more extended or have higher surface brightness. The analysis of Diehl and Statler (2008a) also showed that higher or lower average temperatures tend to

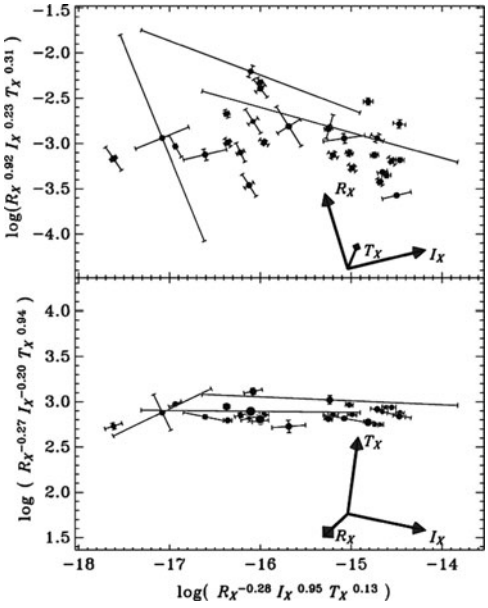

Fig. 7.9 Face-on (*top*) and edge-on (*bottom*) views of the X-ray Gas Fundamental Plane (XGFP). *Symbol sizes* roughly indicate position into and out of the page. *Error bars* indicate 1σ projections of the covariance matrices. *Arrows* indicate the sense of view relative to the measured galaxy properties. (Figure reproduced from Diehl and Statler (2005))

reflect positive or negative temperature gradients. So positive-gradient systems tend to be more extended and brighter than negative-gradient systems. This is consistent with intuitive expectations based on an AGN heating scenario, but a quantitative connection between the XGFP and physical processes has yet to be identified.

Clarifying and quantifying the relative importance of internal (AGN) and environmental effects on hot ISM morphology will undoubtedly require more sophisticated treatment of asymmetries. It may be useful to devise new measures that try to isolate the likely morphological distortions caused by these disparate physical effects. For instance, the influence of ram pressure may be most directly manifested in lopsided $m = 1$ distortions. A novel technique of adaptive binning that explicitly tries to reveal – or at least not obscure – extended linear features, by shaping and aligning bins along brightness contours, has been developed by Sanders (2006). This approach may be worth exploring; however initial applications suggest that the eye-leading property of the oddly-shaped bins may be distracting, encouraging the perception of spurious shell-like features (Diehl and Statler 2006). Nonetheless, more inventive statistical measures that attempt to isolate the expected morphological signs of bubbles/cavities, acoustic waves, or shocks should be devised.

Finally, it should be admitted that questions of pressure support unrelated to the temperature of the X-ray emitting gas are still largely glossed over, including in this chapter. Partial support from cosmic rays and magnetic fields are likely to be important. If these additional pressures are, indeed, significant and are not expressible as monotonic functions of the gas density, then the argument of Sect. 7.1 would require that the gas could not be hydrostatic.

Acknowledgements Support for this work was provided by the National Aeronautics and Space Administration (NASA) through *Chandra* awards G01-2094X and AR3-4011X, issued by the *Chandra* X-Ray Observatory Center, which is operated by the Smithsonian Astrophysical Observatory for and on behalf of NASA under contract NAS8-39073, and by National Science Foundation grants AST-0407152 and AST-0708284. The writing of this chapter was conducted under an Independent Research/Development plan while the author was serving on detail to NSF under the Intergovernmental Personnel Act; any opinion, findings, conclusions, or recommendations expressed in this chapter are those of the author and do not necessarily reflect the views of the National Science Foundation. Finally, the author appreciates the hospitality of the Washington Metropolitan Area Transit Authority, upon whose trains much of this chapter was written.

References

S.W. Allen, R.J.H. Dunn, A.C. Fabian, G.B. Taylor, C.S. Reynolds, The relation between accretion rate and jet power in X-ray luminous elliptical galaxies. Mon. Not. R. Astron. Soc. **372**, 21–30 (2006)

R. Bender, P. Surma, S. Doebereiner, C. Moellenhoff, R. Madejsky, Isophote shapes of elliptical galaxies. II - Correlations with global optical, radio and X-ray properties. Astron. Astrophys. **217**, 35–43 (1989)

B. Boroson, D.-W. Kim, G. Fabbiano, Revisiting with Chandra the Scaling Relations of the X-ray Emission Components (Binaries, Nuclei and Hot Gas) of Early Type Galaxies. ArXiv e-prints, November (2010)
F. Brighenti, W.G. Mathews, Structure and evolution of interstellar gas in flattened, rotating elliptical galaxies. Astrophys. J. **470**, 747–+ (1996)
D.A. Buote, C.R. Canizares, Geometrical evidence for dark matter: X-ray constraints on the mass of the elliptical galaxy NGC 720. Astrophys. J. **427** 86–111 (1994)
D.A. Buote, T.E. Jeltema, C.R. Canizares, G.P. Garmire, Chandra Evidence of a Flattened, Triaxial Dark Matter Halo in the Elliptical Galaxy NGC 720. Astrophys. J. **577**, 183–196 (2002)
P.R. Capelo, P. Natarajan, P.S. Coppi, Hydrostatic equilibrium profiles for gas in elliptical galaxies. Mon. Not. R. Astron. Soc. **407**, 1148–1156 (2010)
M. Cappellari, Y. Copin, Adaptive spatial binning of integral-field spectroscopic data using Voronoi tessellations. Mon. Not. R. Astron. Soc. **342**, 345–354 (2003)
E. Churazov, W. Forman, A. Vikhlinin, S. Tremaine, O. Gerhard, C. Jones, Measuring the non-thermal pressure in early-type galaxy atmospheres: a comparison of X-ray and optical potential profiles in M87 and NGC 1399. Mon. Not. R. Astron. Soc. **388**, 1062–1078 (2008)
L. Ciotti, J.P. Ostriker, Radiative feedback from massive black holes in elliptical galaxies: AGN flaring and central starburst fueled by recycled gas. Astrophys. J. **665**, 1038–1056 (2007)
S. Diehl, T.S. Statler, A fundamental plane relation for the X-Ray gas in normal elliptical galaxies. Astrophys. J. Lett. **633**, L21–L24 (2005)
S. Diehl, T.S. Statler, Adaptive binning of X-ray data with weighted Voronoi tessellations. Mon. Not. R. Astron. Soc. **368**, 497–510 (2006)
S. Diehl, T.S. Statler, The hot interstellar medium of normal elliptical galaxies. I. A chandra gas gallery and comparison of X-Ray and optical morphology. Astrophys. J. **668**, 150–167 (2007)
S. Diehl, T.S. Statler, The hot interstellar medium in normal elliptical galaxies. III. The thermal structure of the gas. Astrophys. J. **687**, 986–996 (2008a)
S. Diehl, T.S. Statler, The hot interstellar medium of normal elliptical galaxies. II. Morphological evidence for active galactic nucleus feedback. Astrophys. J. **680**, 897–910 (2008b)
A. Finoguenov, C. Jones, Chandra observation of M84, a radio lobe elliptical galaxy in the virgo cluster. Astrophys. J. Lett. **547**, L107–L110 (2001)
Y. Fukazawa, J.G. Botoya-Nonesa, J. Pu, A. Ohto, N. Kawano, Scaling mass profiles around elliptical galaxies observed with chandra and XMM-Newton. Astrophys. J. **636**, 698–711 (2006)
M.A. Gendre, P.N. Best, J.V. Wall, The combined NVSS-FIRST galaxies (CoNFIG) sample – II. Comparison of space densities in the Fanaroff-Riley dichotomy. Mon. Not. R. Astron. Soc. **404**, 1719–1732 (2010)
P. Gorenstein, D. Fabricant, K. Topka, F.R. Harnden Jr., W.H. Tucker, Soft X-ray structure of the perseus cluster of galaxies. Astrophys. J. **224**, 718–723 (1978)
P.C. Hanlan, J.N. Bregman, X-Ray Emission from rotating elliptical galaxies. Astrophys. J. **530**, 213–221 (2000)
E. Hubble, No. 324. Extra-galactic nebulae. Contributions from the Mount Wilson Observatory / Carnegie Institution of Washington **324**, 1–49 (1926)
P.J. Humphrey, D.A. Buote, F. Gastaldello, L. Zappacosta, J.S. Bullock, F. Brighenti, W.G. Mathews, A Chandra view of dark matter in early-type galaxies. Astrophys. J. **646**, 899–918 (2006)
J.A. Irwin, A.E. Athey, J.N. Bregman, X-ray spectral properties of low-mass X-Ray binaries in nearby galaxies. Astrophys. J. **587**, 356–366 (2003)
R.I. Jedrzejewski, CCD surface photometry of elliptical galaxies. I - Observations, reduction and results. Mon. Not. R. Astron. Soc. **226**, 747–768 (1987)
C. Jones, W. Forman, A. Vikhlinin, M. Markevitch, L. David, A. Warmflash, S. Murray, P.E.J. Nulsen, Chandra observations of NGC 4636-an elliptical galaxy in turmoil. Astrophys. J. Lett. **567**, L115–L118 (2002)

E. Kellogg, H. Gursky, C. Leong, E. Schreier, H. Tananbaum, R. Giacconi, X-ray observations of the virgo cluster, NGC 5128, and 3c 273 from the UHURU satellite. Astrophys. J. Lett. **165** L49+ (1971)

H.G. Khosroshahi, L.R. Jones, T.J. Ponman, An old galaxy group: Chandra X-ray observations of the nearby fossil group NGC 6482. Mon. Not. R. Astron. Soc. **349**, 1240–1250 (2004)

D.-W. Kim, G. Fabbiano, N.J. Brassington, T. Fragos, V. Kalogera, A. Zezas, A. Jordán, G.R. Sivakoff, A. Kundu, S.E. Zepf, L. Angelini, R.L. Davies, J.S. Gallagher, A.M. Juett, A.R. King, S. Pellegrini, C.L. Sarazin, G. Trinchieri, Comparing GC and field LMXBs in elliptical galaxies with deep Chandra and Hubble data. Astrophys. J. , **703**, 829–844 (2009)

E. Kim, D.-W. Kim, G. Fabbiano, M.G. Lee, H.S. Park, D. Geisler, B. Dirsch, Low-mass X-ray binaries in six elliptical galaxies: connection to globular clusters. Astrophys. J. **647**, 276–292 (2006)

T.R. Lauer, Boxy isophotes, discs and dust lanes in elliptical galaxies. Mon. Not. R. Astron. Soc. **216**, 429–438 (1985)

T.R. Lauer, The cores of elliptical galaxies. Astrophys. J. **292**, 104–121 (1985)

G.A. Mamon, E.L. Łokas, Dark matter in elliptical galaxies – I. Is the total mass density profile of the NFW form or even steeper? Mon. Not. R. Astron. Soc. **362**, 95–109 (2005)

W.G. Mathews, F. Brighenti, Hot gas in and around elliptical galaxies. Ann. Rev. Astron. Astrophys. **41**, 191–239 (2003)

T. Naab, A. Burkert, L. Hernquist, On the formation of Boxy and Disky elliptical galaxies. Astrophys. J. Lett. **523**, L133–L136 (1999)

E. O'Sullivan, T.J. Ponman, R.S. Collins, X-ray scaling properties of early-type galaxies. Mon. Not. R. Astron. Soc. **340**, 1375–1399 (2003)

S.W. Randall, C.L. Sarazin, J.A. Irwin, XMM-Newton observation of diffuse gas and low-mass X-ray binaries in the elliptical galaxy NGC 4649 (M60). Astrophys. J. **636**, 200–213 (2006)

J.S. Sanders, Contour binning: a new technique for spatially resolved X-ray spectroscopy applied to Cassiopeia A. Mon. Not. R. Astron. Soc. **371**, 829–842 (2006)

C.L. Sarazin, J.A. Irwin, J.N. Bregman, Resolving the mystery of X-Ray-faint elliptical galaxies: Chandra X-ray observations of NGC 4697. Astrophys. J. Lett. **544**, L101–L105 (2000)

C.L. Sarazin, J.A. Irwin, J.N. Bregman, Chandra X-ray observations of the X-Ray faint elliptical galaxy NGC 4697. Astrophys. J. **556**, 533–555 (2001)

K. Shurkin, R.J.H. Dunn, G. Gentile, G.B. Taylor, S.W. Allen, Active galactic nuclei-induced cavities in NGC 1399 and NGC 4649. Mon. Not. R. Astron. Soc. **383**, 923–930 (2008)

T.S. Statler, B.R. McNamara, A 15 Kiloparsec X-ray disk in the elliptical galaxy NGC 1700. Astrophys. J. **581**, 1032–1038 (2002)

G. Trinchieri, G. Fabbiano, C.R. Canizares, The X-ray surface brightness distribution and spectral properties of six early-type galaxies. Astrophys. J. **310**, 637–659 (1986)

Chapter 8
Dark Matter in Elliptical Galaxies*

David A. Buote and Philip J. Humphrey

Abstract We review X-ray constraints on dark matter in giant elliptical galaxies ($10^{12}\,M_\odot \lesssim M_{vir} \lesssim 10^{13}\,M_\odot$) obtained using the current generation of X-ray satellites, beginning with an overview of the physics of the hot interstellar medium and mass modeling methodology. Dark matter is now firmly established in many galaxies, with inferred NFW concentration parameters somewhat larger than the mean theoretical relation. X-ray observations confirm that the total mass profile (baryons+DM) is close to isothermal ($M \sim r$), and new evidence suggests a more general power-law relation for the slope of the total mass profile that varies with the stellar half-light radius. We also discuss constraints on the baryon fraction, supermassive black holes, and axial ratio of the dark matter halo. Finally, we review constraints on non-thermal gas motions and discuss the accuracy of the hydrostatic equilibrium approximation in elliptical galaxies.

8.1 Introduction

Cold, non-baryonic dark matter (CDM) is a critical ingredient of the widely accepted Big Bang cosmological paradigm (Feng 2005, Hannestad 2006, Einasto 2009). Although the dark matter (DM) particle has yet to be directly detected in a terrestrial laboratory (Steffen 2009, Irastorza 2009, Ellis and Olive 2010), the total amount of DM is known precisely from observations of the large-scale geometry

*Editor's note: The previous chapter by Statler presents a different viewpoint on the issue of hydrostatic equilibrium. We ask readers to carefully consider the two different positions.

D.A. Buote (✉) · P.J. Humphrey
Department of Physics and Astronomy, 4129 Frederick Reines Hall, University of California at Irvine, Irvine, CA 92697-4575, USA
e-mail: buote@uci.edu, phumphre@uci.edu

D.-W. Kim and S. Pellegrini (eds.), *Hot Interstellar Matter in Elliptical Galaxies*, Astrophysics and Space Science Library 378, DOI 10.1007/978-1-4614-0580-1_8,
© Springer Science+Business Media, LLC 2012

of the Universe, in particular the cosmic microwave background radiation, distant Type Ia supernovas, baryon acoustic oscillations, galaxy cluster mass functions and baryon fractions. These observations indicate that DM comprises about 23% of the energy density budget of the Universe today compared to about 4% for baryonic matter (Amsler et al. 2008, Lahav and Liddle 2010).

While the standard cosmological model describes the large-scale Universe very well, it has encountered interesting tension with observations of DM on galaxy scales. Perhaps most notably, beginning with the seminal studies of rotation curves of dwarf spiral galaxies (Moore 1994, Flores and Primack 1994), it is now generally recognized that both small and large disk galaxies have central radial DM profiles that are flatter than initially predicted by the standard model when considering only the gravitational influence of the DM (Gilmore et al. 2008, Primack 2009, de Blok 2010). Similar cored DM profiles are obtained by optical studies of elliptical galaxies at the center of galaxy clusters (Sand et al. 2002, Kelson et al. 2002, Sand et al. 2004, 2008, Newman et al. 2009), though X-ray observations of some clusters find "cuspy" total mass profiles consistent with theory (Arabadjis et al. 2002, Lewis et al. 2003). This "core-cusp" problem has generated great interest as it may yield information on the nature of the DM that is apparently inaccessible to observations on larger scales. An influential early suggestion to reconcile observation and theory is that the DM particles are self-interacting (Spergel and Steinhardt 2000, Kochanek and White 2000, Firmani et al. 2001, Ahn and Shapiro 2005), though observations apparently do not currently favor that possibility (Arabadjis et al. 2002, Lewis et al. 2003, Randall et al. 2008, Kuzio de Naray et al. 2010).

Alternatively, the core-cusp problem may reveal clues to the influence of baryons on galaxy formation which should be most important near the centers of galaxies. In the standard model slightly over-dense regions in a nearly uniform early DM distribution acted as seeds for future galaxies and clusters. Baryonic material subsequently fell into the potential wells established by the DM. The interplay of the baryons and DM through, e.g., adiabatic contraction and dynamical friction, has likely altered the spatial distributions of both quantities during galaxy formation and evolution (Blumenthal et al. 1984, El-Zant et al. 2004, Gnedin et al. 2007, Romano-Díaz et al. 2008, Del Popolo 2009, Duffy et al. 2010, Abadi et al. 2010). Hence, the DM profiles on galaxy scales can serve as important laboratories for studying galaxy formation and the nature of the DM particle.

Like all the different types of galaxies, giant elliptical galaxies have their own special properties that make them deserving of dedicated study. Unlike disk galaxies or the smallest dwarf elliptical galaxies, giant elliptical galaxies are sufficiently massive that multiple powerful techniques to measure their mass profiles are available for many systems. In particular, only for giant ellipticals can gravitational lensing and X-rays be used to complement the information available from stellar dynamics, the latter of which is also available for smaller galaxies. Also, in contrast to the smallest galaxies, every giant elliptical is thought to host a supermassive black hole (SMBH) at its center, the formation of which is apparently intertwined with the host galaxy (Ferrarese and Merritt 2000, Gebhardt et al. 2000). There is also an increased recognition that galaxies acquire their gas in

two modes that are distinguished by whether or not the in-falling gas is heated (Birnboim and Dekel 2003, Kereš et al. 2005). Both modes can operate in the transition mass regime of giant elliptical galaxies ($10^{12} - 10^{13} M_{\odot}$) (Birnboim et al. 2007).

One of the advantages of using X-ray observations to probe DM and SMBHs in elliptical galaxies is that the hot X-ray-emitting interstellar medium (ISM) fills the three-dimensional galactic potential well, thus providing a continuous tracer from the galactic nucleus out to well past the optical half-light radius where stellar dynamical studies become very challenging. In order to translate an X-ray observation of the hot ISM into a gravitating mass profile and DM measurement, it is required that hydrostatic equilibrium holds to a good approximation throughout the region of interest; i.e., that the thermal gas pressure of the ISM balances the weight of the gas. With X-ray observations providing increasing evidence of morphologically disturbed elliptical galaxies, it is timely to review the accuracy of the approximation of hydrostatic equilibrium in X-ray determinations of their DM profiles. Understanding and quantifying deviations from hydrostatic equilibrium not only will lead to more accurate X-ray mass determinations, but any measured non-hydrostatic gas motions will provide clues to elliptical galaxy formation (Mathews and Brighenti 2003a, Birnboim and Dekel 2003, Kereš et al. 2005, Birnboim et al. 2007, Dekel and Birnboim 2008, Brighenti et al. 2009).

Since giant elliptical galaxies tend to be located in dense environments, it can be difficult to disentangle any DM associated with the elliptical galaxy from its parent halo. Naturally, most of the attention of X-ray studies has been devoted to those systems with the largest X-ray fluxes which has lead to an emphasis on elliptical galaxies located at the centers of the most massive galaxy groups and clusters. While all elliptical galaxies are of interest for DM studies, in this review we address galaxy-sized halos by focusing on the lower mass regime that is still accessible to detailed X-ray study ($10^{12}\,\mathrm{M}_{\odot} \lesssim \mathrm{M}_{\mathrm{vir}} \lesssim 10^{13}\,\mathrm{M}_{\odot}$) We restrict consideration to objects where a single giant elliptical galaxy dominates the stellar light, which at the upper end of the mass range under consideration are often classified as fossil groups (Ponman et al. 1994, Vikhlinin et al. 1999, Jones et al. 2003) which are thought to be highly evolved, relaxed systems (D'Onghia et al. 2005, Dariush et al. 2007, Milosavljević et al. 2006).

In the present review we focus on the constraints on DM in elliptical galaxies obtained using the current generation of X-ray observatories – *Chandra*, *XMM*, and *Suzaku*; constraints from the previous generation of X-ray satellites are reviewed by, e.g., Fabbiano (1989), Buote and Canizares (1998), and Mathews and Brighenti (2003a). While we take care to mention relevant results obtained from other techniques, our review is not intended to be complete from the multi-wavelength perspective. The interested reader is urged to consult the reviews by Gerhard (2006, 2010), Ellis (2010), and Treu (2010) for discussions of the constraints on DM in elliptical galaxies obtained by stellar dynamics and gravitational lensing.

8.2 Hydrostatic Models of the Hot ISM

8.2.1 Preliminaries

The hot ISM of an elliptical galaxy ($T \sim 10^7\,\mathrm{K} \sim 0.9\,\mathrm{keV}/k_B$) has properties that are extremely similar to the (hotter) intracluster medium (ICM) of a massive galaxy cluster (Sarazin 1986, Fabian 1990, Sarazin 1992). While the detailed radiation spectrum is described well by a collisionally ionized *plasma* of electrons and ions obeying the coronal approximation (Mewe 1999), the macro-structure of the hot ISM in an elliptical galaxy is for many purposes also described well by a simple *monatomic ideal gas*. We highlight four key features of the "hot gas" relevant for constructing hydrostatic models to measure the DM content in elliptical galaxies.

8.2.1.1 Collisional Fluid

In a fully ionized plasma, the equipartition timescale for electrons considering only their mutual Coulomb interactions is (Spitzer 1962),

$$\begin{aligned}\tau_{e-e} &= \frac{3m_e^{1/2}\,(k_B T_e)^{3/2}}{4\pi^{1/2} n_e e^4 \ln\,\Lambda_{\rm coul}} \\ &= 1.1\times 10^4\,\left(\frac{T_e}{10^7\,\mathrm{K}}\right)^{3/2}\left(\frac{n_e}{10^{-3}\,\mathrm{cm}^{-3}}\right)^{-1}\,\mathrm{year},\end{aligned} \tag{8.1}$$

where m_e is the electron mass, e is the electric charge, k_B is Boltzmann's constant, n_e is the electron number density, and T_e is the electron temperature. For $T_e > 4\times 10^5$ K the Coulomb logarithm of an electron-proton plasma is (Spitzer 1962),

$$\ln\,\Lambda_{\rm coul} = 35.4 + \ln\left[\left(\frac{T}{10^7\,\mathrm{K}}\right)\left(\frac{n_e}{10^{-3}\,\mathrm{cm}^{-3}}\right)^{-1/2}\right]. \tag{8.2}$$

The mean free path of the electrons for Coulomb collisions is $\mathrm{v}_e\tau_{e-e}$ (Spitzer 1956, Cowie and McKee 1977, Dopita and Sutherland 2003), where $\mathrm{v}_e = \sqrt{3k_B T_e/m_e}$ is the rms thermal velocity of the electrons, so that,

$$\begin{aligned}\text{Coulomb mean free path} &= \frac{3^{1/2}\,(k_B T_e)^2}{4\pi^{1/2} n_e e^4 \ln\,\Lambda_{\rm coul}} \\ &= 243\,\left(\frac{T}{10^7\,\mathrm{K}}\right)^2\left(\frac{n_e}{10^{-3}\,\mathrm{cm}^{-3}}\right)^{-1}\,\mathrm{pc}.\end{aligned} \tag{8.3}$$

Because m_e does not enter the above equation this expression also represents the mean free path for the protons (for $n_e = n_p$ and $T_e = T_p$). The electron

and proton mean free paths are generally much smaller than the length scales of interest for DM studies indicating that the plasma may be treated as a collisional fluid. Still, in the outer regions near the virial radius, where n_e is small, and therefore the Coulomb mean free path is large, it is possible the fluid approximation considering only Coulomb collisions may not always be justified. But the hot ISM of elliptical galaxies may typically possess tangled $\sim 1\mu$ G magnetic fields (Vallée 2004, Mathews and Brighenti 1997). If so, the electron gyroradius, $r_g = \mathrm{v_e}/\omega$, for angular gyrofrequency $\omega = eB/m_e c$,

$$r_g = 3.9 \times 10^{-11}\, Z^{-1} \left(\frac{T}{10^7\,\mathrm{K}}\right)^{1/2} \left(\frac{m}{m_e}\right)^{1/2} \left(\frac{B}{1\,\mu G}\right)^{-1} \mathrm{pc}, \tag{8.4}$$

is vastly smaller than the relevant length scales for DM studies. (The same is true for the proton gyroradius obtained by setting $m = m_p$.) Consequently, if the hot ISM contains (plausible) weak magnetic fields, then it is expected to behave as a collisional fluid on all length scales of interest for DM studies, allowing an isotropic pressure and temperature to be defined for any fluid element.

8.2.1.2 Local Maxwellian Velocity Distribution

In any fluid element in the hot ISM, Coulomb collisions between electrons establish a Maxwellian velocity distribution with kinetic temperature T_e on the time scale given by (8.1). This is much shorter than other time scales associated with the hot ISM in a relaxed elliptical galaxy. In general the ions can reach equilibrium with a kinetic temperature different from that of the electrons. But electron-ion collisions will establish equipartition on a time scale $\approx (m_p/m_e)\tau_{e-e} \approx 1870\tau_{e-e} \approx 10^7$ year for the conditions typical of the hot ISM (Spitzer 1962). Only for galaxies currently undergoing strong dynamical disturbances, particularly in the central regions of some galaxies with AGN, might be evolving dynamically on a comparable time scale so that the electron and ion temperatures could be different. In relaxed elliptical galaxies, however, the hot ISM is expected to behave locally as a Maxwellian velocity distribution with a single kinetic temperature for the electrons and the ions. Therefore, the thermal pressure of the hot ISM is characterized by that of a monatomic ideal gas, $\rho_{\mathrm{gas}} k_B T/\mu m_{\mathrm{a}}$, where μ is the mean atomic weight of the gas and m_{a} is the atomic mass unit. For a fully ionized gas of solar abundances, $\mu = 0.62$.

8.2.1.3 Thermal Pressure Dominates Magnetic Pressure

Observations of radio halos and relics in several massive galaxy clusters indicate that the ICM is magnetized with a field strength of $1 - 10\,\mu$G (Govoni and Feretti 2004). Unfortunately, elliptical galaxies are not observed to possess the large-scale diffuse radio emission observed in some massive clusters, and thus knowledge of

their magnetic fields is derived from systems with embedded radio jets where the inferred $\sim \mu$G fields (Vallée 2004) may not be representative of the typical hot ISM. For fields of this magnitude, with $P_{\rm mag} = B^2/8\pi$ and $P_{\rm therm} = n_{\rm gas}k_BT \approx 1.9n_ek_BT$,

$$\frac{P_{mag}}{P_{therm}} = 0.015 \left(\frac{B}{1\,\mu G}\right)^2 \left(\frac{T}{10^7\,{\rm K}}\right)^{-1} \left(\frac{n_e}{10^{-3}\,{\rm cm}^{-3}}\right)^{-1}, \tag{8.5}$$

which implies a minor, though very uncertain, contribution of magnetic fields to the pressure support of the hot ISM. Many theoretical models of inflowing gas in elliptical galaxies predict that small seed magnetic fields are amplified possibly to this level or larger (Mathews and Brighenti, 2003a, and references therein), although the small gas fractions observed at the centers of groups (Gastaldello et al. 2007, Sun et al. 2009) likely indicates that any hypothetical concentration magnetic fields, e.g., arising from the amplification owing to inflowing gas just described, has been dispersed by feedback. X-ray studies of DM in elliptical galaxies generally neglect the magnetic pressure, an assumption that can be tested indirectly by (1) comparing observed stellar mass-to-light ratios to theoretical stellar population synthesis models and (2) comparing mass profiles obtained by X-ray methods with those obtained from stellar dynamics and gravitational lensing (Sect. 8.8).

8.2.1.4 Thermal Motions Dominate the Hot ISM in Relaxed Galaxies

When the gravitational potential evolves on a time scale longer than the dynamical time, approximately given by the crossing time of the stars,

$$t_{\rm cross} = \frac{d}{\sigma} = 3.9\times10^7 \left(\frac{d}{10\ {\rm kpc}}\right)\left(\frac{\sigma}{250\ {\rm km\ s}^{-1}}\right)^{-1}\ {\rm year}, \tag{8.6}$$

where d is the length scale of the region under consideration and σ is the stellar velocity dispersion within that region, a time-independent description of the gravitational potential is appropriate. This quasi-static description of the gravitational potential is valid regardless of the dynamical state of the hot ISM, because the gas contributes negligibly to the total mass (gas+stars+DM) over most of the radial range within the virial radius of an elliptical galaxy. Radiative cooling of the hot gas acting alone cannot drive evolution on time scales smaller than the cooling time ($\approx 5\times10^6/n_e$ year for $T = 10^7$ K and solar abundances, or 5×10^9 year for $n_e = 10^{-3}$ cm^{-3}) which is generally much longer than $t_{\rm cross}$. But rapid evolution on a time scale $\lesssim t_{\rm cross}$ is expected to prevail in the central regions of galaxies that have experienced recent, strong AGN feedback presumably generated in response to gas cooling. For our purposes, a *relaxed* elliptical galaxy is one in which the structure of the hot ISM is also evolving quasi-statically on a time scale longer than $t_{\rm cross}$ described by a state of hydrostatic equilibrium, which applies provided any non-thermal gas motions (i.e., motions that are not associated with the random

velocities that define the thermal gas pressure) are negligible compared to the sound speed,

$$c_s = \left(\frac{\gamma P_{\rm gas}}{\rho_{\rm gas}}\right)^{1/2} = 473 \left(\frac{T}{10^7\,{\rm K}}\right)^{1/2}\ {\rm km\ s^{-1}}, \tag{8.7}$$

where $\gamma = 5/3$ is the adiabatic index. This implies a sound crossing time similar to the stellar crossing time in (8.6). Turbulence is expected to be introduced into the hot ISM from merging and intermittent AGN feedback. Interesting limits on turbulent motions have been obtained via constraints on resonance scattering in the center ($\lesssim$1 kpc) of the elliptical galaxy NGC 4636 (Werner et al. 2009) and from Doppler broadening of the X-ray emission lines in a small number of elliptical galaxies (NGC 533, NGC 1399, NGC 4261, NGC 5044) from the sample of Sanders et al. (2010) suggesting that any turbulent motions present in the central regions of those systems are highly subsonic. While not expected to dominate, turbulent velocities may not be negligible since cosmological hydrodynamical simulations typically find that turbulence contributes up to $\sim$20% of the pressure support of the ICM in relaxed galaxy clusters (Tsai et al. 1994, Evrard et al. 1996, Nagai et al. 2007, Piffaretti and Valdarnini 2008, Fang et al. 2009). The irregular, subsonic Hα velocities observed at the centers of some elliptical galaxies also suggest turbulent velocities in the hot gas (Caon et al. 2000). It is unlikely that rotation dominates the ISM dynamics on large scales in elliptical galaxies given the lack of flattened disks observed (Hanlan and Bregman 2000), though modest rotational spin-up might occur in the innermost ($\lesssim$ 1 kpc) regions of some galaxies (Brighenti et al. 2009). The expected inflow velocities arising from radiative cooling are negligible (Mathews and Brighenti 2003a), and a recent study of galaxy-scale halos using a cosmological hydrodynamical simulation concludes that their hot ISM is generally quasi-hydrostatic (Crain et al. 2010a,b).

8.2.2 *The Equation of Hydrostatic Equilibrium: Usage Guidelines*

For the relaxed elliptical galaxies under consideration, hydrostatic equilibrium of a fluid element of hot ISM is expressed as the balance between forces per unit volume of gravity and gas pressure,

$$\nabla P_{\rm gas} = -\rho_{\rm gas} \nabla \Phi, \tag{8.8}$$

where Φ is the gravitational potential, $P_{\rm gas}$ is the pressure and $\rho_{\rm gas}$ the density of the ISM. If non-thermal effects are significant that can be represented by a pressure ($P_{\rm nt}$), such as for isotropic random turbulence or a magnetic field, then $P_{\rm gas} = P_{\rm t} + P_{\rm nt}$, where $P_{\rm t}$ is the thermal pressure. For the case of solid-body rotation, Φ can be replaced by an effective potential. For general rotation (and other ordered gas motions) the convective derivative term $(\mathbf{v}\cdot\nabla)\mathbf{v}$ in the Euler equation must be added

to the left-hand side of (8.8). As remarked previously, the hydrostatic approximation is appropriate provided the non-thermal gas motions are subsonic.

In order to measure directly the magnitude of any non-thermal motions present in the hot ISM, it is necessary to measure precisely the Doppler shifts and broadening of emission lines which is beyond the capability of the current X-ray satellites – except possibly for the innermost regions of some galaxies noted above. Consequently, indirect methods are required to assess whether a galaxy is suitably relaxed for the hydrostatic approximation. Assessment of the morphology of the X-ray image is a convenient first step to locate candidate relaxed galaxies for the following reason. Because the total underlying stellar and DM distribution is expected to have a shape close to that of an ellipsoid, the gravitational potential is also expected to be approximately ellipsoidal, though rounder than the generating mass distribution. Since in hydrostatic equilibrium the X-ray emissivity traces the same three-dimensional shape as the potential for any temperature profile (see Sect. 8.6), galaxies that exhibit irregular, non-ellipsoidal features in their X-ray images might not be suitably relaxed for hydrostatic study. The existence of such asymmetrical features (e.g., substructure, cold fronts) does not guarantee large departures from hydrostatic equilibrium, as demonstrated by cosmological hydrodynamical simulations of clusters (Tsai et al. 1994, Evrard et al. 1996, Nagai et al. 2007, Piffaretti and Valdarnini 2008, Fang et al. 2009), especially when the features are sufficiently localized so that they can be easily excluded from study (Buote and Tsai 1995, Nagai et al. 2007).

Another important consideration in hydrostatic analysis is to insure that the X-ray emission that is attributed to hot ISM is not, in fact, heavily contaminated by unresolved discrete sources. A large number of the brightest discrete sources (mostly low-mass X-ray binaries – LMXBs) can be detected and excluded in nearby galaxies using the high spatial resolution of *Chandra* (see Humphrey and Buote, 2008, and references therein); the lower resolution of *XMM* leads to far fewer detections, and only a few sources (if any) can be detected with *Suzaku*. Because the combined spectrum of unresolved LMXBs is spectrally harder than the hot ISM, the spectral signature of the hot ISM can be reliably extracted from the data provided it is not overwhelmed by the unresolved source component. The situation is more problematic in X-ray faint galaxies (having low ratios of X–ray-to-optical luminosity) like NGC 3379, where hydrostatic mass estimates have been attempted (Fukazawa et al. 2006, Pellegrini and Ciotti 2006) but the soft, diffuse X-ray emission attributed to hot ISM most likely originates almost entirely from cataclysmic variable stars and stellar coronae (Revnivtsev et al. 2008, Trinchieri et al. 2008).

Once a suitably relaxed galaxy with sufficient emission from hot ISM has been identified, the accuracy of the hydrostatic equilibrium approximation can be assessed indirectly via consistency checks. First, one may examine if any well-motivated hydrostatic model is able to provide an acceptable fit to the observed density and temperature profiles of the hot ISM. If an acceptable fit is obtained, the data are consistent with, though do not necessarily require, hydrostatic equilibrium. A poor fit – particularly one with sharp discontinuities in the density

and temperature profiles – provides strong evidence for significant violations of the hydrostatic equilibrium approximation.[1] Second, the gravitating mass profile inferred from the X-ray data can be compared to independent measurements using other techniques having different assumptions (stellar dynamics, gravitational lensing). When results obtained from different methods agree, it provides support for the underlying assumptions of each method and implies that systematic errors are well understood (see Sect. 8.8).

Hence, given the limitations of current X-ray data, a sensible approach to apply and assess hydrostatic equilibrium is the following:

8.2.2.1 Guidelines for Applying Hydrostatic Equilibrium in Elliptical Galaxies:

- Select systems which tend to have a regular, approximately cicular or elliptical X-ray image morphology. If the image has asymmetric features, they should be preferably confined to spatial regions that are small compared to the region of interest; e.g., the inner region showing evidence of possible AGN feedback.
- Unresolved discrete sources should not dominate the X-ray emission. As a rough guide, at least half the X-ray luminosity within the optical half-light radius should originate from hot gas.
- Determine whether a hydrostatic model is able to provide an acceptable fit to the density and temperature profiles of the hot ISM over the region of interest.
- When possible, compare the mass profile obtained via the hydrostatic approximation with that obtained by an independent method; e.g., stellar dynamics, gravitational lensing. The hydrostatic equilibrium approximation is judged to be useful if it provides DM measurements of comparable (or better) quality than other techniques – or provides any information when no other technique is available.

The disturbed X-ray image of M 84 is a spectacular example (Cavagnolo et al. 2010) of the profound effect that AGN feedback can have on the hot ISM and is not a galaxy where hydrostatic equilibrium is expected to apply very accurately. But not all elliptical galaxies display such strong, large-scale irregularities in their X-ray images. In Fig. 8.1 we display several elliptical galaxies with mostly regular images suitable for hydrostatic analysis. Two of the them, NGC 720 and NGC 4649, have very regular images deep into their cores (Fig. 8.2). Another two, NGC 4472 and NGC 4261, possess low-level image fluctuations consistent with cavities associated with radio jets that do not greatly interfere with hydrostatic mass analysis. For

[1] Still, even in such cases the hydrostatic approximation might be useful. The core of M 87 – a system more massive than we consider in this review – possesses various spatial and spectral (Forman et al. 2007, Million et al. 2010) irregularities that are very likely associated with sizable non-hydrostatic gas motions. Yet Churazov et al. (2008) found that the gas is close to hydrostatic away from the regions of most significant disturbance.

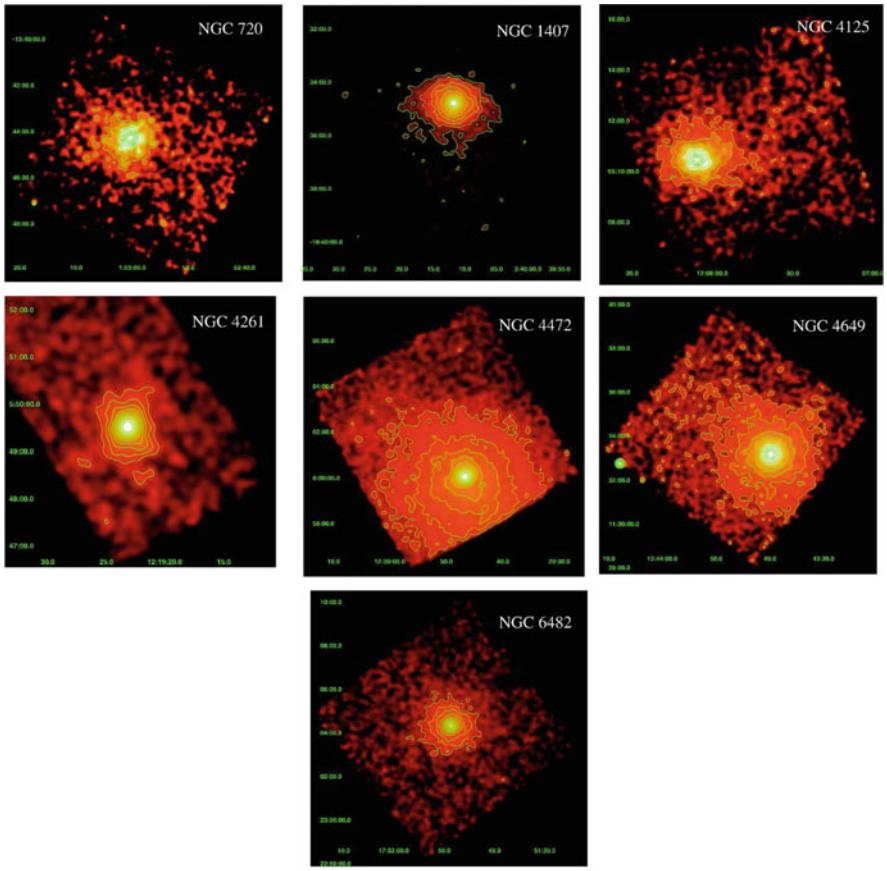

Fig. 8.1 A sample of seven nearby elliptical galaxies that are suitable for hydrostatic analysis, with each possessing regular morphologies as revealed by their *Chandra* images (Humphrey et al. 2006)

several of these galaxies, radial entropy profiles have been computed (Humphrey et al. 2008, 2009, 2010) and found to increase monotonically with radius as also found in groups and clusters (Pratt et al. 2010), indicating that the hot ISM is stable to convection and consistent with approximate hydrostatic equilibrium.

8.2.3 On the Incidence of Relaxed Elliptical Galaxies

In a controversial study, Diehl and Statler (2007) investigated the X-ray and optical isophotal ellipticities in a heterogeneous sample of early-type galaxies to test whether they are consistent with hot ISM obeying hydrostatic equilibrium.

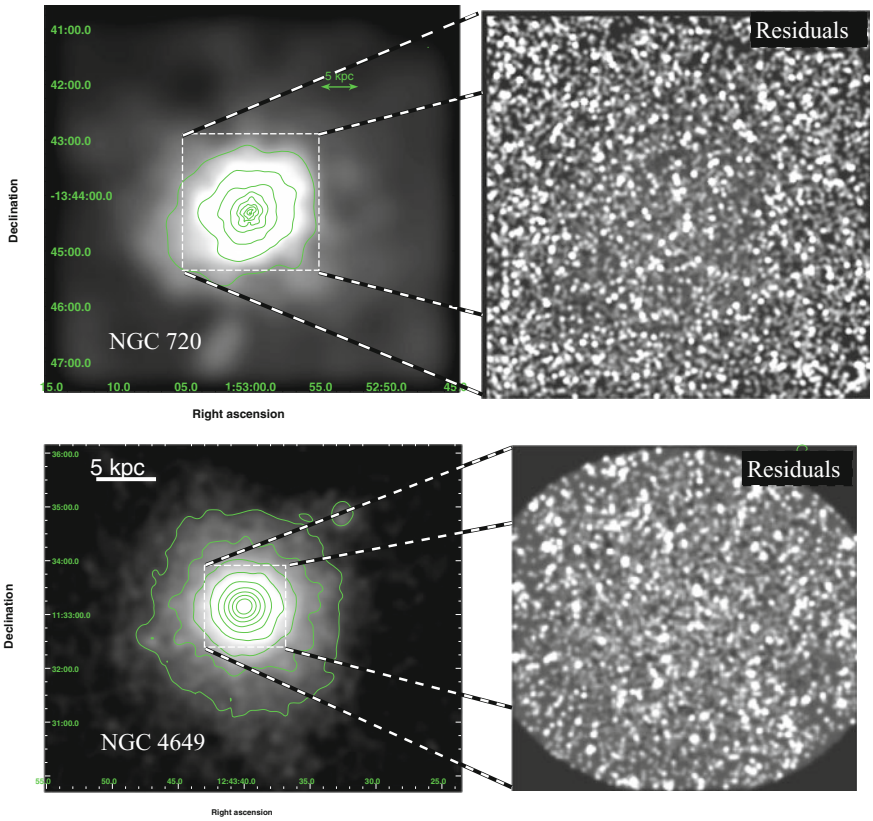

Fig. 8.2 Residual significance images of the central regions of NGC 720 (*top*, adapted from Humphrey et al. 2010) and NGC 4649 (*bottom*), indicating deviations from a smooth model fit to the X-ray isophotes (Humphrey et al. 2008, 2010). Both galaxies appear to be relaxed and symmetrical at all scales accessible to the *Chandra* images

The expected correlation between the ellipticities assumes that both hydrostatic equilibrium holds exactly and mass follows (optical) light, so that the stars define the shape of the gravitational potential and thus the shape of the X-ray emission. In an attempt to mitigate the impact of any DM halo, Diehl and Statler restricted their analysis of each galaxy to within a small radius – 60–90% of the optical half-light radius. When the expected correlation between the X-ray and optical isophotal ellipticities was not found, they concluded that hydrostatic equilibrium is not ubiquitous and, therefore, should never be assumed (even approximately) in mass analysis. They speculate that assuming hydrostatic equilibrium will always result in an error typically as large as the value of the mass measured; i.e., relaxed elliptical galaxies do not exist. While we agree (as detailed in the previous section) that care should be exercised in the application of hydrostatic equilibrium to the

study of elliptical galaxies, we strongly disagree with their general conclusions about the accuracy of X-ray mass measurements.

The observed lack of a correlation does not allow conclusions to be drawn with certainty for an individual object; it only indicates that hydrostatic equilibrium is unlikely to hold perfectly in a galaxy randomly drawn from their sample, provided it is chosen without any consideration of its morphology. As noted above, hydrostatic equilibrium as expressed by (8.8) is an approximation and is not expected to hold exactly given especially the impact of turbulence on the hot ISM induced by past mergers and AGN feedback. In other words, no elliptical galaxy is expected to be perfectly relaxed. The objects displayed in Figs. 8.1 and 8.2 are among the most relaxed elliptical galaxies possessing high-quality X-ray data. But Diehl and Statler's sample also contained galaxies with pronounced large-scale asymmetries that we would not recommend the routine application of hydrostatic mass methods following the guidelines discussed previously (e.g., NGC 4636: Jones et al. 2002 and M 84: Cavagnolo et al. 2010), and since they focused on the smallest scales (where X-ray point-source removal is most challenging and where AGN-driven disturbances are most serious), in contrast to the larger scales that are most important for DM analysis, the implications of their study for DM measurements of morphologically relaxed systems are dubious and provide no basis for claiming typical mass errors $\gtrsim$100% on all scales in such systems.

An example of how conclusions regarding the center of a galaxy need not apply on larger scales is provided by NGC 5044. In this system Diehl and Statler measured an X-ray ellipticity (0.41 ± 0.08) greatly exceeding the optical value (0.07 ± 0.01), which cannot be reconciled easily with hydrostatic equilibrium (unless the gas is also rapidly rotating). But the X-ray ellipticity measurement is confined to the region within the optical half-light radius (<4 kpc) containing obvious disturbances presumed to be associated with AGN feedback (Buote et al. 2003a, Gastaldello et al. 2009, David et al. 2009). (We note, however, that there is recent evidence that turbulent motions of the hot ISM are negligible compared to the sound speed in the center of NGC 5044 (Sanders et al. 2010).) The X-ray emission can be traced out at least to several hundred kpc, about one-third of the virial radius (David et al. 1994, Buote et al. 2004). Outside of the very central region discussed by Diehl and Statler, the X-ray isophotes are largely symmetric and nearly circular, and acceptable fits with hydrostatic models are obtained (Gastaldello et al. 2007).

Now turning our attention to the central regions within the optical half-light radius relevant to the study of SMBHs (Sect. 8.7), we remark that additional factors can introduce scatter into the correlation between the isophotal ellipticities generated by the stars and hot ISM. As noted above, Diehl and Statler assume that the mass traces the same shape as the optical light, whereas both X-ray and optical observations suggest DM distributed differently from the stars typically contributes 20–30% within the half-light radius in giant elliptical galaxies (see Sect. 8.4). Furthermore, their novel technique to create X-ray images of diffuse hot ISM strictly requires there are no spatial variations in the spectral properties; i.e., every galaxy is assumed to be isothermal with constant metallicity throughout, in conflict with observations of many galaxies possessing high-quality X-ray data (Buote 2002,

Buote et al. 2003b, Kim and Fabbiano 2004, Humphrey and Buote 2006, Fukazawa et al. 2006, Matsushita et al. 2007, Rasmussen and Ponman 2007, Komiyama et al. 2009). Finally, ISM rotation might be important in some galaxies and yet have little relation to stellar rotation because slowly rotating inflowing gas at large radius might be spun up to dynamically relevant velocities if angular momentum is conserved. But rotational spin-up is not guaranteed for every galaxy, and instead the gas can be outflowing gently in a subsonic wind greatly reducing the impact of any rotation initially provided by the stars – see discussion in Mathews and Brighenti (2003a).

Before leaving this topic, we caution that a statistical appraisal of the properties of the hot ISM in any sample of elliptical galaxies should consider the sample selection criteria. Our impression of the X-ray properties of elliptical galaxies is obtained within the context of what are essentially optically selected samples. But for the study of ISM properties, it is important to select the sample according to the ISM luminosity and not the total X-ray luminosity which also contains the emission from discrete sources associated with the stellar population. Diehl and Statler follow the common approach of studying a "heterogeneous" sample of elliptical galaxies, which essentially amounts to collecting all objects in the archives with data of sufficient quality. This procedure resulted in a sample containing some well known objects with extended, X-ray luminous ISM (e.g., NGC 4472) and some where virtually all the X-ray emission can be attributed to discrete sources (e.g., NGC 3379 – Revnivtsev et al. (2008), Trinchieri et al. (2008)).

It is instructive, therefore, to consider a sub-sample extracted from their sample of 54 galaxies that is selected based on the X-ray luminosity of the diffuse gas. Using the tabulated diffuse gas luminosities published by Diehl and Statler, we construct such a sub-sample by excluding massive group/cluster systems (gas $L_{\rm x} > 3\times10^{42}$ erg s^{-1}) and gas-poor galaxies (2σ lower limit on gas $L_{\rm x} < 1\times10^{40}$ erg s^{-1}) resulting in a sample of 26 galaxies, give or take a few depending on how we interpret the quoted lower or upper limits for some systems. This sub-sample includes the seven galaxies shown in Fig. 8.1, as well as several other systems with generally regular X-ray images and where hydrostatic equilibrium previously has been profitably employed – NGC 533, NGC 1399, NGC 1404, NGC 3923, NGC 4555, NGC 5044. The sample also contains well-known disturbed systems such as M 84, NGC 4636, and NGC 5846, which are expected to deviate from hydrostatic equilibrium. In sum, an ISM-selected sub-sample culled from Diehl and Statler's heterogeneous sample indicates that approximately 50% of the elliptical galaxies are sufficiently relaxed for hydrostatic analysis.

8.2.4 Methods

The variety of techniques that have been developed to apply hydrostatic equilibrium to the study of the mass distributions in elliptical galaxies (as well as galaxy clusters) can be divided into two broad classes that will be denoted here as *smoothed inversion* and *forward-fitting*. Whereas the forward-fitting approach

assumes parameterized models for the mass profile and one thermodynamical variable of the gas (e.g., temperature profile), smoothed inversion instead introduces one or more arbitrary parameters to guarantee a smooth (physical) mass profile. The decision of whether or not to adopt a particular approach depends on several factors which we discuss below. Generally, the smoothed inversion approach is preferred if one is primarily interested in measuring the value of the enclosed mass within some radius without making any reference to an assumed (parameterized) mass model. If instead one desires to test the viability of an assumed mass model (e.g., power-law, NFW) and to measure its parameters for comparison to other galaxies and theory, the forward-fitting approach is preferred. Whenever possible both approaches should be employed to assess the magnitude of any biases.

We note that in the following it is generally assumed that the gas density and temperature profiles (projected or deprojected) of the hot gas have been already obtained via an analysis of the spatially resolved X-ray spectra. The hydrostatic models then use these measured profiles to constrain the mass distribution. This decoupling of the spectral fitting and mass modeling, though convenient and generally less computationally expensive, is not necessary. The formalism of both of these approaches is reviewed in Appendix B of Gastaldello et al. (2007).

In the following subsections, we outline in more detail how the two broad model classes are implemented.

8.2.4.1 Smoothed Inversion

Pros:

- Mass measured without reference to an input parameterized model.
- Does not require an input parameterized model for the gas temperature, density, pressure, or entropy.

Cons:

- Deprojection requires a high degree of symmetry (usually spherical).
- Cannot self-consistently account for the projection of galaxy emission from any radii outside of the observed data range or, generally, extrapolate the hydrostatic model outside the data range.
- Arbitrary smoothing required to obtain a physical (monotonically increasing) mass profile. The amount of smoothing increases for lower data quality.

The aim of the smoothed inversion approach is to measure the mass profile without reference to an assumed (parameterized) model for the mass distribution or any quantity associated with the hot ISM (gas temperature, density, pressure, or entropy). For this to be achieved, the three-dimensional distribution of the hot ISM must be obtained by non-parametrically deprojecting the data on the sky. This is only possible if the ISM has a high degree of symmetry, and therefore

spherically symmetric deprojection using the well-known "onion peel" method originally developed for clusters is almost always adopted (Fabian et al. 1981, Kriss et al. 1983). Since the onion peeling starts from the outer edge of the galaxy and works its way inward, such deprojection formally requires that the data span the entire size of the galaxy. As this is not generally the case, ad hoc prescriptions are usually employed to estimate the projection of gas from radii larger than the extent of the available data (Nulsen and Bohringer 1995, Buote 2000).

Because no global mass model is assumed, the value of the mass determined within a given shell can be negative due to noise in the data (amplified by deprojection). To circumvent this problem so as to achieve a mass profile that increases monotonically with radius, the inversion procedure must smooth the gas quantities (e.g., temperature and density) and the mass profile itself. The amount and type of smoothing is arbitrary, and typically as the data quality decreases the amount of smoothing required to achieve interesting constraints generally increases. As discussed below, types of smoothing include (1) the use of ad hoc smooth parameterized models for the gas density and temperature, (2) assuming the ISM is constant in spherical shells so that the widths of the shells set the smoothing scales, and (3) one or more parameters in a Bayesian prior. While the smoothing can be well-motivated, it necessarily introduces additional assumptions, usually expressed by additional parameters that must be determined empirically by the data. Consequently, we believe that the terms "non-parametric" or "model-independent" sometimes used to describe smoothed inversion methods are misleading and should be avoided.

In the context of DM studies, smoothed inversion is best suited to providing a measurement of the enclosed mass within a particular radius without assuming a specific parameterized mass model; e.g., measuring M_{500} for the purpose of establishing the mass function of elliptical galaxies. But if one also desires to fit and measure the parameters of a mass model (e.g., global power-law slope, NFW concentration parameter), the ad hoc smoothing adds a barrier between the data and model which is not present in the forward-fitting approach that is more naturally suited for this problem.

8.2.4.2 Traditional Approach: Parameterized Density and Temperature Profiles

For a spherically symmetric galaxy where the hot ISM is supported by ideal gas pressure, (8.8) can be solved for the total gravitating mass (stars, gas, and DM) as a function of the gas density ($\rho_{\rm gas}$) and temperature (T),

$$M(<r) = -\left[\frac{r k_{\rm B} T}{\mu m_{\rm a} G}\right]\left[\frac{d\ln\rho_{\rm gas}}{d\ln r} + \frac{d\ln T}{d\ln r}\right], \tag{8.9}$$

where $k_{\rm B}$ is Boltzmann's constant, μ is the mean atomic weight of the gas, $m_{\rm a}$ is the atomic mass unit, and G is Newton's gravitation constant. Beginning with M 87 over

30 years ago (Mathews 1978, Fabricant et al. 1980), this equation has been widely applied to galaxies and clusters, traditionally by inserting smooth parameterized functions for the density and temperature into (8.9). The ad hoc parameterized functions do not guarantee a physical mass profile that increases monotonically with increasing radius, and their use offsets any gain in rigor from not assuming a specific mass model. Thus, while this traditional approach has the advantage of being conceptually simple and computationally inexpensive, it is best employed as a rough estimate and a check on other methods.

8.2.4.3 Smoothing by Binning

The derivatives in (8.9) may instead be computed directly from the density and temperature values measured in adjacent radial bins rather than by assuming any parameterized models. Because of bin-to-bin statistical fluctuations in the density and temperature (or pressure) profiles, increased binning (i.e., smoothing) of the radial profile is generally required to produce an approximate monotonically increasing mass profile. This method has only been attempted for the brightest galaxy clusters (David et al. 2001, Voigt and Fabian 2006), since only for data of the highest quality can interesting results be obtained without resorting to heavy binning of the data.

Recently, Nulsen et al. (2010) have proposed a scheme that obviates the need for explicit computation of the derivatives by assuming that within any spherical shell the gravitating matter density and gas temperature are constant. By requiring that the gas pressure be continuous across shell boundaries, the gas density is then computed within any shell using an isothermal solution of (8.8). But the pressure continuity condition involves the difference in the gravitational potential between adjacent shells, which is related to a derivative (and is the argument of an exponential). Consequently, the mass profile derived from this procedure remains subject to similar bin-to-bin statistical fluctuations that occur when the derivatives in (8.9) are computed explicitly. To improve the smoothness of the derived mass profile, Nulsen et al. advocate requiring that the gravitating matter density decrease monotonically with increasing radius.

8.2.4.4 Bayesian Inversion with Smoothing Prior

A very general approach to smoothed inversion has been proposed by Das et al. (2010), which is based on the seminal works of Merritt and Tremblay (1994) and Magorrian (1999). Das et al. enforce smoothness via a Bayesian prior which penalizes large second derivatives between radial bins in the temperature, circular velocity (hence the mass), and pressure gradient. The magnitude of the smoothing is controlled by a parameter λ, the value of which is arbitrary and depends on both the number of radial bins and the model grid spacing. For convenience Das et al. use simulations to select a fixed λ for all galaxies. Since the sensitivity of the derived

mass profile to λ should be investigated for any galaxy, a reasonable extension would be to define a prior for λ and then marginalize over λ for each system.

8.2.4.5 Forward-Fitting

Pros:

- No formal restrictions on galaxy geometry (though spherical symmetry usually assumed).
- Allows for self-consistent extrapolation of hydrostatic model and projection of galaxy emission to and from any radii outside the data range.

Cons:

- Requires an input parameterized model for the mass.
- Requires an input parameterized model for one of the following thermodynamic quantities: gas temperature, density, pressure, or entropy.

The forward-fitting approach uses parameterized models for the mass and one thermodynamic variable of the hot ISM (density, temperature, pressure, or entropy). Because the galaxy is completely specified by the models, in principle any geometrical configuration can be accommodated, though spherical symmetry is usually assumed. The model can be extrapolated to radii outside the available data range allowing for self-consistent treatment of the projection of the ISM of the entire galaxy. Forward-fitting can be applied to data that have been deprojected (as with smoothed inversion) or directly to the data on the sky. The ability to fit projected models to data on the sky is especially important for lower quality, noisy data whose integrity would be unacceptably degraded by deprojection noise.

This approach is preferred when it is desired to test the viability of a particular mass model and to measure its parameters. If the assumed model is incorrect, then the measured mass at a given radius may differ systematically from the true value. It is therefore necessary to explore multiple mass models to gauge the magnitude of any bias. Since the measured mass may be sensitive to the assumed mass model, when possible results using forward-fitting should be compared to those from smoothed inversion.

Prior to *Chandra* and *XMM*, when accurate spatially resolved temperature profiles were only available for a few of the most massive galaxies, it was customary to make strong assumptions about the temperature profile in order to obtain an interesting constraint on the DM. Typically the gas was assumed to be isothermal or that it obeyed a polytropic equation of state ($P_{\rm gas} \propto \rho_{\rm gas}^{\gamma}$). The most widely used of these approaches is the well-known isothermal "beta model" (Cavaliere and Fusco-Femiano 1976, 1978; Sarazin and Bahcall 1977). While such procedures still can be useful for obtaining DM estimates from observations of low data quality,

we focus our discussion on methods intended to exploit accurate spatially resolved temperature profiles, as such data are now more widely available.

8.2.4.6 Density-Based

If an assumption is made about the form of the gas density profile, e.g., that it is described by a parameterized function, then taken together with an assumed parameterized mass model the equation of hydrostatic equilibrium (8.8) may be solved to give the temperature,

$$T(r) = T_0 \frac{\rho_{\rm gas,0}}{\rho_{\rm gas}(r)} - \frac{\mu m_{\rm a} G}{k_{\rm B}} \frac{1}{\rho_{\rm gas}(r)} \int_{r_0}^{r} \rho_{\rm gas}(r) \frac{M(<r)}{r^2}\, dr, \tag{8.10}$$

where $T_0 = T(r_0)$ and $\rho_{\rm gas,0} = \rho_{\rm gas}(r_0)$ evaluated at some reference radius r_0. Here and below we assume spherical symmetry unless noted otherwise (i.e., in Sect. 8.6). The parameters of the mass and density models and the normalization T_0 are then constrained by the observation. As with all the types of forward-fitting approaches we discuss, it is common practice first to measure the temperature and density profiles from fitting the spectra and then constrain the free parameters of the hydrostatic model via a simultaneous fit to the measured profiles. Although the gas contribution to the total mass $M(<r)$ in elliptical galaxies can generally be neglected until one approaches close to the virial radius, a self-consistent hydrostatic model should include it. For these density-based models this is straightforward since the gas density profile is assumed, and therefore the gas mass profile is defined before the temperature profile is computed.

An important variation of the density-based approach was proposed by Fabian and colleagues (Fabian et al. 1981, Kriss et al. 1983, White et al. 1997, Allen et al. 2001) which exploits the relatively high statistical quality of the X-ray surface brightness profile. Sometimes referred to as the "Cambridge Method", this approach assumes spherical symmetry and analytically deprojects the surface brightness using the onion peel procedure to give the three-dimensional emissivity profile, $\epsilon \propto \rho_{\rm gas}^2 \Lambda(T,Z)$, where $\Lambda(T,Z)$ is the plasma emissivity which depends on temperature T and metal abundances Z and is integrated over the relevant (broad) wave band. If $\Lambda(T,Z)$ is assumed to be constant over the galaxy, then $\rho_{\rm gas}(r) \propto \sqrt{\epsilon(r)}$. Because of the relatively high statistical quality of the surface brightness (and emissivity), the density profile derived in this way usually can be evaluated in much finer spatial bins than is possible for the temperature profile determined from detailed spectral fitting. This allows the finely binned density profile to be treated as a continuous function by interpolating values between the bins, which can then be inserted (along with a parameterized mass model) into (8.10) to predict the temperature profile for comparison to the values measured from the spectra.

It is a significant advantage of the Cambridge Method that it does not require for input an assumed, possibly oversimplified, parameterized model for the density

profile. Still, the density profile generated assuming a constant Λ leads to hydrostatic solutions that are not self-consistent in the presence of temperature and metallicity gradients. This effect is not expected to be large because variations in Λ within a galaxy or cluster are probably no more than $\sim$20%, which translate to inferred density differences of only $\sim$10%. In principle, the best-fitting temperature profile could be used to define a new spatially varying Λ from which a new density profile could be computed. The process could be iterated to achieve improved self-consistency.

8.2.4.7 Temperature-Based

If an assumption is made about the form of the temperature profile, then in conjunction with a parameterized mass profile the equation of hydrostatic equilibrium (8.8) may be solved for the gas density,

$$\rho_{\rm gas}(r) = \rho_{\rm gas,0}\frac{T_0}{T(r)}\exp\left[-\frac{\mu m_{\rm a} G}{k_{\rm B}}\int_{r_0}^{r}\frac{1}{T(r)}\frac{M(<r)}{r^2}dr\right], \tag{8.11}$$

where spherical symmetry is again assumed. This approach can be especially useful when the temperature profile is poorly constrained by the data. Simple profiles (constant, power-law) can be adopted in order to explore their impact on the inferred mass profile. Unlike the density-based case, the gas mass contribution to $M(<r)$ cannot be included fully self-consistently in the fit. However, because the gas mass can be treated as a small perturbation, an iterative procedure can be employed; i.e., after first taking the gas mass contribution to $M(<r)$ to be zero, use the resultant best-fitting $\rho_{\rm gas}(r)$ to compute a fixed gas mass profile that is added to $M(<r)$ and then fit again.

8.2.4.8 Entropy-Based

Recent studies have suggested that the entropy is the logical thermodynamic variable for which to assume a parameterized model (Humphrey et al. 2008, 2009, Cavaliere et al. 2009, Fusco-Femiano et al. 2009). Consistent with the hydrostatic equilibrium approximation is the requirement that the hot gas be stable against convection at every radius. Convective stability provides an important additional constraint on the mass profile that has been used in the past to set a robust lower limit on the total masses of galaxy clusters (Fabian et al. 1986). For an ideal gas equation of state the first law of thermodynamics can be solved to yield the specific entropy, $s = (3k_{\rm B}/2\mu m_{\rm a})\ln(T\rho_{\rm gas}^{-2/3}) + {\rm constant}$. It is conventional for studies of the hot gas in galaxies and clusters to remove the logarithm and the numerical factor to define the quantity, $S \equiv (k_{\rm B}/\mu m_{\rm a})T\rho_{\rm gas}^{-2/3}$, which we will refer to as the "entropy" in our discussion.

If parameterized models are assumed for both the entropy and mass profiles, then the equation of hydrostatic equilibrium can be rewritten so that,

$$\frac{d\xi}{dr} = -\frac{2}{5}\frac{GM(<r)}{r^2}S^{-3/5}, \qquad \xi \equiv P^{2/5}. \tag{8.12}$$

Solving this equation for ξ gives the profiles of gas density, $\rho_{\rm gas} = (P/S)^{3/5} = S^{-3/5}\xi^{3/2}$, and temperature, $k_{\rm B}T/\mu m_{\rm a} = S^{3/5}P^{2/5} = S^{3/5}\xi$, which are compared to the observation to constrain the parameters of the input S and $M(<r)$ models. Since, however, the total mass $M(<r)$ also includes the gas mass which depends on ξ, (8.12) can be solved for ξ by direct integration only if the gas mass is negligible with respect to the mass of the stars and DM. To include the gas mass self-consistently, (8.12) can be differentiated and rearranged to yield,

$$\frac{d}{dr}\left(r^2 S^{3/5}\frac{d\xi}{dr}\right) + \frac{8\pi r^2 G}{5}S^{-3/5}\xi^{3/2} = -\frac{8\pi r^2 G}{5}\left(\rho_{\rm stars} + \rho_{\rm DM}\right), \tag{8.13}$$

where use has been made of the relation $dM(<r)/dr = 4\pi r^2(\rho_{\rm stars} + \rho_{\rm DM} + \rho_{\rm gas})$. The two boundary conditions for this second-order differential equation require specifying the values of ξ and $d\xi/dr$ at some radius. The value of ξ amounts to specifying the pressure at some radius, which is just a normalization constant determined by the fitting of the density and temperature profiles. As discussed by Humphrey et al. (2008), because the gas mass makes a negligible contribution to the total mass at small radius, (8.12) can be evaluated at such a small radius to give the $d\xi/dr$ boundary condition.

The Schwarzschild criterion for convective stability requires that the entropy increases monotonically with increasing radius, consistent with observations of relaxed elliptical galaxies, for which the entropy profiles are well described by simple models of a constant with a broken power-law (Humphrey et al. 2008, 2009, 2010). The Schwarzschild criterion also effectively limits the magnitude of any temperature gradient. Stronger restrictions on the temperature gradient potentially could be enforced by MTI/HBI instabilities (Balbus 2001, Quataert 2008) that develop in the weakly magnetized plasma characteristic of the hot gas in a galaxy cluster. These instabilities arise when heat and momentum transport occurs only along magnetic field lines, which may happen in regions of a plasma where the gyroradius is much smaller than the the Coulomb mean free path (such as for an elliptical galaxy – see Sect. 8.2.1). But since these instabilities are expected to be weaker for the lower temperatures of elliptical galaxies, and they are also suppressed by small amounts of turbulence (Parrish et al. 2010, Ruszkowski and Oh 2010), their relevance to elliptical galaxies is unclear.

Whereas gas density and temperature profiles display a large range of behavior, a robust result of cosmological simulations considering only gravity is that the radial entropy profile follows a power-law, $S(r) \sim r^{1.1}$ (Tozzi and Norman 2001, Voit et al. 2005). Since the cooling and feedback processes that would modify this relation are expected to be most significant closer to the centers of halos, the $S(r) \sim r^{1.1}$ relation

provides a physically well-motivated asymptotic relation that is particularly useful when extrapolating the hydrostatic model outside the data range (e.g., computing model projections).

8.3 Is DM Required?

Prior to the launches of *Chandra* and *XMM*, the principal limiting factor for X-ray studies of DM in elliptical galaxies was the temperature profile (though see Sect. 8.6). In most cases isothermality was assumed, but the possibility of large radial temperature gradients meant that no firm conclusions on DM could be obtained for most galaxies (Fabbiano 1989). For a small number of the brightest, hottest ($k_{\rm B}T \sim 1$ keV), most massive (few $\times\, 10^{13}{\rm M}_{\odot}$) galaxies, *ROSAT* was able to place interesting constraints on the temperature profiles, from which large amounts of DM were inferred: NGC 1339 (Jones et al. 1997), NGC 4472 (Irwin and Sarazin 1996, Brighenti and Mathews 1997), NGC 4649 (Brighenti and Mathews 1997), and NGC 5044 (David et al. 1994).

Now accurate temperature profiles have been measured with *Chandra* and *XMM* for many galaxies (Fig. 8.3). The shapes of the radial temperature profiles of early-type galaxies can be separated into roughly two classes (Fukazawa et al. 2006, Humphrey et al. 2006, Nagino and Matsushita 2009): (1) those with profiles that rise toward the center, corresponding to galaxies with $M_{\rm vir} \lesssim 10^{13}\, M_{\odot}$ and average temperature $k_{\rm B}T \sim 0.5$ keV, and (2) those with profiles that fall toward the center, corresponding to galaxies with $M_{\rm vir} \gtrsim 10^{13}\, M_{\odot}$ and average temperature $k_{\rm B}T \sim 1$ keV. These temperature profiles enable accurate DM constraints for many galaxies, including lower mass systems (few $\times\, 10^{12}{\rm M}_{\odot}$).

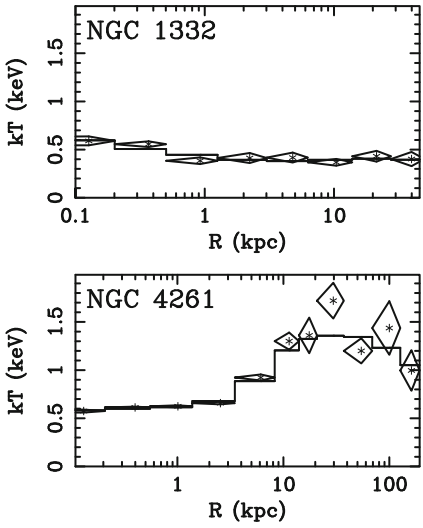

Fig. 8.3 *Chandra* temperature profiles of two galaxies from Humphrey et al. (2009). The *top panel* shows the centrally rising profile of NGC 1332 characteristic of galaxies with $M_{\rm vir} \lesssim 10^{13}\, M_{\odot}$ and average temperature $k_{\rm B}T \sim 0.5$ keV. The *bottom panel* shows the centrally falling profile of NGC 4261 characteristic of galaxies with $M_{\rm vir} \gtrsim 10^{13}\, M_{\odot}$ and average temperature $k_{\rm B}T \sim 1$ keV. The K-band half-light radii are 2.7 and 3.4 kpc, respectively, for NGC 1332 and NGC 4261

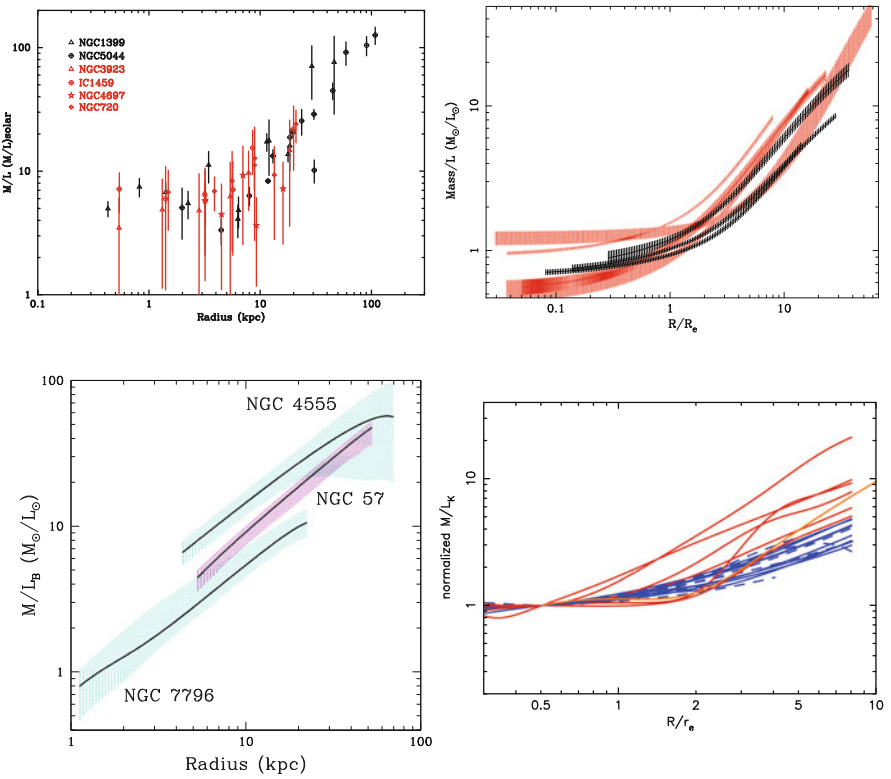

Fig. 8.4 Representative total mass-to-light (M/L) ratios of elliptical galaxies obtained from *Chandra* and *XMM* observations clearly showing rising M/L, and thus the need for DM, outside of $1-2$ optical half-light radii. (*Top Left*) Clear confirmation of rising M/L in the massive galaxies NGC 1399 and NGC 5044 (Fukazawa et al. 2006) found previously with *ROSAT* observations. (*Top Right*) Results for the galaxies displayed in Fig. 8.1 obtained by Humphrey et al. (2006). The *black regions* correspond to the galaxies NGC 720, NGC 4325, and NGC 6482 that have $M_{\rm vir} \lesssim 10^{13}\,M_{\odot}$ while the *red regions* correspond to the galaxies NGC 1407, NGC 4472, NGC 4649, and NGC 4261 that have $M_{\rm vir} \gtrsim 10^{13}\,M_{\odot}$. Each result shown reflects a 1σ confidence region. (*Bottom Left*) 1σ error regions for three galaxies from O'Sullivan and Ponman (2004) and O'Sullivan et al. (2007a), where isothermal temperature profiles have been adopted for NGC 57 and NGC 7796. (*Bottom Right*) Results from Nagino and Matsushita (2009) for M/L profiles of galaxies with temperature profiles that fall toward the center (*red lines*) and for others (*blue lines*)

Equipped with accurate temperature profiles from *Chandra* and *XMM*, precise constraints on mass-to-light ratios (M/L) have now been obtained for many galaxies (Sun et al. 2003, O'Sullivan and Ponman 2004, Fukazawa et al. 2006, Humphrey et al. 2006, Gastaldello et al. 2007, O'Sullivan et al. 2007a,b, Zhang et al. 2007, Humphrey et al. 2008, 2009, Nagino and Matsushita 2009, Humphrey et al. 2010); here M is the total mass and L is the stellar luminosity, each computed within the same radius. Generally, for those galaxies with good constraints on the temperature profile out to a large radius, the data exclude a constant M/L profile at

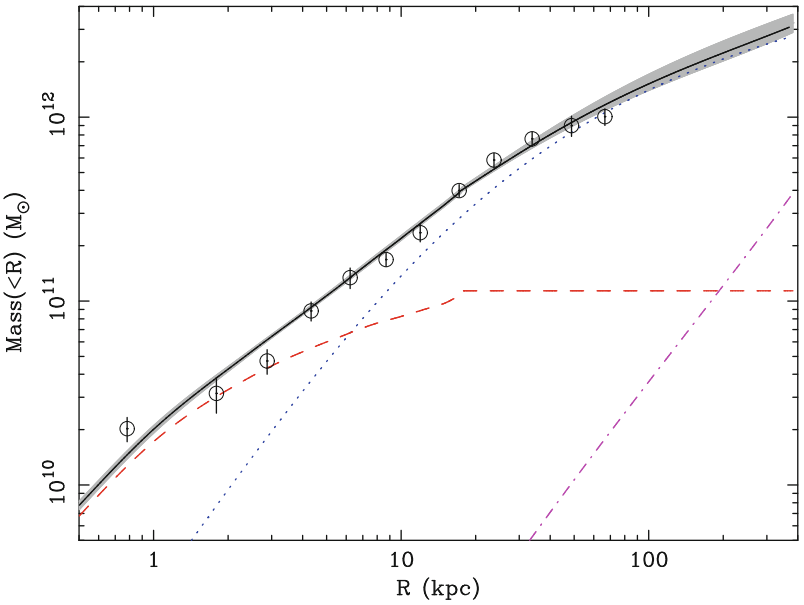

Fig. 8.5 Radial mass profile of NGC 720 obtained by Humphrey et al. (2010) using deep observations with *Chandra* and *Suzaku*. The *solid (black)* line indicates the total enclosed mass, the *dashed (red)* line indicates the stellar mass, the *dotted (blue)* line is the DM contribution, and the *dash-dot (magenta)* line is the gas mass contribution. The *grey shaded* regions indicate the 1σ error on the total mass distribution obtained using the entropy-based forward-fitting method. Overlaid are a set of data points derived from an independent analysis using the traditional smoothed inversion approach; i.e., the model indicated by the shaded region was not obtained by fitting these data points. Notice that DM is clearly required for radii larger than $\sim$ 5 kpc, about $2R_e$, where $R_e = 3.1$ kpc is the K-band half-light radius; see the electronic version for a color version of this figure

high significance, instead requiring that M/L rises with increasing radius outside of 1–2 optical half-light radii (Fig. 8.4). The failure of the constant M/L model provides strong evidence for DM.

It should be stressed that the current generation of X-ray satellites is able for the first time to provide excellent constraints on DM in lower mass galaxies with average temperature $k_{\rm B}T \sim 0.5$ keV. Combining data from deep observations with *Chandra* and *Suzaku*, Humphrey et al. (2010) obtained strong constraints on the mass profile of NGC 720 (see Fig. 8.5) which was found to have a total mass ($M_{2500} = 1.6 \pm 0.2 \times 10^{12}\, M_\odot$) similar to that of the Milky Way.

This X-ray evidence for DM determined individually for a relatively small number of elliptical galaxies ($\sim$15, depending on the upper mass limit) is complemented by evidence from large statistical studies in the optical. Weak lensing (Hoekstra et al. 2005, Kleinheinrich et al. 2006, Mandelbaum et al. 2006, Heymans et al. 2006) and the dynamics of satellite galaxies (Prada et al. 2003) consider the accumulated data from a very large number of galaxies and find that the average halo mass $\sim 10^{12}\, M_\odot$ clearly exceeds that which can be attributed to the stars. As for constraints on

individual systems, strong evidence for DM using sophisticated, orbit-based stellar dynamical models has been found recently for NGC 4649 (Shen and Gebhardt 2010), although the mass somewhat exceeds that inferred by X-rays, a point to which we shall return in more detail in Sect. 8.8.

8.4 Radial DM Profile

Although the need for DM is now established for many elliptical galaxies, the X-ray data do not as of yet clearly favor a specific model for the radial profile. In particular, both the NFW and $\sim r^{-2}$ DM density profiles are consistent with available data. The NFW profile provides a useful means to compare observed DM halos to those predicted by cosmological models. The two parameters which specify the NFW profile are the concentration c_Δ and halo mass M_Δ. The concentration is defined as, $c_\Delta = r_\Delta / r_s$, where r_s is a scale radius (denoting the radius at which the logarithmic denstiy slope is -2), and r_Δ is a reference radius defined so that the average density of the halo within the sphere of radius r_Δ equals the number Δ times the critical density of the Universe. Quoted values for Δ typically range from 100–2,500. The mass, M_Δ, is the mass enclosed within r_Δ. Often Δ is chosen to be the solution to the spherical collapse model at the time of cluster virialization (Bryan and Norman 1998), where $\Delta \sim 100$ at the present epoch in the standard ΛCDM cosmology, in which case the parameters are sometimes referred to as the "virial radius", $r_{\rm vir}$, "virial mass", $M_{\rm vir}$, and "virial concentration", $c_{\rm vir}$.

Dissipationless simulations of the ΛCDM model predict $c_{\rm vir} \approx 10$ for DM halos with an intrinsic scatter of $\approx$0.1 dex over the mass range of elliptical galaxies considered in this review (Bullock et al. 2001, Macciò et al. 2008). Some early measurements obtained much larger concentrations on these mass scales inconsistent with theory. Firstly, Sato et al. (2000) attempted to deconvolve the large, energy-dependent PSF of *ASCA* observations, which is challenging given that the size of the PSF ($>1'$) is generally as large or larger than the optical half-light radii of nearby elliptical galaxies observed in X-rays. Secondly, Wu and Xue (2000) used *ROSAT* observations, but they had to assume the gas is isothermal throughout each galaxy. Finally, one early study using *Chandra* data of NGC 6482 (Khosroshahi et al. 2004) with an accurately measured (non-isothermal) temperature profile also obtained a very large concentration ($c_{200} = 61, c_{\rm vir} \sim 80$).

Mamon and Łokas (2005) proposed that such large concentrations disagreeing with theoretical expectation were primarily an artifact of neglecting to include a component for the stellar mass in X-ray determinations of the DM profile. This bias was confirmed with *Chandra* observations by Humphrey et al. (2006) in their sample of seven galaxies (Fig. 8.6), demonstrating that reliable X-ray measurements of the DM concentration on the galaxy scale definitely require the stellar mass to be modeled accurately. There is good agreement in the concentrations obtained for studies of galaxies like NGC 1407 that include the stellar mass (Humphrey et al. 2006, Zhang et al. 2007). But statistically significant systematic differences

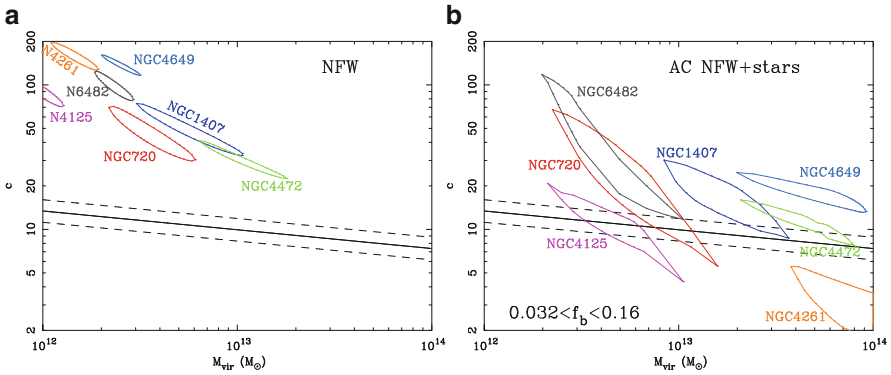

Fig. 8.6 $c_{\rm vir} - M_{\rm vir}$ results (1σ) for the seven elliptical galaxies shown in Fig. 8.1 from Humphrey et al. (2006) where the mass model includes (*Left Panel*) only a single NFW component and (*Right Panel*) an NFW model for the DM and a Hernquist model for the stellar mass. The omission of the stellar component leads to a large overestimate of the concentration parameter as originally suggested by Mamon and Łokas (2005). When including components for both the stars and DM the values are mostly consistent with the theoretical expectation within the errors (*solid line* is median and *dashed lines* 1σ intrinsic scatter), with a weak suggestion that the galaxies lie systematically above the theoretical relation, see the electronic version for a color version of this figure

can arise in some (higher mass) galaxies between studies that include stellar mass (Gastaldello et al. 2007) and those that instead exclude a large portion of the central region (Sun et al. 2009). As emphasized by Gastaldello et al. (2007), since an accurate determination of the DM concentration requires that the NFW scale radius be accurately measured, it is essential that r_s lie within the range of data being fitted. On the other hand, excluding the central region of a galaxy disturbed by AGN feedback is a reasonable approach for hydrostatic analysis. In either case, the systematic error in the adopted analysis choice needs to be investigated and quantified.

The observed $c_{\rm vir} - M_{\rm vir}$ relation for elliptical galaxies inferred from X-rays (Fig. 8.6) is broadly consistent with the cosmological prediction within the estimated observational errors. Despite the relatively large error regions, these measurements on the elliptical galaxy scale, when combined with measurements for groups and massive clusters, were crucial to providing a sufficiently wide mass baseline to establish that the $c_{\rm vir} - M_{\rm vir}$ slope is indeed negative (a robust prediction of CDM models) with a value (-0.17 ± 0.03) close to the theoretical prediction (Buote et al. 2007). However, even when accounting for the stellar mass, the normalization of the $c_{\rm vir} - M_{\rm vir}$ relation on the galaxy scale remains larger than predicted. While the effect is not highly significant for the results shown in Fig. 8.6, the recent analysis of NGC 720 (Humphrey et al. 2010) using deeper *Chandra* data mentioned previously with an improved entropy-based analysis finds $c_{\rm vir} = 26 \pm 5$, $M_{\rm vir} = 3.3 \pm 0.4 \times 10^{12}\, M_\odot$, which exceeds the theoretical prediction (considering intrinsic scatter) by about 2σ. The systematic offset could represent one or more of the following:

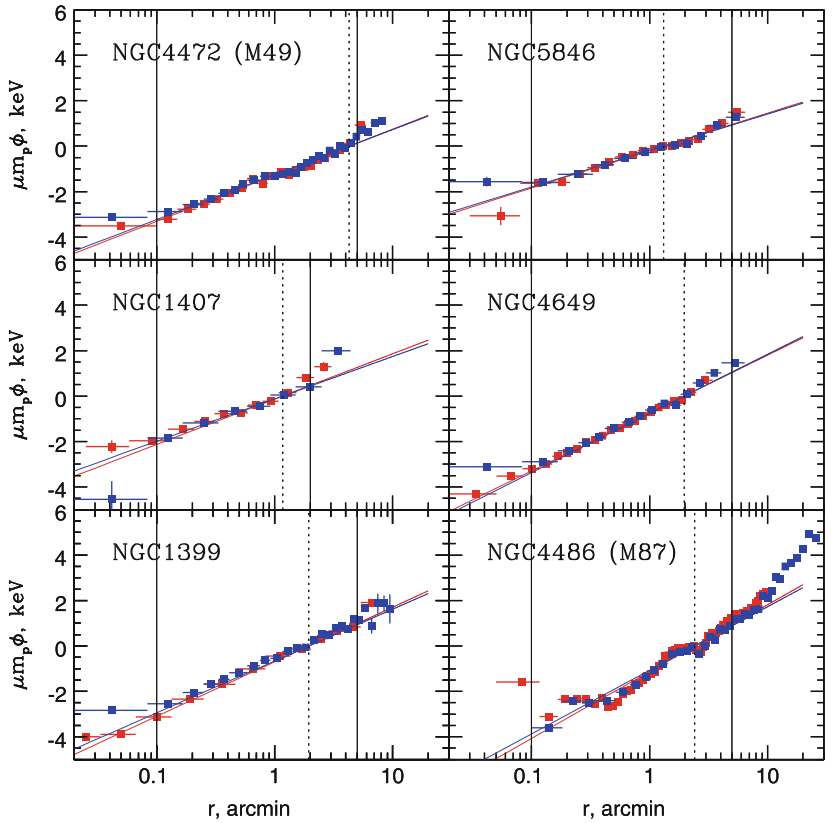

Fig. 8.7 Gravitational potential profiles and power-law fits from Churazov et al. (2010). *Chandra* data are shown in red and *XMM* in *blue*. *Solid vertical lines* indicate the radial range included for the power-law fits, while the *vertical dotted* lines indicate the optical half-light radius, see the electronic version for a color version of this figure

the selection of preferentially early forming systems (NGC 720 is a very relaxed isolated galaxy), departures from hydrostatic equilibrium (underestimate of stellar mass contribution), or the need for a different value of σ_8 or w in the cosmological model (see Buote et al., 2007). Although adiabatic contraction (Blumenthal et al. 1984, Gnedin et al. 2004) can lower the inferred concentrations, the estimated modest reductions still exceed the theoretical prediction (Humphrey et al. 2006, 2010, Gastaldello et al. 2007).

While the NFW profile is a good description of the DM profiles in elliptical galaxies, evidence continues to accumulate that the total gravitating mass is very well approximated by a single power-law over a wide radial range. Prior to *Chandra* and *XMM* many X-ray studies found mass profiles consistent with $\rho \sim r^{-\alpha}$, where $\alpha \approx 2$ (see Churazov et al. 2010, Humphrey and Buote 2010, and references therein), although isothermal gas was generally assumed. These

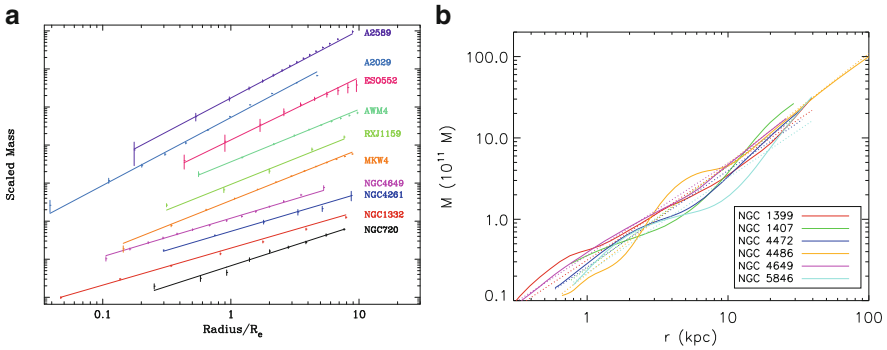

Fig. 8.8 Radial mass profiles and associated power-law fits. (*Left Panel*) Results for ten objects spanning galaxies to clusters from Humphrey and Buote (2010), arbitrarily scaled for clarity. The *solid lines* are the best-fitting profiles determined from an entropy-based forward-fitting procedure, while the data points are determined from the traditional smoothed inversion approach; i.e., the displayed models are not fitted to the data points but are derived independently. (*Right Panel*) Results for six objects from Das et al. (2010) based on X-ray data analyzed by Churazov et al. (2010). *Solid lines* show the mass best-fitting mass profiles, while the *dotted lines* show the best-fitting power-laws to these mass profiles, see the electronic version for a color version of this figure

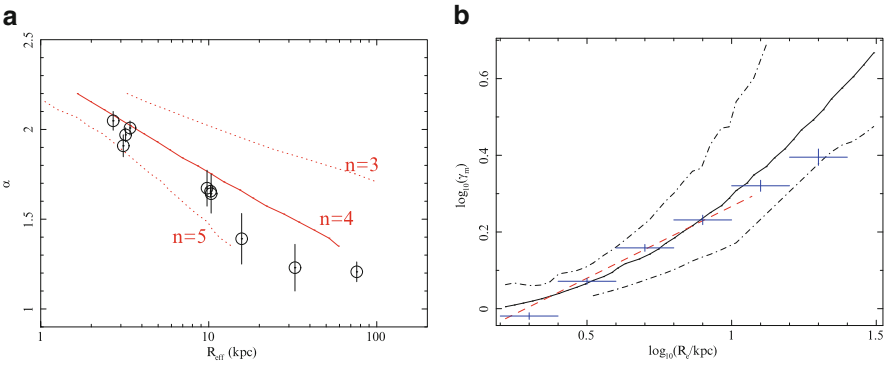

Fig. 8.9 From Humphrey and Buote (2010): (*Left Panel*) X-ray (*black circles*) measurements of logarithmic mass slope plotted against optical half-light radius. The *red lines* are model predictions decomposing a power-law total mass profile into Sersic stellar light and NFW DM profiles (see text). (*Right Panel*) Ratio γ_m of total mass to stellar mass enclosed within R_e plotted vs. R_e. The *solid line* is the model prediction corresponding to the $n = 4$ curve shown in the left panel which agrees well with the data points corresponding to the K-band M/L ratios adapted from the data of La Barbera et al. (2008), see the electronic version for a color version of this figure

results have now been confirmed and strengthened (Figs. 8.7 and 8.8) with accurate temperature profiles measured with *Chandra* and *XMM* (Fukazawa et al. 2006, Humphrey et al. 2006, Churazov et al. 2010, Humphrey and Buote 2010, Das et al. 2010). Furthermore, using *Chandra* data of 10 galaxies spanning a wide range in M_{vir} (including some clusters) and optical half-light radii (R_e), Humphrey and Buote (2010) discovered that the power-law index α decreases systematically with

increasing R_e (Fig. 8.9). This behavior can be explained by the combination of the stellar (Sersic) and DM (NFW) profiles required to produce a power-law total mass profile, which leads to the relation $\alpha = 2.31 - 0.54 \log_{10} R_e$ for a Sersic index $n \approx 4$ corresponding to a stellar de Vaucouleurs profile.

This correlation has recently been confirmed by Auger et al. (2010) using combined central velocity dispersions and strong gravitational lensing in 73 early-type galaxies. These optical results provide very important supporting evidence, but since they essentially determine a mass profile from two mass data points (i.e., at the center and at the Einstein radius of a galaxy), the X-ray measurements remain of critical importance. This relation between α with R_e has far-reaching implications, as Humphrey and Buote (2010) showed that it implies a DM fraction within R_e that varies systematically with the properties of the galaxy in such a manner as to reproduce, without fine tuning, the observed tilt of the Fundamental Plane. Consequently, Humphrey and Buote (2010) speculated that establishing a nearly power-law total mass distribution is a fundamental feature of galaxy formation and the primary factor which determines the tilt of the fundamental plane.

8.5 Baryon Fraction

A major outstanding question in galaxy formation is the location of the "missing baryons" in Milky Way-size halos ($\sim 10^{12}\, M_\odot$) (see Kaufmann et al. 2009, and references therein). In a Hubble time most of the baryons should have cooled, but only about 20% of the baryons in Milky Way-size halos exist as cold gas and stars. It is presently unknown whether the remaining 80% of the baryons exist as low-density hot halos still attached to the galaxies (Maller and Bullock 2004, Fukugita and Peebles 2006) or if the gas has been totally expelled (Dekel and Silk 1986, Oppenheimer and Davé 2006). Direct detection of the extended, low-density hot halos of spiral galaxies from their X-ray emission is very challenging and has not yet been achieved (Rasmussen et al. 2009). Although spiral galaxies are more common, elliptical galaxies would seem better suited for this purpose since they are known to have an extended, luminous hot ISM. Unfortunately, only for massive group-scale systems ($\gtrsim 10^{13}\, M_\odot$) have accurate baryon fractions been computed out to a large fraction of the virial radius (Zhang et al. 2007, Gastaldello et al. 2007, Sun et al. 2009).

But the recent study of NGC 720 (Humphrey et al. 2010) mentioned above, through a combined analysis of deep *Chandra* and *Suzaku* data, mapped the hot ISM out to a large fraction of the virial radius (R_{2500}), obtaining strong constraints on the mass and baryon fraction both within R_{2500} and when evaluated at the virial radius using self-consistent, entropy-based hydrostatic models (Fig. 8.10). The baryon fraction ($f_{b,2500} = 0.10 \pm 0.01$, $f_{b,\rm vir} = 0.16 \pm 0.04$) within $\rm r_{vir}$ is fully consistent with the cosmic value. This measurement provides the first example of a baryonically closed Milky Way–size halo which, if found to be typical, indicates that feedback does not expel a large fraction of baryons from a galaxy (Kaufmann

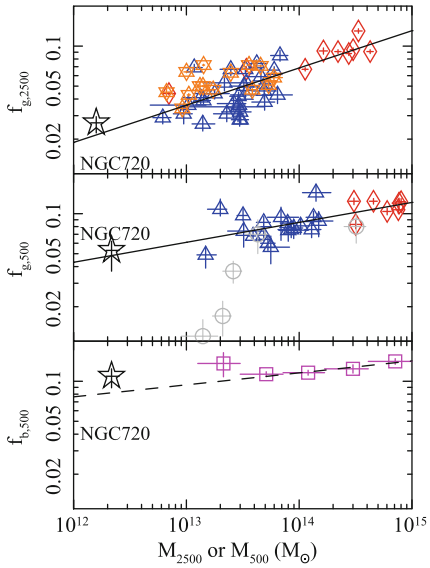

Fig. 8.10 Adapted from Humphrey et al. (2010). *Top Panel*: Gas fraction within r_{2500} shown as a function of M_{2500} for the isolated galaxy NGC 720 (five-pointed star) and a literature sample of groups and clusters (Vikhlinin et al. 2006, *diamonds*, Gastaldello et al. 2007, *six-pointed stars*, Sun et al. 2009, *triangles*). The best power-law fit to the data is shown as a *solid line*. The gas fraction within r_{2500} of NGC 720 is consistent with an extrapolation of the trend for galaxy groups and clusters. *Center Panel*: The same, but within an over-density of 500. Additional data from Dai et al. (2010) from a stacking analysis of *ROSAT* data are overlaid denoted by *circles*. *Bottom Panel*: Baryon fraction within r_{500} as a function of M_{500} for NGC 720 and the mean data from the group and cluster sample of Giodini et al. (2009). The best-fitting power-law relation from Giodini et al. (2009) is overlaid (*dashed line*). NGC 720 is consistent with an extrapolation to low masses, see the electronic version for a color version of this figure

et al. 2009) and has implications for the amount and location of the WHIM (Davé et al. 2010).

8.6 Non-Spherical Constraints

The DM halos formed in cosmological simulations are significantly non-spherical, where the typical flattening within $\approx 0.3 r_{\rm vir}$ can be expressed by an axis ratio $q \sim 0.6$ for halos with $10^{12}\,{\rm M}_\odot \lesssim {\rm M}_{\rm vir} \lesssim 10^{13}\,{\rm M}_\odot$ (Allgood et al. 2006, Macciò et al. 2008). Measurements of global DM flattening from weak lensing yield average constraints consistent with theory with large statistical uncertainties (Mandelbaum et al. 2006, Parker et al. 2007). Joint consideration of strong lensing and central stellar velocity dispersions find an average $q \approx 0.8$ with intrinsic scatter 0.1 (Koopmans et al. 2006), somewhat rounder than the theoretical prediction. This discrepancy may point to the importance of gas dynamics in elliptical galaxy formation (Dubinski

1994, Valluri et al. 2010), which may be especially important for these measurements confined within the stellar half-light radius.

X-ray observations of hydrostatic gas have the capability to provide detailed and fairly robust constraints on DM halo shapes, as pointed out originally in the context of galaxy clusters (Binney and Strimpel 1978). If the hot ISM of an elliptical galaxy obeys (8.8), then, by taking curls of that equation, it follows that $P_{\rm gas}$, $\rho_{\rm gas}$, and Φ have parallel normal vectors; i.e., surfaces of constant Φ are also surfaces of constant $P_{\rm gas}$ and $\rho_{\rm gas}$. These relationships imply that for a single-phase ISM with a unique value of density and temperature at any position ($P_{\rm gas} = P_{\rm gas}(\rho_{\rm gas}, T)$) that surfaces of constant Φ are also surfaces of constant T. Since the X-ray emissivity, $\epsilon \propto \rho_{\rm gas}^2 \Lambda(T, Z)$, is a function only of $\rho_{\rm gas}$, T, and the metal abundances, Z, and the spatial profile of the abundances should closely trace $\rho_{\rm gas}$, it follows that surfaces of constant emissivity are also surfaces of constant Φ. This "X-ray Shape Theorem" (Buote and Canizares 1994, 1996, 1998) means that flattening of the X-ray emission directly reflects flattening in the gravitational potential, independent of any radial temperature and abundance gradients. The observed flattening of the X-ray emission projected onto the sky largely maintains this insensitivity to temperature gradients allowing the intrinsic flattening of the underlying mass distribution to be accurately constrained directly from the X-ray image (Buote and Tsai 1995).

Only for a few galaxies have X-ray measurements of DM shapes been attempted, primarily because of the considerable increase in complexity and computational expense over spherical hydrostatic models. But the number of appropriate targets is also limited by the need to lessen potential effects from ram pressure or tidal distortions on the hot ISM, so that it is desirable to restrict study to relatively isolated elliptical galaxies with bright, extended hot ISM. Analysis of the flattening of the *ROSAT* images of two elliptical galaxies (NGC 720, NGC 3923) and one S0 (NGC 1332) found $q \approx 0.4 - 0.6$ for the total mass distribution, which is also consistent with q of the stellar light (Buote and Canizares 1994, 1996, 1998). Although the limited spatial resolution and soft band pass of *ROSAT* did not allow discrete sources to be identified and excluded from the X-ray images, the effect of unresolved discrete sources on the inferred axial ratios was explored using the hard fluxes measured by *ASCA*. Assuming the hard fluxes measured in the large *ASCA* apertures were spatially distributed as the optical light, adding such a component to the modeling of the *ROSAT* imaging data meant that the axial ratio for the DM in the S0 galaxy NGC 1332 could no longer be constrained. But the effect on the other two elliptical galaxies was estimated to be modest, in particular leading to a systematic $\approx 10\%$ increase in q for NGC 720 (Buote and Canizares 1997).

High-resolution *Chandra* data for NGC 720 (Buote et al. 2002) reveals over 60 discrete sources embedded in the diffuse X-ray emission. After accounting for these sources, a DM axial ratio was obtained, 0.67 ± 0.03 (1σ), consistent with the previous analysis of the *ROSAT* and *ASCA* data where the effect of unresolved sources could only be estimated, and also consistent with the cosmological prediction quoted above. The flattened DM is inconsistent with the nearly spherical halos predicted if the DM is composed of particles that are self-interacting (Spergel and Steinhardt

2000, Feng et al. 2009, 2010). Finally, we mention that the evidence for DM in NGC 720 from X-ray isophote shapes cannot be easily obviated by alternative gravity theories like MOND (Buote and Canizares 1994), though invoking an unseen massive neutrino component may be able to reconcile a MOND explanation without DM as in the spherical analysis of NGC 4125 (Angus et al. 2008).

These results assume rotation of the ISM can be neglected, although one of the expected characteristics of large-scale gas inflows is rotational spin-up. While the exact rotational velocity distribution should be sensitive to the details of where the gas originates and to angular momentum transport due to turbulent viscosity (Nulsen et al. 1984, Brighenti and Mathews 2000), if the rotational velocity is dynamically important, it should nevertheless flatten the X-ray isophotes significantly (Brighenti and Mathews 1996, Fang et al. 2009, Lau et al. 2010). As mentioned previously, the general lack of flattened disks in ellipticals observed in X-rays Hanlan and Bregman (2000) argues against strong rotational support. A possible exception is NGC 1700 where Statler and McNamara (2002) argued the X-ray ellipticity profile suggests the presence of a $\sim$15 kpc, flattened gas disk, rotating at up to $\sim$270 km s^{-1}. Because this conclusion rests to a large extent on a sharp increase in the value of the ellipticity measured at large radius, the possibility of contamination from unresolved point sources requires further attention. Evidence for rotation on smaller scales has been presented for NGC 4649. Using hydrodynamical models that incorporate turbulence, Brighenti et al. (2009) showed that the observed modest flattening of the central ($\lesssim$1 kpc) X-ray isophotes of the galaxy NGC 4649 are characteristic of gas spinning-up as it is accreted. In their models, rotation is the dominant source of non-thermal pressure, and it contributes $\lesssim$30% of the gas support, peaking within $\sim$0.5 kpc.

8.7 SMBHs

Super-massive black holes (SMBHs) are believed to be ubiquitous in galaxy bulges and are increasingly being implicated in helping to shape the structure of their host galaxies. The tight correlations between the black hole mass (M_{BH}) and various properties of the host, such as bulge luminosity and central velocity dispersion (σ_*) provide compelling evidence for this symbiosis (Gebhardt et al. 2000, Ferrarese and Ford 2005). These relations have now become standard observables for testing structure formation scenarios (Hopkins et al. 2006). The physics involved in establishing them is the subject of vigorous ongoing research, and may be tied in to the poorly understood interplay between the cooling gas condensing into stars in the nascent galaxy and feedback from the accreting SMBH (Di Matteo et al. 2005).

Despite the key role that the M_{BH}-σ_* and related relations now play in constraining models of galaxy formation, they are largely determined only from $\sim$40–50 precise, reliable SMBH measurements spanning $\sim$3 orders of magnitude (Gültekin et al. 2009). These measurements were primarily derived from modeling the dynamics of the stars, given the line-of-sight velocity distribution, or the kinematics

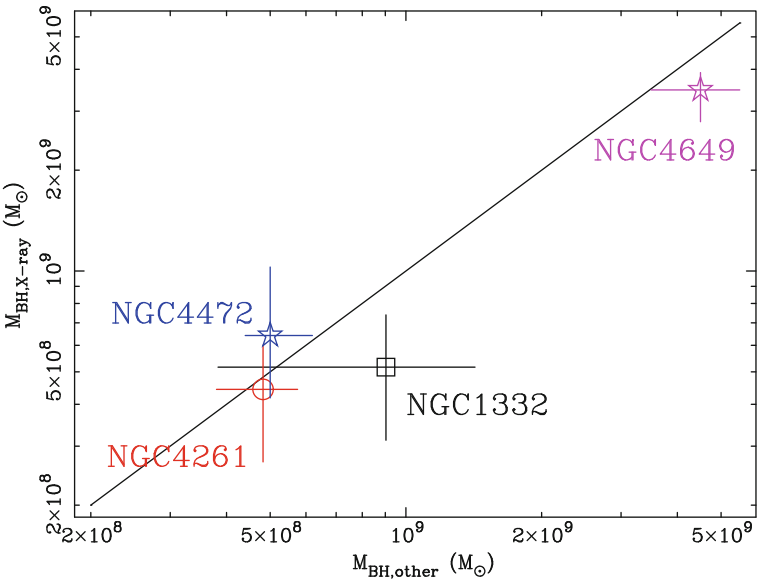

Fig. 8.11 Comparison of the black hole mass measured from the existing *Chandra* data to measurements based on stellar dynamics (*stars*), gas disk dynamics (*circle*) or the M_{BH}-σ_* relation. Adapted from Humphrey et al. (2009), see the electronic version for a color version of this figure

of a central, rotating gas disk (Gebhardt et al. 2003, Ferrarese et al. 1996). Both of these techniques could potentially be subject to significant sources of systematic uncertainty (Valluri et al. 2004, Cappellari et al. 2002), making it essential to assess their accuracy. This is especially true as questions persist over the exact shape of the M_{BH}-σ_* relation that could have implications for how it is established (Ferrarese and Ford 2005, Wyithe 2006, Lauer et al. 2007).

As suggested by Brighenti and Mathews (1999), hydrostatic analysis of the hot ISM can also be used to infer the mass of a SMBH in an elliptical galaxy. Using *Chandra* it is possible to obtain the required gas temperature and density constraints down to ∼100 parsec scales in nearby galaxies without X-ray luminous AGNs, approaching the sphere of influence of the most massive SMBHs. This new technique has been employed by Humphrey et al. (2008, 2009) to measure M_{BH} in four X-ray bright early-type galaxies hosting high-mass SMBHs ($M_{BH} \gtrsim 5 \times 10^8 M_\odot$). In Fig. 8.11 the SMBH masses obtained from the X-ray technique is compared to those found by other methods, and good agreement between the different methods is observed.

This comparison is complementary to similar studies beginning to emerge which compare M_{BH} determined from gas and stellar dynamics (Shapiro et al. 2006, Siopis et al. 2009). The constraints for two of the galaxies in particular, NGC 4649 and NGC 4472, are fairly insensitive to the adopted priors. For the other galaxies, while the lower limit on M_{BH} is more dependent on the priors, the upper limit is tightly

constrained by the X-ray data. While the overall agreement is very encouraging for the accuracy of stellar dynamics techniques incorporating dark matter halos, it also has interesting implications for hydrostatic equilibrium, a point to which we return in the next section.

8.8 Accuracy of the Hydrostatic Equilibrium Approximation

Provided other sources of systematic error are controlled, the accuracy of a mass measurement from X-rays reflects the degree to which non-thermal motions are present in the hot gas. As remarked in Sect. 8.2.1, only limited direct constraints on gas motions are possible with current X-ray detectors, and such measurements that exist suggest subsonic non-thermal motions. An indirect assessment of non-thermal motions can be achieved by comparing the X-ray-determined stellar M/L ratios with those predicted for each galaxy by single-burst stellar population synthesis (SSP) models. For a sample of four galaxies (including NGC 4472 and NGC 4261, both of which have AGN-blown cavities in the ISM), the X-rays and SSP display good overall agreement (Fig. 8.12), implying non-thermal pressure is no larger than ∼20% (Humphrey et al. 2009). Similar agreement was found for NGC 1407 (Zhang et al. 2007). While the SSP models could be in error due to a mixture of differently aged stars in each galaxy or the initial mass function (IMF) differing from that of Kroupa (2001), for non-thermal pressure to be significant, it must exist in a finely balanced conspiracy with the shape of the IMF.

Alternatively, if the three-dimensional gravitational potential can be measured independently, it should be possible to use the measured X-ray properties of the gas to make an (indirect) constraint on non-thermal gas motions. Since elliptical galaxies with X-ray data of sufficient quality for detailed mass analysis are necessarily quite nearby (within $\sim$ 100 Mpc), the only techniques (aside from X-ray tools) currently available to measure the gravitational potential with sufficient accuracy are axisymmetric (or triaxial) stellar dynamical methods. The most sophisticated of these methods employ the full information in the line-of-sight stellar velocity distribution to break the mass-orbit degeneracy (van der Marel and Franx 1993, Gebhardt et al. 2000, van den Bosch et al. 2008, Gebhardt and Thomas 2009), while making minimal assumptions about the orbital structure (Schwarzschild 1979, van der Marel et al. 1998). The fundamentally ill-posed nature of the inversion problem at the heart of these "orbit-based" methods can be mitigated by regularization or a maximum entropy constraint (e.g. van der Marel et al., 1998, Richstone and Tremaine, 1988, Gebhardt et al., 2000).

Only a few studies have attempted to combine the X-ray and optical methods in this way. Assuming spherical symmetry and severely limiting the orbital structure by employing "Jeans modeling", a modest disagreement between the mass inferred from the two techniques has been reported for the galaxy NGC 4472 (Mathews and Brighenti 2003b, Ciotti and Pellegrini 2004). While this may indicate on average ∼20–50% non-thermal pressure support, it could also reflect the limitations of Jeans

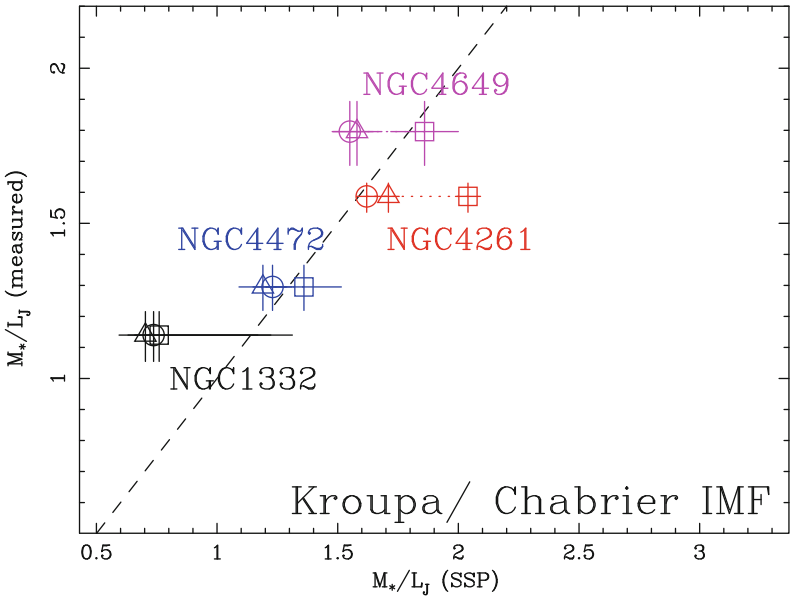

Fig. 8.12 Comparison of the stellar M/L ratios from X-ray mass modeling with those predicted from three sets of SSP models (*squares*: Maraston 2005; *circles*: Fioc and Rocca-Volmerange 1997; *triangles*: Bruzual and Charlot 2003). The *dotted line* is "y = x". The good agreement implies deviations from hydrostatic equilibrium are less than ∼10–20%. Adapted from Humphrey et al. (2009), see the electronic version for a color version of this figure

modeling to recover the orbital structure accurately (e.g., Binney et al., 1990). In contrast, using a similar approach (Romanowsky et al. 2009) argued the X-ray method overestimates the mass distribution in the elliptical galaxy NGC 1407 by ∼70%, which is difficult to understand unless the gas is globally out-flowing. The exact magnitude of this discrepancy, however, is very uncertain due to large systematic errors associated with assumptions in both the X-ray and the optical analysis. (A similar conclusion obtained for the galaxy NGC 3379 (Pellegrini and Ciotti 2006) is also very uncertain since unresolved point sources dominate the X-ray emission in that particular galaxy (Revnivtsev et al. 2008, Trinchieri et al. 2008).) Large systematic uncertainties have also characterized similar studies of 6 galaxies undertaken by Churazov et al. (2008, 2010), who concluded that, on average, the X-ray data are consistent with modest, but highly uncertain, non-thermal support (see Fig. 8.13). They conclude that, although they find ∼30% non-thermal pressure in the systems they studied, "*the uncertainties in [their] model assumptions (e.g., spherical symmetry) are sufficiently large that the contribution [of non-thermal pressure] could be consistent with zero.*" (Churazov et al. 2008). By an extension of this argument, it could also be significantly larger.

A major roadblock to the use of more rigorous axisymmetric (or triaxial) "orbit based" methods for modeling the optical data in such work has been the prohibitive

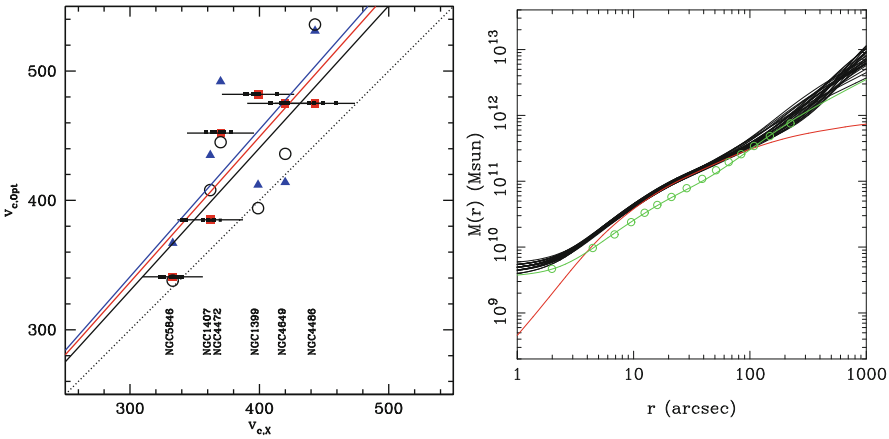

Fig. 8.13 (*Left Panel*) Comparison of circular velocities for six nearby galaxies inferred from hydrostatic X-ray models (horizontal axis) and from a suite of simple stellar dynamical estimates (vertical axis). The observation that the galaxies tend to lie above the *dotted line* representing equal X-ray and optical values implies that the X-ray method tends to underestimate the mass by around 30%, implying significant non-thermal gas motions (Churazov et al. 2010). (*Right Panel*) Stellar dynamics/X-ray comparison for NGC 4649 from Shen and Gebhardt (2010). The *black lines* represent the total mass profile (and 1σ range) from the stellar dynamics. The *green line* is a representation of the mass profile inferred from X-rays (Humphrey et al. 2008), and the *red line* is the stellar mass, see the electronic version for a color version of this figure

computational cost of self-consistently incorporating a DM halo in such a scheme. Recently, however, such models have begun to be developed (e.g., Thomas et al., 2007). In particular, Shen and Gebhardt (2010) found a discrepancy between the mass profile of NGC 4649 from orbit-based models and the (spherical) X-ray mass distribution, implying on average ∼40% non-thermal support. This is significantly larger than was required by the hydrodynamical models of Brighenti et al. (2009) to reconcile the stellar and X-ray ellipticity profiles (although this comparison is not strictly self-consistent as the hydrodynamical models assumed a gravitational potential consistent with the X-ray results). Similarly, Gebhardt and Thomas (2009) found discrepancies for the galaxy M 87, while the X-ray mass profiles were found by Das et al. (2010) to underestimate by ∼20–45% the gravitating mass determined from orbit-based stellar models in the centers of three galaxies, with the sign of the discrepancy reversing at large ($\gtrsim$10 kpc) radii. While inclination effects could conceivably contribute a significant uncertainty into the stellar dynamical analysis of the round galaxies considered in these studies, a similar mismatch between the X-ray and (orbit-based) optical mass estimates (corresponding to ∼50% non-thermal support) has been reported in the central ∼3 kpc region for the edge-on S0 galaxy NGC 1332 (Rusli et al. 2010).

Hence, the current status of comparisons between stellar dynamics and X-rays is that X-rays tend, on average, to underestimate the mass obtained by stellar dynamics by ∼30%, but with considerable uncertainty on many of the measurements, and

the comparison can be complicated by a radial dependence in the discrepancy. To better understand the systematic errors in these comparisons, it is essential in the future that self-consistent comparisons be made; i.e., simultaneous modeling of the X-ray and stellar dynamical data. The X-ray data analysis is subject to numerous potential systematic effects which need to be controlled; e.g., background characterization, measurements of the metal abundances, treatment of unresolved discrete sources, and even uncertainties associated with the mass modeling technique that is adopted (e.g., Humphrey et al., 2009, Das et al., 2010). While many of these systematic errors are modest in absolute terms, they can be comparable to, or at times exceed, the statistical errors. With the detailed comparison between X-ray and optical mass profiles now demanding the interpretation of differences as small as $\sim$20%, precise control of these errors is essential. Until this becomes routine, the accurate radial profiles of possible non-thermal gas motions inferred by comparing mass profiles determined from X-rays and stellar dynamics will remain out of reach.

8.9 Conclusions

With the advent of accurate radial temperature profiles from *Chandra*, *XMM*, and *Suzaku*, the need for DM is now firmly established in many giant elliptical galaxies ($10^{12}\,M_\odot \lesssim M_{vir} \lesssim 10^{13}\,M_\odot$). Current data do not distinguish between NFW and isothermal DM profiles. For the cosmologically motivated NFW model the inferred concentration parameters of elliptical galaxies generally exceed the mean theoretical relation. This discrepancy may be due in large part to the preferential selection of the most relaxed galaxies for X-ray studies. X-ray observations confirm that the total mass profile (baryons+DM) is close to isothermal ($M \sim r$), and new evidence suggests a more general power-law relation for the slope of the total mass profile that varies with the stellar half-light radius. While the global baryon fraction remains difficult to constrain, a recent joint *Chandra-Suzaku* analysis of NGC 720 indicates a global baryon fraction consistent with the cosmological value, suggesting a Milky Way–size galaxy can retain all of its baryons. The axial ratio of the DM inferred from the X-ray isophote shapes of NGC 720 is very consistent with those of halos produced in cosmological simulations. Finally, the unprecedented high spatial resolution of *Chandra* has enabled the first measurements of the mass of SMBHs in a few elliptical galaxies, obtaining a precision comparable to that achieved by traditional optical methods in NGC 4649.

The most important uncertainty in X-ray determinations of DM in elliptical galaxies is no longer the measurement of the temperature profile but now the accuracy of the hydrostatic equilibrium approximation; i.e., the magnitude of non-thermal motions in the hot ISM. The limited direct constraints possible with current data suggest subsonic non-thermal motions, and improved measurements of turbulent motions via Doppler line broadening in the brightest systems is expected from *Astro-H* in a few years. In the meantime, it is essential to perform

self-consistent studies of X-ray and stellar dynamical data of elliptical galaxies to assess the magnitude of non-thermal gas motions and achieve more reliable DM measurements than possible with either technique individually.

Acknowledgements We thank W. Mathews, F. Brighenti, S. Ettori, and K. Gebhardt for discussions related to this work. We are grateful to W. Mathews and F. Gastaldello for providing comments on the manuscript. We also would like to express our appreciation to E. O'Sullivan for providing data included in Fig. 8.4. This work was supported in part by the National Aeronautics and Space Administration under Grant No. NNX10AD07G issued through the Astrophysics Data Analysis Program (ADP).

References

M.G. Abadi, J.F. Navarro, M. Fardal, A. Babul, M. Steinmetz, MNRAS 847 (2010). DOI 10.1111/j.1365-2966.2010.16912.x
K. Ahn, P.R. Shapiro, MNRAS **363**, 1092 (2005). DOI 10.1111/j.1365-2966.2005.09492.x
S.W. Allen, S. Ettori, A.C. Fabian, MNRAS **324**, 877 (2001). DOI 10.1046/j.1365-8711.2001.04318.x
B. Allgood, R.A. Flores, J.R. Primack, A.V. Kravtsov, R.H. Wechsler, A. Faltenbacher, J.S. Bullock, MNRAS **367**, 1781 (2006). DOI 10.1111/j.1365-2966.2006.10094.x
C. Amsler et al., Phys. Lett. **B667**, 1 (2008). DOI 10.1016/j.physletb.2008.07.018
G.W. Angus, B. Famaey, D.A. Buote, MNRAS **387**, 1470 (2008). DOI 10.1111/j.1365-2966.2008.13353.x
J.S. Arabadjis, M.W. Bautz, G.P. Garmire, ApJ **572**, 66 (2002). DOI 10.1086/340296
M.W. Auger, T. Treu, A.S. Bolton, R. Gavazzi, L.V.E. Koopmans, P.J. Marshall, L.A. Moustakas, S. Burles, ApJ **724**, 511 (2010). DOI 10.1088/0004-637X/724/1/511
S.A. Balbus, ApJ **562**, 909 (2001). DOI 10.1086/323875
F. La Barbera, G. Busarello, P. Merluzzi, I.G. de la Rosa, G. Coppola, C.P. Haines, ApJ **689**, 913 (2008). DOI 10.1086/592769
J.J. Binney, R.L. Davies, G.D. Illingworth, ApJ **361**, 78 (1990). DOI 10.1086/169169
J. Binney, O. Strimpel, MNRAS **185**, 473 (1978)
Y. Birnboim, A. Dekel, MNRAS **345**, 349 (2003). DOI 10.1046/j.1365-8711.2003.06955.x
Y. Birnboim, A. Dekel, E. Neistein, MNRAS **380**, 339 (2007). DOI 10.1111/j.1365-2966.2007.12074.x
W.J.G. de Blok, Adv. Astron. **2010** (2010). DOI 10.1155/2010/789293
G.R. Blumenthal, S.M. Faber, J.R. Primack, M.J. Rees, Nature **311**, 517 (1984)
R.C.E. van den Bosch, G. van de Ven, E.K. Verolme, M. Cappellari, P.T. de Zeeuw, MNRAS **385**, 647 (2008). DOI 10.1111/j.1365-2966.2008.12874.x
F. Brighenti, W.G. Mathews, ApJ **539**, 675 (2000). DOI 10.1086/309266
F. Brighenti, W.G. Mathews, P.J. Humphrey, D.A. Buote, ApJ **705**, 1672 (2009). DOI 10.1088/0004-637X/705/2/1672
F. Brighenti, W.G. Mathews, ApJ **470**, 747 (1996). DOI 10.1086/177905
F. Brighenti, W.G. Mathews, ApJ **486**, L83 (1997)
F. Brighenti, W.G. Mathews, ApJ **527**, L89 (1999). DOI 10.1086/312407
G. Bruzual, S. Charlot, MNRAS **344**, 1000 (2003). DOI 10.1046/j.1365-8711.2003.06897.x
G.L. Bryan, M.L. Norman, ApJ **495**, 80 (1998). DOI 10.1086/305262
J.S. Bullock, T.S. Kolatt, Y. Sigad, R.S. Somerville, A.V. Kravtsov, A.A. Klypin, J.R. Primack, A. Dekel, MNRAS **321**, 559 (2001). DOI 10.1046/j.1365-8711.2001.04068.x
D.A. Buote, ApJ **539**, 172 (2000). DOI 10.1086/309224
D.A. Buote, ApJ **574**, L135 (2002). DOI 10.1086/342532

D.A. Buote, F. Brighenti, W.G. Mathews, ApJ **607**, L91 (2004)
D.A. Buote, C.R. Canizares, ApJ **427**, 86 (1994). DOI 10.1086/174123
D.A. Buote, C.R. Canizares, ApJ **457**, 177 (1996). DOI 10.1086/176721
D.A. Buote, C.R. Canizares, ApJ **474**, 650 (1997). DOI 10.1086/303490
D.A. Buote, C.R. Canizares, in *Galactic Halos*, *Astronomical Society of the Pacific Conference Series*, vol. 136, ed. by D. Zaritsky. *Astronomical Society of the Pacific Conference Series*, vol. 136, p. 289 (1998)
D.A. Buote, C.R. Canizares, MNRAS **298**, 811 (1998). DOI 10.1046/j.1365-8711.1998.01663.x
D.A. Buote, F. Gastaldello, P.J. Humphrey, L. Zappacosta, J.S. Bullock, F. Brighenti, W.G. Mathews, ApJ **664**, 123 (2007). DOI 10.1086/518684
D.A. Buote, T.E. Jeltema, C.R. Canizares, G.P. Garmire, ApJ **577**, 183 (2002). DOI 10.1086/342158
D.A. Buote, A.D. Lewis, F. Brighenti, W.G. Mathews, ApJ **594**, 741 (2003a)
D.A. Buote, A.D. Lewis, F. Brighenti, W.G. Mathews, ApJ **595**, 151 (2003b)
D.A. Buote, J.C. Tsai, ApJ **439**, 29 (1995). DOI 10.1086/175148
N. Caon, D. Macchetto, M. Pastoriza, ApJS **127**, 39 (2000). DOI 10.1086/313315
M. Cappellari, E.K. Verolme, R.P. van der Marel, G.A.V. Kleijn, G.D. Illingworth, M. Franx, C.M. Carollo, P.T. de Zeeuw, ApJ **578**, 787 (2002). DOI 10.1086/342653
K.W. Cavagnolo, B.R. McNamara, P.E.J. Nulsen, C.L. Carilli, C. Jones, L. Birzan, ArXiv e-prints (2010)
A. Cavaliere, R. Fusco-Femiano, A&A **49**, 137 (1976)
A. Cavaliere, R. Fusco-Femiano, A&A **70**, 677 (1978)
A. Cavaliere, A. Lapi, R. Fusco-Femiano, ApJ **698**, 580 (2009). DOI 10.1088/0004-637X/698/1/580
E. Churazov, W. Forman, A. Vikhlinin, S. Tremaine, O. Gerhard, C. Jones, MNRAS **388**, 1062 (2008). DOI 10.1111/j.1365-2966.2008.13507.x
E. Churazov, S. Tremaine, W. Forman, O. Gerhard, P. Das, A. Vikhlinin, C. Jones, H. Böhringer, K. Gebhardt, MNRAS **404**, 1165 (2010). DOI 10.1111/j.1365-2966.2010.16377.x
L. Ciotti, S. Pellegrini, MNRAS **350**, 609 (2004). DOI 10.1111/j.1365-2966.2004.07670.x
L.L. Cowie, C.F. McKee, ApJ **211**, 135 (1977). DOI 10.1086/154911
R.A. Crain, I.G. McCarthy, C.S. Frenk, T. Theuns, J. Schaye, MNRAS 967 (2010). DOI 10.1111/j.1365-2966.2010.16985.x
R.A. Crain, I.G. McCarthy, J. Schaye, C.S. Frenk, T. Theuns, ArXiv e-prints (2010)
X. Dai, J.N. Bregman, C.S. Kochanek, E. Rasia, ApJ **719**, 119 (2010). DOI 10.1088/0004-637X/719/1/119
A. Dariush, H.G. Khosroshahi, T.J. Ponman, F. Pearce, S. Raychaudhury, W. Hartley, MNRAS **382**, 433 (2007). DOI 10.1111/j.1365-2966.2007.12385.x
P. Das, O. Gerhard, E. Churazov, I. Zhuravleva, MNRAS 409, 1362 (2010). DOI 10.1111/j.1365-2966.2010.17417.x
R. Davé, B.D. Oppenheimer, N. Katz, J.A. Kollmeier, D.H. Weinberg, MNRAS 1291–+ (2010). DOI 10.1111/j.1365-2966.2010.17279.x
L.P. David, C. Jones, W. Forman, S. Daines, ApJ **428**, 544 (1994). DOI 10.1086/174264
L.P. David, C. Jones, W. Forman, P. Nulsen, J. Vrtilek, E. O'Sullivan, S. Giacintucci, S. Raychaudhury, ApJ **705**, 624 (2009). DOI 10.1088/0004-637X/705/1/624
L.P. David, P.E.J. Nulsen, B.R. McNamara, W. Forman, C. Jones, T. Ponman, B. Robertson, M. Wise, ApJ **557**, 546 (2001). DOI 10.1086/322250
A. Dekel, Y. Birnboim, MNRAS **383**, 119 (2008). DOI 10.1111/j.1365-2966.2007.12569.x
A. Dekel, J. Silk, ApJ **303**, 39 (1986). DOI 10.1086/164050
A. Del Popolo, ApJ **698**, 2093 (2009). DOI 10.1088/0004-637X/698/2/2093
S. Diehl, T.S. Statler, ApJ **668**, 150 (2007). DOI 10.1086/521009
E. D'Onghia, J. Sommer-Larsen, A.D. Romeo, A. Burkert, K. Pedersen, L. Portinari, J. Rasmussen, ApJ **630**, L109 (2005). DOI 10.1086/491651
M.A. Dopita, R.S. Sutherland, *Astrophysics of the Diffuse Universe* (Springer, Berlin, 2003)
J. Dubinski, ApJ **431**, 617 (1994). DOI 10.1086/174512

A.R. Duffy, J. Schaye, S.T. Kay, C. Dalla Vecchia, R.A. Battye, C.M. Booth, MNRAS **405**, 2161 (2010). DOI 10.1111/j.1365-2966.2010.16613.x
J. Einasto, ArXiv e-prints (2009)
R.S. Ellis, Phil. Trans. R. Soc. A **368**, 967 (2010). DOI 10.1098/rsta.2009.0209
J. Ellis, K.A. Olive, Supersymmetric dark matter candidates (Cambridge University Press, 2010), p. 142
A.A. El-Zant, Y. Hoffman, J. Primack, F. Combes, I. Shlosman, ApJ **607**, L75 (2004). DOI 10.1086/421938
A.E. Evrard, C.A. Metzler, J.F. Navarro, ApJ **469**, 494 (1996). DOI 10.1086/177798
G. Fabbiano, ARA&A **27**, 87 (1989). DOI 10.1146/annurev.aa.27.090189.000511
A.C. Fabian, in *NATO ASIC Proc. 300: Physical Processes in Hot Cosmic Plasmas* (1990), pp. 271–297, ed. by W. Brinkmann, A. C. Fabian, F. Giovannelli
A.C. Fabian, E.M. Hu, L.L. Cowie, J. Grindlay, ApJ **248**, 47 (1981). DOI 10.1086/159128
A.C. Fabian, P.A. Thomas, R.E. White, III, S.M. Fall, MNRAS **221**, 1049 (1986)
D. Fabricant, M. Lecar, P. Gorenstein, ApJ **241**, 552 (1980). DOI 10.1086/158369
T. Fang, P. Humphrey, D. Buote, ApJ **691**, 1648 (2009). DOI 10.1088/0004-637X/691/2/1648
J.L. Feng, ArXiv High Energy Physics – Phenomenology e-prints (2005)
J.L. Feng, M. Kaplinghat, H. Tu, H. Yu, JCAP **7**, 4 (2009). DOI 10.1088/1475-7516/2009/07/004
J.L. Feng, M. Kaplinghat, H. Yu, Phys. Rev. Lett. **104**(15), 151301 (2010). DOI 10.1103/PhysRevLett.104.151301
L. Ferrarese, H.C. Ford, W. Jaffe, ApJ **470**, 444 (1996). DOI 10.1086/177876
L. Ferrarese, H. Ford, Space Sci. Rev. **116**, 523 (2005). DOI 10.1007/s11214-005-3947-6
L. Ferrarese, D. Merritt, ApJ **539**, L9 (2000). DOI 10.1086/312838
M. Fioc, B. Rocca-Volmerange, A&A **326**, 950 (1997)
C. Firmani, E. D'Onghia, G. Chincarini, X. Hernández, V. Avila-Reese, MNRAS **321**, 713 (2001). DOI 10.1046/j.1365-8711.2001.04030.x
R.A. Flores, J.R. Primack, ApJ **427**, L1 (1994). DOI 10.1086/187350
W. Forman, C. Jones, E. Churazov, M. Markevitch, P. Nulsen, A. Vikhlinin, M. Begelman, H. Böhringer, J. Eilek, S. Heinz, R. Kraft, F. Owen, M. Pahre, ApJ **665**, 1057 (2007). DOI 10.1086/519480
Y. Fukazawa, J.G. Botoya-Nonesa, J. Pu, A. Ohto, N. Kawano, ApJ **636**, 698 (2006). DOI 10.1086/498081
M. Fukugita, P.J.E. Peebles, ApJ **639**, 590 (2006). DOI 10.1086/499556
R. Fusco-Femiano, A. Cavaliere, A. Lapi, ApJ **705**, 1019 (2009). DOI 10.1088/0004-637X/705/1/1019
F. Gastaldello, D.A. Buote, P.J. Humphrey, L. Zappacosta, J.S. Bullock, F. Brighenti, W.G. Mathews, ApJ **669**, 158 (2007). DOI 10.1086/521519
F. Gastaldello, D.A. Buote, P. Temi, F. Brighenti, W.G. Mathews, S. Ettori, ApJ **693**, 43 (2009). DOI 10.1088/0004-637X/693/1/43
K. Gebhardt, R. Bender, G. Bower, A. Dressler, S.M. Faber, A.V. Filippenko, R. Green, C. Grillmair, L.C. Ho, J. Kormendy, T.R. Lauer, J. Magorrian, J. Pinkney, D. Richstone, S. Tremaine, ApJ **539**, L13 (2000). DOI 10.1086/312840
K. Gebhardt, D. Richstone, J. Kormendy, T.R. Lauer, E.A. Ajhar, R. Bender, A. Dressler, S.M. Faber, C. Grillmair, J. Magorrian, S. Tremaine, AJ **119**, 1157 (2000). DOI 10.1086/301240
K. Gebhardt, D. Richstone, S. Tremaine, T.R. Lauer, R. Bender, G. Bower, A. Dressler, S.M. Faber, A.V. Filippenko, R. Green, C. Grillmair, L.C. Ho, J. Kormendy, J. Magorrian, J. Pinkney, ApJ **583**, 92 (2003). DOI 10.1086/345081
K. Gebhardt, J. Thomas, ApJ **700**, 1690 (2009). DOI 10.1088/0004-637X/700/2/1690
O. Gerhard, in *Planetary Nebulae Beyond the Milky Way*, ed. by L. Stanghellini, J. R. Walsh, N. G. Douglas (Springer, Berlin, 2006), p. 299. DOI 10.1007/3-540-34270-2-47
O. Gerhard, ArXiv e-prints (2010)

G. Gilmore, D. Zucker, M. Wilkinson, R.F.G. Wyse, V. Belokurov, J. Kleyna, A. Koch, N.W. Evans, E.K. Grebel, in *Astronomical Society of the Pacific Conference Series*, *Astronomical Society of the Pacific Conference Series*, vol. 399, ed. by T. Kodama, T. Yamada, K. Aoki. *Astronomical Society of the Pacific Conference Series*, vol. 399, p. 453 (2008)

S. Giodini, D. Pierini, A. Finoguenov, G.W. Pratt, H. Boehringer, A. Leauthaud, L. Guzzo, H. Aussel, M. Bolzonella, P. Capak, M. Elvis, G. Hasinger, O. Ilbert, J.S. Kartaltepe, A.M. Koekemoer, S.J. Lilly, R. Massey, H.J. McCracken, J. Rhodes, M. Salvato, D.B. Sanders, N.Z. Scoville, S. Sasaki, V. Smolcic, Y. Taniguchi, D. Thompson, the COSMOS Collaboration, ApJ **703**, 982 (2009). DOI 10.1088/0004-637X/703/1/982

O.Y. Gnedin, A.V. Kravtsov, A.A. Klypin, D. Nagai, ApJ **616**, 16 (2004)

O.Y. Gnedin, D.H. Weinberg, J. Pizagno, F. Prada, H. Rix, ApJ **671**, 1115 (2007). DOI 10.1086/523256

F. Govoni, L. Feretti, Int. J. Modern Phys. D **13**, 1549 (2004). DOI 10.1142/S0218271804005080

K. Gültekin, D.O. Richstone, K. Gebhardt, T.R. Lauer, S. Tremaine, M.C. Aller, R. Bender, A. Dressler, S.M. Faber, A.V. Filippenko, R. Green, L.C. Ho, J. Kormendy, J. Magorrian, J. Pinkney, C. Siopis, ApJ **698**, 198 (2009). DOI 10.1088/0004-637X/698/1/198

P.C. Hanlan, J.N. Bregman, ApJ **530**, 213 (2000). DOI 10.1086/308357

S. Hannestad, Int. J. Modern Phys. A **21**, 1938 (2006). DOI 10.1142/S0217751X06032885

C. Heymans, E.F. Bell, H. Rix, M. Barden, A. Borch, J.A.R. Caldwell, D.H. McIntosh, K. Meisenheimer, C.Y. Peng, C. Wolf, S.V.W. Beckwith, B. Häußler, K. Jahnke, S. Jogee, S.F. Sánchez, R. Somerville, L. Wisotzki, MNRAS **371**, L60 (2006). DOI 10.1111/j.1745-3933.2006.00208.x

H. Hoekstra, B.C. Hsieh, H.K.C. Yee, H. Lin, M.D. Gladders, ApJ **635**, 73 (2005). DOI 10.1086/496913

P.F. Hopkins, L. Hernquist, T.J. Cox, T. Di Matteo, B. Robertson, V. Springel, ApJS **163**, 1 (2006). DOI 10.1086/499298

P.J. Humphrey, D.A. Buote, ApJ **639**, 136 (2006). DOI 10.1086/499323

P.J. Humphrey, D.A. Buote, ApJ **689**, 983 (2008). DOI 10.1086/592590

P.J. Humphrey, D.A. Buote, MNRAS **403**, 2143 (2010). DOI 10.1111/j.1365-2966.2010.16257.x

P.J. Humphrey, D.A. Buote, F. Brighenti, K. Gebhardt, W.G. Mathews, ApJ **683**, 161 (2008). DOI 10.1086/589709

P.J. Humphrey, D.A. Buote, F. Brighenti, K. Gebhardt, W.G. Mathews, ApJ **703**, 1257 (2009). DOI 10.1088/0004-637X/703/2/1257

P.J. Humphrey, D.A. Buote, C.R. Canizares, A.C. Fabian, J.M. Miller, ApJ **729**, 53 (2011). DOI 10.1088/0004-637X/729/1/53

P.J. Humphrey, D.A. Buote, F. Gastaldello, L. Zappacosta, J.S. Bullock, F. Brighenti, W.G. Mathews, ApJ **646**, 899 (2006). DOI 10.1086/505019

I.G. Irastorza, ArXiv e-prints (2009)

J.A. Irwin, C.L. Sarazin, ApJ **471**, 683 (1996)

C. Jones, W. Forman, A. Vikhlinin, M. Markevitch, L. David, A. Warmflash, S. Murray, P.E.J. Nulsen, ApJ **567**, L115 (2002). DOI 10.1086/340114

L.R. Jones, T.J. Ponman, A. Horton, A. Babul, H. Ebeling, D.J. Burke, MNRAS **343**, 627 (2003). DOI 10.1046/j.1365-8711.2003.06702.x

C. Jones, C. Stern, W. Forman, J. Breen, L. David, W. Tucker, M. Franx, ApJ **482**, 143 (1997). DOI 10.1086/304104

T. Kaufmann, J.S. Bullock, A.H. Maller, T. Fang, J. Wadsley, MNRAS **396**, 191 (2009). DOI 10.1111/j.1365-2966.2009.14744.x

D.D. Kelson, A.I. Zabludoff, K.A. Williams, S.C. Trager, J.S. Mulchaey, M. Bolte, ApJ **576**, 720 (2002). DOI 10.1086/341891

D. Kereš, N. Katz, D.H. Weinberg, R. Davé, MNRAS **363**, 2 (2005). DOI 10.1111/j.1365-2966.2005.09451.x

H.G. Khosroshahi, L.R. Jones, T.J. Ponman, MNRAS **349**, 1240 (2004). DOI 10.1111/j.1365-2966.2004.07575.x

D. Kim, G. Fabbiano, ApJ **613**, 933 (2004). DOI 10.1086/423266

M. Kleinheinrich, P. Schneider, H. Rix, T. Erben, C. Wolf, M. Schirmer, K. Meisenheimer, A. Borch, S. Dye, Z. Kovacs, L. Wisotzki, A&A **455**, 441 (2006). DOI 10.1051/0004-6361:20042606
C.S. Kochanek, M. White, ApJ **543**, 514 (2000). DOI 10.1086/317149
M. Komiyama, K. Sato, R. Nagino, T. Ohashi, K. Matsushita, PASJ **61**, 337 (2009)
L.V.E. Koopmans, T. Treu, A.S. Bolton, S. Burles, L.A. Moustakas, ApJ **649**, 599 (2006). DOI 10.1086/505696
G.A. Kriss, D.F. Cioffi, C.R. Canizares, ApJ **272**, 439 (1983). DOI 10.1086/161311
P. Kroupa, MNRAS **322**, 231 (2001). DOI 10.1046/j.1365-8711.2001.04022.x
R. Kuzio de Naray, G.D. Martinez, J.S. Bullock, M. Kaplinghat, ApJ **710**, L161 (2010). DOI 10.1088/2041-8205/710/2/L161
O. Lahav, A.R. Liddle, ArXiv e-prints (2010)
E.T. Lau, D. Nagai, A.V. Kravtsov, A.R. Zentner, ApJ **734**, 93 (2011). DOI 10.1088/0004-637X/734/2/93
T.R. Lauer, S.M. Faber, D. Richstone, K. Gebhardt, S. Tremaine, M. Postman, A. Dressler, M.C. Aller, A.V. Filippenko, R. Green, L.C. Ho, J. Kormendy, J. Magorrian, J. Pinkney, ApJ **662**, 808 (2007). DOI 10.1086/518223
A.D. Lewis, D.A. Buote, J.T. Stocke, ApJ **586**, 135 (2003)
A.V. Macciò, A.A. Dutton, F.C. van den Bosch, MNRAS **391**, 1940 (2008). DOI 10.1111/j.1365-2966.2008.14029.x
J. Magorrian, MNRAS **302**, 530 (1999). DOI 10.1046/j.1365-8711.1999.02135.x
A.H. Maller, J.S. Bullock, MNRAS **355**, 694 (2004). DOI 10.1111/j.1365-2966.2004.08349.x
G.A. Mamon, E.L. Łokas, MNRAS **362**, 95 (2005). DOI 10.1111/j.1365-2966.2005.09225.x
R. Mandelbaum, U. Seljak, G. Kauffmann, C.M. Hirata, J. Brinkmann, MNRAS **368**, 715 (2006). DOI 10.1111/j.1365-2966.2006.10156.x
C. Maraston, MNRAS **362**, 799 (2005). DOI 10.1111/j.1365-2966.2005.09270.x
R.P. van der Marel, N. Cretton, P.T. de Zeeuw, H. Rix, ApJ **493**, 613 (1998). DOI 10.1086/305147
R.P. van der Marel, M. Franx, ApJ **407**, 525 (1993). DOI 10.1086/172534
W.G. Mathews, ApJ **219**, 413 (1978). DOI 10.1086/155794
W.G. Mathews, F. Brighenti, ARA&A **41**, 191 (2003a)
W.G. Mathews, F. Brighenti, ApJ **599**, 992 (2003b). DOI 10.1086/379537
W.G. Mathews, F. Brighenti, ApJ **488**, 595 (1997). DOI 10.1086/304728
K. Matsushita, Y. Fukazawa, J.P. Hughes, T. Kitaguchi, K. Makishima, K. Nakazawa, T. Ohashi, N. Ota, T. Tamura, M. Tozuka, T.G. Tsuru, Y. Urata, N.Y. Yamasaki, PASJ **59**, 327 (2007)
T. Di Matteo, V. Springel, L. Hernquist, Nature **433**, 604 (2005). DOI 10.1038/nature03335
D. Merritt, B. Tremblay, AJ **108**, 514 (1994). DOI 10.1086/117088
R. Mewe, in *X-Ray Spectroscopy in Astrophysics*, *Lecture Notes in Physics, Berlin Springer Verlag*, vol. 520, ed. by J. van Paradijs, J.A.M. Bleeker. *Lecture Notes in Physics*, vol. 520 (Springer Verlag, Berlin, 1999) p. 109
E.T. Million, N. Werner, A. Simionescu, S.W. Allen, P.E.J. Nulsen, A.C. Fabian, H. Böhringer, J.S. Sanders, MNRAS **407**, 2046 (2010). DOI 10.1111/j.1365-2966.2010.17220.x
M. Milosavljević, C.J. Miller, S.R. Furlanetto, A. Cooray, ApJ **637**, L9 (2006). DOI 10.1086/500547
B. Moore, Nature **370**, 629 (1994). DOI 10.1038/370629a0
D. Nagai, A. Vikhlinin, A.V. Kravtsov, ApJ **655**, 98 (2007). DOI 10.1086/509868
R. Nagino, K. Matsushita, A&A **501**, 157 (2009). DOI 10.1051/0004-6361/200810978
A.B. Newman, T. Treu, R.S. Ellis, D.J. Sand, J. Richard, P.J. Marshall, P. Capak, S. Miyazaki, ApJ **706**, 1078 (2009). DOI 10.1088/0004-637X/706/2/1078
P.E.J. Nulsen, H. Bohringer, MNRAS **274**, 1093 (1995)
P.E.J. Nulsen, S.L. Powell, A. Vikhlinin, ApJ **722**, 55 (2010). DOI 10.1088/0004-637X/722/1/55
P.E.J. Nulsen, G.C. Stewart, A.C. Fabian, MNRAS **208**, 185 (1984)
B.D. Oppenheimer, R. Davé, MNRAS **373**, 1265 (2006). DOI 10.1111/j.1365-2966.2006.10989.x
E. O'Sullivan, T.J. Ponman, MNRAS **354**, 935 (2004). DOI 10.1111/j.1365-2966.2004.08257.x

E. O'Sullivan, A.J.R. Sanderson, T.J. Ponman, MNRAS **380**, 1409 (2007). DOI 10.1111/j.1365-2966.2007.12229.x
E. O'Sullivan, J.M. Vrtilek, D.E. Harris, T.J. Ponman, ApJ **658**, 299 (2007). DOI 10.1086/511778
L.C. Parker, H. Hoekstra, M.J. Hudson, L. van Waerbeke, Y. Mellier, ApJ **669**, 21 (2007). DOI 10.1086/521541
I.J. Parrish, E. Quataert, P. Sharma, ApJ **712**, L194 (2010). DOI 10.1088/2041-8205/712/2/L194
S. Pellegrini, L. Ciotti, MNRAS **370**, 1797 (2006). DOI 10.1111/j.1365-2966.2006.10590.x
R. Piffaretti, R. Valdarnini, A&A **491**, 71 (2008). DOI 10.1051/0004-6361:200809739
T.J. Ponman, D.J. Allan, L.R. Jones, M. Merrifield, I.M. McHardy, H.J. Lehto, G.A. Luppino, Nature **369**, 462 (1994). DOI 10.1038/369462a0
F. Prada, M. Vitvitska, A. Klypin, J.A. Holtzman, D.J. Schlegel, E.K. Grebel, H. Rix, J. Brinkmann, T.A. McKay, I. Csabai, ApJ **598**, 260 (2003). DOI 10.1086/378669
G.W. Pratt, M. Arnaud, R. Piffaretti, H. Böhringer, T.J. Ponman, J.H. Croston, G.M. Voit, S. Borgani, R.G. Bower, A&A **511**, A85 (2010). DOI 10.1051/0004-6361/200913309
J.R. Primack, New J. Phys. **11**(10), 105029 (2009). DOI 10.1088/1367-2630/11/10/105029
E. Quataert, ApJ **673**, 758 (2008). DOI 10.1086/525248
S.W. Randall, M. Markevitch, D. Clowe, A.H. Gonzalez, M. Bradač, ApJ **679**, 1173 (2008). DOI 10.1086/587859
J. Rasmussen, T.J. Ponman, MNRAS **380**, 1554 (2007). DOI 10.1111/j.1365-2966.2007.12191.x
J. Rasmussen, J. Sommer-Larsen, K. Pedersen, S. Toft, A. Benson, R.G. Bower, L.F. Grove, ApJ **697**, 79 (2009). DOI 10.1088/0004-637X/697/1/79
M. Revnivtsev, E. Churazov, S. Sazonov, W. Forman, C. Jones, A&A **490**, 37 (2008). DOI 10.1051/0004-6361:200809889
D.O. Richstone, S. Tremaine, ApJ **327**, 82 (1988). DOI 10.1086/166171
E. Romano-Díaz, I. Shlosman, Y. Hoffman, C. Heller, ApJ **685**, L105 (2008). DOI 10.1086/592687
A.J. Romanowsky, J. Strader, L.R. Spitler, R. Johnson, J.P. Brodie, D.A. Forbes, T. Ponman, AJ **137**, 4956 (2009). DOI 10.1088/0004-6256/137/6/4956
S.P. Rusli, J. Thomas, P. Erwin, R.P. Saglia, N. Nowak, R. Bender, ArXiv e-prints (2010)
M. Ruszkowski, S.P. Oh, ApJ **713**, 1332 (2010). DOI 10.1088/0004-637X/713/2/1332
D.J. Sand, T. Treu, R.S. Ellis, ApJ **574**, L129 (2002). DOI 10.1086/342530
D.J. Sand, T. Treu, R.S. Ellis, G.P. Smith, J. Kneib, ApJ **674**, 711 (2008). DOI 10.1086/524652
D.J. Sand, T. Treu, G.P. Smith, R.S. Ellis, ApJ **604**, 88 (2004). DOI 10.1086/382146
J.S. Sanders, A.C. Fabian, R.K. Smith, MNRAS **410**, 1797 (2011). DOI 10.1111/j.1365-2966.2010.17561.x
C.L. Sarazin, Rev. Modern Phys. **58**, 1 (1986). DOI 10.1103/RevModPhys.58.1
C.L. Sarazin, in *NATO ASIC Proc. 366: Clusters and Superclusters of Galaxies* (1992), p. 131, ed. by A. C. Fabian
C.L. Sarazin, J.N. Bahcall, ApJS **34**, 451 (1977). DOI 10.1086/190457
S. Sato, F. Akimoto, A. Furuzawa, Y. Tawara, M. Watanabe, Y. Kumai, ApJ **537**, L73 (2000). DOI 10.1086/312772
M. Schwarzschild, ApJ **232**, 236 (1979). DOI 10.1086/157282
K.L. Shapiro, M. Cappellari, T. de Zeeuw, R.M. McDermid, K. Gebhardt, R.C.E. van den Bosch, T.S. Statler, MNRAS **370**, 559 (2006). DOI 10.1111/j.1365-2966.2006.10537.x
J. Shen, K. Gebhardt, ApJ **711**, 484 (2010). DOI 10.1088/0004-637X/711/1/484
C. Siopis, K. Gebhardt, T.R. Lauer, J. Kormendy, J. Pinkney, D. Richstone, S.M. Faber, S. Tremaine, M.C. Aller, R. Bender, G. Bower, A. Dressler, A.V. Filippenko, R. Green, L.C. Ho, J. Magorrian, ApJ **693**, 946 (2009). DOI 10.1088/0004-637X/693/1/946**********
D.N. Spergel, P.J. Steinhardt, Phys. Rev. Lett. **84**, 3760 (2000). DOI 10.1103/PhysRevLett.84.3760
L. Spitzer, Jr., ApJ **124**, 20 (1956). DOI 10.1086/146200
L. Spitzer, *Physics of Fully Ionized Gases* (Interscience, New York, 1962)
T.S. Statler, B.R. McNamara, ApJ **581**, 1032 (2002). DOI 10.1086/344362
F.D. Steffen, Eur. Phys. J. C **59**, 557 (2009). DOI 10.1140/epjc/s10052-008-0830-0
M. Sun, W. Forman, A. Vikhlinin, A. Hornstrup, C. Jones, S.S. Murray, ApJ **598**, 250 (2003). DOI 10.1086/378887

M. Sun, G.M. Voit, M. Donahue, C. Jones, W. Forman, A. Vikhlinin, ApJ **693**, 1142 (2009). DOI 10.1088/0004-637X/693/2/1142
J. Thomas, R.P. Saglia, R. Bender, D. Thomas, K. Gebhardt, J. Magorrian, E.M. Corsini, G. Wegner, MNRAS **382**, 657 (2007). DOI 10.1111/j.1365-2966.2007.12434.x
P. Tozzi, C. Norman, ApJ **546**, 63 (2001). DOI 10.1086/318237
T. Treu, ARA&A **48**, 87 (2010). DOI 10.1146/annurev-astro-081309-130924
G. Trinchieri, S. Pellegrini, G. Fabbiano, R. Fu, N.J. Brassington, A. Zezas, D. Kim, J. Gallagher, L. Angelini, R.L. Davies, V. Kalogera, A.R. King, S. Zepf, ApJ **688**, 1000 (2008). DOI 10.1086/592287
J.C. Tsai, N. Katz, E. Bertschinger, ApJ **423**, 553 (1994). DOI 10.1086/173834
J.P. Vallée, New Astron. Rev. **48**, 763 (2004). DOI 10.1016/j.newar.2004.03.017
M. Valluri, V.P. Debattista, T. Quinn, B. Moore, MNRAS **403**, 525 (2010). DOI 10.1111/j.1365-2966.2009.16192.x
M. Valluri, D. Merritt, E. Emsellem, ApJ **602**, 66 (2004). DOI 10.1086/380896
A. Vikhlinin, A. Kravtsov, W. Forman, C. Jones, M. Markevitch, S.S. Murray, L. Van Speybroeck, ApJ **640**, 691 (2006). DOI 10.1086/500288
A. Vikhlinin, B.R. McNamara, A. Hornstrup, H. Quintana, W. Forman, C. Jones, M. Way, ApJ **520**, L1 (1999). DOI 10.1086/312134
L.M. Voigt, A.C. Fabian, MNRAS **368**, 518 (2006). DOI 10.1111/j.1365-2966.2006.10199.x
G.M. Voit, S.T. Kay, G.L. Bryan, MNRAS **364**, 909 (2005). DOI 10.1111/j.1365-2966.2005.09621.x
N. Werner, I. Zhuravleva, E. Churazov, A. Simionescu, S.W. Allen, W. Forman, C. Jones, J.S. Kaastra, MNRAS **398**, 23 (2009). DOI 10.1111/j.1365-2966.2009.14860.x
D.A. White, C. Jones, W. Forman, MNRAS **292**, 419 (1997)
X. Wu, Y. Xue, ApJ **529**, L5 (2000). DOI 10.1086/312451
J.S.B. Wyithe, MNRAS **365**, 1082 (2006). DOI 10.1111/j.1365-2966.2005.09721.x
Z. Zhang, H. Xu, Y. Wang, T. An, Y. Xu, X. Wu, ApJ **656**, 805 (2007). DOI 10.1086/510281

Index

D.-W. Kim and S. Pellegrini (eds.), *Hot Interstellar Matter in Elliptical Galaxies*, Astrophysics and Space Science Library 378, DOI 10.1007/978-1-4614-0580-1,

© Springer Science+Business Media, LLC 2012